

THE UNIVERSITY OF HULL

THE INDUSTRIAL MINERALOGY OF
MAGNESITE AND HUNTITE FROM EASTERN IRAN.

being a Thesis submitted for the Degree of
Doctor of Philosophy
in the University of Hull

by

Khosrow EBRAHIMI NASRABADI,
B.Sc. (Mashhad), M.Sc. (Hull)

May 1990.

ABSTRACT

Vein and hydrothermal - sedimentary types of magnesite from eastern Iran probably originated from ascending hydrothermal solutions. The host rocks are part of an ophiolite unit. The cryptocrystalline magnesites are very pure although they have a variable CaO/SiO₂ ratio. The magnesite is compact with a very fine and uniform texture.

The mineralogy of samples of dead burned magnesites calcined at different temperatures and times are variable and can be predicted from phase equilibria studies. The textural relationships studied using scanning electron microscopy show that matrix is concentrated at periclase crystal boundaries particularly at the triple points. The Periclase crystals are larger at increased calcination temperatures and times. The amount of periclase - periclase grain contact reduces by increasing the amount of impurities. Electron microprobe results confirm that CaO and FeO in periclase increase steadily with the increase in the CaO/SiO₂ ratio and FeO content of the bulk chemistry respectively.

The mineral chemistry of forsterite, monticellite, merwinite, dicalcium silicate and tricalcium silicate in dead burned magnesite indicates some solid solution between some phases, although sometimes it is difficult to analyse single phases. The observations indicate that high quality dead burned magnesia bricks can be produced from Iranian natural magnesite with low CaO and SiO₂ impurities and by maintaining

the CaO/SiO₂ ratio of around 2:1.

The effects of time and temperature on the transformation of the Iranian natural magnesite into caustic calcined magnesia have been used to establish the optimum industrial properties for the chemical and allied industries. High quality magnesia can be produced by calcination at 600°C for 2 hours. A medium quality product can be made rapidly (within 30 min) between 800 - 1000°C, but at lower temperatures (600 - 800°C), the formation of medium quality magnesia is largely independent of time in the range of 2-8 hours.

Many occurrences of huntite are present near to the magnesite deposits. Three different modes of occurrence are recognised: 1) in veins as a weathering products of magnesite, 2) As sporadic nodules near fault zones between ultrabasic rocks and 3) in low temperature and near surface environments as a result of alteration of Mg-rich solutions with pre-existing weathered carbonate fragments in alluvial sediments. The mineralogy, chemistry, microstructure and industrial properties of huntite suggest that it may make an excellent white filler in paint.

*IN THE NAME OF GOD *

"And help one another in goodness
and piety and do not help one
another in sin and aggression"

This work is dedicated to my wife,
Parvin, who rendered valuable
assistance in the task and in
checking the final manuscript, and
whose patience and understanding
during its writing added much to
whatever merit it may have.

ACKNOWLEDGEMENTS

I am immensely grateful to my supervisors Dr. P.W. Scott and Professor A.C. Dunham for their invaluable guidance and constructive comments and especially their encouragement throughout my work.

I would like to thank Dr A.G. Fraser for his helpful advice and supervision of X-ray analysis.

My sincere thanks goes to Mr T. Sinclair for scanning electron microscopy, Mr F.C. Wilkinson for electron microprobe, Mr R.Middleton in chemical analysis and computing, J. Garner's photography, Mrs Munday for transmission electron microscopy and Dr N. Kimyongur for his fruitful discussion. Special thanks are due to Mr Kiyasat and Mr Amini for their help during field work.

I would also like to present my deep appreciation to Mr R. Miles and Mr E. Thompson of the School of Engineering and Computing for their generously given time and expertise in using laser printer when it was most needed, even though people responsible for the job in the University Computer Centre refused to do it. Special thanks to Mrs M. Lawson and all other geology department staff and research students in particular Mr R. kitturkar.

Finally I should like to express my love and gratitude to my wife, children, Davoud and Danial and my mother for their understanding, patience and support at all stages.

TABLE OF CONTENTS

ABSTRACT

ACKNOWLEDGEMENTS

LIST OF TABLES

LIST OF FIGURES

LIST OF PLATES

CHAPTER 1

INTRODUCTION

1.1	Magnesite	1
1.2	Huntite	2
1.3	Reasons for this research	3

CHAPTER 2 GEOLOGY AND TECHNOLOGY OF MAGNESITE AND HUNTITE SECTION 1 (MAGNESITE)

2.1.1	Geological occurrences	5
2.1.1.1	Endogenic (hydrothermal) deposits	6
2.1.1.1.a	Metasomatic type	6
2.1.1.1.b	Vein type	7
2.1.1.2	Transitional hydrothermal-sedimentary deposits	7
2.1.1.3	Exogenic deposits	8
2.1.1.3.1	Sedimentary deposits	8
2.1.1.3.1.a	Saliferous type	8
2.1.1.3.1.b	Detrital type	9
2.1.1.3.2	Deposits resulting from weathering	9
2.1.2	Possible source of magnesium	10
2.1.2.1	Magmatic source	10
2.1.2.2	Chemistry of water	10
2.1.2.3	Ocean water	10
2.1.2.4	River water	11
2.1.3	Prospecting and exploration	11
2.1.4	Mining and processing	11
2.1.5	Production	12
2.1.5.1	Yugoslavia, Greece, Turkey, Iran, Pakistan ultrabasic belt	13
2.1.6	Uses	14
2.1.6.1	Crude magnesite	14

2.1.6.2	Dead burned magnesite	15
2.1.6.3	Caustic calcined magnesite	15
2.1.7	Tests and specification	16
2.1.7.1	Refractory magnesia	16
2.1.7.2	Caustic calcined magnesia	17
2.1.8	Properties of refractory materials	17
2.1.8.1	Physical properties	18
2.1.8.1.a	Porosity	18
2.1.8.1.b	Density	19
2.1.8.1.c	Thermal expansion	19
2.1.8.1.d	Refractoriness	19
2.1.8.1.e	Thermal conductivity, heat capacity and thermal diffusivity	20
2.1.8.1.f	Accuracy of size and shape	20
2.1.8.1.g	High temperature stability	20
2.1.8.2	Mechanical properties	20
2.1.8.2.a	Modulus of rupture	20
2.1.8.2.b	Spalling resistance	21
2.1.9	Chemical properties	21
2.1.10	Economical features	22
2.1.11	Impurities	23
2.1.12	Sea water magnesia	26
2.1.12.1	Introduction	26
2.1.12.2	Sea water magnesia process	27
2.1.12.3	Control of chemical properties	28
2.1.12.3.a	Limestone/dolomite impurities	28
2.1.12.3.b	Sea water impurities	28
2.1.13	Properties of sea water magnesia	29
2.1.13.1	High temperature strength	29
2.1.13.2	Density	31
2.1.13.3	Microstructure	31
2.1.13.4	Hydration resistance	32
2.1.14	History and future of magnesite refractory	32
SECTION 2 (HUNTITE)		
2.2.1	Introduction	35
2.2.2	Physical and optical properties	35
2.2.3	Geological occurrences	36
2.2.4	Industrial application	37

CHAPTER 3	GEOLOGY AND MINERALOGY OF MAGNESITE FROM KHORASAN PROVINCE, EASTERN IRAN.	
3.1	Introduction	38
3.2	A review of geological formation of Khorasan Province	39
3.2.1	The Koppeh Dagh mountain system	39
3.2.2	Binalud range	39
3.2.3	The ophiolite Melange zone	40
3.3	Geography and Geology of the investigated area	43
3.3.1	Physiography	43
3.3.1.1	Location	43
3.3.1.2	Climate	43
3.3.1.3	Vegetation	43
3.4	Main geological units	44
3.4.1	Ophiolite complex	44
3.4.2	Coloured Melange zone	44
3.4.3	Flysch sediments	45
3.5	Magnesite deposits of eastern Iran	54
3.5.1	Regional geology	54
3.5.2	Description of magnesite deposits	58
3.5.2.1	Torshak magnesite deposit	58
3.5.2.2	Afzalabad magnesite deposit	66
3.6	Sampling and sample location	67
3.7	Chemical composition of natural magnesite from Iran	72
3.7.1	Introduction	72
3.7.2	Factors affecting analysis by X-ray fluorescence spectrometry	72
3.7.3	Results	73
3.7.3.1	Major constituents	76
3.7.3.1.a	MgO	76
3.7.3.1.b	LOI	76
3.7.3.2	Minor constituents	77
3.7.3.2.a	CaO	77
3.7.3.2.b	SiO ₂	77
3.7.3.2.c	Fe ₂ O ₃	78
3.7.3.2.d	Al ₂ O ₃	78
3.8	Mineralogy and petrography	80
3.8.1	Experimental	80
3.8.2	Petrographic description	80
3.8.2.1	Magnesite	80
3.8.2.2	Host rock	81
3.8.3	X-ray diffraction	88

3.8.3.1	Sample preparation	88
3.8.3.2	Instrumental	88
3.8.3.3	Results	89
3.9	Microstructure (SEM)	93
3.10	Mineral chemistry	98
3.10.1	General	98
3.10.2	Instrumental	98
3.10.3	Results and discussion	99
CHAPTER 4	MINERALOGY, MICROSTRUCTURE, MINERAL CHEMISTRY AND PHYSICAL PROPERTIES OF DEAD BURNED MAGNESITE	
4.1	Introduction	105
4.2	Experimental procedure and sample descriptions	
4.3	Mineralogy (XRD)	108
4.3.1	Instrumental	108
4.3.2	Sample preparation	108
4.3.3	Results	108
4.3.3.1	Sample A3	113
4.3.3.2	Sample A14	113
4.3.3.3	Sample T2	114
4.3.3.4	Sample T15	114
4.3.3.5	Sample T26	115
4.3.4	Discussion	115
4.4	Microstructure	117
4.4.1	Introduction	117
4.4.2	Optical microscopy	117
4.4.2.1	Sample A3	118
4.4.2.2	Sample A14	118
4.4.2.3	Sample T2	118
4.4.2.4	Sample T15	118
4.4.2.5	Sample T26	119
4.4.3	Scanning electron microscopy	119
4.4.3.1	Experimental	120
4.4.3.2	The SEM micrographs	122
4.4.3.3	Elemental analysis by SEM	122
4.4.3.4	Description of Microstructures	123
4.4.4	Mean grain size	124
4.4.5	Results	125
4.4.5.1	Sample A3	125
4.4.5.1.1	Major phase (periclase)	126
4.4.5.1.2	Interstitial or matrix materials	127
4.4.5.1.3	rare features	127
4.4.5.2	Sample A14	136
4.4.5.2.1	Major phase (periclase)	137
4.4.5.2.2	Interstitial or matrix materials	137
4.4.5.2.2.a	Forsterite - Monticellite	138
4.4.5.2.2.b	Tricalcium silicate - tricalcium aluminate	138
4.4.5.2.2.c	Monticellite - Dicalcium silicate	138

4.4.5.2.2.d	Dicalcium silicate - Tricalcium silicate	138
4.4.5.3	Sample T2	146
4.4.5.3.1	Major phase (periclase)	146
4.4.5.3.2	Interstitial or matrix phases	147
4.4.5.3.3	Rare feature	156
4.4.5.4	Sample T15	156
4.4.5.4.1	Major phase (periclase)	157
4.4.5.4.2	Interstitial or matrix phases	157
4.4.5.4.3	Rare feature	158
4.4.5.5	Sample T26	167
4.4.5.5.1	Major phase (periclase)	167
4.4.5.5.2	Interstitial or matrix materials	168
4.5	Mineralogy as determined by electron microprobe	
4.5.1	Introduction	180
4.5.2	Experimental	180
4.5.3	Analytical difficulties	181
4.5.4	Accuracy, precision and detection limits of electron microprobe analysis	182
4.5.5	Results	183
4.5.5.1	Sample A3	184
4.5.5.1.a	Sample A3 (1600°C, 108 hrs)	184
4.5.5.1.b	Sample A3 (1500°C, 24 hrs)	185
4.5.5.1.c	Sample A3 (1400°C, 6 hrs)	186
4.5.5.2	Sample A14	186
4.5.5.2.a	Sample A14 (1600°C, 108 hrs)	186
4.5.5.2.b	Sample A14 (1500°C, 24 hrs)	186
4.5.5.2.c	Sample A14 (1400°C, 6 hrs)	187
4.5.5.3	Sample T2	189
4.5.5.3.a	Sample T2 (1600°C, 108 hrs)	189
4.5.5.3.b	Sample T2 (1500°C, 24 hrs)	189
4.5.5.3.c	Sample T2 (1400°C, 6 hrs)	190
4.5.5.4	Sample T15	190
4.5.5.4.a	Sample T15 (1600°C, 108 hrs)	190
4.5.5.4.b	Sample T15 (1500°C, 24 hrs)	191
4.5.5.4.c	Sample T15 (1400°C, 6 hrs)	191
4.5.5.5	Sample T26	193
4.5.5.5.a	Sample T26 (1600°C, 108 hrs)	193
4.5.5.5.b	Sample T26 (1500°C, 24 hrs)	193
4.5.5.5.c	Sample T26 (1400°C, 6 hrs)	196
4.5.6	Discussion	196
4.6	Mineral chemistry	198
4.6.1	Periclase	198
4.6.1.1	General	198
4.6.1.2	Results	201
4.6.1.2.a	CaO in periclase	201
4.6.1.2.b	FeO in periclase	203
4.6.1.2.c	Al ₂ O ₃ in periclase	203
4.6.1.2.d	SiO ₂ in periclase	205
4.6.1.3	Discussion and conclusion	205
4.6.2	Monticellite	206
4.6.2.1	General	206
4.6.2.2	Results	208

4.6.3	Forsterite	211
4.6.3.1	General	211
4.6.3.2	Results and discussion	213
4.6.4	Dicalcium silicate	217
4.6.4.1	General	217
4.6.4.2	Polymorphism of dicalcium silicate	217
4.6.4.3	Solid solution of dicalcium silicate	220
4.6.4.4	Results and discussion	222
4.6.5	Tricalcium silicate	225
4.6.5.1	General	225
4.6.5.2	Solid solution	226
4.6.5.3	Results and discussion	227
4.6.6	Merwinite	229
4.6.6.1	General	229
4.6.6.2	Results and discussion	231
4.7	Summary and conclusion	234
4.7.1	Phase assemblages	234
4.7.2	Discussion of the predicted and determined phase assemblages	237
4.7.3	Industrial implications	242
4.7.3.1	Bulk chemistry	243
4.7.3.2	Mineralogy	243
4.7.3.3	Bulk density, porosity and specific gravity	244
4.7.3.4	Porosity and its distribution	245
4.7.3.5	Degree of direct periclase-periclase bonding	245
4.7.3.6	Hydration tendency	246
CHAPTER 5	CALCINATION PROPERTIES OF CRYPTOCRYSTALLINE MAGNESITE FROM IRAN	
5.1	Introduction	247
5.2	Experimental	248
5.3	Sample characteristic and sample preparation for calcination	249
5.4	Decomposition of magnesite	250
5.5	X-ray diffraction	250
5.5.1	Phase transformation of magnesite (MgCO ₃) to periclase (MgO)	252
5.5.2	Mean crystallite size determination by X-ray powder diffractometry	254
5.6	Loss on ignition	256
5.6.1	Method of measurement	259
5.6.2	Results	259
5.7	Surface area	261
5.7.1	Results	262

5.8	Determination of iodine adsorption number	264
5.8.1	Results	265
5.9	Microstructure	267
5.10	Relationship of determined industrial properties	271
5.11	Assessment of industrial properties	274
5.12	Discussion	276
CHAPTER 6	GEOLOGY, MINERALOGY AND TECHNOLOGY OF HUNTITE	
6.1	Introduction	279
6.2	Regional geology	279
6.3	Description of huntite deposits	280
6.3.1	Vein type huntite	280
6.3.2	Nodular type huntite	283
6.3.3	Alluvial type huntite	283
6.3.4	Nesquehonite	286
6.4	Sampling and sample locations	291
6.5	Mineralogy and petrography	294
6.5.1	Physical and optical properties	294
6.5.2	X-ray diffraction	295
6.5.2.1	Instrumental	295
6.5.2.2	Results	296
6.5.2.3	Discussion	299
6.5.3	Differential thermal analysis (DTA)	299
6.5.3.1	Results	300
6.5.3.1.a	Huntite [$\text{CaMg}_3(\text{CO}_3)_4$]	300
6.5.3.1.b	Magnesite (MgCO_3)	300
6.5.3.1.c	Nesquehonite	301
6.5.3.1.d	Hydromagnesite - huntite	301
6.5.4	Transmission electron microscopy	303
6.5.4.1	Results	303
6.6	Bulk chemistry	308
6.6.1	Results	308
6.7	Microstructure	310
6.8	Apparent porosity, bulk density and apparent specific gravity	317
6.8.1	Method of measurement	318
6.8.2	Results and discussion	318
6.9	Acid insoluble residue (AIR)	320
6.9.1	Method of measurement	320

6.9.2	Results and discussion	320
CHAPTER 7	INDUSTRIAL POTENTIAL OF HUNTITE	
7.1	Introduction	322
7.2	Oil absorption	322
7.2.1	Method of measurement	323
7.2.2	Results	323
7.2.3	Discussion	324
7.3	Colour measurement	325
7.3.1	Importance of colour of industrial mineral powders	325
7.3.2	Method of measurement and preparation of specimens	325
7.3.3	Results	326
7.3.4	Discussion	328
7.4	Dead burned huntite	331
7.4.1	Microstructure	331
7.4.2	Description of microstructures	332
7.4.2.1	Dead burned alluvial type huntite	333
7.4.2.2	Dead burned vein type huntite	334
7.4.2.3	Dead burned nodular type huntite	334
7.4.2.4	Dead burned hydromagnesite - huntite	334
7.4.2.5	Dead burned magnesite - dolomite	335
7.4.2.6	Dead burned nesquehonite	335
7.5	Mineralogy and mineral chemistry of dead burned huntite, Hydromagnesite - huntite, magnesite - dolomite and nesquehonite.	345
7.5.1	General	345
7.5.2	Instrumental	345
7.5.3	Results	345
7.5.3.1	Dead burned alluvial type huntite	346
7.5.3.2	Dead burned vein type huntite	347
7.5.3.3	Dead burned nodular type huntite	347
7.5.3.4	Dead burned nesquehonite	348
7.5.3.5	Dead burned magnesite - dolomite	349
7.5.3.6	Dead burned hydromagnesite - huntite	349
7.6	Mineral chemistry	352
7.6.1	Periclase	352
7.6.1.1	Results	352
7.6.1.1.a	CaO in periclase	352
7.6.1.1.b	FeO in periclase	354
7.6.1.1.c	Al ₂ O ₃ in periclase	354
7.6.1.1.d	SiO ₂ in periclase	354
7.6.2	Lime	354
7.6.2.1	Results	355
7.6.2.1	MgO in lime	355

7.6.2.2	SiO ₂ in Lime	355
7.6.2.3	Al ₂ O ₃ and FeO in Lime	355
7.6.3	Monticellite	358
7.6.4	Forsterite	360
7.6.5	Merwinite	360
7.6.6	Dicalcium silicate	360
7.6.7	Tricalcium silicate	364
7.7	Comparison and evaluation	368
7.7.1	Discussion of the predicted and determined phase assemblages	368
CHAPTER 8 SUMMARY AND CONCLUSION		
8.1	Natural magnesite	371
8.2	Dead burned magnesite	372
8.2.1	Comparison and recommendation	376
8.3	Caustic calcined magnesite	380
8.3.1	Recommendation	382
8.4	Huntite	383
8.4.1	Exploitation and processing	385
APPENDICES		
Appendix 1	Hand specimen description of magnesite	387
Appendix 2	Bulk chemistry	390
Appendix 3	X-ray diffraction analysis	396
Appendix 4	Electron microprobe analyses of natural magnesite	402
Appendix 5	Scanning electron microscope	409
Appendix 6	Polished blocks preparation	413
Appendix 7	Electron microprobe analyses of dead burned magnesite	416
APPENDIX 8	Loss on ignition	441
Appendix 9	Surface area measurement	443
Appendix 10	Determination of iodine adsorption number	449
Appendix 11	Measurement of apparent porosity, apparent	

specific gravity and bulk density	452
Appendix 12 Determination of acid insoluble residue (AIR)	459
Appendix 13 Determination of oil absorption value	462
Appendix 14 Colour measurement of mineral powders	465
Appendix 15 Electron microprobe analyses of dead burned huntite	475

LIST OF TABLES

2.1	A genetic classification of magnesite deposits	5
2.2	World production of crude magnesite	14
2.3	Physical and mechanical properties of refractory products	18
2.4	World production of sea water magnesia	27
3.1	Bulk chemical analyses of natural magnesite	75
3.2	Statistical presentation of 13 analyses of natural magnesite from Afzalabad deposit, analysed by XRF	75
3.3	Statistical presentation of 27 analyses of natural magnesite from Torshak deposit	75
3.4	The mineralogy of Afzalabad and Ablah magnesite deposits as determined by XRD	90
3.5	The mineralogy of Torshak magnesite deposit as determined by XRD	91
3.6	Microprobe analyses of magnesite and dolomite	100
3.7	Minimum, maximum, mean and standard deviation of major and minor oxides present in samples from Afzalabad magnesite deposit	101
3.8	Minimum, maximum, mean and standard deviation of major and minor oxides present in samples from Torshak magnesite deposit	101
4.1	Chemical composition of natural magnesite samples used for calcination	106
4.2	Minerals identified in sample A3 (XRD)	109
4.3	Minerals identified in sample A14 (XRD)	109
4.4	Minerals identified in sample T2 (XRD)	110
4.5	Minerals identified in sample T15 (XRD)	110
4.6	Minerals identified in sample T26 (XRD)	110
4.7	The average atomic number of the phases which can be found in dead burned magnesites	123
4.8	Mean grain sizes of periclase in dead burned magnesites calcined at different conditions	124
4.9	Phases present in the calcined magnesite samples as determined by energy dispersive X-ray analysis (sample A3)	125
4.10	Phases present in the calcined magnesite samples as determined by energy dispersive X-ray analysis (Sample A14)	136
4.11	Phases present in the calcined magnesite samples as determined by energy dispersive X-ray analysis (Sample T2)	146
4.12	Phases present in the calcined magnesite samples as determined by energy dispersive X-ray analysis (Sample T15)	156

4.13	Phases present in the calcined magnesite samples as determined by energy dispersive X-ray analysis (Sample T26)	167
4.14	Minerals identified in dead burned magnesites	184
4.15	A selection of periclase analysis	202
4.16	A selection of monticellite analysis	209
4.17	A selection of forsterite analysis	
4.18	A selection of dicalcium silicate analysis	223
4.19	A selection of tricalcium silicate	232
4.20	Predicted and determined phase assemblage (1400°C, 6hrs)	239
4.21	Predicted and determined phases (1500°C, 96 hrs)	240
4.22	Predicted and determined phases (1600°C, 108 hrs)	241
4.23	Melting points of phases present in dead burned magnesites	241
4.24	Porosity (P), density (B) and specific gravity (T) values of natural dead burned magnesite (sample A3) determined at different temperature	244
5.1	The surface area (SA), iodine adsorption number (IN), loss on ignition (LOI) and crystallite size (CS) of the calcined magnesite in the temperature range 500 - 1200°C and time range 1/4 - 8 hours	257
5.2	Comparison of impurities of studied samples with those of commercial products	275
5.3	The industrial properties of Spanish natural calcined magnesite and synthetic caustic magnesia and the material under this investigation	275
5.4	The industrial properties of samples under present investigation	
6.1	The mineralogy of huntite, hydromagnesite - huntite and nesquehonite as determined by XRD	297
6.2	The bulk chemical composition of huntite, hydromagnesite - huntite, magnesite - dolomite and nesquehonite as determined by XRF	309
6.3	Apparent porosity (P), density (B) and apparent specific gravity (T) values of huntite, hydromagnesite - huntite, nesquehonite, magnesite - dolomite and magnesite.	
6.4	Acid insoluble residue of specimens from Iran and Greece	320
7.1	Oil absorption values	324
7.2	Percentage reflectance at given wavelengths	327
7.3	Derivation of chromaticity coordinates	328
7.4	Phases determined in the calcined huntite (SEM)	332
7.5	The mineralogy of huntite, hydromagnesite - huntite, magnesite - dolomite and nesquehonite calcined at 1500°C for 96 hours	346
7.6	A selection of periclase analysis	353
7.7	A selection of lime analysis	356
7.8	Monticellite analysis	359
7.9	Forsterite analysis	361

7.10	Merwinite analysis	362
7.11	Dicalcium silicate analysis	365
7.12	Tricalcium silicate analyses	366
7.13	Predicted and determined phase assemblages of natural dead burned huntite, hydromagnesite - huntite, magnesite - dolomite and nesquehonite	
A2.1	Chemical analysis of larvikite	393
A2.2	XRF instrumental condition	395
A11.1	Data obtained after repetitive tests of magnesite	
A13.1	Mass of pigment for test	

LIST OF FIGURES

<u>Figure</u>	<u>page</u>
3.1 Tectono-sedimentary map of Iran	42
3.2 Tectonic sketch map showing Lut Block and Flysch Zone of East Iran	49
3.3 Geological map of the Nehbandan area	55
3.4 Sketch map showing magnesite locations of eastern Iran (Birjand - Nehbandan area)	60
3.5 Geological sketch map of the Torshak magnesite deposit	61
3.6 Geological sketch map of the Afzalabad magnesite deposit	69
3.7 Plots to show the chemical variation in magnesite from the Afzalabad and Torshak deposits	79
3.8 X-ray diffraction traces of magnesite and dolomite	92
3.9 Triangular plots showing CaO-MgO-SiO ₂ and CaO-MgO-FeO ratios of all microprobe analyses of natural magnesite (wt.%)	104
4.1 A selection of X-ray diffraction traces of dead burned magnesites	111
4.2 A selection of X-ray diffraction traces of dead burned magnesites.	112
4.4 Triangular plots showing CaO-MgO-SiO ₂ ratios of dead burned magnesite (wt.%)	192
4.5 Triangular plots showing CaO-MgO-SiO ₂ ratio of all microprobe analyses of dead burned magnesite (wt.%)	192
4.6 Triangular plots showing CaO-MgO-SiO ₂ ratio of all microprobe analyses of dead burned magnesite (wt.%)	194
4.7 Triangular plots showing MgO-Al ₂ O ₃ -SiO ₂ , and CaO-Al ₂ O ₃ -MgO ratios of all microprobe analyses of dead burned magnesite (wt.%).	195
4.8 Triangular plot (wt.%) and cation relationship of periclase	204
4.9	
4.10 Triangular plot (wt.%) and cation relationships of monticellite	210
4.11 Triangular plot (wt.%) and cation relationships of forsterite	216
4.12 Stability diagram of dicalcium silicate polymorphs	219
4.13 Triangular plot (wt.%) and cation relationships of dicalcium silicate	224
4.14 Triangular plot (wt.%) and cation relationships of merwinite	233
4.15 Phase relationship in the solid state in the system MgO-CaO-SiO ₂ -Fe ₂ O ₃ , where MgO occurs as a phase	235
4.16 Isothermal diagrams	238
5.1 The DTA curve of magnesite	251
5.2 The Time - Temperature - Transformation (TTT) diagram of magnesite	253

5.3	Crystallite size (CS) (\AA) as plotted against	
	A) Time	
	B) Time - Temperature (contour)	258
5.4	Loss on ignition (LOI) (%) as plotted against	
	A) Time	
	B) Time - Temperature (contour)	260
5.5	Surface area (SA) (m^2/g) as plotted against	
	A) Time	
	B) Time - Temperature (contour)	263
5.6	Iodine adsorption number (IN) (mg/g) as plotted against	
	A) Time	
	B) Time - Temperature (contour)	266
5.7	Relationship between the determined parameters	272
5.8	Time - Temperature regions within which high quality, and medium quality caustic calcined magnesia can be made under laboratory conditions	278
6.1	X-ray diffraction traces of huntite, hydromagnesite and nesquehonite	298
6.2	Differential thermal curves of studied specimens	302
7.1	Spectrophotometric curves of studied materials	330
7.2	Triangular plots showing CaO-MgO-SiO ₂ ratios of all microprobe analyses of dead burned huntite, nesquehonite, magnesite - dolomite and hydromagnesite - huntite (wt.%)	350
7.3	Triangular plots showing CaO-Al ₂ O ₃ -SiO ₂ , MgO-Al ₂ O ₃ -SiO ₂ , CaO-MgO-SiO ₂ , CaO-SrO-SiO ₂ and CaO-SrO-MgO ratios of all microprobe analyses of dead burned huntite and magnesite - dolomite (wt.%)	351
7.4	Triangular plots (wt.%) and cation relationship of periclase (a,b,c) and lime (d,e,f,g)	357
7.5	Triangular plots (wt.%) and cation relationship of monticellite (a,b), forsterite (c,d) and merwinite (e)	363
7.6	Triangular plots (wt.%) and cation relationship of dicalcium silicate (a,b) and tricalcium silicate (c,d,e,f)	
7.7	Chemical analyses of huntite as plotted on CaO-MgO-SiO ₂ diagram	369
A2.1	XRF calibration curves	
A5.1	Schematic showing SEM/EDX system	412
A9.1	Areometer II used for measuring surface area	447
A9.2	Areometer II nomogram	448
A11.1	Apparatus for measuring suspended weight	454
A14.1	EEL reflectance spectrophotometer and components of the powder press	

LIST OF PLATES

<u>Plate</u>	<u>Page</u>
1. Ophiolite and coloured melange	51
2. Flysch sediments	53
3. Flysch and continental sediments	57
4. Torshak magnesite deposit	63
5. Closer view of Torshak magnesite deposit	65
6. view of vein type magnesite deposits	71
7. Hand specimen photographs of natural magnesites	83
8. Transmitted light micrographs of cryptocrystalline magnesites	85
9. Transmitted light micrographs of serpentinite	87
10. Scanning electron micrographs of fracture surface of natural magnesite, dolomite and serpentinite	95
11. Scanning electron microscope photographs in backscattered mode of polished thin section of natural magnesite	97
12. Colour photograph of dead burned magnesites	107
13. Scanning electron micrographs of the surface of natural dead burned magnesite (sample A3)	129
14. Scanning electron micrographs of impurity phases on the surface of dead burned magnesite	131
15. Backscattered electron micrographs of dead burned magnesite (sample A3)	133
16. Backscattered electron micrographs of impurity phases in dead burned magnesite (Sample A3)	135
17. Scanning electron micrographs of the surface of magnesite grains (sample A14)	141
18. Backscattered electron micrographs of dead burned magnesite (sample A14)	143
19. Backscattered electron micrographs of dead burned magnesite (sample A14)	145
20. Scanning electron micrographs of the surface of dead burned magnesite (sample T2)	149
21. Scanning electron micrographs of the surface of dead magnesite (sample T2)	151
22. Backscattered electron micrographs of dead burned magnesite (sample T2)	153
23. backscattered electron micrographs of minor phases of dead burned magnesite (sample T2)	155
24. Scanning electron micrographs of the surface of dead burned magnesite (sample T15)	160
25. Scanning electron micrographs of the surface of dead burned magnesite (sample T15)	162
26. Backscattered electron micrographs of dead burned magnesite (sample T15)	164
27. Backscattered electron micrographs of impurity phases associated with periclase grains in dead burned magnesite (sample T15)	166
28. Scanning electron micrographs of the surface of dead	

	burned magnesite (sample T26)	171
29.	Scanning electron micrographs of detailed study of impurities in natural dead burned magnesite (sample T26)	173
30.	Backscattered electron micrographs of dead burned magnesite (sample T26)	175
31.	Backscattered electron micrographs of detailed study of impurities in sample T26	177
32.	Backscattered electron micrographs of detailed study of matrix and porosity	179
33.	Scanning electron micrographs of the surface of caustic calcined magnesite	270
34.	Vein type huntite deposit	282
35.	Nodular type huntite deposit	285
36.	Alluvial type huntite deposit	288
37.	Dry river beds covered by a thin layer of nesquehonite	290
38.	Hand specimen photographs of different huntite	293
39.	Transmission electron micrographs of huntite	305
40.	Transmission electron micrographs of nesquehonite	307
41.	Scanning electron micrographs of fracture surface of different huntite specimens	312
42.	Scanning electron micrographs of fracture surface of comparison study of fracture surface of magnesite - dolomite, magnesite and hydromagnesite - huntite	314
43.	Scanning electron micrographs of fracture surface of nesquehonite	316
44.	Scanning electron micrographs of the surface of dead burned products of huntite, magnesite - dolomite and nesquehonite	337
45.	Backscattered electron micrographs of dead burned huntite	339
46.	Backscattered electron micrographs of dead burned huntite and hydromagnesite - huntite	341
47.	Backscattered electron micrographs of dead burned magnesite - dolomite and nesquehonite	343
48.	Colour photograph of dead burned huntite	344

CHAPTER 1

INTRODUCTION

1.1 Magnesite

Magnesite (MgCO_3), is the magnesium end member of an isomorphous series of carbonates. An increasing content of calcium produces first dolomite and ultimately calcite, the calcium end member, increasing iron produces breunnerite and then siderite, the iron end member. Pure magnesite, theoretically 47.8% MgO and 52.2% CO_2 , is rarely found. Magnesite in its natural crude state has very limited applications, the use of high purity natural magnesite as an anti-caking agent in ammonium nitrate fertilizers is a notable exception. Magnesite dissociates upon heating to form magnesia (periclase) (MgO) and carbon dioxide (CO_2).

Magnesia (MgO), whether used to line a kiln or an upset stomach, is basic to modern society. In industry, its inertness and high melting point allows magnesia to be used as a refractory. Dead burned magnesite (refractory magnesia), and caustic calcined magnesite are essentially magnesia differing mainly in density and crystal development as the result of different levels of heat application.

The term dead burned magnesite refers to the granular product produced by firing magnesite, magnesium hydroxide, or other material reducible to magnesia at temperatures in excess of 1600°C and for enough time to produce a dense, stable product, suitable for use in the manufacture of

refractory materials. Of the approximately 8 million tonnes of magnesia consumed each year, four fifths goes into the production of refractories.

Caustic calcined magnesia (or light burned magnesia) is produced when magnesite or material reducible to magnesia by heat, is heated to such a degree that less than 10% ignition loss remains and the product displays high adsorptive capacity or activity. The degree of sintering is much less than the case of refractory magnesia, and commonly the firing temperature is in the range of 700-1000°C. Caustic calcined magnesia is used in a variety of products, including animal feed-stuff, special cement, fertilizer and a variety of magnesium chemicals including the familiar "milk of magnesia".

1.2 Huntite

Huntite [$Mg_3Ca(CO_3)_4$], is a rare mineral, first identified by Faust (1953) and was named in honour of professor Walter F. Hunte. Huntite is a naturally occurring rhombohedral carbonate and forms either as a weathering product of carbonates in a near surface environment, or by interaction between Mg rich solution with the basic and ultrabasic rocks. Huntite occurs as sporadic nodules near fault zones between serpentinite rocks. Huntite also can originate by direct precipitation from Mg rich solutions or as a result of interaction of these solutions with pre-existing weathered carbonate fragments.

The physical and industrial properties of huntite such

as its snowy white colour, hardness of 1-2, its softness which is low enough to leave marks on a dark surface, porous and crumbling in water, grain size of less than one micron, high brightness and purity suggest that huntite may make an excellent white filler in paint.

1.3 Reasons for this research

Iran could be one of the largest producers of industrial minerals. However because of vast production of metals, oil and gas, the potential for industrial minerals have never been determined in detail. The principal objective of the author's researches on industrial minerals from Iran such as feldspars (Nasrabadi, 1986), and magnesite and huntite in the present investigation is to provide information on the geological, mineralogical, chemical, physical and particularly industrial properties of these raw materials to evaluate their potential for variety of uses.

Magnesite and its dead burned and caustic calcined products have been studied over a long period of time and a very extensive literature exist on this subject, but there is almost no systematic or detailed chemical, mineralogical, microstructural and especially industrial mineralogical study of huntite available.

Thus, the aims of this research are:

1. To determine the geology, mineralogy, chemistry and microstructure of natural magnesite deposits of eastern Iran, in order to confirm their mode of occurrence and in particular the factors influencing their utilisation.

2. A systematic and detailed study of dead burned magnesites from Iran. a) To determine their mineralogy, physical and industrial properties. b) To establish their microstructural characteristics. c) To determine quantitative analysis of each mineral phases, and the extent of solid solutions; and finally, d) To compare the determined phases in each dead burned product with those of predicted phases from phase equilibrium studies, and hence the applicability of the prediction of mineralogy to the actual products.
3. To examine the calcination characteristics of some natural cryptocrystalline magnesite from Iran, by decomposing granular material over a range of temperatures and time in a laboratory furnace; and to establish the ideal industrial properties of these caustic calcined magnesias to compete with the available high quality commercial products.
4. To determine the geology, mineralogy, chemistry, physical properties, microstructure and industrial properties of huntite deposits of eastern Iran in order to evaluate the industrial potential of huntite.

CHAPTER 2

GEOLOGY AND TECHNOLOGY OF MAGNESITE AND HUNTITE

SECTION 1 (MAGNESITE)

2.1.1 Geological occurrences

Of the types of magnesite deposits so far known in the world, only the vein and hydrothermal - sedimentary types are found in eastern Iran. Metasomatic, and exogenic type deposits have not yet been observed in Iran. The geological occurrences of magnesite deposits are summarized in Table 2.1.

Table 2.1 A genetic classification of magnesite deposits.

1. Endogenic (hydrothermal) deposits
 - a) Metasomatic type
 - b) Vein type
2. Transitional hydrothermal - sedimentary deposits
3. Exogenic deposits
 - a) Sedimentary deposits
 - i) Saliferous type
 - ii) Detrital type
 - b) Deposits resulting from weathering
(infiltration type)

2.1.1.1 Endogenic (hydrothermal) deposits

2.1.1.1.a Metasomatic type

The hydrothermal - metasomatic type forms extensive magnesite bodies (beds, lenses, stocks) within limestones and dolomites. The largest and economically most important deposits in the world are of this type (Manchuria, Korea, Soviet Union, Austria, Czechoslovakia, Spain, and North America).

Deposits of this type are relatively few but they usually have large reserves from a few million to several tens of million tonnes, and sometimes several hundred million and even several thousand million tonnes.

In this type of deposit the mechanism whereby magnesite replace the country rock is thought to involve magnesium rich fluids entering the strata via fissures, cleavage planes and capillary openings

Magnesite deposits of metasomatic type have not so far been discovered in eastern Iran. In metasomatic deposits magnesite occurs as granular, usually very coarse grained aggregates so that these are often called deposits of crystalline or spathic magnesite. Magnesite grains range from less than a millimetre to several centimetres in size. Their colour is usually white or yellowish, but can also be grey to completely black, with a hardness of 3.5 - 4, and specific gravity of 3.02. The main undesirable impurities are lime and iron oxides.

A large group of geologists (Bain, 1924, Petrascheck, 1931, Himmelbaue, 1933, Redlich, 1934, Tatarinov, 1946) state

that these deposits formed by metasomatic replacement of limestones and dolomites by hot magnesium-charged hydrothermal solutions, while another group (Nishihara, 1956, Martin, 1956, Deliaarena, 1959) believe that these deposits formed by sedimentation.

2.1.1.1.b Vein type

The hydrothermal vein type of magnesite occurs mainly in the form of veins or veinlets (stockworks) in ultrabasic rock masses (peridotite and serpentinite). They constitute only a comparatively small portion of world production, but in eastern Iran they are the commonest and most important sources of magnesite. The important deposits of vein type are those in the USSR, Austria, Poland, India, South Africa, USA and Iran.

Reserves of vein magnesite in individual deposits range from several hundred thousand to several million tonnes. The magnesite in vein deposits is cryptocrystalline (amorphous), or less often microcrystalline. It is very dense and has a conchoidal fracture. It is usually snowy white in colour but it can be tinted yellow, orange, or buff, with a hardness of 3.5-5, and a specific gravity of 2.9-3.0.

2.1.1.2 Transitional hydrothermal - sedimentary deposits

The hydrothermal - sedimentary type of magnesite occurs in the form of lenses and beds in sedimentary strata of fresh water basins. The Torshak deposit, eastern Iran is of this type. A characteristic feature of hydrothermal - sedimentary

magnesite deposits is that they usually have the form of large magnesite bodies occurring singly or in groups and contain considerable reserves (from several hundred thousand to several million tonnes). They are mostly mined by open pit method.

The magnesite found in hydrothermal - sedimentary deposits is microcrystalline to cryptocrystalline, dense, and often with a conchoidal fracture. Its colour is usually white but it can also be grey. Magnesite of hydrothermal - sedimentary deposits is of appreciably lower grade than that of vein deposits. This magnesite is often intercalated with marls and shales, and its main impurities are high contents of lime, silica and sometimes alumina.

2.1.1.3 Exogenic deposits

2.1.1.3.1 Sedimentary deposits

2.1.1.3.1.a Saliferous type

The saliferous type of magnesite deposits is rather rare and is formed under very specific conditions (Bain, 1924, Destombes, 1956, Kazakove et al. 1957, and Petrascheck, 1961 have reported this type of deposit).

Kazakov (1957), established that the precipitation of sedimentary magnesite is determined by the following:

1. A relatively high concentration of magnesium bicarbonate, i.e. a high PH.
2. A comparatively high content of carbon dioxide in the water.
3. a low calcium content in the water.

Special conditions such as arid climate, isolation of the sedimentary basin, unusual chemical characteristic of the water (e.g. sodium or carbo-magnesium type of water), high content of CO₂ and high salinity are required for the formation of deposits of this type.

This form of deposit is very rare. Magnesite formed in this way is found in the rock salt deposits of Hall (Tyrol) and Saint Pandelone (France).

2.1.1.3.1.b Detrital type

The detrital type of magnesite deposits has been discovered by Ilic (1966). This form of deposit has been produced by mechanical disintegration of existing magnesite deposits (vein or hydrothermal-Sedimentary) and re-deposition of the magnesite detritus in a nearby basins. Examples of this type of deposit are in Yugoslavia and Greece.

2.1.1.3.2 Deposits resulting from weathering (infiltration type)

The infiltration type of magnesite deposit occurs in the crusts of weathering of ultrabasic rocks (peridotite and serpentinite). Although genetically very interesting these deposits generally have no economic importance.

Weathering crusts of ultrabasic rocks are formed in arid and wet climates under the action of air, surface and ground water and living organisms. Under conditions of lateritisation of ultrabasic rocks, descending solutions containing carbonic acid leach magnesium from the upper zones

of the crust of weathering, transport it in the form of bicarbonate and deposit in fissures and cavities in the lowermost zone, thus forming magnesite stockworks and small nodules. Deposits of this type have a rather small vertical extent of 10-15 m, (for more detail see Ilic, 1968).

2.1.2 Possible source of magnesium

2.1.2.1 Magmatic source

According to Clark (1924) the average igneous rock contains 2.09% magnesia. Magnesia is used up in the crystallization of olivine, the pyroxenes, amphiboles and finally biotite.

There is a relatively low magnesia content in felsic rocks as compared with the mafic rocks. Residual fluids, gases, or liquids, from the crystallization of magma contain little or no magnesium.

2.1.2.2 Chemistry of water

Analyses of waters from springs are subject to the criticism that the hot water may have dissolved certain substances from the wall rock of the passage ways. Analyses of water show magnesium salts in amounts that rarely reach 16.45% of total salts, or about 0.06 gram of magnesium per cubic metre of water.

2.1.2.3 Ocean water

Magnesium salts forms 15.84% of all dissolved salts in ocean water (Clark, 1924). Of this 3.77% is Mg. This

accumulation of Mg occurs mostly from the destruction and dissolution of Mg bearing rocks and minerals.

2.1.2.4 River waters

The salinity of river water varies from 14 - 1500 PPM dissolved solids. Of this Mg salts form 1.22 - 10.71%. (for more detail see Nishihara 1956).

2.1.3 Prospecting and exploration

The search for deposits of any type of magnesite should be guided by consideration of the probable origin of magnesite. In the case of crystalline magnesite, possible locations of deposits are areas of limestone or dolomite that have been subjected to folding or igneous activity. In the case of cryptocrystalline magnesite possible locations are areas of ultrabasic rocks which show extensive alteration to serpentinite. In both cases, the search can be confined within the boundaries of the areas that show evidence of dynamic geologic activity. Magnesite formations are generally more resistant to weathering than associated formations. Thus they stand out as features.

Magnesite to be commercially acceptable, should contain at least 95% magnesium carbonate, an amount which, depending on the accessory oxides, would result in a dead burned product containing 90-94% MgO.

2.1.4 Mining and processing

Nearly all major magnesite deposits are mined by open pit methods, although in certain cases narrow and deep deposits are mined by underground drifts and stopes or surface opening.

The mined ore is rarely shipped or used in crude form, but is processed to yield refractory magnesia or caustic calcined magnesia. In the most crystalline deposits, in which magnesite occurs in association with dolomite, processing consists of preliminary crushing followed by heavy media separation for coarser material and floatation for fines. Other beneficiation techniques such as the use of high intensity magnetic separators are also used some times. There is also usually a blending and mixing stage before calcination. For cryptocrystalline magnesite, in which white veins of magnesite occur in a dark matrix of serpentine and related minerals, it is now common in modern plants to use optical separation technique, after a crushing and washing stage. Secondary stages are again involve combination of heavy media, floatation and magnetic separation techniques. For both types of magnesite, the fine floatation concentrate is briquetted (and sometimes pre-calcined and briquetted) before the final dead burning stage. Dead burning is generally carried out in rotary kilns although modern designs of vertical shaft kiln are favoured by some producers (For more detail see Foroglou et al. 1981, Coope, 1981 and Wicken, 1984).

2.1.5 Production

The total world production capacity of crude natural magnesite is around 11.4 million tonnes, over a third being derived from Eastern Bloc countries, (Table 2.2).

From crude magnesite, two main commercial grades of magnesia are derived, caustic calcined magnesia, produced at 700-1000°C and dead burned magnesia at 1500-1750°C. The latter is the main refractory grade, about 5 million tonnes being produced from the 11.4 million tonnes per year of crude magnesia mined.

2.1.5.1 Yugoslavia, Greece, Turkey, Iran, Pakistan ultrabasic belt

A belt of ultrabasic rock stretching from Yugoslavia through Albania, Greece and Turkey, then eastwards to Iran and Pakistan, is a major source of minerals. These include magnesite, chromite, iron ore, nickel ore, laterite and asbestos. Yugoslavia, Greece and Turkey have a combined magnesite production of about 2 million tonnes per year.

Table 2.2 World production of crude natural magnesite (tpa) (1981).

USSR	2,100,000
China	2,000,000
N.Korea	1,900,000
Austria	1,158,852
Greece	930,000
Turkey	772,966
Czechoslovakia	664,000
Spain	500,000
India	453,410
Brazil	350,000
Yugoslavia	300,000
USA	150,000
TOTAL	11,400,000

Source: Institute of Geological Sciences London (for more detail see Harben and Bates, 1984).

2.1.6 Uses

2.1.6.1 Crude magnesite

Crude magnesite has been used in negligible quantities for the preparation of such chemicals as Epsom salts.

2.1.6.2 Dead burned magnesite

Dead burned magnesite is used almost entirely as a refractory material. It can be used directly as a grain product or as a constituent of a brick. The refractories made from magnesia have a wide variety of uses but their main use is in iron and steel manufacture, which currently accounts for about three-quarters of the total consumption of refractory materials on a worldwide basis. The remaining refractory demand is divided among cement, glass, copper, non-ferrous metals and ceramic industries. The great merit of magnesia based refractories is their ability to resist basic slag at high temperatures.

High quality grade of refractory magnesia are produced by dead burning beneficiated magnesite ore at temperatures up to 2000°C in shaft or rotary kilns.

2.1.6.3 Caustic calcined magnesite

Caustic magnesia is a type of magnesium oxide which is obtained by decomposing magnesium carbonate or magnesium hydroxide just above the temperature of thermal decomposition. It is obvious that such a type of thermal treatment gives materials which have a high reactivity.

There are many fields of application for caustic magnesia; the most important consumers are the following:

1. Building industry (for light weight building boards and flooring).
2. For the preparation of fertilizer and animal feed.
3. For the paper industry.
4. For manufacture of grinding wheels and discs.
5. For the rubber, ceramic and resin industries.
6. For the metallurgical industry and the steel industry in particular.
7. For the petrochemical and pharmaceutical industries.
8. For beneficiating waste water.
9. As additive in power plants to combine sulphur with MgO from oil.

2.1.7 Tests and specifications

2.1.7.1 Refractory magnesia

Resistance to hydration is an important determination often made. The presence of free lime in dead burned magnesite is deleterious and can result in shattered refractories as hydration take place. In most dead burned magnesite, lime is not free but is combined with other oxides in stable mineral combination, which are resistant to hydration.

In synthetic and high purity magnesias, the size of the periclase crystal is considered important and is checked under a microscope. The presence and relationship of trace

elements are important, as is the density of grain of the final product.

2.1.7.2 Caustic calcined magnesia

The specification for magnesia of this type are as varied as the uses. In general specific requirements such as the particle size, colour, ignition loss, chemical composition, bulk density, and activity may have to be met.

When caustic calcined magnesia is calcined at extremely high temperature (fused MgO), The product is used in special refractory and electrical applications. These products are usually very expensive (for more detail see Wicken, 1984, and Mortl, 1986).

2.1.8 Properties of refractory materials

The most important properties of refractories are those which directly determine their ability to withstand conditions during service in furnaces and fireboxes.

The properties of refractory materials can be divided into four groups: Physical, mechanical and chemical properties and economic features. Physical and mechanical properties are summarised in Table 2.3. (for more detail see Duncan et al. 1981, Wicken, 1984, Mortl, 1986 and Coope, 1981, 1983, 1987).

Table 2.3 Physical and mechanical properties of refractory products

<u>Physical</u>	<u>Mechanical</u>
1. Porosity & bulk density	1. Crushing strength
2. Pore size	2. Creep in compression
3. Thermal expansion	3. Modulus of rupture
4. Refractoriness	4. Creep in torsion or bend
5. Thermal conductivity	5. Spalling resistance
6. Specific heat	6. Abrasion resistance
7. Accuracy of size and shape	7. Impact resistance
8. Permanent dimension	

Probably the most important properties of refractory materials are their chemical composition, refractoriness, high temperature stability, hot strength, cold crushing strength, porosity and the spalling resistance.

2.1.8.1 Physical properties

2.1.8.1.a Porosity

Porosity is the ratio of the pore or voids to the volume of the entire brick and is usually expressed as a percentage. The lower the porosity, the greater the amount of material to resist chemical attack. At the same time a very low porosity could adversely effect certain mechanical properties.

The nature of porosity is important as well. Most evidence suggests that a fine pore size distribution reduces liquid slag penetration.

2.1.8.1.b Density

Bulk density is inversely related on true (open and closed pores) and apparent porosity (open pores). As the porosity decreases. The bulk density and hence the apparent porosity can be measured by the extent to which water or other liquid penetrate the refractory brick.

2.1.8.1.c Thermal expansion

Upon heating, refractories expand. Mostly they resume their original volume when cooled. This thermal expansion, sometimes known as "reversible" expansion, is distinct from the additional "permanent" expansion caused by changes in phase composition and structure of the refractory. The thermal expansion governs the stresses occurring in the refractory when rapidly heated or cooled and thus has a substantial effect on the spalling resistance. Thermal expansion depends solely on the chemical and mineralogical composition of the given material.

2.1.8.1.d Refractoriness

At fairly high temperature refractory materials soften and ultimately will flow as liquids of various degree of viscosity. The refractoriness of the material is, in part, its ability to withstand the effect of high temperature without losing its dimensional stability.

2.1.8.1.e Thermal conductivity, heat capacity and thermal diffusivity

Conduction of heat in refractories is very important in determining the loss of heat through the walls and roof of the furnace. Heat conduction also affects their spalling resistance. The thermal conductivity of ordinary refractories increases as the heating temperature is raised, but if the porosity increases, the heat conductivity is reduced.

The thermal diffusivity is the rate at which the temperature is propagated when a body is heated.

2.1.8.1.f Accuracy of size and shape

The size and shape of refractory bricks is important in prolonging the service life of linings. A lining with thin seams not exceeding 3 mm, and in more critical cases 0.5 mm, can be obtained only with a regularly shaped and accurately dimensioned brick.

2.1.8.1.g High temperature stability

This is a measure of the volume change after being heated at specific temperature for known lengths of time.

2.1.8.2 Mechanical properties

Among the mechanical properties presented in Table 2.3, the more important mechanical properties are:

2.1.8.2.a Modulus of rupture

Hot strength is determined by measuring the modulus of

rupture. For this, a specimen is suspended between two bearing surface, and an increasing load is applied until failure occurs.

2.1.8.2.b Spalling resistance

Spalling is defined as "the breaking or cracking of the refractory brick in service to such extent that pieces are separated or fall away, leaving new surfaces of the brick exposed." There are three types of spalling, thermal, mechanical and structural.

Variations in the temperature of a refractory lining in furnaces may cause cracking. The ability of a refractory to resist repeated temperature variation without being destroyed is called its spalling resistance.

2.1.9 Chemical properties

Chemical analysis is an important measurement, first of all as a means of classifying the refractory, but also to determine its impurity content.

The chemical composition of a refractory and of the raw material depends on the degree of purity of the raw material. Sometimes the chemical composition of the refractory raw material may be used as an advantage in ensuring the required phase composition of the refractory product.

Chemical composition is directly linked to refractoriness and volume stability at high temperature and it markedly affects the properties, texture and in particular, high temperature mechanical properties.

In itself the chemical quality is directly linked to slag resistance, the other properties that are dependent on chemical quality merely adding to, or detracting from, this resistance. Slag erosion is the principal reason for the destruction of most refractory materials. Slag erosion depends on the chemical nature of the slag and the refractory. The action of basic slag on an acid refractory or acid slag on a basic refractory at high temperatures causes formation of low-melting compounds, which will quickly destroy the refractory.

2.1.10 Economical features

The cost/unit volume is very relevant and is a major factor in assessing the technical/economic performance by which refractories are selected (for more detail see Budnikov, 1964, Norton, 1968, Webster et al. 1975 and Coope, 1981).

2.1.11 Impurities

The undesirable impurities in magnesite refractories are lime, silica and iron compounds. The CaO-MgO system does not show the formation of any liquid phase below 2370°C. Thus fluxing by lime does not occur under normal steelmaking conditions. However, free lime renders the final product prone to hydration by atmospheric moisture.

The most important impurity is silica, which is not only detrimental in itself, but also combines with other impurities to form undesirable compounds e.g. clinoenstatite ($\text{MgO} \cdot \text{SiO}_2$), which melts incongruently at 1557°C, and forsterite ($2\text{MgO} \cdot \text{SiO}_2$), which melts congruently at about 1900°C. The combination of silica and lime is extremely important in magnesia refractories in that the lime/silica ratio determines the nature of the compounds formed in the bond between the magnesia grains.

Relatively refractory minerals such as dicalcium silicate (m.pt. 2130°C) are tolerable, but less refractory minerals such as wollastonite (CaO, SiO_2) (m.pt. 1544°C), merwinite (m.pt. 1575°C) or monticellite (m.pt. 1502°C) are undesirable. If the lime content of the magnesite is high, considerable quantities of dicalcium silicate may be formed during dead burning and this can lead to "dusting" of the refractories in service when they are allowed to cool below 675°C. The dusting results from the transformation in the dicalcium silicate which is accompanied by a 10% volume change.

In general, a CaO/SiO₂ ratio of about 2:1 is desirable. With a higher ratio the possibility exists for forming low melting dicalcium ferrite (2CaO,Fe₂O₃), aluminate and spinel (Spencer et al. 1971). The formation of such a liquid phase between the magnesia grains reduces the resistance to deformation or rupture of the hot refractory.

It is found (Palfreyman, 1974) that CaO/SiO₂ ratio greater than 2:1 were required to maximise high temperature strength and that the lower the SiO₂ content the greater the CaO/SiO₂ required to maximise strength. The results are consistent with established fact that part of the CaO enters into solid solution in the periclase phase resulting in a lower CaO/SiO₂ ratio in the silicate phase than in the overall composition.

The result of CaO entering solid solution in MgO is to lower the actual CaO/SiO₂ ratio of the silicate phase with formation of merwinite (C₃MS₂) and monticellite (CMS), which liquify at lower temperatures than dicalcium silicate (C₂S). Excess CaO is required to maintain the CaO/SiO₂ to produce the refractory C₂S second phase. The lower the SiO₂ content the more critical the effect of CaO solubility in the periclase phase and the greater the overall CaO/SiO₂ ratio in the MgO in order to maintain a C₂S second solid phase. The higher the application temperature, the greater the CaO solubility in the periclase and hence higher CaO/SiO₂ ratios are required to maintain the silicate in the form of C₂S.

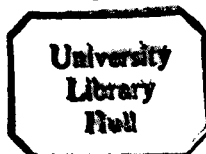
The occurrence of alumina (Al₂O₃) as an impurity in magnesite is normally very minor and in magnesia refractories

the alumina and silica together are mostly less than 2%. The system MgO-Al₂O₃-SiO₂ shows an eutectic which melts at 1355°C, but much melting at this temperature would not be expected to be present in a magnesia refractory which contains very low amounts of Al₂O₃ (for more detail see Palfreyman, 1974).

The effect of B₂O₃ in sea water magnesia is critical in the 0.01 to 0.1% addition range. The lower the SiO₂ content the more critical the effect of B₂O₃. At a constant SiO₂ level the higher the CaO/SiO₂ ratio the lower the strength decrease caused by the B₂O₃ addition.

The strength reduction caused by the Al₂O₃, B₂O₃, Cr₂O₃ and Fe₂O₃ additions varies with the SiO₂ content, the CaO/SiO₂ ratio and test temperature. In equivalent weight basis the Fe₂O₃ is the least deleterious of the investigated impurities. B₂O₃ is approximately 10 times more deleterious than Al₂O₃ which, in turn, is 6 times more deleterious than Cr₂O₃ and 17 times more deleterious than Fe₂O₃ at this particular MgO composition (Spencer, 1972).

Further low SiO₂ and R₂O₃ content grades of MgO should contain high CaO/SiO₂ ratios in order to maximise strength. It is also desirable to control the CaO/SiO₂ ratio above the optimum ratio due to the marked strength decrease that occurs when the ratio falls below the optimum. A high CaO/SiO₂ ratio MgO is also considered important for slag resistance. The ability of magnesia bricks containing high CaO/SiO₂ ratios to deform under stress without fracturing may also contribute to longer service lives of the material (Spencer, 1972).

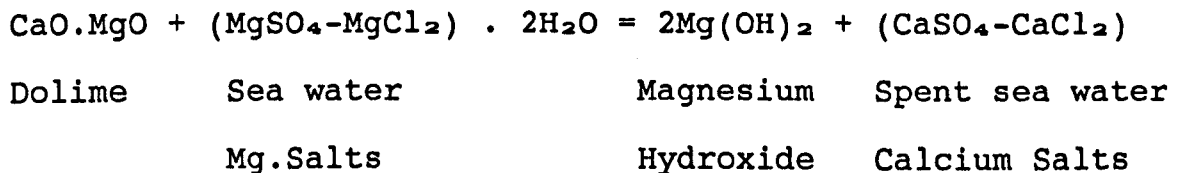


2.1.12 Sea water magnesia

2.1.12.1 Introduction

Magnesia raw materials for use in basic refractories are obtained either by dead burning naturally occurring magnesite, or by dead burning (i.e. rotary kiln calcining at temperatures greater than 1600°C) magnesium hydroxide, $\{(\text{Mg}(\text{OH})_2)\}$ precipitated from sea water or brine solutions by alkali. The extraction of magnesia from sea water for refractory applications originated in the major steel producing countries which did not have available a source of high quality natural magnesite.

Essentially the process consists of burning dolomite to dolomitic lime (Dolime) and reacting this with sea water to precipitate magnesium hydroxide. The chemical reaction is shown below:



Over the last 30 years major improvement have been made to the physical and chemical qualities of synthetic magnesia and it is now accepted that the highest qualities give superior performance compared with the best qualities of beneficiated, dead burned natural magnesites in a number of refractory applications.

Current production of magnesia from sea water and brines represents approximately 40% of the total magnesia for refractory usage. It should be noted that the sea water magnesia process is also used for production of chemical grade magnesia (e.g. for use in the paper industry) and as a precursor for the production of magnesium metal.

TABLE 2.4 World production of sea water magnesia (tpa) (1981).

Japan	715,000
USA	460,000
UK	250,000
Italy	180,000
Eire	175,000
Norway	120,000
USSR	100,000
Canada	60,000
Mexico	50,000
China	10,000

(for more detail see Bates, 1969 and Harben & Bates, 1984)

2.1.12.2 Sea water magnesia process

The siting of a sea water magnesia plant is dependent on the following main factors:

- a) The sea water requires to be of approximately constant composition. No major rivers or other sources of dilution should be present in the locality.

- b) The sea should be free from silt and should be sheltered to minimise sand contamination.
- c) A source of high quality limestone or dolomite should be available.
- d) Fresh, clean water for washing the precipitate should be available.

2.1.12.3 Control of chemical impurities

Impurities in sea water magnesia arise predominantly from two sources, those inherent in the limestone or dolomite which is used as the source of alkali and those present in the sea water.

2.1.12.3.a Limestone/dolomite impurities

The major impurities derived from this source are SiO_2 , Fe_2O_3 , Al_2O_3 and CaO . Small amounts of other impurities may also be present in the raw stone at levels approx. 0.05%, such as MnO .

2.1.12.3.b Sea water impurities

SiO_2 and Al_2O_3 impurities present in the sea water as suspended sand or silt particles are decreased to an acceptable level by centrifuging the sea water prior to the reaction tanks. Potential CaO contamination resulting from the CO_2 present in the water may be removed by acid pretreatment or by precipitation as CaCO_3 as previously indicated.

Boron contamination from sea water has received the most

attention in recent years. Sea water contains boron, as boric acid, to the extent of 15 p.p.m. (as B_2O_3) (Sverdrup et al., 1942). This has been a problem for a considerable time for plants producing sea water magnesia for magnesium metal production. The capacity of the $Mg(OH)_2$ precipitate for adsorption of boron is such that contamination can be as high as 0.4% B_2O_3 on MgO . Although boron is a critical impurity in high duty MgO bricks, it is not as deleterious in materials used in the manufacture of chrome magnesia and magnesia chrome bricks and may even be an advantage in promoting spinel bonding. The need for low boron content MgO only becomes critical with the advent of the basic oxygen steelmaking processes (for more detail see Hall and Spencer, 1973).

2.1.13 Properties of sea water magnesia

2.1.13.1 High temperature strength

High temperature strength measurements are important since they give an indication of the stress that the material can withstand in service. They also provide a measurement of the refractoriness and structural characteristics of the material at temperatures approaching those experienced in its working environment. Generally, as soon as the impurity phase in magnesia begins to soften, the strength of the material decreases markedly. Three major impurities are responsible for the poor hot strength properties.

1. It is found necessary to increase the CaO/SiO_2 ratio of the silicate impurity phase in the MgO to approximately

2:1 to correspond to the refractory dicalcium silicate phase.

2. It is necessary to reduce the B_2O_3 impurity to below 0.05%.
3. Further research has shown that part of the CaO present in dead burned magnesia enters into solid solution in the MgO phase and hence the CaO/SiO₂ ratio in the silicate impurity phase was lower than that present in the overall material (Jones & Melford, 1969 and Henry & Jones, 1969). The effect of this CaO solid solubility becomes more critical as the SiO₂ impurity in the MgO is decreased. When these adjustments are made to the sea water magnesia it is found that bricks with hot strength properties at least equivalent to those made from the best qualities of naturally occurring magnesite can be obtained (Gilpin, 1969).

Benefits from high CaO/SiO₂ ratios in the impurity contents in low SiO₂ content sea water magnesias are thought to be to:

1. Maximise the refractoriness of the silicate phase at application temperature.
2. Reduce the sensitivity to fluxing of the silicate phase by small B_2O_3 impurity contents.
3. Maximise grain and brick densities.
4. Optimise microstructure.
5. Improve resistance to initial SiO₂ rich slag experienced in basic oxygen steelmaking prior to the solution of the lime addition to form of basic slag.

This may also improve the hot face spalling resistance of the bricks. It should be noted that there are disadvantages for very high CaO/SiO₂ ratio material. The main factors are:

1. Increasing CaO/SiO₂ decreases hydration resistance. It is thought that there should be only sufficient excess CaO in the material to saturate the MgO phase and maintain a dicalcium silicate second solid phase. The presence of a separate CaO phase causes a marked deleterioration in the hydration resistance and decrease the resistance to slag containing a high Fe₂O₃ content.
2. The presence of small Al₂O₃ and Fe₂O₃ contents lowers the refractoriness of the silicate phase particularly at high CaO/SiO₂ ratios (White, 1970).

A quantitative assessment of the relative deleterious effects of B₂O₃, Al₂O₃ and Fe₂O₃ on the hot strength of magnesia grain has been made by Spencer (Spencer, 1972).

2.1.13.2 Density

Refractory grade magnesia should have a high density to maximise slag resistance and high temperature strength properties. It is generally considered that the raw material should have a density of at least 3.35-3.40 g/ml, to achieve these properties.

2.1.13.3 Microstructure

The chemical impurities and firing treatment control the microstructure of the dead burned magnesite. The raw material

for high duty MgO bricks should have a structure consisting of;

1. angular shaped MgO crystals.
2. a high degree of direct MgO-MgO crystal contact.
3. a minimum amount of impurity phase isolated in pockets at MgO crystal intersections.
4. a crystal diameter in the 40-90 micron range.
5. Pores that are present should preferably be isolated within the crystals and should not form a continuous network at the crystal boundaries. Crystal shape and diameter is dependent on firing temperature, time and chemical quality, particularly with respect to the CaO/SiO₂ ratio. (Spencer and Coleman, 1970)

2.1.13.4 Hydration resistance

The relatively poor hydration resistance properties of sea water MgO grades produced during the infancy of the process were soon overcome by lowering the CaO impurity to a level which eliminated the presence of free CaO in the dead burned product and by increasing the fired bulk density. Present day sea water magnesias have excellent resistance to hydration (Hall and Spencer, 1973).

2.1.14 History and future of magnesite refractory

Magnesite was used as refractory throughout the nineteenth century in small quantities. By about 1890 magnesite bricks found applications in convertors, open hearth furnaces and in cement kilns.

The past thirty years has seen an almost complete change in the steel industry particularly from the use of open hearth furnaces and the Bessemer to basic oxygen convertors (BOF) and electric arc furnaces. The linings commonly used in the open hearth furnace consist of basic brick. The Bessemer convertor, on the other hand, commonly uses either silica, fireclay, or a combination of both. Both the BOF and the electric arc furnaces use predominately basic linings made from magnesia and dolomite, although the roof of the arc furnace is usually lined with high alumina (80-85% Al_2O_3) bricks.

With steelmaking temperatures in the region of 1800-1900°C, the number of possible refractories for use as lining roofs, side walls and other exposed positions has become very limited of magnesite, chrome-magnesite, dolomite and high alumina. If temperature approach 2000°C, dolomite and high alumina can not be used. The situation, of course represent a considerable challenge to the refractory industry, the solution is the development of magnesite and magnesite-based refractories.

The general trend, over the last 30 years or so has been towards higher and higher purity, but even for high purity magnesite, at high temperature (1800°C), they continue to shrink and creep when held at high temperature for long periods of time. High purity may not solve these remaining problems. According to Laming (1971), high hot strength in magnesite may require the presence of a second solid phase at high temperature whose main function is to prevent the

penetration of liquid between adjacent MgO grains. The properties required for the magnesite refractory of the future are:

1. High strength at high temperature.
2. Low creep rates at high temperature.
3. High resistance to basic slag.

These can only be achieved by:

1. decreasing its porosity.
2. decreasing its content of fluxing impurities.
3. controlling the proportions of certain constituents.
4. controlling the spatial distribution of the low melting constituents in the fired brick.
5. controlling the rates of reactions leading to failure. (White, 1962, 1963, 1966, 1968), (Laming, 1971) and (Dickson, 1981).

SECTION 2 (HUNTITE)

2.2.1 Introduction

Huntite, $Mg_3Ca(CO_3)_4$, was first identified by Faust (1953) from Current Creek, Nevada, and was named in honour of Professor Walter Hunt. Huntite is a naturally occurring rhombohedral carbonate whose composition lies half way between dolomite, $CaMg(CO_3)_2$, and magnesite, $MgCO_3$.

2.2.2 Physical and optical properties

Huntite generally occurs as compact, chalk like masses which have an even to subconchoidal fracture. It is brittle when cut with knife and is soft enough to leave a mark on a dark surface. The compact masses are easily cut by the fingernail. It is porous and a fragment dropped into water crumbles, emitting crackling noises as it breaks into smaller fragments. This crackling is accompanied by a hissing sound produced by the displacement of air bubbles from the porous mass. Huntite has a smooth feel and adheres to the tongue. The specific gravity is 2.696 at 4°C. Huntite is colourless in thin section. No determinations of the optical properties of huntite were possible by the usual immersion techniques, owing to the very small size of the crystals. An attempt to determine the refractive index by oil immersion methods gave a value of 1.615. It should be pointed out that this determination was for fibrous aggregates. Examination in thin section shows that the birefringence is very strong. Electron micrographs of huntite show that it is very fine grained (1 micron and less). Huntite has a platy habit.

2.2.3 Geological occurrences

After huntite was recognised by Faust (1953) as a new mineral, being deposited at shallow depths by late stage meteoric solutions, it has been found in many other localities and in association with some other carbonate minerals.

1. In Australia huntite has been reported: a) from Tea Tree Gully, South Australia, as a weathering product of dolomitic rock (Skinner, 1958), b) from Northern Territory, as localised nodules in a soil layer overlying weathered basalt (Veen and Arndt, 1973), c) from Deer Park, Victoria, as filling vesicles of the weathered basalt in the form of nodules in the indurated fossil soil, d) as small nodules in narrow basalts (Cole and Lancucki, 1975), and e) recently, Shayan and Sandy (1983) found huntite in large vesicles (already lined with a mixture of dolomite and magnesite) of altered basalt. This huntite contained 1.86% SrO.
2. In Iran huntite occurs as sporadic nodules in the fault zones between highly weathered serpentinite, as a weathering product of magnesite associated with magnesite and within the lower part of alluvium in a low temperature and near surface environment. As with the Australian material, these huntites contain SrO, (maximum of 2.94% SrO).
3. In China huntite containing 0.43% SrO is reported by Baogui and Yueming (1975).

2.2.4 Industrial application

The result of specific mineralogical and technological investigations which are presented in Chapters 6 and 7, suggest that huntite may make an excellent white filler in paint.

CHAPTER 3

GEOLOGY AND MINERALOGY OF MAGNESITE FROM KHORASAN PROVINCE, EASTERN IRAN.

3.1 Introduction

Magnesite, the carbonate of magnesium, has been found in a wide range of geological environments, as a replacement mineral in carbonate rocks, an alteration product in ultrabasic rocks, in sedimentary rocks, and as a vein-filling material (Bain, 1924). One of the most important commercial types of deposit occurs in belts of ultramafic rocks and consists of cryptocrystalline magnesite resulting from the alteration of serpentinite.

In the last decade an important group of cryptocrystalline magnesite deposits were discovered in the south east of Birjand, eastern Iran. These magnesite deposits have formed within the flysch and ophiolite melange belt of eastern Iran. The most important formation exposed in the area consists of Upper Cretaceous ophiolites and the Upper Cretaceous - Middle Eocene flysch formations. The latter contain lightly metamorphosed shale, siltstone and sandstones. The ophiolite unit, mainly serpentinite, is the host rock of the magnesite deposits. Several generations of magnesite can be recognised in the area ranging from Middle Eocene and continuing until the present (according to some unpublished reports, magnesite has been recognised on the top of the Neogene conglomerates and Quaternary terraces).

The Geological Survey of Iran studied the deposits at the request of and in cooperation with the Iran Magnesia Company.

3.2 A review of the geological formation of Khorasan province

Three important geological units have been described by the geological survey of Iran (G.S.I) in the Khorasan province north east of Iran.

3.2.1 The Koppeh Dagh mountain system

This is made up mainly of Jurassic - Cretaceous marine miogeosynclinal sediments, which contain a core of Precambrian to Triassic rock units with basic volcanics tightly folded and sliced in an early Kimmerian - late Hercynian tectonic phase. This core is separated by a marked angular unconformity from later Jurassic sandstones and shales of the Koppeh Dagh sedimentary sequence. The Koppeh Dagh belt is dissected by numerous dextral transcurrent faults in two directions, north and north east, which are still active. Many destructive earthquakes have been recorded in these faults.

In the Hezar Masjed mountains, the Koppeh Dagh reaches altitudes of more than 3000 metres. The Jurassic - Cretaceous rock units of Koppeh Dagh sequence extend into the Binalud mountains of the eastern Alborz range, (Figure 3.1).

3.2.2 Binalud range

These mountains rise on regular, gentle dip slopes of

Upper Jurassic and Lower Cretaceous limestones to an altitude over 3000 metres. They are cut and uplifted on the south west side by faults against down-thrown Neogene - Paleogene rock units. The eastern Binalud range has metamorphic cores near Mashhad with ultrabasic and Pre Middle Jurassic granite intrusions. These are terminated by north west to south east faults against the tightly folded Lower Jurassic slate and Paleozoic carbonate and sandstone units of central Binalud range (Figure 3.1).

3.2.3 The Ophiolite Melange zone

The Coloured Melange and ultrabasic zones (Ophiolite Melange) with pelagic micritic and siliceous Upper Cretaceous marine sediments are products of local deep rifting and cumulated build up of oceanic crust. These rift zones were separated and enclosed by local submarine horsts, on which Jurassic to Lower Cretaceous platform sediments (orbitolina limestone) were preserved. Partial filling of rift fault systems by basic igneous rocks in late Cretaceous time was followed by sagging and tensional deformation which formed a graben during the Paleogene. These were filled by flysch sediments from the adjacent horsts. These are called the Coloured Melange which contain evaporites and form sequences up to several thousand metres thick. In the Neogene period, acidic magma from underthrust sialic crust wedges was mobilized under the northern zone of the Coloured Melange intruded at its margins as porphyrite domes and dacite lavas.

The complex of the metamorphic Flysch and Coloured Melange to the south east of Birjand (2790 m), with direction of south east - north west surround the north - eastern limit of Lut Block (Figure 3.2) (for more details see Nabavi, 1976, Stocklin et al., 1977 and McCall 1985).

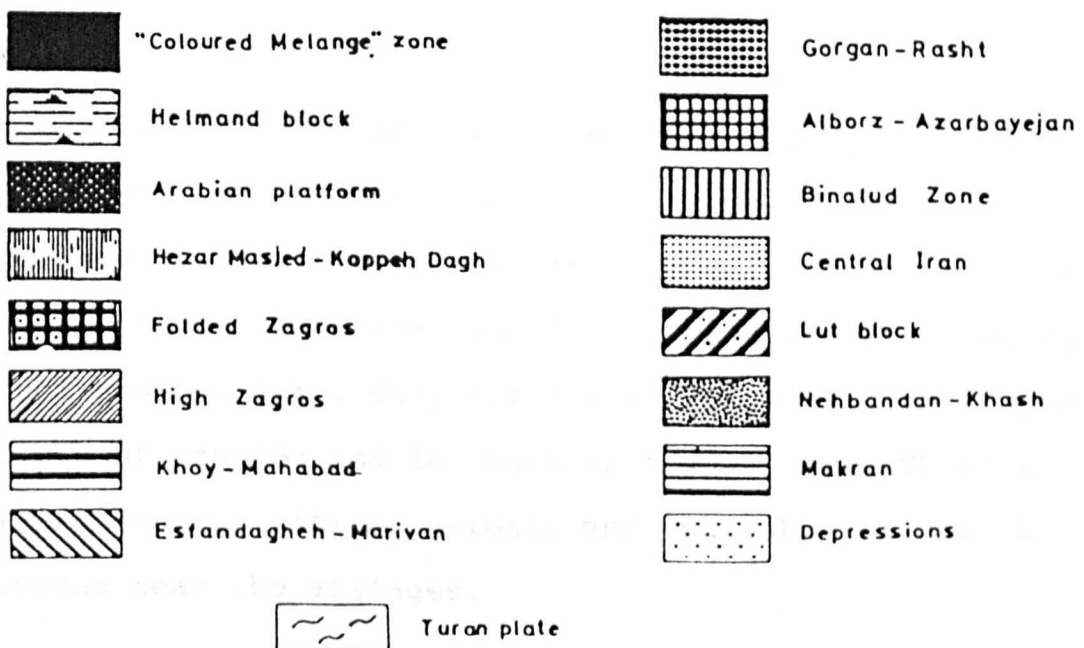
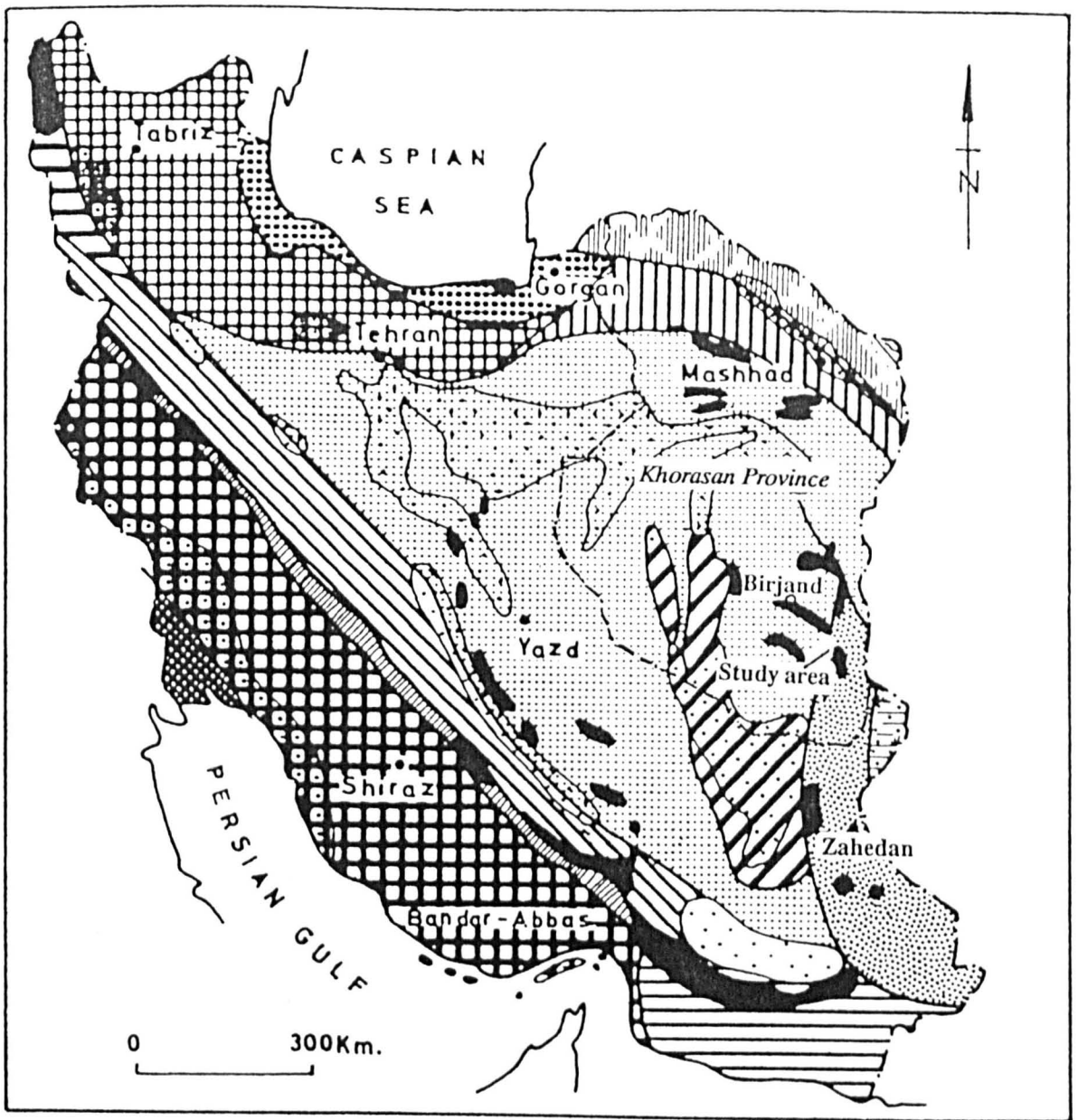


Figure 3.1 Tectono-sedimentary map of Iran (after Nabavi 1976)

3.3 Geography and geology of the investigated area

3.3.1 Physiography

3.3.1.1 Location

The investigated area is situated in the Khorasan province of eastern Iran approximately 170 Km south - east of Birjand (Figure 3.2).

3.3.1.2 Climate

The climate is dry and the landscape is semi-desert. Temperatures show strong daily and seasonal variations. The yearly rainfall is less than 200 mm. In summer, day temperatures commonly exceed 30°C. There are a number of villages in the mountain valleys and most of them can be reached on driveable desert tracks that are connected with the Birjand - Zahedan main road.

3.3.1.3 Vegetation

The entire project area is poorly vegetated. The mountains are bare and rocky and covered only by sparse scrub of grasses, bushes and stunted trees. The river channels are followed by growth of bushes including oleander, but there are no grassy flat areas at all, the valley floors being rough and bouldery. Only after rain there is a thin ephemeral growth of grasses and low bush in the valleys. There are plantations of citrus, cereals and vegetables along the water courses near the villages.

3.4 Main geological units

3.4.1 Ophiolite complex

In the Mediterranean area, numerous ophiolite belts were emplaced in Paleozoic to Mesozoic times. In Iran three ophiolite belts have been recognised (Figure 3.1), one Paleozoic belt restricted to the north part of Iran and two Mesozoic belts. The first one running north west - south east called the Zagros - Oman - Baluchistan belt was possibly developed from Triassic to the Turonian times, whereas the second one borders the central east Iran microplate. The investigated area is situated in this latter complex. There, the ophiolites, mainly of Upper Cretaceous age, are associated with Melanges (Takin, 1972). An examination of the geological map of Birjand area (Figure 3.2) shows that the main Ophiolite body in the area has been fringed in the northern and eastern parts by flysch type sediments and cored by younger sedimentary and volcanic rocks in the southern part. In other words, they form collectively as arcuate fragments, so that the Tertiary volcanic rocks emplaced in the centre of the arc, and flysch type sediments and ophiolites accreted tectonically to the flank of the arc.

The main ophiolite body of Birjand, which is situated in eastern part of Iran, have formed before the Tertiary along the crust of the continental margin. This intercontinental fragment is arcuate in shape (Figure 3.2) and indicates incorporation of ocean floor materials into the continental

margin. Two contrasted facies, namely ophiolites and flysch sediments, have been placed close together by regional subduction, along which the ocean floor complex slides beneath the Continental margin (Figure 3.2).

The investigated area contains arcuate ophiolite fragments which have been formed since the Late Cretaceous (Figure 3.2, Plate 1a). These ophiolite fragments are the result of convergence and collision between two different continental segments and a small region of oceanic crust. Convergence of the continental segment began in the Cretaceous by subduction of oceanic crust and continued until complete disappearance of the oceanic crust. During the collision of two continental segments, the primary plates were fragmented within the marginal parts into a more complex array of small fragments. The characteristics of the movement and deformation of these fragments are typical of the Alpine - Himalayan system.

3.4.2 Coloured Melange zone

The name Coloured Melange was derived from a combination of "Coloured series" as used by Iranian Oil Company geologist and "Ankara Melange" as referred to by Sticklin et al. (1977). The name is now commonly applied in Iran to a peculiar rock association presenting a wild colourful aspect due to a chaotic mixture of various sedimentary, igneous and metamorphic blocks ranging in size from pebbles and blocks to huge highly contorted and crushed rock masses. The most characteristic rock types are radiolarites, red and green

siliceous shales, thin bedded pink limestone contains globotruncana and various basic and ultrabasic rocks such as pyroxenite, peridotite, serpentinite, olivine basalt, gabbro, and dunite. Among the less frequent components are nummulitic limestones, coral and rudist limestones, agglomerates, amygdaloidal basalts, granodiorite and various metamorphic rocks including marble (Figure 3.2, Plate 1b).

In the eastern parts, the Coloured Melange complex is overlain by Middle Eocene Flysch type sediments, and Late Cretaceous to Early Tertiary various marine beds occurring in the Iran - Pakistan border regions (Figure 3.2).

3.4.3 Flysch sediments

The Flysch Zone is characterized structurally by tight, linear folding and longitudinal faulting in the Cretaceous flysch and by chaotic structure in the Coloured Melange complex. The rocks are rather uniform, argillaceous, silty and sandy shales of green-grey colour, with intercalations of thin sandstones and occasional calcareous shales. The flysch Zones form the mountain belt between the Lut Block in the west and the Iran - Afghanistan and Iran - Pakistan borders in the east. It covers an area with a north-south extension of about 800 Km and a width of up to 200 Km. In the north, several branches of the main zone extend north westwards into the Birjand area (Figure 3.2, plate 2a, b).

Flysch formation contains great thicknesses of predominantly shaley and sandy deep water sediments with subordinate radiolarites and pelagic limestones and with

variable admixtures of submarine, mainly diabase and andesite volcanics and lenses of ultrabasic rocks. No rocks older than Cretaceous have been recognised anywhere in the Flysch Zone. As a rather foreign element in the Flysch Zone appears the large granodiorite batholith of Kuh-e-Sefid (plate 1). This intrusive body is believed to have been formed during the Tertiary. The origin of the Flysch Zone may be viewed within the concept of plate tectonics. Takin (1972) conceived the Lut Block as a part of a large central and east Iranian microcontinent, and the Flysch and Coloured Melange Zone to the east of it as part of a former narrow ocean basin. The Lut Block has, in fact all the characteristics of a continental crust, with a granitic substratum and a relatively thin cover of shelf type sediments. The sharp eastern edge of the Lut Block could represent the western face of a deep split in a once coherent continental crust, the eastern face being represented by the equally sharp eastern border of the Flysch Zone now situated near the Iran - Afghanistan border. Widening of the initial fracture by the formation of an oceanic crust within the rift could have resulted in the development of a narrow Red Sea type oceanic trough, in which submarine pillow lavas were deposited together with deep water sediments and clastic material derived from the continental margin (Flysch). Continuous spreading of the ocean floor could eventually have led to underthrusting (subduction) of the oceanic crust below the Continental margin, a mechanism that might explain the tectonic emplacement of upper mantle material (ultrabasic

rocks) and its intermingling with the sedimentary and volcanic fill of the ocean trough (Coloured Melange). It is assumed that the primary fracture and its subsequent widening to an oceanic trough took place in Cretaceous time. And the absence of Pre-Cretaceous sediments from the Flysch zone would be a satisfactory explanation. Similarly, subduction, if expressed in terms of overthrusting and related emergence of the continental plate, could explain the evident near contemporaneity of deep sea sedimentation and melange formation in the Flysch trough and non sedimentation on the Lut Block in late Cretaceous time (for more information see Stocklin et al., 1972 and Ohanian, 1983).

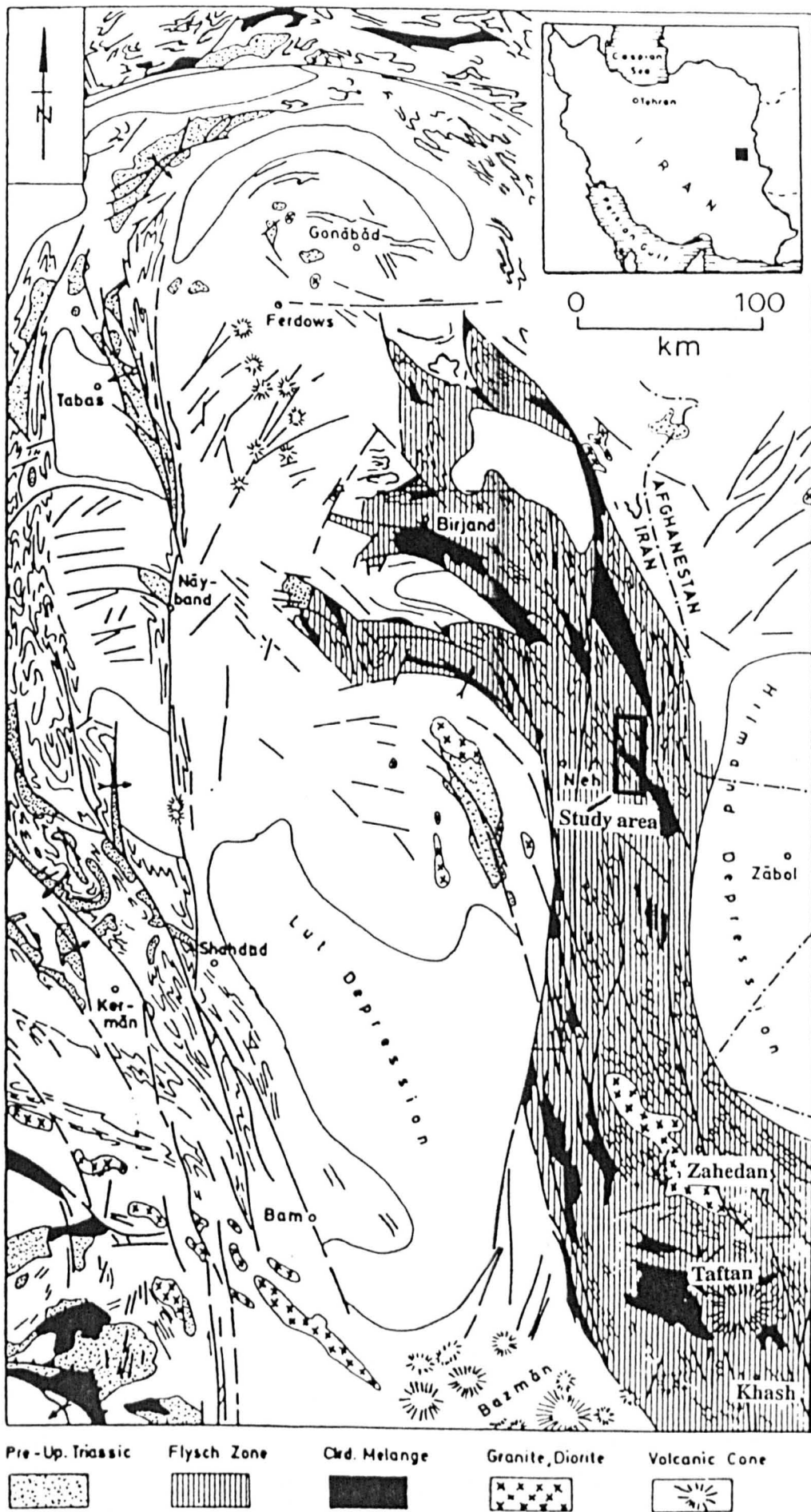


Figure 3.2 Tectonic sketch map showing Lut Block and Flysch Zone of East Iran (after Stocklin et al. 1972)

PLATE 1.a

View of Ophiolite complex which surrounds the Kuh-e-Sefid granodiorite batholith (background - right). This complex consists mostly of peridotite, serpentinite and harzburgite. Alteration of greenish serpentinite to the pale yellow ophicarbonates are quite visible especially near to the fault zones (foreground - right). The Kuh-e-Sefid granodiorite may have played an important role in the genesis of magnesite.

PLATE 1.b

View of Coloured Melange formation on north east of Shusf (village). This complex contains radiolarites, red and green siliceous shales, thin bedded limestones and various igneous rocks such as pyroxenite, peridotite, serpentinite, olivine basalt, gabbro and dunite. Limonitisation and alteration are quite visible especially near the main faults. In the background of photograph, the Kuh-e-Sefid granodiorite batholith (white in colour) is in view.

PLATE 1

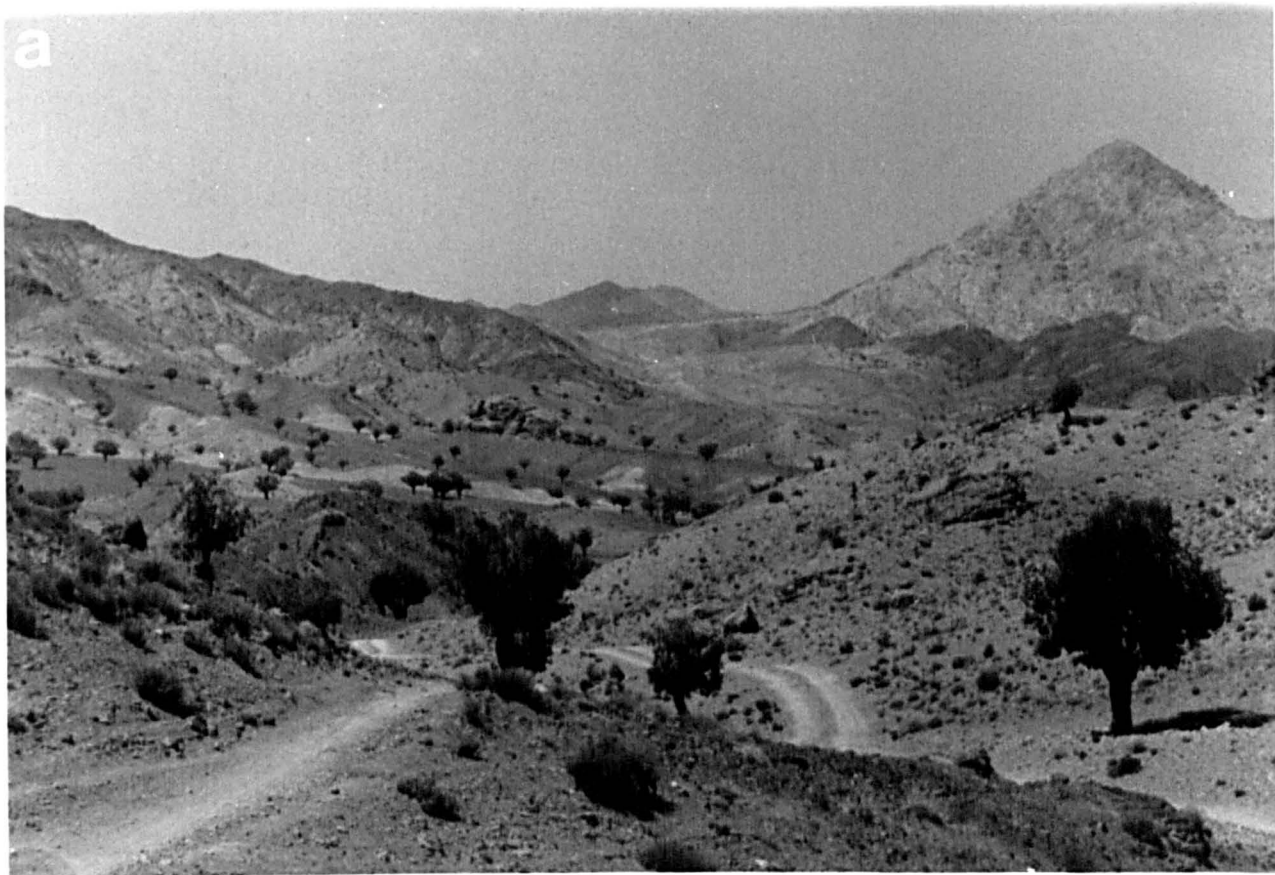


PLATE 2.a

View from West to the thick sequence of Paleocene shallow marine sediments, includes both carbonate and non-carbonate clastics; generally weakly deformed. These sediments are situated to the east of Afzalabad magnesite deposit.

PLATE 2.b

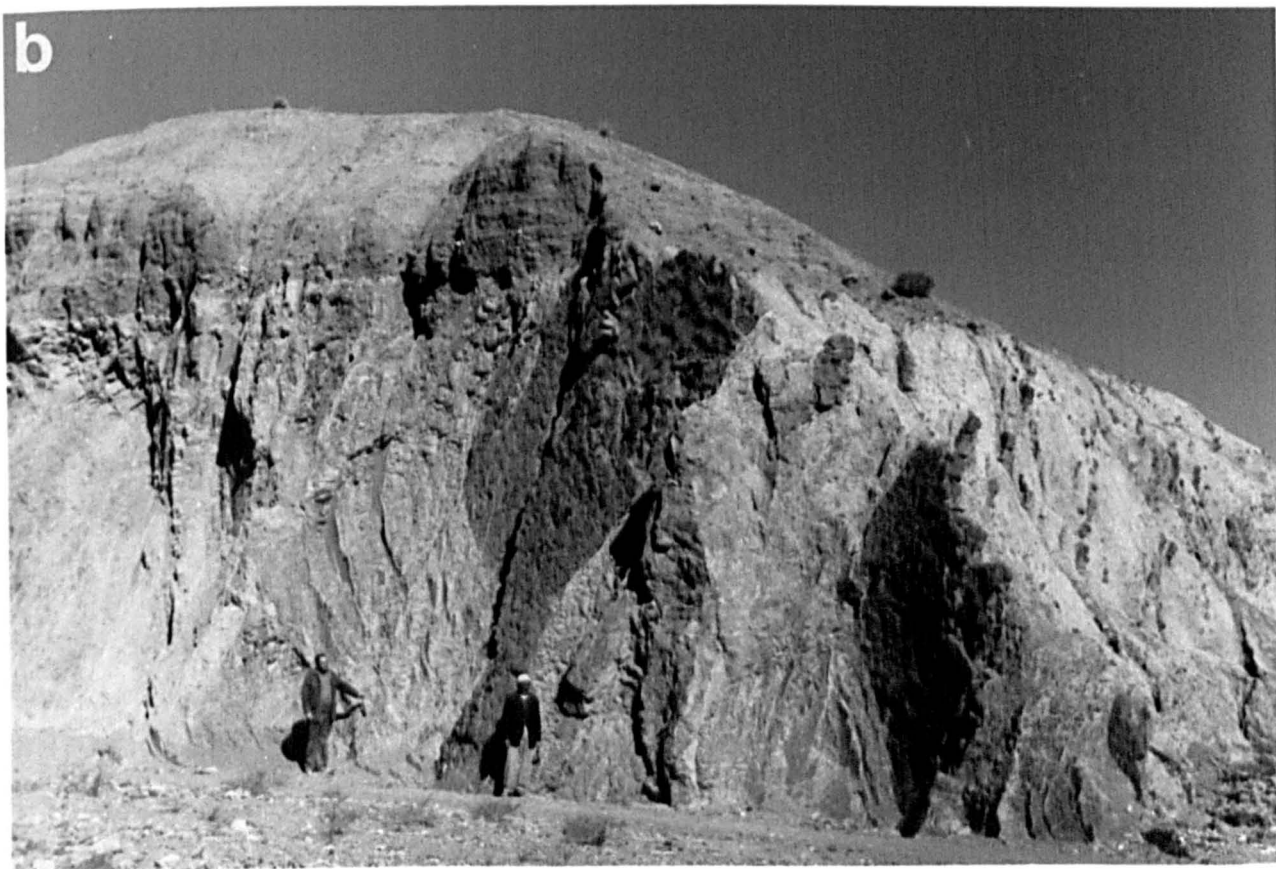
Thick layers of paleocene non-carbonate flysch sediments principally include green shale and sandstones which have been slightly metamorphosed and folded. These flysch sediments are located to the west of Torshak magnesite deposit.

PLATE 2

a



b



3.5 Magnesite deposits of eastern Iran

3.5.1 Regional geology

A geological map of the area around the magnesite and huntite deposits, extracted from 1/250,000 scale, metallogenic map of south east Iran is shown in Figure 3.3. The area is almost exclusively within the Flysch and Ophiolite-Melange belt of eastern Iran and is situated in Khorasan Province, about 170 Km south east of Birjand, not far from the border with Afghanistan (Figure 3.2).

The most important formation which is exposed in the area consists of Upper Cretaceous strata. They include various flysch type formations (Plate 2a, b), volcanic, ophiolitic units, and metamorphic rocks. The major fault zone of the area has a trend of NNW - SSE. These faults are still active and, as a result of this activity, limonitisation, slickenside and fault mylonites in this area are quite visible (Plate 3a).

The sedimentary rocks of the Melange which are partly folded and metamorphosed are largely identical with those forming the bedded Flysch successions. The rocks are argillaceous and silty shales and sandstones of green-grey colour, green radiolarite and dense pink pelagic limestone and micro conglomeratic layers. Slight phyllitization has also affected the Flysch type shales and tuffs (Plate 3b).

The igneous components comprise ultrabasic rocks, mainly serpentized peridotite and serpentinite (Plate 1a).

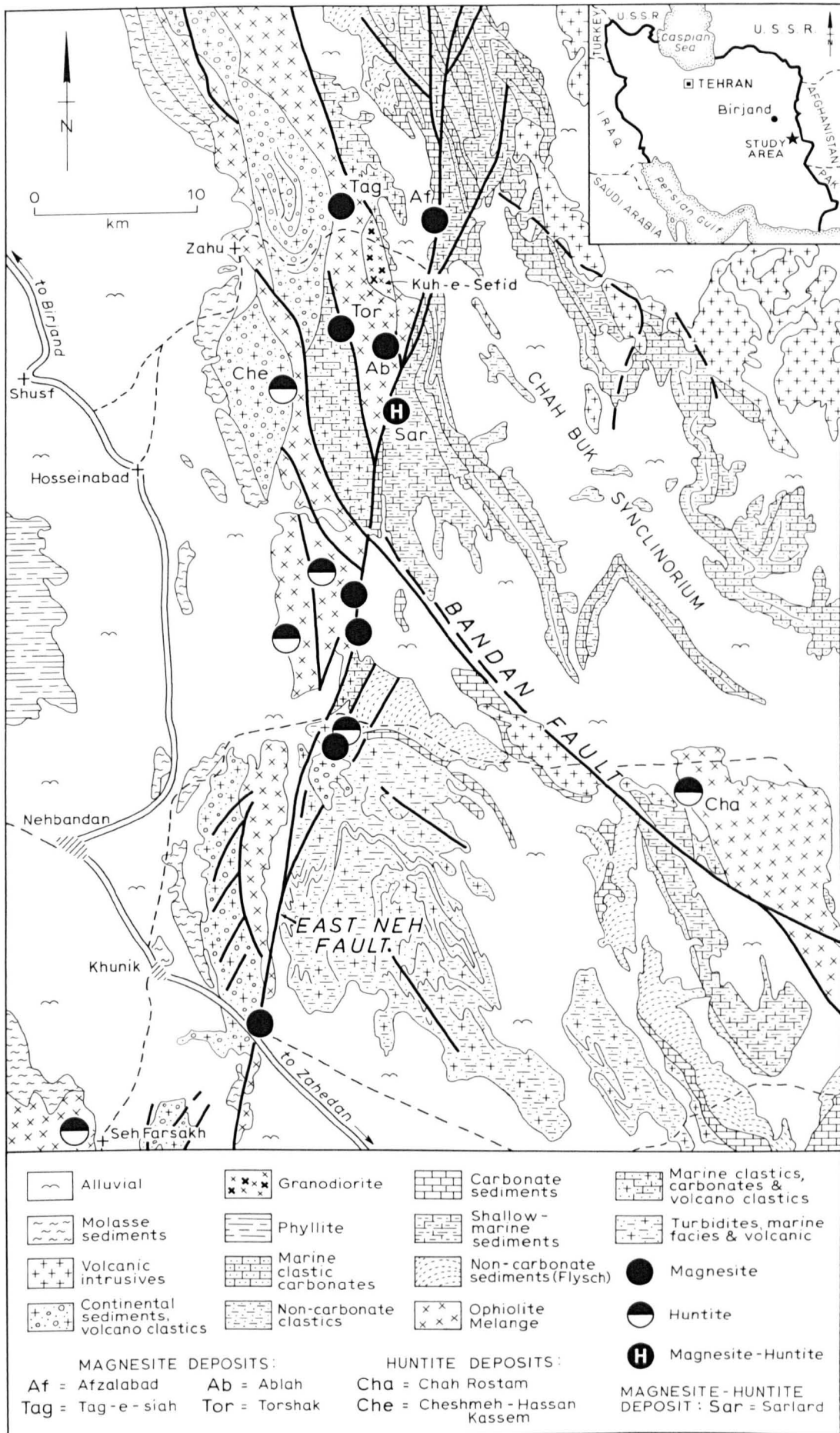


Figure 33 Geological map of the Nehbandan area
(after Geological Survey of Iran)

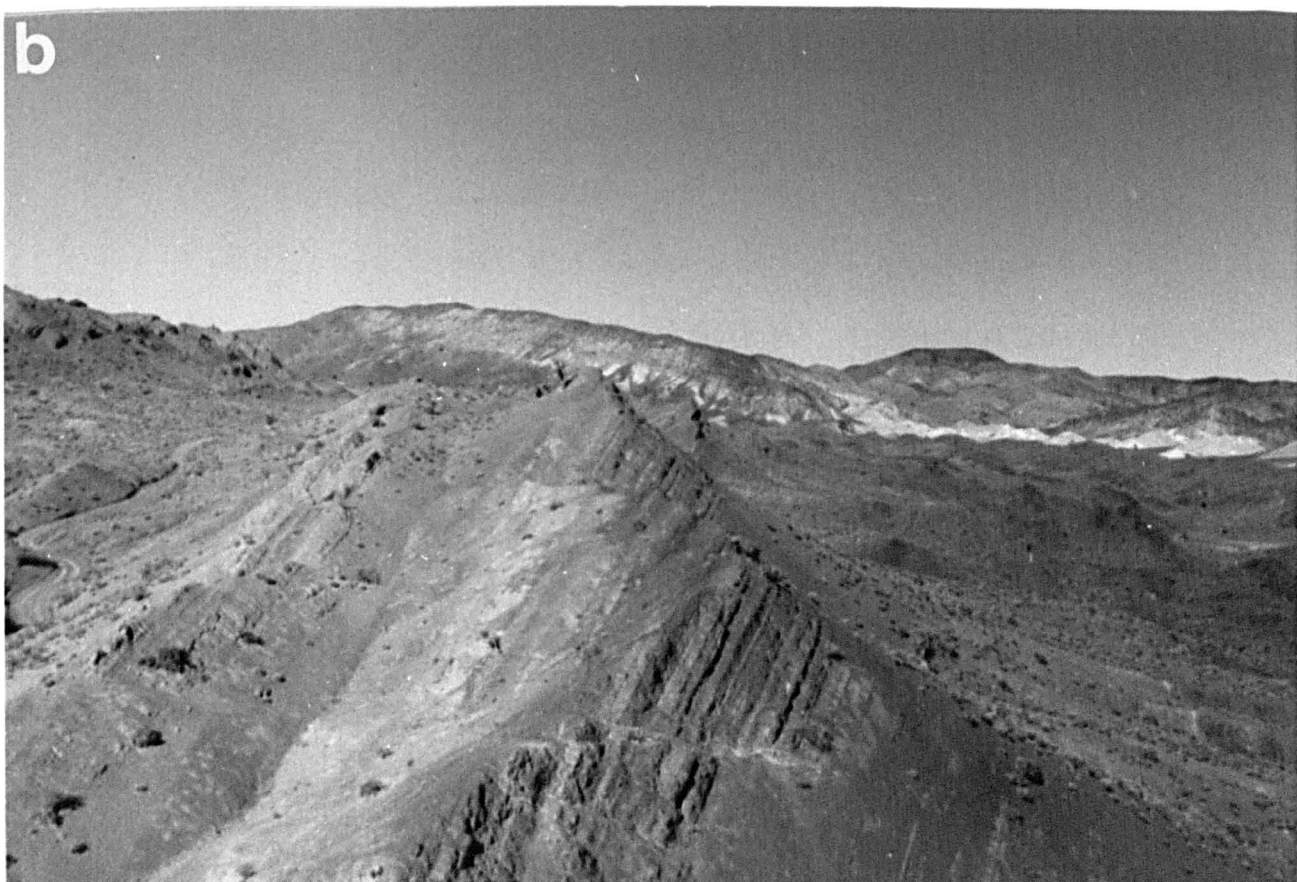
PLATE 3.a

Flysch type sediments have been highly broken near the main fault zone. These formations show great limonitisation. Also fault mylonite and slickenside are quite visible near major faults zones which have a trend of N-NW and S-SE.

PLATE 3.b

View looking south to the Oligocene - Miocene continental sediments, volcanoclastics and volcanic flows, including greenish - grey shales, silts, sandstone, conglomerate, and alkali rich volcanics. These sediments are located to the north west of Torshak magnesite deposit. The normal strike and dip of these sediments are N5°W, 45°SW.

PLATE 3



3.5.2 Description of magnesite deposits

In the south east of Birjand, numerous magnesite deposits have been recognised by the Geological Survey of Iran and the Iran Magnesia Company. According to their unpublished reports, these deposits together have approximately 5.1 million tonnes of magnesite. Figure 3.4 shows the location of these deposits. The two important and largest magnesite deposits (Torshak and Afzalabad) have been chosen for this study. The investigated occurrences are located in the north east of Shusf (village) approximately 170 Km south east of Birjand. Geological maps of Torshak and Afzalabad magnesite deposits are presented in Figures 3.5 and 3.6).

3.5.2.1 Torshak magnesite deposit

This deposit is situated approximately 170 Km south east of Birjand, at 1650 metre altitude from sea level. (Longitude : $60^{\circ}, 15'$ and latitude : $31^{\circ}, 49'$) (Figure 3.5).

At first sight the deposit gives the impression of massive, widespread mineralisation of magnesite which covers about one Km^2 , where presumably a quality in the range of 95% MgO can be expected (Plate 4a, b). Some parts of the deposit have been eroded under the influence of the desert climate, and loose magnesite typically occurs in the top part of a cryptocrystalline magnesite deposit, which covers the whole area (Plate 5b). According to Keyvanfar (1987), the total estimated reserves of the deposit are 1,545,996 tonnes of

magnesite.

The ultrabasic body, which here belongs to the Upper Cretaceous is the oldest formation in the area, and consists mainly of peridotite and serpentinite. This body is the host rock for the magnesite deposits. It has a tectonised boundary with the younger and slightly metamorphosed flysch sediments, which belong to the Upper Cretaceous to Middle Eocene. Flysch sediments are made of grey shale and sandstone, with red and yellow marls.

The generation of magnesite started after the Middle Eocene, and the deposit is positioned on top of flysch sediments. In addition magnesium rich solutions have filled all the empty spaces and cracks within the sediments (Plate 5a). The shape of this deposit is lenticular which is formed within the flysch sediments. Finally some parts of deposit are covered by the Quaternary sediments.

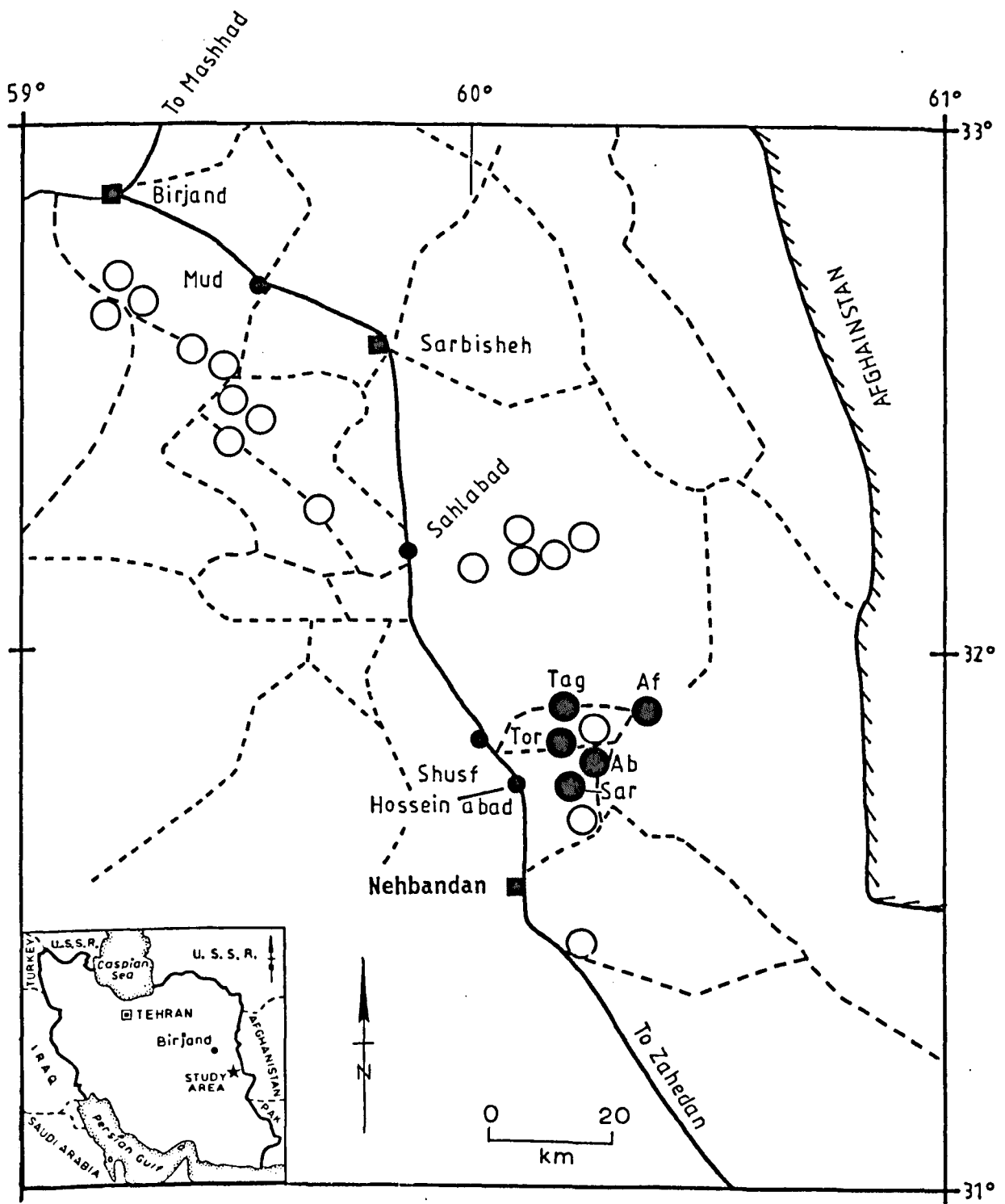
The main development of the deposit has taken place near the surface, and a maximum of 25 metres depth for magnesite in this deposit have been reported (Keyvanfar, 1987)

Two main fault zones, which controlled the development of magnesite have been recognised in the Torshak magnesite deposit area:

1. East Nehbandan fault, with the direction of NE - SW.
2. Kuh-e-Sefied fault, with the direction of NW - SE.

These faults are approximately vertical and cut all the formations (Figure 3.3).

Flysch sediments in the area have a general strike direction of NW - SE with a range of dip between 65-90



- = magnesite deposits
 - = Studied magnesite deposits
 - Tor = Torshak magnesite deposit
 - Af = Afzalabad magnesite deposit
 - Tag = Tag-e-siah magnesite deposit
 - Ab = Ablah magnesite-dolomite deposit
 - city
 - village
 - major road
 - - - minor road
- Sar = Sarlard magnesite-huntite deposit

Figure 3.4 Sketch map showing magnesite deposits of eastern Iran (Birjand-Nehbandan area)

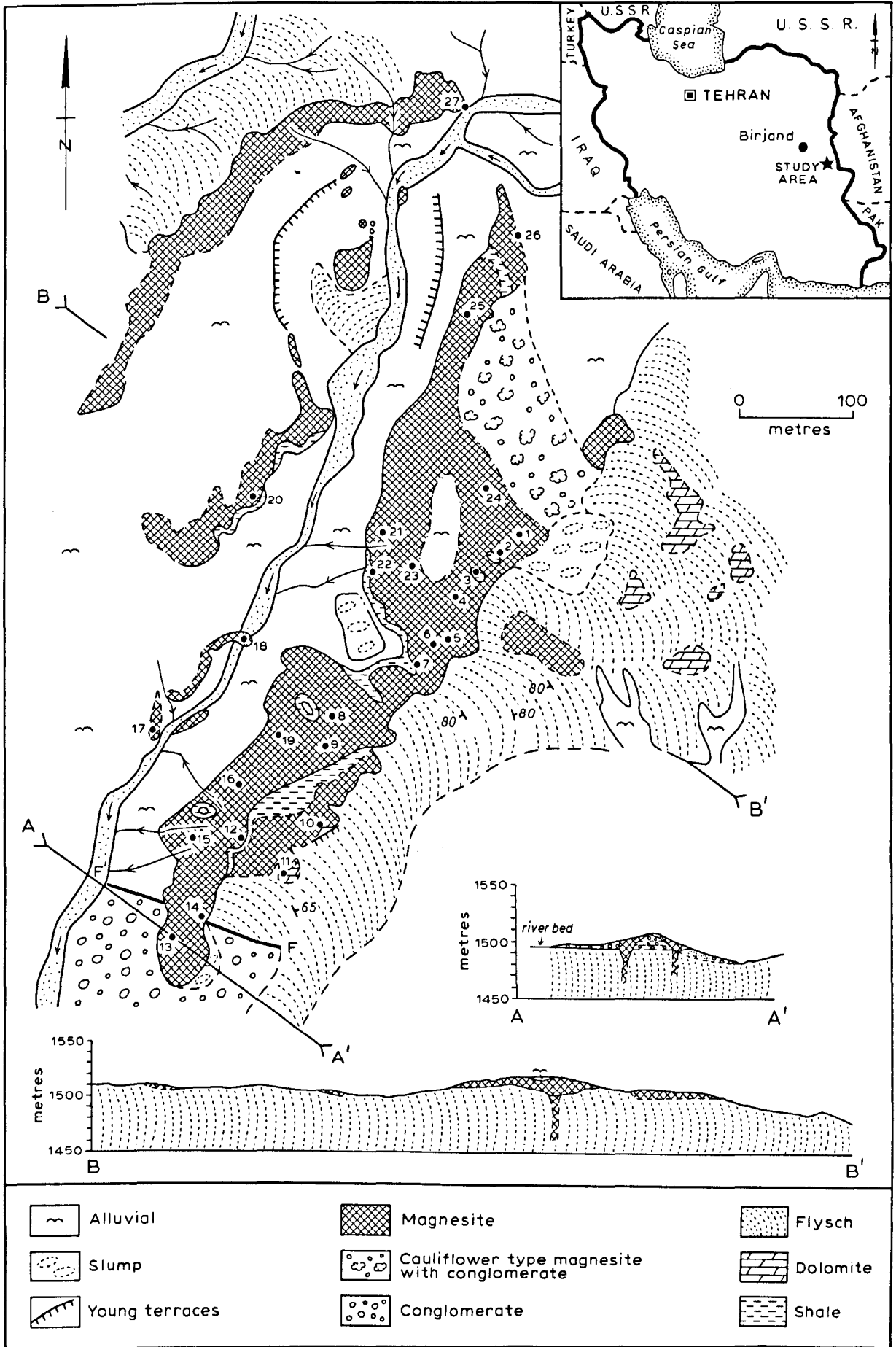


Figure 5 Geological sketch map of the Torshak magnesite deposit

PLATE 4.a

The Torshak magnesite deposit occurring in the form of lenses and beds in the country rocks, which consist mainly of dolomite, shale, and sandstones. This magnesite deposit presumably belongs to the hydrothermal - sedimentary type deposits. A characteristic feature of this type of deposit is that they are usually large. The magnesite is associated with ultramafic rocks such as serpentinite.

PLATE 4.b

Closer view of Torshak magnesite deposit which shows in detail the main ore body and the country rocks. The main magnesite body is deposited between the flysch type sediments such as green shales (foreground), sandstone, dolomite, and conglomerate. The main ore body is younger than Neogene conglomerates.

PLATE 4



PLATE 5.a

Closer view to the Neogene conglomerate situated on top of flysch sediments (see plate 4.b). This conglomerate contains some pebbles of magnesite, but as is visible in plate 4.b, the main ore body is deposited on the top of this conglomerate. The magnesium rich solution filled all of cracks, pores and any empty spaces within this conglomerate. These are strong evidence that there are several generations of magnesite in the area. Magnesite formation presumably started in late Upper Cretaceous - early Tertiary.

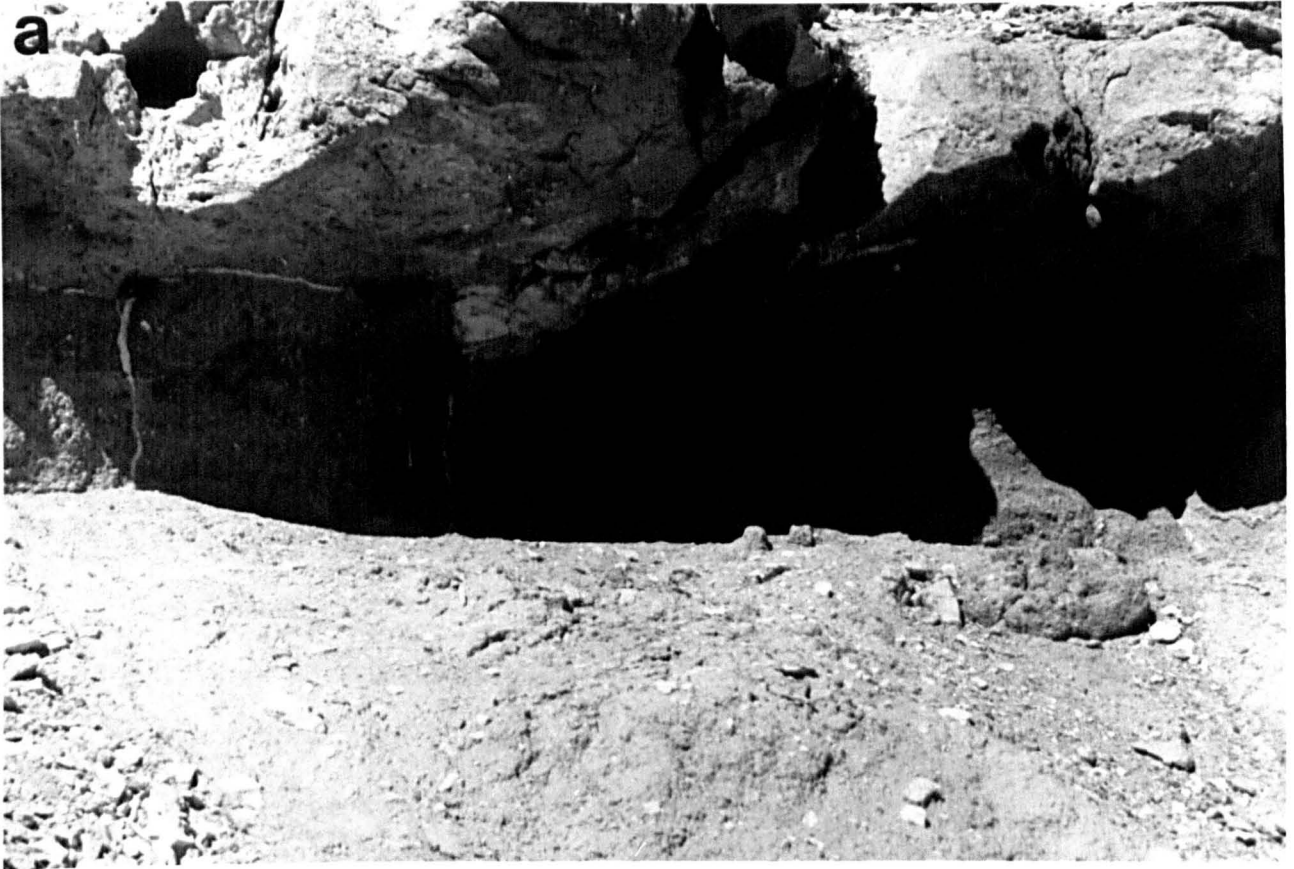
PLATE 5.b

Common view of desert climate weathering. A considerable parts of Torshak deposit has been heavily eroded. Loose magnesite, which is the best quality, and typically occurs in the top parts of Torshak magnesite deposits cover the whole area.

The ultrabasic body which is mainly of serpentinised peridotite and serpentinite is believed to be the host rock for this deposit.

PLATE 5

a



b



degrees.

Magnesite in this deposit lies on the flysch sediments, and partly covered by the Quaternary continental sediments.

3.5.2.2 Afzalabad magnesite deposit

This deposit occurs north east of Shusf (village), approximately 170 Km south east of Birjand, at 1650 metres altitude (longitude : 60°, 17' and Latitude : 31°, 52').

Magnesite in this deposit occurs as a massive vein approximately 1000 metres long and maximum 8 metres wide (Figure 3.6), between the ophiolite body and flysch sediments. The magnesite vein extends parallel to the regional north south strike with nearly vertical dip. Views of the Afzalabad magnesite vein are shown in Plates 6b.

Magnesite veinlets which are later than the main vein, cut the ultrabasic rocks (serpentinite) and flysch in all directions. The veinlets range in size from a few millimetres up to 30-40 centimetres. According to Keyvanfar (1987) the total estimated reserves of the deposit are 692,881 tonnes of magnesite.

The magnesite is snowy white, very compact, dense, cryptocrystalline and sometimes has a conchoidal fracture surface. (Plate 7).

In the Afzalabad area the following formations can be recognised:

1. The ultrabasic rocks, which include peridotite, serpentinite and ophicarbonates, are the oldest formations. These belong to the Upper Cretaceous. The

boundary of these ophiolites with the younger rock units is tectonised.

2. The second oldest rock units are the metamorphosed sediments; green and yellow shales together with some limestone, which belong to the Upper Cretaceous and are situated to the west of deposit.
3. Flysch sediments such as shale, siltstone, sandstone and limestone which are belong to Upper Cretaceous to Paleocene and situated to the east of deposit.
4. Eocene limestone situated to the west of Afzalabad dry river bed.
5. Quaternary and river sediments.

The Afzalabad magnesite deposit is an excellent example of a vein type deposit (Plate 6b). The magnesite vein has a complex internal structure, resulting from the crystallization of several generations of magnesite.

The tectonic activity in Afzalabad area started during the Upper Cretaceous and continued after several generations of magnesite formation. As a result, the deposit is highly broken and slickensides can be observed on the surface of the magnesite vein (plate 6a, b).

3.6 Sampling and sample location

Magnesite specimens were collected from both Torshak and Afzalabad deposits as representative of the occurrences. Neither deposits have been worked on a commercial scale. Sampling of Torshak magnesite deposit was carried throughout the body, while at Afzalabad, the vein was sampled along its

length. Host rock samples were also collected from near the magnesite mineralisation.

In this study samples collected from Afzalabad and Torshak occurrences are numbered from (A1-A14) for Afzalabad, and (T1-T27) for Torshak magnesite deposits. The location of all samples can be found on the Figures 3.5 and 3.6, (numbers 1-14 for Afzalabad, and 1-27 for Torshak magnesite deposits). Representative magnesite hand specimens photograph and their descriptions are presented in Plate 7.

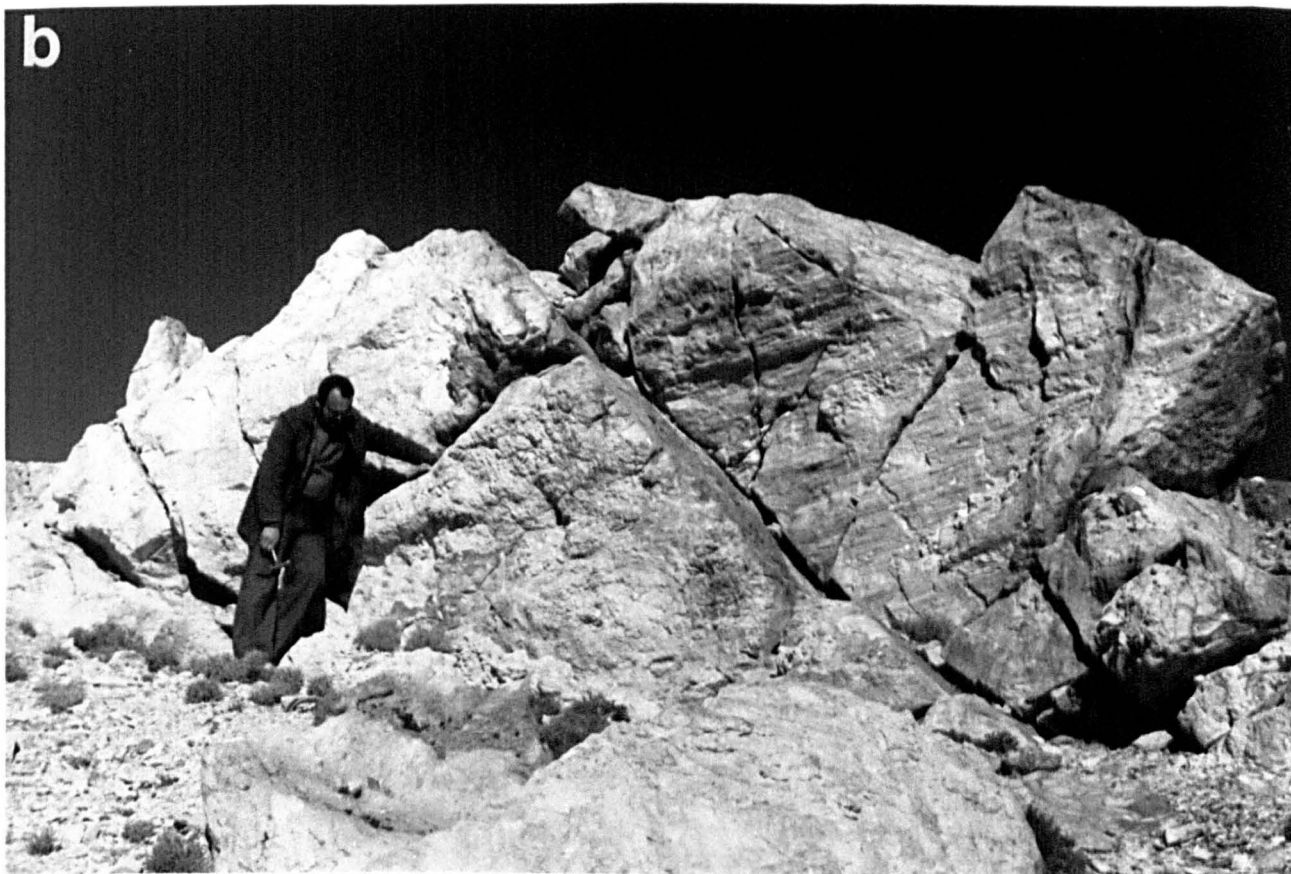
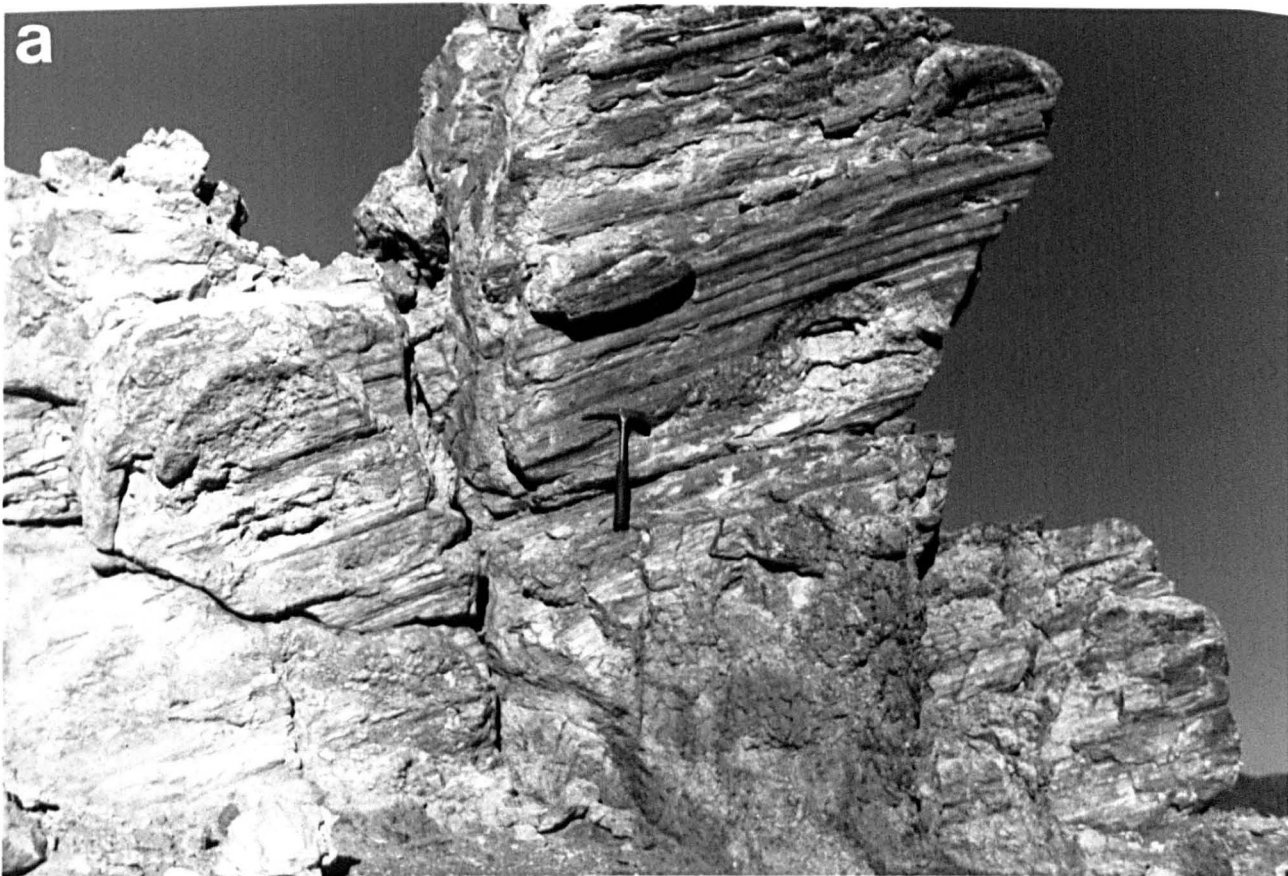
PLATES 6.a, b

Typical views of vein type magnesite deposits (Tag-e-Siah, and Afzalabad deposits). These deposits belong to the hydrothermal - vein type magnesite deposits which occur in the form of veins and veinlets (stock works) in the ultrabasic rock masses, mostly of serpentinite and peridotite.

Magnesite in these deposits are usually snowy white in colour, cryptocrystalline, very dense and of conchoidal fracture. This type of deposit is always closely associated with fault zones. As a result these deposits are highly broken and slickensides can be observed on the surface of magnesite veins. These deposits have a great length, thickness and vertical extent.

The major fault zone in this area is the eastern Iranian fault zones (Nehbandan fault branches) which are still active, with the normal strike and dip of N-S, 75-85° W. The host rocks for this deposits are peridotite and serpentinitized peridotite.

PLATE 6



3.7 Chemical composition of natural magnesite from Iran

3.7.1 Introduction

The chemical composition of 40 natural magnesite samples collected from the Torshak and Afzalabad deposits, Khorasan province of eastern Iran, was determined using a Philips PW 1212 automatic X-ray fluorescence spectrometer (XRF). The XRF technique was chosen because it is rapid compared to the wet chemical methods. Major and minor oxides (SiO_2 , Al_2O_3 , TiO_2 , Fe_2O_3 , MgO , CaO , Na_2O and K_2O) were analysed using pressed powder pellets. Previously analysed magnesites (Kimyongur, 1984) were used in obtaining calibration curves. Details of the method of sample preparation, determination of calibration factors and instrumental conditions are outlined in Appendix 2. The loss on ignition at 1000°C was also measured for each samples as an indication of the amount of CO_2 present. The method is described in Appendix 8.

3.7.2 Factors affecting analysis by X-ray fluorescence spectrometry

In XRF analysis the intensity of the characteristic radiation emitted by the sample in response to excitation by high energy X-rays is a measure of the concentration of the element. However the intensity of the emitted X-rays is also affected by the physical and chemical conditions of the sample. The most significant effect is the absorption of the X-rays in the sample. The greater this absorption, which

increases with the increased atomic weight of the elements combined in the sample, the more the characteristic X-rays are weakened. This is because the irradiating X-rays penetrate less into samples containing elements with high atomic weights. A second factor is that characteristic radiation emitted from some elements will in turn excite other elements to emission. These two influencing factors are known collectively as the inter-element effects. However, the standards used in this investigation have compositions close to those of the unknowns, essentially nullifying these effects.

3.7.3 Results

The chemical analyses, and loss on ignition values for the magnesites are presented in Table 3.1. Maximum, minimum, mean and standard deviations for each element in the two deposits are given in Tables 3.2 and 3.3.

In the following XRF analyses, the higher value of the total in those samples with higher percentages of silica is due to the difficulty of analysing MgO in pressed powder pellets.

Table 3.1 The bulk chemical composition of magnesite samples from Afzalabad (A) and Torshak deposits of eastern Iran

Sample	A1	A2	A3	A4	A5	A6	A7	A8	A9	A10
SiO2	0.06	1.19	0.08	0.17	0.23	4.43	1.39	0.77	0.47	2.45
Al2O3	0.02	0.16	0.01	0.02	0.01	0.03	0.05	0.00	0.01	0.01
TiO2	0.00	0.00	0.00	0.00	0.00	0.00	0.00	0.05	0.00	0.00
Fe2O3	0.50	0.87	0.49	0.73	0.78	0.65	0.92	0.52	0.30	0.30
MgO	43.90	45.10	45.93	45.43	45.02	44.41	45.19	46.06	46.03	45.08
CaO	2.79	0.74	0.24	0.16	0.54	0.89	0.54	0.15	0.34	1.59
Na2O	0.02	0.04	0.03	0.03	0.04	0.04	0.02	0.04	0.04	0.03
K2O	0.00	0.01	0.00	0.00	0.00	0.00	0.00	0.00	0.00	0.00
LOI	52.12	51.36	52.10	52.10	51.91	48.82	51.03	51.89	51.52	50.44
TOTAL	99.41	99.47	98.88	98.64	98.53	99.27	99.14	99.48	98.71	99.90

Sample	A11	A12	A14	T1	T2	T3	T4	T5	T6	T7
SiO2	0.29	0.21	3.12	0.27	0.99	0.13	0.77	2.96	0.65	6.18
Al2O3	0.02	0.05	0.96	0.06	0.01	0.01	0.15	0.53	0.08	0.37
TiO2	0.00	0.00	0.03	0.00	0.00	0.00	0.00	0.02	0.00	0.01
Fe2O3	1.25	0.85	0.30	0.01	0.00	0.00	0.04	0.17	0.01	0.10
MgO	44.91	45.31	43.85	45.46	43.79	46.37	45.86	44.28	45.64	43.06
CaO	0.64	0.64	2.24	1.96	2.51	1.55	1.80	1.90	2.17	3.12
Na2O	0.06	0.03	0.14	0.03	0.04	0.11	0.00	0.07	0.02	0.04
K2O	0.00	0.01	0.18	0.01	0.00	0.00	0.03	0.09	0.01	0.07
LOI	51.78	51.97	49.90	51.63	51.45	51.68	51.25	49.98	51.39	48.29
TOTAL	98.95	99.07	100.72	99.43	98.79	99.85	99.90	100.00	99.97	101.24

Sample	T8	T9	T10	T11	T12	T13	T14	T15	T16	T17
SiO2	0.28	0.58	0.17	2.18	2.17	4.29	7.79	5.41	0.71	1.29
Al2O3	0.05	0.11	0.01	0.40	0.31	0.01	0.01	0.01	0.22	0.35
TiO2	0.00	0.00	0.00	0.02	0.01	0.00	0.00	0.00	0.01	0.01
Fe2O3	0.01	0.02	0.00	0.12	0.08	0.00	0.00	0.00	0.05	2.12
MgO	44.78	45.65	43.96	44.94	45.69	44.73	44.12	44.38	45.92	44.86
CaO	1.73	2.23	1.39	1.47	1.51	2.79	1.75	2.44	0.80	0.23
Na2O	0.04	0.05	0.03	0.06	0.05	0.04	0.03	0.04	0.33	0.23
K2O	0.01	0.00	0.00	0.08	0.06	0.00	0.00	0.01	0.05	0.07
LOI	51.90	50.95	51.77	50.54	50.19	49.07	47.88	48.58	51.98	51.07
TOTAL	98.80	99.59	97.33	99.81	100.07	100.93	101.58	100.87	100.07	100.23

Sample	T18	T19	T20	T21	T22	T23	T24	T25	T26	T27
SiO2	1.23	0.12	0.05	9.10	0.46	0.17	1.09	1.22	0.12	0.92
Al2O3	0.35	0.04	0.02	2.56	0.12	0.02	0.01	0.17	0.02	0.01
TiO2	0.02	0.00	0.00	0.08	0.00	0.00	0.00	0.00	0.00	0.00
Fe2O3	0.09	0.00	0.00	0.64	0.04	0.00	0.00	0.04	0.00	0.00
MgO	46.14	46.49	45.19	41.22	45.07	46.75	45.37	45.19	46.58	44.60
CaO	1.16	0.94	0.81	2.45	2.33	0.81	2.03	2.22	1.33	2.58
Na2O	0.15	0.02	0.30	0.10	0.05	0.03	0.04	0.03	0.04	0.41
K2O	0.06	0.01	0.01	0.40	0.03	0.00	0.00	0.03	0.00	0.01
LOI	51.07	52.06	52.34	45.44	51.36	51.85	51.12	51.25	51.79	51.63
TOTAL	100.27	99.68	98.72	101.99	99.46	99.63	99.66	100.15	99.88	100.16

Table 3.2 Statistical presentation of 13 analyses of natural magnesite from Afzalabad deposit, analysed by XRF.

Oxides	Min	Max	Mean	SD
SiO ₂	0.08	4.43	1.14	1.38
Al ₂ O ₃	0.00	0.96	0.10	0.26
TiO ₂	0.00	0.05	0.007	0.02
Fe ₂ O ₃	0.30	1.25	0.65	0.29
MgO	43.85	46.06	45.09	0.72
CaO	0.15	2.79	0.88	0.82
Na ₂ O	0.02	0.14	0.04	0.03
K ₂ O	0.00	0.18	0.02	0.05
LOI	48.82	52.12	51.30	1.01

SD = Standard deviation

Table 3.3 Statistical presentation of 27 analyses of natural magnesite from Torshak deposit.

Oxides	Min	Max	Mean	SD
SiO ₂	0.05	9.10	1.90	2.48
Al ₂ O ₃	0.01	2.56	0.22	0.49
TiO ₂	0.00	0.08	0.007	0.02
Fe ₂ O ₃	0.00	2.12	0.13	0.42
MgO	41.22	46.75	45.04	1.19
CaO	0.23	3.12	1.78	0.70
Na ₂ O	0.00	0.41	0.09	0.11
K ₂ O	0.00	0.40	0.04	0.08
LOI	45.44	52.14	50.72	1.59

SD = Standard deviation

3.7.3.1 Major constituents:

3.7.3.1.a MgO

In the Torshak magnesite deposit MgO varies from 41.22% (T21) to 46.75% (T23), while in the Afzalabad deposit these vary between a minimum of 43.85% and a maximum of 46.06%.

The mean values of 45.09% for the Afzalabad deposit and 45.04% for the Torshak magnesite deposit are closely similar. There is a broad inverse correlation between MgO and CaO (Figure 3.7a).

3.7.3.1.b LOI

The LOI which includes CO₂ and other volatile constituents such as water ranges from 45.44% (T21) to 52.14% (T20), in Torshak deposit.

When magnesite is pure the LOI value is 52.2%. The presence of impurities such as silica (SiO₂) and lime (CaO) dilutes the magnesite. Samples with a higher percentage of silica, have higher percentages of lime (CaO). The relation between the amount of SiO₂, LOI, and MgO + CaO are presented in Figures 3.7c). The value of silica shows a close inverse correlation with LOI (Figure 3.7d).

The mean LOI in the Afzalabad magnesite specimens is higher (51.30%) than the mean value of LOI in samples from Torshak deposit (50.72%). This probably reflects an overall slightly higher impurity level (i.e. SiO₂ and CaO) in the Torshak deposit. The higher percentage of silica and lime is due to the formation of Torshak magnesite deposit within the

flysch sediments. According to the Geological Survey of Iran, Flysch sediments of eastern Iran have the following chemical composition:

SiO_2 = 60-65 (%)

Al_2O_3 = 10-15 (%)

Fe_2O_3 = 3-5 (%)

CaO = 3-5 (%)

MgO = 3-5 (%)

Na_2O = 1-2 (%)

K_2O = 1-2 (%)

3.7.3.2 Minor constituents

3.7.3.2.a CaO

Sample T7 has the highest CaO (3.12%), While samples T2, T13, T15, T21, T27, and A1 have relatively high values of CaO (more than 2.4%). Sample A8 has only 0.15% CaO. The mean value of CaO in Torshak magnesite deposit (1.78%) is higher than the Afzalabad deposit (0.88%).

3.7.3.2.b SiO_2

The silica content varies from a minimum value of 0.05% in sample T20 and a maximum value of 9.10% in sample T21. The Mean value of SiO_2 for Afzalabad magnesite deposit (1.14%) is lower than Torshak deposit (1.90%). The silica content dilutes the magnesite. Samples with a higher percentage of silica, carry higher percentage of CaO (Figure 3.7a).

3.7.3.2.c Fe₂O₃

The highest percentage of Fe₂O₃ was obtained in sample T17 (2.12%). Fe₂O₃ is below the detection limit in samples T2, T3, T10, T13, T14, T15, T19, T20, T23, T24, T26 and T27.

The mean value of Fe₂O₃ for the Afzalabad deposit (0.65%) is higher than the Torshak deposit (0.13%). The higher percentage of Fe₂O₃ in the Afzalabad deposit is probably due to the close proximity of this deposit to a very active fault zone, in which activity continued after the formation of Afzalabad magnesite deposit (Plate 6, Figure 3.7e).

3.7.3.2.d Al₂O₃

The range of Al₂O₃ is very narrow. The mean value of Al₂O₃ in Afzalabad magnesite deposit is 0.1% while in Torshak deposit it is 0.22%. The higher percentage of Al₂O₃ in Torshak is due to formation of Torshak deposit within the Flysch sediments with a range of 10-15% Al₂O₃.

The percentage of the other minor oxides such as TiO₂, Na₂O and K₂O are very low. The mean values of TiO₂ in both deposits are similar and very low (0.007%). The mean percentage value of Na₂O and K₂O for Afzalabad is 0.04 and 0.02 which are nearly similar to Torshak deposit (0.09 and 0.04 percentage).

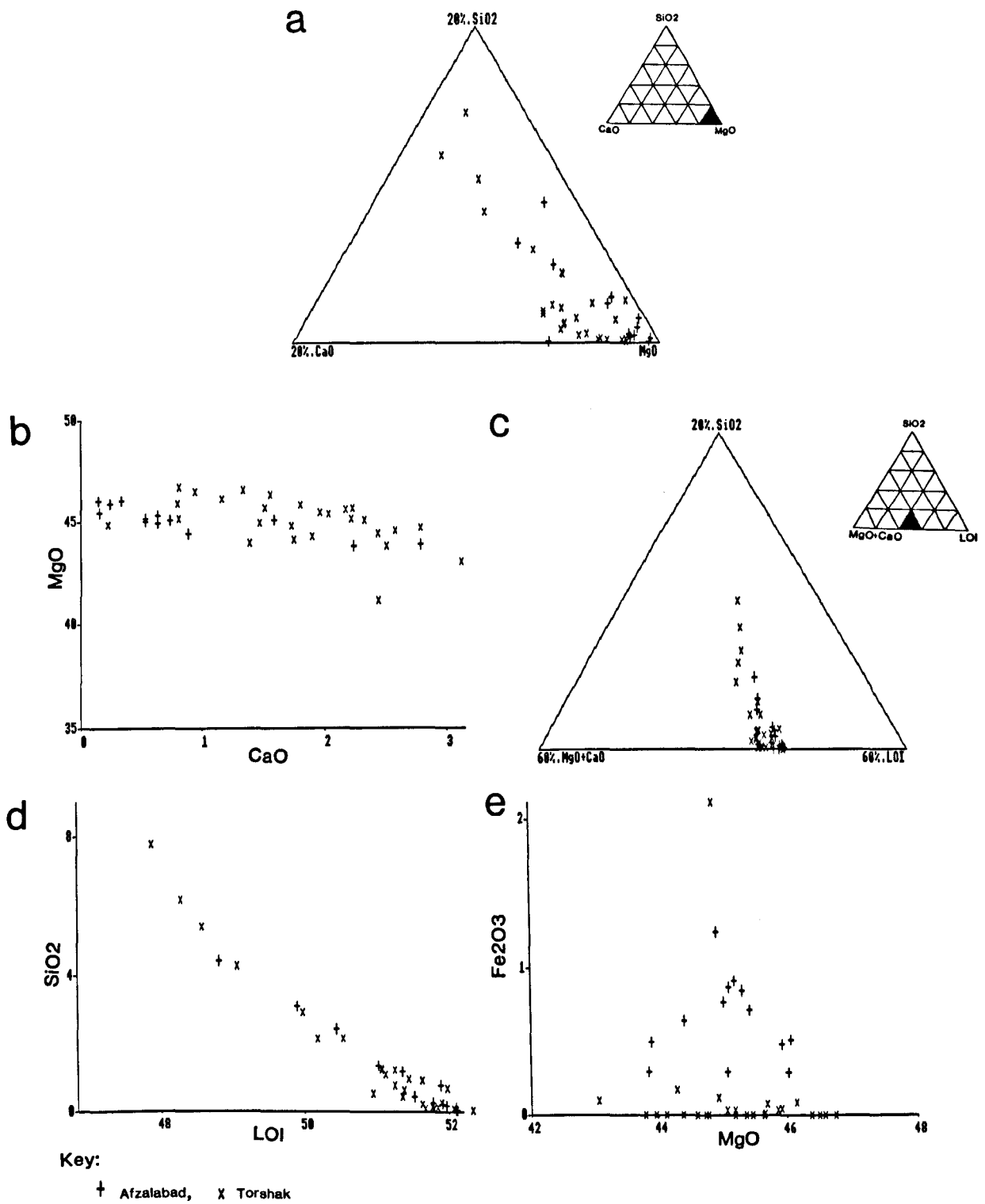


Figure 3.7 Plots to show the chemical variation in magnesite from the Afzalabad and Torshak deposits

3.8 Mineralogy and petrography

The mineralogy and petrography of the natural magnesites have been determined using the following techniques:

1. Hand specimen description.
2. Thin section description using optical microscope.
3. X-ray diffraction (XRD).
4. Scanning electron microscopy (SEM).
5. Electron microprobe analysis (EPMA).

Representative magnesite hand specimen photographs and their descriptions are presented in Plate 7. Complete hand specimen descriptions of all samples are presented in Appendix 1.

3.8.1 Experimental

polished thin sections of the natural magnesite and their host rock were prepared for the optical microscopic investigation, scanning electron microscopy and electron microprobe. For the SEM and EPMA the natural magnesite polished thin sections were coated with a thin layer of carbon (approx. 200 Å) prior to analysis.

3.8.2 Petrographic description

3.8.2.1 Magnesite

Microscopic study shows that the most of magnesites are compact, cryptocrystalline and have a very fine uniform texture. The magnesite crystals are of very similar sizes (1-5 μ m) especially in the Afzalabad deposit. Two or three generations of magnesite have been found. Some of the narrow

veins are displaced as a result of faulting after the formation of magnesite (Plate 8F).

In the Afzalabad magnesite deposit, larger magnesite crystals have been found in fissures, holes and other spaces between the compact and very fine grained magnesite (Plate 8d).

The examination of thin sections of natural magnesite specimens from Torshak deposit shows they are uniform and not many veinlets of secondary magnesite have been observed in comparison with Afzalabad deposit (which is situated very close to the major fault zone).

Traces of quartz and dolomite are present in magnesites from both Torshak and Afzalabad deposits. Quartz grains are observed in fissures as individual crystals. Optical micrographs of natural cryptocrystalline magnesite specimens and their descriptions are presented in Plate 8.

3.8.2.2 Host rock

Optical microscopic investigation of host rocks in Torshak, Afzalabad and Tag-e-Siah magnesite deposits shows altered olivine and serpentine. In places, serpentinite is cut by veinlets of magnesite, quartz, calcite, and dolomite. The hand specimens of serpentinites are green to dark bluish green in colour and contain in addition to serpentine, appreciable amounts of olivine. The presence of olivine in these specimens indicates incomplete alteration of dunite to serpentinite, (Plate 9a).

PLATE 7

Hand specimen photographs of natural magnesites from Iran and their host rock, (serpentinite).

- a) Conchoidal fracture surface of white cryptocrystalline magnesite, (sample T3).
- b) Very pure, white and cryptocrystalline magnesite, (cut surface of sample T14).
- c) Conchoidal fracture and cauliflower structure in natural cryptocrystalline magnesite, (sample T21).
- d) Earthy luster (soily), and white cryptocrystalline magnesite, (sample T22).
- e) Highly broken natural magnesite as a result of active tectonism, (sample T25).
- f) Different generation of magnesite. The magnesite in the darker patches contain iron oxides, but the whiter areas do not contain any iron, (sample A12).
- g) Magnesite with small amounts of host rock, (serpentinite) which is the darker patches, (sample A14).
- h) Dark green serpentinite as a host rock of magnesite.

PLATE 7

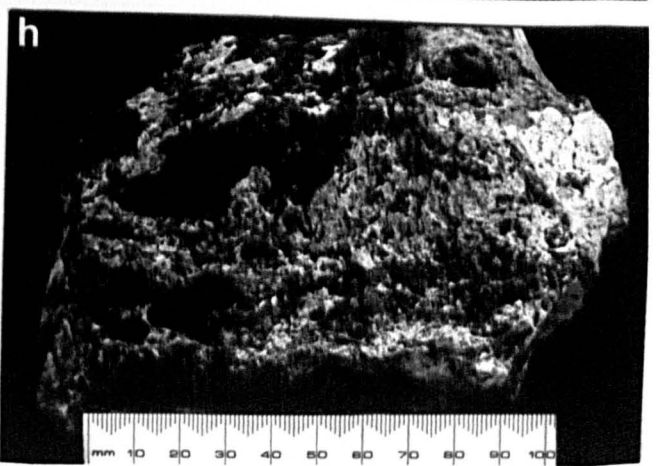
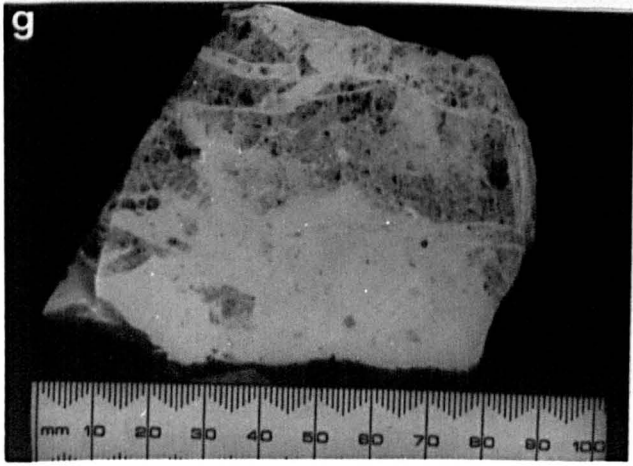
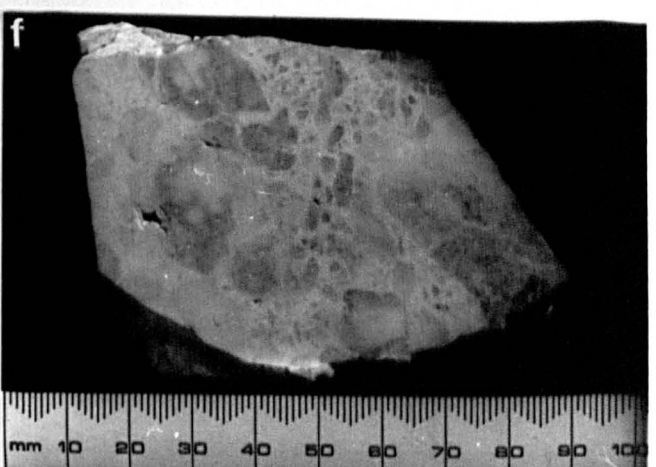
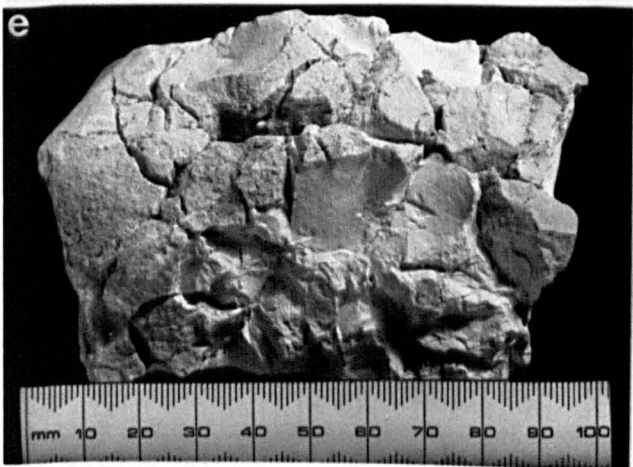
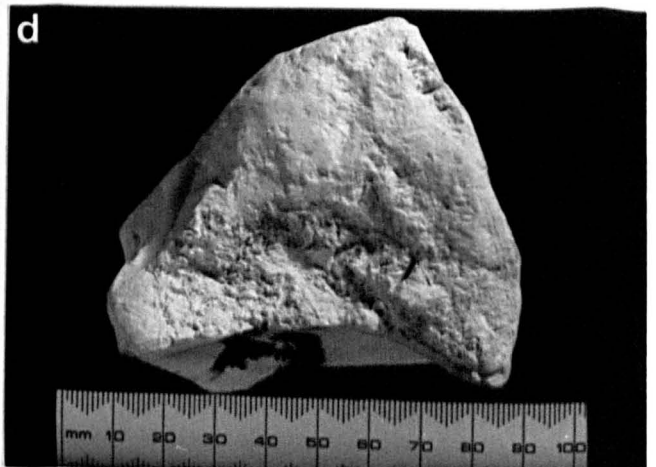
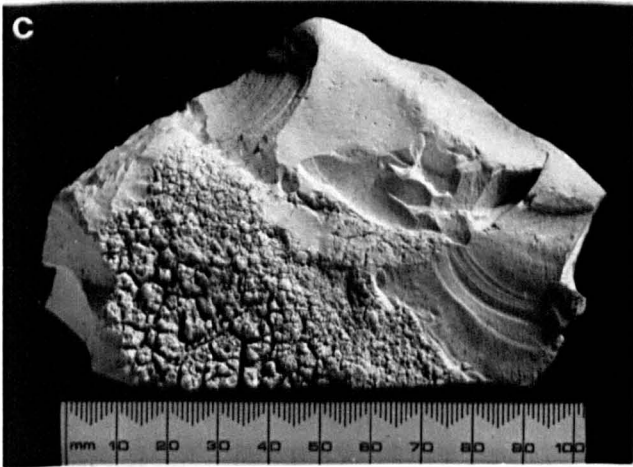
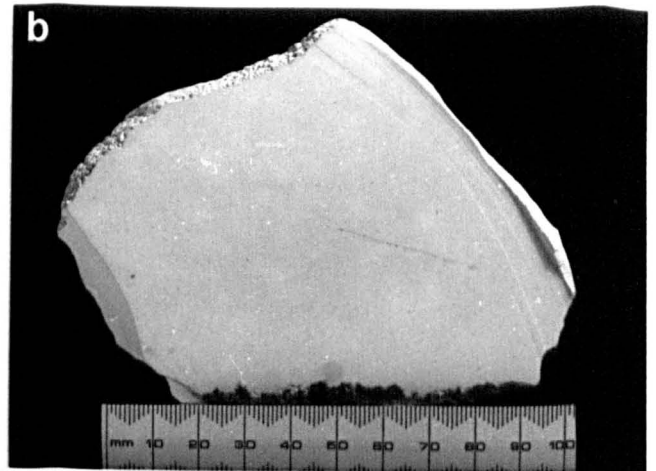
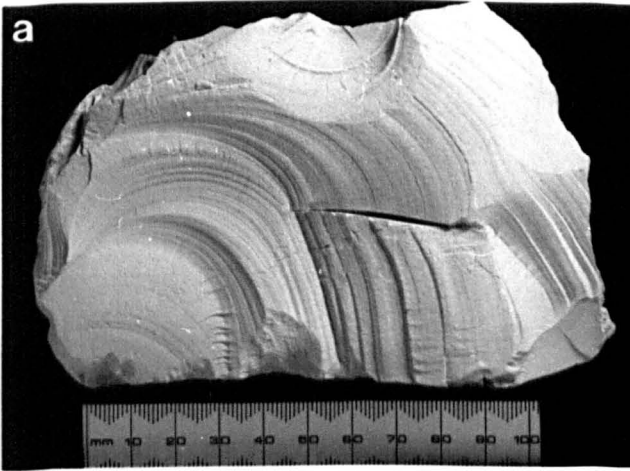


PLATE 8

Transmitted light micrographs of cryptocrystalline magnesite from Iran. All photographs have been taken under crossed polars.

- a) Uniform, granular texture of cryptocrystalline magnesite.
- b) Two generation of magnesite. Previously formed magnesite fragments are broken probably as a result of active tectonism. These broken particles are cemented with magnesite of a second generation.
- c) Coarse radial growth of magnesite lining small cavities.
- d) Coarse magnesite crystals developed in a fissure veinlet within cryptocrystalline magnesite.
- e) Several generation of magnesite showing earlier formed magnesites cut by later and purer magnesite veinlets.
- f) Magnesite veinlets showing fracturing probably as a result of tectonism. The fracture has subsequently healed. The whiter magnesite contains some Fe oxides.
- g) Radial growth of magnesite crystals.
- h) Detail of radial growth in magnesite.

PLATE 8

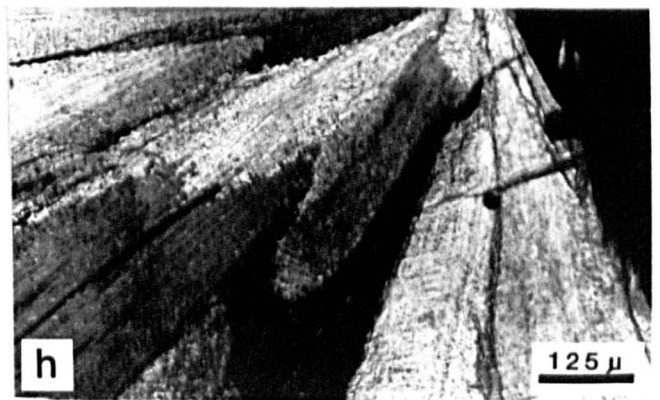
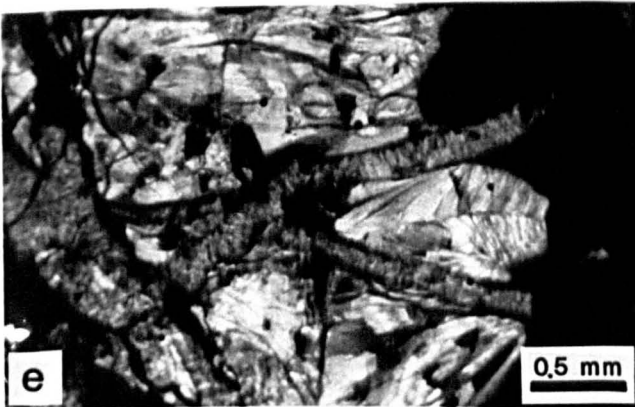
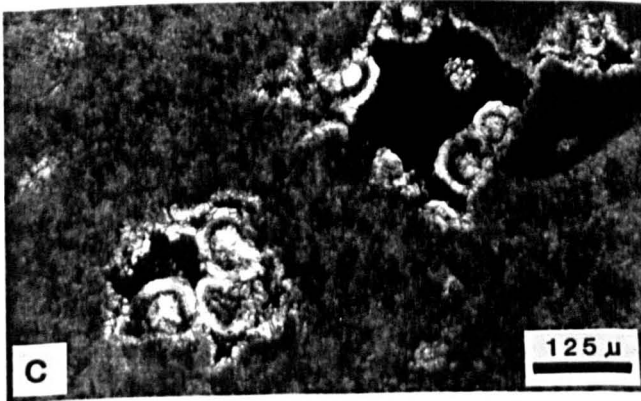
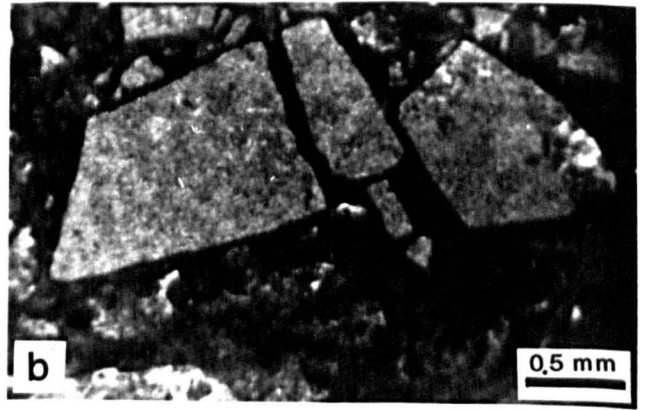
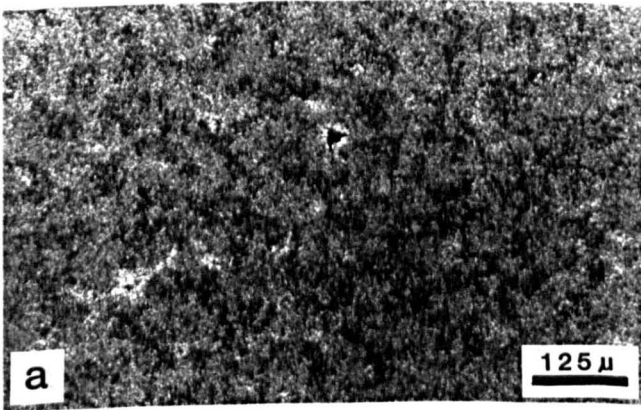
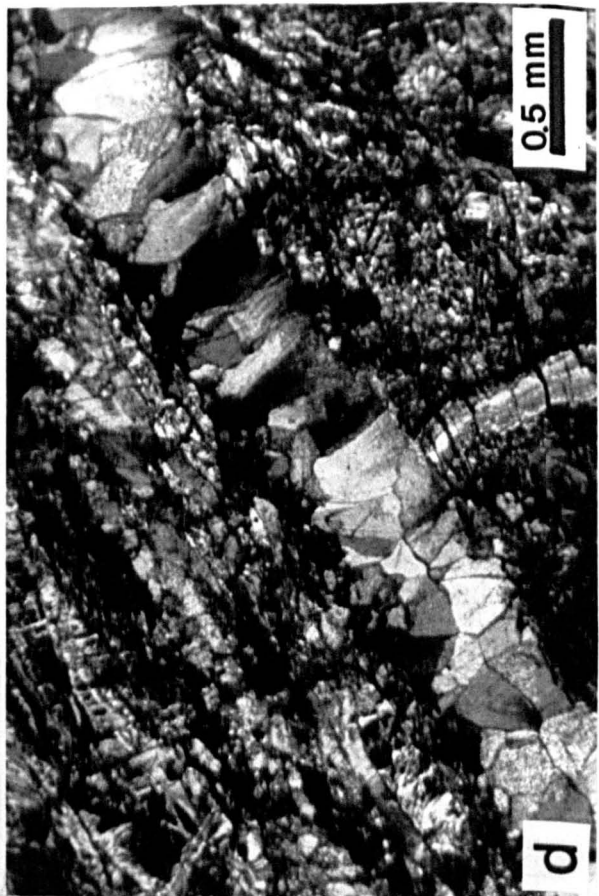
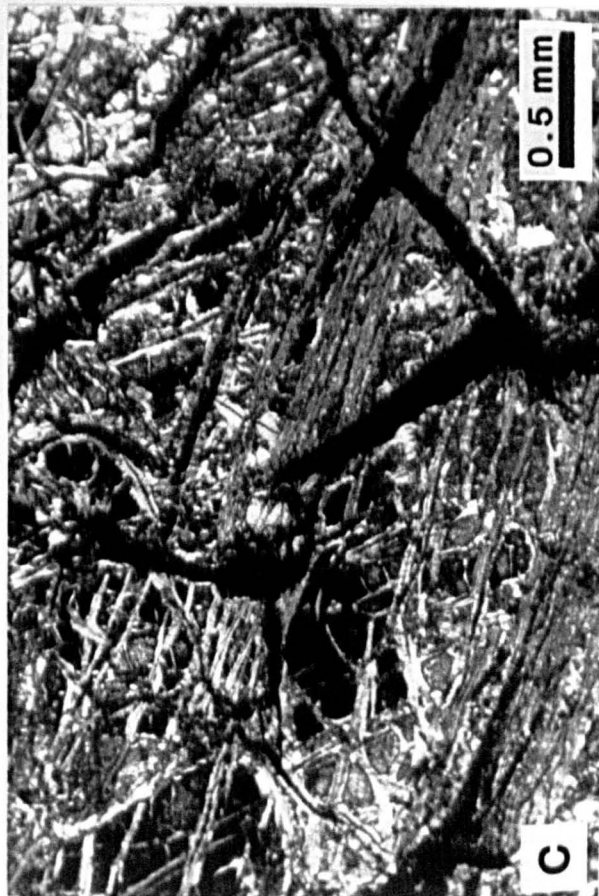


PLATE 9

Transmitted light micrographs of serpentinite (magnesite host rocks) showing different stages of alterations from olivine (a), to a mixture of olivine and serpentine (b), to serpentine (c), and magnesite veinlets (d). All photographs have been taken under crossed polars.

- a) Original olivine grains show striations possibly due to high oxidation. Most of the altered material is serpentine.
- b) First stage of alteration of olivine, showing both oxidized olivine and the alteration product (serpentine) together.
- c) Typical serpentinite with no residual olivine or development of magnesite.
- d) Magnesite in the form of veinlets within serpentinite.

PLATE 9



3.8.3 X-ray diffraction

X-ray diffraction was used for qualitative analysis. This technique identifies minerals on the basis of their crystal structure. As each mineral has a unique crystal structure with individual interplaner spacings (d), incident X-rays satisfy the Bragg equation of $n\lambda=2d \sin\theta$ at different angles of incidence (θ). By identifying the angles at which reflections occur it is possible to relate these angle to the (d) spacing in a crystal. This phenomenon forms a basic experimental procedure for identifying minerals.

3.8.3.1 Sample preparation

The particle size suitable for X-ray diffraction work is less than 40 microns (Zussman, 1977). In order to achieve a similar size range for the natural, caustic calcined and dead burned magnesite specimens, the samples were first crushed by fly press to less than 2 cm, and then hand ground in an agate pestle and mortar.

3.8.3.2 Instrumental

Ni filtered, CuK-alpha radiation was used for all analyses on a Philips X-ray diffraction unit in the range of $5-60^\circ 2\theta$. Operation conditions as shown below:

tube current	40 Kv, 30 mA
count rate	1×10^3 cps
time Constant	4 seconds
scanning speed	$1/2^\circ 2\theta/\text{min}$
chart speed	10 mm/min

3.8.3.3 Results

A list of minerals identified by XRD in samples from Afzalabad, Ablah and Torshak magnesite deposits are given in Tables 3.4 and 3.5. Figure 3.8. shows representative X-ray diffraction traces of different samples, where A4 is pure magnesite from Afzalabad deposit, T21 is magnesite with some impurities from Torshak deposit, Ab1 is a natural mixture of magnesite and dolomite from Ablah deposit and A13 is dolomite.

The peak positions were measured at half peak height above the background with a scanning range of $5-60^\circ 2\theta$ which encompasses the majority of peaks produced by the major minerals. The intensities (cps) are measured for the major reflection for each mineral.

All samples from Afzalabad, Ablah and Torshak magnesite deposits contain minor amounts of impurities. The main impurities which are present in majority of samples from all deposits are dolomite and chlorite, but also some other impurities such as quartz, calcite, mica and plagioclase are present to a minor extent in some samples.

Table 3.4 The mineralogy of Afzalabad and Ablah magnesite deposits as determined by XRD.

Sample	VS	S	MS	MD	MW	W	VW
A1	M	-	-	-	-	C	P, Ca
A2	M	-	-	D	-	C	-
A3	M	-	-	-	-	C	-
A4	M	-	-	-	-	C	Ca
A5	M	-	-	-	-	C	Ca
A6	M	-	-	D	-	C	Q
A7	M	-	-	-	-	C	Ca
A8	M	-	-	-	-	C	D, Mica
A9	M	-	-	-	-	C	Ca
A10	M	D	-	-	-	Q, C, Ca	Mica
A11	M	-	-	-	-	C, D	Ca
A12	M	-	-	-	-	C	Q, Ca
A13	D	-	-	-	-	-	-
A14	M	-	Q, D	-	-	C	Mica, P
Ab1	M	D	-	-	C, Ha	-	-
Ab2	M	D	-	-	Ha	c	-
Ab3	M	D	-	-	Ha	c	-

Where:

VS = very strong (>1000 cps).

S = strong (250-1000 cps).

MS = moderate strong (125-250 cps).

MD = moderate (62.5-125 cps).

MW = moderate weak (37.5-62.5 cps).

W = weak (12.5-37.5 cps).

VW = very weak (<12.5 cps), and minerals are: M = magnesite, D = dolomite, C = chlorite, Ca = calcite, Q = quartz, Ha = halite and P = plagioclase. Samples are A1-A14, all collected from Afzalabad magnesite deposit, and Ab1-Ab3 are from Ablah magnesite deposit.

Note: The intensities (cps) are measured for the major reflection for each mineral (cps).

Table 3.5 The mineralogy of Torshak magnesite deposit as determined by XRD.

Sample	VS	S	MS	MD	MW	W	VW
T1	M	-	-	-	-	C, D	-
T2	M	-	-	-	-	C	-
T3	M	-	-	-	-	C	-
T4	M	-	-	-	-	D, C	-
T5	M	-	-	-	-	C	-
T6	M	-	D	-	-	C	-
T7	M	-	-	D	-	C	-
T8	M	-	-	-	-	C	-
T9	M	-	-	-	-	C, D	-
T10	M	-	-	-	-	C	Q
T11	M	-	-	-	D, Q	C	-
T12	M	-	-	-	-	D, C	Q
T13	M	-	-	-	D	C	-
T14	M	-	-	-	-	C	D
T15	M	-	-	-	-	C, D	-
T16	M	-	-	-	-	C, D	Q, Ca
T17	M	-	-	D	-	Q, C	-
T18	M	-	-	-	-	Q, C, D	P
T19	M	-	-	-	-	C	-
T20	M	-	-	-	D	C	Ca
T21	M	-	Q	D	P	Mica, C	-
T22	M	-	-	-	-	C	-
T23	M	-	-	-	-	C	-
T24	M	-	-	D	-	C	-
T25	M	-	-	D	-	C	-
T26	M	-	-	D	-	C	-
T27	M	-	-	-	-	C, D	Q

Where:

VS = very strong (>1000 cps).

S = strong (400-1000 cps).

MS = moderate strong (250-400 cps).

MD = moderate (125-250 cps).

MW = moderate weak (50-125 cps).

W = weak (20-50 cps).

VW = very weak (<20 cps), and minerals are: M = magnesite, D = dolomite, C = chlorite, Ca = calcite, Q = quartz, P = plagioclase. Samples are T1-T27, all collected from Torshak magnesite deposit.

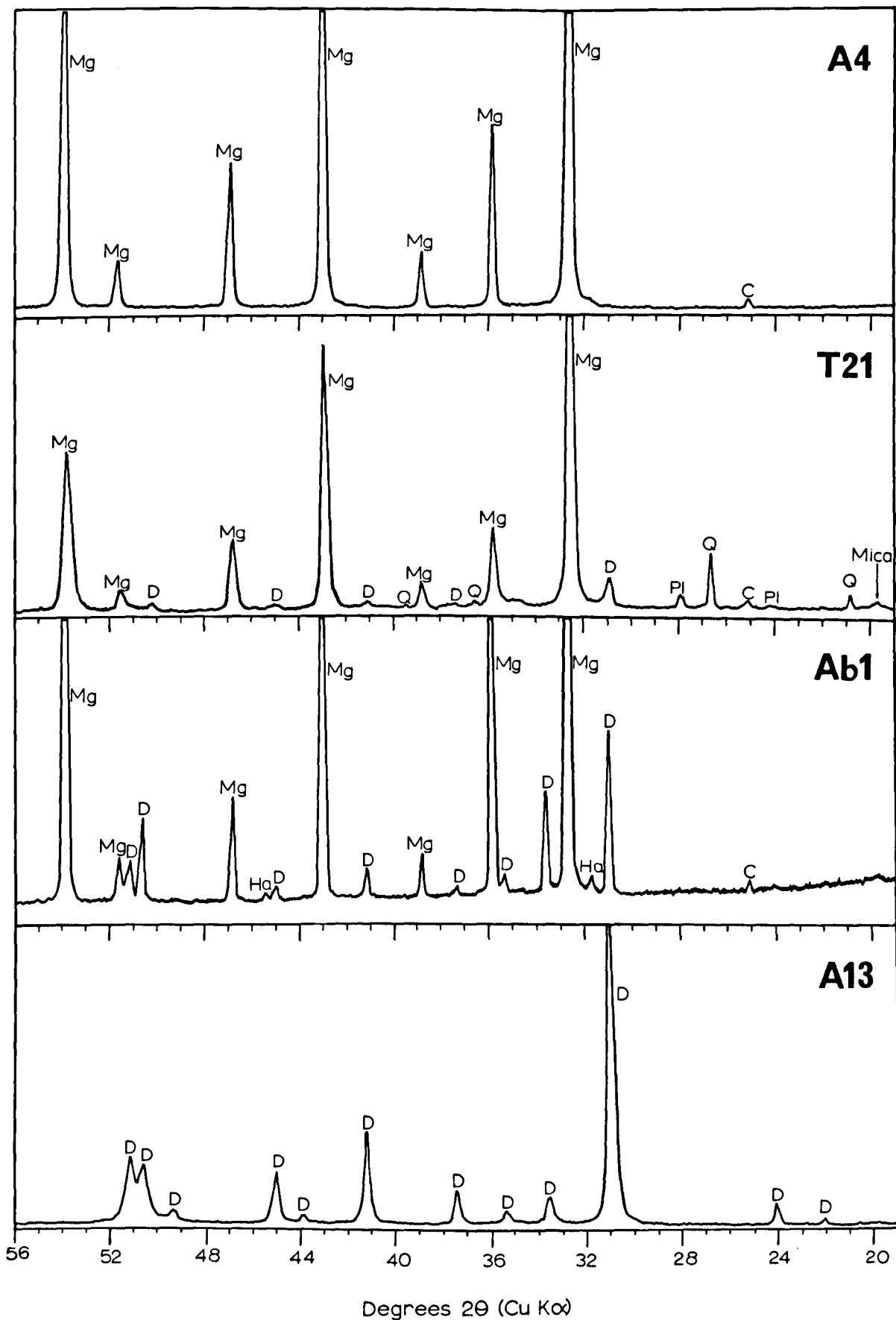


Figure 3.8 X-ray diffraction traces of magnesite and dolomite.

Mg = Magnesite, D = Dolomite, C = Chlorite, Q = Quartz,

PI = Plagioclase, Ha = Halite.

3.9 Microstructure.

The microstructure of natural magnesite specimens have been studied in both secondary and backscattered modes, using two Cambridge scanning electron microscopes Models 360 and 600.

Scanning electron micrographs of fracture surface of natural magnesites are presented in Plate 10, displaying their cryptocrystalline ($<2^{\mu\text{m}}$), and compact nature. The fracture cleavage can be seen in Plate 10c, and their perfect rhombohedral crystals are shown in Plates 10g and h. Also fracture surface of dolomite and serpentinite have been studied. Compact structure of dolomite and fibrous nature of serpentinite are shown in Plates 10d, and 10e and f respectively.

Back scattered electron micrographs of polished thin sections of natural magnesites indicates, pure magnesite which are dark grey, and impure magnesite (magnesite with Ca and Fe in solid solution) white grey in colour. The main impurities which are mostly of dolomite and calcite (white areas) appear in two forms of either vein filling, or as a separate patches (Plate 11).

PLATE 10

Scanning electron micrographs of fracture surfaces of natural magnesite, dolomite and serpentinite (host rock).

a,b) Uniform cryptocrystalline magnesite. The grain sizes are less than one micron.

c) Perfect fracture cleavage appearance of coarse magnesite.

d) Common view of the fracture surface of dolomite.

e,f) Serpentinite showing irregular fibrous structure.

g,h) Perfect rhombohedral magnesite crystals.

PLATE 10

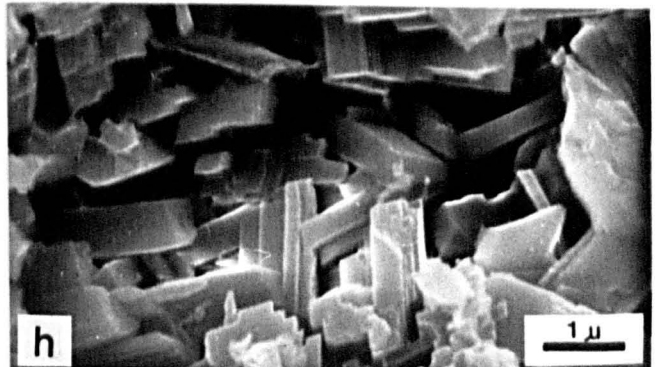
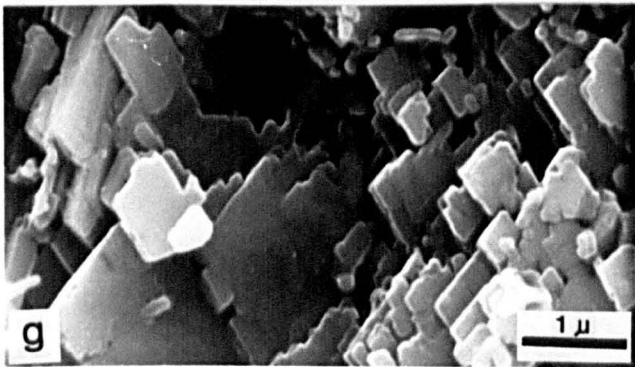
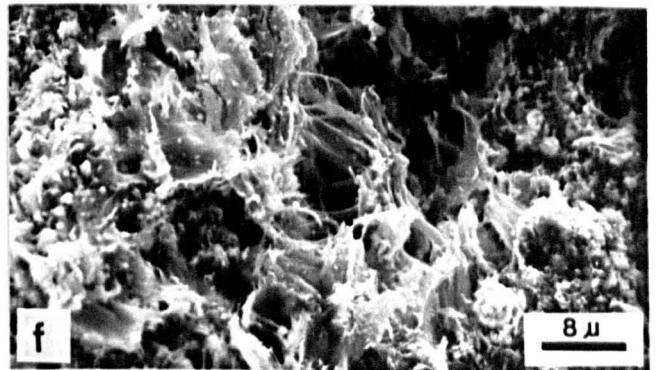
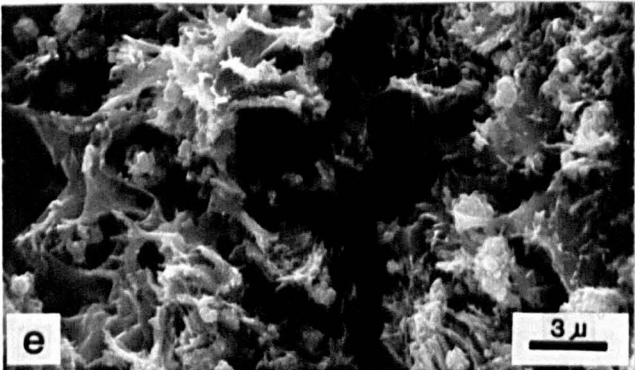
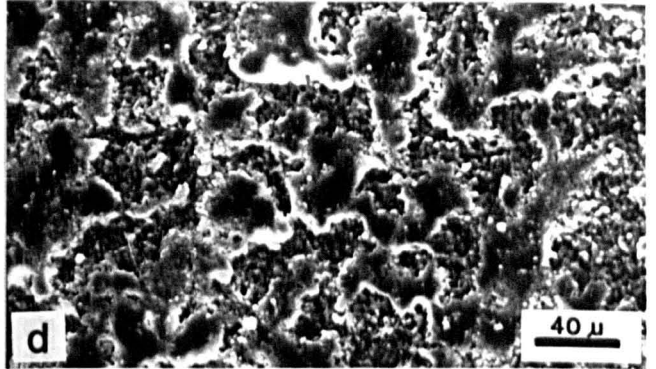
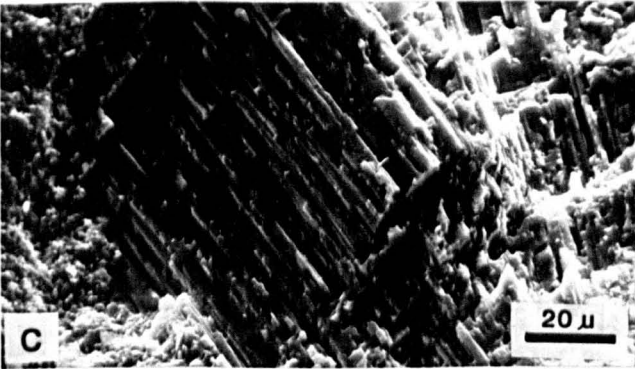
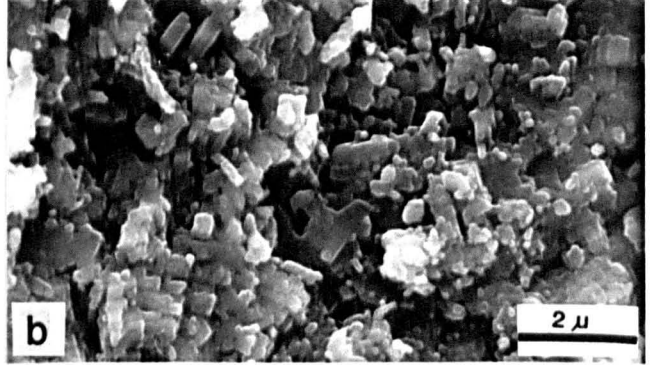
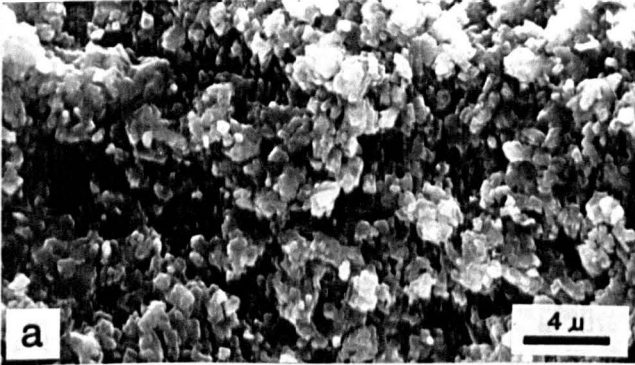
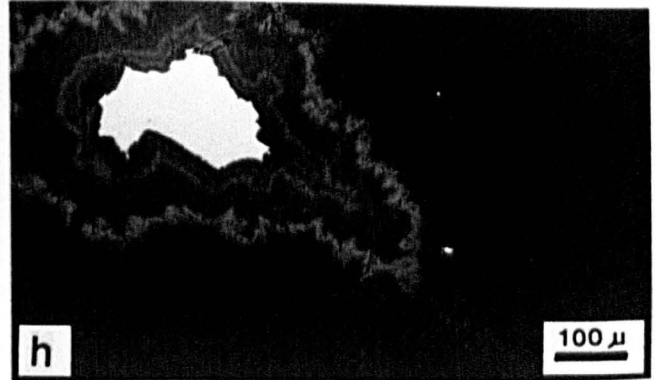
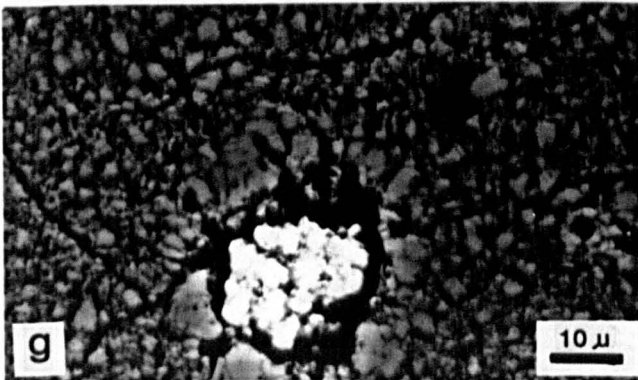
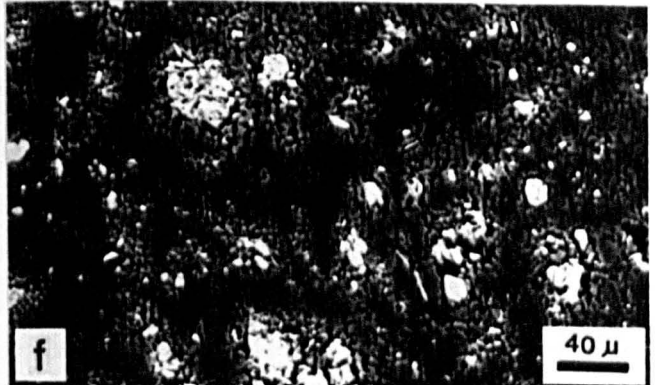
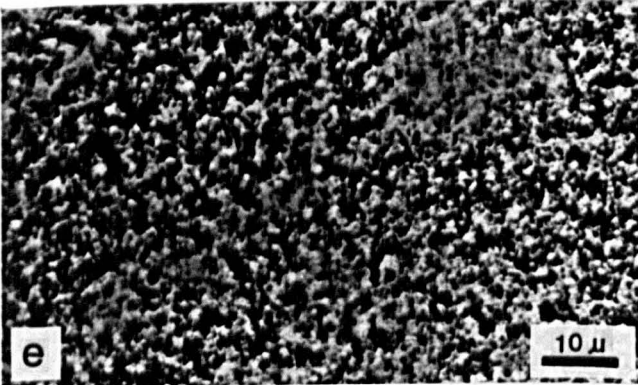
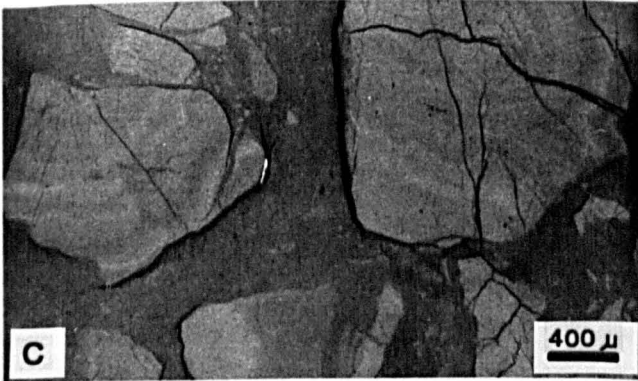
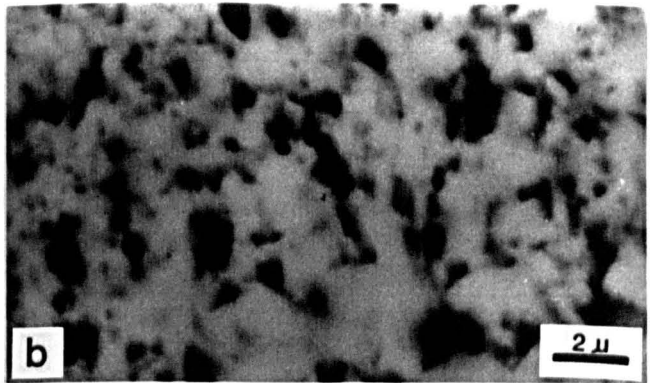
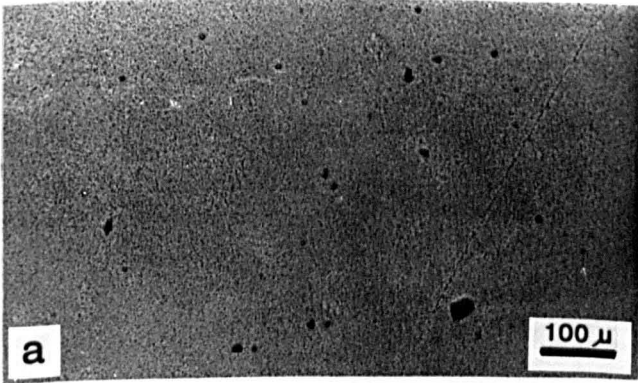


PLATE 11

Scanning electron microscope photographs in backscattered mode of polished thin sections of natural magnesite, containing the following phases, pure magnesite (dark grey), impure magnesite (magnesite with Ca and Fe in solid solution) (white grey). The main impurities which are mostly of dolomite and calcite (white areas) appear in two forms of either vein filling, or as a separate patches.

- a) Very pure and uniform cryptocrystalline magnesite.
- b) Detail of cryptocrystalline magnesite showing microporosity (black).
- c,d) Two generation of magnesite. The whiter parts which are darker in hand specimen have more Ca, and Fe. The darker parts which are whiter in hand specimen are pure magnesite. The small white vein filling material (more visible in plate 11d) is dolomite.
- e) Detail of high microporosity distribution (black) within magnesite grains (greyish white).
- f,g) Large dolomite patches (white) within a host of microcrystalline magnesite (grey). This magnesite contains only minor amounts of Ca.
- h) Concentric arrangement of alternating calcium and magnesium rich phases (calcite, magnesite, dolomite) around calcite nucleus.

PLATE 11



3.10 Mineral chemistry

3.10.1 General

Magnesite is the magnesium end member of the carbonate group of minerals and crystallizes in the trigonal system. The structure of magnesite is similar to that of calcite, but with a slightly smaller unit cell due to the smaller size of the magnesium ion. (for more information see Hurlbut and Klein, 1977 and Deer et al., 1962, 1983).

There is a complete solid solution series between magnesite and siderite (FeCO_3). The ferroan rich magnesite, breunnerite, extends from 5 to 50 mole percent FeCO_3 . The substitutions of Mn for Mg and Ca for Mg are both limited in amount due to the greater difference in ionic radius (see Reeder, 1983, Goldsmith, 1983).

Experimental work shows evidence of minor solid solution of Ca in magnesite.

3.10.2. Instrumental

The mineral chemistry of natural magnesites have been made using a Link system model 290-2Kx energy dispersive spectrometer, fitted to a Cambridge Geoscan Electron Microprobe. The method used, is the same as described by Dunham & Wilkinson (1978) using an accelerating potential of 15 KV and 100 live-second, counting time. Detection limits vary a little according to the mineral being analysed, but are approximately

<u>Oxide</u>	<u>Detection Limit (wt.%)</u>
SiO ₂	0.21
TiO ₂	0.18
Al ₂ O ₃	0.26
Cr ₂ O ₃	0.19
FeO	0.19
MnO	0.18
MgO	0.21
CaO	0.14
Na ₂ O	0.27
K ₂ O	0.13

3.10.3 Results and discussion

Electron microprobe analyses of magnesite and dolomite were carried out on samples from Afzalabad and Torshak magnesite deposits (samples beginning with A and T respectively). Complete results are presented in Appendix 4. A selection of these analyses with their carbonate compositions recalculated as wt.% are given in Table 3.6. The CO₂ is recalculated.

The microprobe analyses were carried out on 98 spots on three samples from the Afzalabad deposit (A1, A6 and A12) and 42 spots on three samples of Torshak deposit (T2, T15 and T26).

Magnesite is the main mineral identified in all analyses. Dolomite have been analysed only in samples A1 and T26. Tables 3.7 and 3.8 compare, minimum, maximum, mean and

Table 3.6 A selection of magnesite and dolomite analyses as determined by electron microprobe

Sample Code	A1 MG-M	A1 MG-C	A1 MG-C	A1 MG-M	A1 MG-C	A1 MG-C	A1 MG-C	A1 MG-M	A1 MG-C	A6 MG-C	Sample Code	A1 DL-C	A1 DL-M	A1 DL-C	A1 DL-M	A1 DL-C	A1 DL-C	A1 DL-M	A1 DL-C	A1 DL-C	T26 DL-C
SPOT	4	10	12	16	17	20	21	22	27	3	SPOT	1	2	5	6	9	13	23	24	25	1
SiO2	0.18	n.d.	0.19	n.d.	n.d.	n.d.	n.d.	n.d.	n.d.	n.d.	SiO2	n.d.	n.d.	n.d.	0.22	n.d.	0.31	n.d.	n.d.	n.d.	n.d.
TiO2	n.d.	n.d.	n.d.	n.d.	n.d.	n.d.	n.d.	n.d.	n.d.	n.d.	TiO2	n.d.									
Al2O3	n.d.	n.d.	n.d.	n.d.	n.d.	n.d.	n.d.	n.d.	n.d.	n.d.	Al2O3	n.d.									
Cr2O3	n.d.	n.d.	n.d.	n.d.	n.d.	n.d.	n.d.	n.d.	0.22	n.d.	Cr2O3	n.d.									
FeO	n.d.	1.79	0.87	n.d.	n.d.	n.d.	0.25	2.99	n.d.	0.67	FeO	0.68	0.53	0.87	1.81	n.d.	n.d.	1.87	n.d.	0.30	n.d.
MnO	n.d.	n.d.	n.d.	n.d.	n.d.	n.d.	n.d.	n.d.	n.d.	n.d.	MnO	n.d.									
MgO	41.31	40.86	41.03	41.93	40.98	42.51	42.23	40.77	43.33	40.88	MgO	21.30	21.03	21.20	21.10	20.94	20.66	21.85	21.36	21.85	18.46
CaO	0.55	0.48	0.31	0.67	0.19	0.15	0.39	1.02	0.43	1.48	CaO	28.08	28.09	26.98	27.01	29.22	29.76	28.82	30.11	29.53	33.49
K2O	n.d.	n.d.	n.d.	n.d.	n.d.	n.d.	n.d.	n.d.	n.d.	n.d.	K2O	n.d.									
CO2	45.54	46.09	45.58	46.31	44.90	46.54	46.57	47.15	47.65	46.21	CO2	45.72	45.35	44.86	45.36	45.81	45.92	47.63	46.96	47.22	46.45
TOTAL	87.58	89.22	87.98	88.91	86.07	89.20	89.44	91.93	91.63	89.24	TOTAL	95.78	95.00	93.91	95.50	95.97	96.64	100.17	98.44	98.89	98.40
Formula on the basis of 100 cations											Formula on the basis of 100 cations										
Ca	0.95	0.82	0.53	1.14	0.33	0.25	0.66	1.70	0.71	2.51	Ca	48.22	48.63	47.20	46.74	50.08	50.87	47.49	50.33	49.09	56.60
Mn	0.00	0.00	0.00	0.00	0.00	0.00	0.00	0.00	0.00	0.00	Mn	0.00	0.00	0.00	0.00	0.00	0.00	0.00	0.00	0.00	0.00
Mg	99.05	96.80	98.30	98.86	99.67	99.75	99.01	94.42	99.29	96.60	Mg	50.88	50.65	51.62	50.81	49.92	49.13	50.10	49.67	50.52	43.40
Fe2	0.00	2.38	1.17	0.00	0.00	0.00	0.33	3.89	0.00	0.89	Fe2	0.91	0.72	1.18	2.45	0.00	0.00	2.41	0.00	0.38	0.00
CaCO3	0.98	0.86	0.55	1.20	0.34	0.27	0.70	1.82	0.77	2.64	CaCO3	50.12	50.14	48.15	48.20	52.15	53.11	51.43	53.75	52.71	59.77
MgCO3	86.41	85.47	85.83	87.71	85.72	88.92	88.34	85.28	90.64	85.51	MgCO3	44.56	43.99	44.36	44.15	43.80	43.21	45.71	44.68	45.70	38.62
FeCO3	0.00	2.89	1.40	0.00	0.00	0.00	0.40	4.82	0.00	1.08	FeCO3	1.09	0.86	1.40	2.93	0.00	0.00	3.02	0.00	0.48	0.00
MnCO3	0.00	0.00	0.00	0.00	0.00	0.00	0.00	0.00	0.00	0.00	MnCO3	0.00	0.00	0.00	0.00	0.00	0.00	0.00	0.00	0.00	0.00
Sample Code	A6 MG-C	A6 MG-C	A6 MG-C	A6 MG-C	A12 MG-C	A12 MG-M	A12 MG-C	A12 MG-C	A12 MG-C	A12 MG-M	Sample Code	T26 DL-C	T26 DL-M	T26 DL-C	T26 DL-C	T26 DL-M					
SPOT	4	6	12	19	1	2	5	7	12	18	SPOT	3	5	7	9	11	13	16	18	20	21
SiO2	0.17	0.86	n.d.	0.17	n.d.	0.22	n.d.	n.d.	n.d.	0.22	SiO2	n.d.	0.17								
TiO2	n.d.	n.d.	n.d.	n.d.	n.d.	n.d.	n.d.	n.d.	n.d.	n.d.	TiO2	n.d.									
Al2O3	n.d.	n.d.	n.d.	n.d.	n.d.	n.d.	n.d.	n.d.	n.d.	n.d.	Al2O3	n.d.									
Cr2O3	n.d.	n.d.	n.d.	n.d.	n.d.	n.d.	n.d.	n.d.	n.d.	n.d.	Cr2O3	n.d.									
FeO	0.36	0.39	n.d.	n.d.	1.87	0.58	2.55	n.d.	0.20	0.45	FeO	n.d.									
MnO	n.d.	n.d.	n.d.	n.d.	n.d.	n.d.	n.d.	n.d.	n.d.	n.d.	MnO	n.d.									
MgO	41.49	41.03	41.66	41.90	40.56	41.26	40.62	41.54	41.41	41.11	MgO	21.84	19.21	21.04	19.67	21.94	21.45	23.54	18.96	21.86	25.66
CaO	0.96	0.57	0.54	0.95	0.84	0.68	1.14	0.89	1.03	1.00	CaO	30.45	32.81	29.76	33.35	28.94	30.40	26.45	32.81	31.29	26.94
K2O	n.d.	n.d.	n.d.	n.d.	n.d.	n.d.	n.d.	n.d.	n.d.	n.d.	K2O	n.d.									
CO2	46.28	45.49	45.92	46.50	46.10	45.95	46.82	46.06	46.15	45.95	CO2	47.75	46.74	46.34	47.65	46.68	47.29	46.47	46.46	48.44	49.16
TOTAL	89.26	88.34	88.12	89.52	89.37	88.69	91.13	88.49	88.79	88.73	TOTAL	100.03	98.76	97.15	100.67	97.56	99.15	96.47	98.23	101.59	101.93
Formula on the basis of 100 cations											Formula on the basis of 100 cations										
Ca	1.63	0.98	0.92	1.60	1.43	1.16	1.91	1.52	1.75	1.71	Ca	50.06	55.11	50.42	54.93	48.67	50.46	44.68	55.43	50.71	43.01
Mn	0.00	0.00	0.00	0.00	0.00	0.00	0.00	0.00	0.00	0.00	Mn	0.00	0.00	0.00	0.00	0.00	0.00	0.00	0.00	0.00	0.00
Mg	97.90	98.49	99.08	98.40	96.08	98.06	94.75	98.48	97.98	97.69	Mg	49.94	44.89	49.58	45.07	51.33	49.54	55.32	44.57	49.29	56.99
Fe2	0.48	0.53	0.00	0.00	2.49	0.77	3.34	0.00	0.27	0.60	Fe2	0.00	0.00	0.00	0.00	0.00	0.00	0.00	0.00	0.00	0.00
CaCO3	1.71	1.02	0.96	1.70	1.50	1.21	2.03	1.59	1.84	1.78	CaCO3	54.34	58.57	53.12	59.52	51.65	54.26	47.21	58.55	55.85	48.07
MgCO3	86.79	85.83	87.14	87.65	84.84	86.31	84.97	86.89	86.62	85.99	MgCO3	45.68	40.18	44.02	41.14	45.90	44.88	49.25	39.66	45.73	53.67
FeCO3	0.58	0.63	0.00	0.00	3.02	0.94	4.11	0.00	0.32	0.73	FeCO3	0.00	0.00	0.00	0.00	0.00	0.00	0.00	0.00	0.00	0.00
MnCO3	0.00	0.00	0.00	0.00	0.00	0.00	0.00	0.00	0.00	0.00	MnCO3	0.00	0.00	0.00	0.00	0.00	0.00	0.00	0.00	0.00	0.00

standard deviation of major and minor oxide present in Afzalabad and Torshak magnesite deposits:

Table 3.7 Minimum, maximum, mean and standard deviation of major and minor oxides present in samples from Afzalabad magnesite deposit.

Field	Min	Max	Mean	SD
SiO ₂	0.00	0.19	0.04	0.08
FeO	0.00	2.98	0.66	0.98
MgO (A1)	40.63	43.33	41.56	0.76
CaO	0.13	1.02	0.44	0.26
SiO ₂	0.00	4.97	1.16	1.47
FeO	0.00	0.99	0.33	0.34
MgO (A6)	39.43	42.28	41.04	0.76
CaO	0.22	1.48	0.66	0.22
SiO ₂	0.00	0.73	0.06	0.14
FeO	0.00	3.46	1.56	1.00
MgO (A12)	38.85	41.98	40.65	0.71
CaO	0.37	1.56	0.90	0.32

Table 3.8 Minimum, maximum, mean and standard deviation of major and minor oxides present in samples from Torshak magnesite deposit.

Field	Min	Max	Mean	SD
SiO ₂	0.19	3.68	0.80	0.99
MgO (T2)	38.86	41.64	40.70	0.83
CaO	2.02	2.94	2.32	0.25
SiO ₂	0.11	6.39	3.12	1.82
MgO (T15)	33.23	38.92	35.43	2.01
CaO	2.09	4.62	2.48	0.87
SiO ₂	0.00	0.26	0.13	0.12
MgO (T26)	38.22	40.57	39.68	0.90
CaO	0.84	3.05	1.54	0.95

In Figure 3.9, 98 analyses have been plotted from the Afzalabad magnesites using CaO, MgO and SiO₂ as end members. The analyses indicate that magnesite and dolomite are the main phases present in sample A1, since samples A6 and A12 only contain magnesite.

Microprobe analyses of 42 spots are carried out on three samples of T2, T15 and T26 collected from Torshak deposit. Magnesite and dolomite are the main phases identified in sample T26, but samples T2 and T15 only contain magnesite. In these samples the percentage of FeO is below detection limit, but they contain a higher percentage of CaO and SiO₂ than samples from Afzalabad.

Figure 3.9 compare the CaO-MgO-SiO₂ and CaO-MgO-FeO diagrams of samples collected from Afzalabad and Torshak deposits.

As described earlier 3-4 different generation of magnesites are recognised in Afzalabad deposit. The electron microprobe analyses indicate that the narrow magnesite veins which cut the previous magnesites are purer (Plate 11d).

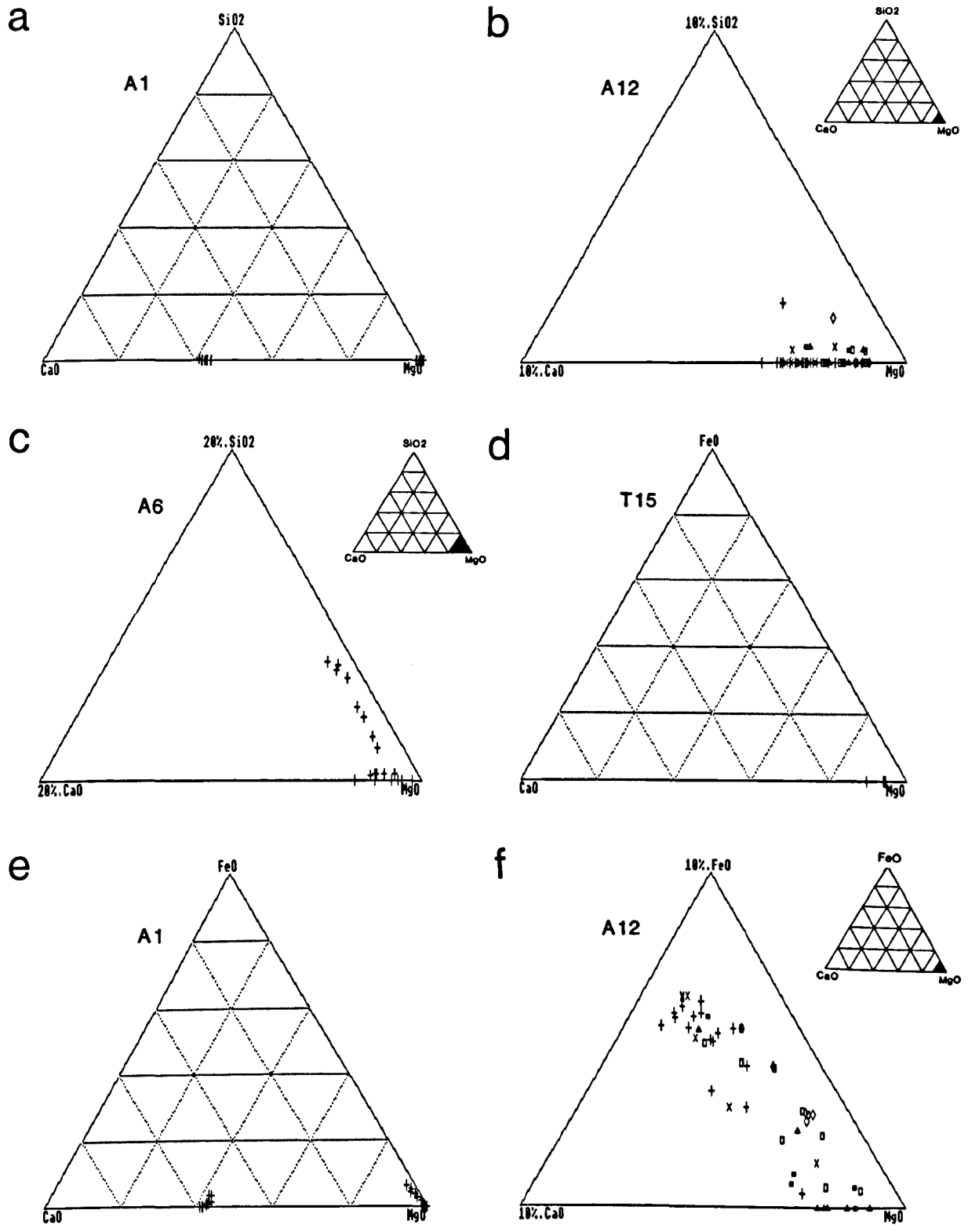
SiO₂ is found to be present in the majority of samples. It varies between below detection limit and 4.97% in Afzalabad samples and 0.26-6.39% in Torshak. The higher percentage of SiO₂ can be picked up from the surrounding impurity grains due to the small size of the magnesite crystals (the probe beam penetrating more than a single crystal of magnesite).

FeO is found to be present in majority of magnesite

specimens from Afzalabad deposit, but magnesites from Torshak deposit are free of FeO.

CaO is present as a solid solution in all samples and varies between 0.13-1.56% in samples from Afzalabad deposit, and 0.84~2.5% in Torshak magnesite deposit. The higher percentage of CaO in samples from Torshak magnesite deposit is due to the presence of dolomite (Figure 3.9).

The total in all analyses is low, due to presence of microporosities.



Key:

- White magnesite (core) ◇ White magnesite (margin) † Green-grey magnesite (core) X Green-grey magnesite (margin)
- ▲ Narrow white magnesite veinlets cutting others (core) ■ Narrow white magnesite veinlets cutting others (margin)

Figure 3.9 Triangular plots showing CaO-MgO-SiO₂ and CaO-MgO-FeO ratios of all microprobe analyses of natural magnesite (wt.%)

CHAPTER 4

MINERALOGY, MICROSTRUCTURE, MINERAL CHEMISTRY AND PHYSICAL PROPERTIES OF DEAD BURNED MAGNESITE

4.1 Introduction

More than 80% of the world's magnesite production is consumed in a dead burned form as a refractory to line the furnaces and kilns in the steel, cement, nonferrous metal industries and the like.

The term dead burned is used for a magnesite that has been calcined to a temperature several hundreds of degrees (usually more than 1600°C) above the minimum decomposition temperature at atmospheric pressure (approx. 700°C). In the dead burned form the resulting periclase crystals have hopefully been able to grow >40 microns in size and become relatively unreactive.

4.2 Experimental Procedure and sample descriptions

Five specimens which are different in bulk chemistry (Table 4.1) were chosen from the Torshak and Afzalabad deposits of eastern Iran for the purpose of studying the dead burned properties of the magnesite. Separate samples were calcined in an electric laboratory furnace at different temperatures (1400, 1500 and 1600°C) for various periods of times (6, 24, 96 and 108 hrs). Although air hydration of products was unlikely, the dead burned materials were stored in a vacuum desiccator.

The mineralogy, microstructure, mineral chemistry and physical properties of the calcined products have been studied using X-ray diffraction, optical microscopy, scanning electron microscopy and electron microprobe.

Table 4.1 Chemical composition of the natural magnesite samples used for calcination.

sample	A3	A14	T2	T15	T26
SiO ₂	0.08	3.12	0.99	5.41	0.12
Al ₂ O ₃	0.01	0.96	0.01	0.01	0.02
TiO ₂	0.00	0.03	0.00	0.00	0.00
Fe ₂ O ₃	0.49	0.30	0.00	0.00	0.00
MgO	45.93	43.85	43.79	44.38	46.58
CaO	0.24	2.24	2.51	2.44	1.33
Na ₂ O	0.03	0.14	0.04	0.04	0.04
K ₂ O	0.00	0.18	0.00	0.01	0.00
LOI	52.10	49.90	51.41	48.58	51.79
TOTAL	98.88	100.72	98.75	100.87	99.88
CaO/SiO ₂	3.21	0.77	2.72	0.48	11.88
Al ₂ O ₃ /Fe ₂ O ₃	0.23	5.00	0.00	0.00	0.00

(Note: CaO/SiO₂ and Al₂O₃/Fe₂O₃ are in mole ratio).

As a result of different chemical composition of natural magnesite raw materials, some of the dead burned magnesite products show differences in colour, physical properties, mineralogy and microstructure.

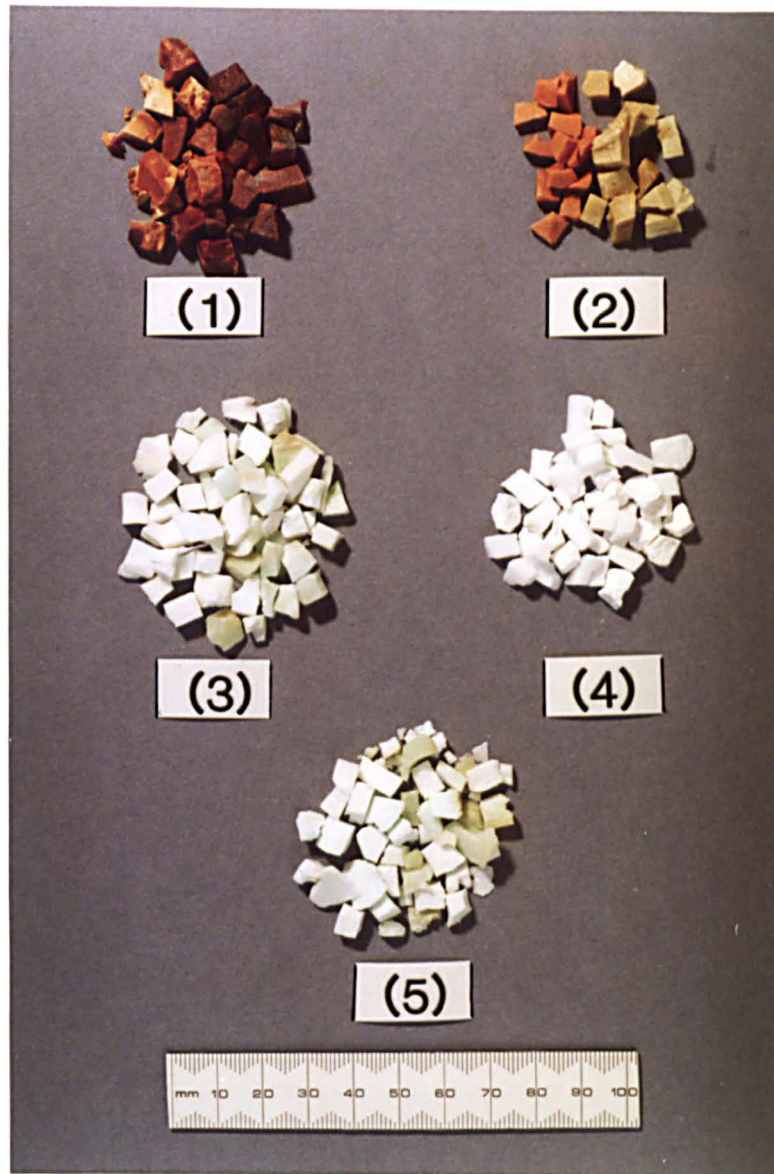


PLATE 12 A Colour photograph of dead burned magnesite products showing different colours due to variation in the chemical compositions.

Following are the sample numbers.

(1) A₃ (2) A₁₄ (3) T₂ (4) T₁₅ (5) T₂₆

4.3 Mineralogy (XRD)

X-ray diffraction using Ni filtered, CuK-alpha radiation was used to determine the crystalline phases present in each dead burned magnesite product.

4.3.1 Instrumental

The operating conditions of the Philips X-ray diffraction unit are shown below:

Tube current	40 Kv, 40 mA
Count rate	4×10^2 cps
Time constant	4 second
Chart speed	10mm/min

Cavity mounted specimens were scanned from $20-65^\circ 2\theta$, which covers most of the reflections of the phases expected in these dead burned products. All the specimens were run under the same instrumental condition. Thus direct comparison of results can be made.

4.3.2 Sample preparation

The calcined magnesite samples were ground by hand grinding in an agate pestle and mortar to less than 40 microns which is the suitable particle size for X-ray diffraction (Zussman 1977).

4.3.3 Results

The crystalline phases have been identified by comparing the determined d-spacing with those in the (JCPDS) powder diffraction files. The mineralogy of natural dead burned

magnesites as determined by XRD are given in Tables 4.2 - 4.6 and a selection of their X-ray diffraction traces are presented in Figures 4.1 and 4.2. The comparative intensities of the major reflections of each phase is taken as a rough guide to the changes in mineralogy occurring between different temperatures and times of calcination.

Table 4.2 Minerals identified in sample A3

Minerals Degrees (2θ)	Q	C ₂ S	C ₃ MS ₂ &/orC ₂ S	M	C	Sp
	26.7	32.2	33.5	43.0	54.0	31.2
(Temp/Time)						
(1600°C, 108 hrs)	-	32	12	>400	-	12
(1600°C, 6 hrs)	16	20	22	>400	-	8
(1500°C, 96 hrs)	28	20	28	>400	24	-
(1500°C, 24 hrs)	13	-	-	>400	12	-
(1500°C, 6 hrs)	22	-	-	>400	12	-
(1400°C, 96 hrs)	18	-	-	>400	20	-
(1400°C, 24 hrs)	20	-	-	>400	24	-
(1400°C, 6 hrs)	28	-	-	>400	30	-

Table 4.3 Minerals identified in sample A14

Minerals Degrees (2θ)	Q	Sp&/orC ₂ S	CMS	M ₂ S	M	C ₂ S
	26.7	31.2	33.7	36.3	43.0	33.5
(Temp/Time)						
(1600°C, 108 hrs)	-	12	60	24	>400	-
(1600°C, 6 hrs)	20	9	76	14	>400	-
(1500°C, 96 hrs)	18	4	72	-	>400	48
(1500°C, 24 hrs)	20	12	86	-	>400	40
(1500°C, 6 hrs)	16	12	98	-	>400	68
(1400°C, 96 hrs)	16	16	96	24	>400	60
(1400°C, 24 hrs)	22	12	112	28	>400	52
(1400°C, 6 hrs)	24	14	132	36	>400	-

The following abbreviations are used in Tables 4.2 - 4.6: Q = Quartz, C₂S = Dicalcium silicate, C₃MS₂ = Merwinite, M = Periclase, C = Lime, Sp = Spinel, CMS = Monticellite, M₂S = Forsterite, C₃S = Tricalcium silicate. (Note: Intensities shown are the measured counts per second of the most intense reflection for each mineral, which is shown in degrees 2θ.

Table 4.4 Minerals identified in sample T2

Minerals Degrees (2θ)	Q 26.7	C ₃ S 32.6	C ₂ S&/orC ₃ MS ₂ 33.5	C 37.4	M 43.0
(Temp/Time)					
(1600°C, 108 hrs)	-	64	20	36	>400
(1600°C, 6 hrs)	15	84	60	76	>400
(1500°C, 96 hrs)	16	48	32	80	>400
(1500°C, 24 hrs)	14	44	40	72	>400
(1500°C, 6 hrs)	20	44	52	48	>400
(1400°C, 96 hrs)	16	60	32	32	>400
(1400°C, 24 hrs)	36	52	36	96	>400
(1400°C, 6 hrs)	28	36	32	104	>400

Table 4.5 Minerals identified in sample T15

Minerals Degrees (2θ)	Q 26.7	CMS 33.7	M ₂ S 36.5	M 43.0
(Temp/Time)				
(1600°C, 108 hrs)	-	84	92	>400
(1600°C, 6 hrs)	16	108	66	>400
(1500°C, 96 hrs)	10	124	92	>400
(1500°C, 24 hrs)	10	152	100	>400
(1500°C, 6 hrs)	10	176	84	>400
(1400°C, 96 hrs)	20	204	100	>400
(1400°C, 24 hrs)	20	200	112	>400
(1400°C, 6 hrs)	16	200	116	>400

Table 4.6 Minerals identified in sample T26

Minerals Degrees (2θ)	Q 26.7	C 32.3	M 43.0	C ₂ S&/orC ₃ S 34.3
(Temp/Time)				
(1600°C, 108 hrs)	-	48	>400	18
(1600°C, 6 hrs)	10	36	>400	8
(1500°C, 96 hrs)	10	52	>400	-
(1500°C, 24 hrs)	10	44	>400	-
(1500°C, 6 hrs)	8	36	>400	16
(1400°C, 96 hrs)	12	52	>400	-
(1400°C, 24 hrs)	10	60	>400	28
(1400°C, 6 hrs)	12	60	>400	-

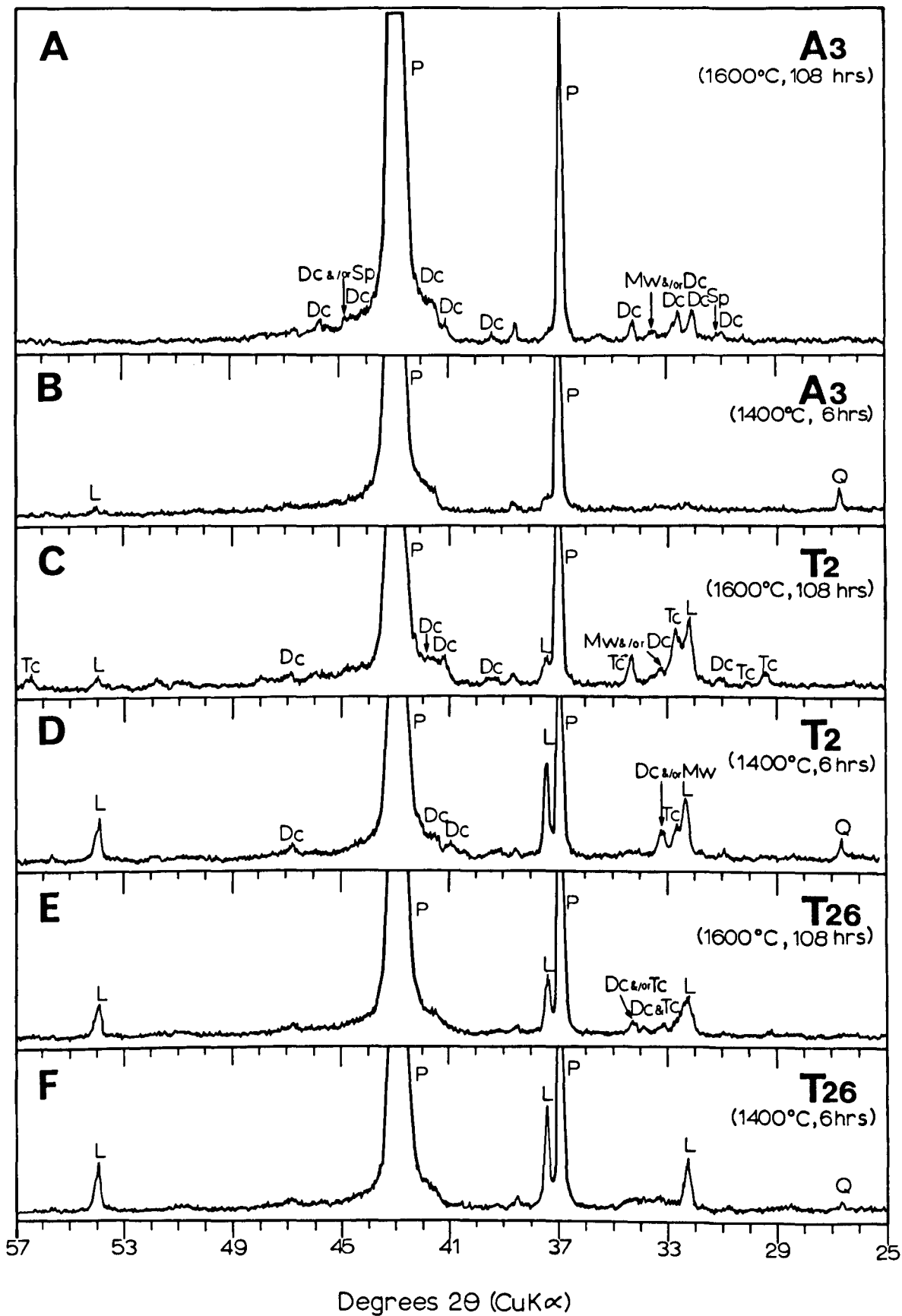


Figure 4.1 A selection of X-ray diffraction traces of dead burned magnesites.

P=periclase, Dc=Dicalcium silicate, Mw = Merwinite,
 Sp = spinel, L=lime, Tc = Tricalcium silicate, Q= Quartz.

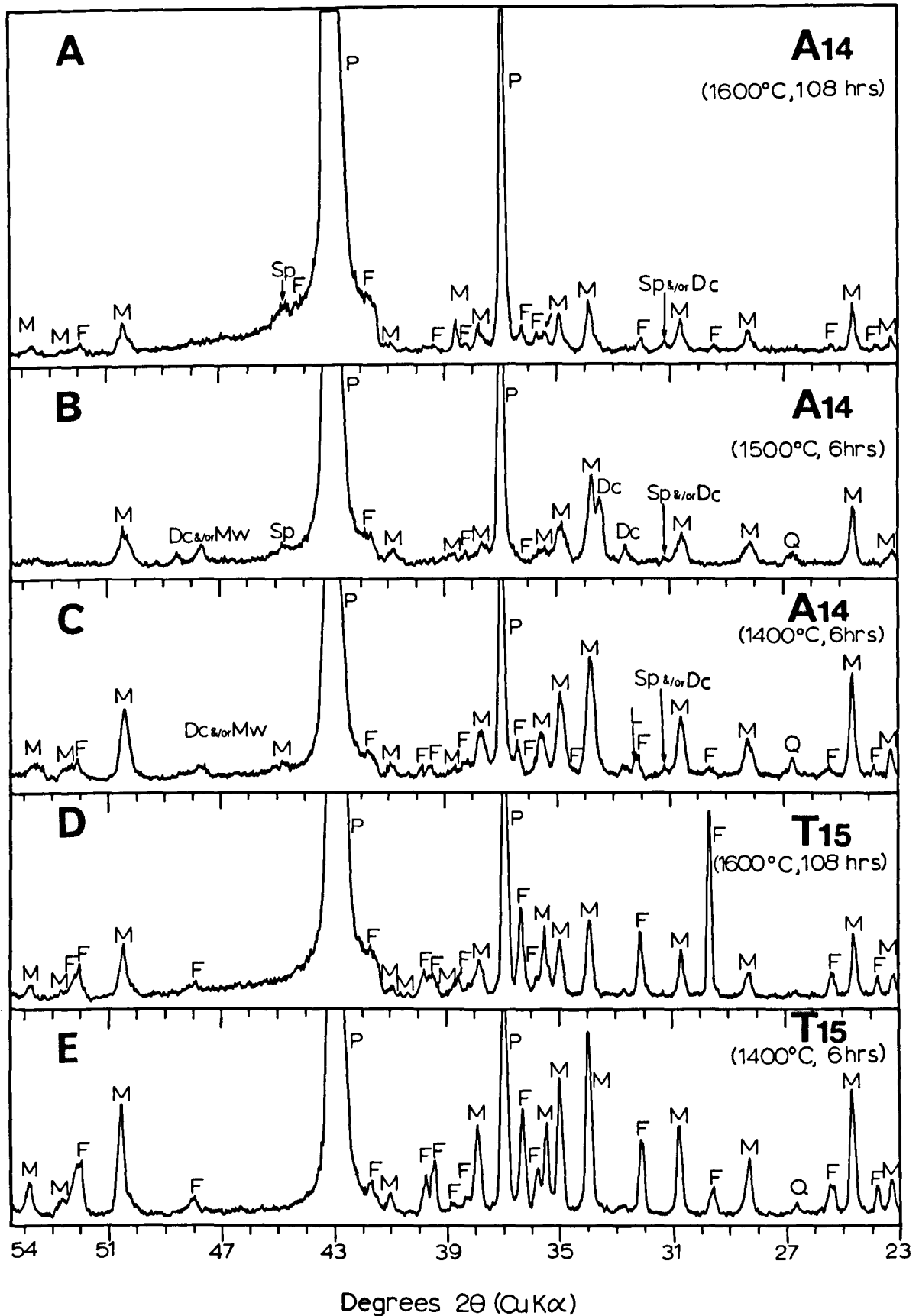


Figure 4.2 A selection of X-ray diffraction traces of dead burned magnesites
P= Periclase, M= Monticellite, F= Forsterite,
Dc= Dicalcium silicate, L= Lime, SP= Spinel,
Mw = Merwinite, Q= Quartz.

4.3.3.1 Sample A3

Minerals identified in this sample calcined at different times and temperatures are given in Table 4.2. Periclase, dicalcium silicate, merwinite and/or dicalcium silicate, lime, spinel, and quartz are present. Quartz is present in constant amounts, but it disappears completely at 1600°C and 108 hours). Lime is also present more or less with similar intensities of reflection throughout but absent at higher temperatures of calcination. In contrast dicalcium silicate and merwinite begin to form at higher temperatures, i.e (1500°C, 96 hrs) increasing their intensities with higher temperature. Spinel is only present in very small amounts at higher firing temperature (1600°C).

4.3.3.2 Sample A14

Minerals identified in sample A14 calcined different condition are given in Table 4.3. Periclase, monticellite, forsterite, dicalcium silicate and/or merwinite, quartz and spinel are present.

Monticellite is present in all firing conditions, its intensity decreasing gradually by increasing calcination temperatures. Forsterite is present in lower amounts compared with monticellite. It disappears at 1500°C, which is probably due to sample heterogeneity. Quartz is present nearly in constant intensity, but it completely disappears at (1600°C, 108 hrs). Dicalcium silicate and/or merwinite is almost constant. The amount of forsterite in this sample is much

lower compared with sample T15 is much lower, possibly due to presence of dicalcium silicate. Lime is present in very low amounts.

4.3.3.3 Sample T2

Minerals identified in this sample are given in Table 4.4 which are mainly of periclase, tricalcium silicate, lime, dicalcium silicate and/or merwinite and quartz.

Quartz is present in nearly similar intensities, but it disappears completely at 1600°C, 108 hrs. Lime loses its intensity gradually by increasing the calcination temperature. In contrast to quartz and lime^{which} disappear or have reduced intensities at higher temperatures, tricalcium silicate develops at higher temperatures which is probably due to reaction between lime and quartz in higher temperatures. Dicalcium silicate and/or merwinite are present in all conditions, their intensities increase up to 1600°C, but after that decrease with increased time.

4.3.3.4 Sample T15

Minerals identified in sample T15 calcined at different conditions are presented in Table 4.5. Periclase, monticellite, forsterite and quartz are the phases which identified.

Monticellite and forsterite appear throughout. Monticellite reduces in intensity at higher temperature. Forsterite also shows comparatively lower intensities in higher temperatures. Quartz has similar intensities at all

calcination conditions except it completely disappears at 1600°C and 108 hrs.

4.3.3.5 Sample T26

Minerals identified in sample T26 are presented in Table 4.6. The phases are periclase, lime, dicalcium silicate and/or tricalcium silicate and quartz. Quartz is present with similar intensities but disappears at 1600°C and 108 hrs. Lime also gradually reduces in intensity at higher calcination temperatures. In contrast to lime and quartz, dicalcium silicate and/or tricalcium silicate appear to form at higher temperatures.

4.3.4 Discussion

The mineral phases identified in each dead burned product of the studied samples depend to a large extent on the chemical composition of their raw materials (Table 4.1).

To be commercially acceptable magnesite should contain around 95% magnesium carbonate, an amount which depending on the accessory oxides, would result in a dead burned product containing 90-94% MgO. The most frequently present impurities which produce the main impurity phases are CaO and SiO₂. Al₂O₃ and Fe₂O₃ which are present to a lower extent form spinel solid solutions and ferrites (rarely found).

The combination of SiO₂ and CaO is extremely important in magnesia refractories in which the CaO/SiO₂ ratio determines the nature of compounds formed in the bond between magnesia grains. In general CaO/SiO₂ ratio of approximately

2:1 is desirable, in this case such as samples A3 and T2 relatively refractory matrix phases such as dicalcium and tricalcium silicates with the melting point of more than 2000°C are produced which is tolerable. With the lower CaO/SiO₂ ratios (sample A14 and T15), less refractory interstitial materials such as monticellite (m.pt. 1502°C) and merwinite (m.pt. 1575°C which are undesirable are produced.

The lower the SiO₂ content, the more critical the effect of CaO. In sample T26 for example the percentage of SiO₂ is very low (0.12%). Relatively small amounts of CaO (1.33%) can produce a very high CaO/SiO₂ ratio (increasing CaO/SiO₂, decrease hydration resistance). In this case CaO is not entirely bound, leaving some CaO in the free state. The presence of free lime in dead burned magnesite is deleterious and can result a shattered refractories as hydration take place. In general good refractories may be produced with low amount of CaO and SiO₂ with a CaO/SiO₂ ratio of around 2:1.

4.4 Microstructure

4.4.1 Introduction

The detailed microstructural investigation of the different phases developed in the dead burned products of natural magnesites calcined at different temperatures (1400, 1500 and 1600°C) for various times (6, 24, 96 and 108 hours), has been made using scanning electron microscopy (SEM) and energy dispersive X-ray analysis (EDX).

This section provides details of the identification of each phases, their mutual relationships, and other important factors such as distribution of porosity, size, shape and texture of the grains.

This part of study was made using two Cambridge Scanning Electron Microscopes (SEM 360 and SEM 600). Both the surfaces of the grains using secondary electron emission (SE), and flat polished surfaces of samples (polished blocks), using backscattered electron emission (BSE) have been studied.

4.4.2 Optical microscopy

The most widely used technique of studying ceramic microstructure is reflected light microscopy. In dead burned magnesite, the reflectivity of silicates are very similar and specially in purer material, these minor phases are very small in size. Higher magnifications than the optical microscope range are necessary. The optical microscopy observations are summarized below:

4.4.2.1 Sample A3

Polygonal periclase crystals show a direct grain contact. Occasionally small amounts of interstitial material with the same reflectivity of periclase are present at the triple points. Periclase grains show rough and smooth surface. Lots of cracks and few holes are visible. Where the amounts of interstitial materials are higher, the periclase grains are rounded.

4.4.2.2 Sample A14

The periclase grains are mostly rounded and interstitial impurities are present between them. Interstitial silicates show similar reflectivity to periclase. Periclase grains exhibit rough and smooth appearance on the surface.

4.4.2.3 Sample T2

In this sample the periclase grains are very small with rough and smooth surface structure. The periclase grains are mostly polygonal and interstitial impurities appear at the triple points. When the matrix phases are higher in amount, they form between the periclase grains, resulting in rounded periclase grains.

4.4.2.4 Sample T15

High amount of impurities are present between the rounded periclase grains. Periclase grains have smooth and rough surface appearance. The interstitial materials have the

same reflectivity as periclase which indicate the interstitial materials are silicate.

4.4.2.5 Sample T26

In this sample the periclase grains are very small and impurities form between the periclase grains. In some parts of sample which contain lower amounts of impurities, the bigger polygonal periclase grains are present. Periclase grains appear either with smooth or rough surface structure.

In all samples described above, the periclase grains grow considerably at higher temperatures and longer times of calcination.

4.4.3 Scanning electron microscopy

The introduction of SEM with EDX system, enables identification of very small impurity phases and examination of their distribution and microstructures. Other advantages of scanning electron microscopes are their greater depth of field compared with that possible with light microscope.

The most reliable way to identify minerals through the SEM is to compare their morphologies with the elemental compositions by the EDX system. This chapter includes both SEM micrographs and EDX spectra.

Identifications were compared with the results obtained by X-ray diffraction analysis of the powdered dead burned samples (see section 4.3). Plates illustrating the mineralogy and textures consist of a series of eight micrographs

normally arranged in order of increasing calcination temperature. They are accompanied by brief interpretive description. The Energy Dispersive X-ray Spectra for the main phases identified are presented in Figure 4.3.

4.4.3.1 Experimental

Polished blocks and the surface of dead burned magnesite were prepared for this study. The polished blocks were prepared first by embedding representative pieces of dead burned magnesia in epoxy resin, secondly by grinding, using four grades of carborundum (400, 600, 800, 1200) and finally, by polishing them for approximately two hours each in a polishing machine using three grades of diamond paste (6, 3, 1 micron). Paraffin was used instead of water in the whole preparation process to prevent hydration. The procedure followed in the polished block preparation in this study is presented in Appendix 6.

Uncontaminated pieces of dead burned magnesite were attached to a specimen stub with epoxy adhesive. The sample must be small enough to fit into the SEM sample chamber. The specimens were then coated with carbon. There are two reasons for coating specimens prior to insertion into the scanning electron microscope. First because non conducting specimens build up a surface charge through which secondary electron information is unable to penetrate. Therefore the image may be distorted both in signal level and image form. Second, in order to provide a surface layer that produces a higher secondary electron yield than the specimen material. The

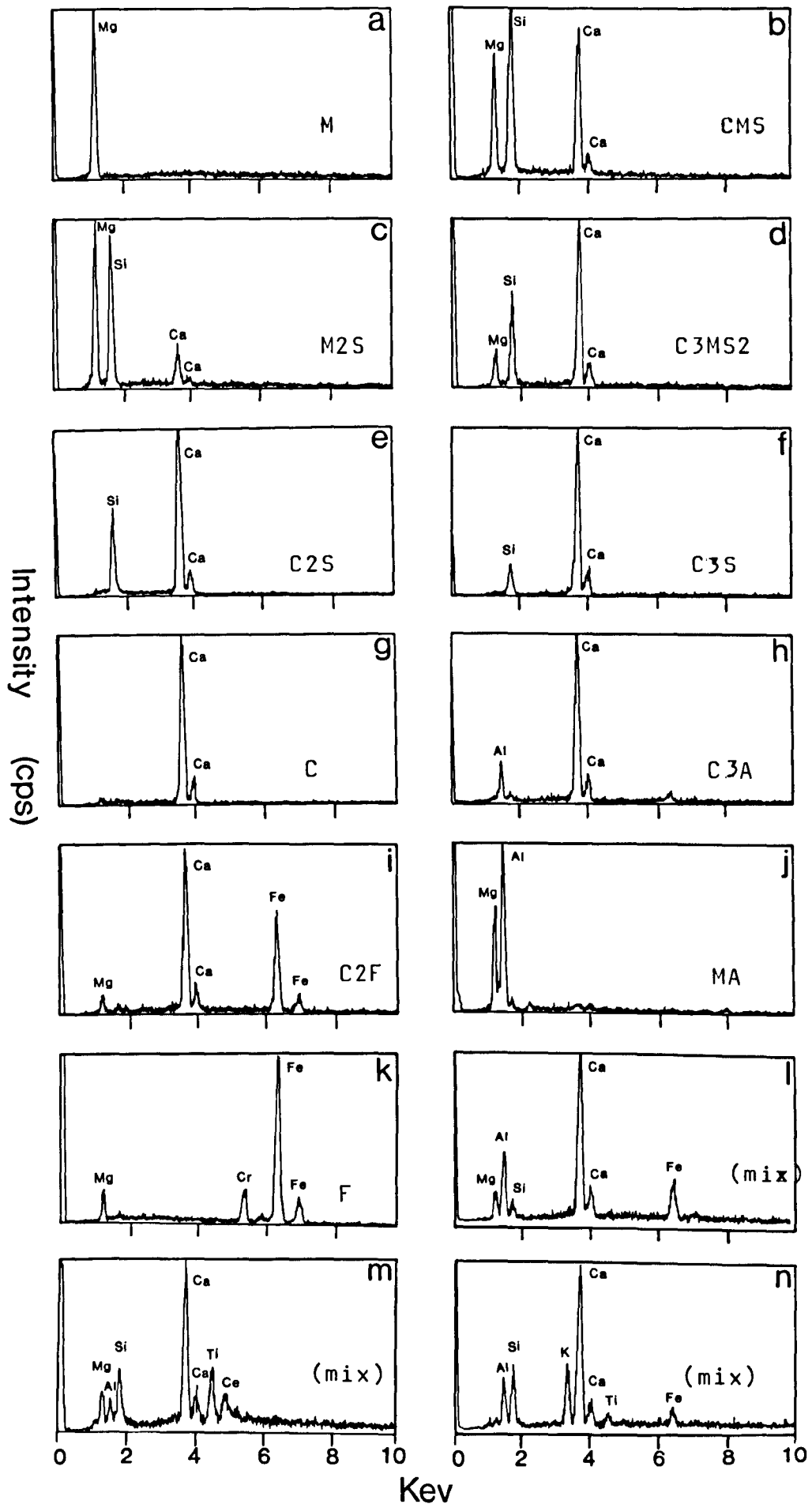


Figure 4.3 Energy Dispersive X-Ray Spectra (EDX)

coating is so thin (200 Å) that it does not hinder the identification of specific minerals.

4.4.3.2 The SEM micrographs

The three dimensional image (SEM micrograph) is formed by collecting the secondary electrons generated by the primary beam, these are low energy electrons, so only those formed near the surface (50-500 Å deep for insulating materials such as rocks) are able to escape (Wells, 1974). The electrons emitted are collected by the secondary electron detector mounted in the SEM sample chamber and processed into the familiar SEM image. This image is either displayed on a TV screen or it can be photographed with an attached camera.

The microstructural study in two dimensions is carried out using back scatter electron images.

4.4.3.3 Elemental analysis by SEM

Elemental analysis of a sample is obtained by collecting the characteristic X-ray generated as the electron beam scans the sample. The X-ray detector is mounted adjacent to the secondary electron detector (see Appendix 5, for more detail). Each elements in the sample produces X-ray with characteristic energies. These X-rays can be analysed by using a Si(Li) detector in an energy dispersive system (EDX).

In general, the EDX system can only be used for semi-quantitative analyses of elements above atomic number (Z) of 11 (sodium). The average atomic number of the phases which can be found in natural dead burned magnesites are

presented in Table 4.7.

Table 4.7 The average atomic number of the phases which can be found in dead burned magnesites.

Phase	Formula	Average atomic number (Z)
Periclase	MgO	10.41
Forsterite	2MgO.SiO ₂	10.58
Monticellite	CaO.MgO.SiO ₂	12.77
Merwinite	3CaO.MgO.2SiO ₂	13.71
Akermanite	2CaO.MgO.2SiO ₂	13.12
Dicalcium silicate	2CaO.SiO ₂	14.56
Tricalcium silicate	3CaO.SiO ₂	15.06
Lime	CaO	16.58
Magnesioferrite	MgO.Fe ₂ O ₃	18.54
Spinel	MgO.Al ₂ O ₃	10.58
Dicalcium ferrite	2CaO.Fe ₂ O ₃	19.93
Brownmillerite	4CaO.Al ₂ O ₃ .Fe ₂ O ₃	16.65
Tricalcium aluminate	3CaO.Al ₂ O ₃	14.34
Tricalcium phosphate	3CaO.P ₂ O ₅	14.05

4.4.3.4 Description of microstructures

For the purpose of this investigation, five natural magnesite specimens (A3, A14, T2, T15, T26), with a wide variety in bulk composition (Table 4.1) were calcined at different temperatures and times. Each calcined products showed different colours, due to their chemical composition variability, (e.g. sample A3 which contain higher percentage of iron oxide is dark brown) (Plate 12).

The microstructure of each sample was examined in the polished blocks (two dimension) using backscattered (BSE) mode and the surface of the dead burned magnesite was examined using the secondary electron detector.

4.4.4 Mean grain size

The mean grain size of periclase (D) from the polished sections can be measured using a relationship derived by Fullman (1953). For this purpose a grid of lines are drawn on the photographs and the mean size (D) is calculated from

$$D = 1.5 L$$

Where L is the mean length of the intercepts of individual grains on the lines. This relationship is derived assuming spherical grains of uniform size. It is said to be valid when the grain size varies over a fairly narrow range (White 1968). In this work, at least 200 grains were measured for each sample calcined at each temperatures and times.

Table 4.8 Mean grain sizes of periclase in dead burned magnesites calcined at different conditions.

Temp/time	Samples				
	A3	A14	T2	T15	T26
1600°C, 108 hrs	122.3	88.2	18.6	78.6	25.4
1600°C, 6 hrs	78.4	37.3	8.6	40.5	20.2
1500°C, 96 hrs	48.4	70.8	7.4	63.0	23.6
1500°C, 24 hrs	39.6	40.0	6.0	34.3	16.2
1500°C, 6 hrs	34.2	36.2	3.8	26.5	10.7
1400°C, 96 hrs	44.4	42.2	5.0	- -	12.9
1400°C, 24 hrs	35.1	33.3	4.1	5.1	12.4
1400°C, 6 hrs	25.2	16.1	2.7	- -	- -

Note:

All grain sizes are in micron.
 - - = not possible to determine.

Larger periclase grains are produced when magnesite is

calcined at higher temperatures and times. Normally periclase grains calcined for longer times, exhibit larger grains in comparison with materials calcined at higher temperatures, but for shorter calcination times, (e.g. periclase grains are bigger at 1400°C, for 96 hours, compare with 1500°C, for 6 hours).

4.4.5 Results

4.4.5.1 Sample A3

The different phases found in sample A3 in both secondary (SE) and backscattered modes (BSE) are summarized in Table 4.9 and the micrographs are presented in Plate 13-16.

Table 4.9 Phases present in the calcined magnesite samples as determined by energy dispersive X-ray analysis (sample A3).

Temp/Time	(SE)	(BSE)
(1600°C, 108 hrs)	M, C ₂ S, C ₃ S, C ₃ A	M, C ₃ S, C ₃ A, C ₂ F, SP, C, C ₂ S
(1600°C, 6 hrs)	M, C ₂ S, C ₃ S	M, C ₃ S, C ₂ S &/or C ₃ MS ₂
(1500°C, 96 hrs)	M, C ₂ S, C ₃ S, C ₃ MS ₂	M, C ₃ S
(1500°C, 24 hrs)	M, C ₃ S	M, C ₃ S, C
(1500°C, 6 hrs)	M	M, C ₃ S
(1400°C, 96 hrs)	M, C ₃ S	M, C ₂ S &/or C ₃ MS ₂
(1400°C, 24 hrs)	M, C ₂ F	M, C ₃ S
(1400°C, 6 hrs)	M, C, C ₂ S, C ₃ MS ₂	M, C ₃ S, C, C ₂ F

Where:

M = periclase, C₂S = dicalcium silicate, C₃S = Tricalcium silicate, C₃A = tricalcium aluminate, C₂F = dicalcium ferrite, C = Lime, C₃MS₂ = Merwinite.

Details of identification of each phases and their mutual relationships are as follow:

4.4.5.1.1 Major phase (periclase)

Periclase grains, normally grow to similar sizes with high degree of direct grain contact (Plate 13 and 15). The periclase grain sizes are presented in Table 4.8. The surface of periclase grains in sample A3 either have a smooth surface structure appearance (Plate 13e), or an irregular aggregate like texture (Plate 13h).

Step like growth are present on the surface of some periclase grains (Plate 13b).

Periclase grains grow large at higher calcination temperatures and longer times (compare plates 15a and 15b). With more impurities there is less periclase - periclase grain contact. However high purity is not always the most important factor required by industry. For example sample A3 which is pure, cracked after calcination (Plate 15f). The presence of a few percentage of impurities may reduce this undesirable effect. Lower percentage of impurities concentrate at the triple points of periclase grains (Plate 15g). In samples with higher amounts of impurities, the increased amounts of matrix results in smaller and rounded periclase grains with less direct contact (Plate 16a).

Periclase grains appear in two main shapes, spherical mostly when the percentage of matrix is high, such as Plate 16a and polygonal when in purer material (Plate 15c). The

periclase grains have two main surface structures, namely rough and smooth (Plate 15d). The microprobe analyses indicated that the total is lower in the rough surface structure periclase grains which presumably results from the higher percentage of microporosity.

4.4.5.1.2 Interstitial or matrix materials

In sample A3, the matrix materials which are mainly of dicalcium and tricalcium silicates with smaller amount of merwinite usually form at the triple points, also they can form as rounded masses on the surface of periclase grains (Plates 14a, e). Sometimes dicalcium silicate is presented in large amount, and cover almost completely some parts of the periclase grains (Plate 14g).

c) 4.4.5.1.3 Rare features

Ferrite, spinel, tricalcium aluminate and lime are the rare phases in this sample. They normally appear with other interstitial phases. Detailed textural relationship between tricalcium silicate, tricalcium aluminate, spinel and ferrite are shown in Plate 16d. Tricalcium silicate (white) forms as irregular elongated crystals. Spinel (dark grey) shows a mesh like texture with tricalcium aluminate (pale grey). Tricalcium aluminate generally form between the periclase grains boundaries and ferrites appear between the periclase grains boundaries as very small and very white inclusions respectively.

Lime inclusions in periclase are also observed, they

PLATE 13

Scanning electron micrographs of the surface of natural dead burned magnesite (sample A3), containing 0.08% SiO₂, 0.49% Fe₂O₃, 0.24% CaO and a CaO/SiO₂ mole ratio of 3.21, calcined at temperatures of 1400, 1500 and 1600°C and for different period of calcination times (6, 24, 96 and 108 hours).

- a) Polygonal and semi-rounded periclase with a moderate to high direct bonding of periclase grains. Tricalcium silicates, (small rounded and white grains) are present at the triple point between periclase grains. This also results in their appearance on the surface of periclase calcined at 1400°C, for 96 hours.
- b) Step like growth on the surface of polygonal periclase. There is a high degree of direct bonding of grains (1400°C, 24 hrs).
- c) Semi rounded periclase grains with only minor direct grain bonding. The main impurity phases (tricalcium and dicalcium silicate), separates the periclase (1500°C, 6 hrs).
- d) Detail of step like growth on the surface of periclase. The rounded grains on the surface are tricalcium silicate, which are separated from the periclase by dicalcium ferrite (1500°C, 6 hrs).
- e) Typical view of polygonal magnesia grains having smooth and rough surface structure. The periclase grains are separated from each other by tricalcium silicate. Step like growth are visible in some of the grains (1500°C, 96 hrs).
- f) Semi-rounded to polygonal periclase grains with a minor direct grain bonding. The impurity phase (dicalcium silicate) appears within periclase grains. This also results in their appearance on the surface of periclase grains (1600°C, 108 hrs).
- g) Irregular periclase with almost no direct bonding and a large amount of pore space. The periclase grains have low amounts of Ca and Fe as impurities (1600°C, 6 hrs).
- h) Semi-rounded to polygonal and rough surface periclase grains with moderate amount of direct bonding. The matrix phase which is present between the periclase grains is dicalcium silicate (1600°C, 6 hrs).

PLATE 13

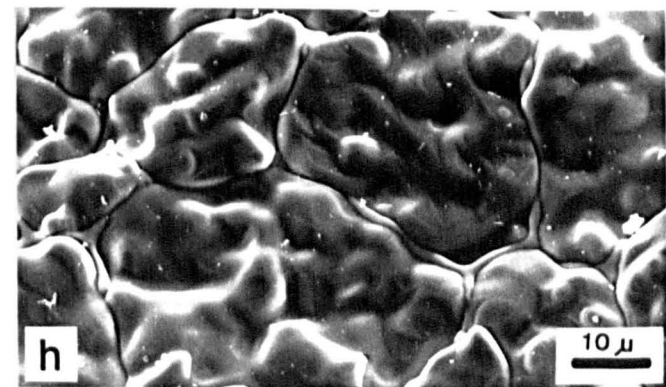
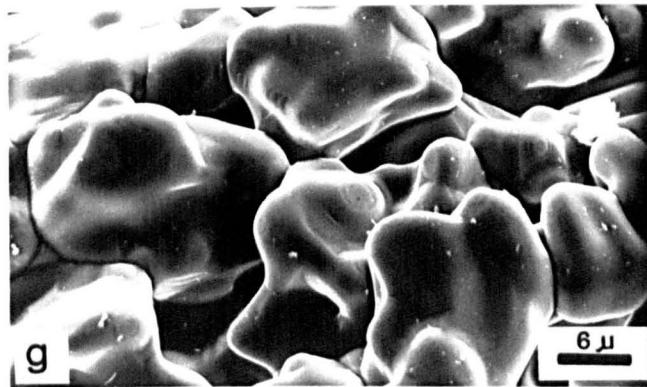
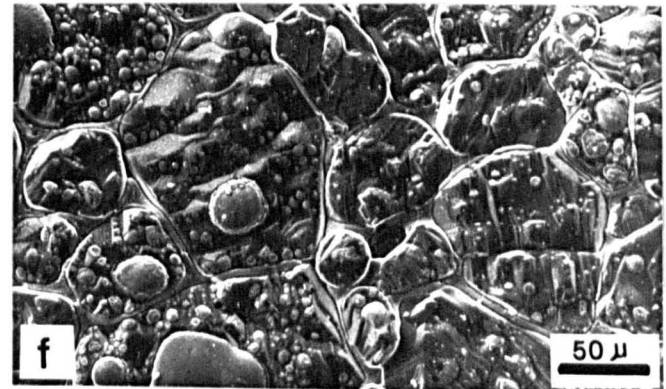
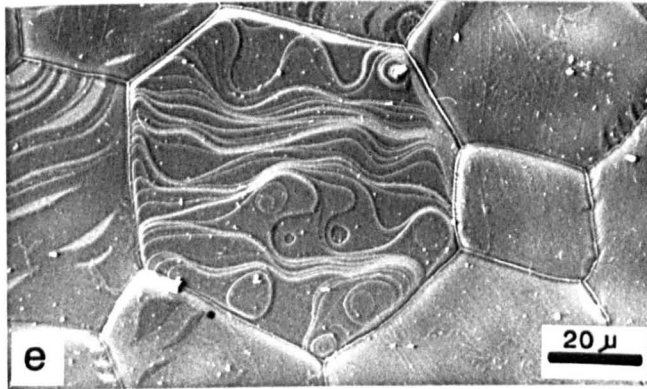
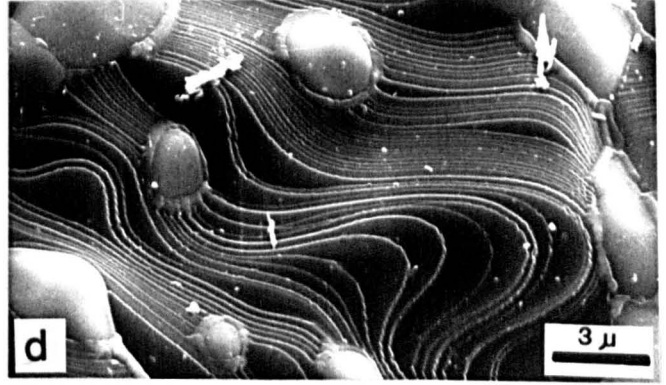
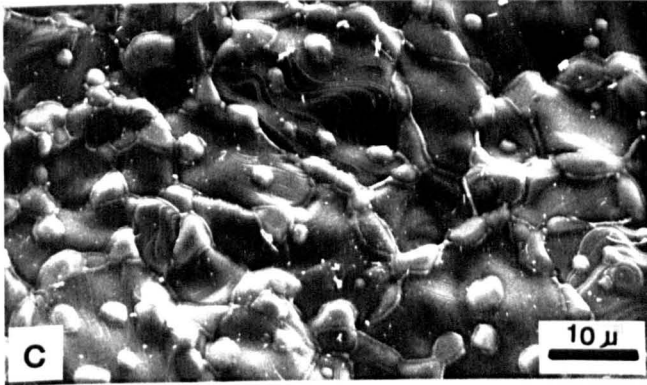


PLATE 14

Scanning electron micrographs of impurity phases on the surface of dead burned natural magnesite (sample A3) containing 0.08% SiO₂, 0.49% Fe₂O₃, 0.24% CaO and a CaO/SiO₂ mole ratio of 3.21. Most of the rounded grains on the surface of periclase grains are dicalcium silicate. This sample calcined at (1400, 1500 and 1600°C) for (6, 24, 96 and 108 hours).

- a) Rounded, white tricalcium silicate on the surface of periclase grains calcined at 1500°C for 24 hours.
- b) Detail of rounded, white tricalcium silicate grains on the surface of periclase grains (1500°C, 96 hrs).
- c) Rounded merwinite grains on the surface of periclase grains. Perfect cubic cleavage is visible within the periclase grains (1600°C, 108 hrs).
- d) Detail rounded merwinite grains on the surface of periclase. The small white and rounded inclusions in the merwinite are richer in Al (1600°C, 108 hrs).
- e) Dicalcium silicate impurities are formed as a rounded grains on the surface (1600°C, 108 hrs). If the percentage of impurities are high they can cover some part of the whole surface of sample, e.g. plate 14g.
- f) Triple point between three periclase grains without any impurity formed at the contact (1600°C, 108 hrs).
- g) Small rounded dicalcium silicate grains on the surface of and between periclase grains (1600°C, 108 hrs).
- h) Rounded elongate growth on dicalcium silicates possibly due to hydration (1600°C, 108 hrs).

PLATE 14

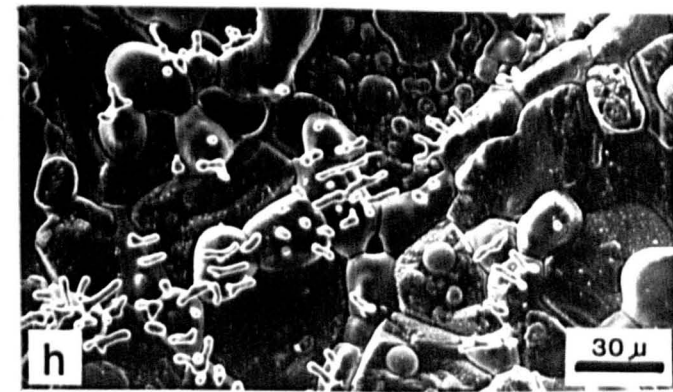
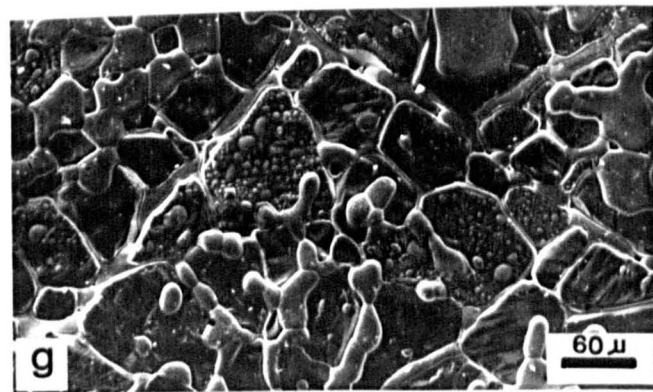
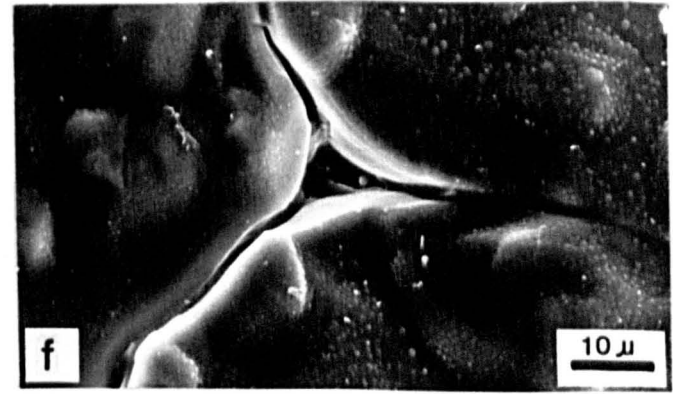
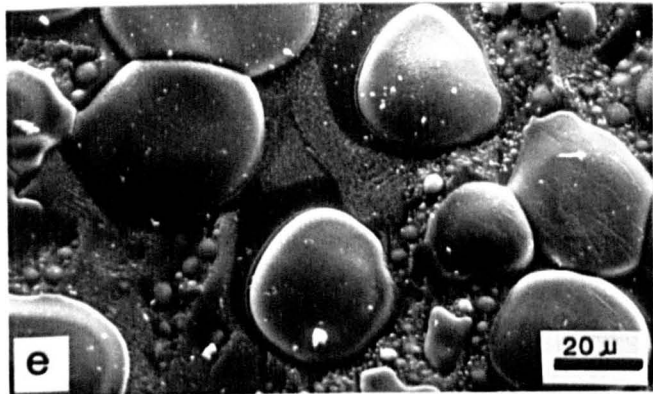
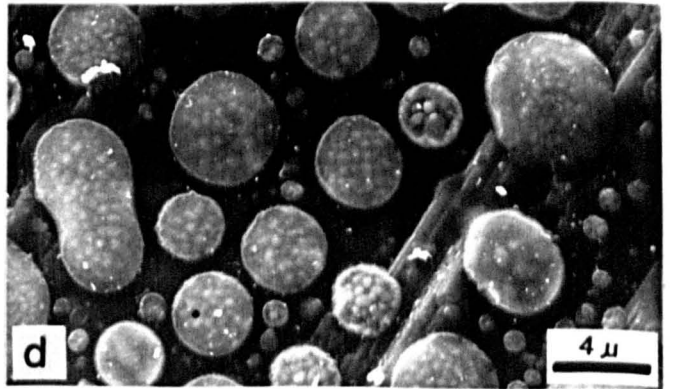
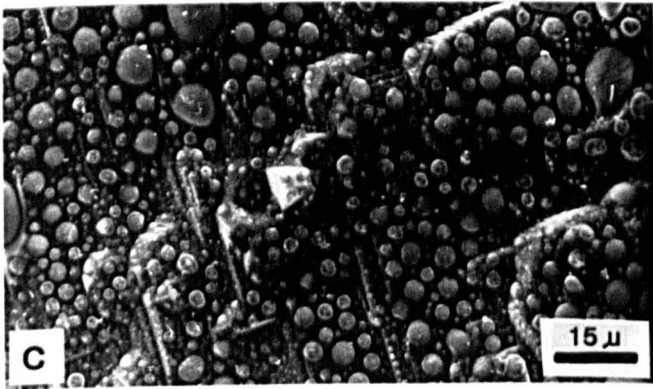
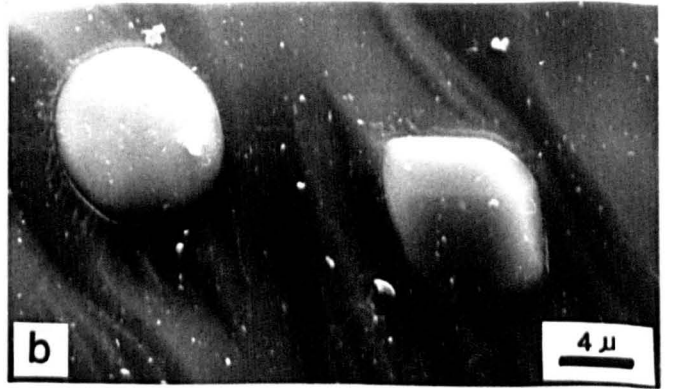
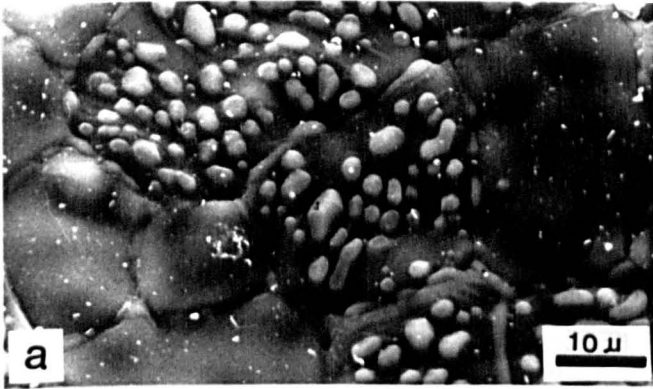


PLATE 15

Backscattered scanning electron micrographs of polished blocks of natural dead burned magnesite (sample A3), containing 0.08% SiO₂, 0.49% Fe₂O₃, 0.24% CaO, and a CaO/SiO₂ mole ratio of 3.21. This sample calcined at different temperatures (1400, 1500 and 1600°C), for different period of calcination times (6, 24, 96 and 108 hours).

- a) Very porous structure within indistinct periclase crystals (1400°C, 6 hrs).
- b) periclase grains showing colour differences due to smooth and rough surface structures. When they are smooth, their colour is white and when they have got rough surface, their colour is black (possibly due to higher microporosities). There is a high amount of direct periclase - periclase contact. Very small rounded and white interstitial materials are lime and dicalcium ferrite (1400°C, 6 hrs).
- c) Polygonal periclase grains having very good direct grain contact. The periclase grains usually contain minor amounts of FeO in solid solution. Smooth and rough surface structure are visible. The small rounded holes are hydrated lime and dicalcium ferrite (1400°C, 24 hrs).
- d) Detailed view of the smooth and rough surface structures on the surface of periclase grains, with high direct bonding. Lime and dicalcium ferrite impurities appear as a little rounded white grains on the surface of periclase grains which are usually hydrated and a hole is remained (1400°C, 96 hrs).
- e) comparison of contrast between backscattered and secondary electron mode of imaging (1400°C, 96 hrs).
- f) Periclase grains with direct contact at grain boundaries associated with cracks (1500°C, 96 hrs).
- g,h) Semi-rounded periclase grains with smooth and rough surface structures with little direct grain contact. Dicalcium silicate occurs as a white patches between the periclase grains. Very small rounded and white inclusions within periclase grains are lime, which can hydrate easily and as a result normally a hole remains. The calcination conditions are: (1600°C, 6 hrs) and (1600°C, 108 hrs) for (g,h) respectively.

PLATE 15

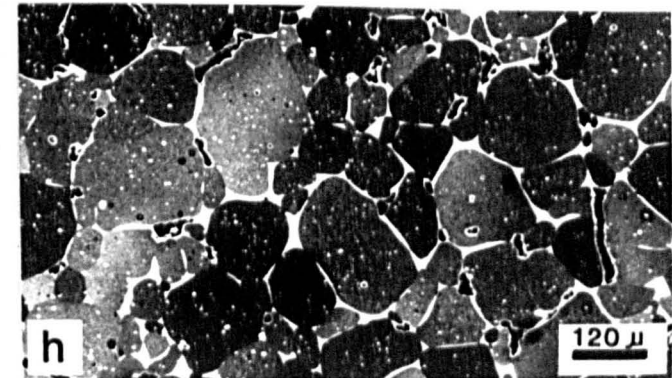
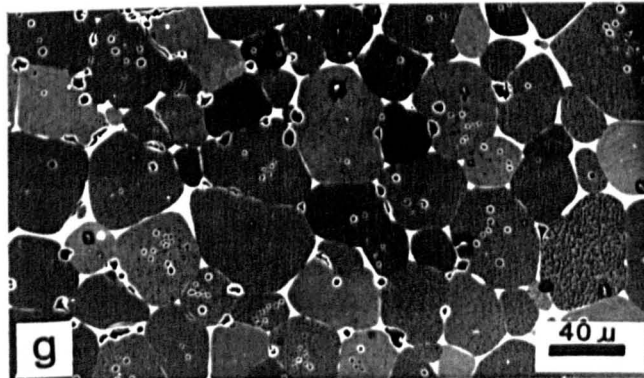
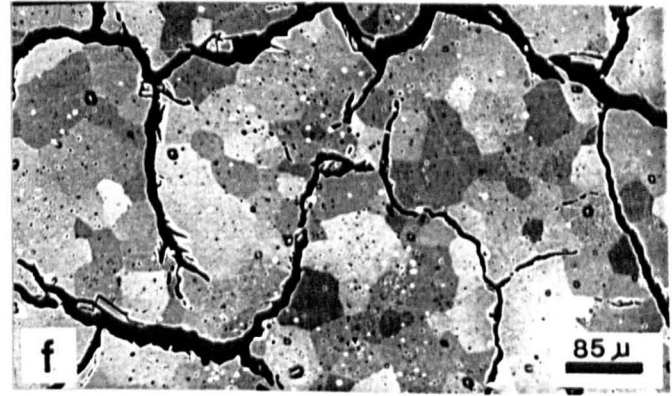
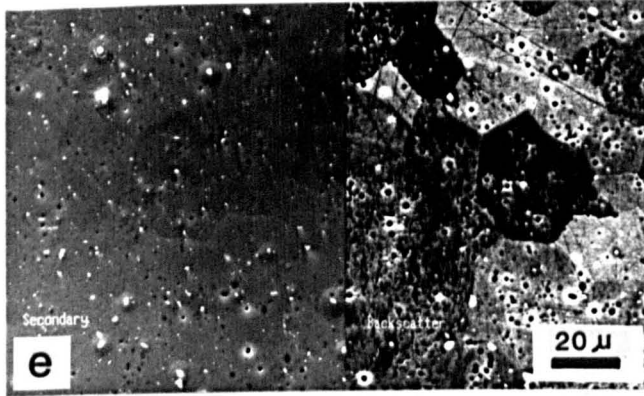
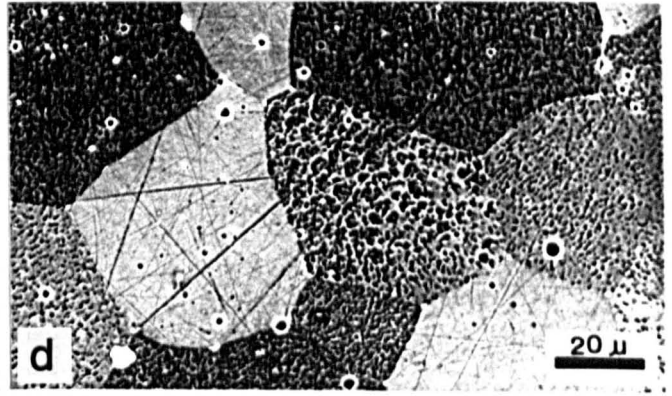
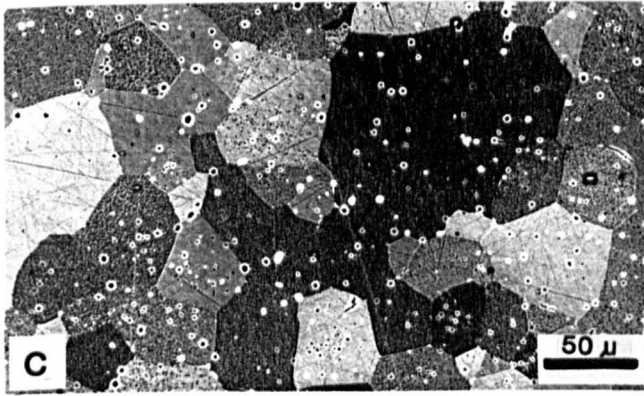
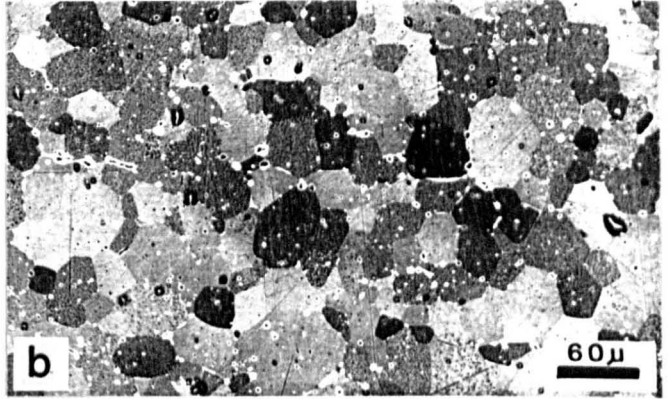
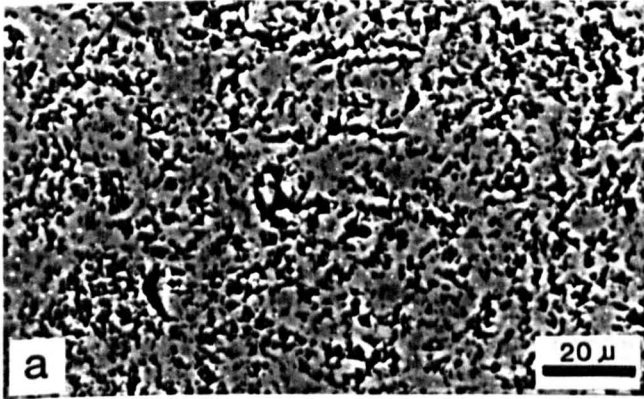
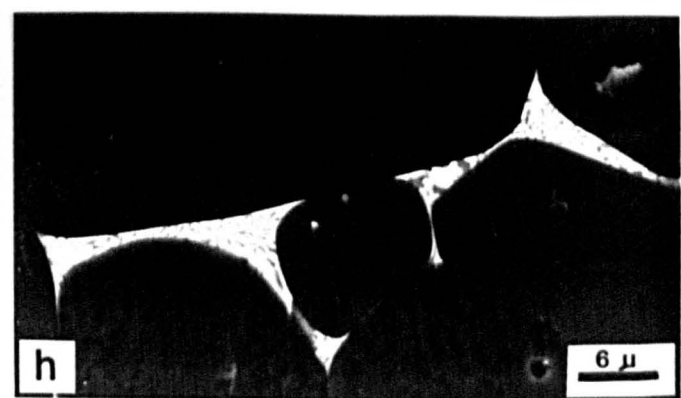
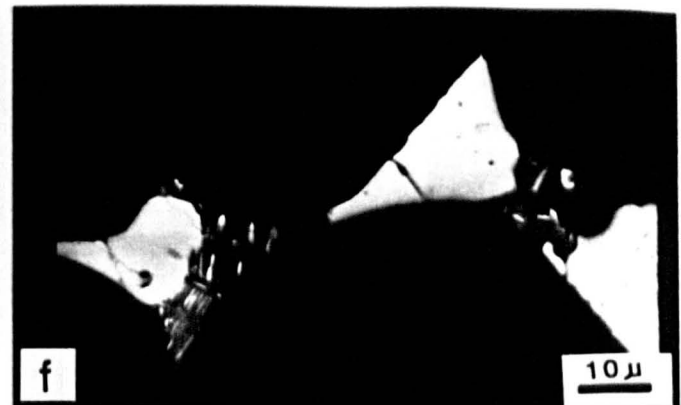
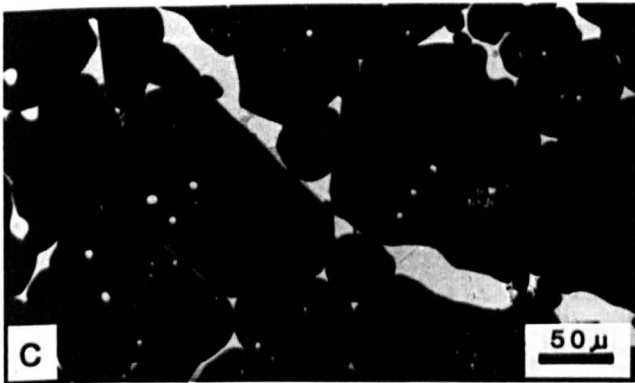
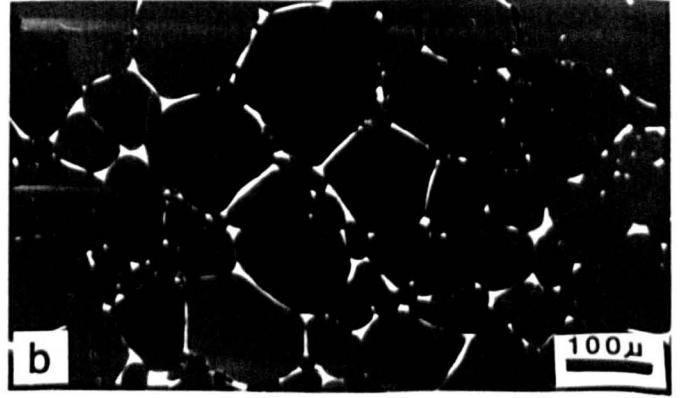
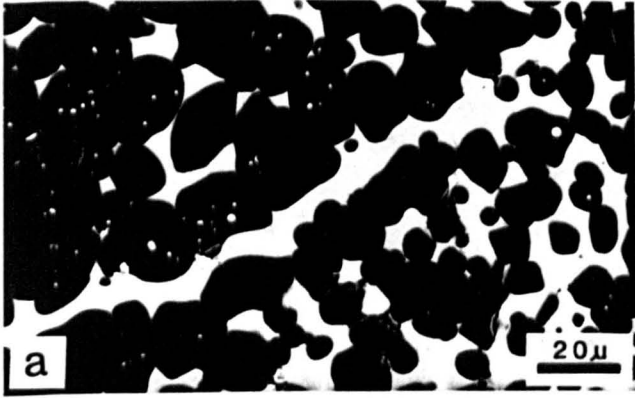


PLATE 16

Backscattered electron micrographs of impurity phases in natural dead burned magnesite (sample A3). The main impurity phases are C_3S , lime, C_3A and C_2F .

- a) White Tricalcium silicate appears between the spherical periclase (black) grains, or coalesce to form a narrow white vein. Some impurities specially free limes and C_2F , are formed as a little rounded grains on the surface of periclase grains. These small white and rounded inclusions are usually hydrated. There is a very poor direct boundary between the periclase grains. As it can be seen in this photograph, when the percentage of calcium silicate matrix is high, the crystal development of periclase is low (1500°C, 96 hrs).
- b) Polygonal periclase grains with no direct grain contact and a white dicalcium silicate matrix (1600°C, 108 hrs).
- c) General view to the periclase grains (black) and the matrix (white). The white impurities (C_3S) are appear in two forms, either filling the veinlets or as a small and rounded white inclusions between periclase grains. The grey patches within the tricalcium silicate impurities are C_3A (1600°C, 108 hrs).
- d) Closer view of the white area in the middle of plate 16c. In this photograph, black grains are periclase, the white parts are tricalcium silicate and the grey part is C_3A . Very little white grains inside the grey part are ferrites, and the darker greys are spinel (1600°C, 108 hrs).
- e) Dead burned magnesite containing black periclase grains together with white (tricalcium silicate) and grey (tricalcium aluminate) matrix. Spinel also formed as a darker grey patches between the tricalcium silicate grains (top right of photograph) (1600°C, 108 hrs).
- f) Closer view to one part of plate 16e. In this photograph, the white patches are tricalcium silicates, between these white grains, there are some darker areas which are tricalcium aluminate. The little white grains inside the grey area are ferrite (1600°C, 108 hrs).
- g) Common view of periclase (black grains) and the matrix (white). The white grains are tricalcium silicate. The percentage of tricalcium aluminate (grey) increase near the edge of matrix (1600°C, 108 hrs).
- h) Combination of periclase grains (dark-grey) and the matrix fillings spaces between them. In this photograph the white grains are C_2F and the little pale grey patches between them are C_3S (1400°C, 6 hrs).

PLATE 16



hydrate very easily and as a result only small rounded holes may remain (Plate 15c).

4.4.5.2 Sample A14

Phases determined in sample A14 in both secondary (SE) and backscattered (BSE) modes are summarized in Table 4.10 and the electron micrographs are presented in Plate 17-19.

Table 4.10 Phases present in the calcined magnesite samples as determined by energy dispersive X-ray analysis. (sample A14).

Temp/Time	(SE)	(BSE)
(1600°C, 108 hrs)	M, CMS	M, CMS, M ₂ S, SP, C ₂ S
(1600°C, 6 hrs)	M, C ₂ S, C ₃ S	M, C ₃ S, C ₂ S & / or C ₃ MS ₂
(1500°C, 96 hrs)	M, C ₂ S, C, C ₃ MS ₂	M, C ₂ S & / or C ₃ MS ₂
(1500°C, 24 hrs)	M, M ₂ S	M, C ₂ S & / or C ₃ MS ₂ , M ₂ S
(1500°C, 6 hrs)	M, C ₂ S & / or C ₃ MS ₂	M, C ₂ S & / or C ₃ MS ₂
(1400°C, 96 hrs)	M, CMS	M, C ₃ MS ₂ & / or C ₂ S
(1400°C, 24 hrs)	M, CMS, M ₂ S	M, CMS, C ₂ S & / or C ₃ S, C
(1400°C, 6 hrs)	M, CMS, M ₂ S, C, MF	M, M ₂ S, C ₃ S, C ₂ S & / or C ₃ MS ₂

Where:

M = periclase, C₂S = dicalcium silicate, C₃S = Tricalcium silicate, C₃A = tricalcium aluminate, C₂F = dicalcium ferrite, C = Lime, C₃MS₂ = Merwinite. Sp = Spinel

Details of identification of each phases and their mutual relationship are as follow:

4.4.5.2.1 Major phase (Periclase)

Sample A14 is an impure magnesite (Table 4.1). Periclase grains vary in size from one grain to another in samples calcined at different temperatures, but always they are larger at increasing temperatures and durations of calcination. In general the periclase grains are larger when calcined at increasing temperatures and times (Table 4.8). In this sample the periclase grains are rounded and separated from each other by large amounts of interstitial material (Plate 18e). Periclase grains are mostly spherical, but occasionally some polygonal crystals have been found (Plate 18b). The former is common and usually surrounded by a comparatively large amount of matrix phase (Plate 19a). When periclase grains are polygonal, they have usually six or more sides (Plate 18b), and in this case normally the impurities concentrate at the triple points of the periclase grains.

The amount of porosity in this sample is low and periclase grains at the surface either have a smooth appearance (Plate 17g) or an irregular aggregate like texture (Plate 17a).

4.4.5.2.2 Interstitial materials and their mutual relationship:

The impurities form a matrix between periclase grains, and as a result most of periclase grains are rounded (Plate 17g). At longer period of calcination, the interstitial

phases appear more crystalline (see Plate 17f in compare with Plate 17e).

4.4.5.2.2.a Forsterite - Monticellite

The phase relationship, between forsterite (grey) and monticellite (white) are given in Plate 18c. The matrix phases (monticellite, forsterite) are most concentrated at the triple point between periclase grains.

4.4.5.2.2.b Tricalcium silicate - Tricalcium aluminate

The phase relationship, between tricalcium silicate (white) and tricalcium aluminate (pale grey) are given in Plate 19g. Tricalcium silicate is almost spherical in shape. Tricalcium aluminate appears mostly between the tricalcium silicate and periclase grains. This combination of phases is rarely present.

4.4.5.2.2.c Monticellite - Dicalcium Silicate

The textural relationships between monticellite and dicalcium silicates are shown in Plates 19c, d and e. Dicalcium silicate forms as irregular elongated crystals, almost parallel and sometimes as irregular aggregates. Their intimate relationship perhaps indicates simultaneous crystallization.

4.4.5.2.2.d Dicalcium silicate - Tricalcium silicate

The phase relationship, between dicalcium silicate (white) and tricalcium silicate (very white) are given in

Plate 19a. Tricalcium silicate appears in this sample mostly as very small and rounded whiter grains between the dicalcium silicate. This phase combination is rare.

PLATE 17

Scanning electron micrographs of the surface of magnesia grains (sample A14), containing 3.12% SiO₂, 0.96% Al₂O₃, 0.30% Fe₂O₃, CaO/SiO₂ mole ratio of 0.77 and a Al₂O₃/Fe₂O₃ mole ratio of 5.00, after calcining at different temperatures (1400, 1500 and 1600°C), for different period of calcination times (6, 24, 96 and 108 hrs). Major impurities are formed between the periclase grains and when their percentage are high, they cover some parts of surface.

- a) Irregular, aggregate like small periclase grains causes by insufficient calcination temperature (1400°C, 6 hrs).
- b) Irregular aggregate like appearance of periclase grains. Most of periclase grains have polygonal shape. The grey and smooth patches between periclase grains are forsterite (1400°C, 24 hrs).
- c) Rosette like and hydrated lime (white) grains on the surface of periclase (1400°C, 6 hrs).
- d) Concentration of dicalcium silicate impurities as small rounded grains on the surface of periclase. The main matrix between the periclase grains is monticellite (1500°C, 24 hrs).
- e) Smooth and semi-rounded periclase grains with minor periclase grain contact. The impurities such as dicalcium silicates are beginning to develop between the periclase grains (1500°C, 6 hrs).
- f) Similar to Plate 17e but the minor interstitial phases appear more crystalline between the periclase grains. No direct bonding of periclase is visible. The grey and smooth surface material is forsterite. (1500°C, 96 hrs).
- g) Rounded to semi-polygonal periclase grains with very poor direct periclase grain contact. Impurities are present between the periclase grains (1600°C, 6 hrs).
- h) Polygonal and semi-rounded rough surface periclase grains with minor direct periclase grain contact (1600°C, 108 hrs).

PLATE 17

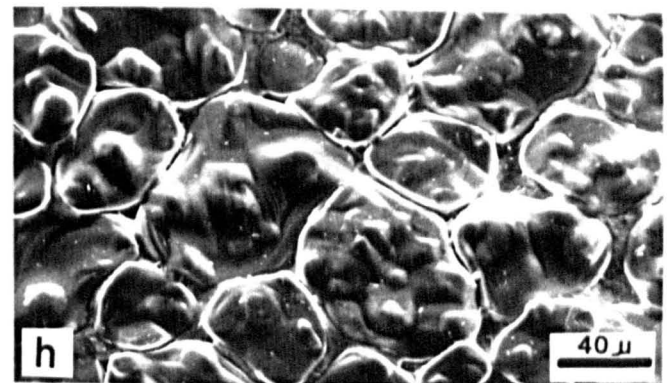
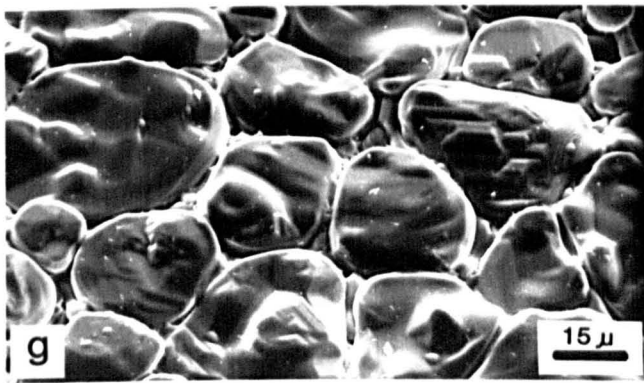
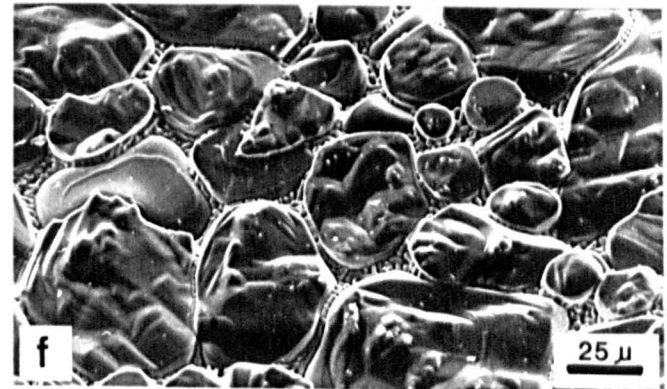
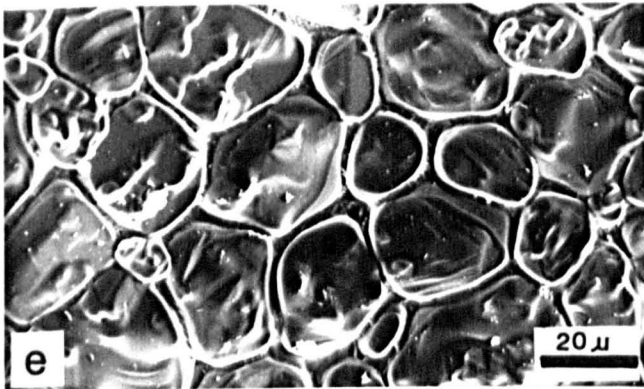
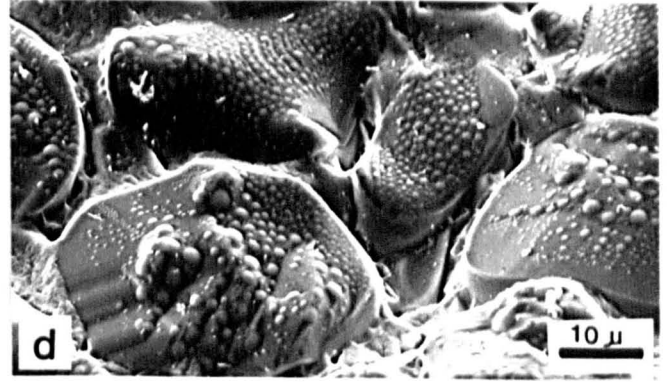
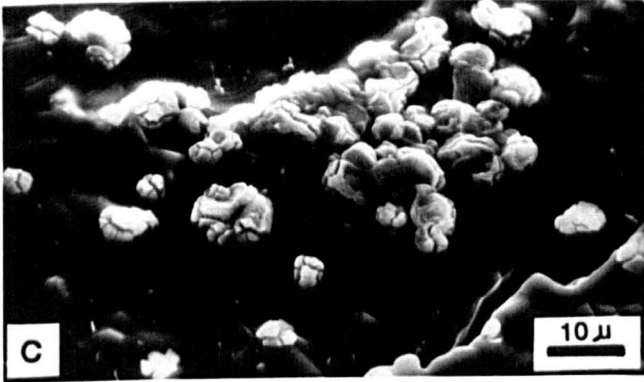
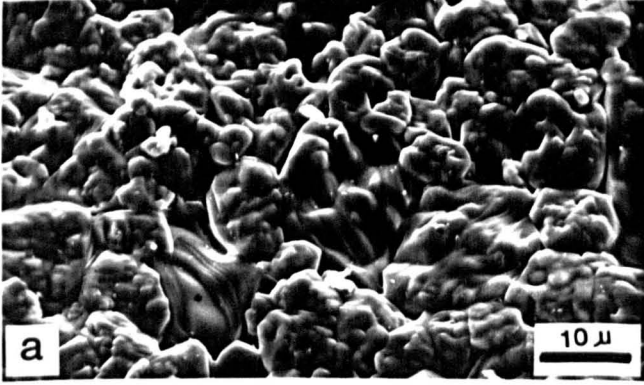


PLATE 18

Backscattered electron micrographs of natural dead burned magnesite (sample A14) containing 3.12% SiO₂, 0.96% Al₂O₃, 0.30% Fe₂O₃, CaO/SiO₂ mole ratio of 0.77 and a Al₂O₃/Fe₂O₃ mole ratio of 5.00.

- a) Rounded periclase grains having smooth (dark grey) and rough (dark) surface structures with very poor direct periclase grain contact. Two other main phases are visible, Forsterite (grey) and monticellite (white) calcined at 1400°C, for 24 hours.
- b) Detailed view of the different surface appearance of periclase grains. Where periclase has a rough surface structure, it is darker. A smooth surface is paler. The periclase grains are surrounded by a white matrix of monticellite. No direct contact between the periclase grains are visible (1500°C, 6 hrs).
- c) Rounded periclase grains (black) with no direct grain contact. The interstitial phases are forsterite (grey) and monticellite (white). A few large pores mainly at the periclase boundary are visible (1500°C, 24 hrs).
- d) This is a higher magnification of Plate 18c, showing the rounded periclase grains (black) with no direct grain contact. Forsterite (grey) and monticellite (white) are present between the periclase grains. Forsterite grains contain minor amounts of Ca in solid solution (1500°C, 24 hrs).
- e) Common view of the sample containing rounded periclase grains without grain contact, together with forsterite (grey) and monticellite (white) (1500°C, 24 hrs).
- f) Monochrome print taken from a pseudo colour image to enhance minor chemical differences. The rounded black grains are periclase. The matrix is dicalcium silicate which increases its Al content at the contact with the MgO grains. The increase is shown by the thin white rims at the contact with the periclase grains (1500°C, 24 hrs).
- g,h) General view of combination of periclase (black), forsterite (grey) and monticellite (white), (1600°C, 108 hrs).

PLATE 18

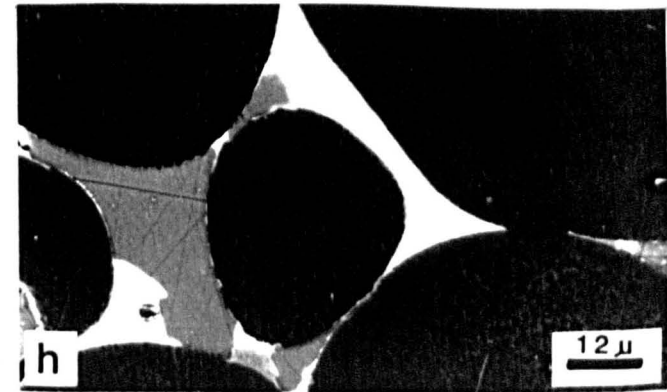
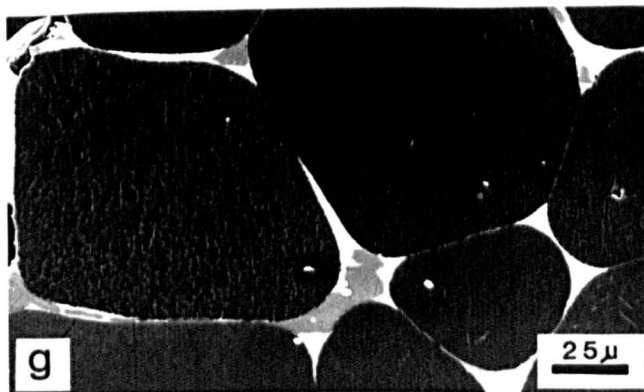
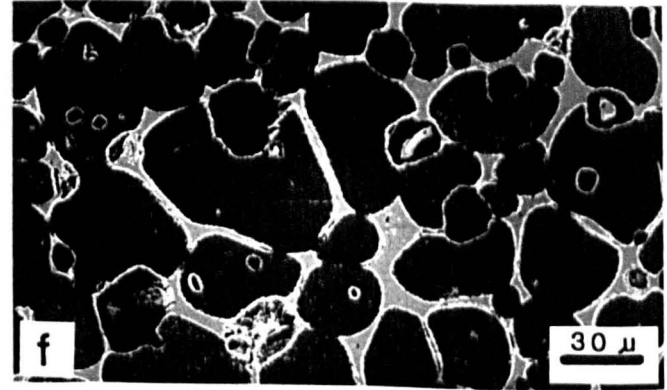
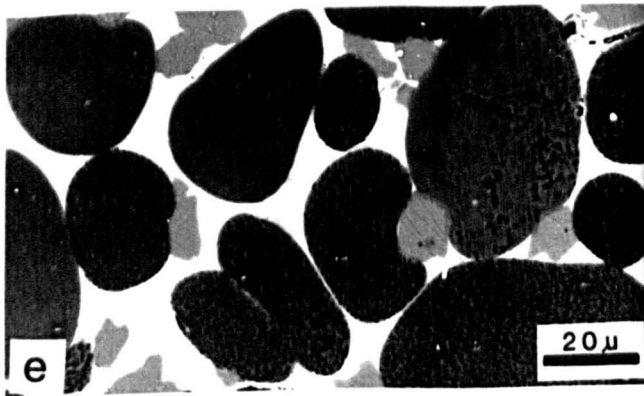
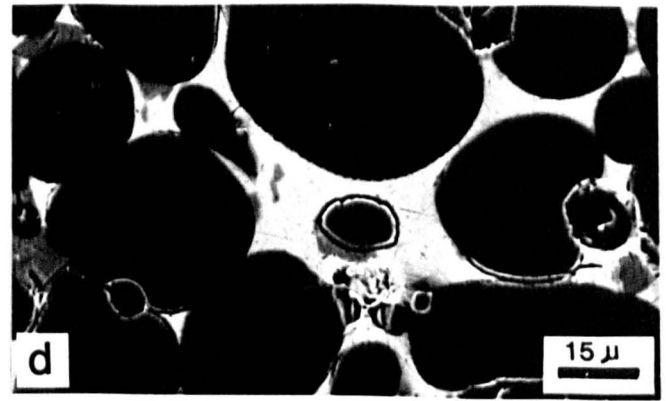
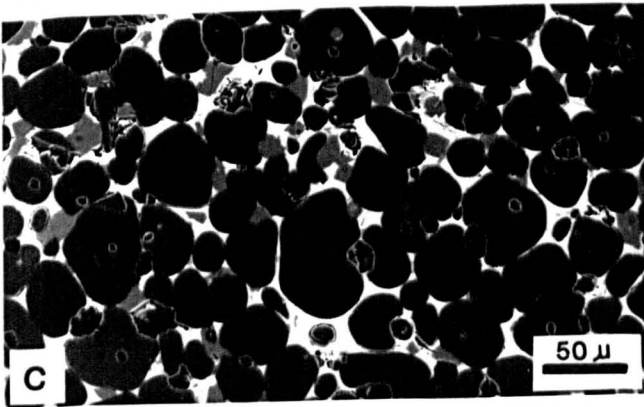
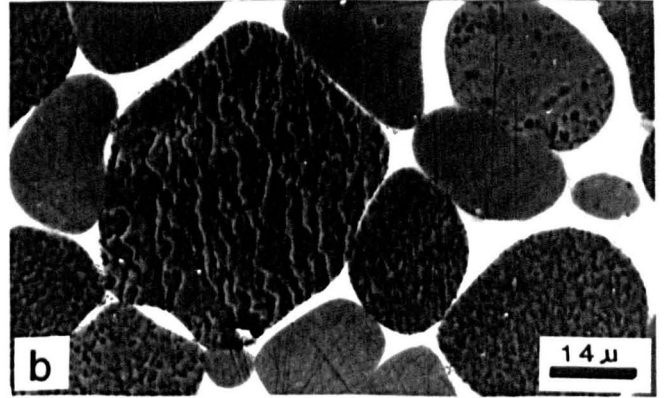
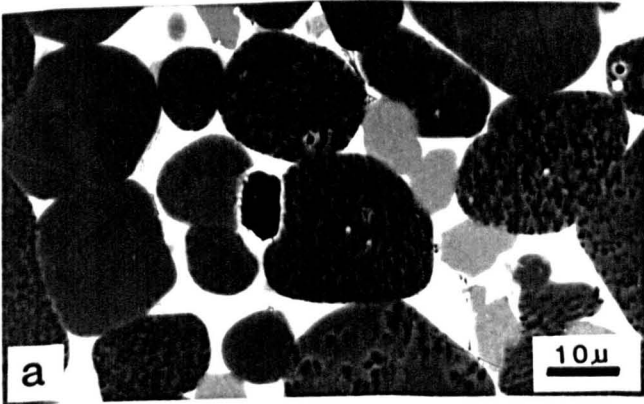
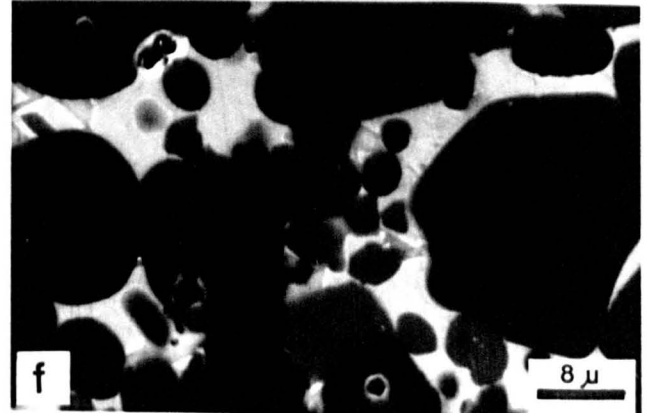
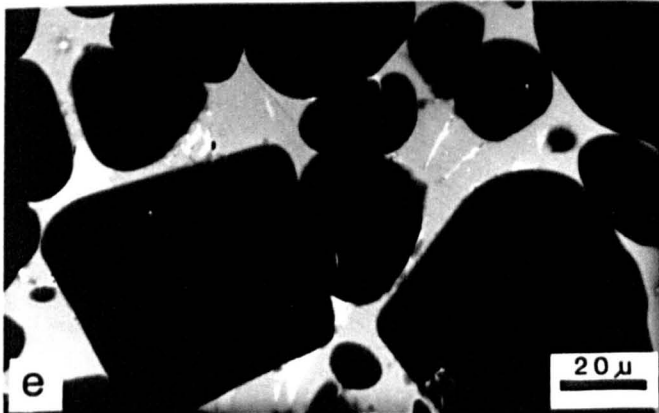
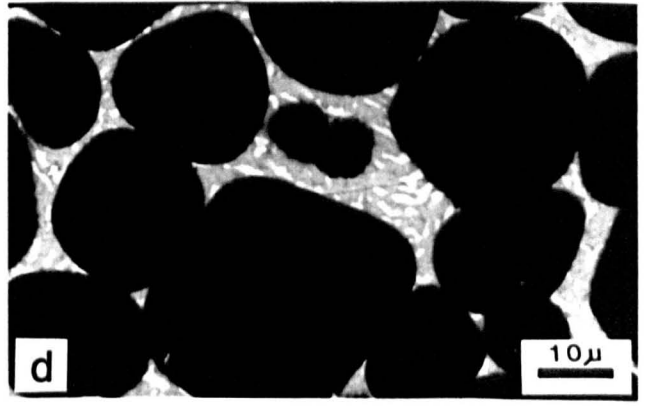
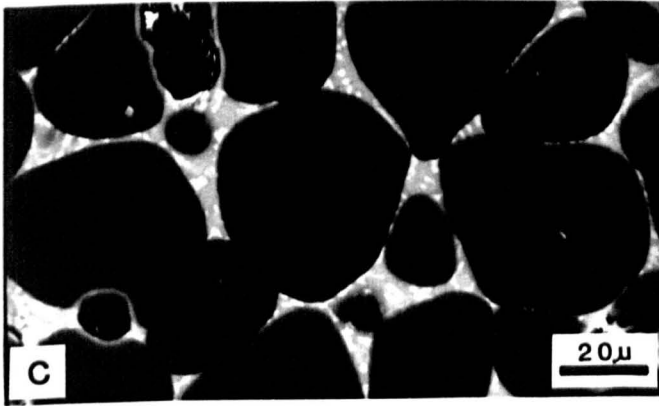
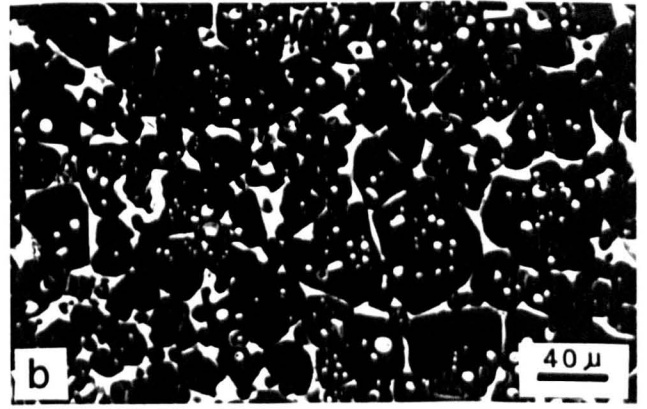


PLATE 19

Backscattered electron micrographs of natural dead burned magnesite (sample A14) containing 3.12% SiO₂, 0.96% Al₂O₃, 0.30% Fe₂O₃, CaO/SiO₂ mole ratio of 0.77 and a Al₂O₃/Fe₂O₃ mole ratio of 5.00.

- a) Individual rounded and small periclase grains (black) without any direct periclase - periclase grain contact. These periclase grains are surrounded by dicalcium silicates. The small whiter patches in the middle of photograph within dicalcium silicates are tricalcium silicate (1400°C, 96 hrs).
- b) General view of the matrix phase distribution between the periclase grains. The white impurities (C₃S) are mainly formed between the semi-rounded periclase (black) grains. Also few percentage of tricalcium silicate are present on the surface of periclase grains like round grains. These little rounded inclusions can hydrate very easily and as a result little holes remain. In this sample the following phases are identified, periclase (black), tricalcium silicates (white), and hydrated limes (grey), (1400°C, 24 hrs).
- c,d,e) Common views of the combination of periclase and the matrix phases. In these photographs, the rounded black grains are periclase. The greyish white phase between periclase grains are monticellite, and the white elongate areas between monticellite phase are dicalcium silicate. The calcination conditions are (1600°C, 6 hrs), (1500°C, 6 hrs), and (1400 °C, 96 hrs) for (Plates 19c, d, e) respectively.
- f) In this photograph the following phases are identified, periclase (black), monticellite (white), forsterite with some Ca solid solution (dark grey) and finally little pale grey grains between the white patches are of an unidentified phase containing Ca, K, Si, Al, Fe and Mg (Figure 4.3n) (1400°C, 6 hrs).
- g) Periclase (black) and matrix phases. The white matrix is C₃S and the grey patches between the white areas are C₃A. (1600°C, 6 hrs).
- h) Detailed view to the combination of periclase (black), monticellite (white), and forsterite (grey) (1600°C, 108 hrs).

PLATE 19



4.4.5.3 Sample T2

Phases determined in sample T2 in both secondary (SE) and backscattered modes (BSE) are summarized in Table 4.11 and their electron micrographs are presented in Plates 20-23.

Table 4.11 Phases present in the calcined magnesite samples as determined by energy dispersive X-ray analysis (sample T2).

Temp/Time	(SE)	(BSE)
(1600°C, 108 hrs)	M, C ₂ S, C ₃ S, C ₃ A	M, C ₂ S, C ₃ S, C
(1600°C, 6 hrs)	M, C ₂ S	M, C ₃ S, C ₃ A
(1500°C, 96 hrs)	M, C ₂ S, C ₃ S	M, C ₃ S, C ₃ A
(1500°C, 24 hrs)	M, C ₂ S, C ₃ S, C	M, C ₃ S, C
(1500°C, 6 hrs)	M, C ₂ S	M, C ₃ S, C ₂ S
(1400°C, 96 hrs)	M, C ₂ S	M, C
(1400°C, 24 hrs)	M, C ₂ S, C ₃ S	M, C ₃ S, C
(1400°C, 6 hrs)	M, SP	M, C ₃ S, C

Where:

M = Periclase, C₂S = dicalcium silicate, C₃S = tricalcium silicate, C₃A = tricalcium aluminate, C = lime, Sp = spinel.

Details of identification of each phases and their mutual relationship are as follow:

4.4.5.3.1 Major phase (periclase)

In sample T2 generally the amount of impurities are low and thus there is a high amount of contact between the

periclase grains (Plate 21c). Periclase grains sizes vary considerably and a perfect cubic cleavage can be seen on the surface of some grains. Grain size measurements are presented in Table 4.8.

Periclase grains either have smooth (Plate 20h) or irregular appearance (Plate 20e). Occasionally both types of textures are found in one sample.

Only small periclase crystals develop (Plate 20a) at low temperature. Both spherical and polygonal periclase grains have been recognised and shown in Plates 20h and 21f respectively. Plate 21b shows the concentric step like growth of periclase crystals.

Periclase grains in this sample are smaller in size than those from other samples. This is probably due to the level and type of impurities, (Insley and Frechette, 1955, Chesters, 1973 and Turkdogan, 1980. Insufficient sintering results in a very small crystal size (Plate 22a). Two main surface structures are present, smooth and rough surface structures (Plate 22h).

4.4.5.3.2 Interstitial materials (matrix phases)

The matrix phases which are mostly of dicalcium silicate and tricalcium silicate are present at the triple points between the periclase grains (Plate 22). In this case periclase grains are mostly polygonal. Larger amounts of impurities when present give increased separation of periclase grains (Plate 23a) and results in rounded periclase grains.

PLATE 20

Scanning electron micrographs of the surface of natural dead burned magnesite (sample T2) calcined at different temperatures (1400, 1500 and 1600°C) for different period of calcination (6, 24, 96 and 108 hours). This sample contains 0.99% SiO₂, 2.51% CaO and a CaO/SiO₂ mole ratio of 2.72.

- a) Very small cubic periclase crystals. There is minor Ca impurities in some whiter grains calcined at 1400°C for 24 hours.
- b) Step like growth on the surface of periclase grains (1400°C, 96 hrs).
- c) Step like growth on the surface of periclase grains. The whiter and very smooth surfaces are interstitial dicalcium silicate (1500°C, 6 hrs).
- d) Periclase grains with high direct periclase - periclase grain contact. On the periclase grains, step like growth is visible. Dicalcium silicate impurities form like a very small rounded grains on the surface of periclase grains. (1500°C, 96 hrs).
- e) Irregular aggregate-like periclase grains (1500°C, 96 hrs).
- f) Tricalcium silicate with rounded surface present in large amounts covering underneath periclase grains (1500°C, 24 hrs).
- g) Variable crystal size of periclase grains (1500°C, 6 hrs).
- h) Closer view of the larger periclase grains from plate 20g. The periclase grains are rounded and there is much void space between them (1500°C, 6 hrs).

PLATE 20

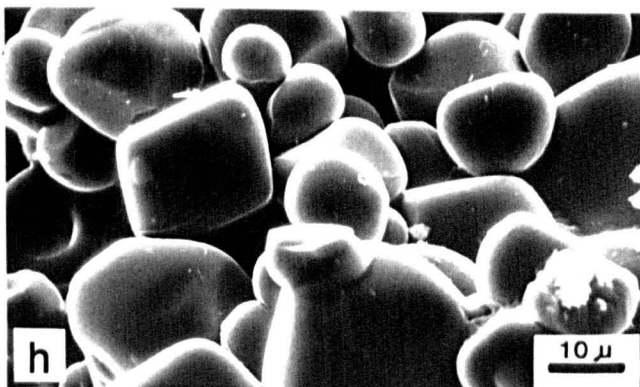
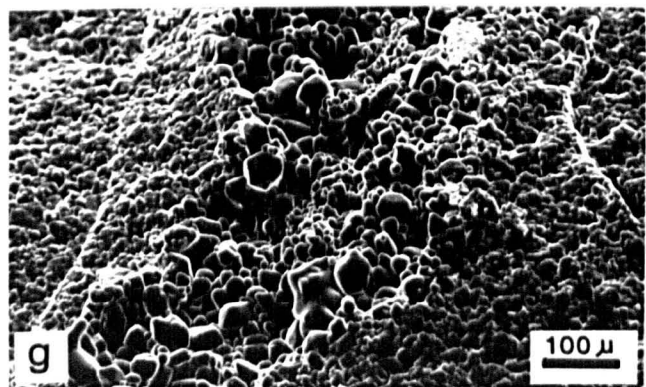
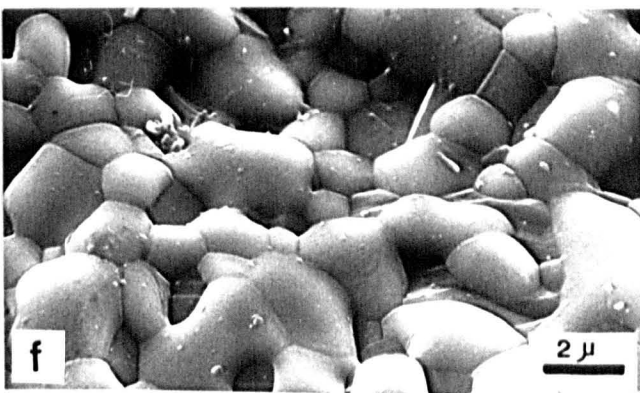
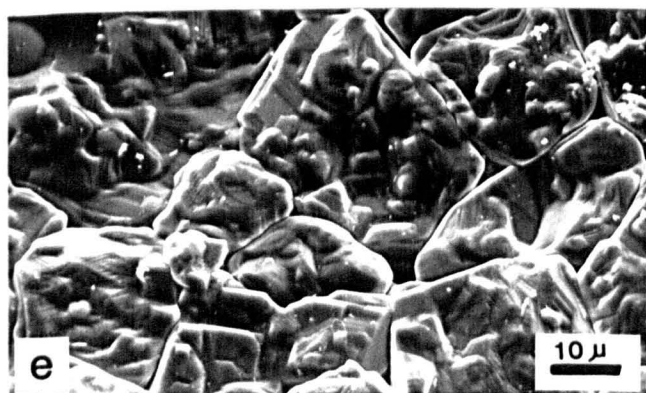
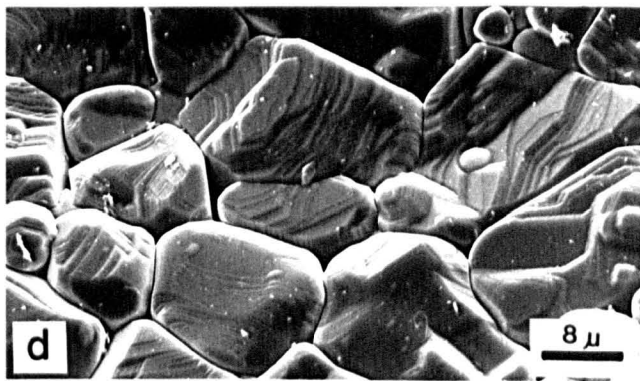
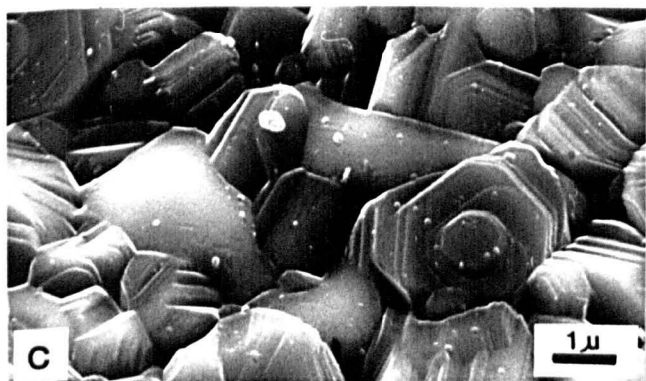
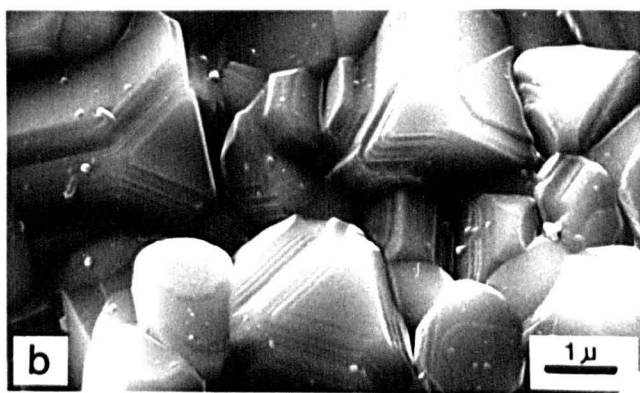
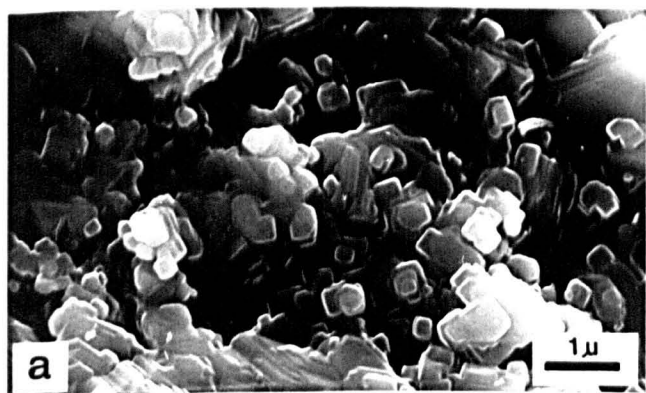


PLATE 21

Scanning electron micrographs of the surface of natural dead burned magnesite (sample T2) containing 0.99% SiO₂, 2.51% CaO and a CaO/SiO₂ mole ratio of 2.72. In this sample the main impurities are dicalcium and tricalcium silicate, calcined at different temperatures of 1400, 1500 and 1600°C for various calcination times of 6, 24, 96 and 108 hours.

- a) Periclase grains with step like growth structure, with a matrix of smooth appearance which is dicalcium silicate. This sample calcined at 1600°C for 6 hours).
- b) Detail of the surface of one periclase grain showing step like growth (1600°C, 6 hrs).
- c) Periclase grains, with dicalcium silicate in very minor amounts present between periclase grains and as a small globules on the surface of periclase grains (1600° C, 6 hrs).
- d) Periclase grains with step like growth structure, with a matrix of smooth appearance, which is dicalcium silicate (1600°C, 108 hrs).
- e,f) Dense aggregate of periclase grains showing step-like growth, with dicalcium silicate present in very minor amounts typically as small globules (1600°C, 108 hrs).
- g) Rounded merwinite grains are present on the surface of periclase grains (1600°C, 108 hrs).
- h) Irregular elongate growth sometimes present on the surface of samples due to the hydration of lime (1600°C, 108 hrs).

PLATE 21

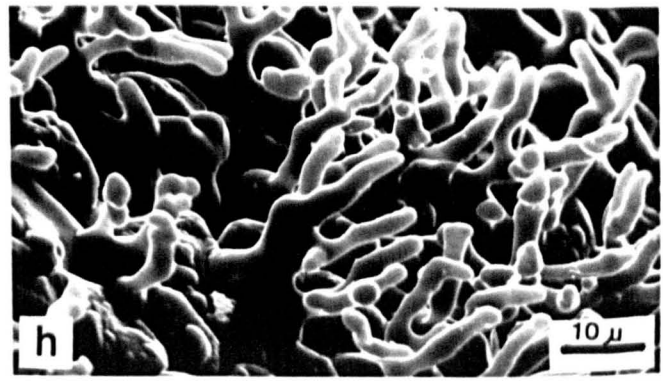
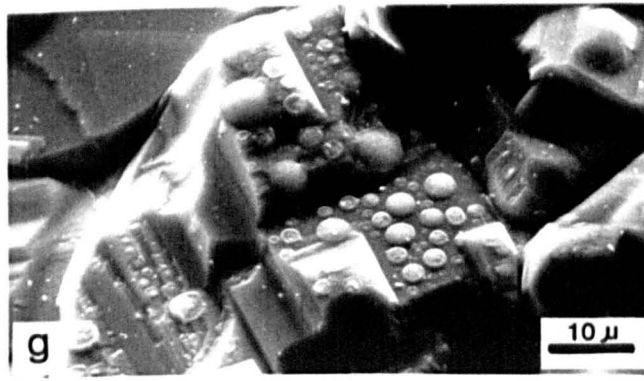
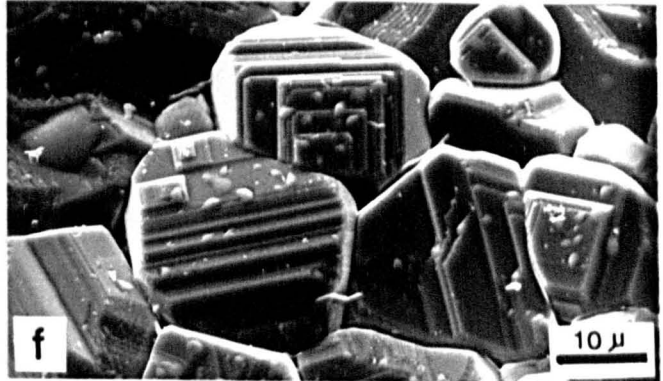
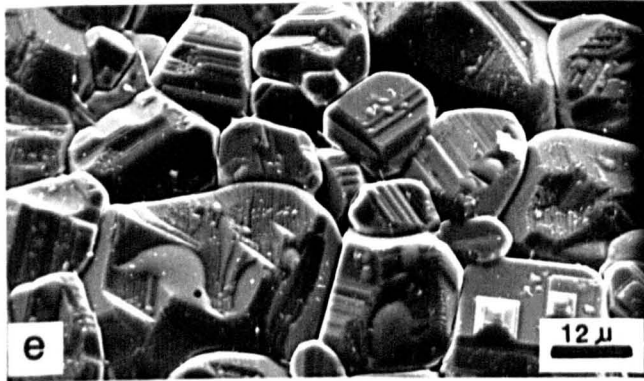
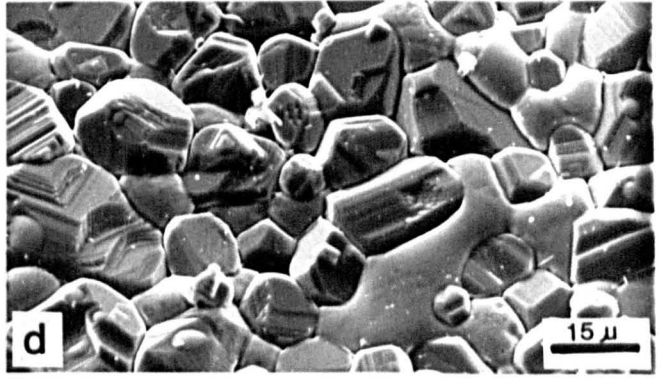
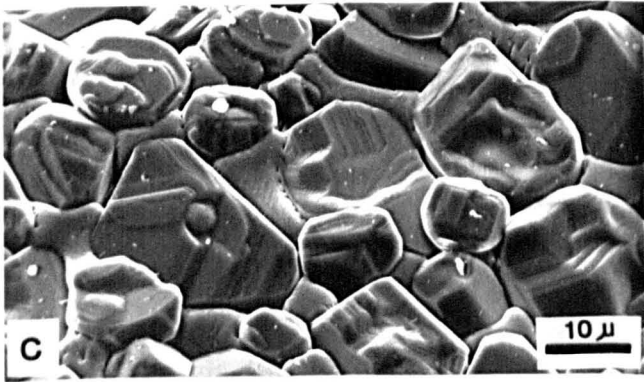
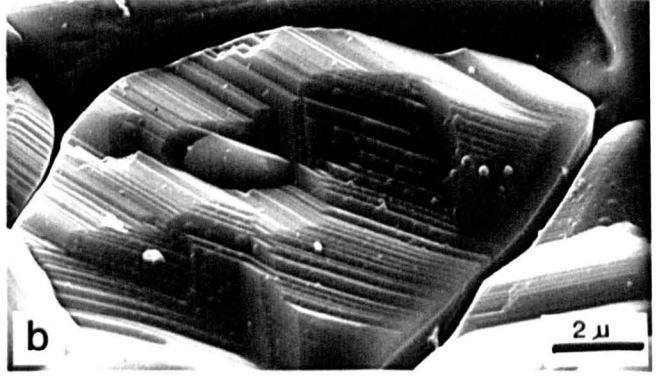
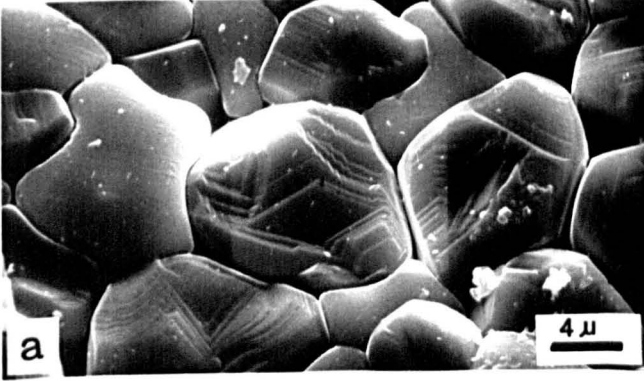


PLATE 22

Backscattered electron micrographs of natural dead burned magnesite (sample T2) containing 0.99% SiO₂, 2.51% CaO and a CaO/SiO₂ mole ratio of 2.72. In this sample which is quite pure the percentage of impurities such as Fe₂O₃ which promote crystal growth in periclase grains are below detection limit, so the the periclase grain size are very small.

- a) Periclase (grey) and irregular distribution of other phases such as dicalcium and tricalcium silicates and lime are poorly developed, calcined at 1400°C for 6 hours).
- b) Closer view to the periclase (black) and other phases which are tricalcium silicate (white) and C₃A (grey patches) (1400°C, 24 hrs).
- c) Small periclase grains (grey). The matrix phase contain mainly of tricalcium silicate and lime as a little white grains, (1400°C, 6 hrs).
- d) Similar to (c) but more crystal growth as a result of longer calcination time (1400°C, 96 hrs).
- e, f, g) Common views of three samples calcined in different times and temperatures. Three main phases are present: periclase (dark grey), dicalcium silicate, tricalcium silicate and lime (white) Normally the little rounded grains which are formed on the surface of periclase grains are lime. The calcination conditions are: (1500°C, 24 hrs), (1500°C, 96 hrs), and (1600°C, 6 hrs), for Plate 22e, f and g respectively.
- h) At the higher calcination temperatures (1600°C) and for the longer firing time, the periclase grains grow larger. Periclase grains (grey) are surrounded by white dicalcium and tricalcium silicate impurity phases. The periclase grains have shown two main surface structures mainly of smooth (grey) and rough (darker grey) (1600°C, 108 hrs).

PLATE 22

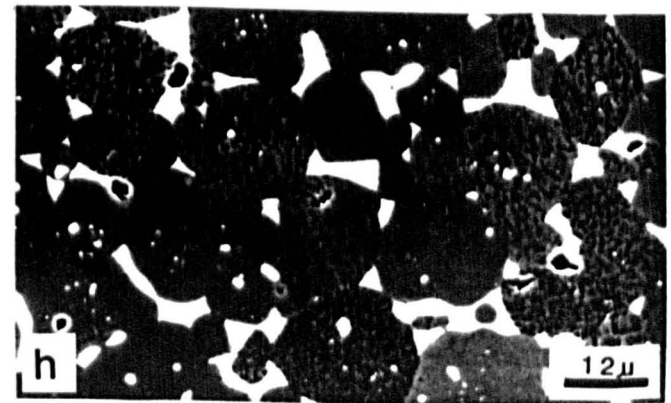
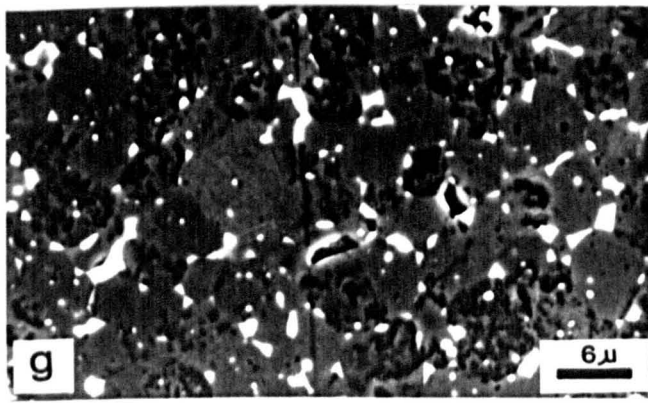
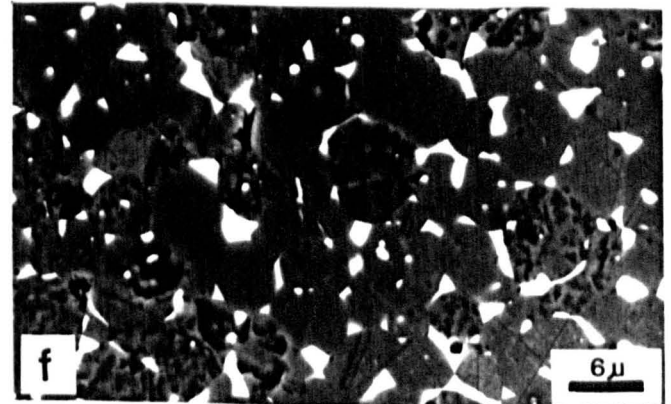
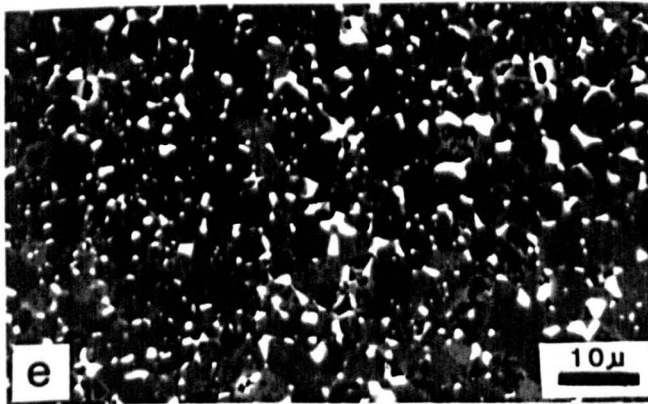
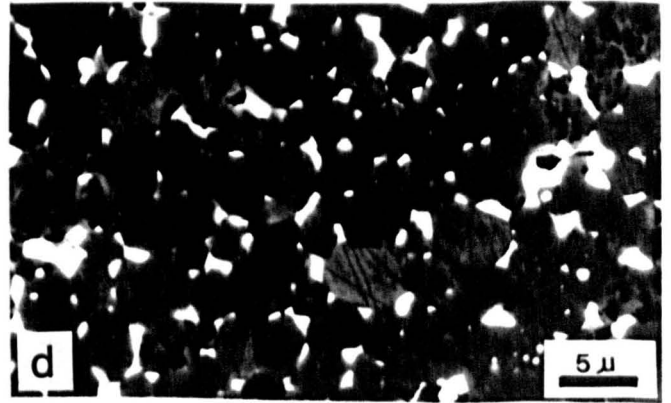
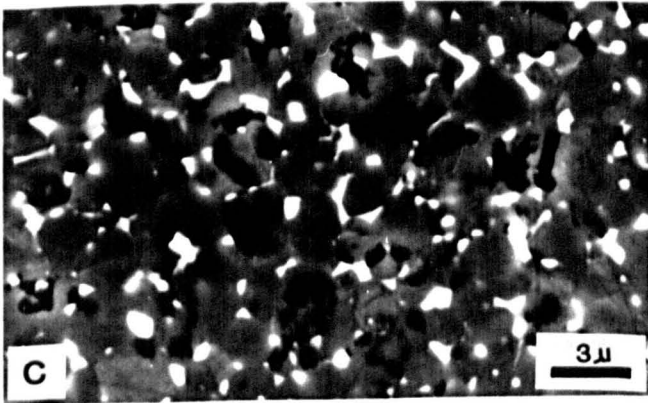
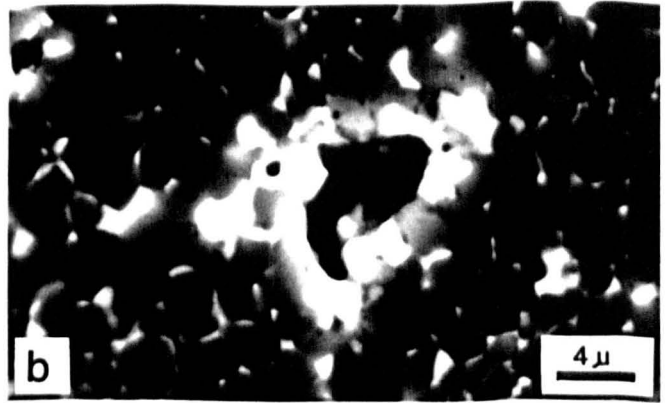
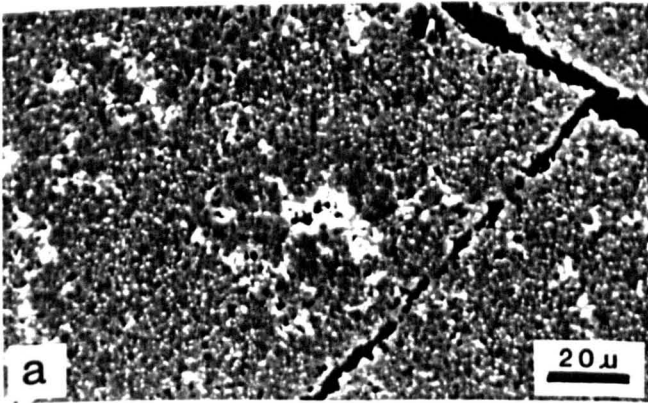
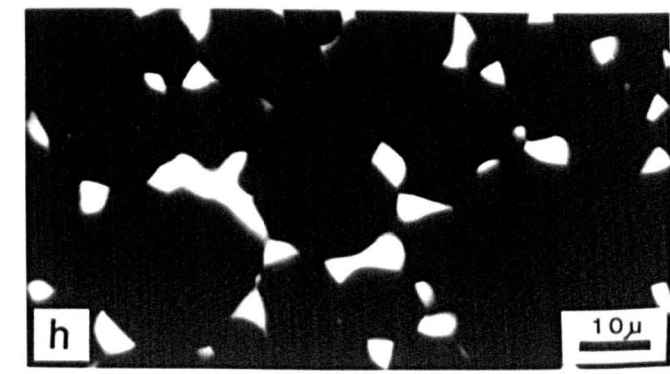
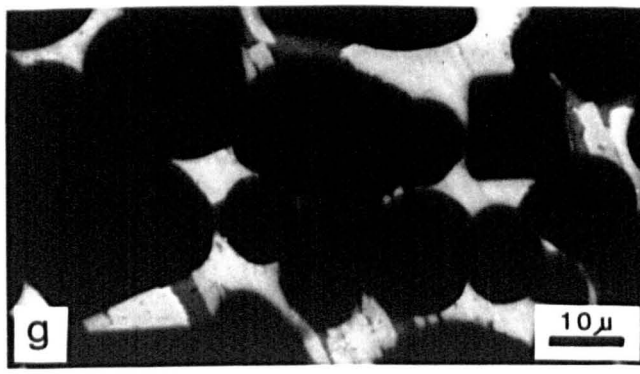
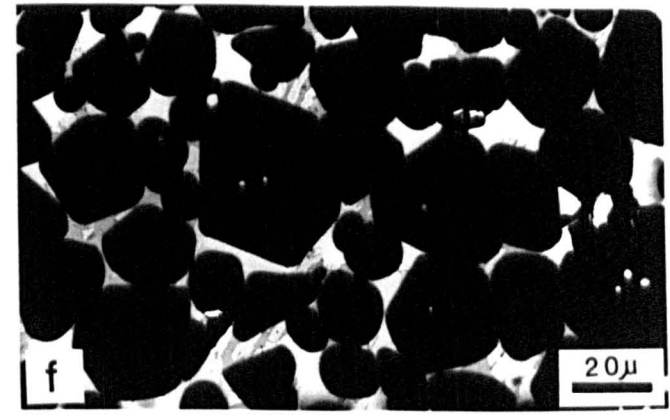
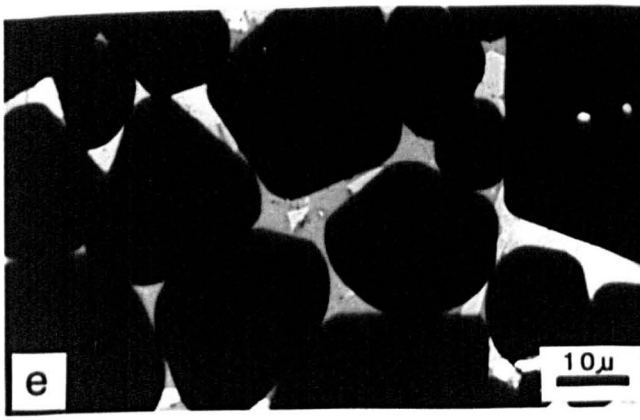
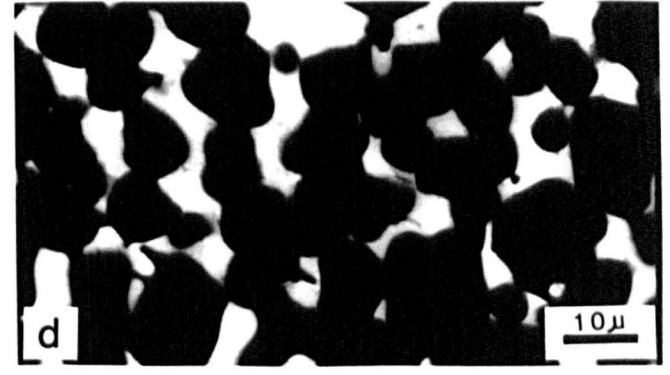
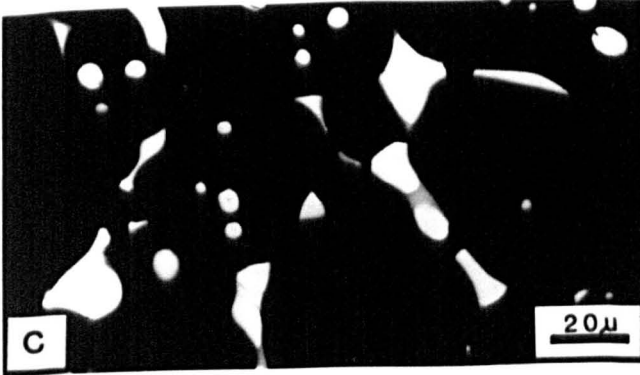
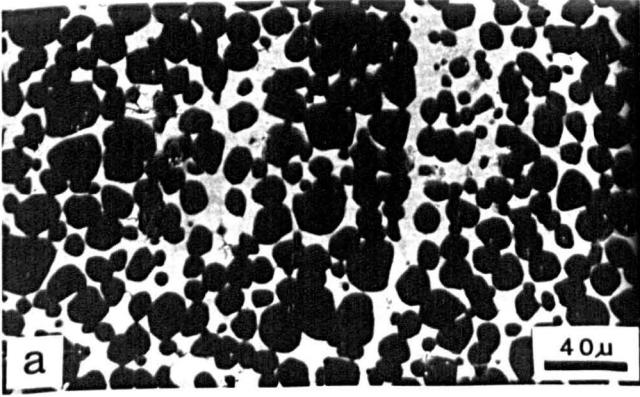


PLATE 23

Backscattered electron micrographs of minor phases of natural dead burned magnesite, (sample T2) containing 0.99% SiO_2 , 2.51% CaO and a CaO/SiO_2 mole ratio of 2.72. This sample calcined at different temperatures of 1400, 1500 and 1600°C for various calcination times of 6, 24, 96 and 108 hours.

- a,b) Spherical periclase grains (black), with very poor direct bonding. The matrix of tricalcium silicate (white) are present between the periclase grains, calcined at 1600°C, for 108 hours).
- c) Periclase grains (black) with interstitial matrix of tricalcium silicate (white), and tricalcium aluminate (pale grey) (1500°C, 96 hrs).
- d) Common view to the combination of periclase (black) and dicalcium silicates (white) grains, (1500°C, 24 hrs).
- e,f,g) Common view of three main phases in sample T2. Periclase grains which are mostly rounded without direct grain boundary, C_3S (white) and C_3A which appear in grey colour, (1600°C, 6 hrs).
- h) Common view to the sample T2 with two main phases, periclase (black) and dicalcium silicate (white) (1600°C, 108 hrs).

PLATE 23



Impurities are present also in very minor amounts as small globules on the surface of periclase grains (Plate 21g). Larger amounts of impurities can cover entirely surface of sample (Plate 20f).

The porosity in sample T2 is very low.

4.4.5.3.3 Rare feature

Tricalcium aluminate (grey) appears as small rod-like grains within tricalcium silicate (white) (Plate 23g).

4.4.5.4 Sample T15

Different phases determined in sample T15 using both secondary (SE) and backscattered (BSE) modes are summarized in Table 4.12 and the electron micrographs are presented in Plate 24-27.

Table 4.12 Phases present in the calcined magnesite samples as determined by energy dispersive X-ray analysis (sample T15).

Temp/Time	(SE)	(BSE)
(1600°C, 108 hrs)	M, CMS	M, CMS, M ₂ S, C, C ₂ S
(1600°C, 6 hrs)	M, CMS	M, C ₃ MS ₂ , M ₂ S
(1500°C, 96 hrs)	M, CMS, M ₂ S, C, C ₂ S	M, CMS, C ₃ MS ₂
(1500°C, 24 hrs)	M, CMS, M ₂ S	M, CMS, M ₂ S, C ₃ MS ₂
(1500°C, 6 hrs)	M, C ₃ S, C	M, CMS, M ₂ S, C ₃ MS ₂
(1400°C, 96 hrs)	M, M ₂ S	M, M ₂ S, C ₃ MS ₂
(1400°C, 24 hrs)	M, CMS	M, CMS, M ₂ S, C ₃ MS ₂
(1400°C, 6 hrs)	M, CMS, M ₂ S, C ₂ S &/or C ₃ S	M, CMS, M ₂ S, C ₂ S &/C ₃ MS ₂

Where:

M = Periclase, C₂S = dicalcium silicate, C₃S = tricalcium silicate, C₃A = tricalcium aluminate, C = lime, Sp = spinel.

Details of identification of each phases and their mutual relationship are as follow:

4.4.5.4.1 Major phase (periclase)

Periclase grains are larger at increased calcination temperature and time. Most of periclase grains are rounded (Plate 25c).

The amount of porosity in this sample is higher than the others. The closed pores are mainly at the periclase boundaries and they have irregular shapes. Periclase grains either have a smooth appearance (Plate 25c) or an irregular aggregate like texture (Plate 24d). Small periclase crystals which are shown in Plate 24a result from low temperature sintering.

Periclase grains are spherical and surrounded by a comparatively large amount of matrix (monticellite and forsterite) phases. No direct periclase - Periclase grain contacts are visible. The grain size of periclase varies in different samples (Table 4.8). This variation depends on the calcination temperatures and times and the amount of impurities. Low temperatures result in a very small crystal size (Plate 26a).

4.4.5.4.2 Interstitial materials (matrix Phases)

The matrix phases, mainly of monticellite and forsterite are present between the periclase grains as separate patches (Plate 26h) or as veinlets (Plate 26f).

In most parts of sample monticellite as a matrix phase completely surrounds periclase grains (Plate 24h), higher amounts of impurities can cover all the surface of periclase grains (Plate 24c).

Forsterite and monticellite exhibit a variety of textures, these textures are presented in Plate 26 and 27. Plate 26a shows poorly developed monticellite and forsterite appearing as separate patches. This texture appear only at low temperatures of sintering. Forsterite veinlets crossing the magnesia grains are presented in Plate 26f. Forsterite may have taken advantage of cracks in the material flowing into them before crystallizing. When the amount of both forsterite and monticellite are very high, they segregate as separate patches (Plates 26h). More frequently, monticellite tends to concentrate at the triple points and forms "bridges" between the periclase grains, but monticellite also forms as separate and rounded grains (Plate 27d).

4.4.5.4.3 Rare feature

Dicalcium and tricalcium silicates are rarely observed at the triple points of periclase grains (Plate 25g). Lime is occasionally found as small and partly hydrated grains (grey) between the whiter calcium silicate matrix.

PLATE 24

Scanning electron micrographs of the surface of natural dead burned magnesite (sample T15) containing 5.41% SiO₂, 2.44% CaO and a CaO/SiO₂ mole ratio of 0.48. The main impurity phase is monticellite, but the little rounded grains on the surface of periclase grains are normally C₂S.

- a) Small periclase grains with large voids between them. Low calcination temperature is the main reason for small periclase grains. This sample calcined at 1400°C for 24 hours.
- b) Detail of a showing cubic periclase crystals (1400°C, 6 hrs).
- c) Forsterite covering periclase grains (1400°C, 96 hrs).
- d) Spherical periclase grains in different grain size. At the top left of photograph, the monticellite has flowed around the periclase grains probably in the molten state (monticellite m.pt. = 1502°C). Calcined at 1500°C for 6 hours.
- e) More details on the surface of periclase grains and the impurities such as monticellite which are flowed around the periclase grains (1500°C, 6 hrs).
- f) Periclase grains associated with impurities of dicalcium silicate which forms between the periclase grains or appear as small rounded and white grains on the surface of periclase (1500°C, 24 hrs).
- g,h) Detailed study of periclase grains and the impurities which are mainly of monticellite. (1500°C, 96 hrs).

PLATE 24

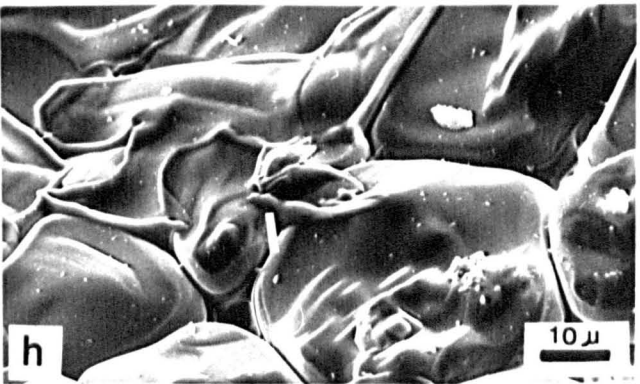
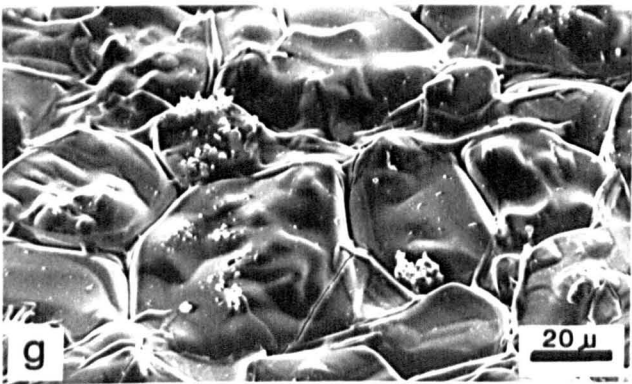
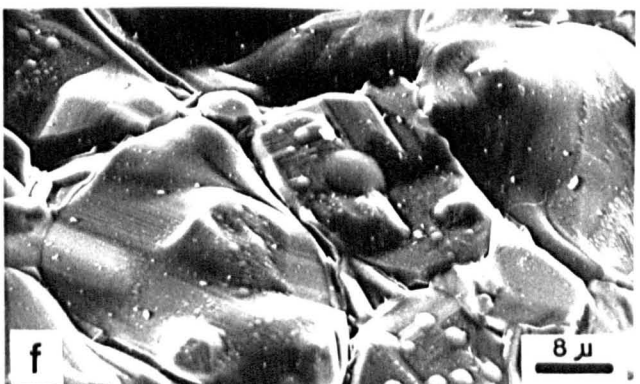
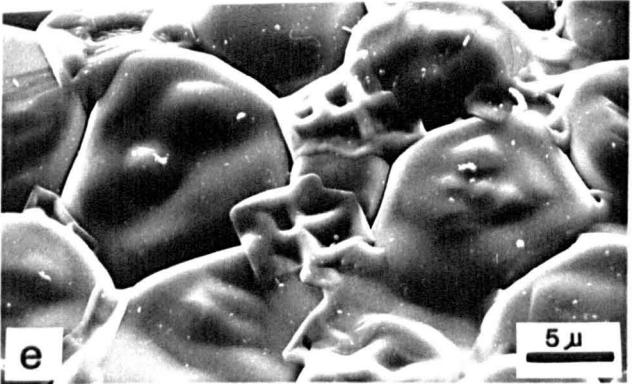
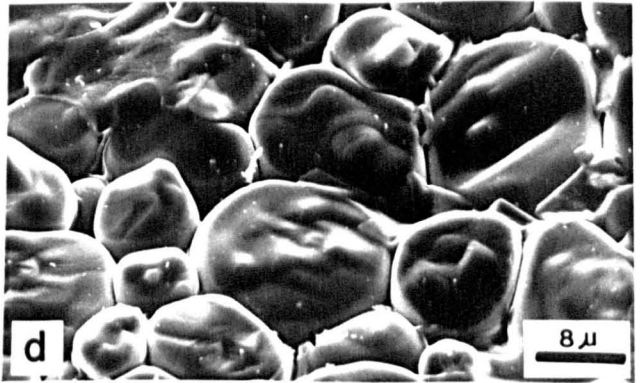
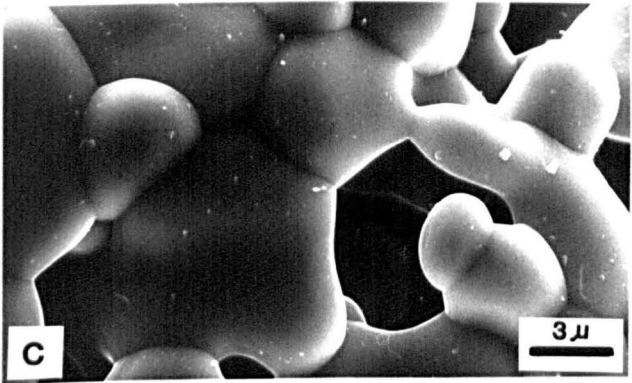
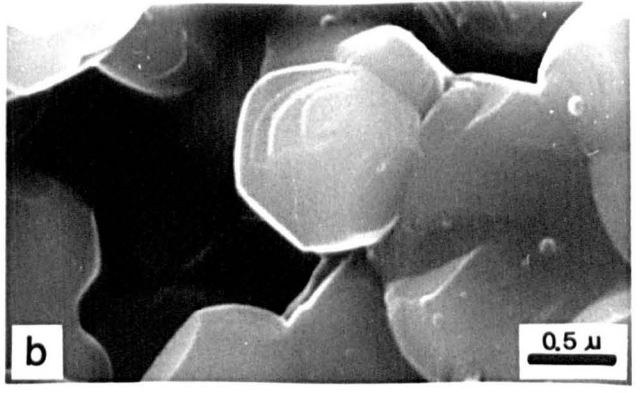
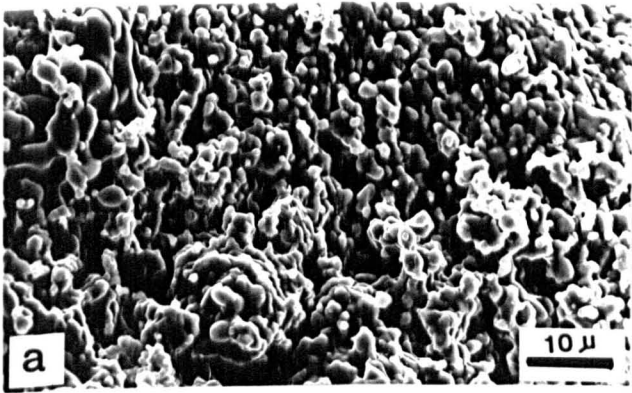


PLATE 25

Scanning electron micrographs of the surface of natural dead burned magnesite, (sample T15) containing 5.41% SiO₂, 2.44% CaO and a CaO/SiO₂ mole ratio of 0.48. This sample calcined at different temperatures of 1400, 1500 and 1600°C, for various calcination times of 6, 24, 96 and 108 hours.

- a,b,c) Various magnification showing periclase grains with variable amount of interstitial monticellite. The monticellite has flowed around the periclase grains, probably in the molten state (monticellite melting point is 1502°C). Calcined at 1600°C for 6 hours.
- d) General view to the different size periclase grains having little knob on the surface, These little knobs are periclase as well with few percentage of si and ca solid solution (1600°C, 108 hrs).
- e,f) The Impurity phases are concentrated in separate patches. These are monticellite and forsterite with smooth appearance. Their grains are larger than the surrounding periclase (1500°C, 6 hrs).
- g) Periclase with high amount of grain contact. Impurities such as dicalcium silicate are present at the triple points (1600°C, 108 hrs).
- g) Polygonal periclase grains having direct periclase grain boundary. Impurities such as dicalcium silicate are formed between the periclase grains (1600°C, 108 hrs).
- h) Acicular (rod like) crystals of dicalcium silicates (1500°C, 24 hrs).

PLATE 25

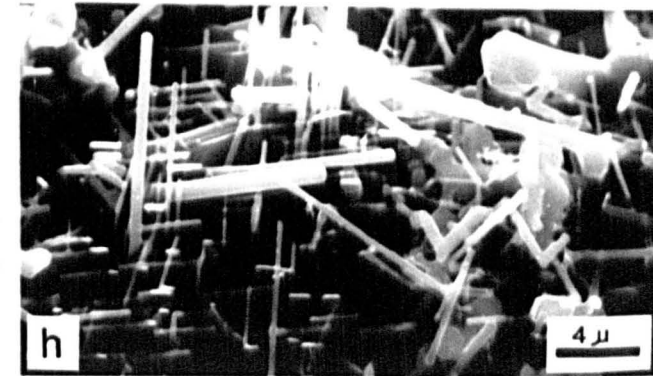
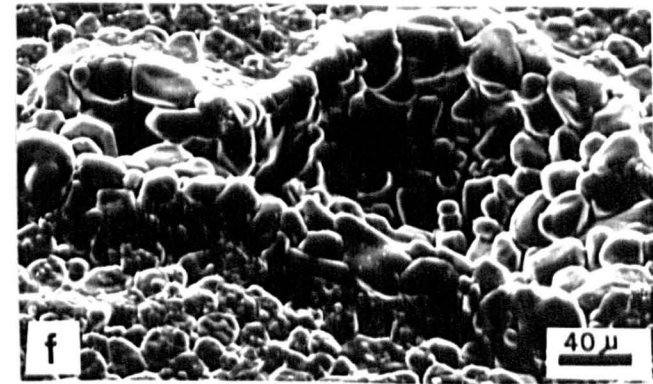
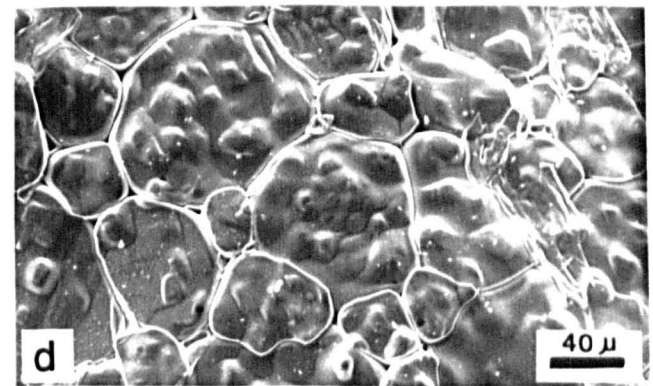
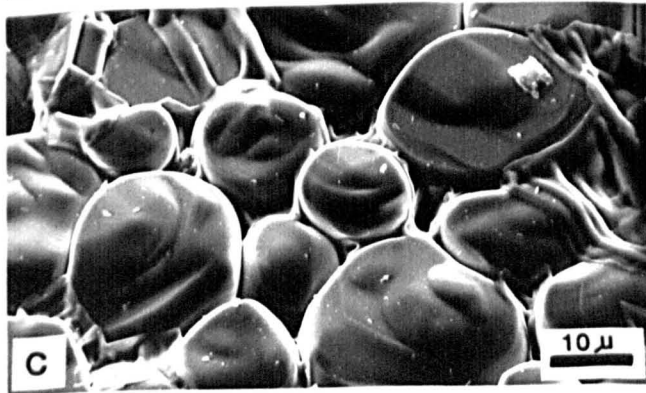
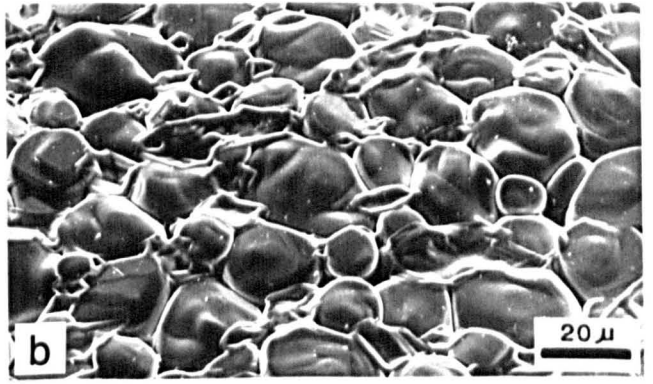
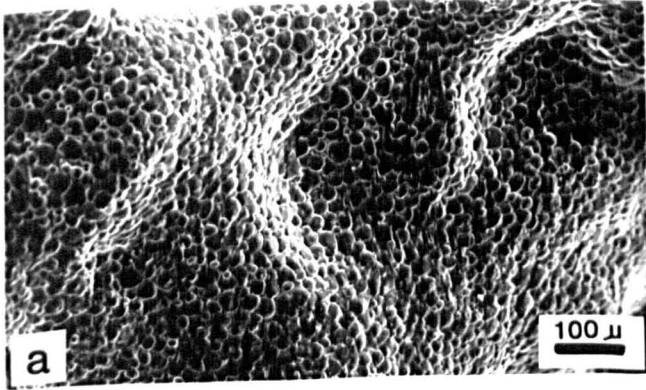


PLATE 26

Backscattered electron micrographs of natural dead burned magnesite (sample T15) contains 5.41% SiO₂ and 2.44% CaO, with a CaO/SiO₂ mole ratio of 0.48. Periclase, forsterite, monticellite and possibly spinel are present. The main white impurities are monticellite but in certain area the smaller ones are dicalcium silicates.

- a) Small periclase grains (dark grey) with high porosity. The impurity phases are concentrated in patches. These are monticellite (white), and forsterite (grey) calcined at 1400°C for 6 hours).
- b) Detailed view of very small periclase grains (grey) and high porosity. Plate 26b is a part of plate 26a. (1400°C, 6 hrs).
- c) Closer view of one of the impurity patches containing monticellite (white) and forsterite (grey). Periclase grains are black, (1400°C, 96 hrs).
- d) Periclase grains (black) with lower porosity crossing through the middle of photograph (1500°C, 6 hrs).
- e) Concentration of mixture of monticellite (white) and forsterite (grey) within impurity patches. These impurities also can appear as a vein crossing through the sample containing spherical periclase grains. There is no direct periclase grain contact where impurities are high (1500°C, 24 hrs).
- f) Concentration of forsterite (grey) as a veinlets through the periclase aggregate. Monticellite grains (white) are situated normally between the periclase grains (1500°C, 6 hrs).
- g,h) Concentration of impurities of monticellite (white) and forsterite (grey) in certain area with black periclase grains (1500°C, 24 hrs).

PLATE 26

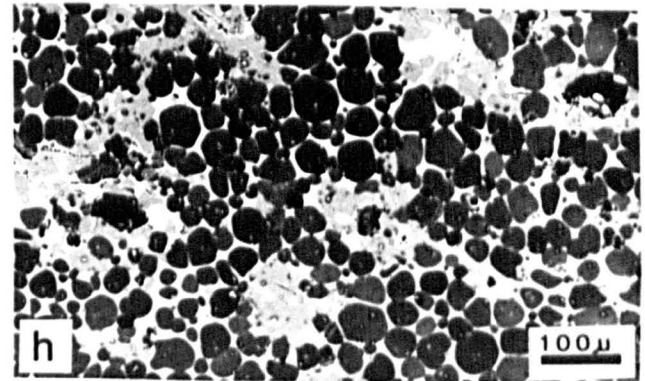
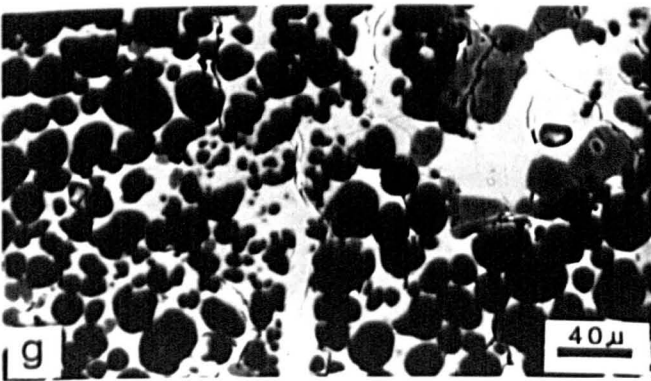
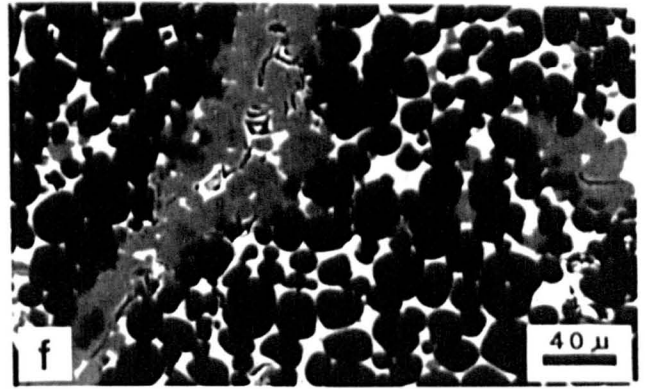
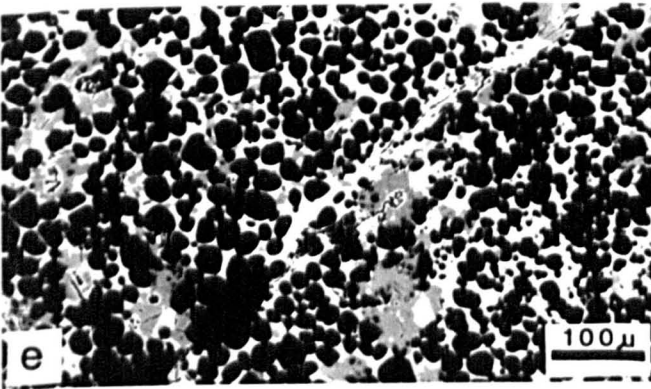
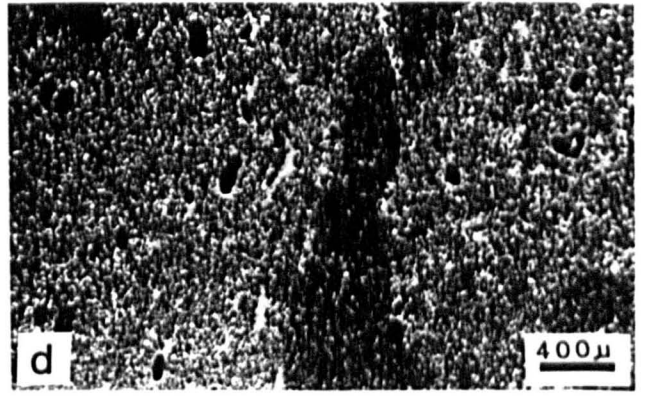
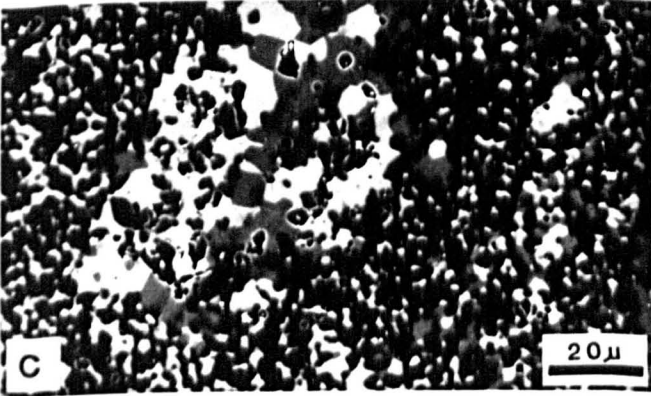
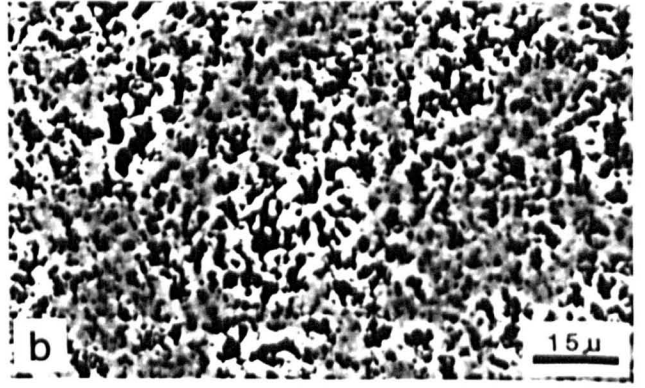
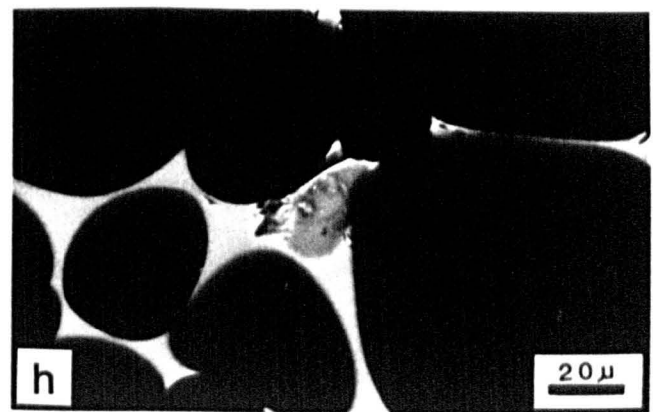
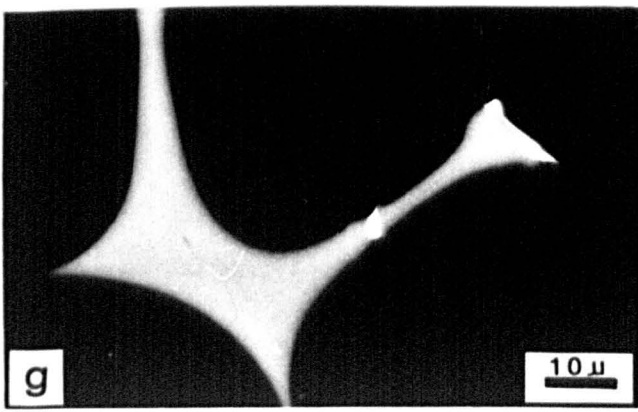
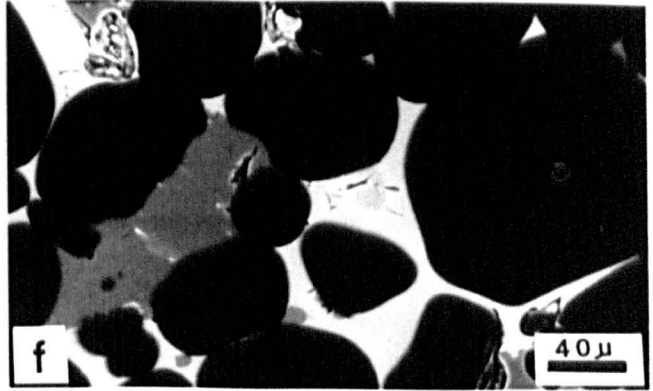
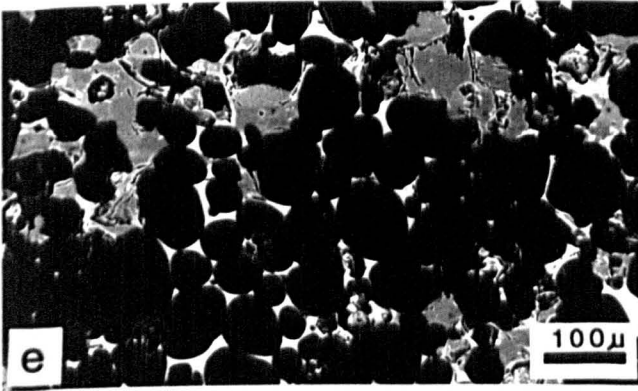
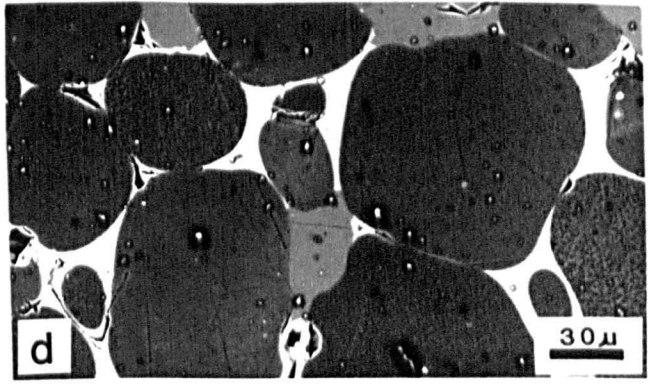
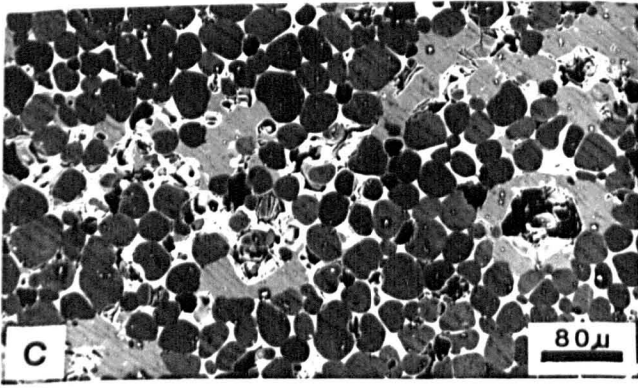
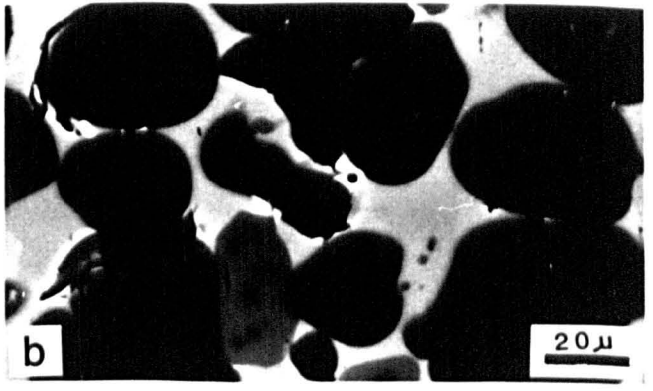
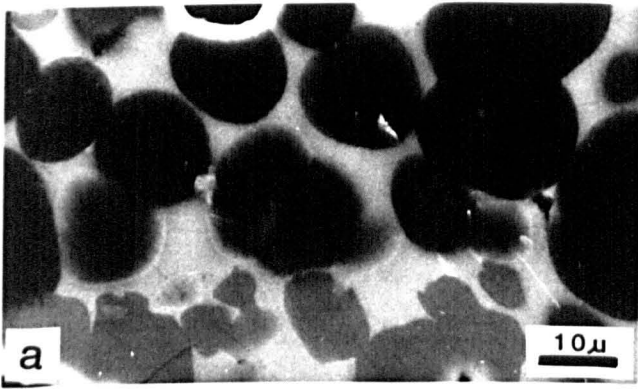


PLATE 27

Backscattered electron micrographs of impurity phases associated with periclase grains in dead burned magnesite (sample T15), containing 5.41% SiO₂, 2.44% CaO and a CaO/SiO₂ mole ratio of 0.48.

- a) Detailed view to spherical periclase grains (black) with no direct grain contact, separated by forsterite (grey) and monticellite (white) (1500°C, 6 hrs).
- b) Common view to the sample with the following different phases, Periclase (black) which are rounded and have no direct grain contact. The white part which covered most of the spaces between the periclase grains is monticellite. Forsterite is grey, and the very small whiter grains between the matrix is a mixed phase containing (Ca, Ti, Si, Mg, Ce, Al) (Figure 4.3 m) (1500°C, 96 hrs).
- c) Rounded periclase grains (dark grey) mostly separated by monticellite (white) with isolated concentration of forsterite (grey) (1500°C, 6 hrs).
- d) Rounded periclase (dark grey) grains with rounded forsterite (pale grey) and interstitial monticellite (white) (1600°C, 108 hrs).
- e) Rounded periclase grains (black), with patches of forsterite (grey). Monticellite impurities (white) are formed mostly at the triple point boundaries of periclase grains (1600°C, 108 hrs).
- f) In this photograph a combination of different phases are visible, The black and rounded grains are periclase. The white matrix is monticellite and the grey phase is forsterite. Within the white matrix in some places, there are some slightly darker grains which are hydrated lime. Forsterite with higher percentage of Ca solid solution is whiter (1600°C, 108 hrs).
- g) In this photograph between the white tricalcium silicate grains, there are some little whiter grains which are quite difficult to analyse with EDX system due to their size. These grains contain Ca, Ti, Ce, Si, Mg, and Al (Figure 4.3m) which is probably a mix phase. (1600°C, 108 hrs).
- h) Common view of lime (grey) (partly hydrated) between the whiter calcium silicate matrix (1600°C, 108 hrs).

PLATE 27



4.4.5.5 Sample T26

The phases determined in sample T26 in both secondary (SE) and backscattered modes (BSE) are summarized in Table 4.13. The electron micrographs are presented in Plate 28-31.

Table 4.13 Phases present in the calcined magnesite samples as determined by energy dispersive X-ray analysis (sample T26).

Temp/Time	(SE)	(BSE)
(1600°C, 108 hrs)	M, C ₂ S &/or C ₃ S	M, C ₂ S, C ₃ S, C, C ₃ A, C ₃ MS ₂
(1600°C, 6 hrs)	M, C ₃ S, C	M, C ₃ S, C
(1500°C, 96 hrs)	M, C	M, C ₃ S, C
(1500°C, 24 hrs)	M, C ₃ S, C ₂ F	M, C
(1500°C, 6 hrs)	M	M, C
(1400°C, 96 hrs)	M	M, C
(1400°C, 24 hrs)	M	M, C ₃ S, C
(1400°C, 6 hrs)	M, C ₃ S &/or C ₂ S	M, C

Where:

M = Periclase, C₂S = dicalcium silicate, C₃S = tricalcium silicate, C₃A = tricalcium aluminate, C = lime, Sp = spinel, C₃MS₂ = merwinite

Details of identification of each phases and their mutual relationship are as follow:

4.4.5.5.1 Major phase (periclase)

Periclase grains are larger at increased calcination temperatures and time (compare Plate 30c and

30h). Periclase grains appear in two main shapes, spherical, mostly when the percentage of matrix is high (Plate 31d) and polygonal in purer material (Plate 30f). Periclase grains have two main surface structures, namely rough and smooth appearance (Plate 30e).

The periclase grains are very small in this sample comparing to others, and some part of surface are covered by lime. The porosity is low, pores being mainly at the periclase grain boundaries, and they have irregular shape. The surface of dead burned sample T26 with a high matrix (tricalcium silicate) content is shown in Plates 28h. The periclase grains are surrounded by the matrix.

Periclase grains in this sample are small during calcination. This is due to the level and type of impurities which is shown in Plate 31a, b. Periclase grains are larger when the amount of Ca impurities are lower (top left Plate 31b). The periclase grain sizes are presented in Table 4.8.

4.4.5.5.2 Interstitial materials and their relationship

In this sample lime (white) is present as a large separate patches surrounded by fine grained periclase (Plate 30a), and as small and rounded grains within periclase (Plate 31h).

Lime appear as a very white and small grains on the surface (Plate 28g). Impurities when present in higher concentration appear on the surface of periclase (Plate

29e). Some effect of hydration of lime are shown in Plate 29g and h. Step like growth is visible on the surface of some periclase grains.

Tricalcium aluminate (grey) appears as small patches within the tricalcium silicates (white) (Plate 31g).

PLATE 28

Scanning electron micrographs of the surface of natural dead burned magnesite (sample T26) containing 0.12% SiO₂, 1.33% CaO and a CaO/SiO₂ mole ratio of 11.88. The periclase grains do not grow very well. Periclase grains in some cases have some knobs on the surface which have very little Ca solid solution. The major impurities are lime and tricalcium silicate. In this sample limes are mostly hydrated and some percentage of Mg from surrounding periclase grains can be catch.

- a) Very small periclase crystals. The whiter Periclase grains contain higher amount of Ca solid solution (1400°C, 6 hrs).
- b) Step like growth on periclase grains (1400°C, 24 hrs).
- c,d) Closer view of the step like growth of periclase grains. The calcination conditions are (1400°C, 24 hrs) and (1400°C, 96 hrs), for (Plate 28c, d) respectively.
- e) Step like growth on the surface of periclase grains (1500°C, 24 hrs).
- f) Periclase crystals with smaller (whiter) crystals of equidimensional lime on the surface (1500°C, 96 hrs).
- g) Pure periclase grains showing step-like growth. The very white grain in the middle of micrograph is lime. (1500°C, 96 hrs).
- h) Periclase grains showing step-like growth with interstitial tricalcium silicate (white) (1500°C, 6 hrs).

PLATE 28

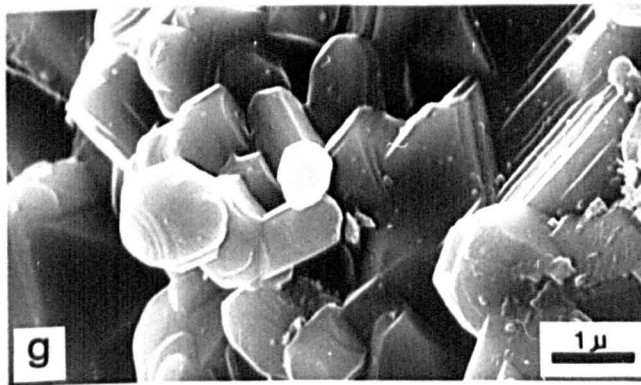
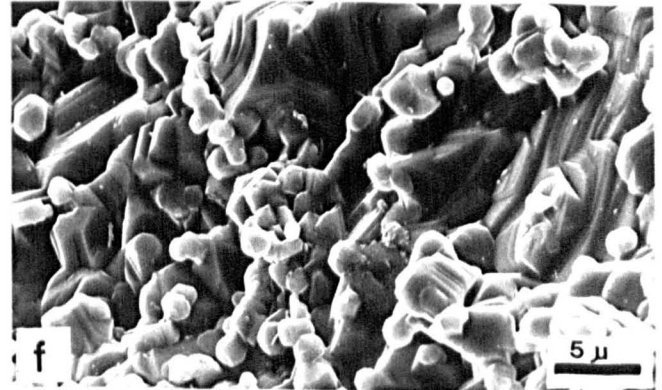
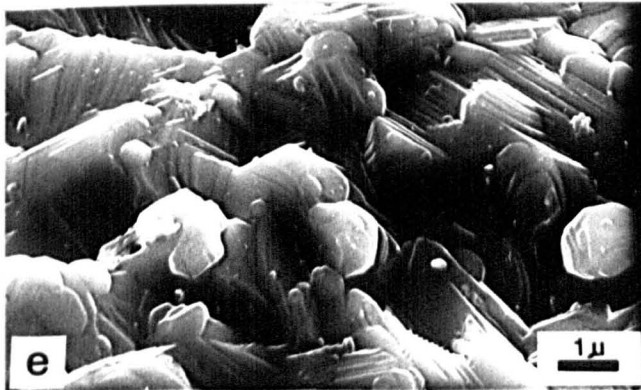
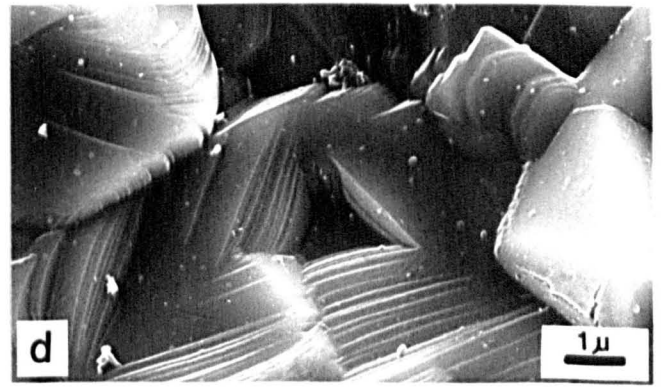
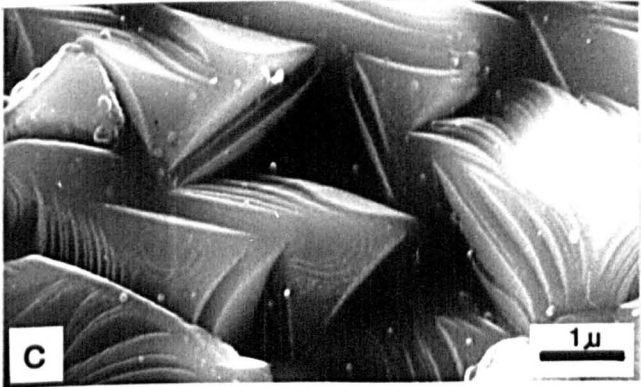
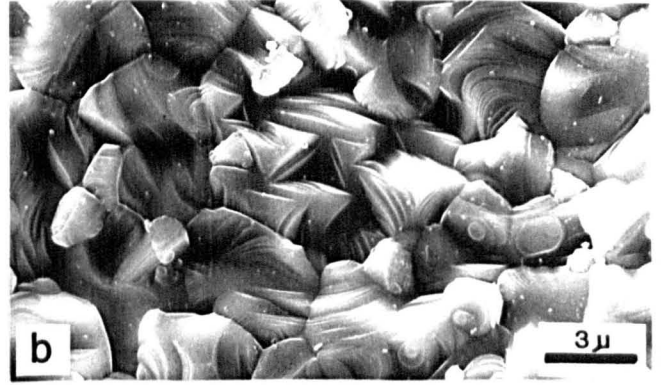
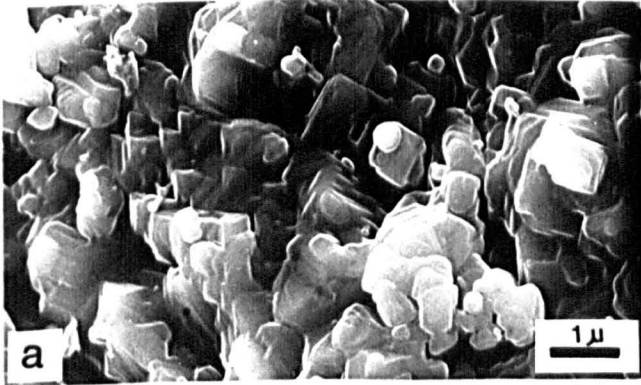


PLATE 29

Scanning electron micrographs of detailed study of impurities in natural dead burned magnesite (sample T26), containing 0.12% SiO₂, 1.33% CaO and a CaO/SiO₂ mole ratio of 11.88. Normally the whiter grains in this sample have more Ca or they are lime.

- a) Periclase grains, having some step like growth on the surface (1600°C, 6 hrs).
- b) Detail view of Step like growth on the surface of periclase grains (1600°C, 6 hrs).
- c) Small irregular shaped tricalcium silicate on the surface and between the periclase grains (1600°C, 108 hrs).
- d) Rod-like tricalcium silicate on the surface of periclase grain (1600°C, 108 hrs).
- e) Impurities covered most parts of sample. These rounded grains are dicalcium silicate (1600°C, 108 hrs).
- f) Tricalcium silicate (white) occurring between periclase grains (1600°C, 108 hrs).
- g,h) Rounded elongate growth on tricalcium silicate and lime possibly due to hydration (1600°C, 108 hrs).

PLATE 29

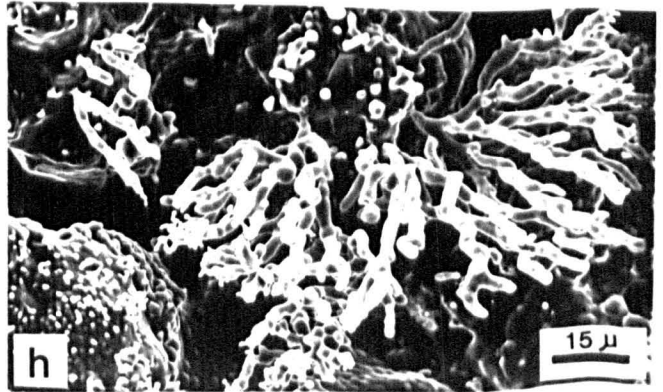
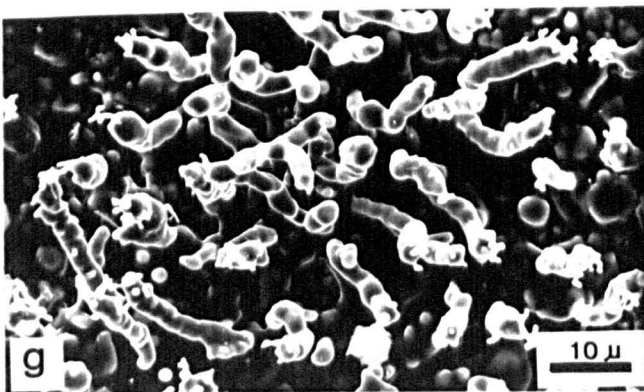
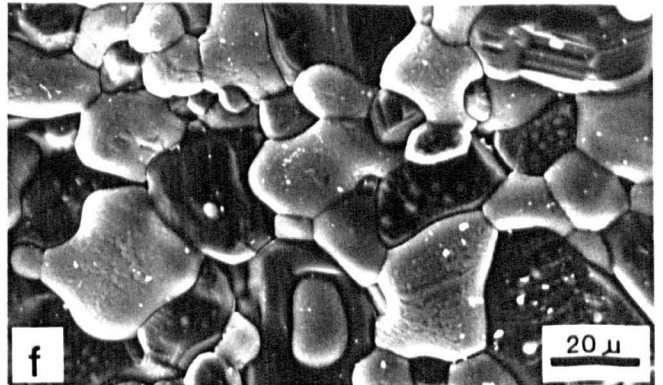
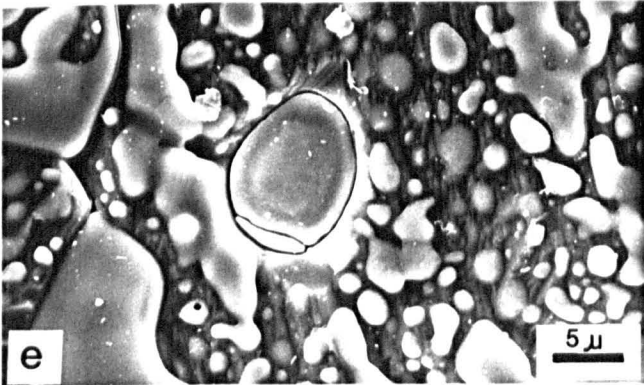
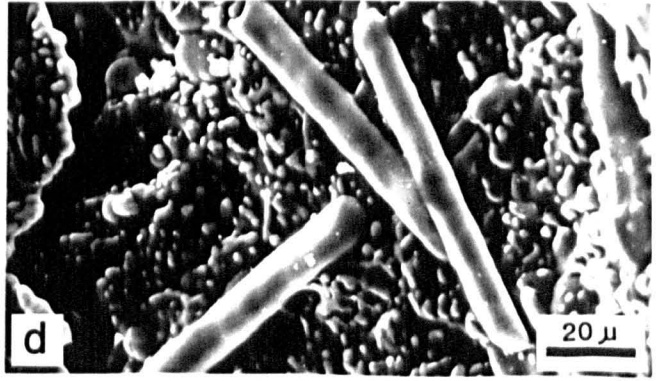
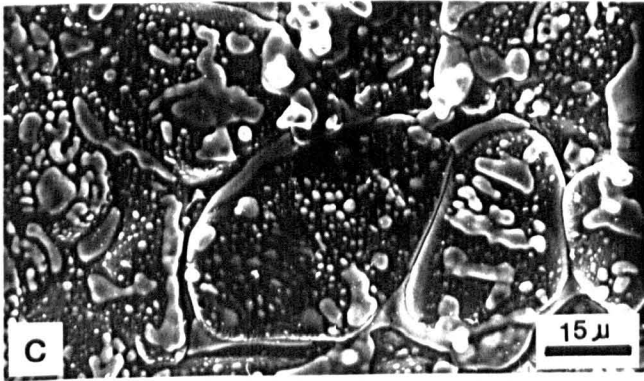
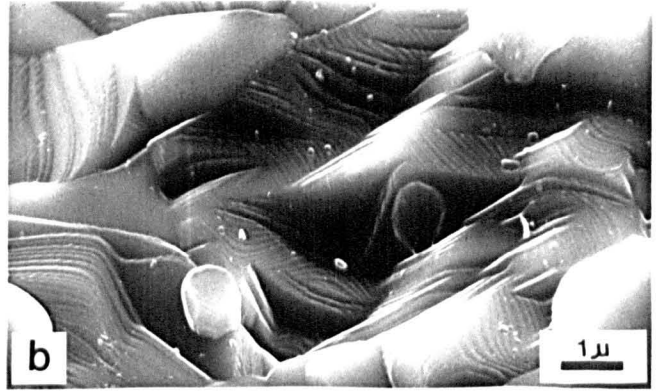
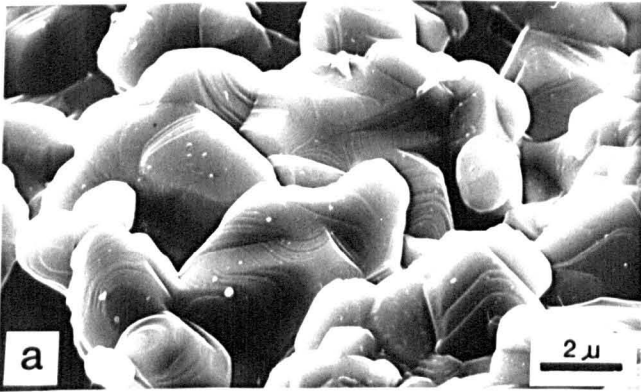


PLATE 30

Backscattered electron micrographs of natural dead burned magnesite (sample T26), containing 0.12% SiO₂, 1.33% CaO and a CaO/SiO₂ mole ratio of 11.88. In these photographs three main phases are determined, periclase (dark), lime mainly as a separate patches and to lesser extent tricalcium silicate.

- a) Lime present as a large patch within very small aggregate of periclase (1400°C, 6 hrs).
- b) Detailed view of the very porous lime patches of plate 30a, (1400°C, 6 hrs).
- c) Mixture of very small periclase grains and lime (white) (1400°C, 6 hrs).
- d,e) Larger periclase grains with rather porous appearance. Rounded white areas are lime within periclase. The periclase grains are mostly in direct contact with each other. The calcination conditions are: (1400°C, 24 hrs) and (1500°C, 6 hrs) for (Plate 30d, e) respectively.
- f) Large periclase grains with rather porous appearance. Rounded white areas are lime within periclase (mostly hydrated). The periclase grains are in direct contact with each others (1500°C, 96 hrs).
- g,h) Similar calcination temperature with different time. Periclase grains are developed and they have direct MgO-MgO grain boundary. The periclase grains have rough (darker) and smooth (whiter) surface structure. Impurities (lime) can appear either on the surface of periclase grains or between them, and mostly can hydrate easily. In lower temperatures, the impurities are lime, but in higher temperatures they change to tricalcium silicate. The calcination conditions are (1600°C, 6 hrs) and (1600°C, 108 hrs) for (Plate 30g, h) respectively.

PLATE 30

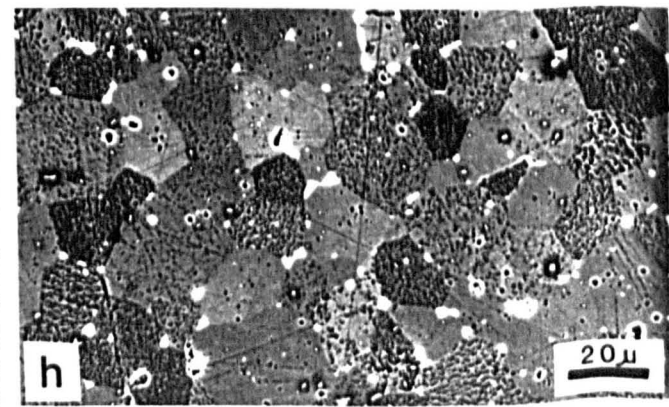
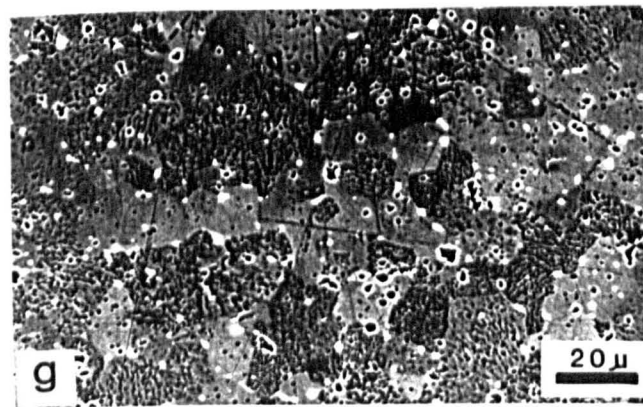
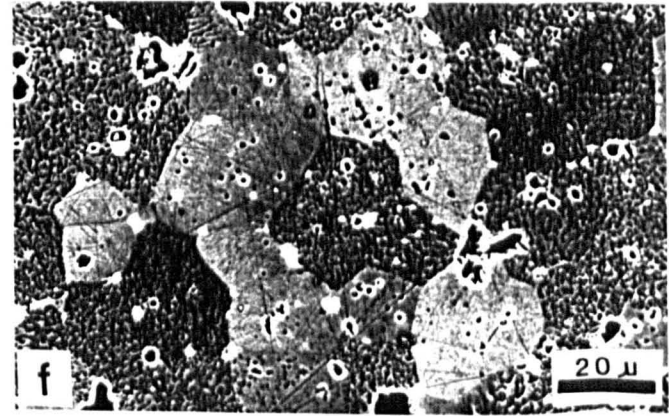
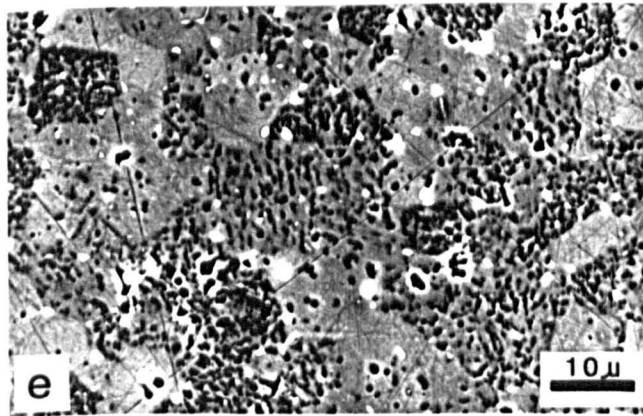
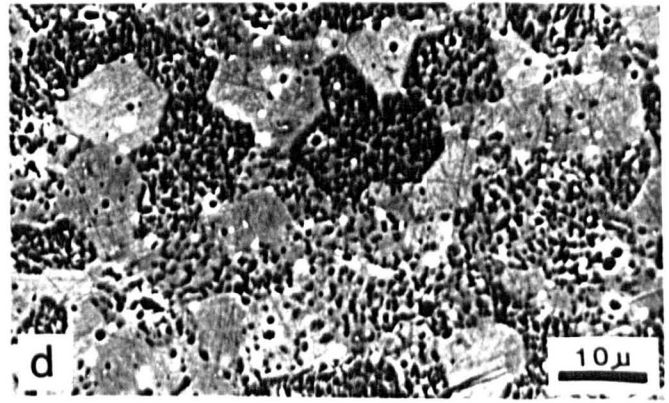
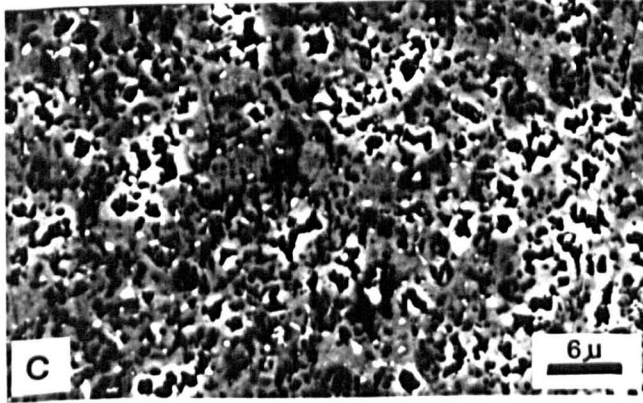
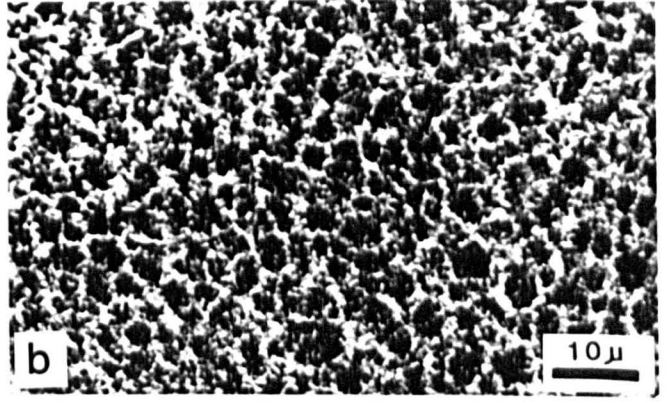
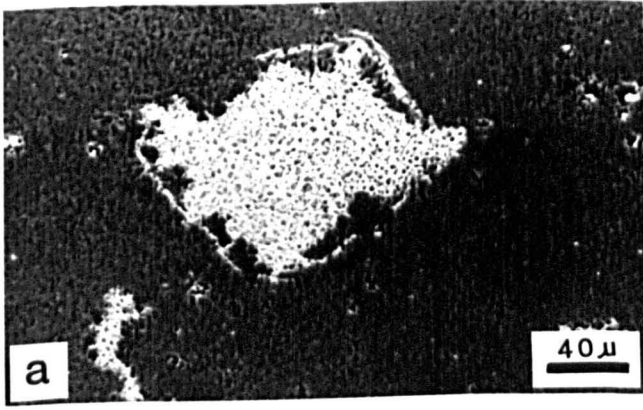


PLATE 31

Backscattered electron micrographs of detailed study of impurities in sample T26 containing 0.12% SiO₂, 1.3% CaO and a CaO/SiO₂ mole ratio of 11.88.

- a) Low magnification view showing heterogeneous nature of sample and irregular distribution of phases (1600°C, 108 hrs).
- b) Closer view to the different parts of sample with higher and lower impurity places. Periclase grains have grown better when the percentage of Tricalcium silicate impurities is less (top-left). The main impurity (white) grains are tricalcium silicate. In some of the rounded C₃S grains a few percentage of Al is present. Also between C₃S grains some grey phases are present which are C₃A. (1600°C, 108 hrs).
- c) Closer view of the impure part of sample. There is no direct periclase grain bonding in this sample because of the high percentage of impurities (C₃S) (1600°C, 6 hrs).
- d) Tricalcium silicate impurities (white) are appeared mostly between the periclase grains (black), but sometimes they can formed as very little rounded grains on the surface of periclase grains (1600°C, 108 hrs).
- e) Closer view to the part of sample with lower percentage of impurities. In this part periclase grains are larger (1600°C, 108 hrs).
- f,g) Detailed view to the matrix phase between the periclase grains. The white phase is tricalcium silicate, and grey is tricalcium aluminate. Mixture of lime and Mg have been found in the middle of plate 31g (1600°C, 108 hrs).
- h) Small rounded inclusions of lime within periclase (1600°C, 108 hrs).

PLATE 31

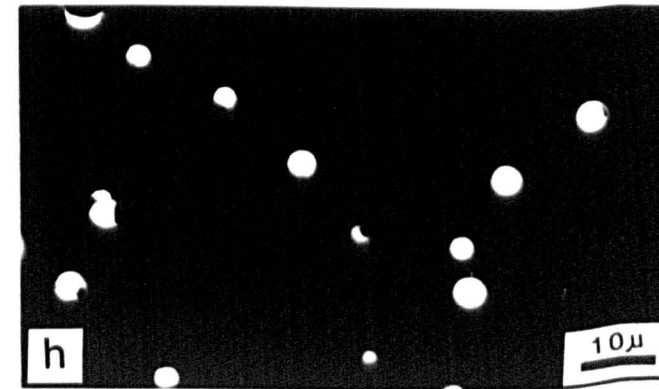
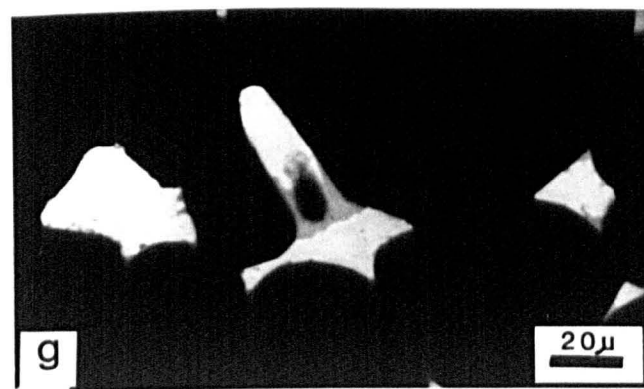
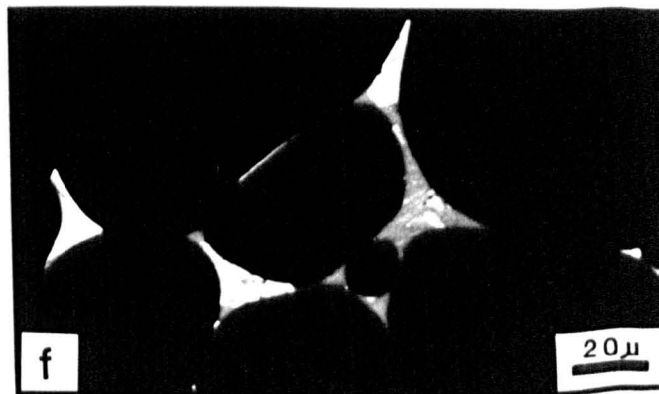
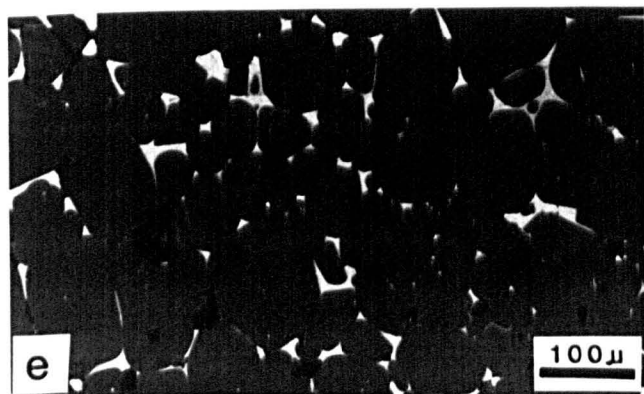
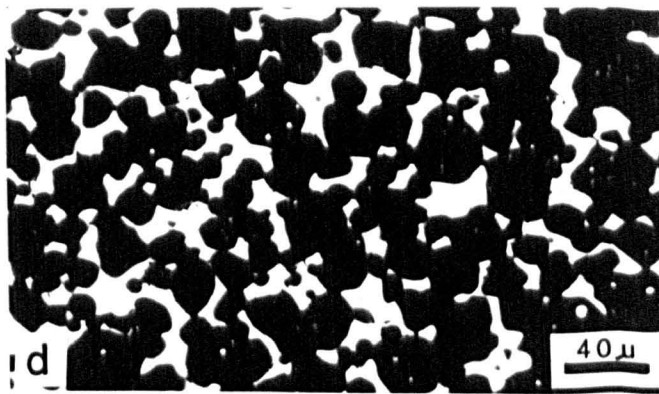
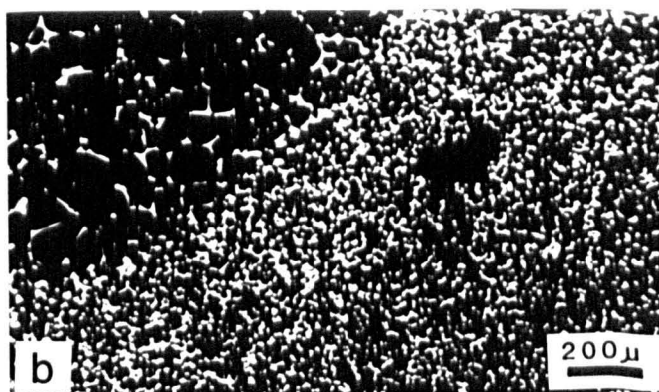
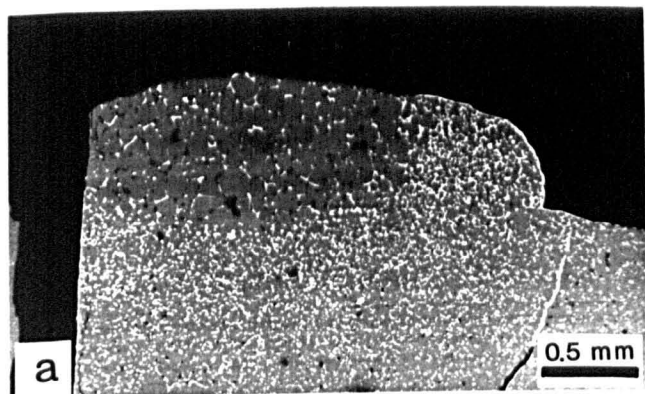
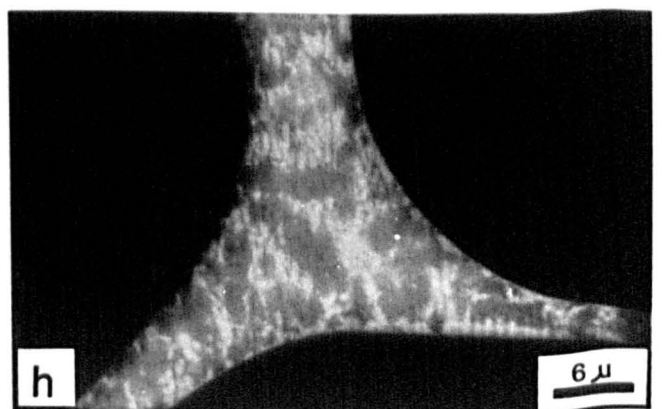
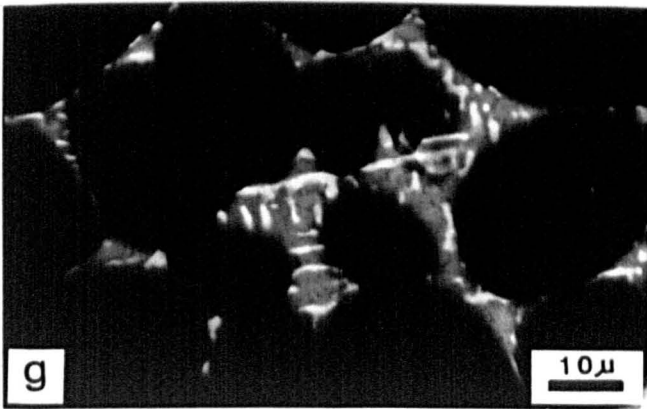
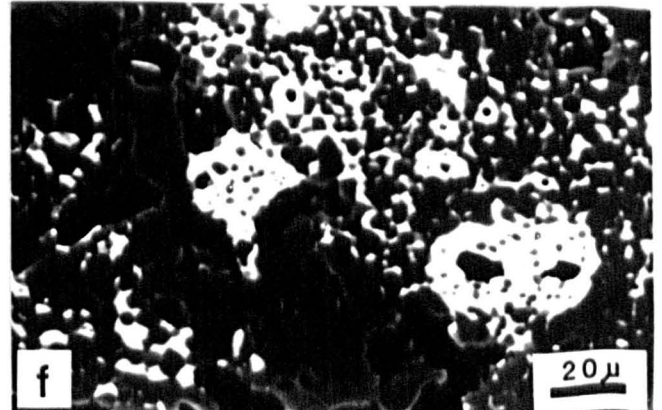
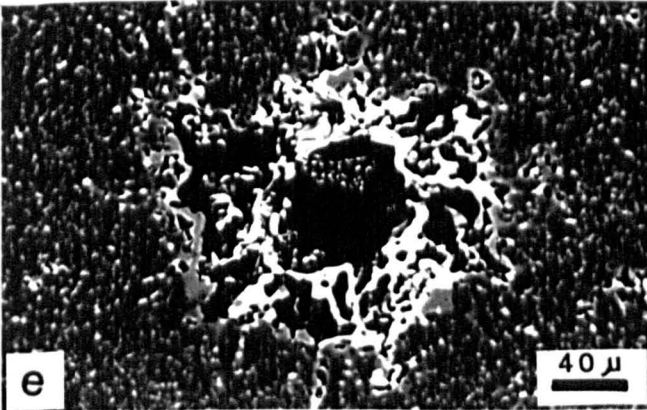
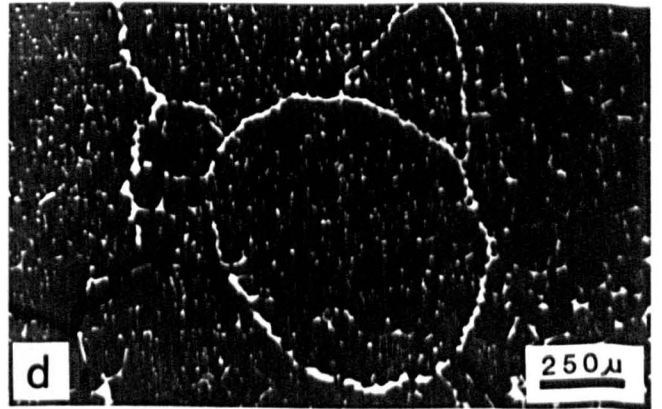
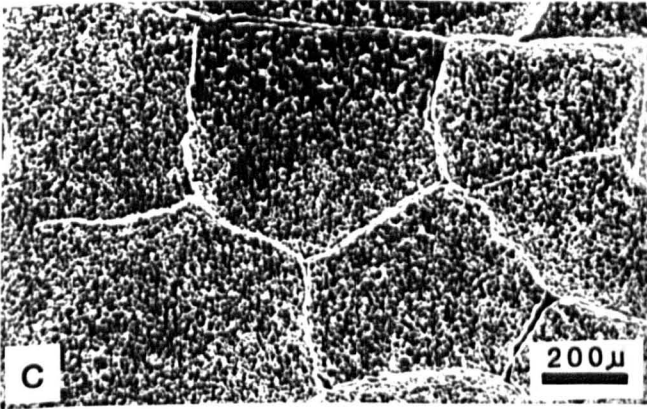
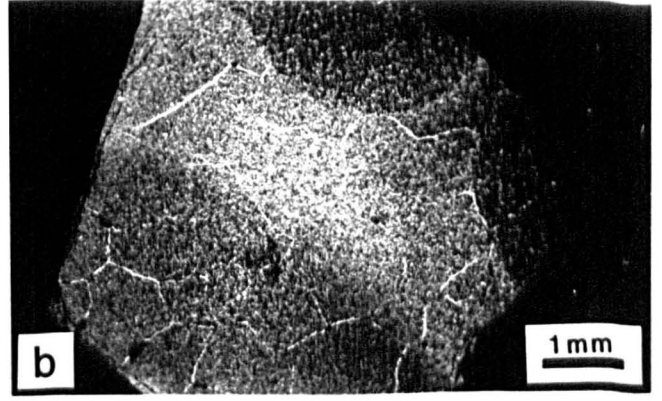
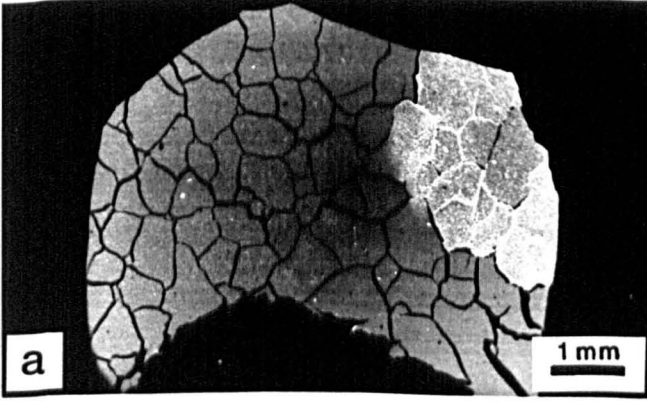


PLATE 32

Backscattered electron micrographs of detailed study of matrix and porosity.

- a,b) Single pieces of dead burned magnesite (sample T2). The impurities are distributed unevenly within the original magnesite resulting in part of dead burned product having a similar uneven distribution of impurities. The calcination condition are: (1600°C, 108 hrs) and (1600°C, 6 hrs) for Plate 32a and b respectively.
- c) Concentration of matrix (tricalcium silicate and lime) in veinlets and within periclase grains in sample T2 (1600°C, 108 hrs).
- d) Concentration of matrix as a rounded veinlets and within periclase grains. Porosities are mainly present at the periclase boundaries in sample A3 (1600°C, 108 hrs).
- e) Concentration of matrix, monticellite (white) and forsterite (grey) in certain area with high percentage of porosity in sample T15. In this temperature periclase grains are not very large as a result of insufficient calcination temperature (1400°C, 96 hrs).
- f) Concentration of tricalcium silicate matrix (white) in certain area, in sample A3 with high amount of porosity (1400°C, 24 hrs).
- g) Detail of highly skeletal dicalcium silicate grains (white) that may occupy the most field of view with monticellite (grey) in sample A14. These matrix grains are formed between the periclase grains (black) (1500°C, 6 hrs).
- h) Detailed view to the matrix between the periclase grains. The whiter patches are tricalcium silicates and the grey patches are merwinite. (1500°C, 96 hrs).

PLATE 32



4.5 Mineralogy as determined by electron microprobe

4.5.1 Introduction

The aims of the microprobe study can be briefly described as follows:

1. To determine different mineral phases present in each dead burned magnesite product.
2. To achieve fully quantitative analyses of each mineral phase in these materials.

The samples used were representative specimens of natural dead burned magnesites calcined at different temperature for different times (1400°C, 6 hrs), (1500°C, 24 hrs) and (1600°C, 108 hrs).

4.5.2 Experimental

Detailed description of the electron microprobe analysis technique and instrumentation are given by Anderson (1972), Reed (1975), Long (1977) and Goldstein et al. (1981).

The electron microprobe employed in this study is a 'Cambridge Geoscan' fitted with a fully quantitative 'Link system models 290-2KV, and QX-200 energy dispersive spectrometers'. The take off angle is 75°. All analyses were carried out using 15 KV accelerating potential and specimen current of 3nA on Co metal. Livetime of 100 seconds has been used for all measurements. The input count rate from Co metal is approximately 2000 counts per second. A computer program which contains a full ZAF (atomic number, absorption,

fluorescence) correction facility was used in the data collection and processing. The standards used for the elements analysed were as follows:

<u>Element</u>	<u>Standard</u>
Ca	Wollastonite
Mg	Periclase (synthetic)
Si	Wollastonite
Fe	Iron metal
Ti	Rutile
P	Apatite
Mn	Mn metal
Cr	Cr metal
Al	Pure alumina

The same polished blocks previously used in the microstructural study were used for electron microprobe analyses. Full details of polished block preparation are presented in Appendix 6. The polished blocks were coated with a thin layer of carbon (Approx. 200 Å) in order to ensure their electrical conductivity during the analyses.

4.5.3 Analytical difficulties

The following analytical difficulties have been encountered during the electron microprobe analysis.

1. Periclase grains generally show higher relief than the surrounding matrix phases. These changes in relief slightly effect the total in the matrix phase analyses.

2. The microporosity of matrix phase appears to be higher than periclase. This is considered to be the main factor responsible for the comparatively low total of the matrix phase analyses.
3. In the case of very small phases, when the grain size of the phase is small ($<5\mu\text{m}$), it is not possible to obtain an analysis of a single phase. The resulting analysis is a mixture of the contributing phases.
4. It is difficult to analyse Na_2O in periclase, because the NaK-alpha and MgK-alpha peaks slightly overlap, i.e. in completely pure periclase grains Na_2O is also found. This point also was confirmed by XRF analysis of natural magnesites. For example the wt.% of Na_2O from XRF in sample A3 is in order of 0.03%, in comparison with 0.57-1.19 wt.% Na_2O present in periclase microprobe analyses. As periclase constitutes 94-96 percentage of the phases in these products, the results of Na_2O from both techniques of XRF and EPMA should be roughly in the same order.

4.5.4 Accuracy, precision and detection limits of electron microprobe analysis.

Dunham and Wilkinson (1978) have studied the accuracy, precision and detection limits of energy dispersive electron microprobe analysis of silicates.

The detection limits of elements analysed as the weight percentage of oxide, at livetime 100 seconds, are given below:

<u>Oxide</u>	<u>Detection limit (wt.%)</u>
MgO	0.21
CaO	0.14
SiO ₂	0.21
Al ₂ O ₃	0.26
FeO	0.19
TiO ₂	0.18
Cr ₂ O ₃	0.19
MnO	0.18

4.5.5 Results

Five representative samples of dead burned magnesite made from the Afzalabad and Torshak deposits of eastern Iran have been chosen for the purpose of the electron microprobe study. The magnesite had been calcined at temperatures of 1600°C for 108 hours, 1500°C for 24 hours and 1400°C for 6 hours. The mineral phases identified for each sample calcined at different conditions are presented in Table 4.14. As MgO, CaO and SiO₂ are the main components in these materials, the microprobe analyses have been plotted on CaO-MgO-SiO₂ triangular diagrams. Where other oxides are found in considerable amounts, the analyses are also plotted on appropriate diagrams, e.g. CaO-Al₂O₃-SiO₂, MgO-Al₂O₃-SiO₂ and CaO-Al₂O₃-MgO.

Interpretation of the data is made in accordance with other observations, i.e. X-ray diffraction, and scanning electron microscopy results.

The complete electron microprobe analyses of natural dead burned magnesites are given in Appendix 7.

Table 4.14 Minerals identified in dead burned magnesites by electron microprobe (EPMA)

Sample	Temp/Time	Phases determined
A3	(1600°C, 108 hrs)	M, C ₂ S, SP, (mix)
A3	(1500°C, 24 hrs)	M, C ₂ S, C ₃ MS ₂ , (mix)
A3	(1400°C, 6 hrs)	M, C ₂ F, (mix)
A14	(1600°C, 108 hrs)	M, CMS, M ₂ S, SP, (mix)
A14	(1500°C, 24 hrs)	M, CMS, M ₂ S, (mix)
A14	(1400°C, 6 hrs)	M, CMS, M ₂ S, SP, (mix)
T2	(1600°C, 108 hrs)	M, C ₂ S, C ₃ S, (mix)
T2	(1500°C, 24 hrs)	M, C ₂ S, C ₃ S, CA, (mix)
T2	(1400°C, 6 hrs)	M, C ₂ S, (mix)
T15	(1600°C, 108 hrs)	M, CMS, M ₂ S, C ₃ MS ₂ , (mix)
T15	(1500°C, 24 hrs)	M, CMS, M ₂ S, SP, (mix)
T15	(1400°C, 6 hrs)	M, CMS, M ₂ S, (mix)
T26	(1600°C, 108 hrs)	M, C ₂ S, C ₃ S, C ₃ A, CA, SP, (mix)
T26	(1500°C, 24 hrs)	M, C, (mix)
T26	(1400°C, 6 hrs)	M, C, (mix)

Where:

M = magnesia (periclase), C₂S = dicalcium silicate, Sp = spinel, C₂F = dicalcium ferrite, CMS = monticellite, M₂S = forsterite, C₃S = tricalcium silicate, C₃A = tricalcium aluminate, C = lime. All contain mixed analyses (mix), C₃MS₂ = Merwinite.

4.5.5.1 Sample A3

4.5.5.1.a Sample A3 (calcined at 1600°C for 108 hours):

Minerals identified by EPMA in sample A3 (1600°C, 108 hrs) are given in Table 4.14. The CaO-MgO-SiO₂ diagram of 91 analyses carried out on 5 magnesia grains of sample A3 (1600°C, 108 hrs) are given in Figure 4.4a. The main phases are periclase and dicalcium silicate. The analyses plotting slightly away from theoretical composition of dicalcium silicate and on the join between periclase and dicalcium silicate, are mixed analyses.

In general, oxides other than MgO, CaO and SiO₂ are Al₂O₃ and FeO. These are either below detection limit or present in very low quantities. When comparatively high proportion of Al₂O₃ and FeO are found, it is probably from the presence of small amounts of tricalcium aluminate, ferrite and spinel as suggested from the SEM observations. The presence of the latter is confirmed by MgO-Al₂O₃-SiO₂ diagram (Figure 4.7a).

4.5.5.1.b Sample A3 (1500°C, 24 hrs):

The major mineral phases are periclase, merwinite and dicalcium silicate.

The CaO-MgO-SiO₂ diagram of 23 analyses of sample A3 (1500°C, 24 hrs) are presented in Figure 4.4b. Three analyses lying between merwinite and periclase are probably mixed analyses of both phases. Where the matrix phases are very small in size (<5^{um}) it is difficult to obtain unmixed

analyses. The only point plotting near dicalcium silicate shows a clear trend towards merwinite and is probably a mixed analysis of both phases.

4.5.5.1.c Sample A3 (1400°C, 6 hrs):

The relatively low temperature and short time of calcination for this sample (1400°C, 6 hrs) is not sufficient to allow the growth of grains which are large enough for separate analysis by the microprobe (Figure 4.4c). Almost all analyses are a mixture of two or more phases.

4.5.5.2 Sample A14

4.5.5.2.a Sample A14 calcined at 1600°C for 108 hours.

The mineral phases present in this sample are periclase, monticellite, forsterite and spinel (Table 4.14). The CaO-MgO-SiO₂ diagram of 57 spot analyses carried out on 3 magnesia grains are given in Figure 4.4d. The MgO-Al₂O₃-SiO₂ diagram is presented in Figure 4.7b.

Points plotting near monticellite show a wide range of composition, and display a trend towards forsterite, probably as a result of solid solution between monticellite and forsterite (Figure 4.4d). Other analyses lying on the join between monticellite with periclase are mixed analyses.

The forsterite analyses are concentrated in an area slightly away from the theoretical composition, towards monticellite. This results from the presence of a small amount of Ca within the forsterite, and indicates the existence of minor amount of solid solution between

forsterite and monticellite.

4.5.5.2.b Sample A14 calcined at 1500°C for 24 hours.

The CaO-MgO-SiO₂ diagram of 34 spot analyses carried out on 2 magnesia grains of sample A14 (1500°C, 24 hrs) are given in Figure 4.4e. As it can be seen from the diagram, the analyses show the presence of periclase, monticellite and forsterite plus mixed phases (Table 4.14). Two analyses which plot between monticellite and akermanite (C₂MS₂) may be a mixture of these two minerals. Other analyses lying on the join between monticellite with periclase, are mixed analyses.

As above the forsterite analyses plot slightly away from the theoretical composition and towards monticellite. This is due to presence of monticellite solid solution in forsterite.

4.5.5.2.c Sample A14 calcined at 1400°C for 6 hours:

A total of 59 analyses were performed on two magnesia grains of sample A14. The mineral phases identified in this sample are presented in Table 4.14. The analyses are plotted on the CaO-MgO-SiO₂, and MgO-Al₂O₃-SiO₂ diagrams as shown in Figures 4.4f and 4.7b.

In this calcination temperature and time, (1400°C, 6 hrs) because of the small grain size of the matrix, it is not easy to obtain analyses of a single phase. Thus the results show a considerable scatter on the CaO-MgO-SiO₂ diagram.

The main phases are periclase, monticellite and forsterite (Figure 4.4f). Spinel may also be present as indicated from the MgO-Al₂O₃-SiO₂ diagram (Figure 4.7b).

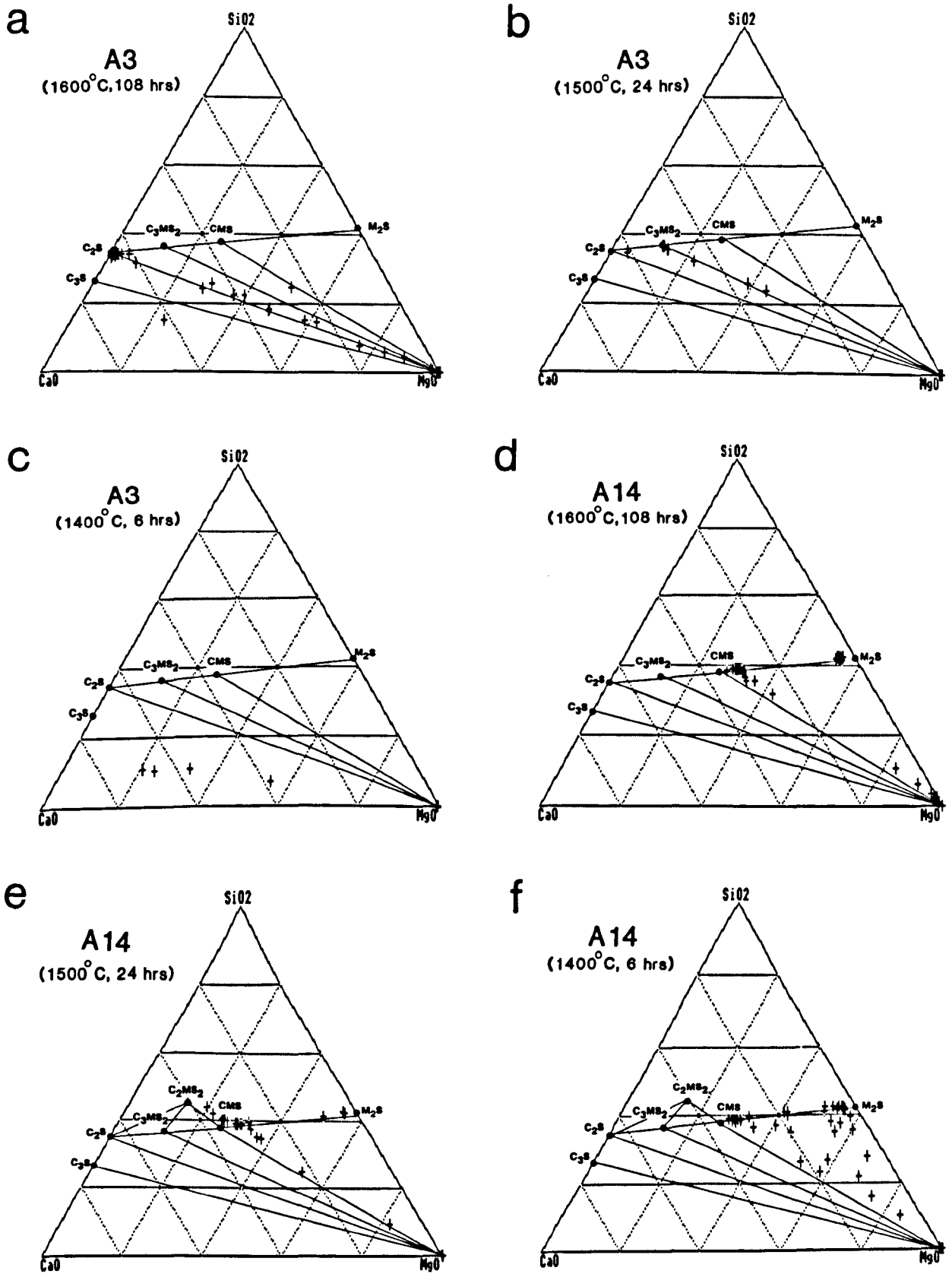


Figure 4.4 Triangular plots showing CaO-MgO-SiO₂ ratios of all microprobe analyses of dead burned magnesite (wt.%)

There is a clear trend between monticellite and forsterite, which is due to solid solution of monticellite in forsterite.

4.5.5.3 Sample T2

4.5.5.3.a Sample T2 calcined at 1600°C for 108 hours:

The CaO-MgO-SiO₂ diagram of 58 spot analyses carried out on 4 magnesia grains of sample T2 (1600°C, 108 hrs) is given in Figure 4.5a.

As it can be seen from the diagram, the data show the presence of mainly periclase and dicalcium silicate. The points which plot near dicalcium silicate show a wide range of composition (Figure 4.5a). The dicalcium silicate analyses showing a trend towards merwinite and towards periclase indicate mixed analyses of two or three components.

Table 4.14 present the mineral phases determined in sample T2 (1600°C, 108 hrs). The analyses lying on the line joining periclase and tricalcium silicates (Figure 4.5a) may indicate the presence of tricalcium silicate, the analyses being possibly a mixture of tricalcium silicate and periclase.

4.5.5.3.b Sample T2 calcined at 1500°C for 24 hours:

The CaO-MgO-SiO₂ diagram of electron microprobe analyses of sample T2 (1500°C, 24 hrs) are given in Figure 4.5b. As it can be seen from the diagram, the analyses show the presence of periclase and dicalcium silicate. Pure tricalcium silicate has not been found in this sample, possibly because of its

small grain size. Points plotting near dicalcium silicate are slightly away from its theoretical composition. This may indicate some solid solution of MgO in dicalcium silicate or a small and constant amount of merwinite.

4.5.5.3.c Sample T2 calcined at 1400°C for 6 hours:

The relatively low temperature and short time of calcination for this sample (1400°C, 6 hrs) is not sufficient to allow the growth of grains which are large enough for separate analysis by microprobe.

The CaO-MgO-SiO₂ diagram of 41 spot analyses of sample T2 (1400°C, 6 hrs) is given in Figure 4.5c. The only phase which is possible to analyse is periclase, and it shows a wide composition range. The periclase analyses show a clear trend towards dicalcium and tricalcium silicates, which are probably the other phases.

4.5.5.4 Sample T15

4.5.5.4.a Sample T15 calcined at 1600°C for 108 hours:

The CaO-MgO-SiO₂ diagram of 77 spot analyses of 4 magnesia grains of sample T15 (1600°C, 108 hours) are given in Figure 4.5d. The main phases are periclase, monticellite and forsterite. The points plotting near monticellite display a trend towards forsterite probably due to solid solution between forsterite and monticellite. Forsterite analyses show a wider range of composition (Figure 4.5d), with a clear trend towards monticellite. This results from the presence of small amount of Ca within the forsterite, and indicates solid

solution between forsterite and monticellite. Two analyses lying on the join between merwinite and periclase may be mixed analysis of these two phases.

4.5.5.4.b Sample T15 calcined at 1500°C for 24 hours:

The CaO-MgO-SiO₂ and MgO-Al₂O₃-SiO₂ diagrams of 45 spot analyses carried out on two magnesia grains of sample T15 (1500°C, 24 hrs) are given in Figures 4.5e and 4.7c.

The main phases determined in sample T15 (1500°C, 24 hrs), are periclase, monticellite, and forsterite.

Monticellite analyses which are lying away from the theoretical point, display a wide range of composition having a trend towards forsterite which is due to forsterite solid solution in monticellite.

Forsterite analyses are all almost identical but they plot away from the theoretical composition, with a trend towards monticellite. This indicates minor amounts of solid solution between monticellite and forsterite (Figure 4.5e).

Two impure spinel phases have been analysed in this sample which is plotted in MgO-Al₂O₃-SiO₂ diagram (Figure 4.7c).

4.5.5.4.c Sample T15 calcined at 1400°C for 6 hours:

The CaO-MgO-SiO₂ diagram of 23 spot analyses of sample T15 (1400°C, 6 hrs) are given in Figure 4.5f. Three main phases are present which are periclase, monticellite and forsterite (Table 4.14). Most of the analyses show a wide range of composition with a clear trends towards each other.

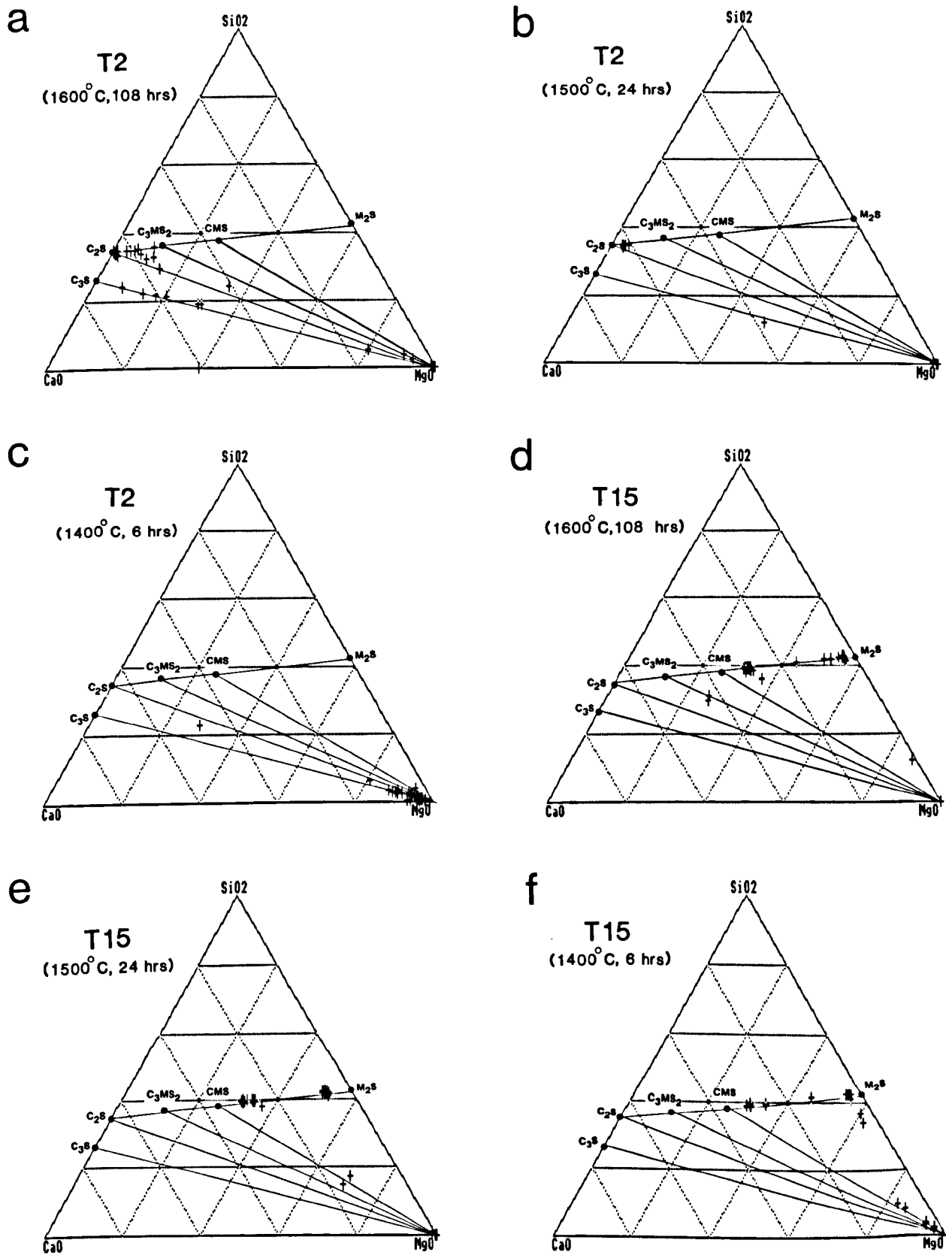


Figure 4.5 Triangular plots showing CaO-MgO-SiO₂ ratios of all microprobe analyses of dead burned magnesite (wt.%)

This is mainly due to relatively low temperature and short time of calcination which is not sufficient to allow the growth of grains which are large enough for separate analysis by microprobe.

4.5.5.5 Sample T26

4.5.5.5.a Sample T26 calcined at 1600°C for 108 hours:

The CaO-MgO-SiO₂ diagram of 46 spot analyses of 4 grains of sample T26 (1600°C, 108 hrs) are given in Figure 4.6b. Periclase and dicalcium silicate are the main phases identified in this sample. The analysis lying on the line joining periclase and tricalcium silicate may indicate the presence of tricalcium silicate mixed with periclase.

As scanning electron microscopy indicates, sample T26 have small grain size. Mixed analyses of dicalcium silicate and periclase are also present.

4.5.5.5.b Sample T26 calcined at 1500°C for 24 hours.

The calcination temperature of 1500°C is insufficient for analysable grains phases to be produced other than periclase.

The CaO-MgO-SiO₂ diagram of sample T26 calcined at 1500°C indicates that the only phase which is possible to analyse is periclase (Figure 4.6c). The electron microscopy results of this sample indicates that lime appears in separate patches and amounts of CaO in periclase fluctuate considerably. The changes in CaO content of periclase are most probably due to lime inclusions. The analyses lying on

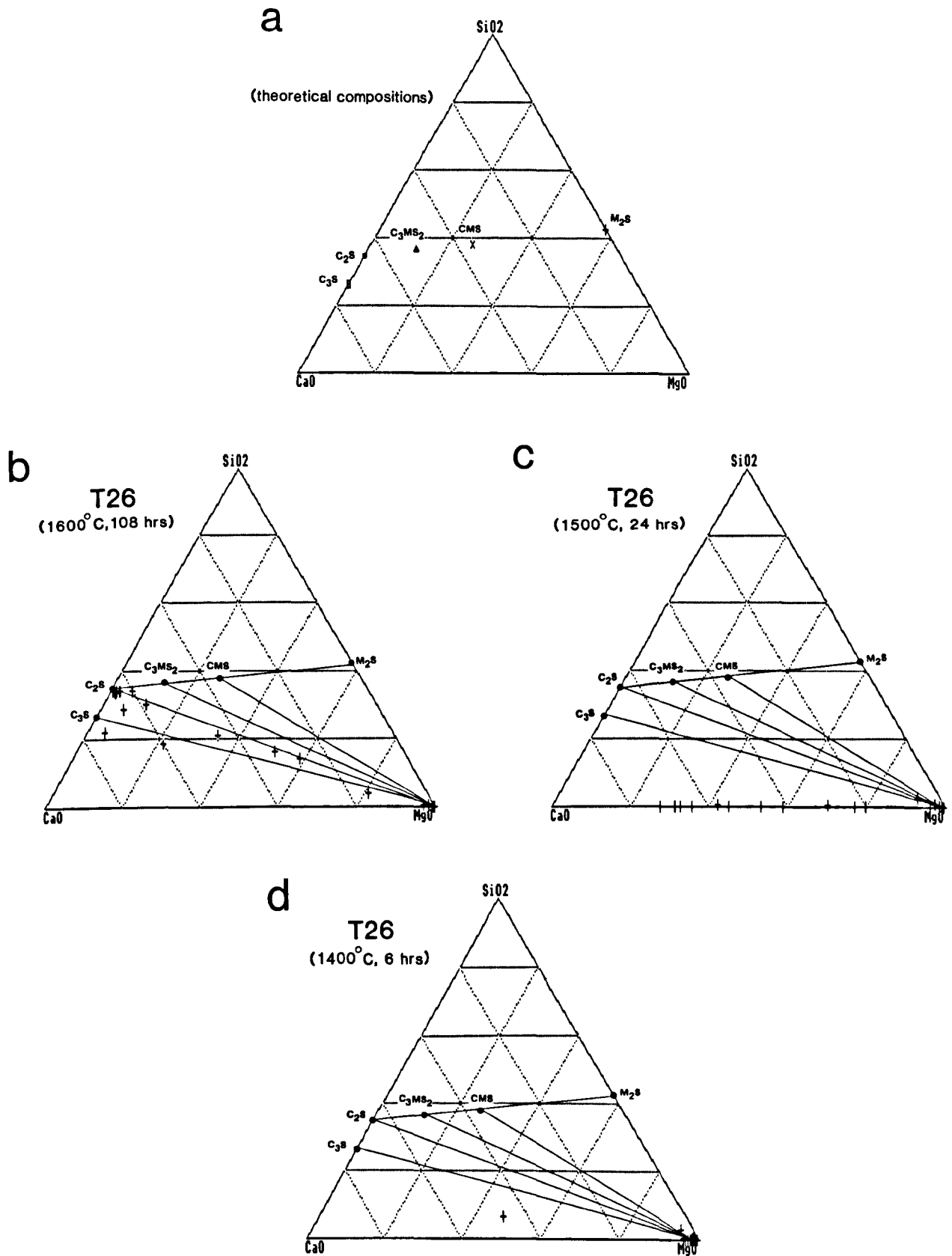


Figure 4.6 Triangular plots showing CaO–MgO–SiO₂ ratios of all microprobe analyses of dead burned magnesite (wt.%)

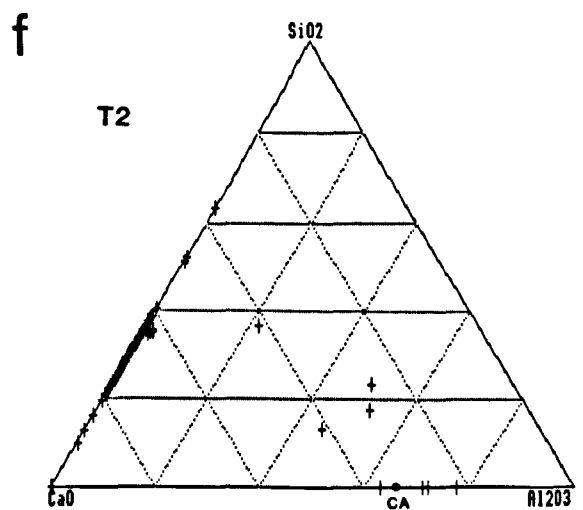
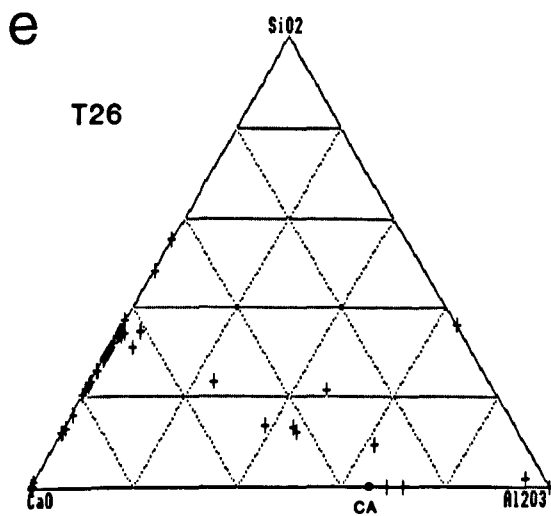
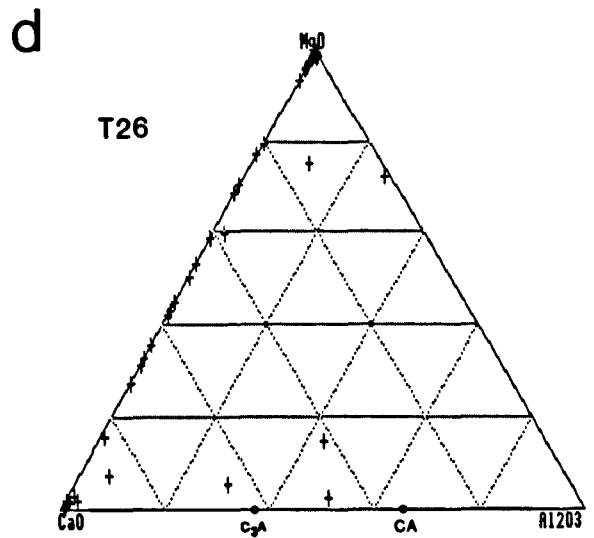
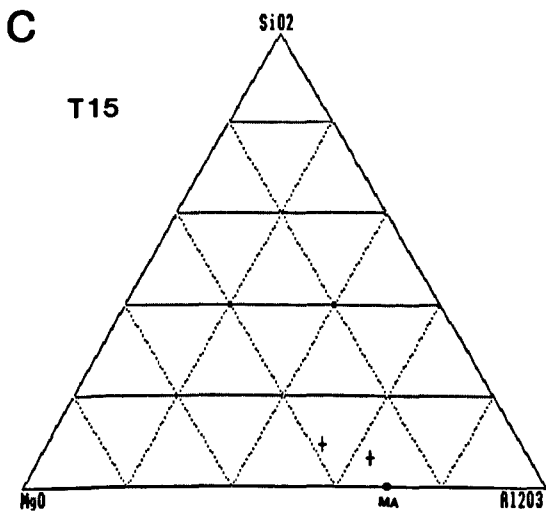
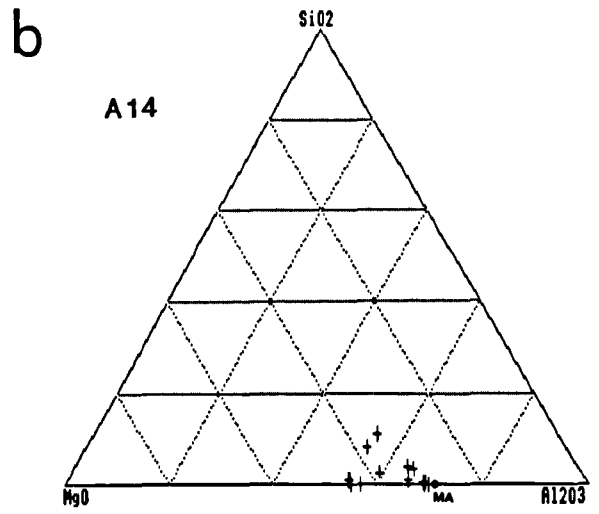
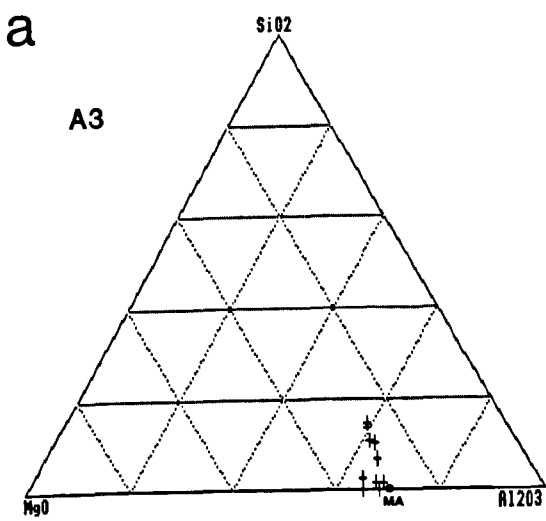


Figure 4.7 Triangular plots showing MgO-Al₂O₃-SiO₂, CaO-Al₂O₃-SiO₂ and CaO-Al₂O₃-MgO ratios of all microprobe analyses of dead burned magnesite (wt.%)

the join between periclase and lime (CaO) are mixed analyses of two phases.

4.5.5.5.c Sample T26 calcined at 1400°C for 6 hours:

The calcination temperature of 1400°C is not sufficient for crystal growth of this sample. The grain size especially in matrix is very small in size ($<5\mu\text{m}$). It is not possible to obtain any microprobe analysis of matrix without mixing with the adjacent periclase grains.

As it can be seen from the CaO-MgO-SiO₂ diagram, the only phase which can be positively identified is periclase (Figure 4.6d).

4.5.6 Discussion

The crystal growth of different phases produced in dead burned magnesites are controlled by a number of factors such as chemical composition of materials, temperature and period of calcination. For example under similar conditions of calcination, samples A3, A14, T2, T15 and T26 while having different chemical compositions (Table 4.1) have experienced different crystalline growth rate; samples A3, A14, and T15 are coarser than samples T2 and T26 at all temperatures, but every sample has larger periclase and interstitial grains at higher temperatures.

Like other analytical instruments, electron microprobe analysis has its limitations. The size of the phase to be analysed is the most important factor. Generally fully quantitative and un-mixed analyses can be obtained when the

grain size of the phase is larger than 5 μm in diameter (note that the effective beam diameter of electron microprobe is around 5 μm in diameter). When the size of phases are less than 5 microns, mixed analyses are obtained. In this case, the presence of phases may be indicated by plotting the electron microprobe data on the relevant triangular diagrams.

Normally the number of phases identified by the electron microprobe in each dead burned magnesite specimen is less than the number observed by the SEM (Table 4.20-4.22).

By combination of XRD, SEM, and EPMA it is possible to identify the mineralogy of the various dead burned magnesites calcined at different temperatures.

The mineralogical determination of different phases present in each sample determined by electron microprobe are in close agreement with the XRD and SEM observations.

4.6 Mineral chemistry

4.6.1 Periclase

4.6.1.1 General

Periclase (MgO) crystallises in the cubic system. The structure of periclase is similar to that of halite (NaCl), with magnesium and oxygen ions occupying the sites of sodium and chlorine respectively. The cell edge is 4.212\AA with $Z = 4$ (Deer et al., 1962, 1983). The physical properties of periclase as described by Deer et al. (1962, 1983) are as follows:

$n = 1.735$

Dispersion: moderate

Cleavage: (001) perfect, (111) imperfect

Twinning: spinel-type twins on (111) in synthetic crystals.

Colour: Greyish white to yellow or brown, colourless in thin section, soluble in dilute HCl.

Density: 3.56-3.68

The melting point of periclase as reported by Chesters 1973 is 2825°C . A maximum presence of 1% CaO in MgO is found in the temperature range of $1600-1800^{\circ}\text{C}$ (Levin et al., 1964.)

According to Jones and Melford (1969) 0.5-1.4% CaO can dissolve in MgO, but they mentioned of no solubility of SiO_2 in periclase at high temperatures. But Schlaudt and Roy (1965) (referred to by White, 1970) in their revision of MgO- SiO_2 phase diagram, indicated of approximately 8% SiO_2 is

soluble in MgO at 1590°C, and increases to 12% at 1780°C.

Foroglou et al. (1980) reported the solubility of CaO in MgO as 0.85-1.25% and SiO₂ in MgO as very low.

According to Spencer et al. (1971) at constant SiO₂ content the degree of solid solubility of CaO in the periclase phase generally rose as the CaO/SiO₂ ratio of the matrix increased. Henney and Jones (1969) found by X-ray analysis that the amount of CaO in solution in MgO at 1750°C rose to a maximum as the merwinite, dicalcium silicate, or tricalcium silicate content of periclase-silicate mixture were progressively increased. They also mentioned very low solubility of SiO₂ in MgO.

The lattice parameter of the MgO decreased slightly in quenched specimens to 4.211 Å but no systematic variation with SiO₂ content is found. The fact that forsterite was observed with only 0.5% SiO₂ indicates that the solid solubility of SiO₂ in MgO is very low at 1750°C. This does not agree with work by Schlaudt and Roy (1966), who estimate the solid solubility of SiO₂ in MgO is of the order of several percent at this temperature.

There is a complete solid solution between (MgO, FeO), and (MgO, MnO), indicated by the phase diagrams, but Al₂O₃ and Cr₂O₃ are reported to be partially soluble in periclase with rising temperature higher than 1000°C (White 1970).

According to White (1970) about 13.6% Cr₂O₃ is found to be soluble in MgO at 1600°C, rising to 18% at 1700°C. The solubility of Al₂O₃ in the periclase is much lower than that of Cr₂O₃ at a given temperature. Reported values are 1.8% at

1600°C, 2% at 1680°C, and 3% at 1700°C.

A number of researchers referred to by Dewendra et al., 1982 have studied the system MgO-Fe₂O₃ in air and have shown that up to about 70% iron oxide can combine with MgO to form a magnesio-wustite solid solution at 1700°C; the value falls to about 40% at 1400°C.

The presence of iron oxide increases the solubility of Cr₂O₃ in periclase. The presence of Cr₂O₃ appears to enhance the solubility of Al₂O₃ in periclase whilst that of iron oxide had the reverse effect. (Dewendra et al., 1982).

In the present work the composition of periclase has been determined from a variety of dead burned natural magnesites calcined at different temperatures and times (1400°C, 6hrs), (1500°C, 24 hrs), (1600°C, 108 hrs). Certain oxides such as CaO and FeO are found to be present often in the periclase analyses. SiO₂ and Al₂O₃, are also observed in periclase, but to a lesser extent. Obviously some of the analyses are of mixed analyses. especially at lower temperatures of calcination, when the periclase grains are very small. In the following, mixed analyses are not included and the discussion refers to the mineral chemistry of periclase.

4.6.1.2 Results

A selection of representative Periclase analyses determined in the natural dead burned magnesites are presented in Table 4.15, under the code beginning with P. Complete electron microprobe analyses of dead burned

magnesites are presented in Appendix 7.

The mineral formula of periclase is calculated on the basis of 1 oxygen. Cation relationships in periclase are presented in Figure 4.8.

As can be seen from the Table 4.15 in the samples collected from the Afzalabad deposit, (i.e. A3, A14) Fe and Al are sometimes present in periclase, but in samples from the Torshak deposit (T2, T15 and T26) Ca and Si are the most common elements present in periclase. These results are confirmed by SEM observations.

a) 4.6.1.2.a CaO in periclase:

The electron microprobe analyses of periclase in each dead burned magnesite show varying amounts of CaO in different temperatures. Some analyses contain no CaO (i.e. are below detection limit), but others contain a small percentage. In the case of lower calcination temperatures some of the CaO may be picked up from the adjacent Ca silicate grains (Table 4.15). Variation in the amount of CaO has been explained in terms of different associated minor phases, especially silicates, present with the periclase and also in terms of the bulk chemistry. The highest values of CaO content in periclase are found in lower calcination temperatures, i.e. 1400-1500°C, which are undoubtedly due to mixed analyses. There is a direct relationship between CaO/SiO₂ ratio of different samples and the amount of CaO in periclase is determined (Figure 4.9a). In general, however, CaO in periclase, in a single magnesia grain, is less

Table 4.15 A selection of periclase analyses as determined
in natural dead burned magnesite

Sample Code	A3-1A PC16	A3-1A PC16	A3-1A PM16	A3-1A PC16	A3-1B PM16	A3-1B PC16	A3-2B PC16	A3-2B PM16	A3 PM15	A3 PM15	Sample Code	T2-2A PM16	T2-2A PC16	T2-2A PM16	T2-2B PC16	T2-1A PC16	T2-1A PC16	T2-1B PC16	T2 PC15	T2 PC15	T2 PC14
SPOT	3	11	18	23	3	15	2	17	11	15	SPOT	10	14	19	9	12	14	3	8	14	38
SiO2	n.d.	n.d.	n.d.	n.d.	n.d.	0.18	n.d.	0.23	n.d.	n.d.	SiO2	0.32	0.34	n.d.	0.23	0.19	n.d.	n.d.	0.23	n.d.	1.05
TiO2	n.d.	n.d.	n.d.	n.d.	n.d.	n.d.	n.d.	n.d.	n.d.	n.d.	TiO2	n.d.	n.d.	n.d.	n.d.	n.d.	n.d.	n.d.	n.d.	n.d.	n.d.
Al2O3	n.d.	n.d.	n.d.	n.d.	n.d.	n.d.	n.d.	n.d.	n.d.	n.d.	Al2O3	n.d.	n.d.	n.d.	n.d.	n.d.	n.d.	n.d.	n.d.	0.48	0.54
Cr2O3	n.d.	n.d.	n.d.	n.d.	n.d.	n.d.	n.d.	n.d.	n.d.	n.d.	Cr2O3	n.d.	n.d.	n.d.	n.d.	n.d.	n.d.	n.d.	n.d.	n.d.	n.d.
FeO	0.56	0.38	0.40	0.55	0.45	0.70	0.75	1.07	2.00	1.95	FeO	n.d.	n.d.	n.d.	n.d.	n.d.	n.d.	n.d.	n.d.	n.d.	0.23
MnO	n.d.	n.d.	n.d.	n.d.	n.d.	n.d.	n.d.	n.d.	n.d.	n.d.	MnO	n.d.	n.d.	n.d.	n.d.	n.d.	n.d.	n.d.	n.d.	n.d.	n.d.
MgO	98.75	100.10	100.07	99.93	99.43	99.26	99.74	98.81	96.65	96.99	MgO	100.07	99.73	100.69	99.01	100.50	100.75	99.42	98.94	100.08	95.58
CaO	n.d.	n.d.	n.d.	n.d.	n.d.	0.19	n.d.	n.d.	0.37	n.d.	CaO	0.29	0.32	0.24	0.85	0.58	0.57	0.91	0.26	0.21	3.11
K2O	n.d.	n.d.	n.d.	n.d.	n.d.	n.d.	n.d.	n.d.	n.d.	n.d.	K2O	n.d.	n.d.	n.d.	n.d.	n.d.	n.d.	n.d.	n.d.	n.d.	n.d.
Cations on the basis of 1 oxygen											Cations on the basis of 1 oxygen										
Si	0.00	0.00	0.00	0.00	0.00	0.00	0.00	0.00	0.00	0.00	Si	0.00	0.00	0.00	0.00	0.00	0.00	0.00	0.00	0.00	0.01
Fe2	0.00	0.00	0.00	0.00	0.00	0.00	0.00	0.01	0.01	0.01	Fe2	0.00	0.00	0.00	0.00	0.00	0.00	0.00	0.00	0.00	0.00
Mn	0.00	0.00	0.00	0.00	0.00	0.00	0.00	0.00	0.00	0.00	Mn	0.00	0.00	0.00	0.00	0.00	0.00	0.00	0.00	0.00	0.00
Mg	1.00	1.00	1.00	1.00	1.00	0.99	1.00	0.98	0.99	0.99	Mg	0.99	0.99	1.00	0.99	0.99	1.00	0.99	0.99	0.99	0.96
Ca	0.00	0.00	0.00	0.00	0.00	0.00	0.00	0.00	0.00	0.00	Ca	0.00	0.00	0.00	0.01	0.00	0.00	0.01	0.00	0.00	0.02
Al	0.00	0.00	0.00	0.00	0.00	0.00	0.00	0.00	0.00	0.00	Al	0.00	0.00	0.00	0.00	0.00	0.00	0.00	0.00	0.00	0.00
Sample Code	A3 PC14	A3 PM14	A14-1A PM16	A14 PC16	A14-A PC15	A14-B PC15	A14-1B PM15	A14-A PC14	A14-B PC14	T2-2A PC16	Sample Code	T15-1A PC16	T15-1A PM16	T15-1A PM16	T15-1B PC16	T15-1C PC16	T15-2 PM16	T15-B PC15	T15 PC14	T26-1A PC16	T26-1A PM16
SPOT	2	11	8	10	3	1	4	17	3	3	SPOT	2	3	5	9	5	4	18	17	1	2
SiO2	0.30	0.19	n.d.	n.d.	n.d.	n.d.	n.d.	0.23	0.19	n.d.	SiO2	n.d.	n.d.	0.20	n.d.	0.22	n.d.	n.d.	0.77	0.18	n.d.
TiO2	n.d.	n.d.	n.d.	n.d.	n.d.	n.d.	n.d.	n.d.	n.d.	n.d.	TiO2	n.d.	n.d.	n.d.	n.d.	n.d.	n.d.	n.d.	n.d.	n.d.	n.d.
Al2O3	n.d.	n.d.	n.d.	0.44	n.d.	n.d.	n.d.	0.49	0.63	n.d.	Al2O3	n.d.	n.d.	n.d.	n.d.	n.d.	n.d.	n.d.	n.d.	0.32	n.d.
Cr2O3	n.d.	n.d.	n.d.	n.d.	n.d.	n.d.	n.d.	n.d.	n.d.	n.d.	Cr2O3	n.d.	n.d.	n.d.	n.d.	n.d.	n.d.	n.d.	n.d.	n.d.	n.d.
FeO	1.55	1.50	0.54	0.44	0.56	0.57	0.69	0.62	0.88	n.d.	FeO	n.d.	n.d.	n.d.	n.d.	n.d.	n.d.	n.d.	n.d.	n.d.	n.d.
MnO	n.d.	n.d.	n.d.	n.d.	n.d.	n.d.	n.d.	n.d.	n.d.	n.d.	MnO	n.d.	n.d.	n.d.	n.d.	n.d.	n.d.	n.d.	n.d.	n.d.	n.d.
MgO	98.02	98.34	98.49	99.10	98.74	98.92	98.57	99.07	97.92	100.29	MgO	100.92	100.19	101.09	100.96	99.53	99.54	100.06	97.20	98.46	99.90
CaO	0.46	0.32	n.d.	n.d.	n.d.	n.d.	n.d.	n.d.	n.d.	0.27	CaO	n.d.	n.d.	n.d.	n.d.	n.d.	n.d.	n.d.	0.50	n.d.	0.23
K2O	n.d.	n.d.	n.d.	n.d.	n.d.	n.d.	n.d.	n.d.	n.d.	n.d.	K2O	n.d.	n.d.	n.d.	n.d.	n.d.	n.d.	n.d.	n.d.	n.d.	n.d.
Cations on the basis of 1 oxygen											Cations on the basis of 1 oxygen										
Si	0.00	0.00	0.00	0.00	0.00	0.00	0.00	0.00	0.00	0.00	Si	0.00	0.00	0.00	0.00	0.00	0.00	0.00	0.01	0.00	0.00
Fe2	0.01	0.01	0.00	0.00	0.00	0.00	0.00	0.00	0.00	0.00	Fe2	0.00	0.00	0.00	0.00	0.00	0.00	0.00	0.00	0.00	0.00
Mn	0.00	0.00	0.00	0.00	0.00	0.00	0.00	0.00	0.00	0.00	Mn	0.00	0.00	0.00	0.00	0.00	0.00	0.00	0.00	0.00	0.00
Mg	0.98	0.99	1.00	0.99	1.00	1.00	1.00	0.99	0.98	1.00	Mg	1.00	1.00	1.00	1.00	1.00	1.00	1.00	0.99	0.99	1.00
Ca	0.00	0.00	0.00	0.00	0.00	0.00	0.00	0.00	0.00	0.00	Ca	0.00	0.00	0.00	0.00	0.00	0.00	0.00	0.00	0.00	0.00
Al	0.00	0.00	0.00	0.00	0.00	0.00	0.00	0.00	0.01	0.00	Al	0.00	0.00	0.00	0.00	0.00	0.00	0.00	0.00	0.00	0.00

variable. There is an inverse relationship between Ca and Mg cations (Figure 4.8b).

4.6.1.2.b FeO in periclase:

FeO is only present in samples A3, and A14. But unlike CaO, it can be present in larger amounts (up to 2.23% in sample A3). Very high values of FeO in periclase in these samples are thought to have resulted from dicalcium ferrite inclusions in periclase, as observed by scanning electron microscopy.

The relationship between FeO in periclase and $\text{Fe}_2\text{O}_3/\text{Al}_2\text{O}_3$ ratio shown in Figure 4.9b. It is clear that FeO in periclase increases as the Fe_2O_3 content of the material increases. The Mg-Fe₂ cation relationship is presented in Figure 4.8g.

4.6.1.2.c Al_2O_3 in periclase:

Al_2O_3 , is rarely detected in periclase. In a few magnesia grains of A3, A14, T2 and T26, Al_2O_3 is more frequently present with a maximum of 2.12, 1.18, 0.81 and 1.18% respectively. It is possible that high values resulted from the presence of spinel. As it can be seen from Figure 4.8f, most of the Al_2O_3 analyses are below detection limit, others have a poor relationship with Mg.

4.6.1.2.d SiO_2 in periclase:

SiO_2 is detected in low percentage in all of the periclase grains in dead burned magnesites. It is usually

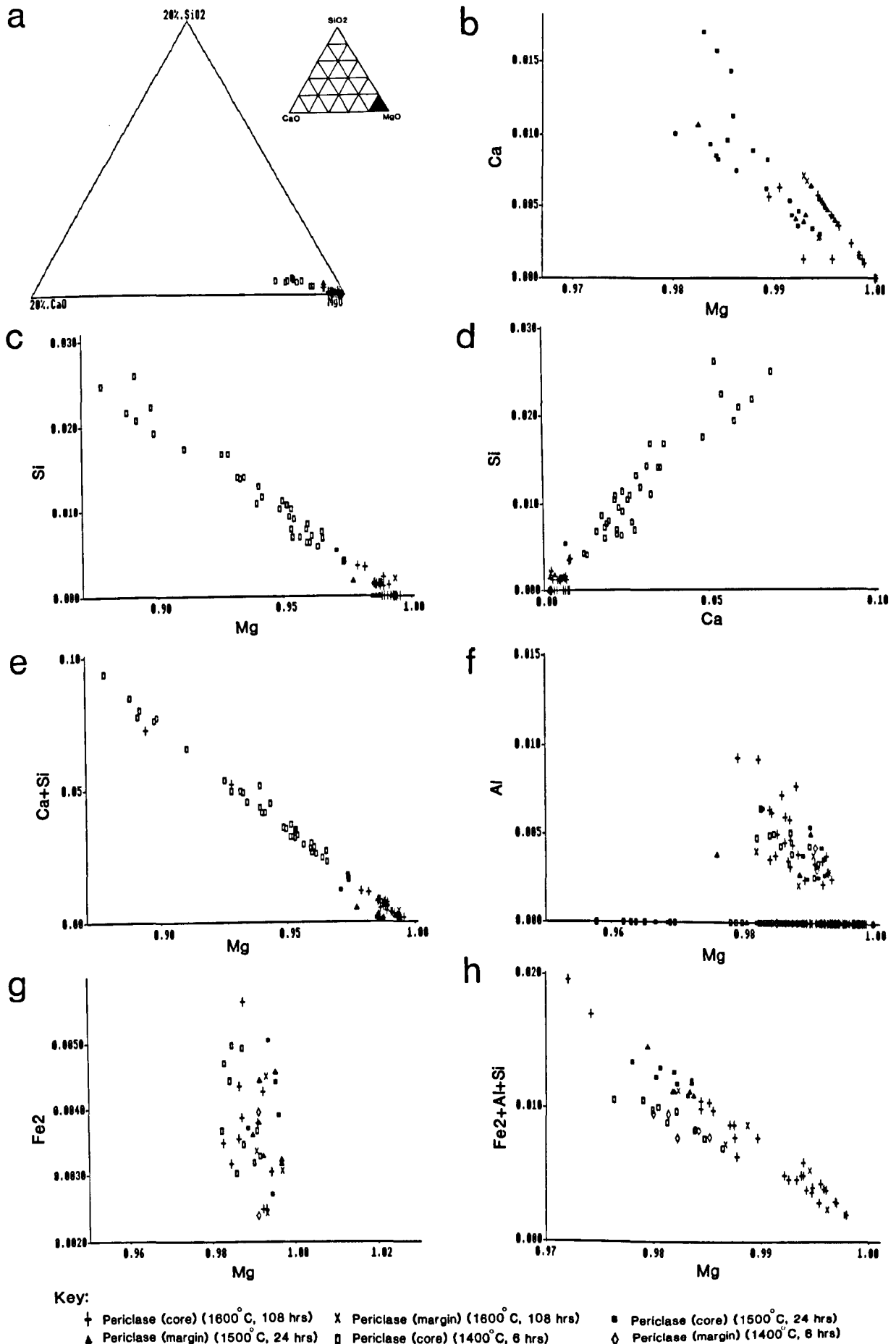


Figure 4.8 Triangular plot (wt.%) and cation relationships of periclaise

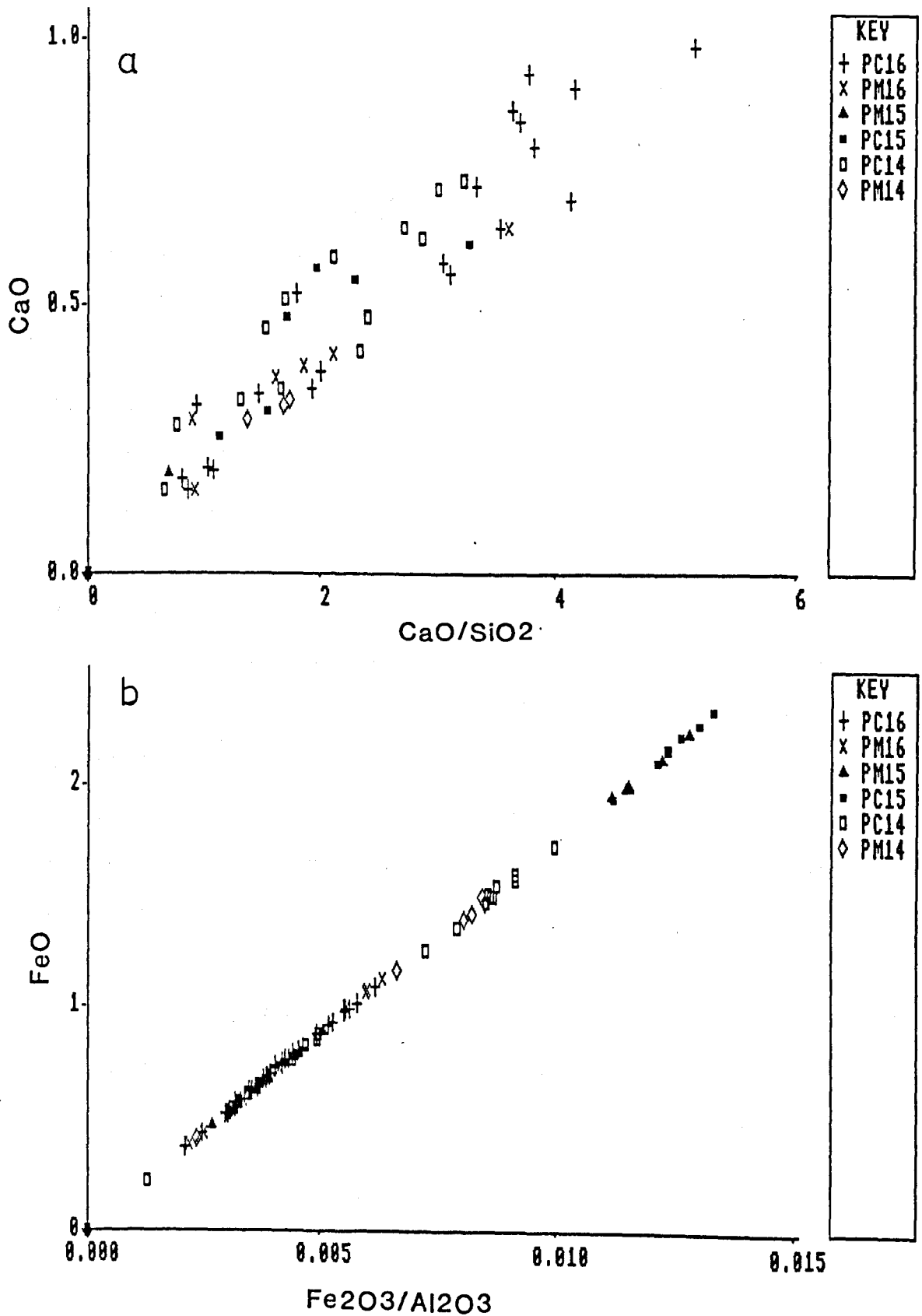


Figure 4.9 Relationship between CaO and FeO in periclase with CaO/SiO₂ and Fe₂O₃/Al₂O₃ Ratios

less than 1% except in some possibly mixed analyses. Comparatively high values of SiO_2 in periclase most probably resulted from other phases such as forsterite and calcium silicates. The Si-Mg cation relationship is presented in Figure 4.8c.

4.6.1.3 Discussion and conclusion

Electron microprobe analyses of periclase in natural dead burned magnesites shows that CaO and to a lower extent FeO and Al_2O_3 are the most frequently present constituents with comparatively wide range of composition. Correlation is made between the level of these oxides in periclase, and the mineralogy and also bulk chemistry. CaO in periclase increases steadily with the increase in the CaO/ SiO_2 ratios of the bulk composition (Figure 4.9a). Also when the CaO/ SiO_2 ratio of the associated silicate phase increases, higher percentage of CaO can dissolve in periclase.

The amount of FeO in periclase in the dead burned magnesites is found to rise with the rising Fe_2O_3 content of the bulk analyses.

4.6.2 Monticellite

4.6.2.1 General

Monticellite (CaMgSiO_4) is a member of the olivine group and like forsterite, it crystallizes with orthorhombic symmetry.

The physical properties of monticellite according to Deer et al. (1982, 1983) are presented below.

$$\alpha = 1.638-1.654$$

$$\beta = 1.646-1.664$$

$$\gamma = 1.650-1.674$$

$$\Delta = 0.012-0.020$$

$$2V = 69-88$$

$$D = 3.05-3.27$$

$$H = 5.5$$

Dispersion $r > v$

Cleavage (010) poor, moderate.

Twinning (031)

Colour - colourless or grey, colourless in thin section.

The cell parameter of synthetic monticellite as determined at 24°C and 1 atmosphere pressure are: $a:4.821 \text{ \AA}$, $b:11.091 \text{ \AA}$ and $c:6.373 \text{ \AA}$ (Warner and Luth, 1973). The number of formula unit per cell (Z) is 4 and the space group is Pbnm (see Deer et al. 1982).

The monticellite structure is principally similar to other olivines. The unit cell expands due to the replacement of half of the (Mg,Fe) by Ca. In monticellite Ca ions occupy

the sites of the mirror planes (M2 sites) and Mg ions are at the centres of symmetry (M1 sites (for more details see Deer et al., 1982)).

The stability of monticellite in the system CaO-MgO-SiO₂ is presented by Osborn and Muan (1960). Monticellite melts incongruently at 1490°C.

A number of workers have reported a limited degree of solid solution of forsterite in monticellite. Ferguson and Merwin (1919) (referred to by Warner and Luth 1973) in their study of CaO-MgO-SiO₂ system at 1 atmosphere indicated that approximately 10 wt.% forsterite may be present in monticellite, but up to 30 wt.% of forsterite in monticellite at 1490°C have been reported by Ricker and Osborn (1954).

Biggar and O'Hara (1969) estimated the crystalline solution of 8-25 mol.% forsterite at 1490°C and 7-11 mol.% forsterite at 1200°C in monticellite.

According to Yi Yang (1973), the amount of forsterite in monticellite ranges between 16.2-18.0 wt.% at 1440°C to 27.2-28.7 wt.% at 1490°C. The extent of forsterite solid solution in monticellite decrease rapidly as the temperature decreases. Schlaudt and Roy (1966) who studied the joint monticellite - dicalcium silicate, report no solid solution of merwinite in monticellite.

4.6.2.2 Results and discussion

Monticellite is one of the most common matrix phases in the samples A14 and T15. The monticellite analyses are plotted on the CaO-MgO-SiO₂ diagram as Wt.% which is shown in

Figure 4.10a. The monticellite analyses show a wide composition range, with a very clear trend towards forsterite and periclase. They plot slightly away from the theoretical composition.

The mineral formulae of monticellite are calculated on the basis of four oxygens. A selection of these analyses with their mineral formula are given in Table 4.16 under the code beginning with M.

The relationship between the cations are shown in Figure 4.10. There is an inverse relationship between Mg and Ca (Figure 4.10b). A great majority of the analyses are higher in Mg and lower in Ca than the theoretical composition of monticellite. These are the analyses which lie between monticellite and forsterite and periclase.

Si shows no significant variation when plotted against Mg and Ca (Figure 4.10c). Fe and Al are the minor cations which are occasionally present. There are no definite relationships between these minor cations with Mg or Ca.

Table 4.16 A selection of monticellite analyses as determined in natural dead burned magnesite

Sample Code SPOT	A14-1A MC16 1	A14-1A MC16 12	A14-1A MC16 13	A14-1A MC16 20	A14-1A MC16 21	A14-1B MC16 4	A14-1B MC16 8	A14-1B MC16 16	A14-1B MC16 21	A14-1B MC16 22
SiO2	39.01	38.83	38.73	35.37	38.91	39.18	37.66	38.87	38.52	38.55
TiO2	n.d.	n.d.	n.d.	n.d.	n.d.	n.d.	n.d.	n.d.	n.d.	0.23
Al2O3	n.d.	n.d.	n.d.	2.00	n.d.	0.38	n.d.	0.44	n.d.	0.37
Cr2O3	n.d.	n.d.	n.d.	n.d.	n.d.	n.d.	n.d.	n.d.	n.d.	n.d.
FeO	n.d.	n.d.	n.d.	0.47	n.d.	n.d.	n.d.	n.d.	n.d.	n.d.
MnO	n.d.	n.d.	n.d.	n.d.	n.d.	n.d.	n.d.	n.d.	n.d.	n.d.
MgO	29.61	28.50	29.76	35.55	29.23	30.33	31.14	29.66	29.00	30.35
CaO	30.58	31.71	30.72	27.84	31.42	30.65	29.85	31.29	31.07	30.17
K2O	n.d.	n.d.	n.d.	n.d.	n.d.	n.d.	n.d.	n.d.	n.d.	n.d.
TOTAL	99.20	99.04	99.21	101.23	99.56	100.54	98.65	100.26	98.59	99.67

Cations on the basis of 4 oxygens

Si	1.01	1.01	1.00	0.90	1.00	1.00	0.98	1.00	1.00	0.99
Al	0.00	0.00	0.00	0.06	0.00	0.01	0.00	0.01	0.00	0.01
Fe2	0.00	0.00	0.00	0.01	0.00	0.00	0.00	0.00	0.00	0.00
Mn	0.00	0.00	0.00	0.00	0.00	0.00	0.00	0.00	0.00	0.00
Mg	1.14	1.10	1.15	1.35	1.12	1.15	1.21	1.13	1.13	1.17
Ca	0.85	0.88	0.85	0.76	0.87	0.84	0.83	0.86	0.87	0.83

Sample Code SPOT	A14-A MC15 12	A14-A MC15 16	A14-B MC15 7	A14-B MC15 9	A14-B MC15 11	A14-B MC15 13	A14-B MC15 16	A14-A MC14 11	A14-A MC14 13	A14-A MC14 14
SiO2	38.77	38.11	30.72	38.48	38.76	37.12	39.63	37.55	39.02	37.42
TiO2	0.26	0.25	n.d.	n.d.	n.d.	n.d.	n.d.	n.d.	n.d.	0.35
Al2O3	1.12	3.10	n.d.	n.d.	0.37	n.d.	0.39	1.45	0.40	2.23
Cr2O3	n.d.	n.d.	n.d.	n.d.	n.d.	n.d.	n.d.	n.d.	n.d.	n.d.
FeO	0.43	0.50	n.d.	n.d.	n.d.	n.d.	n.d.	n.d.	n.d.	n.d.
MnO	n.d.	n.d.	n.d.	n.d.	n.d.	n.d.	n.d.	n.d.	n.d.	n.d.
MgO	29.06	25.38	28.98	30.35	29.63	32.67	32.17	29.07	30.03	27.85
CaO	31.50	31.93	30.99	30.07	31.24	28.16	28.10	30.80	30.26	31.05
K2O	n.d.	n.d.	n.d.	n.d.	n.d.	n.d.	n.d.	0.19	n.d.	0.18
TOTAL	101.14	99.27	90.69	98.90	100.00	97.95	100.29	99.06	99.71	99.08

Cations on the basis of 4 oxygens

Si	0.99	0.99	0.89	1.00	1.00	0.97	1.00	0.98	1.00	0.97
Al	0.03	0.09	0.00	0.00	0.01	0.00	0.01	0.04	0.01	0.07
Fe2	0.01	0.01	0.00	0.00	0.00	0.00	0.00	0.00	0.00	0.00
Mn	0.00	0.00	0.00	0.00	0.00	0.00	0.00	0.00	0.00	0.00
Mg	1.10	0.98	1.25	1.17	1.13	1.27	1.21	1.13	1.15	1.08
Ca	0.86	0.89	0.96	0.83	0.86	0.79	0.76	0.86	0.83	0.87

Sample Code SPOT	A14-B MC14 1	A14-B MC14 17	T15-1B MC16 5	T15-1C MC16 8	T15-2 MC16 6	T15-2 MC16 16	T15-2 MC16 17	T15-A MC15 8	T15 MC14 8
SiO2	38.76	38.78	39.09	38.81	39.24	39.09	39.51	39.56	39.05
TiO2	0.29	n.d.	n.d.	n.d.	n.d.	0.28	n.d.	n.d.	n.d.
Al2O3	0.36	0.44	n.d.	n.d.	n.d.	n.d.	n.d.	n.d.	n.d.
Cr2O3	n.d.	n.d.	n.d.	n.d.	n.d.	n.d.	n.d.	n.d.	n.d.
FeO	n.d.	n.d.	n.d.	n.d.	n.d.	n.d.	n.d.	n.d.	n.d.
MnO	n.d.	n.d.	n.d.	n.d.	n.d.	n.d.	n.d.	n.d.	n.d.
MgO	28.25	30.41	31.02	32.65	32.09	31.20	30.67	30.52	29.72
CaO	30.61	29.33	30.11	28.34	28.55	29.27	29.55	29.46	30.55
K2O	n.d.	n.d.	n.d.	n.d.	n.d.	n.d.	n.d.	n.d.	n.d.
TOTAL	98.27	98.96	100.22	99.80	99.88	99.84	99.73	99.54	99.32

Cations on the basis of 4 oxygens

Si	1.01	1.00	1.00	0.99	1.00	1.00	1.01	1.01	1.01
Al	0.01	0.01	0.00	0.00	0.00	0.00	0.00	0.00	0.00
Fe2	0.00	0.00	0.00	0.00	0.00	0.00	0.00	0.00	0.00
Mn	0.00	0.00	0.00	0.00	0.00	0.00	0.00	0.00	0.00
Mg	1.10	1.17	1.18	1.24	1.22	1.19	1.17	1.17	1.14
Ca	0.86	0.81	0.82	0.78	0.78	0.80	0.81	0.81	0.84

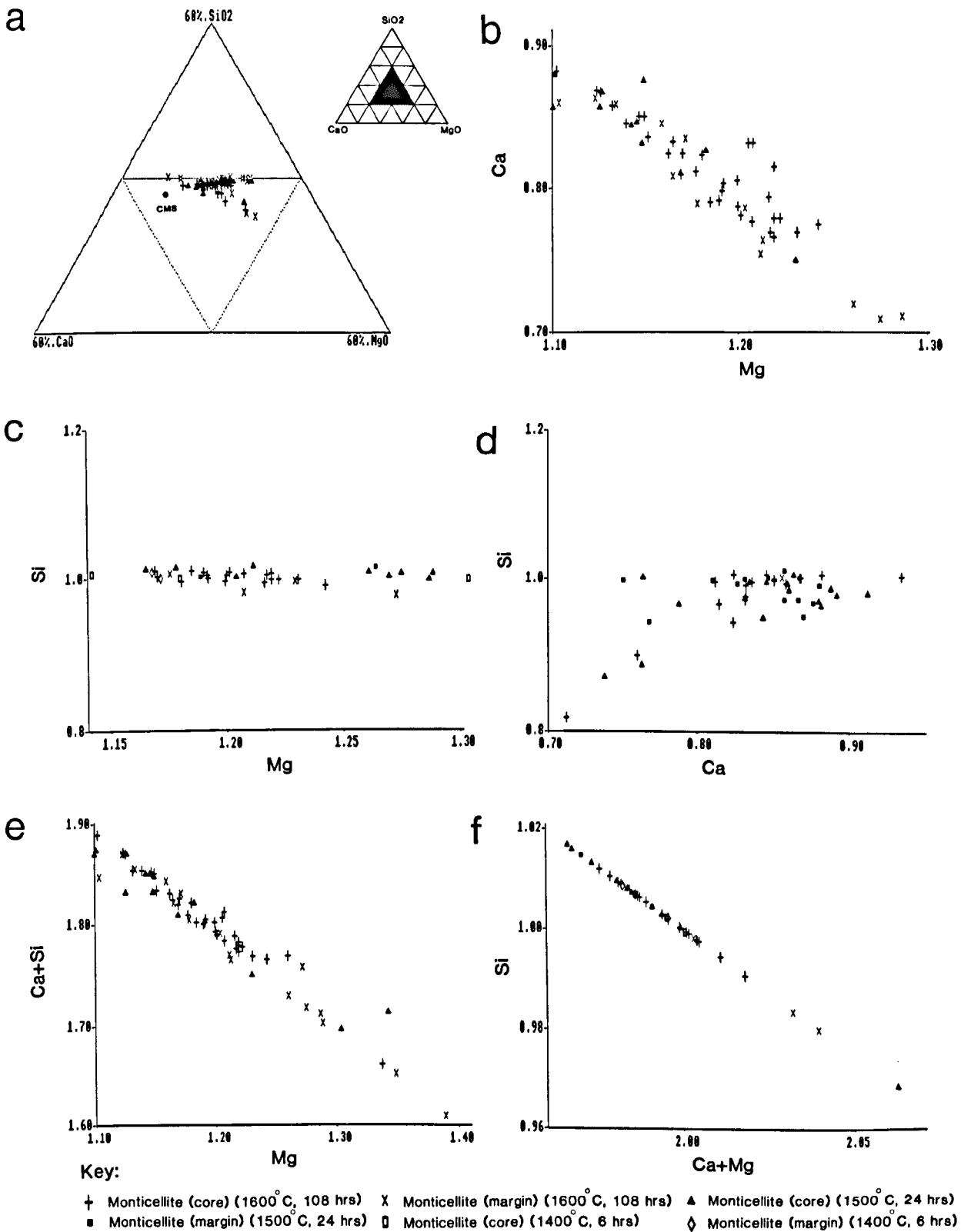


Figure 4.10 Triangular plot (wt.%) and cation relationships of monticellite

4.6.3 Forsterite

4.6.3.1 General

Forsterite (Mg_2SiO_4) is an end member of the olivine group which possess orthorhombic symmetry. There is a complete solid solution between the olivine end members (forsterite (Mg_2SiO_4) and fayalite (Fe_2SiO_4)).

The physical properties of forsterite as described by Deer et al. (1982, 1983) are given below:

$$\alpha = 1.635$$

$$\rho = 1.651$$

$$\gamma = 1.670$$

$$\Delta = 0.03$$

$$2V = 82$$

Dispersion: $r > v$

$$D = 3.222$$

$$H = 7$$

Cleavage (010), (100) imperfect

Twinning (011), (012), (031)

Colour: green, lemon-yellow, colourless in thin section.

Unit cell

$$a: 4.7540 \text{ \AA}$$

$$b: 10.1971 \text{ \AA}$$

$$c: 5.9806 \text{ \AA}$$

$$Z = 4$$

The structure of olivine was first determined by Bragg and Brown (1926) (referred to by Deer et al., 1962, 1982, 1983). The structure consists of individual silicon oxygen

tetrahedra attached by magnesium atoms (each having six nearest oxygen neighbours). The oxygens lie in sheets nearly parallel to the (100) plane with a hexagonal close-packing arrangement. In accordance with full orthorhombic symmetry the silicon-oxygen tetrahedra point alternately either way along both X and Y directions. M atoms (Mg,Fe) occupy half of the available octahedral sites and Si atoms one-eighth of the available tetrahedral sites. The magnesium atoms do not occupy a single set of equivalent lattice positions: half are located at the centres of symmetry and half on reflection planes. These are known as M1 and M2 site respectively (for more detail see Deer et al., 1982).

The structure of olivine has been studied by a number of researchers such as Belov et al. (1951), Hanke and Zeman (1963), Hanke (1965), Birle et al. (1968), Kuroda (1969), and Wenk and Raymond (1973). (for more detail see Deer et al. 1982).

Osborn and Muan (1960) have studied the stability of forsterite in the system of CaO-MgO-SiO_2 . According to them forsterite melts congruently at 1900°C .

According to Riker and Osborn (1954) in their study on the system CaO-MgO-SiO_2 , the maximum solubility of monticellite in forsterite is 30 wt.% at 1500°C and 18 wt.% at 1200°C . Biggar and O'Hara (1969) estimate the maximum solubility of 20.7% monticellite in forsterite at 1490°C and 7.7 wt.% at 1200°C . Yang (1973) showed that the amount of monticellite soluble in forsterite is 17.2 - 18.7 wt.% at 1496°C .

Warner and Luth (1973) indicate that the maximum amount of monticellite which may be dissolved in forsterite is less than 5.5 wt.% under conditions likely to exist in natural system.

Hatfield and Richmond (1970) determined the solubility limit of monticellite in forsterite in the system MgO-CMS-M₂S. The results show that the field of forsterite solid solution is not as extensive as previously reported. The maximum solubility of monticellite in forsterite was found to be 9 wt.% at 1500°C, decreasing to 4 wt.% at 1700°C, higher percentage of monticellite in forsterite at 1500°C as a solid solution are confirmed in the present study (Figure 4.11c, d, e).

4.6.3.2 Results and discussion

The electron microprobe analysis of forsterite are plotted on the system CaO-MgO-SiO₂ as wt.% (Figure 4.11a). Forsterite and monticellite are associated together at different temperatures and times of calcination. As mentioned in the previous section, electron microprobe analyses of forsterite shows a wide composition range with a very clear trend towards monticellite. This, results from the presence of small amount of Ca within the forsterite, and indicates a minor amount of solid solution between forsterite and monticellite. Other analyses lying on the join between forsterite and periclase indicating mixed analyses of two components mainly due to their small grain size results from relatively low temperature and short time of calcination. The

forsterite analyses are recalculated on the basis of four oxygens and a selection of these analyses with their mineral formula are presented in Table 4.17 under the code beginning with F. The cation relationships are shown in Figure 4.11. There is an inverse relationship between Mg and Ca (Figure 4.11c) but Si is almost constant (Figure 4.11d). Fe and Al are occasionally present in forsterite in sample A14. There is no trace of Fe and Al have been found in sample T15. Ca on the other hand, is present in all of the forsterite analyses.

The presence of Ca in all forsterite analyses, however indicates some solid solution between monticellite and forsterite.

Table 4.17 A selection of forsterite analyses as determined in natural dead burned magnesite

Sample Code	A14-1A FC16 SPOT 15	A14-1A FC16 16	A14-1B FM16 2	A14-1B FC16 6	A14-1B FC16 13	A14-B FC15 5	A14-B FC15 14	A14-B FC14 5	A14-B FC14 7	T15-1A FC16 9
SiO2	42.05	41.97	41.22	441.97	42.24	42.66	42.46	41.85	41.81	42.37
TiO2	n.d.	n.d.	n.d.	n.d.	n.d.	n.d.	n.d.	n.d.	n.d.	n.d.
Al2O3	0.68	1.02	0.40	0.69	0.37	n.d.	n.d.	n.d.	0.52	n.d.
Cr2O3	n.d.	n.d.	n.d.	n.d.	n.d.	n.d.	n.d.	n.d.	n.d.	n.d.
FeO	0.44	0.31	0.37	0.29	n.d.	n.d.	n.d.	n.d.	n.d.	n.d.
MnO	n.d.	n.d.	n.d.	n.d.	n.d.	n.d.	n.d.	n.d.	n.d.	n.d.
MgO	53.15	54.08	52.80	52.81	53.01	54.22	53.76	54.64	54.36	54.50
CaO	3.73	3.12	4.15	4.41	4.83	3.02	3.19	2.92	3.25	3.12
K2O	n.d.	n.d.	n.d.	n.d.	n.d.	n.d.	n.d.	n.d.	n.d.	n.d.
TOTAL	100.05	100.50	98.94	500.17	100.45	99.90	99.41	99.41	99.94	99.99

Cations on the basis of 4 oxygens

Si	1.00	0.99	0.99	1.82	1.00	1.01	1.01	0.99	0.99	1.00
Al	0.02	0.03	0.01	0.00	0.01	0.00	0.00	0.00	0.01	0.00
Fe2	0.01	0.01	0.01	0.00	0.00	0.00	0.00	0.00	0.00	0.00
Mn	0.00	0.00	0.00	0.00	0.00	0.00	0.00	0.00	0.00	0.00
Mg	1.88	1.90	1.89	0.32	1.87	1.91	1.90	1.94	1.92	1.92
Ca	0.09	0.08	0.11	0.02	0.12	0.08	0.08	0.07	0.08	0.08

Sample Code	T15-1A FC16 SPOT 10	T15-1A FM16 15	T15-1B FC16 1	T15-1B FC16 3	T15-1B FC16 10	T15-1B FM16 14	T15-2 FC16 5	T15-2 FM16 18	T15-2 FC16 19	T15-2 FC16 22
SiO2	42.77	42.64	42.21	42.91	42.71	42.89	42.16	42.76	42.87	42.78
TiO2	n.d.	n.d.	n.d.	n.d.	n.d.	n.d.	n.d.	n.d.	n.d.	n.d.
Al2O3	n.d.	n.d.	n.d.	n.d.	n.d.	n.d.	n.d.	n.d.	n.d.	n.d.
Cr2O3	n.d.	n.d.	n.d.	n.d.	n.d.	n.d.	n.d.	n.d.	n.d.	n.d.
FeO	n.d.	n.d.	n.d.	n.d.	n.d.	n.d.	n.d.	n.d.	n.d.	n.d.
MnO	n.d.	n.d.	n.d.	n.d.	n.d.	n.d.	n.d.	n.d.	n.d.	n.d.
MgO	54.74	54.71	54.06	54.56	53.85	53.49	55.13	54.19	54.53	53.99
CaO	3.03	2.90	2.89	2.93	3.28	4.19	3.04	3.24	3.12	3.06
K2O	n.d.	n.d.	n.d.	n.d.	n.d.	n.d.	n.d.	n.d.	n.d.	n.d.
TOTAL	100.54	100.25	99.16	100.40	99.84	100.57	100.33	100.19	100.52	99.83

Cations on the basis of 4 oxygens

Si	1.00	1.00	1.00	1.01	1.01	1.01	0.99	1.01	1.01	1.01
Al	0.00	0.00	0.00	0.00	0.00	0.00	0.00	0.00	0.00	0.00
Fe2	0.00	0.00	0.00	0.00	0.00	0.00	0.00	0.00	0.00	0.00
Mn	0.00	0.00	0.00	0.00	0.00	0.00	0.00	0.00	0.00	0.00
Mg	1.92	1.92	1.92	1.91	1.90	1.88	1.94	1.90	1.91	1.90
Ca	0.08	0.07	0.07	0.07	0.08	0.11	0.08	0.08	0.08	0.08

Sample Code	T15-2 FM16 SPOT 23	T15-A FC15 4	T15-A FC15 6	T15-A FC15 16	T15-B FC15 3	T15 FM14 7	T15 FC14 19
SiO2	43.21	41.99	41.88	42.07	42.07	42.30	42.30
TiO2	n.d.	n.d.	n.d.	n.d.	n.d.	n.d.	n.d.
Al2O3	n.d.	n.d.	n.d.	n.d.	n.d.	n.d.	n.d.
Cr2O3	n.d.	n.d.	n.d.	n.d.	n.d.	n.d.	n.d.
FeO	n.d.	n.d.	n.d.	n.d.	n.d.	n.d.	n.d.
MnO	n.d.	n.d.	n.d.	n.d.	n.d.	n.d.	n.d.
MgO	54.31	50.34	51.39	51.11	50.77	53.93	54.13
CaO	2.90	6.92	6.64	6.53	6.79	3.65	3.45
K2O	n.d.	n.d.	n.d.	n.d.	n.d.	n.d.	n.d.
TOTAL	100.42	99.25	99.91	99.71	99.63	99.88	99.88

Cations on the basis of 4 oxygens

Si	1.01	1.01	1.00	1.01	1.01	1.00	1.00
Al	0.00	0.00	0.00	0.00	0.00	0.00	0.00
Fe2	0.00	0.00	0.00	0.00	0.00	0.00	0.00
Mn	0.00	0.00	0.00	0.00	0.00	0.00	0.00
Mg	1.90	1.80	1.83	1.82	1.81	1.90	1.91
Ca	0.07	0.18	0.215	0.17	0.17	0.09	0.09

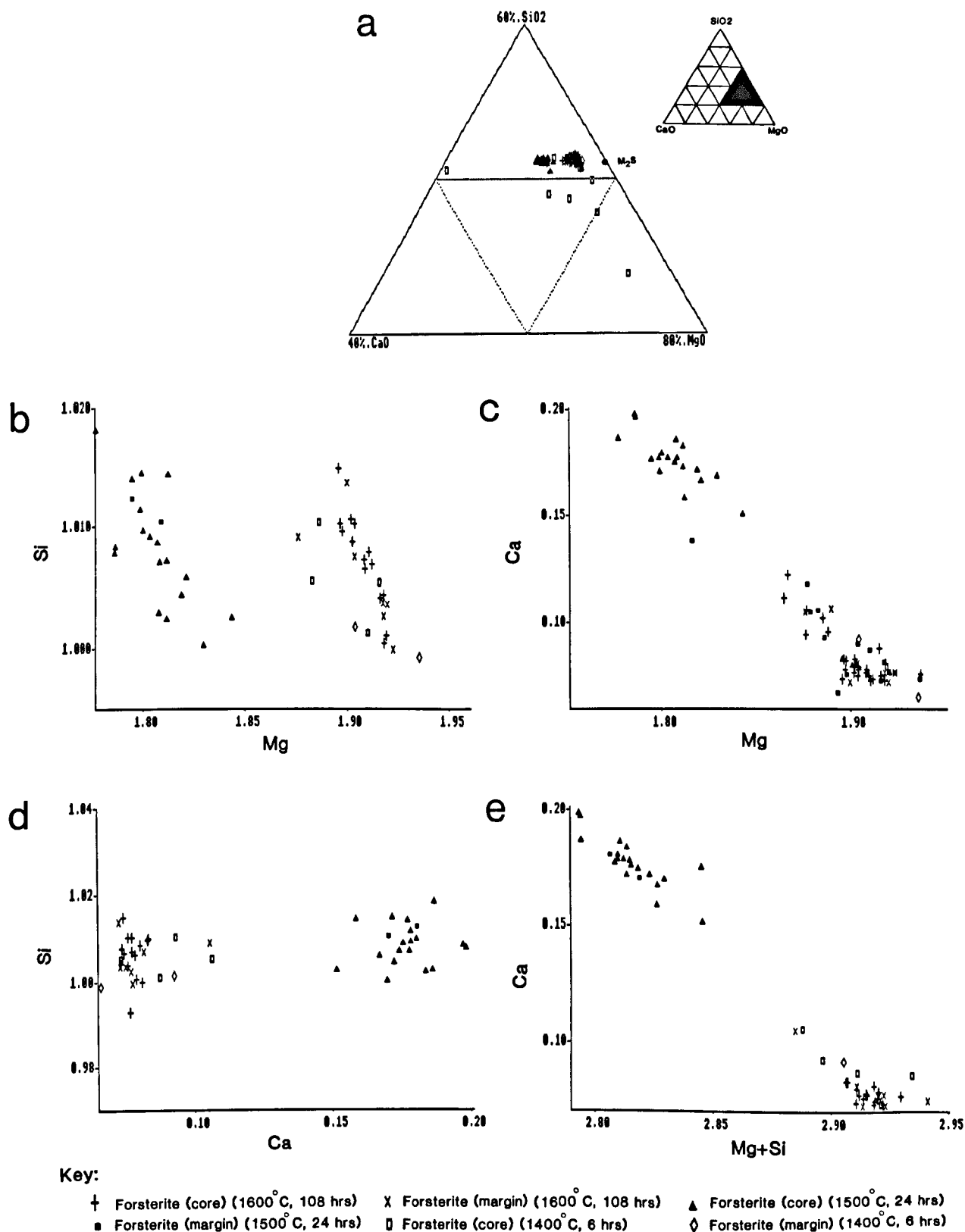


Figure 4.11 Triangular plot (wt.%) and cation relationships of forsterite

4.6.4 Dicalcium silicate

4.6.4.1 General

Dicalcium silicate (Ca_2SiO_4) is of vital importance in several fields of silicate science, such as cement, refractories and slags. It exists in several polymorphic forms of which one (the Y-form) is stable at room temperature without any stabiliser. The b-form is commonly found in ordinary portland cement in association with stabilising ions.

4.6.4.2 Polymorphism of dicalcium silicate

Dicalcium silicate occurs in several polymorphic forms, Y-form is stable at room temperature. The most widely known polymorphs, a, a', b, and Y were reported by Bredig (1950). Later the a' polymorph was reported to exist in two forms, aH and a'L (Guinier and Regourd, 1968) Later, Midgley (1974) (referred to by Gutt and Nurse, 1974) reported another monoclinic form called a'M. Besides these well characterized polymorphs, the existence of a cubic b'-phase (1600°C), a metastable b-phase and a-dicalcium silicate phase stabilised at 600°C with SiO_2 are also reported. The a form has the stability range ($1425-2130^\circ\text{C}$ while the a'L and a'H forms are stable in the ranges $675-1160^\circ\text{C}$) and $1160-1420^\circ\text{C}$, respectively. The a'M form is reported to be stable in the range $711-979^\circ\text{C}$.

The revised stability diagram and the phase transitions

reported by Midgley (1974) based on thermal studies are shown in Figure 4.12.

The a' and b-forms occur as the natural minerals called bredigite and larnite respectively (Bredig, 1950).

According to Smith et al. (1965) who studied the structure of Y-dicalcium silicate polymorph, it has an olivine type of structure. The structure of b-form (larnite) was determined by Midgley (1952) and this has been revised by Jost et al. (1977). The structure consists of isolated (SiO₄) tetrahedra and (CaO)₇ and (CaO)₈ polyhedra. The (CaO)_x polyhedra are densely packed in columns parallel to b, sharing triangular faces. The columns are cross-linked by shared edges and corners.

The stability range of different dicalcium silicate polymorphs are as follows:

a: 1425-2130°C (melting point).

a'H: 1420-1160°C.

a'L: 1160-675°C.

Y: 675°C-room temperature.

b-form is metastable.

On heating, changes are: Y or b to a'L to a'H to a. On cooling high temperature a changes to a' in a reversible manner. On further cooling, changes may follow four paths as described by Muan and Osborn (1965):

1. a' may persist to room temperature.
2. a' may invert to b, which then persists to room temperature.
3. a' may invert to Y.

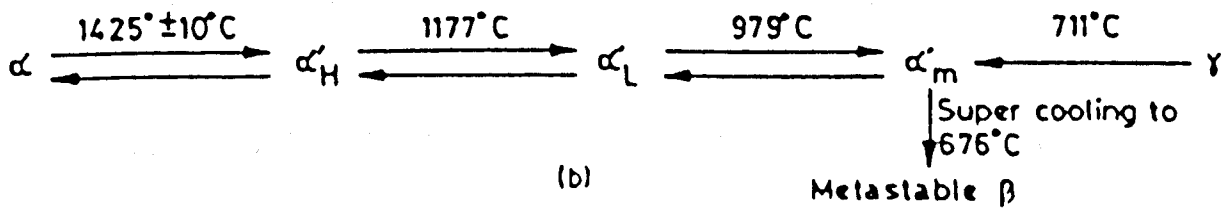
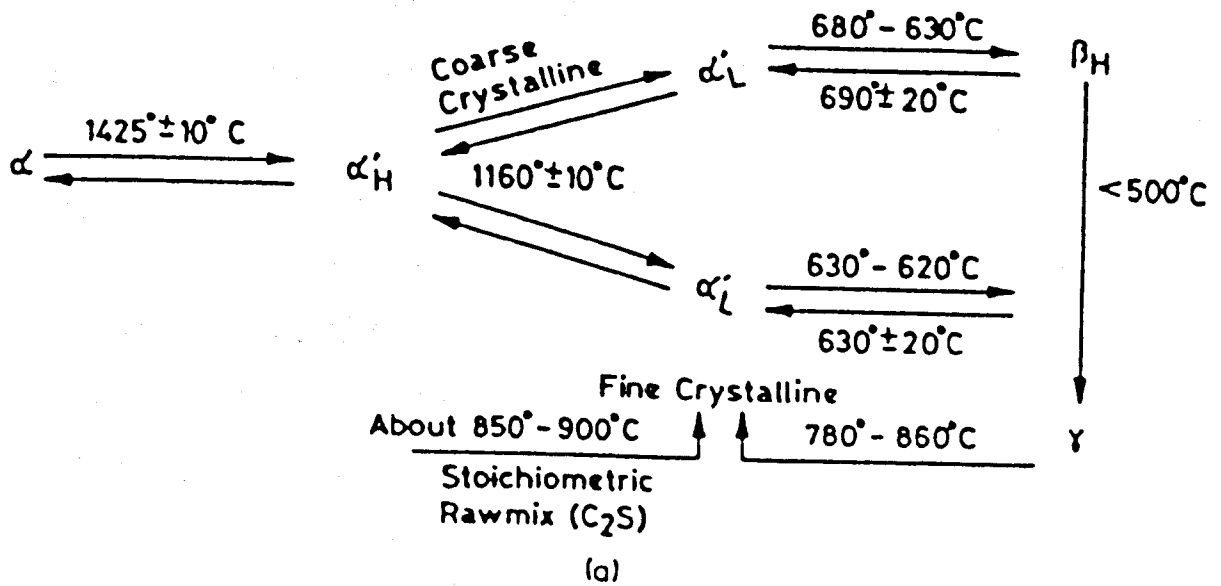


Figure 4.12

Stability diagram of dicalcium silicate polymorphs, a) as reported (Niesel 1972), b) as indicated (Midgley 1974) (from Ghosh et al. 1979)

4. a' may invert to b which then inverts to Y.

When b changes to Y a large increase in volume (approximately 10%) takes place. This is most commonly known as "dusting". In order to avoid dusting which causes disintegration, the high temperature forms of dicalcium silicate have to be stabilised by the addition of stabilising agents (inhibitors) (Nurse, 1952), or by rapid cooling (Ghosh et al. 1979). b form can be stabilised by the addition of B_2O_3 , Na_2O , K_2O , BaO , MnO_2 , Cr_2O_3 , or by a combination of these (Midgely, 1952).

a and a'-forms on the other hand are reported to be stabilised by MgO , Al_2O_3 , Fe_2O_3 , BaO , K_2O , P_2O_5 and Cr_2O_3 (see Ghosh et al. 1979).

4.6.4.3 Solid solution of dicalcium silicate

The position in this case is simpler, since the inversion in dicalcium silicate take place over a temperature range where the parent phase is stable.

Yamaguchi, Ono and Kawamura (1962) stated that in the presence of 2% MgO , dicalcium silicate is stable in the presence of C_3A and C_4AF when Al_2O_3 and Fe_2O_3 are added. The solubility of Al_2O_3 is between 2-3% by weight in the a-form (1400-1500°C) and less than 1% in the a'-form (1300-1350°C); the solubility of Fe_2O_3 is 1.5% in the a-form at 1400°C, 2.5% in the a-form at 1500°C, and less than 1% in the a'-form at 1300-1350°C.

Gutt (1965) also investigated the system dicalcium silicate - merwinite; he noted some solubility of merwinite

in a-dicalcium silicate but did not give a limit; Schlaudt and Roy (1966) give equivalent of 1.5% MgO in a-dicalcium silicate at 1600°C. For a'-dicalcium silicate at 1400°C Gutt (1965) gives 2% as against Schlaudt and Roy's (1966) 1.0% of MgO, but his diagram shows the solid solution in contact with phase (T) ($C_{1.7}M_{0.3}S$), not merwinite.

Gutt (1965) described a new compound (T) with the composition of ($C_{1.7}M_{0.3}S$) stable in contact with dicalcium silicate (C_2S) at sub solidus temperatures. Schlaudt and Roy (1966) thought that it decomposed at 1381°C and was therefore unstable with respect to a-dicalcium silicate, but Gutt (1965) shows a-dicalcium silicate and (T) phase in co-existence, (T) phase decompose at 1460°C.

Biggar (1971) identifies bredigite with the ($Ca_{1.8}Mg_{0.20}$) SiO_4 and ($Ca_{1.70}Mg_{0.30}$) SiO_4 range, which is the phase (T) referred to by Gutt (1965), and does not consider it to be a dicalcium silicate polymorph. Midgley (1974) (referred by Gutt and Nurse, 1974) considers that bredigite and phase (T) are polymorphs of a'L.

The solubility of P_2O_5 in dicalcium silicate can be seen in the system $2CaO.SiO_2-3CaO.P_2O_5$ (Nurse et al., 1959). The maximum solid solution of P_2O_5 in b-form is approximately 0.9 wt.% P_2O_5 (approximately 2 wt.% tricalcium phosphate), in a'-form is approximately 15 wt.% P_2O_5 (approximately 34 wt.% tricalcium phosphate). There is a continuous solid solution series between a'-dicalcium silicate and a'-tricalcium phosphate.

4.6.4.4 Results and discussion

Dicalcium silicate has been found in the natural dead burned magnesite samples A3, T2, T26, and natural dead burned huntite (Chapter 7). The microprobe analyses of dicalcium silicates are plotted on the CaO-MgO-SiO₂ phase diagram as wt.%, and given in Figure 4.13a. A selection of representative analysis of dicalcium silicate are presented in Table 4.18 under the code beginning with D.

There is a distinct trend towards merwinite. The presence of minor oxides mainly of MgO, Al₂O₃ and FeO are probably responsible for this. A comparatively higher content of Al₂O₃ was determined when dicalcium silicate is present with tricalcium aluminate. It is possible that Al₂O₃ in dicalcium silicate resulted from mixed analyses of dicalcium silicate with tricalcium aluminate.

Dicalcium silicate analyses are calculated on the basis of four oxygens.

Cation relationships of dicalcium silicate are shown in Figure 4.13. There is an inverse relationship between Ca and Mg and (Mg+Al+Fe₂) against Ca (Figure 4.13c, e). Si is almost constant when plotted against Mg and Ca (Figures 4.13b, d). It must be mentioned that some of the dicalcium silicate analyses have comparatively lower totals, which is mainly due to the presence of microporosities. The minor impurity oxides are MgO, Al₂O₃ and to a lower extent FeO. The level of MgO and Al₂O₃, varies considerably, which is probably because, they are picked up from the minor phases present in the matrix during the analyses (mixed analyses).

Table 4.18 A selection of dicalcium silicate analyses as determined by EPMA in dead burned magnesite

Sample Code SPOT	A3-1A DM-A 13	A3-1A DC16 21	A3-1A DC16 22	A3-1A DC16 26	A3-1B DC16 1	A3-1B DC16 6	A3-1B DC16 8	A3-1B DC16 9	A3-2A DM16 2	A3-2A DC16 6
SiO2	33.53	33.80	33.37	34.14	34.23	33.79	33.90	33.86	33.41	33.79
TiO2	n.d.	n.d.	n.d.	n.d.	n.d.	n.d.	n.d.	n.d.	n.d.	n.d.
Al2O3	0.40	0.24	1.30	0.46	0.28	0.79	0.31	0.49	0.26	n.d.
Cr2O3	n.d.	n.d.	n.d.	n.d.	n.d.	n.d.	n.d.	n.d.	n.d.	n.d.
FeO	n.d.	n.d.	n.d.	n.d.	n.d.	n.d.	n.d.	n.d.	0.37	n.d.
MnO	n.d.	n.d.	n.d.	n.d.	n.d.	n.d.	n.d.	n.d.	n.d.	n.d.
MgO	0.40	1.87	0.68	1.07	0.82	1.89	0.34	1.80	0.32	0.70
CaO	65.22	63.31	63.96	64.04	64.33	62.93	65.81	63.67	64.67	64.17
K2O	n.d.	n.d.	n.d.	n.d.	n.d.	n.d.	n.d.	n.d.	n.d.	n.d.
TOTAL	99.55	99.22	99.31	99.71	99.66	99.40	100.36	99.82	99.03	98.66

Cations on the basis of 4 oxygens

Si	0.97	0.98	0.96	0.98	0.98	0.97	0.97	0.97	0.97	0.98
Al	0.01	0.01	0.04	0.02	0.01	0.03	0.01	0.02	0.01	0.00
Fe2	0.00	0.00	0.00	0.00	0.00	0.00	0.00	0.00	0.00	0.00
Mn	0.00	0.00	0.00	0.00	0.00	0.00	0.00	0.00	0.00	0.00
Mg	0.02	0.08	0.03	0.05	0.04	0.08	0.01	0.08	0.01	0.03
Ca	2.02	1.96	1.98	1.97	1.98	1.94	2.02	1.96	2.02	2.00

Sample Code SPOT	A3-2A DC16 7	A3-2A DC16 10	A3-2A DC16 12	A3-2A DM16 13	A3-2B DC16 5	A3-2B DM16 8	A3-2B DC16 10	A3-2B DC16 14	A3 DC16 4	T2-2A DC16 4
SiO2	34.28	33.68	33.75	34.28	33.68	33.38	33.99	33.93	33.85	64.31
TiO2	0.23	n.d.	n.d.	n.d.	n.d.	n.d.	n.d.	n.d.	n.d.	n.d.
Al2O3	n.d.	0.45	0.39	0.51	0.63	0.54	0.29	0.35	n.d.	n.d.
Cr2O3	n.d.	n.d.	n.d.	n.d.	n.d.	n.d.	n.d.	n.d.	n.d.	n.d.
FeO	n.d.	n.d.	n.d.	n.d.	n.d.	0.35	n.d.	n.d.	n.d.	n.d.
MnO	n.d.	n.d.	n.d.	n.d.	n.d.	n.d.	n.d.	n.d.	n.d.	n.d.
MgO	0.48	0.20	1.73	1.44	0.58	0.44	n.d.	0.46	0.38	0.67
CaO	64.73	64.97	63.02	63.50	64.17	64.05	64.73	64.34	64.92	64.56
K2O	n.d.	n.d.	n.d.	n.d.	n.d.	n.d.	n.d.	n.d.	n.d.	n.d.
TOTAL	99.72	99.30	98.89	99.73	99.06	98.76	99.01	99.08	99.15	129.54

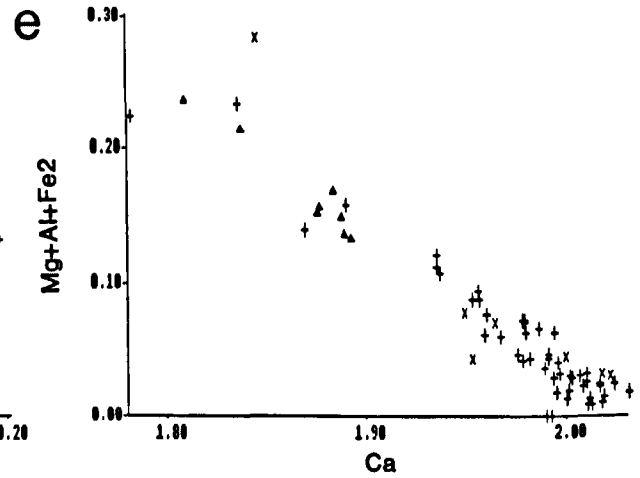
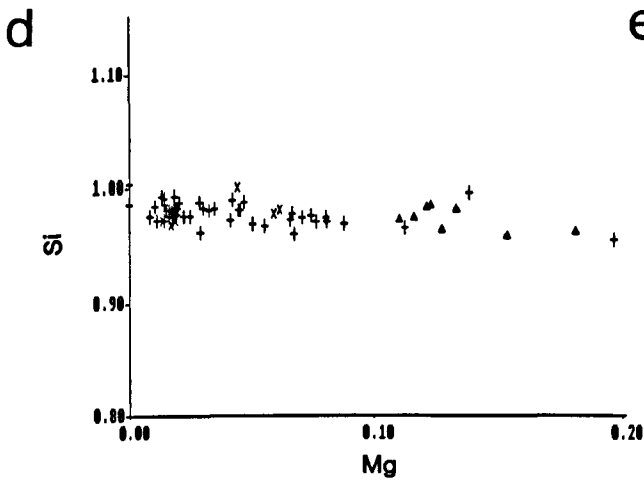
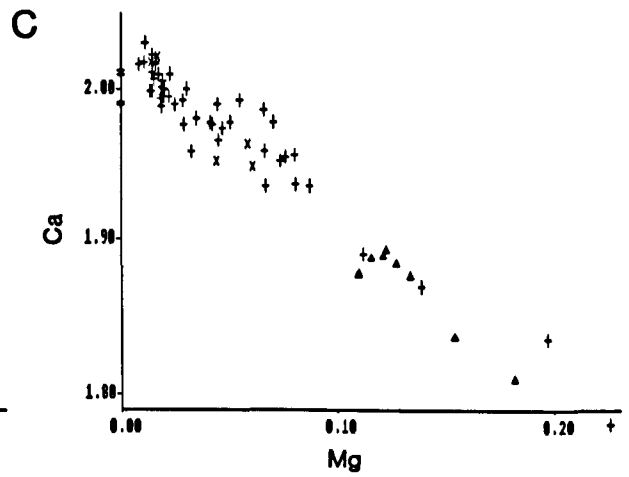
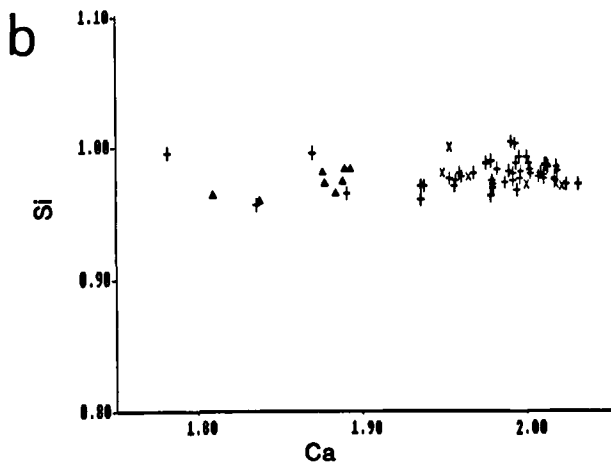
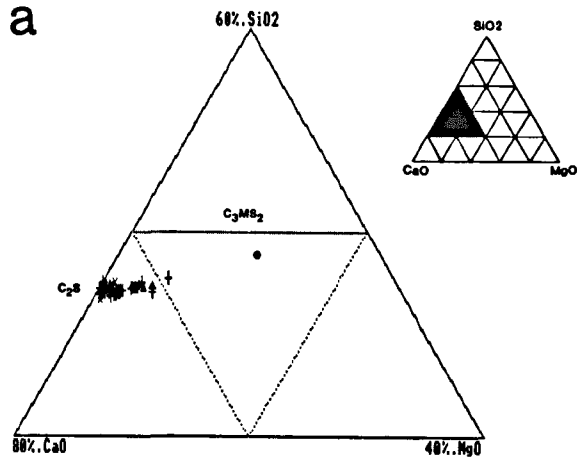
Cations on the basis of 4 oxygens

Si	0.99	0.98	0.98	0.98	0.98	0.97	0.99	0.98	0.98	1.29
Al	0.00	0.02	0.01	0.02	0.02	0.02	0.01	0.01	0.00	0.00
Fe2	0.00	0.00	0.00	0.00	0.00	0.01	0.00	0.00	0.00	0.00
Mn	0.00	0.00	0.00	0.00	0.00	0.00	0.00	0.00	0.00	0.00
Mg	0.02	0.01	0.07	0.06	0.03	0.02	0.00	0.02	0.02	0.02
Ca	2.00	2.02	1.95	1.95	1.99	2.00	2.01	2.00	2.02	1.39

Sample Code SPOT	T2-2A DM16 22	T2-1A DC16 1	T2-1A DC16 4	T2-1A DC16 6	T2-1A DC16 13	T2-1A DC16 17	T2 DC15 6	T2 DC15 7	T26-1A DC16 17
SiO2	34.85	35.50	34.42	33.98	34.21	34.40	34.36	34.52	33.77
TiO2	n.d.	n.d.	n.d.	n.d.	n.d.	n.d.	n.d.	n.d.	n.d.
Al2O3	n.d.	n.d.	n.d.	n.d.	n.d.	n.d.	0.41	0.29	0.65
Cr2O3	n.d.	n.d.	n.d.	n.d.	n.d.	n.d.	n.d.	n.d.	n.d.
FeO	n.d.	n.d.	n.d.	n.d.	n.d.	n.d.	n.d.	n.d.	n.d.
MnO	n.d.	n.d.	n.d.	n.d.	n.d.	n.d.	n.d.	n.d.	n.d.
MgO	1.04	33.32	0.43	1.66	1.10	0.99	2.85	2.89	0.97
CaO	63.45	62.22	64.54	64.38	63.81	64.17	61.59	61.77	64.15
K2O	n.d.	n.d.	n.d.	n.d.	n.d.	n.d.	n.d.	n.d.	n.d.
TOTAL	99.34	131.04	99.39	100.02	99.12	99.56	99.21	99.47	99.54

Cations on the basis of 4 oxygens

Si	1.00	0.76	0.99	0.97	0.99	0.99	0.98	0.99	0.97
Al	0.00	0.00	0.00	0.00	0.00	0.00	0.01	0.01	0.02
Fe2	0.00	0.00	0.00	0.00	0.00	0.00	0.00	0.00	0.00
Mn	0.00	0.00	0.00	0.00	0.00	0.00	0.00	0.00	0.00
Mg	0.04	1.06	0.02	0.07	0.05	0.04	0.12	0.12	0.04
Ca	1.95	1.42	2.00	1.98	1.98	1.98	1.89	1.89	1.98



Key:

† Dicalcium silicate (core) (1600°C, 108 hrs)

× Dicalcium silicate (margin) (1600°C, 108 hrs)

▲ Dicalcium silicate (core) (1500°C, 24 hrs)

Figure 4.13 Triangular plot (wt.%) and cation relationships of dicalcium silicate

4.6.5 Tricalcium silicate

4.6.5.1 General

Tricalcium silicate (Ca_3SiO_5), is an important component of portland cement and to a lesser extent in some kinds of basic refractories and in basic steel making. Six crystalline forms of tricalcium silicate have been reported by Guinier and Regourd (1968) as follows: one rhombohedral, (R), two monoclinic (M1, M2) and three triclinic (T1, T2, T3). The rhombohedral form is stable between its incongruent melting at approximately 2070°C and 1050°C. The conversion temperatures of different tricalcium silicate polymorphs as pointed out by Guinier and Regourd (1968) are given below:

at 1050°C R to M2
at 990°C M2 to M1
at 980°C M1 to T3
at 920°C T3 to T2
at 600°C T2 to T1

Uchikawa and Tsukiyama (1971) indicated four modification of T2 and two modification of T1.

According to Guinier and Regourd (1968), in pure tricalcium silicate, in both heating and cooling conditions, the transformation of polymorphs occurs rapidly and reversibly. But by adding small amounts of Fe_2O_3 , Al_2O_3 , Cr_2O_3 , MgO , TiO_2 , Na_2O , K_2O , the polymorphs can be stabilised.

The structure of tricalcium silicate has been determined

by Jeffery (1952) (referred to by Guinier and Regourd, 1968). The structure is trigonal with approximately $a:7 \text{ \AA}$, $c:25 \text{ \AA}$ (hexagonal rotation) and space group R_{3m} . The structure consists essentially of independent (SiO_4) tetrahedra and octahedrally coordinated calcium ions, which link the tetrahedra and three free oxygen ions (for more detail see Jeffery 1952 and Guinier and Regourd 1968).

Three (SiO_4) tetrahedra and three free oxygen ions which are not linked to silicon are situated at the trigonal axis, at different heights. As a result, the octahedra is distorted and leaves large holes to accommodate other atoms.

4.6.5.2 Solid solutions

The limits of solubility of different oxides in tricalcium silicate at 1550°C as reported by Fletcher (1965) are given below:

MgO	2.0%
Al_2O_3	1.0%
Fe_2O_3	1.1%
Cr_2O_3	1.4%
$\text{Al}_2\text{O}_3+\text{MgO}$	2.2%
$\text{Fe}_2\text{O}_3+\text{MgO}$	2.0%
C_3A	2.0%

1. Mg^{2+} can enter the structure of tricalcium silicate to the extent of 2.0% MgO at 1500°C . Mg^{2+} replace Ca^{2+} and can stabilise the monoclinic form on quenching to room

temperature.

2. Al^{3+} can enter the structure of tricalcium silicate to the extent of about 0.9% Al_2O_3 at 1500°C. 4Al^{3+} replace 3Si^{4+} , the balance of charge is maintained, and the 'O' and Ca packing in the unit cell is unchanged. Al^{3+} alone does not stabilise the monoclinic form on quenching to room temperature.
3. In the presence of Al^{3+} to extent of 0.9% Al_2O_3 about 1% MgO can stabilise the monoclinic form on quenching to room temperature. Further MgO substitution can occur up to a maximum of about 1.7% MgO, resulting in a slight change in the monoclinic structure. The conclusions regarding the mode of substitution of Mg^{2+} and Al^{3+} alone still apply when they are introduced together.
4. If Mg^{2+} and Al^{3+} together are reduced below about three quarters of the amount required to saturate the structure, the triclinic form occurs on quenching to room temperature (for more detail see Midgley and Fletcher 1963).

Gutt (1965) has since revised the temperature of incongruent melting of tricalcium silicate to 2150°C.

4.6.5.3 Results and discussion

Pure tricalcium silicate has been found only in dead burned product of Ablah natural mixture of magnesite and dolomite calcined at 1500°C. In other dead burned magnesites (samples A3, T2 and T26), tricalcium silicate has been found normally mixed with periclase. The microprobe analyses of tricalcium silicate are plotted on the CaO-MgO-SiO₂ diagram

as Wt.% and it is given in Chapter 7, Figure 7.6c. As it can be seen from the CaO-MgO-SiO₂ diagram, the analyses plotted slightly away from the theoretical composition of tricalcium silicate showing a trend towards periclase, that means some of MgO is picked up from the periclase during analyses (i.e. mixed analyses).

The tricalcium silicate analyses are calculated on the basis of five oxygens. All analyses are presented in Chapter 7, Table 7.12 under the code beginning with T.

The cation relationship of tricalcium silicate analysis are presented in Figures 7.6d, e, and f).

4.6.6 Merwinite

4.6.6.1 General

Merwinite $[\text{Ca}_3\text{Mg}(\text{SiO}_4)_2]$ crystallizes with monoclinic symmetry. The physical properties of merwinite as described by Deer et al. (1986) are presented as below:

$$\alpha = 1.702-1.710$$

$$\beta = 1.710-1.714$$

$$\gamma = 1.718-1.728$$

$$\Delta = 0.008-0.021$$

$$2V = 66-76$$

Dispersion $r > v$, weak

$$D = 3.15-3.22$$

$$H = 6$$

Cleavage (100) poor, (010) very poor

Twinning: Lamellar twins common (100); also twins on (611) giving lamellar twin intersection 42.

Colour: White; colourless in thin section.

Unit cell

$$a = 13.261 \text{ \AA}$$

$$b = 5.301 \text{ \AA}$$

$$c = 9.331 \text{ \AA}$$

Z = 4 Space group P21/a

Merwinite as a minor constituents of a refractory brick produced by firing impure magnesite, or a mixture of dolomite and sand, or dolomite at temperature varying between 1500°C and 1650°C.

Merwinite was first described by Larson and Foshag

(1921) (referred to by Speer and Ribbe, 1982). Merwinite can begin to form at a temperature of 1375°C. At this temperature monticellite and calcium orthosilicates are also components of the refractory bricks. The formation of merwinite can be controlled in firing mixtures of lime, magnesia and silica by maintaining the ratio of CaO/SiO_2 between $1.4 < \text{CaO/SiO}_2 < 1.8$. The product after firing will contain both b-dicalcium silicate and merwinite.

In 1943, Phemister described the results of experiments undertaken to test the reactions between lime - forsterite and lime - akermanite. After firing at 1250°C, for two minutes akermanite was completely and forsterite 80% destroyed. In both cases the final products were b-dicalcium silicate and MgO, but intermediate compounds, monticellite and merwinite in the case of experiments with forsterite and merwinite in the case of akermanite, were formed as transient products. The authors also report as transient products mixed crystals between merwinite and b-dicalcium silicate and between monticellite and b-dicalcium silicate. In contrast to the calcium orthosilicate, merwinite does not appear to undergo transformation in the solid state.

Nurse (1952), Yamaguchi and Suzuki (1967), have studied the atomic arrangement of merwinite. Detailed structural investigation was carried out by Moor and Araki (1972). The structure consists of $(\text{Mg})_6$ octahedra and SiO_4 tetrahedra, which link every corner of the octahedra, defining a 'pinwheel'. The pinwheels link to form slabs parallel to (100). Moor and Araki (1972) pointed out that the merwinite

structure has a profound pseudo-hexagonal character.

According to Speer and Ribbe, (1982), Fe^{2+} and Mn may substitute for Mg. Osburn and Muan (1960) have presented the stability of merwinite in the system CaO-MgO-SiO_2 . Merwinite melts incongruently at 1575°C .

Roy (1956), who studied the subsolidus phase relationship in the system dicalcium silicate - monticellite in the $600-900^\circ\text{C}$ temperature range, and Gutt (1965), who examined the system dicalcium silicate - merwinite, indicated no solid solution of coexisting phase. Schlaudt and Roy (1966) report up to 10 mol.% monticellite in merwinite at 1485°C but no solubility of dicalcium silicate.

4.6.6.2 Results and discussion

Merwinite has been analysed in sample A3. The microprobe analyses of merwinites are plotted on the CaO-MgO-SiO_2 diagram as wt.%, which is given in Figure 4.14a. The microprobe analyses of merwinite are presented in Table 4.19 under the code beginning with "MR".

The amount of FeO in merwinite varies from below detection limit up to 0.42%, it may suggest that high levels of FeO is derived from an iron rich separate phase. Consequently some of the merwinite analyses are mixed analyses. Cation relationships, with the cations calculated on the basis of eight oxygens, are shown in Figure 4.14b, c, and d. There is an inverse relationship between (Ca+Si) with Mg, and a direct relationship between Si with Ca.

Table 4.19 The microprobe analyses of merwinite as determined by EPMA in dead burned magnesite

Sample Code	A3 MR15					
SPOT	1	3	19	20	21	22
SiO2	36.56	36.16	36.35	35.35	37.27	34.90
TiO2	n.d.	n.d.	n.d.	n.d.	n.d.	n.d.
Al2O3	n.d.	n.d.	n.d.	n.d.	n.d.	n.d.
Cr2O3	n.d.	n.d.	n.d.	n.d.	n.d.	n.d.
FeO	n.d.	n.d.	0.42	n.d.	0.31	n.d.
MnO	n.d.	n.d.	n.d.	n.d.	n.d.	n.d.
MgO	12.18	11.98	12.14	13.44	12.37	13.51
CaO	50.29	50.43	50.10	49.65	51.82	48.90
K2O	n.d.	n.d.	n.d.	n.d.	n.d.	n.d.
TOTAL	99.03	98.57	99.01	98.44	101.77	97.31

Cations on the basis of 8 oxygens

Si	2.01	2.01	2.01	1.96	2.00	1.96
Al	0.00	0.00	0.00	0.00	0.00	0.00
Fe2	0.00	0.00	0.02	0.00	0.01	0.00
Mn	0.00	0.00	0.00	0.00	0.00	0.00
Mg	1.00	0.99	1.00	1.11	0.99	1.13
Ca	2.97	3.00	2.97	2.96	2.99	2.94

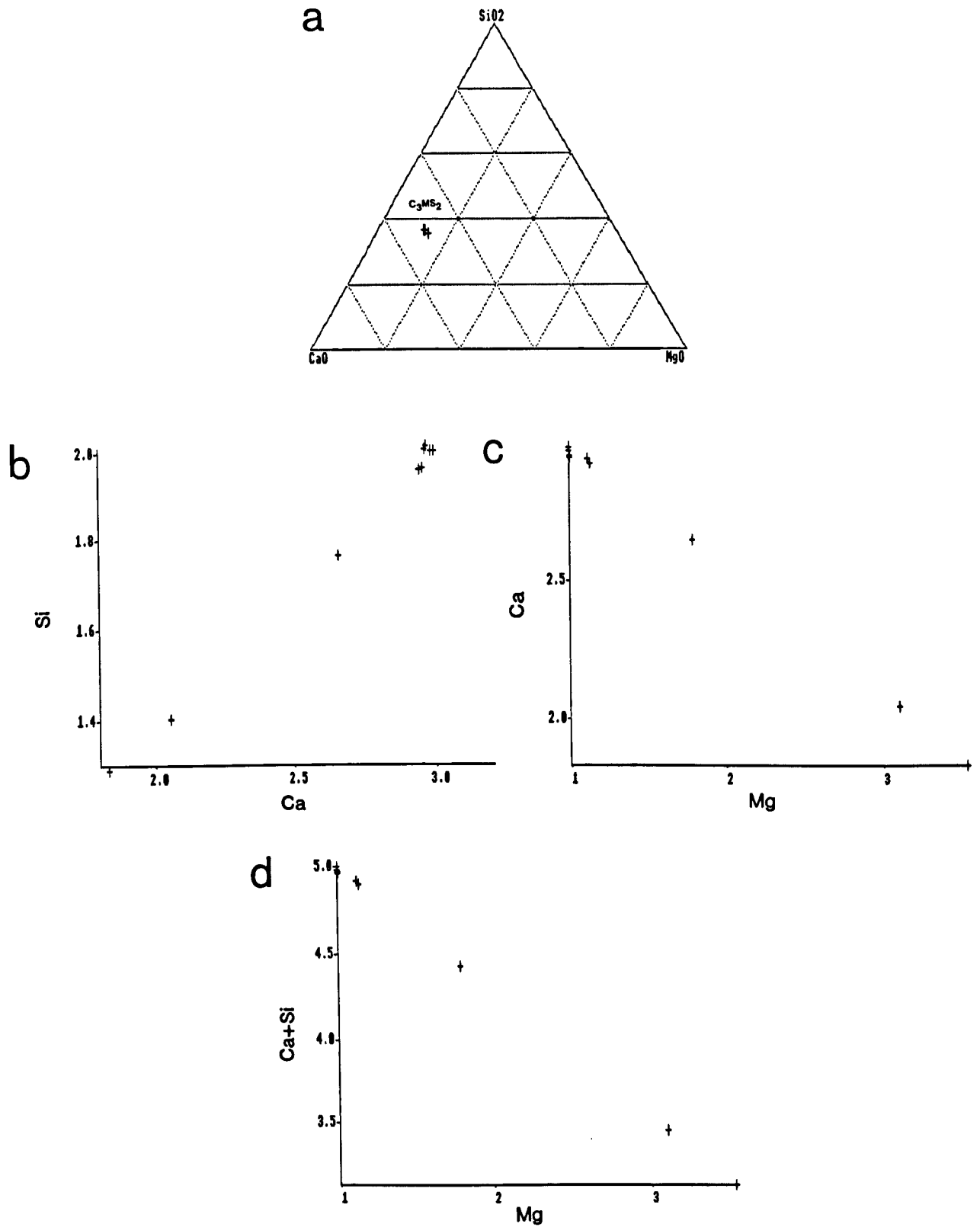


Figure 4.14 Triangular plot (wt.%) and cation relationships of merwinite

4.7 Summary and conclusions

The mineralogy, microstructure and mineral chemistry of the phases of dead burned natural magnesites calcined at 1400, 1500 and 1600°C, for 6, 24, 96 and 108 hours are presented in the previous sections. It is now appropriate to compare the mineral phases determined using XRD, SEM and EPMA with those which can be predicted from phase equilibrium diagram and see whether the predicted phases match the experimental results.

4.7.1 Phase assemblages

The mineral composition of dead burned magnesite may be deduced from the five component system, CaO-MgO-SiO₂-Fe₂O₃-Al₂O₃. There are six possible phase assemblages coexisting in solid state magnesia compounds depending on the CaO/SiO₂ ratio. (for more detail see Rait (1950), White (1962, 1970) and Baumgart (1984). Rigby et al. (1947) described a general method of calculating the mineralogical composition of magnesite brick.

White (1962, 1970) presented the four component system CaO-MgO-SiO₂-Fe₂O₃, and the main features of phase assemblages can be clearly seen from the relevant part of the system. The phase assemblages which can occur in the presence of free MgO (periclase) in the four component system MgO-CaO-SiO₂-Fe₂O₃ is presented in Figure 4.15.

The mineral composition of dead burned magnesites may be deduced from the five component system,

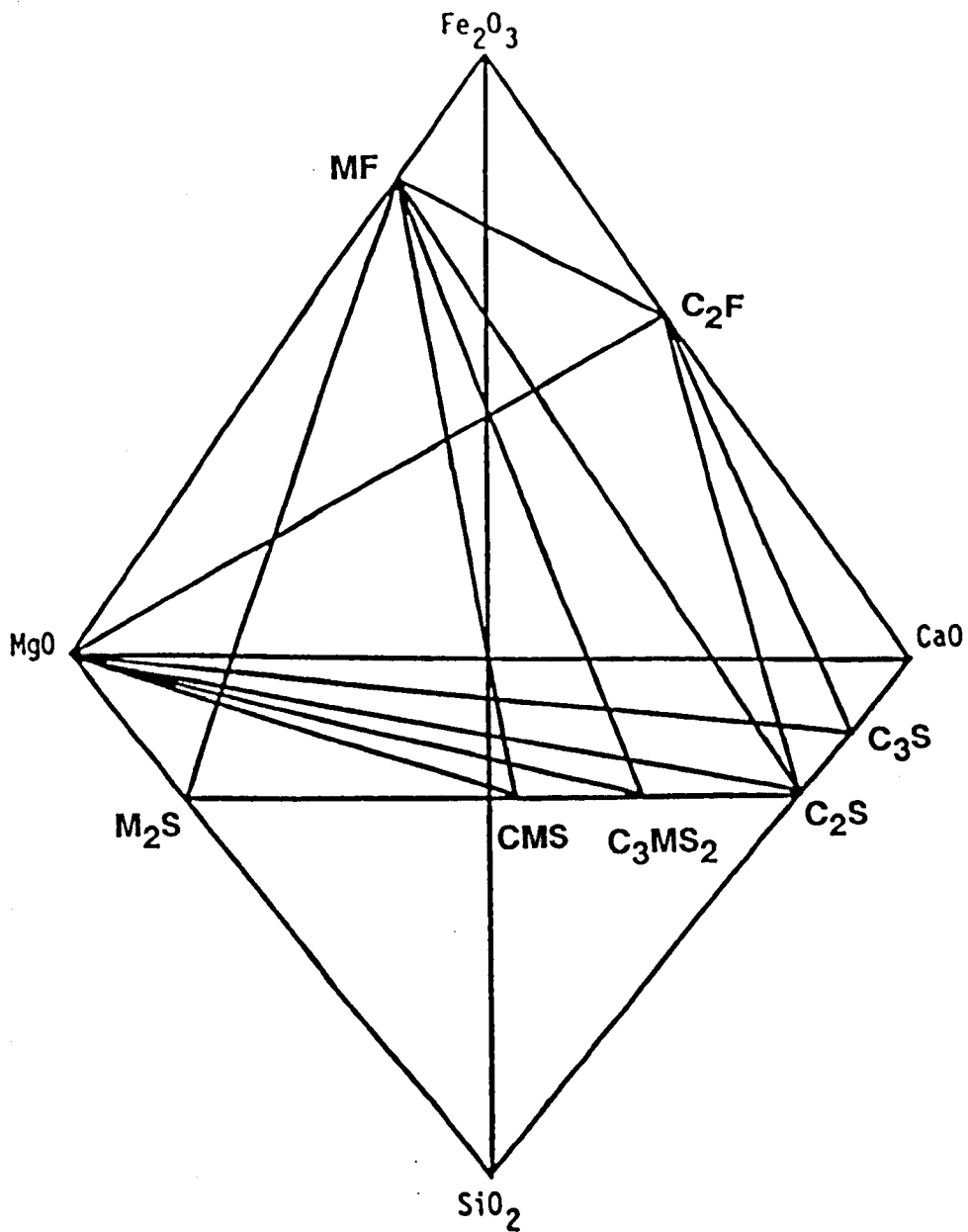


Figure 4.15 Phase relationship in the solid state in the System MgO-CaO-SiO₂-Fe₂O₃ where MgO occurs as a phase (after White 1970).

CaO-MgO-SiO₂-Fe₂O₃-Al₂O₃ by Baumgart (1984) as follows: There are six possible phase assemblages coexisting in solid state magnesia compounds depending on the CaO/SiO₂ ratio.

1. When the CaO/SiO₂ mole ratio is <1:1, the predicted phase assemblage is (M, CMS, M₂S, MA, MF). CaO being present in smaller amount than SiO₂ has formed monticellite (CMS). Al₂O₃ and Fe₂O₃ for magnesioaluminate (MA) and magnesioferrite (MF).
2. CaO/SiO₂ mole ratio between 1:1 - 1.5:1, forsterite (M₂S) is replaced by merwinite (C₃MS₂). The phase assemblage is (M, CMS, C₃MS₂, MA, MF).
3. CaO/SiO₂ mole ratio 1.5:1 - 2:1, monticellite is replaced by dicalcium silicate (C₂S). The predicted phase assemblages is (M, C₂S, C₃MS₂, MA, MF). According to Baumgart (1984) with a CaO/SiO₂ mole ratio of exactly 2:1, the (M, C₂S, MA, MF) is present, but this assemblage is too specific to happen in practice.
4. with a further increase in CaO/SiO₂ mole ratio, the Al₂O₃/Fe₂O₃ ratio partly controls the mineralogy which gives 5 possible assemblages:

(M, C₂S, C₄AF, C₃A, C₅A₃)

(M, C₂S, C₄AF, CA, C₅A₃)

(M, C₂S, C₄AF, CA, MA)

(M, C₂S, C₄AF, C₂F, MF)

(M, C₂S, C₄AF, MA, MF)

5. With more CaO, the phase assemblage resembles a stabilised dolomite brick. The reactive free lime is transformed into more stable tricalcium silicate (C₃S). Brownmillerite

(C₄AF) is always present. The formation of C₂F, or C₃A depends on the Al₂O₃/Fe₂O₃ ratio. There are no more MgO-containing compounds.

6. This mineral assemblage corresponds to the composition of limestone and dolomite after calcination. CaO is not entirely bound leaving some CaO in the free state.

The phase assemblages of the dead burned magnesites, as predicted from the phase equilibrium studies and practically determined mineral phases at different calcination temperatures of 1400, 1500, and 1600°C using XRD, SEM and EPMA are given in Tables 4.20-4.22. Plots of bulk composition (wt.%) of the natural dead burned magnesites on the CaO-MgO-SiO₂ isothermal diagrams at 1400, 1500 and 1600°C, are presented in Figure 4.16.

4.7.2 Discussion of the predicted and determined phase assemblages.

The maximum number of phases which can be present in the dead burned magnesite in the six component system MgO-CaO-SiO₂-Al₂O₃-Fe₂O₃-FeO, at equilibrium conditions, are two silicates (or one silicate and lime), one spinel (or spinel solid solution), and one ferrite (or ferrite solid solution).

As it can be seen from Tables 4.20-4.22, samples A3, A14, T2, T15 and T26 contain most commonly two and occasionally three silicate phases, with a maximum of one spinel and one ferrite phase. Where a higher number of silicate phases is present, equilibrium within the grains is

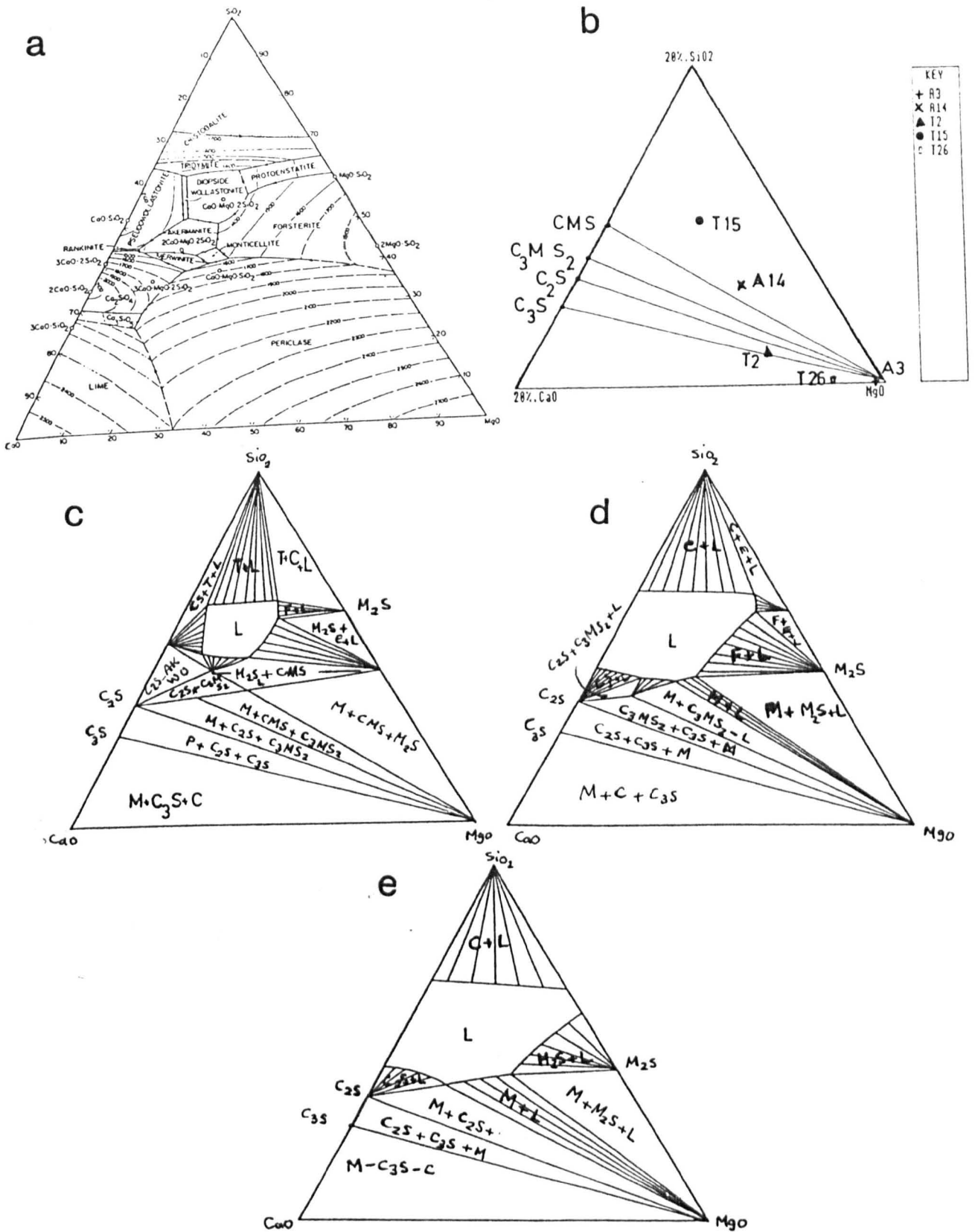


Figure 4.16 a) Phase diagram for the system CaO-MgO-SiO₂ (wt.%) (after Osborn and Muan, 1960). b) Plots of the bulk chemistry of the natural magnesites on CaO-MgO-SiO₂ diagram (wt.%). c,d,e) Isothermal diagrams for 1400°C, 1500°C, 1600°C temperatures

Table : 4.20 Predicted and determined phase assemblages of the natural dead burned magnesites calcined at 1400°C for 6 hours.

Sample	CaO/SiO ₂ mole ratio	Al ₂ O ₃ /Fe ₂ O ₃ mole ratio	Predicted phase Assemblages	Determined phase assemblages	
A3	3.21	0.23	M-C2S-C3S-C-C2F-C3A	XRD	M-C-g
				SEM	M-C3S-C-C2S-C2F
				EPMA	M-C2F-(mix)
A14	0.77	5.00	M-CMS-M2S-MF-MA	XRD	M-CMS-M2S-SP&/orC2S-g
				SEM	M-M2S-C2S&/orC3MS2-CMS-C3S-SP
				EPMA	M-CMS-M2S-SP-(mix)
T2	2.72	0.00	M-C2S-C3S-C2F-C3A	XRD	M-C-C3S-C2S&/orC3MS2-g
				SEM	M-C3S-C-SP
				EPMA	M-C2S-(mix)
T15	0.48	0.00	M-CMS-M2S-MF7-MA	XRD	M-CMS-M2S-g
				SEM	M-M2S-CMS-C2S&/orC3MS2
				EPMA	M-CMS-M2S-(mix)
T26	11.88	0.00	M-C3S-C-(C2F-C3A)	XRD	M-C-g
				SEM	M-C-C2S&/orC3S
				EPMA	M-C-(mix)

Table : 4.21 Predicted and determined phase assemblages of the natural dead burned magnesites calcined at 1500°C for 24 hours.

Sample	CaO/SiO ₂ mole ratio	Al ₂ O ₃ /Fe ₂ O ₃ mole ratio	Predicted phase Assemblages	Determined phase assemblages	
A3	3.21	0.23	M-C2S-C3S-C-C2F-C3A	XRD	M-C-g
				SEM	M-C-C3S-(mix)
				EPMA	M-C2S-C3MS2-(mix)
A14	0.77	5.00	M-CMS-M2S-MF-MA	XRD	M-CMS-SP&/orC2S-C2S-g
				SEM	M-C2S&/orC3MS2-M2S-CMS
				EPMA	M-CMS-M2S-(mix)
T2	2.72	0.00	M-C2S-C3S-C2F-C3A	XRD	M-C2S&/orC3MS2-C-g-C3S
				SEM	M-C3S-C2S-C
				EPMA	M-C2S-C3S-CA-(mix)
T15	0.48	0.00	M-CMS-M2S-MF?MA	XRD	M-CMS-M2S-g
				SEM	M-CMS-M2S-C3MS2
				EPMA	M-CMS-M2S-SP-(mix)
T26	11.88	0.00	M-C3S-C-(C2F-C3A)	XRD	M-C-g
				SEM	M-C-C3S-C2F
				EPMA	M-C-(mix)

Table : 4.22 Predicted and determined phase assemblages of the natural dead burned magnesites calcined at 1600°C for 108 hours.

Sample	CaO/SiO2 mole ratio	Al2O3/Fe2O3 mole ratio	Predicted phase Assemblages	Determined phase assemblages	
A3	3.21	0.23	M-C2S-C3S-C-C2F-C3A	XRD	M-C2S-C3MS2&/orC2S-SP
				SEM	M-C2S-C3S-C2F-C3A - C - Sp - (mix)
				EPMA	M-C2S-SP-(mix)
A14	0.77	5.00	M-CMS-M2S-MF-MA	XRD	M-CMS-M2S-SP&/orC2S
				SEM	M-CMS-M2S-SP-C-C3A-C2S-C3S
				EPMA	M-CMS-M2S-SP-(mix)
T2	2.72	0.00	M-C2S-C3S-C2F-C3A	XRD	M-C3S-C2S&/orC3MS2-C
				SEM	M-C2S-C3S-C-C3A
				EPMA	M-C2S-C3S-(mix)
T15	0.48	0.00	M-CMS-M2S-MF-MA	XRD	M-CMS-M2S
				SEM	M-CMS-M2S-C2S&/orC3MS2-C
				EPMA	M-CMS-M2S-C3MS2-(mix)
T26	11.88	0.00	M-C3S-C-C2F-C3A	XRD	M-C-C2S&/orC3S
				SEM	M-C3S-C-C3A-C2S-(mix)
				EPMA	M-C2S-C3S-C3A-CA-SP-C-(mix)

not completely achieved. This may suggest that equilibrium is partially attained especially at higher calcination temperatures (1500 and 1600°C).

As it can be seen from the Tables 4.20-4.22 almost all the predicted phases are among the determined phases. The phase assemblages determined in the magnesia grains are variable within each sample. The chemical inhomogeneity of natural magnesites is the major cause of mineralogical variation within the natural dead burned magnesites. As the close agreement between the predicted and the determined phases indicates, it is possible to predict the mineralogy of the final product from the bulk chemical analysis using a knowledge of phase equilibria.

Tricalcium silicate is unstable below 1250°C and decomposes into dicalcium silicate and lime. Hence, the predicted phase products containing tricalcium silicate and lime may contain dicalcium silicate depending on the firing temperature and cooling conditions.

The chemical homogeneity of the raw material prior to calcination is thought to be the main factor contributing to the homogeneous mineralogy of the final product.

4.7.3 Industrial implications

In chapter 2 the mineralogy, geology and industrial properties of dead burned magnesites are reviewed in detail. The main aim of this section is to assess the dead burned magnesites from eastern Iran as basic refractory raw materials. The following properties, such as mineralogy, bulk

density, microstructure, grain size, degree of bonding, porosity and hydration tendency need to be considered. Judgment on the basis of one property of dead burned magnesite alone is confusing. For example, a material which is chemically pure but has a low bulk density and poor crystal development, such as sample T26, cannot be considered as a good quality refractory material.

4.7.3.1 Bulk chemistry

The level of impurities varies considerably in the investigated natural dead burned magnesite products. The total impurities range between 0.85-7.91%. On the basis of total impurities, the natural dead burned magnesites can be classified in order of decreasing impurity content as follows, T15 (7.91%), A14 (6.97%), T2 (3.55%), T26 (1.51%), A3 (0.85%).

The highest levels of Fe_2O_3 and Al_2O_3 are found in samples A3 and A14 respectively both from the Afzalabad magnesite deposit.

4.7.3.2 Mineralogy

The mineralogy of the natural dead burned magnesites, as described earlier, is not completely homogeneous throughout which causes slight mineral phase variety in different grains of each sample.

Considering the dominant mineral phases, however, the high temperature resistance of the natural dead burned magnesites may be classified as follows in increasing order

A14, T15, T2, A3, T26. Table 4.23 present the melting point of mineral phases present in natural dead burned magnesites.

Table 4.23 Melting points (or dissociation temperatures) of phases present in dead burned magnesites (Kimyongur 1984)

Mineral	Composition	Melting point °C
Periclase	MgO	2800
Forsterite	2MgO.SiO ₂	1900
Monticellite	CaO.MgO.SiO ₂	1502*
Merwinite	3CaO.MgO.2SiO ₂	1575*
Dicalcium silicate	2CaO.SiO ₂	2130
Tricalcium silicate	3CaO.SiO ₂	2070
Brownmillerite	4CaO.Al ₂ O ₃ .Fe ₂ O ₃	1410
Dicalcium ferrite	2CaO.Fe ₂ O ₃	1438*
Magnesioferrite	MgO.Fe ₂ O ₃	1713*
Magnesioaluminate	MgO.Al ₂ O ₃	2135
Tricalcium aluminate	3CaO.Al ₂ O ₃	1535*
Lime	CaO	2570
Tricalcium phosphate	3CaO.P ₂ O ₅	1800

* dissociation temperature (incongruently melting)

4.7.3.3 Bulk density, porosity and specific gravity

Bulk density (B), porosity (P) and specific gravity (T) of natural dead burned magnesites have been determined by using a modified version of the (ASTM C20-80a) procedure. Details are given in Chapter 6 and Appendix 11. The repetability of this method was tested by determination of ten separate portions of one magnesite sample. The results are presented in Table A11.1 (Appendix 11).

Table 4.24 Porosity (P), density (B) and specific gravity (T) values of natural dead burned magnesite (sample A3) determined at different temperatures.

Temp/time	P (%)	B	T
1600°C	6.87	3.55	3.71
1500°C	7.98	3.47	3.66
1400°C	11.64	3.33	3.64

4.7.3.4 Porosity and its distribution

Porosity in a refractory raw material should be very low and it should be present as closed, isolated pores. When the porosity is high and the pores are interconnected. Slag can easily migrate through the refractory, which shortens its serviceable use. In the dead burned magnesites studies, the pores are usually isolated at the periclase boundaries, but also within the crystals. The pore sizes vary considerably from a fraction of a micrometer up to approximately 100 microns (Plate 32d, f).

4.7.3.5 Degree of direct periclase - periclase bonding

Degree of direct bonding in the natural dead burned magnesites not only changes from one sample to another, but also within a single magnesia grain. At the particle boundaries where there are large amounts of interstitial phases, there is almost no direct contact between periclase crystals (Plate 19a). A similar condition exists when the matrix is locally concentrated (Plate 32a) or its overall

content in a particle is high.

Generally samples containing monticellite and forsterite as interstitial phases exhibits comparatively lower periclase - periclase grain contact (Plates 16h, 18a). With an increase in CaO/SiO₂ ratio of the silicate phase, the bonding, in general is found to increase. Higher degree of direct bonding have been observed when they contain comparatively lower amounts of matrix (Plate 15d). Generally in this case, the matrix is distributed and concentrated at the triple points (Plate 15g).

4.7.3.6 Hydration tendency

When a refractory raw material is insufficiently dead burned, or when it contains lime, it can easily hydrate when exposed to the atmosphere (Plate 29g, h). This can ultimately cause the refractory to disintegrate.

CHAPTER 5

CALCINATION PROPERTIES OF CRYPTOCRYSTALLINE MAGNESITE FROM IRAN

5.1 Introduction

Magnesium oxide (magnesia or periclase) is used in two forms by industry.

- a) As dead burned magnesia, which is made by calcining the Mg carbonate or hydroxide at high temperatures ($>1600^{\circ}\text{C}$) and is used as the major raw material for basic refractory manufacture.
- b) Caustic magnesia is a type of magnesium oxide (MgO) which can be obtained by decomposition of magnesium carbonate or magnesium hydroxide just above the temperature of thermal decomposition ($700 - 1200^{\circ}\text{C}$). In this case the products are more reactive and are suitable for variety of chemical and other applications.

There are many uses for caustic magnesia, the most important of which are the following:

1. building industry (for light weight boards and flooring)
2. fertilizer and animal feed preparation
3. paper processing
4. grinding wheels and discs manufacture
5. rubber, ceramic, glass, and resin industries
6. metallurgical and steel industries
7. petrochemical and pharmaceutical industries
8. waste water beneficiation

The major factors affecting caustic calcined magnesite usage are the quality of the raw material, the chemical activity and the bulk density (Chapter 2 gives more details about caustic calcined magnesite).

The main objective of this work is to examine the calcination characteristics of some natural cryptocrystalline magnesites from Iran by decomposing granular material over a range of temperatures and times in a laboratory furnace and establish the ideal industrial properties of these caustic calcined magnesias to compete with the available high quality commercial products.

5.2 Experimental

The experimental work has been carried out by calcining granular material for various temperatures of (500 - 1200°C) at 100°C intervals and times (1/4, 1/2, 1, 2, 4 and 8 hours), identifying the industrial properties, phase transformations and microstructure. The following tests were made for assessment of caustic magnesia quality:

1. X-ray diffraction - to determine phases present after calcination to establish the (TTT) diagram and to measure the mean crystallite size by X-ray diffraction line broadening.
2. Differential thermal analysis - to determine the decomposition temperature of magnesite.
3. Loss on ignition - for measurement of residual CO₂ content.
4. Scanning electron microscopy - for direct observation of

microstructure and crystal growth.

5. Surface area measurement by nitrogen adsorption using Strohlein Area-meter. II
6. Iodine adsorption number determination - an indirect measure of surface area by adsorption of iodine from carbon tetrachloride solution.

The important physical properties are crystallite size and surface area. These determine the reactivity of the magnesia; small crystallite size and large surface area being needed for high quality markets.

5.3 Sample characteristic and sample preparation for calcination

The caustic calcined investigation has been carried out on the natural cryptocrystalline magnesite samples collected from Torshak deposit, eastern Iran (see Chapter 3). The specimens chosen for this reason are T1, T3, T4, T8, T16, T19 and T23 which are closely similar in bulk composition. These samples were mixed and crushed together to provide sufficient mass of material and to give a product representative of the deposit before the experimental work started. The bulk chemical analyses of these samples are given in chapter 3, Table 3.1. The major impurities present in these samples are: CaO: 0.80-1.96%, SiO₂: 0.12-0.77%, Fe₂O₃: <0.05%, and Al₂O₃: 0.01-0.22%.

The materials were crushed into sizes between 2.0-5.0 mm which is similar to those used in commercial calcination conditions. 30g of crushed samples were weighed and calcined

at different temperatures from 500°C to 1200°C for times ranging from 15 minutes up to 8 hours. A muffle furnace was used for the calcination and in all experiments the material was placed in the furnace when the required temperature was stable. The calcined specimens were air quenched after the calcination just for a short while, then samples were kept in a vacuum desiccator at all times to prevent any possibility of hydration.

5.4 Decomposition of magnesite

The differential thermal analysis (DTA) of the cryptocrystalline magnesite as determined with 8°C/min heating rate is given in Figure 5.1. The endothermic peak of the magnesite is at 594°C. The endothermic decomposition starts at approximately 340°C and is almost complete at 620°C. The greatest decomposition takes place between approximately 550°C and 600°C. The values found for the endothermic decomposition are lower than published data (Webb and Heystek, 1957) which are 660-710°C.

5.5 X-ray diffraction

X-ray diffraction has been used for two purposes in this study to determine:

- a) The transformation of magnesite to periclase.
- b) The crystallite size of periclase.

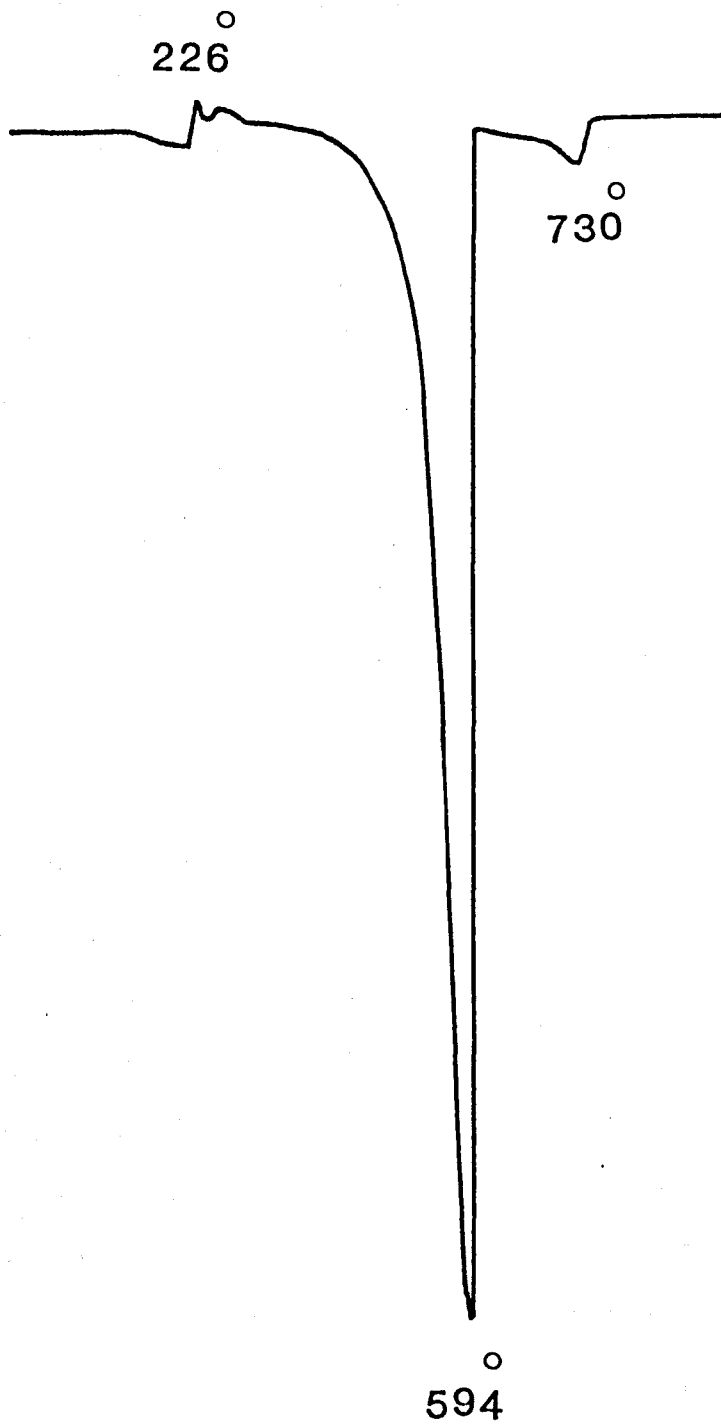


Figure 5.1 The DTA curve of magnesite

5.5.1 Phase transformation of magnesite (MgCO_3) to periclase (MgO)

The caustic calcined magnesite specimens were ground to a suitable size ($<40\mu\text{m}$), using an agate pestle and mortar. A cavity mount of the specimen was then prepared and the analyses were carried out with a Philips PW 1050 X-ray diffractometer using Ni-filtered Cu radiation at 40 Kv and 40 mA. Operation conditions are as follows:

count rate	4×10^2 cps
time constant	4 second
scanning range	30-80 degrees
scanning rate	$1/2^\circ$ $2\theta/\text{min}$
chart speed	10 mm/min

For some samples it was necessary to change the count rate to 2×10^3 cps.

The presence and absence of magnesite and periclase in different patterns were determined to establish the time - temperature - transformation diagram of caustic calcined magnesite (Figure 5.2).

The time - temperature - transformation of magnesite to periclase is distinguished by a narrow zone between two curves where both magnesite and periclase phases are found. Curve (A) represents the initiation of the reaction, periclase appearing in X-ray diffraction traces above this line, and the curve (B) shows the time and temperature at which the transformation of magnesite to periclase is complete. Magnesite is absent above this curve which

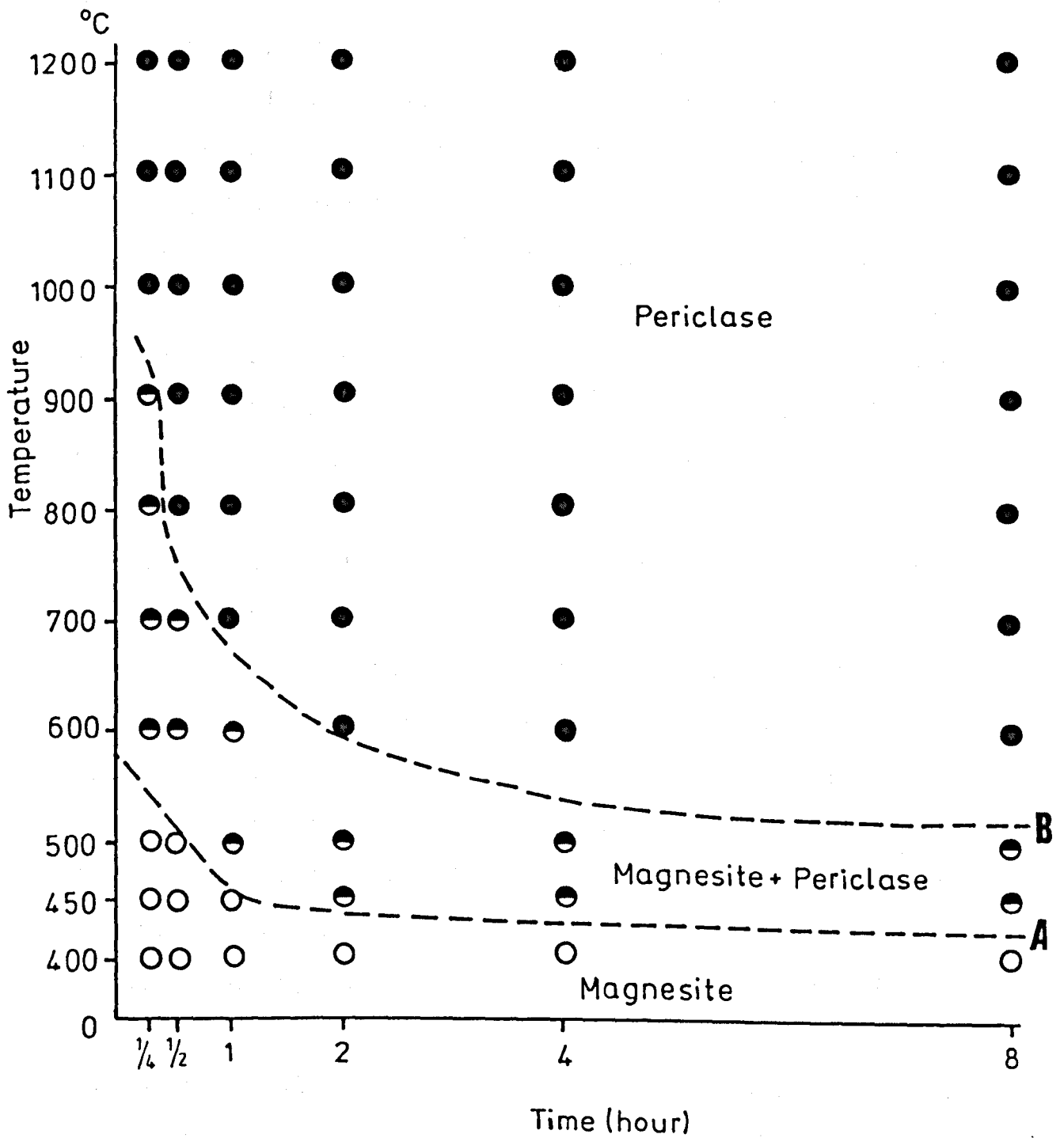


Figure 5.2 The Time-Temperature-Transformation (TTT) diagram of magnesite

corresponds to a loss on ignition of around 5% residual CO₂. The area between these two curves represents the transitional stage where both magnesite and periclase are present. As it can be seen from the (TTT) diagram at the lower calcination temperatures the phase transformation is taking place slowly and longer calcination times are required for complete transformation, for example at 600°C the transformation starts at less than 15 minutes and around two hours is required for almost complete decomposition. At 800°C the phase transformation is completed in less than 30 minutes, but at 500°C more than 8 hours are required.

5.5.2 Mean crystallite size determination by X-ray powder diffractometry

The basis for the determination of crystallite size using X-ray powder diffraction is a phenomenon termed "Diffraction Broadening". Two sets of factors contribute to the degree of diffraction broadening;

1. Pure diffraction broadening effects; these are caused by the physical nature of the crystallites namely crystallite size and crystal imperfections such as strain and twinning.
2. Instrumental broadening; this is due to such factors as non-surface planarity of the sample, slight polychromicity of the X-ray beam and the separation of K-alpha and K-beta radiation, although the latter is important only at high angles of 2θ .

These two sets of factors combine to produce a peak of finite breadth (B) which is a function of these factors, as opposed to the line which the Bragg equation would generate. The degree of Diffraction Broadening is inversely proportional to the crystallite size, as the deviation from the Bragg condition for reflection, i.e. the degree of scatter increases for decreasing crystallite size. (Klug and Alexander, 1974). The above two sets of factors are related to the mean crystallite size of the sample by the Scherrer equation;

$$D = \frac{K\lambda}{\beta \cos\theta} \quad \text{Where } \beta = \sqrt{B^2 - b^2}$$

D = Mean crystallite size in Angstrom

λ = wavelength of radiation (CuK-beta = 1.3922 Å)

β = Pure Diffraction Broadening

b = Instrumental Broadening

B = Total Difference Breadth

θ = Diffraction angle in degree 2 theta converted to radians

K = Crystallite shape constant - this is a function of the linear dimension of the crystal under analysis.

In this experiment a value of K = 0.9 was chosen. Measurement of the line breadth (β) is taken at half the peak height.

A quartz standard assumed to be strain free and a narrow size distribution (1-10 microns) was used to determine the instrumental broadening (b) of the machine at half the peak height above the background (Kimyongur, 1984). (details are

given in Appendix 3). Calculation of the mean crystallite size necessitated the use of the "low angle reflection curve" after Klug and Alexander (1974) illustrated in Appendix 3, Figure A3.1, which give the relationship between b/B and β/B for low angle reflections and enables the pure diffraction breadth to be determined.

The tabulated results for the mean crystallite sizes (CS) of the Caustic calcined magnesite are given in Table 5.1.

The periclase crystallite size as plotted against time and contoured on a time - temperature graph are given in Figure 5.3a and b. As the calcination temperature and time increase, larger periclase crystals develop and as it can be seen from the Figure 5.3a and b the crystallite size increases comparatively sharply at temperatures higher than 1100°C for larger calcination times, but at temperatures between 600°C and 1000°C the increase in the crystallite size with the time is small.

5.6 Loss on ignition

The loss on ignition (LOI) is the amount of volatile constituents in a sample. The LOI of the caustic calcined magnesite in the temperature range of 500-1000°C is determined by grinding the granular specimens and igniting them in a muffle furnace at 1000°C for two hours. The LOI can be calculated as follows:

Table 5.1 The surface area (SA)^{m²/g}, iodine adsorption number (IN)^{m²/g}, loss on ignition (LOI)[%] and crystallite size (CS)^Å of the calcined magnesite in the temperature range 500-1200°C and time range 1/4 - 8 hours.

TEMP	500	500	500	500	500	500	600	600	600	600
TIME	0.25	0.5	1	2	4	8	0.25	0.5	1	2
SA	2.87	3.28	5.36	9.45	11.49	23.09	3.46	7.14	31.20	93.07
IN	3.16	4.72	7.74	9.24	15.63	34.88	1.55	6.31	53.90	106.79
LOI	51.13	50.34	48.07	47.00	37.27	27.75	49.11	42.03	27.60	6.94
CS	n.d.	n.d.	216.00							
TEMP	600	600	700	700	700	700	700	700	800	800
TIME	4	8	0.25	0.5	1	2	4	8	0.25	0.5
SA	77.36	63.99	25.90	64.78	57.20	47.34	40.17	35.72	66.11	65.02
IN	81.33	75.31	26.44	87.78	78.36	70.29	68.50	65.04	75.39	97.87
LOI	4.61	2.45	37.91	15.41	2.65	1.28	1.07	0.92	15.44	1.64
CS	233.00	247.00	n.d.	n.d.	236.00	276.00	326.00	339.00	189.00	262.00
TEMP	800	800	800	800	900	900	900	900	900	900
TIME	1	2	4	8	0.25	0.5	1	2	4	8
SA	44.53	43.50	35.04	30.47	63.41	41.89	33.03	29.40	27.67	27.37
IN	80.10	67.07	59.12	58.40	65.32	60.95	59.03	58.40	56.50	52.40
LOI	0.84	0.60	0.57	0.38	5.30	1.70	1.52	1.09	1.02	0.90
CS	335.00	376.00	427.00	542.00	245.00	352.00	506.00	546.00	682.00	708.00
TEMP	1000	1000	1000	1000	1000	1000	1100	1100	1100	1100
TIME	0.25	0.5	1	2	4	8	0.25	0.5	1	2
SA	30.38	29.42	20.09	15.62	14.40	15.91	28.79	28.91	13.76	15.30
IN	57.71	58.52	42.62	38.69	23.44	22.10	37.69	36.30	19.92	20.52
LOI	1.26	1.08	1.06	0.67	0.41	0.27	n.d.	n.d.	n.d.	n.d.
CS	533.00	580.00	782.00	848.00	994.00	1094.00	647.00	645.00	912.00	1044.00
TEMP	1100	1100	1200	1200	1200	1200	1200	1200		
TIME	4	8	0.25	0.5	1	2	4	8		
SA	9.26	4.44	15.77	10.90	3.78	3.38	1.59	1.58		
IN	9.06	3.10	15.04	13.73	5.93	1.48	0.85	0.37		
LOI	0.00	n.d.								
CS	1529.00	1611.00	1178.00	1568.00	1945.00	2494.00	2694.00	3052.00		

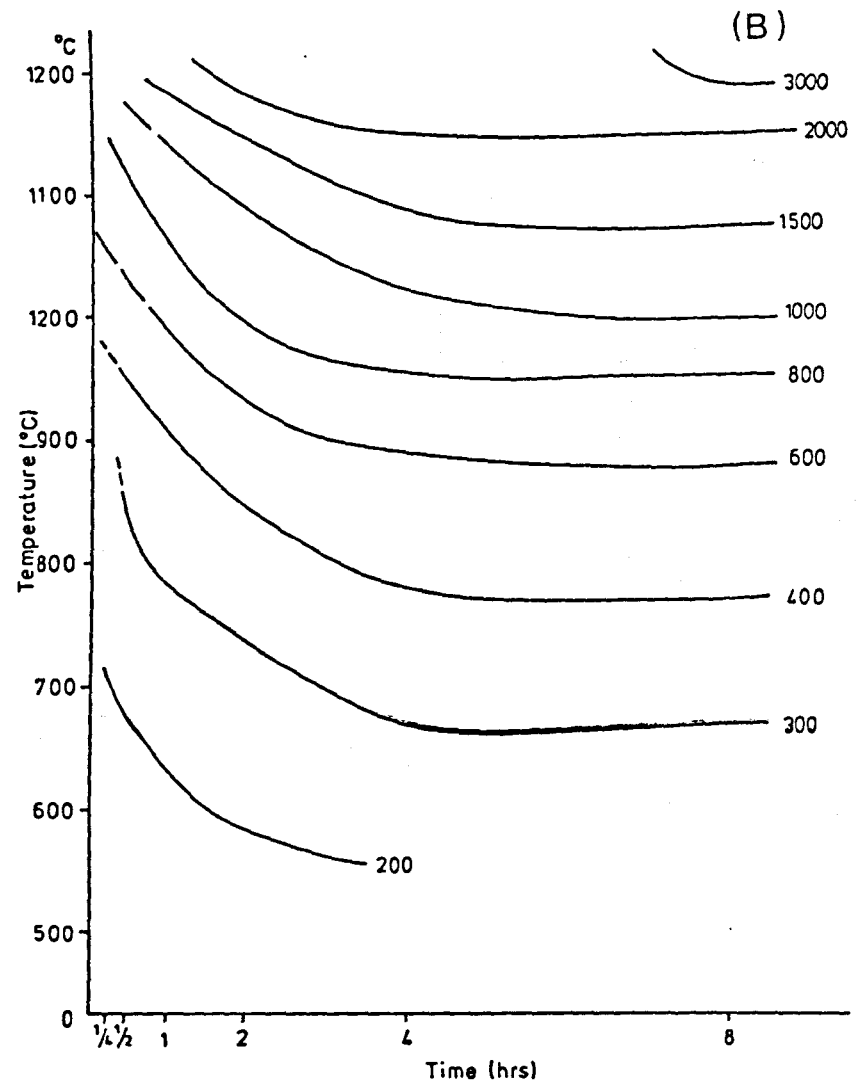
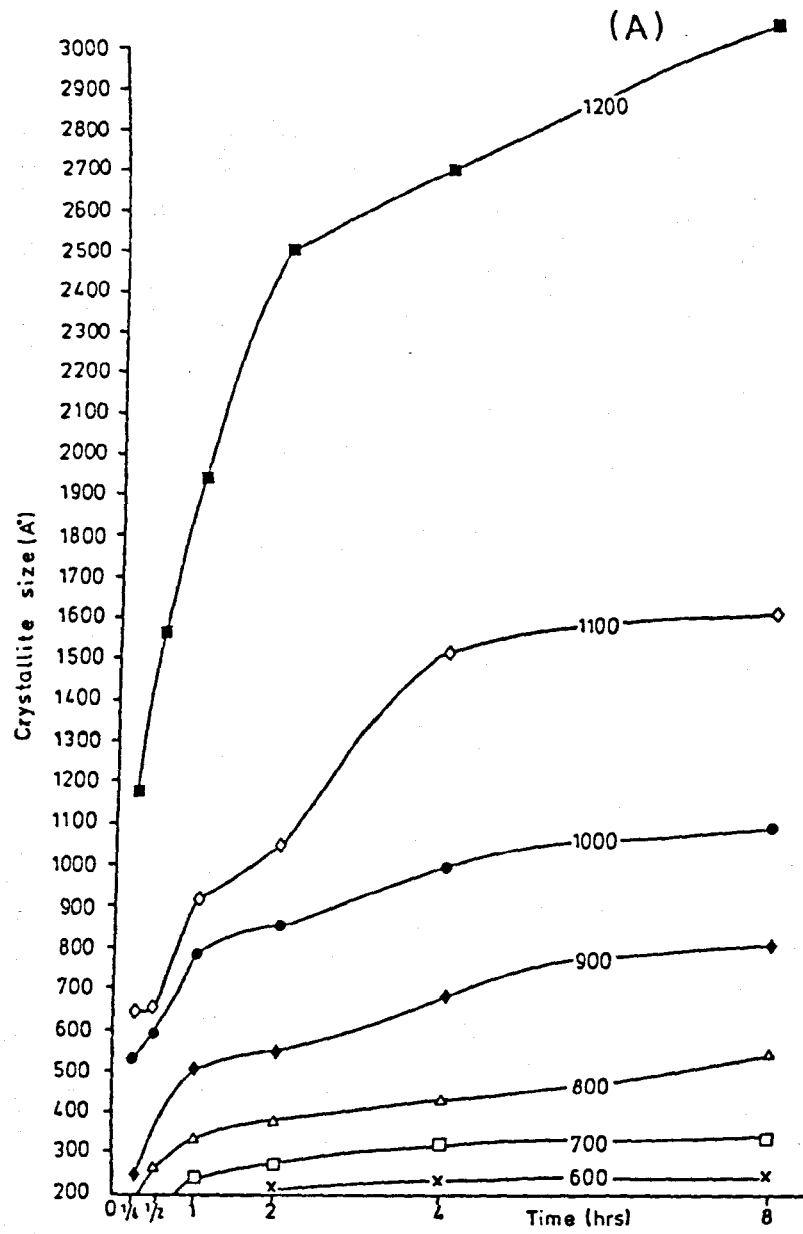


Figure 5.3 Crystallite size (CS) (A) as plotted against
A) Time
B) Time-Temperature (contour)

$$\text{LOI (\%)} = \frac{W_1 - W_2}{W_1} \times 100$$

Where:

W1 : Weight of the calcined specimen before ignition

W2 : Weight of sample after ignition at 1000°C

5.6.1 Method of measurement

The LOI was determined using the procedure given in Appendix 8. Measurement were made on duplicate samples for comparison.

5.6.2 Results

Results of LOI measurements of caustic calcined magnesites from Iran are given in Table 5.1.

The loss on ignition values are plotted against time and contoured on a time - temperature graph in Figure 5.4a and b respectively.

The LOI decreases as the calcination temperature and time increase. The LOI values are very high at 500°C for all of the calcination times and decrease gradually with increasing time. At temperatures of 600°C, 700°C and 800°C the loss on ignition decreases rapidly at short calcination times, i.e. for 600°C between 1/4 and 2 hours, for 700°C between 1/4 and 1 hour, and at 800°C between 1/4 and 1/2 hour (Figure 5.4a).

The loss on ignition values are less variable with different times at 900°C and almost constant at 1000°C for all the calcination times.

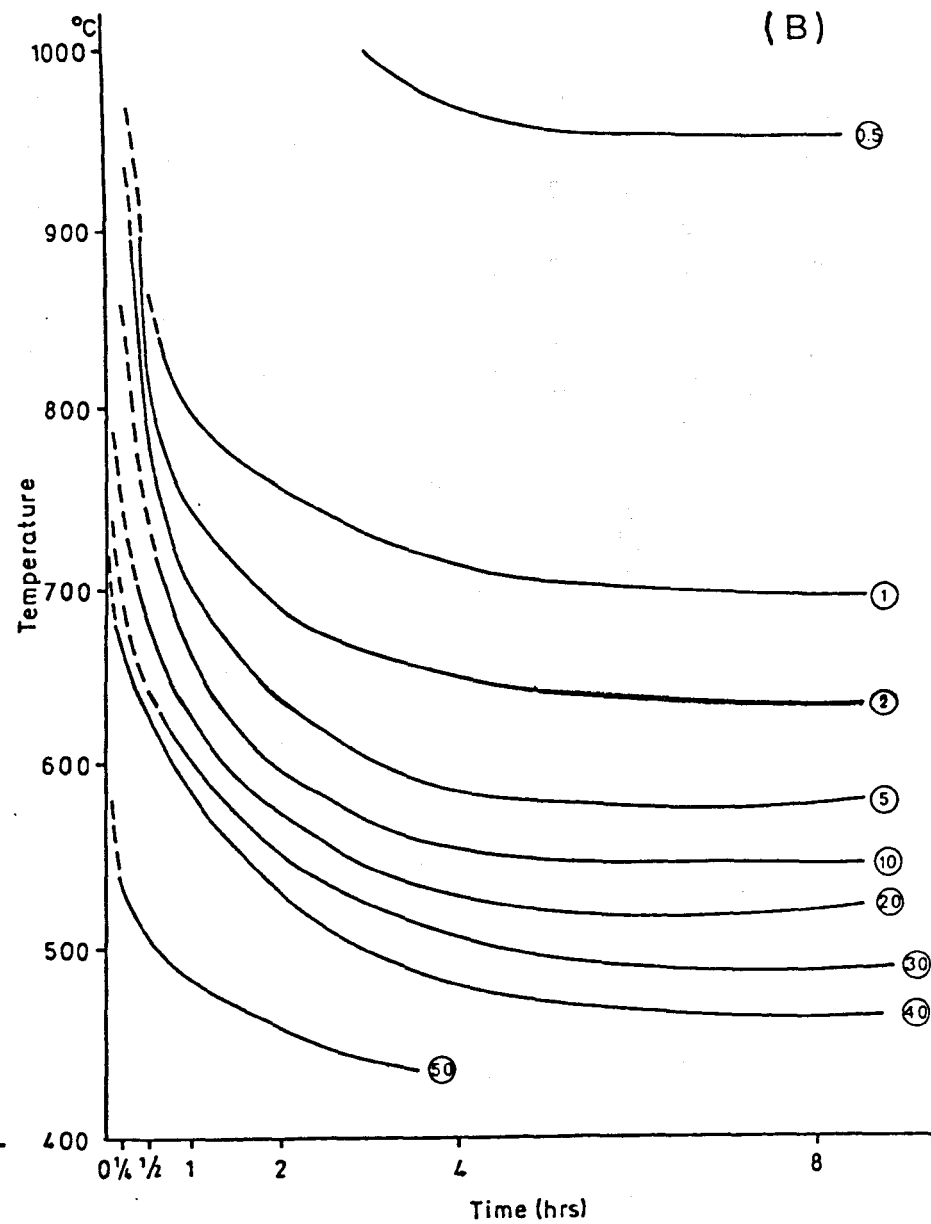
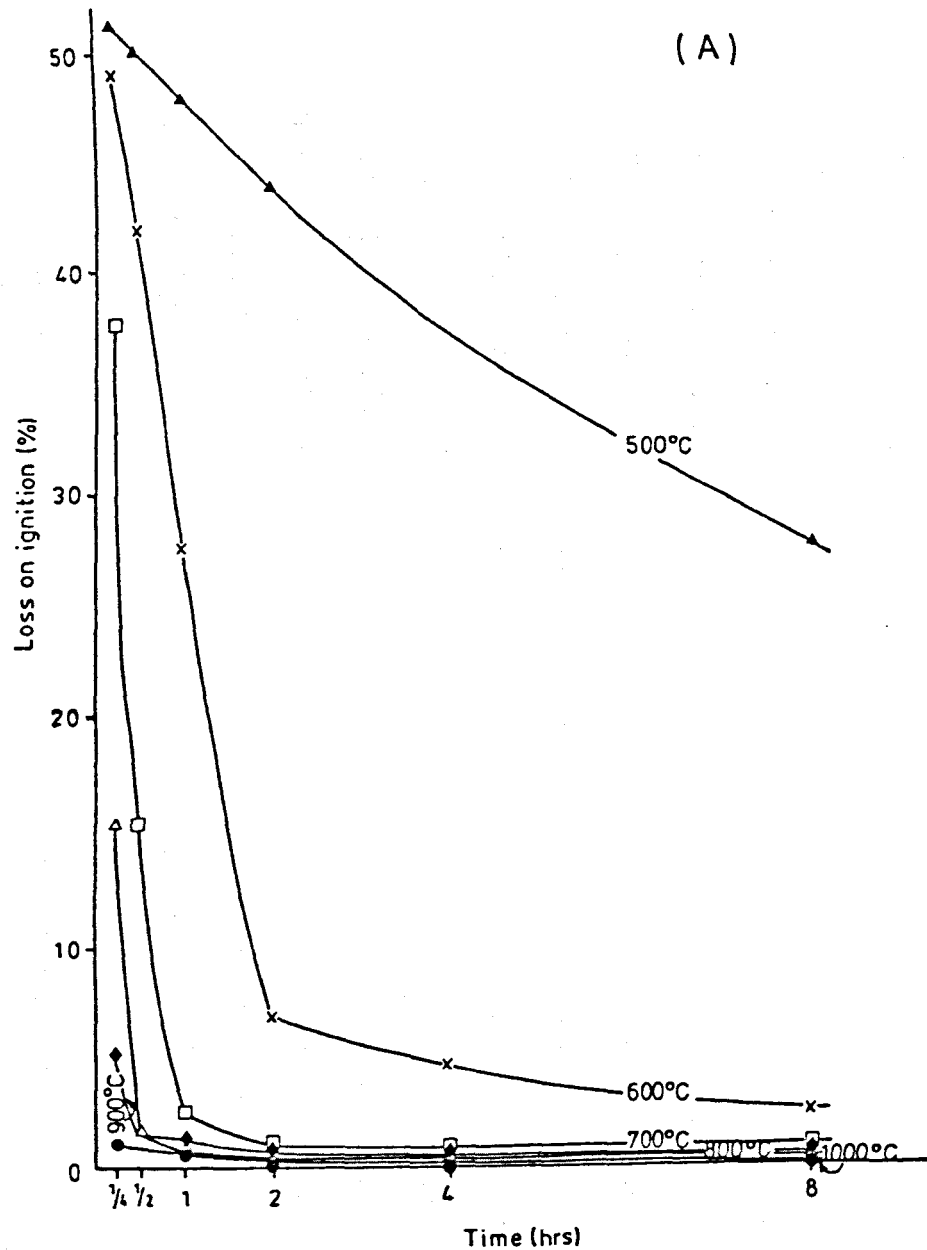


Figure 5.4 Loss on ignition (LOI) (%) as plotted against

A) Time
B) Time-Temperature (contour)

When the LOI values are plotted on the (TTT) diagram (Figure 5.4b), the contours are parallel to the time - temperature - transformation (TTT) curve (Figures 5.2).

The main source of errors in measurement of LOI is difficulty during stabilization and weighing samples which results in the hydration of calcined material particularly for the specimens with high surface area and iodine adsorption number, which are highly reactive.

5.7 Surface area

One of the most significant physical properties of periclase obtained from caustic calcined magnesite is its surface area. The higher the surface area, the greater the rate of reaction (e.g. hydration). This property is precisely related to the porosity and time and temperature of calcination

Under ideal conditions of calcination due to release of carbon dioxide, a high surface area can be developed in a porous periclase. As it can be seen in Figure 5.5a, b and Table 5.1) with increasing the temperature of burning, the crystallite size becomes larger, and as a result the internal pores becomes smaller and a dense product with low surface area will result. Increasing the calcination conditions to a higher temperatures for a longer times causes grain growth with effective decrease in surface area and loss in reactivity.

Determination of surface area has been made using a Strohlein "Areometer II". This uses a single point

determination based on the recognised BET method. The principal of the method is to determine the amount of nitrogen needed to form a monomolecular layer on the surface of sample by adsorption at the temperature of -195°C , which is the boiling point of liquid nitrogen at atmospheric pressure. This amount of nitrogen can be read from a differential manometer.

The area occupied by the nitrogen molecule in the adsorbed condition is generally assumed to be that derived from the density of liquid nitrogen; that is, each molecule of nitrogen is assumed to occupy the volume it would occupy in the liquid state. The pressure difference obtained for a certain amount of sample and known barometric pressure is measured and the surface area can be calculated by using a nomogram.

Full details about the procedure used to determine the specific surface area are given in Appendix 9.

5.7.1 Results

The surface area (SA) values are presented in Table 5.1. The surface area values are plotted against time, and are contoured on a time - temperature graph. These graphs are presented in Figure 5.5a and b.

For lower calcination temperature such as 600°C and 700°C , the surface area goes through a maximum and after this time the surface area values start to decrease with increasing the time. There is no maximum peak recognised at 500°C probably because of insufficient calcination time

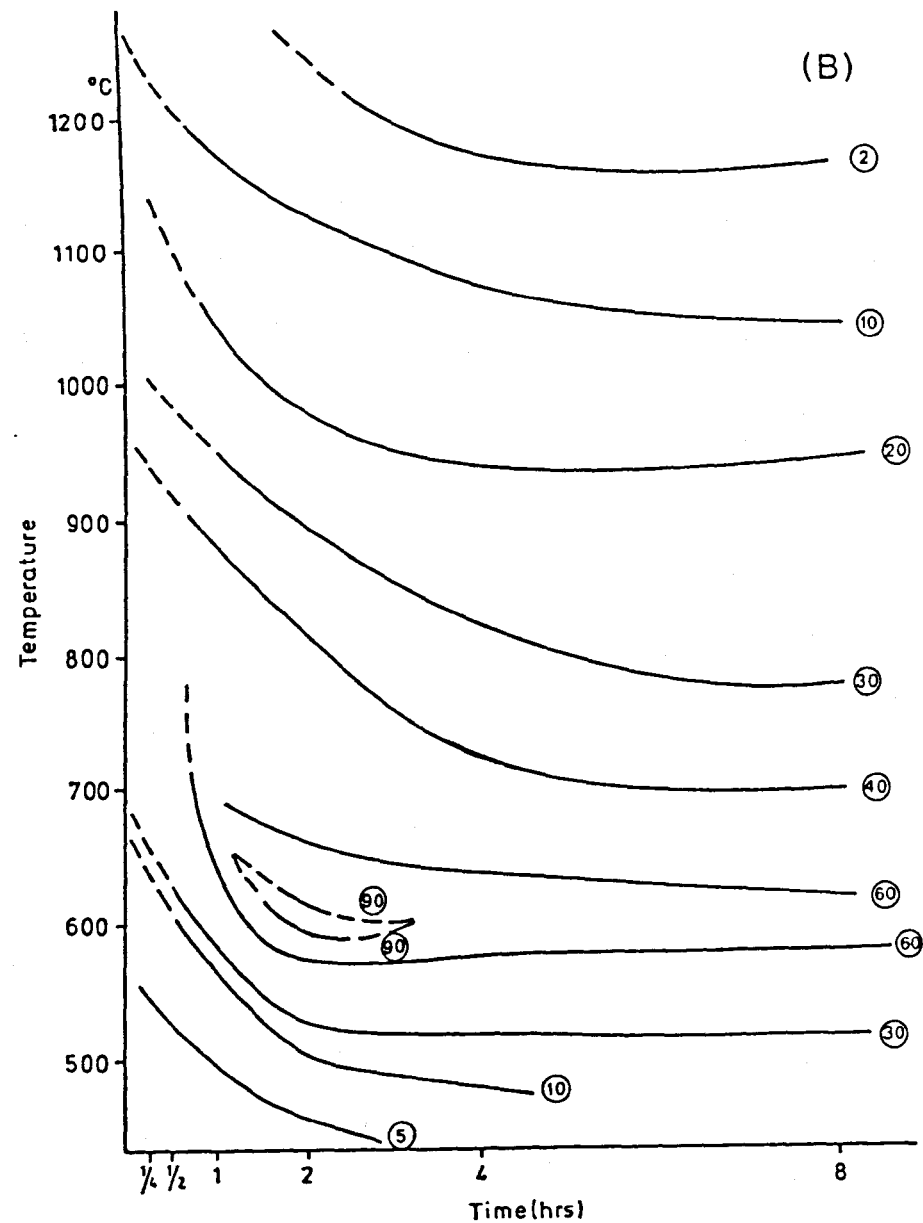
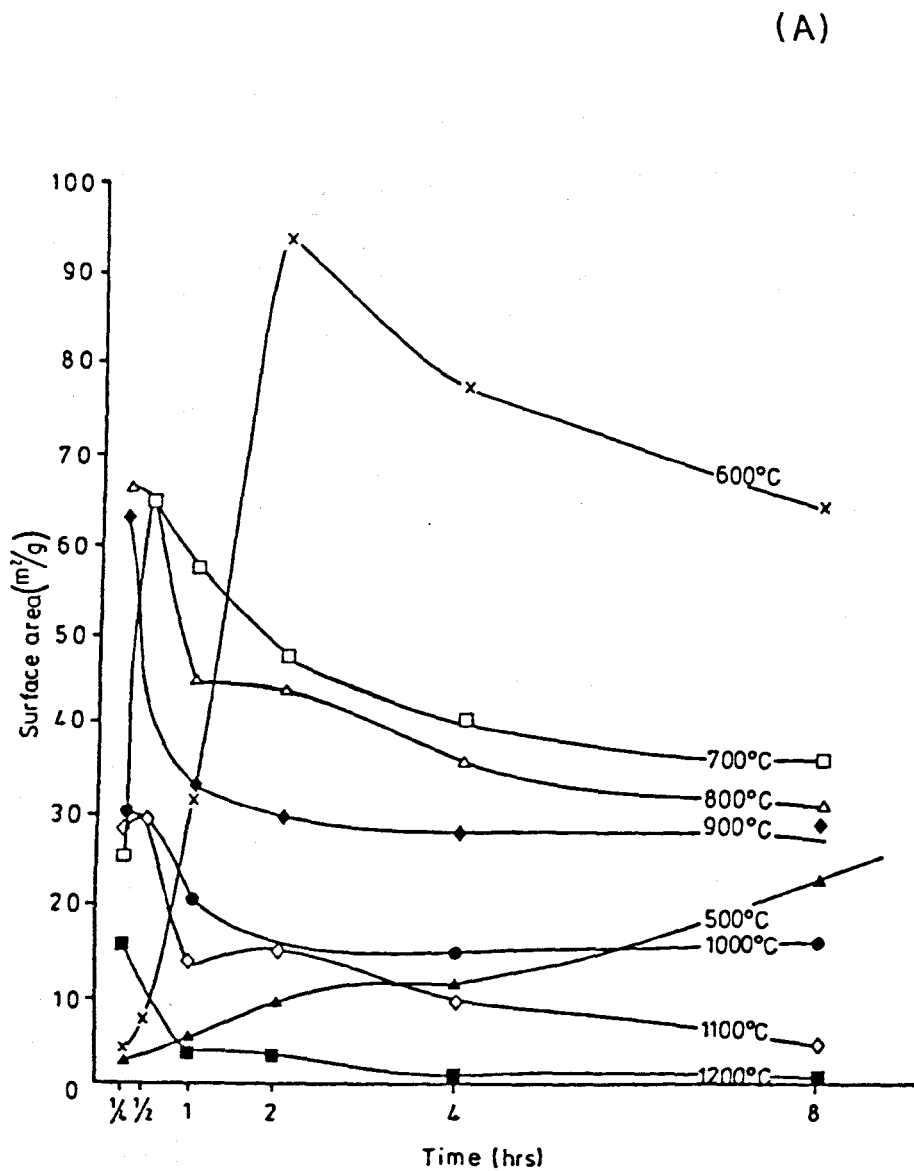


Figure 5.5 Surface area (SA) (m^2/g) as plotted against

A) Time
B) Time-Temperature (Contour)

(maximum 8 hours in this study).

The highest value of surface area is obtained for a sample calcined at 600°C for two hours time (93.07 m²/g), but this corresponds to a high residual loss on ignition of 5-10%.

The surface area changes rapidly with different times for the temperatures between 500°C to 900°C, but for temperatures higher than 1000°C, the surface area values show only small differences with various calcination times.

When the surface area values are plotted against time - temperature (Figure 5.5b), the contours are nearly parallel to those on the time - temperature - transformation diagram (Figure 5.2). There is a closed area with surface area >100 m²/g around 600°C and 2 hours calcination.

5.8 Determination of iodine adsorption number

The iodine adsorption number values of caustic calcined magnesites have been determined as in British Standard 4398 (1969). The iodine number is the amount of iodine in milligrams adsorbed per gram of periclase (MgO).

The principal of the method is to mix thoroughly a known portion of sample (2g) with a measured volume (100 ml) of iodine solution, using a mechanical shaker. Then the mixture is centrifuged and a measured volume of iodine solution is titrated with a standard solution of sodium thiosulphate, until a colourless solution appears. By reading the titration value for known weight of sample, the iodine adsorption number can be calculated.

Full details about the procedure used to determine the iodine number are given in Appendix 10.

5.8.1 Results

The tabulated results of iodine adsorption number (IN) of caustic calcined magnesite are given in Table 5.1. The iodine adsorption values have been plotted against time and contoured on a time - temperature graph, (Figure 5.6a, b) The iodine number curves and contours are similar in shape to the surface area measurements. However, the errors in this method is higher than the surface area measurement.

For lower calcination temperatures such as 600-900°C, the iodine number values goes through a maximum and after this time the iodine adsorption numbers start to decrease with increasing the time. At 500°C there is no maximum peak recognised, because of shortage of calcination time (Max. 8 hours in this study).

The greatest value of iodine adsorption number at 500°C of calcination is probably after calcination time of greater than 8 hours.

The highest iodine number is found at 600°C and two hours calcination time (106.79 mg/g) and a closed contour showing a maximum can be drawn around this point. The iodine adsorption values varies considerably for different calcination temperatures between 500°C to 800°C. But for temperatures higher than 900°C the iodine adsorption values comparatively show smaller differences with various calcination times.

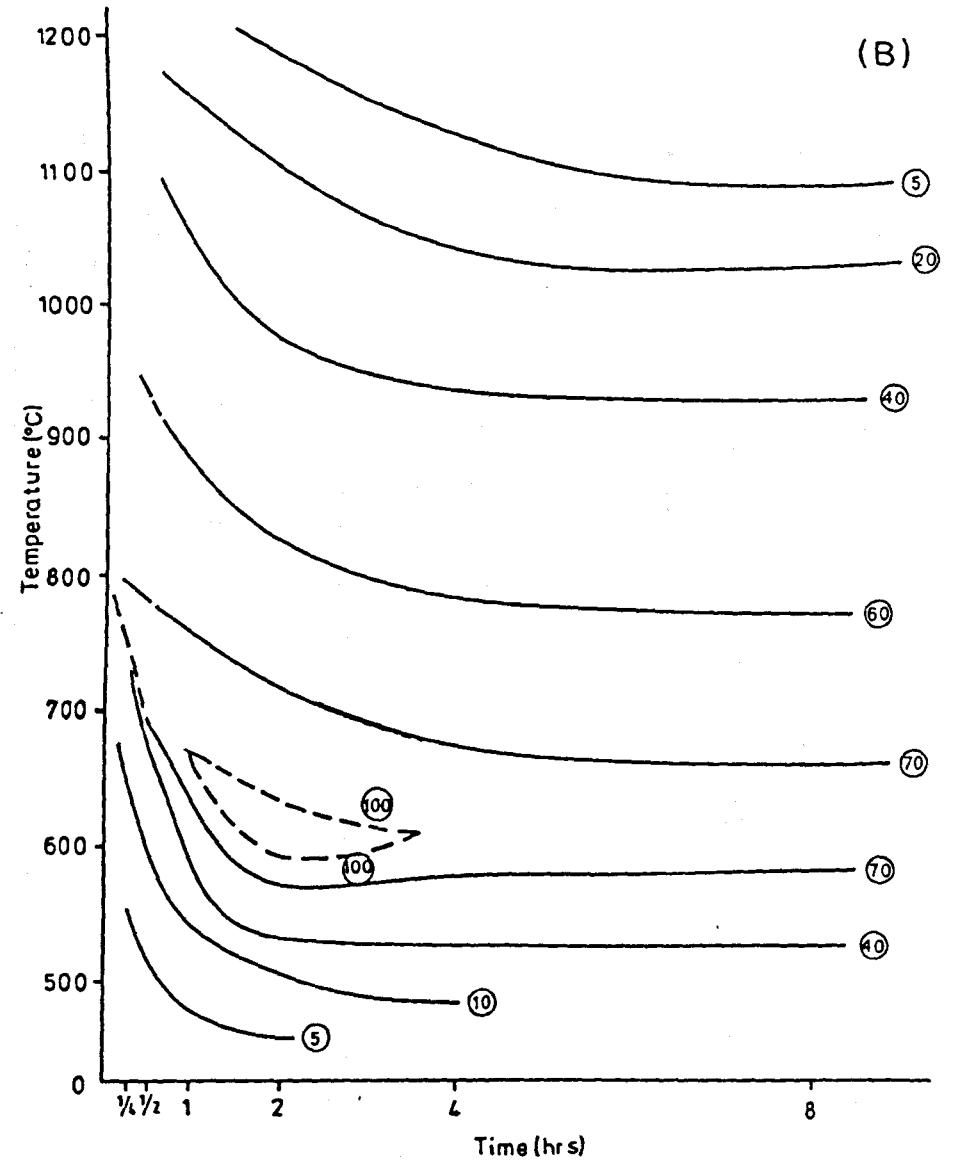
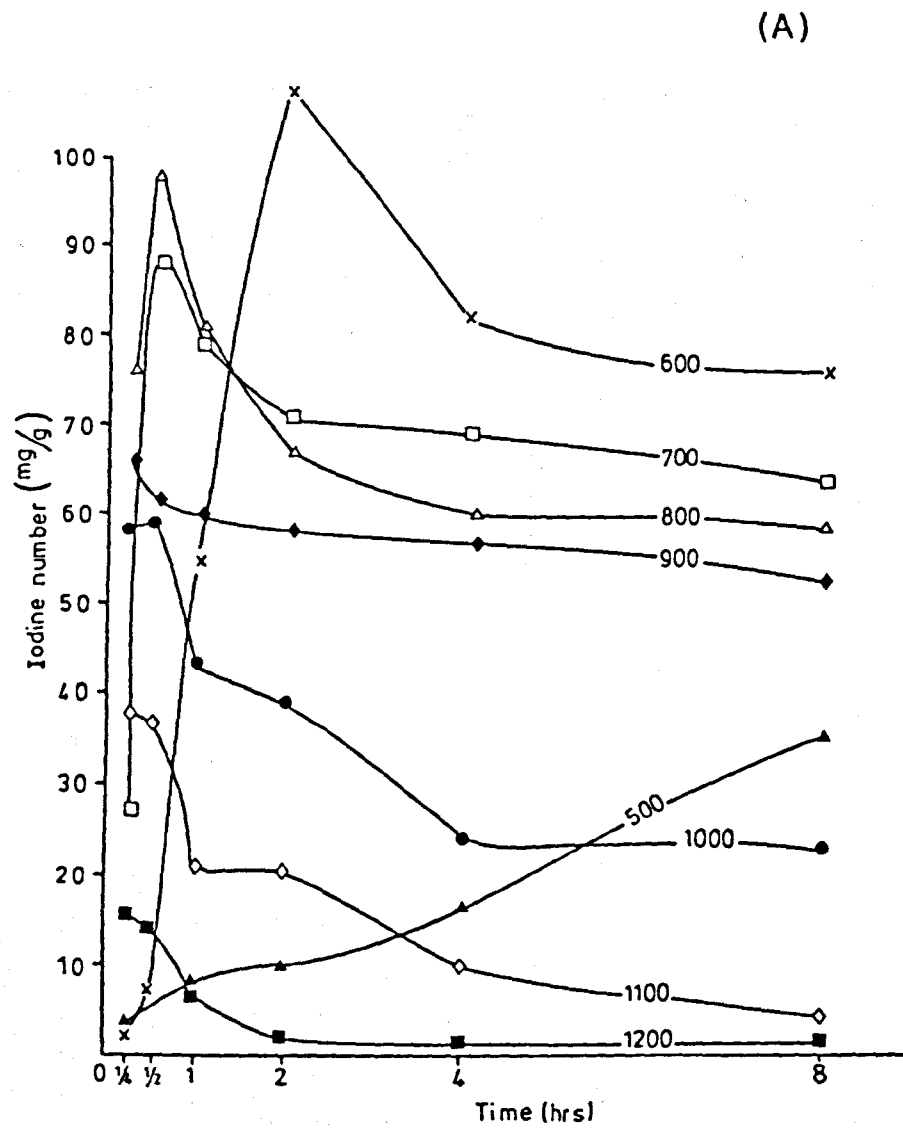


Figure 5.6 Iodine adsorption number (IN) (mg/g) as plotted against

A) Time
B) Time-Temperature (contour)

As mentioned before, at higher temperatures and times of calcination, the amount of surface area decreases, which will decrease the volume of iodine adsorbed per gram of sample (Figure 5.6b and 5.2).

5.9 Microstructure

The microstructural study of caustic calcined magnesites have been carried out by using a Cambridge Scanning Electron Microscope (SEM 360). Plate 33 is a selection of electron micrographs of caustic calcined magnesites which clearly show the transformation of magnesite to periclase at different calcination temperatures of 500 - 1200°C for various calcination temperatures of 1/4 - 8 hours.

Perfectly shaped magnesite crystals are visible at lower calcination conditions e.g. at 500°C, for 1/4 hour (Plate 33a).

As the calcination temperature and time increases, the magnesite crystals first start losing their perfect rhombohedral shape and slowly transfer to cubic periclase crystals. The remaining pseudorhombohedral shape of magnesite crystals were recognised up to 700°C (Plate 33f).

As the time - temperature - transformation (TTT) study by XRD also indicates, a mixture of magnesite and periclase grains remain in material calcined up to 800°C for 1/4 hour, but at higher temperatures or for longer calcination times pseudorhombohedral magnesite crystals completely disappear and periclase crystals start to develop (Plate 33g). At 1200°C, the sintering of magnesia grains are perfectly clear.

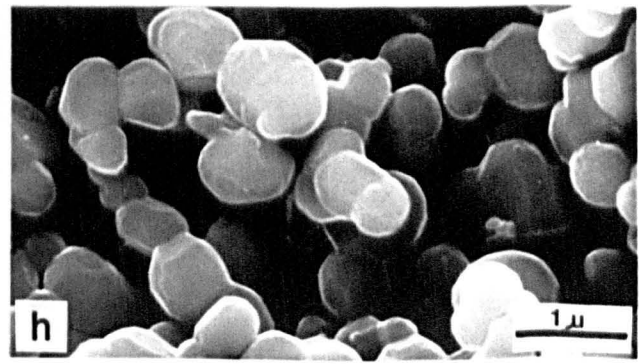
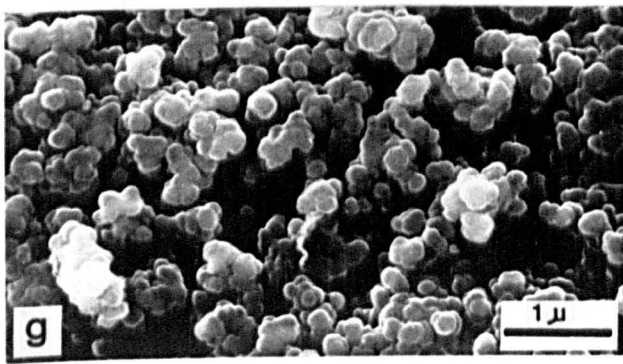
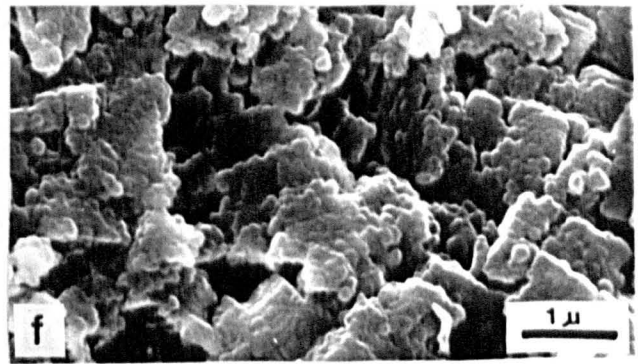
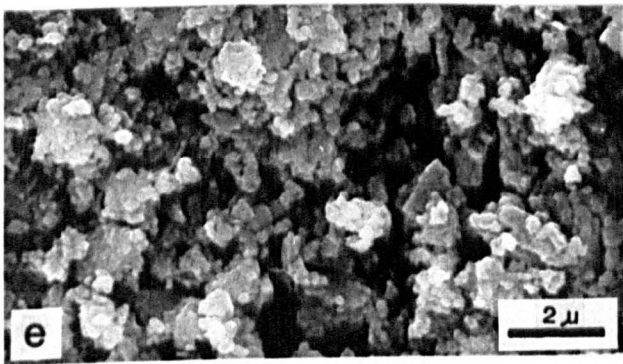
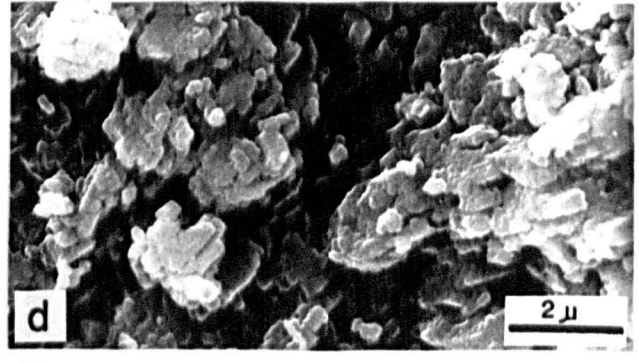
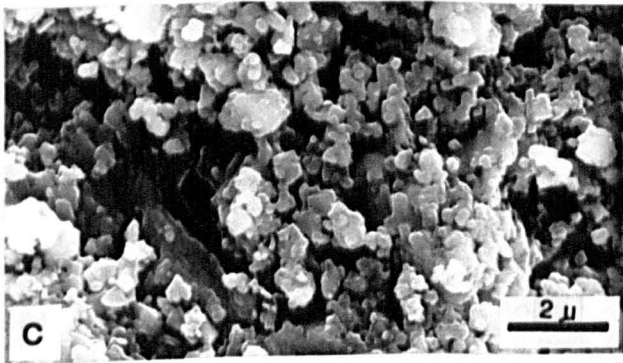
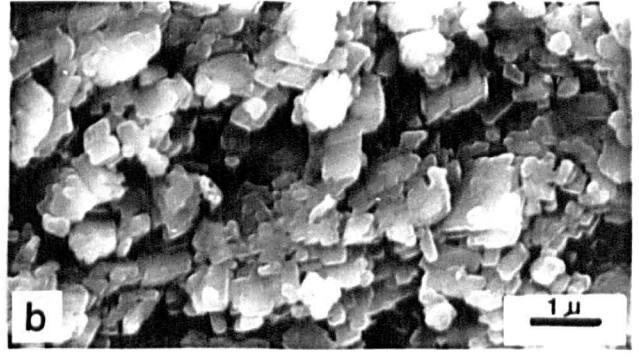
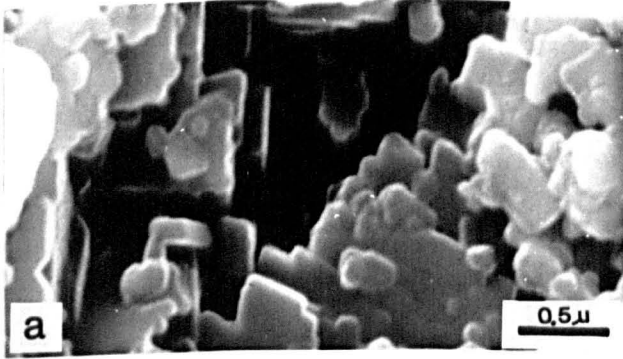
Magnesia crystals (cubic) around half a micron in size which is in close agreement with the study of X-ray line broadening have been recognised at 1200°C and 8 hours calcination (plate 33h).

PLATE 33

Scanning electron micrographs of the surface of caustic calcined magnesite calcined at different temperatures of 500 - 1200°C at 100°C intervals for different period of times (15 and 30 mins., 1, 2, 4 and 8 hours).

- a) This sample calcined at 500°C for 0.25 hour, which is not sufficient to change much of the magnesite to periclase. Unchanged rhombohedral magnesite grains are visible.
- b) Combination of magnesite and periclase grains (most of grains are magnesite) (500°C, 1 hour).
- c) Similar to b, Combination of magnesite and periclase calcined at 600°C for 15 minutes.
- d) Very small rounded periclase grains start to develop, but still the magnesite structure is visible (600°C, 8 hrs).
- e) Mixture of periclase and magnesite, the little rounded grains are periclase, but the rhombohedral shape grains are remaining magnesites (700°C, 30 mins).
- f) Small periclase grains in aggregates which resemble rhombohedral magnesite (700°C, 2 hrs).
- g) Mostly small rounded periclase grains (900°C, 15 mins).
- h) The periclase crystals have grown considerably compared with the other temperatures (1200°C, 8 hrs).

PLATE 33



5.10 Relationship of determined industrial properties

The relationship between determined industrial properties of caustic calcined magnesites such as surface area (SA), iodine adsorption number (IN), loss on ignition (LOI) and crystallite size (CS) are given in Figure 5.7

The surface area and iodine adsorption number values show a linear relationship (Figure 5.7a). The surface area values display an inverse relationship with higher values of loss on ignition (line 1- increase of surface area due to loss of CO_2 from magnesite). There is a direct relationship between surface area with the lower values of loss on ignition (line 2- decrease of surface area due to crystal growth and loss of CO_2) (Figure 5.7b).

Figure 5.7c exhibits the relationship between surface area and crystallite size. Surface area gradually decreases with increase in crystallite values.

The relationship between iodine number with loss on ignition and crystallite size are similar with those between surface area with loss on ignition and crystallite size as it can be seen from Figure 5.7d and e.

Crystallite size and loss on ignition show high loss of ignition values at very small crystallite sizes (Figure 5.7f).

The variation of surface area and iodine adsorption with calcination temperature and time can be explained by reference to the time - temperature - transformation curve and loss on ignition. In general, there is a good agreement

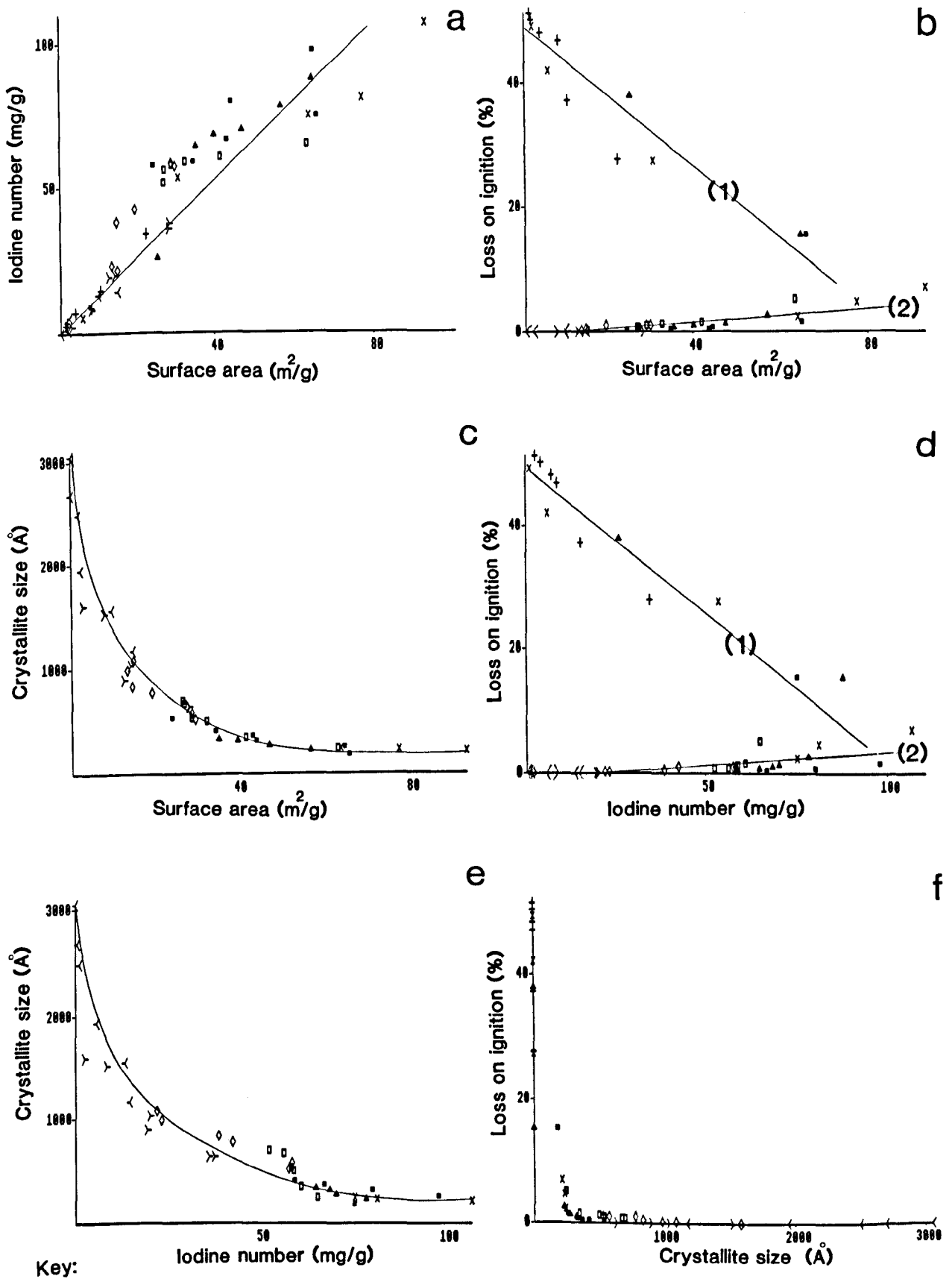


Figure 5.7 Relationship between the determined parameters

between the observed phase transformation and the loss on ignition (Figure 5.2 and 5.4).

The highest values of surface area and iodine number are obtained when the decomposition of magnesite is just complete. Relatively high values for surface area and iodine adsorption number are also found at intermediate decomposition, i.e. when magnesite and periclase are present together, which is the area bounded by the two curves. The starting and complete transformation curves in Figure 5.2 (the area shown as "periclase + magnesite"). In the fields of magnesite and periclase in Figure 5.2, the values of surface area and iodine adsorption number are lower. Hence an increase in surface area and iodine number with rising time at a certain temperature, corresponds to an increase in the decomposition of magnesite, up to complete dissociation. This can be seen in Figures 5.7b and d line 1. The decrease in surface area and iodine number with rising time and a fixed temperature is due to complete dissociation and an increase in densification which is accompanied by an increase in crystallite size. Line 2 in Figure 5.7b and d which show a decrease of surface area and iodine number with a decrease in loss on ignition corresponds to the decomposition stage, i.e. following complete dissociation (the field "periclase" in Figure 5.2).

The densification is very clear at 1200°C and for periods of calcination larger than 2 hours, where there is a sudden decrease in surface area and iodine number and sharp rise in crystallite size (Figure 5.3).

5.11 Assessment of industrial properties

Assessment of the Iranian natural magnesite for the production of caustic calcined magnesia has been made by comparing the industrial properties with the existing commercial products.

A comparison of the bulk chemical composition of material under study with the existing available products suggests that the studied materials are very pure, for example, Table 5.2 compare the impurities of studied natural magnesites from Iran, with those of commercial produced synthetic caustic magnesias by Steetley Mineral Ltd. The results indicate the purity of the Iranian natural magnesites.

Table 5.2 Comparison of impurities of studied samples with those of commercial products

Oxides	(Steetley Minerals Ltd)	(Studied samples)
CaO:	0.7-2.6%	1.37%
SiO ₂	0.5-1.0%	0.35%
Fe ₂ O ₃	0.1-1.4%	0.02%
Al ₂ O ₃	0.1-0.6%	0.08%

(Steetley Minerals information sheets referred to by Kimyongur and Scott 1986).

The industrial properties of the magnesia made from Spanish natural magnesite and synthetic caustic magnesias are given in Table 5.3 (Kimyongur and Scott 1986). Table 5.4 presents the industrial properties of materials under this study.

The best quality calcined magnesite with reasonably low loss on ignition which can be produced from the Iranian natural magnesite compares well with the high quality existing synthetic caustic magnesias which is used for variety of applications.

Table 5.3 The industrial properties of Spanish natural calcined magnesite and synthetic caustic magnesia (Kimyongur and Scott 1986)

Industrial properties	Natural calcined Magnesite**	Synthetic caustic magnesia (Medium quality)	Synthetic caustic magnesia (High quality)*
LOI (%)	1	1-3	4-10
SA (m ² /g)	4	20-40	60-150
IN (mg/g)	11	20-40	60-150
CS (A ^o)	3300	-	-

Table 5.4 The industrial properties of samples under present investigation

Industrial properties	medium quality	high quality
LOI (%)	<5	5-10
SA (m ² /g)	30-60	70-100
IN (mg/g)	50-70	80-110
CS (A ^o)	250-500	200-230

Where:

LOI = loss on ignition, SA = surface area, IN = iodine adsorption number, CS = crystallite size, ** = Spanish calcined magnesite, * = Steetley Minerals information sheets

5.12 Discussion

Caustic calcined magnesia with different industrial properties can be made by varying the calcination temperature and time. As is shown in Table 5.3, the commercial products indicate a wide range of properties. For example the low quality Spanish natural caustic magnesia are used for animal feedstuff. High impurity levels in this material (85% MgO), may promote sintering at relatively low temperatures. Alternatively, a comparison with values obtained in the present experiments (Table 5.4) could illustrate unnecessary overburning and consequent energy wastage in the manufacture of this product.

High quality magnesias (Table 5.3) indicate a large variation in surface area and iodine adsorption number values and specification for individual products span a large part of this range. This probably reflects a difficulty in manufacture on a commercial scale which is to be expected given the narrow zone of time - temperature parameters resulting in high values. Residual loss on ignition is high and, as the experimental results indicate, this is necessary to achieve the high surface area. The industrial properties (SA, IN, LOI and CS) of natural caustic magnesia from Iran determined in present investigation have been plotted on the time - temperature graph to show the fields within which a medium and high quality magnesia can be made under laboratory conditions. As it can be seen from Figure 5.8, high quality magnesia can be produce in a narrow range dependent on both

temperature and time. Medium quality caustic magnesia can be made within a wide range of laboratory parameters. e.g. the medium quality product can be made rapidly (within 30 min.) between 800-1000°C. At lower temperatures (600-800°C) formation of this medium quality magnesia, which is superior to existing synthetic products, is largely independent of time in the range of 2-8 hours. Temperature is the most important factor effecting the production of medium quality magnesia. Increase of calcination temperature beyond 800°C is likely to lead a rapid deterioration of surface area and hence product quality.

This work has been done in laboratory conditions and obviously there are differences between laboratory and commercial instruments, e.g. size of kiln, kiln atmosphere, rate and mechanism of heat transfer, difference in particle size distribution of raw material, particle size distribution, and quantity of caustic calcined materials. Nevertheless according to Kimyongur and Scott (1986) there is no fundamental difference preventing the manufacture of a high quality caustic magnesia from a natural magnesite of high quality. As with the existing products from synthetic source, extremely careful control of calcination is required.

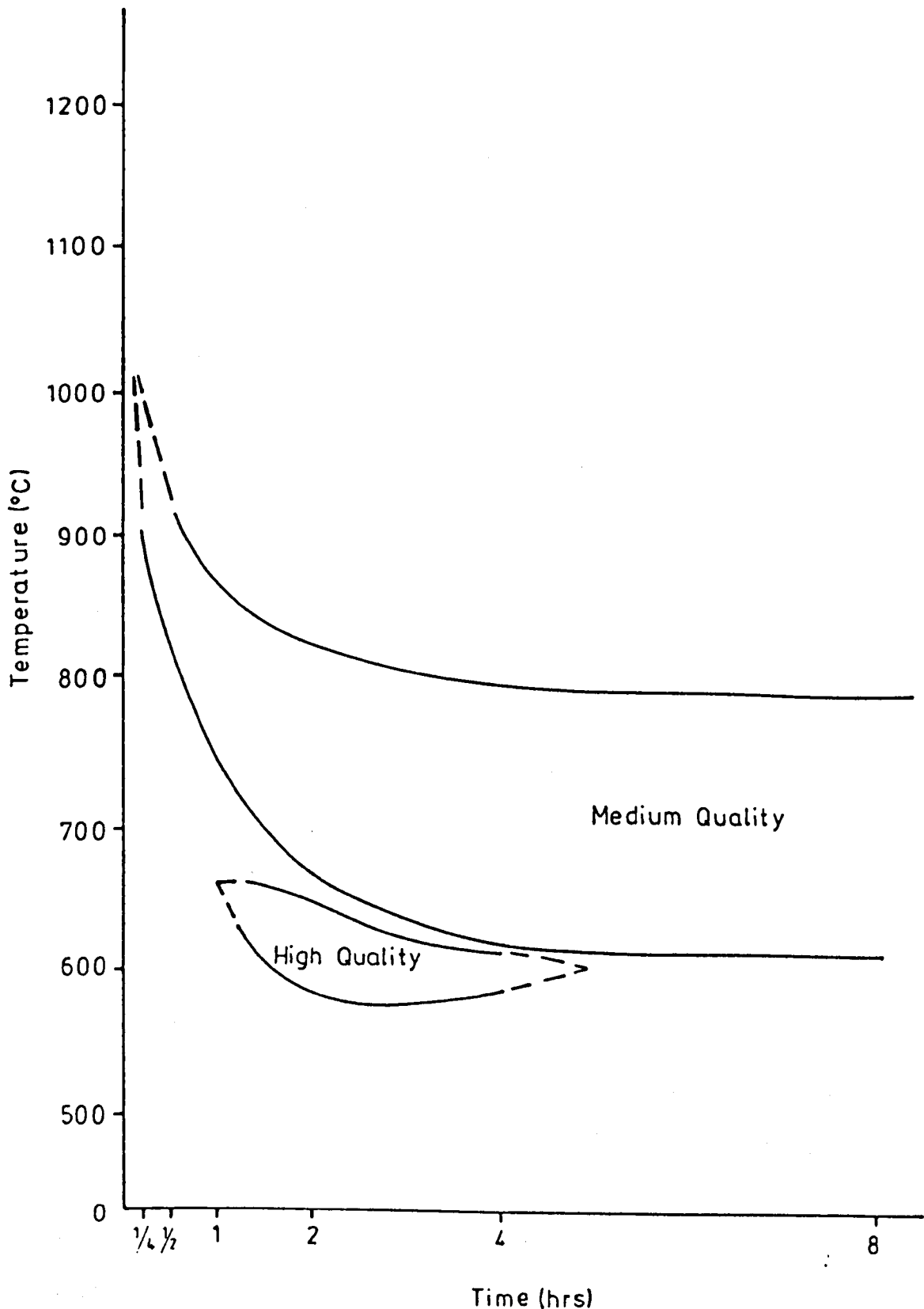


Figure 5.8 Time-Temperature regions within which high quality (loss on ignition <10%, surface area >70 m²/g, crystallite size <230 Å), and medium quality (loss on ignition <5%, surface area >30 m²/g, iodine number 750 mg/g, crystallite size <500 Å) caustic calcined magnesia can be made under laboratory conditions (samples are collected from Torshak magnesite deposit of eastern Iran)

CHAPTER 6

GEOLOGY, MINERALOGY AND TECHNOLOGY OF HUNTITE

6.1 Introduction

Many occurrences of huntite [$Mg_3Ca(CO_3)_4$] are present very close to the magnesite deposits in the Nehbandan area, south east of the town of Birjand. This area lies within the Ophiolite complex of eastern Iran, and is 170 Km from Birjand by road and 250 Km from Zahedan, Capital of Baluchistan Province. In the investigated area three different modes of occurrence of huntite have been recognised, vein type, nodular type, and alluvial type huntite.

Huntite deposits of eastern Iran are presumably formed from alteration products of magnesite deposits which themselves are an alteration product of ultrabasic rocks such as serpentinite.

6.2 Regional geology

The geological map of the area around the magnesite and huntite deposits, extracted from 1/250,000 scale, metallogenic map of south east Iran is shown in Chapter 3, Figure 3.3. The area in which the huntite occurs is almost exclusively within the Flysch and Ophiolite-Melange belt of eastern Iran, and is situated in the Khorasan province, about 170 Km south east of Birjand, not far from the border with Afghanistan (Chapter 3, Figure 3.2).

The most important formations exposed in the area

consist of Upper Cretaceous strata. They include various Flysch type formations, volcanic, ophiolitic units and metamorphic rocks. The major fault zone of the area has a trend of north north west - south south east. These faults are still active and, as a result of this activity, limonitization, slickensides and fault mylonites in this area are common.

The sedimentary rocks of the Melange which are partly folded and metamorphosed are largely identical with those forming the bedded Flysch succession. The rocks are argillaceous and silty shales and sandstones of green-grey colour, green radiolarite and dense pink pelagic limestone and micro conglomeratic layers. Slight phyllitization has also affected the Flysch type shales and tuffs.

The igneous components comprise ultrabasic rocks, mainly serpentized peridotite and serpentinite.

6.3 Description of huntite deposits

Three different modes of occurrence of huntite have been recognised by the author as follows:

6.3.1 Vein type huntite

Vein type huntite deposits have been found in the Sarlard area, 30 Km east of Shusf village (Figure 3.3, Chapter 3). (Altitude from sea level 1600 metres, Longitude 60°, 20' and latitude 31°, 70'). In this deposit a mixture of magnesite and huntite occurs. Hand specimens of huntite are softer than magnesite. Huntite crumbles in water, has a

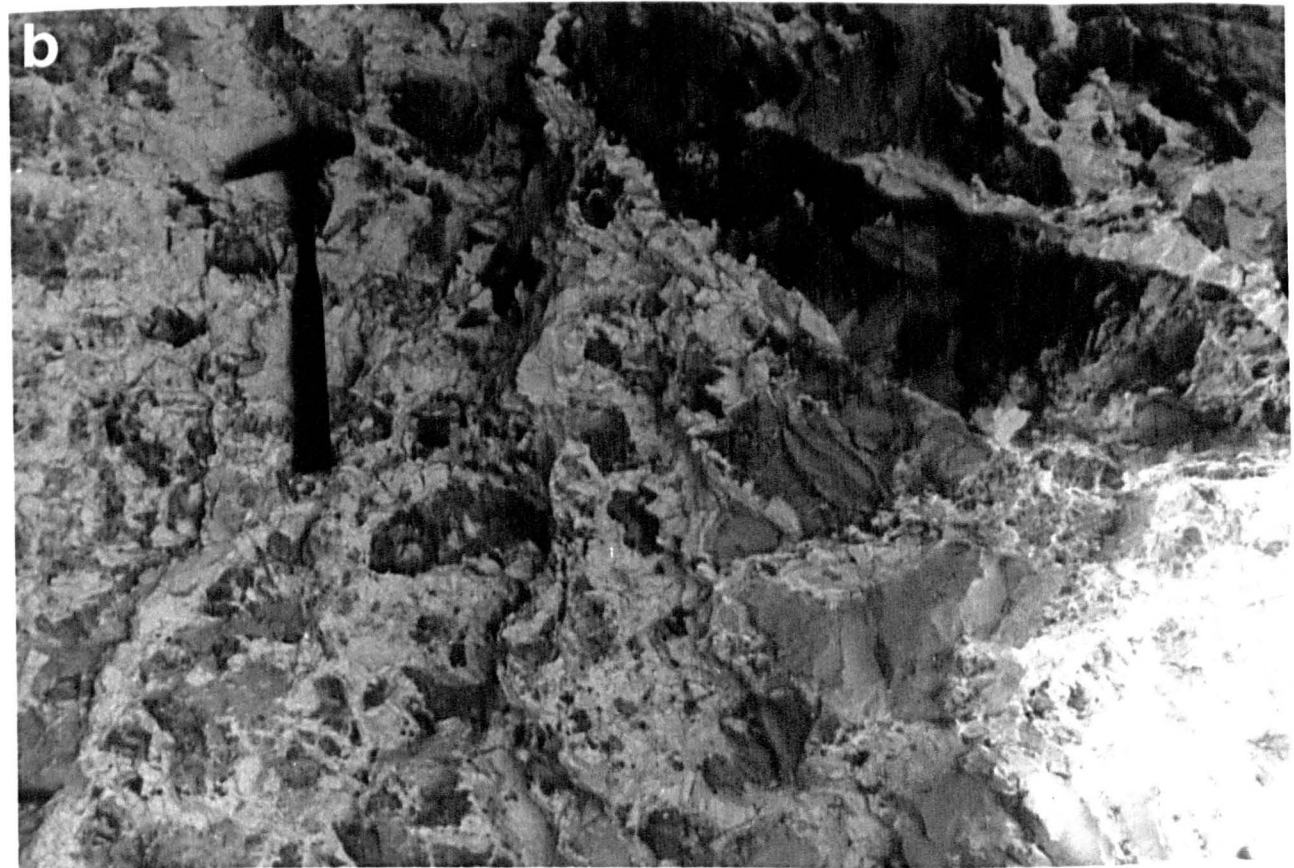
PLATE 34.a

Typical view of vein type huntite deposit, (Sarlard deposit). In this deposit, a mixture of magnesite and its weathering product (huntite) formed in vein shape inside the country rocks, which are green sandstone. Magnesite and huntite veins are between 5 cm to 1m thick.

PLATE 34.b

More detail of magnesite and huntite narrow veins within the green sandstone.

PLATE 34



smooth feel and adheres to the tongue.

Huntite occurs in veins in this deposit as a weathering product of magnesite in a near surface environment. Magnesite and huntite veinlets cut the adjacent green sandstones. Magnesite and huntite veins are between 5 cm to 1m thick and few metres long. The vein type huntite deposits are illustrated in Plate 34a and b.

6.3.2 Nodular type huntite

Nodular type huntite deposits occur in Chah-Rostam area east of Nehbandan, north west of Hajat asbestos mine (Chapter 3, Figure 3.3). (Altitude from sea level 1600 metres, Longitude : 60°, 27', and latitude 31°, 55).

At first sight the huntite nodules cannot be seen (Plate 35a) but after digging, the sporadic nodules are visible inside the highly weathered serpentinite rocks (Plate 35b). This type of deposit may have formed either by interaction between Mg-Ca rich solutions and the ultrabasic rocks such as serpentinite, or as a result of the weathering process in previously formed magnesite nodules inside the serpentinite rocks.

This kind of huntite deposit can be found in highly weathered serpentinite situated close to the major and active fault zones in the area.

6.3.3 Alluvial type huntite

Alluvial type huntite deposits are situated in Cheshmeh Hassan Kassem area approximately 20 Km east of Shusf village

PLATE 35.a

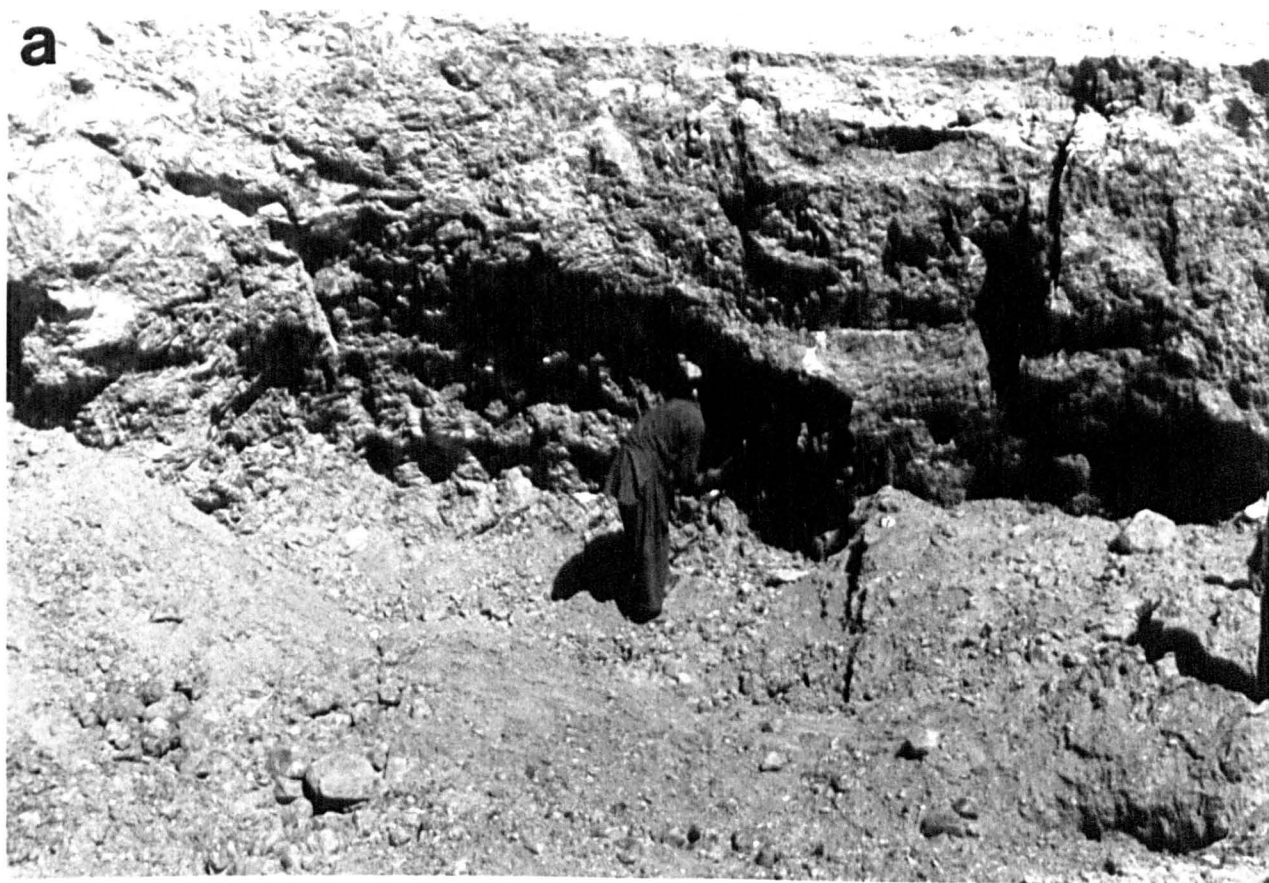
Looking from east to the Nodular type huntite deposit, (Chah Rostam deposit). In this deposit huntite formed by interaction between Mg rich waters and previously formed and altered ultrabasic rocks (serpentinite) near the faults zones.

PLATE 35.b

Huntite has been developed as sporadic nodules inside any space and cracks within the weathered serpentinite rocks.

PLATE 35

a



b



(chapter 3, Figure 3.3). (Altitude from sea level 1600 metre, Latitude 60°, 10' and Longitude 31°, 75').

Huntite in this kind of deposit occurs within the lower part of Quaternary alluvium in a low temperature and near surface environment. It probably originates by direct precipitation from Mg rich aqueous solutions, or as a result of interaction of Mg-rich solutions with pre-existing weathered carbonate fragments between the alluvial sediments.

The present alluvial terrace and soil profile is 1-2 metres thick and appears to be derived by weathering of carbonate and non-carbonate formations. The dominant carbonate in the soil is calcite. The calcite remains in the soil or infills joints and cracks in the rocks. Faults and breccia zones localize deep weathering processes below the soil level and provide an obvious channel way for descending surface waters. It is in these deep weathering zones that huntite occurs. The huntite nodules and lenses are always found in the most porous zone. (plate 36a, b).

6.3.4 Nesquehonite ($MgCO_3 \cdot 3H_2O$)

On the surface of dry rivers bed of the investigated area, located to the east of Shusf village, approximately 170 Km south east of Birjand, some yellowish white sediments which are soft and have a thickness of 1-5 cm are present (Plate 37a). These thin sediments which covers nearly all of the dry river surfaces in the area, appear to be forming as a direct precipitation from some small streams under hot weather conditions (Plate 37b). Atomic Absorption

PLATES 36.a and b

Typical views of alluvial type huntite deposit (Cheshmeh Hassan Kassem deposit). In this deposit huntite is developed within the Quaternary sediments.

PLATE 36



PLATE 37.a

Typical view of some white sediments which cover all of dry river surfaces. These sediments are nesquehonite and appear to be forming as a direct precipitation from Mg-rich solutions.

PLATE 37.b

Closer view to one of the very small Mg-rich water streams which precipitates yellowish white nesquehonite sediments, normally radial in shape around vegetation.

PLATE 37



Spectrophotometry analysis of water from these streams indicate that they are rich in Mg (0.64 g/l MgO, 0.0274 g/l CaO). The X-ray diffraction pattern shows that this yellowish white material is nesquehonite ($\text{MgCO}_3 \cdot 3\text{H}_2\text{O}$).

Nesquehonite normally grows around vegetation in the water and for this reason they show a radial shape (Plates 40a and 43a). The presence of Mg rich ground water and the nesquehonite shows that Mg rich hydrothermal fluids are still active in the area.

6.4 Sampling and sample locations

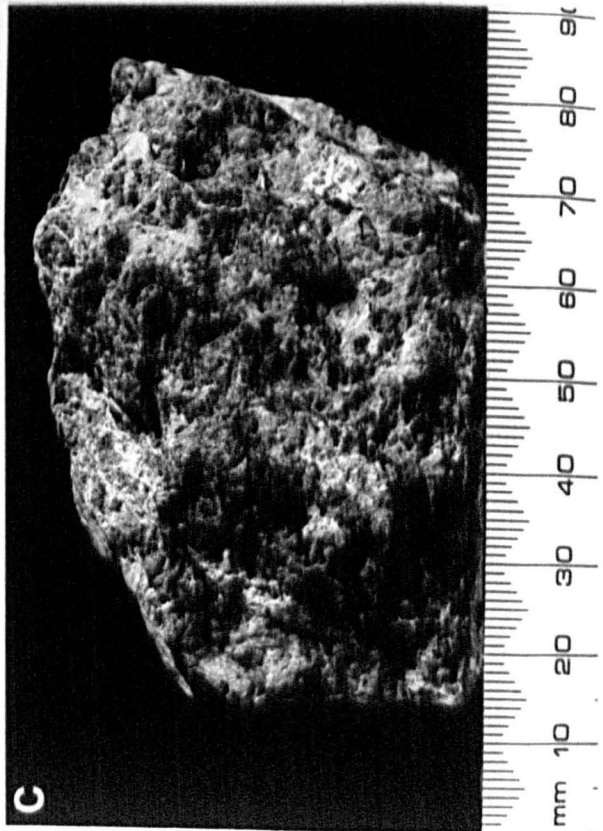
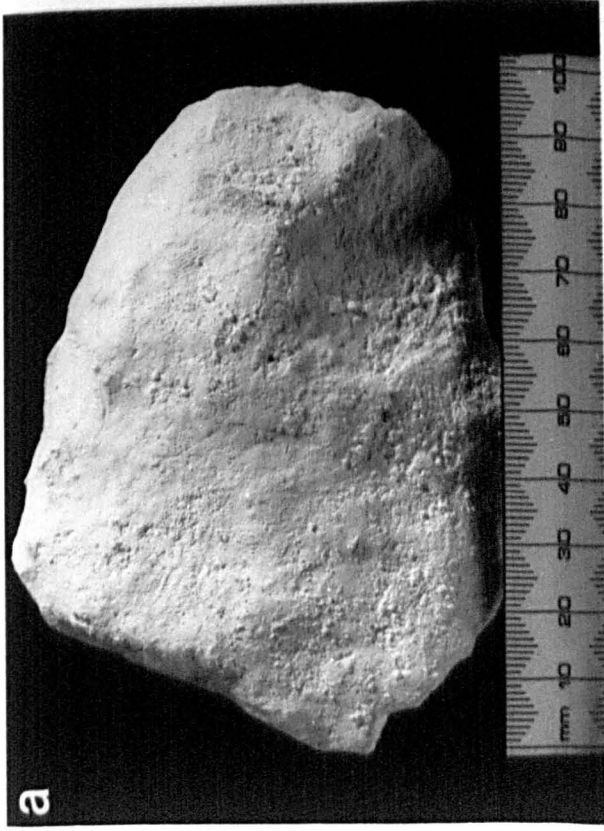
Huntite specimens were collected from unmined deposits as representative of the occurrences. Samples which are collected from nodular type huntite deposits, are usually covered with a thin skin of serpentinite, while in vein type huntite deposits, specimens are always mixed with magnesite. The alluvial type huntite deposits are easily separated from the neighbouring rocks and pure samples can be obtained. Figure 3.3 in Chapter 3, shows the locality of huntite deposits in the investigated area. Representative huntite hand specimen photographs are presented in Plate 38.

PLATE 38

Hand specimen photographs of different huntite samples from Iran.

- a) Very pure and white, with soily smooth alluvial type huntite.
- b) very white combinations of huntite with few percentage of magnesite (vein type huntite).
- c) Common view to unprocessed nodular type huntite which is covered with serpentinite.
- d) Nodular type huntite after hand cleaning and removing the serpentinite skin.

PLATE 38



6.5 Mineralogy and petrography

The mineralogy and petrography of the huntites, hydromagnesite - huntite, and nesquehonite have been determined using the following techniques:

1. Optical microscope
2. X-ray diffraction (XRD)
3. Differential thermal analyses (DTA)
4. Transmission Electron microscope (TEM)
5. Scanning electron microscope (SEM)
6. Electron Microprobe analyses (EPMA) have been employed to determine different phases occurring as a result of dead burning huntite in 1500°C for a period of 96 hours to compare the results to that of dead burned magnesite.

The grain size of less than two microns does not allow the use of the electron microprobe to analyse natural huntite.

6.5.1 Physical and optical properties

The Iranian samples occurs as compact chalk like masses which have an even to subconchoidal fracture. They are brittle when cut with a knife and are soft enough to leave a mark on a dark surface. The compact masses are easily cut by the finger nail. They are porous and a fragment dropped into water crumbles, emitting crackling and accompanied by a hissing sound, produced by the displacement of air bubbles from the porous mass. Huntite has a smooth feel and adheres to the tongue.

The grain size of less than two microns does not allow

the optical properties to be determined satisfactorily. An attempt was made to determine the refractive index of huntite by an oil immersion method which gave a value of $1.605 < RI \leq 1.615$. It should be pointed out that this determination was for fibrous aggregates. The refractive index of nesquehonite also determined which gave a value of $1.480 < RI < 1.485$. Representative huntite hand specimen photographs are presented in Plate 38.

6.5.2 X-ray diffraction

X-ray powder diffraction data has been obtained for the huntite samples by diffractometer technique using filtered CuK-alpha radiation. The X-ray diffraction pattern indicates that except in vein type huntite which contain a small amount of magnesite as an impurity, the samples are pure huntite and they show excellent agreement with those from Nevada analysed by Faust (1953).

6.5.2.1 Instrumental

The analyses of different type of huntite, nesquehonite, a natural mixture of magnesite and dolomite powders all collected from eastern Iran and samples of commercial hydromagnesite - huntite in natural and processed form from Greece (courtesy of Microfine Minerals and Chemicals Ltd), were carried out with a Philips PW 1050 diffractometer using Ni filtered Cu radiation. The operation condition are shown below:

Tube current	40 Kv, 40 mA
scanning rate	1/2°2θ/min
time constant	4 second
count rate	1x10 ³ cps

6.5.2.2 Results

Cavity mounted specimens were scanned from 5-65°2θ which covers most of the reflections of the phases expected in these materials.

A list of minerals identified by XRD in huntite, hydromagnesite - huntite, and nesquehonite are given in Table 6.1, and Figure 6.1 gives a representative X-ray powder diffraction traces of different samples, where A is a pure alluvial type huntite, B is a mix vein type huntite - magnesite, C is an impure nodular hydromagnesite - huntite (unprocessed), D is a Grecian hydromagnesite - huntite product, and E is nesquehonite.

The peak positions were measured at half peak height above the background and the intensities (cps) are measured for the major reflection for each mineral.

Table 6.1 The mineralogy of huntite, hydromagnesite - huntite and nesquehonite as determined by XRD

Sample	VS	S	MS	MD	MW	W	VW
A-H1	H	-	-	-	-	-	-
A-H2	H	-	-	-	-	-	-
A-H3	H	-	-	-	-	-	-
A-H4	H	-	-	-	-	-	-
A-H5	H	-	-	-	-	M	-
A-H6	H	-	-	-	-	-	-
A-H7	H	-	-	-	Q	-	-
A-H8	H	-	-	-	-	-	-
A-H9	H	-	-	-	-	M	-
A-H10	H	-	-	-	-	Q	-
V-H1	H	M	-	-	-	-	-
V-H2	H	-	-	M	-	-	-
V-H3	H	-	M	-	-	-	-
V-H4	H	M	-	-	-	-	-
V-H5	H	-	M	-	-	-	-
V-H6	H	-	-	M	-	-	-
V-H7	H	-	M	-	-	-	-
V-H8	H	M	-	-	-	-	-
V-H9	H	-	-	M	-	-	-
V-H10	H, M	-	-	-	-	-	-
N-H1	H	-	-	-	-	-	-
N-H2	H	-	-	-	-	-	-
N-H3	H	-	-	-	-	-	-
N-H4	H	-	-	-	-	-	-
N-H5	H	-	-	-	-	-	-
N-H6	H	-	-	-	-	-	-
N-H7	H	-	-	-	-	-	-
N-H8	H	-	-	-	-	-	-
N-H9	H	Se	-	-	-	-	-
N-H10	Se	Hm	-	H	-	-	-
G-Hm, H	Hm	H	-	-	-	-	-
G-P	H, Hm	-	-	-	-	-	-
NES1	N	Q	Hm	Dp	-	-	-
NES2	N	Q	Hm	Dp	-	-	-
NES3	N	-	Q	Hm, Dp	-	-	-
NES4	N	Q	Hm	Dp	-	-	-

Where:

VS = very strong (>1000 cps), S = strong (250-1000 cps), MS = moderate strong (125-250 cps), MD = moderate (62.5-125 cps), MW = moderate weak (37.5-62.5 cps), W = weak (12.5-37.5 cps), VW = very weak (<12.5 cps). Samples are: A-H = Alluvial type huntite, V-H = vein type huntite, N-H nodular type huntite, G-Hm, H = Grecian natural hydromagnesite - huntite, G-P = Grecian product, and NES = Nesquehonite. Minerals are: H = huntite, M = magnesite, Hm = hydromagnesite, Q = quartz, N = nesquehonite, Se = serpentinite, Dp = Dypingite.

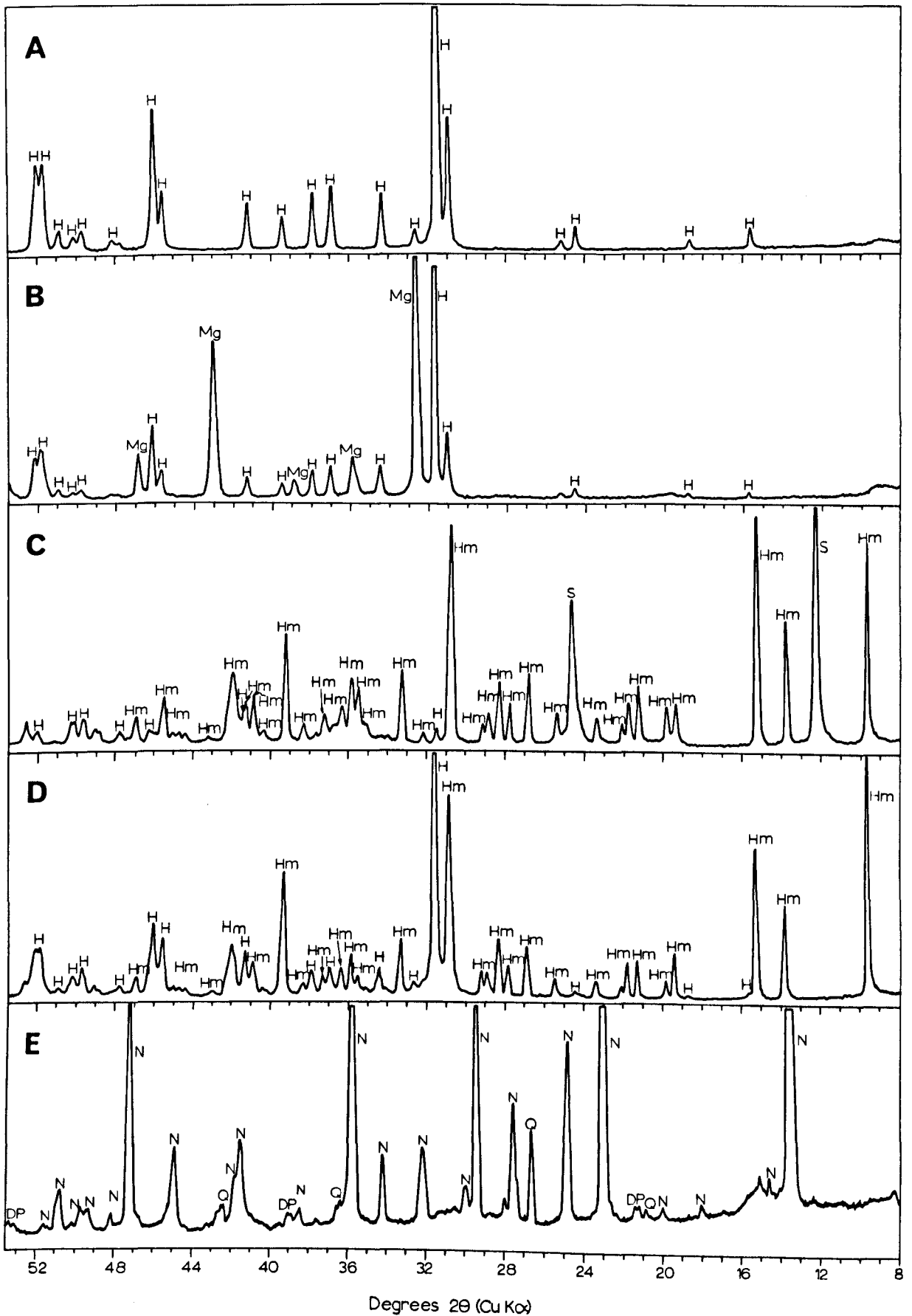


Figure 6.1 X-ray diffraction traces of Huntite, Hydromagnesite, and Nesquehonite.
 H = Huntite. Hm = Hydromagnesite. N = Nesquehonite. Mg = Magnesite.
 S = Serpentinite. Dp = Dypingite. Q = Quartz.

6.5.2.3 Discussion

As it can be seen from the Table 6.1, the majority of alluvial and nodular type huntites are entirely pure huntite. Magnesite and quartz are rarely present as impurities in alluvial type huntite, and serpentinite and hydromagnesite are the main impurities in nodular type huntite.

Vein type huntite as explained earlier is a mixture of huntite and magnesite. All vein type huntite samples contain a various amount of magnesite. Natural and processed samples from Greece are not pure huntite, they contain mostly hydromagnesite and huntite. The main impurities present on nesquehonite samples are quartz, hydromagnesite and dypingite $[Mg_5(CO_3)_4(OH)_2 \cdot 5H_2O]$

6.5.3 Differential thermal analysis (DTA)

The differential thermal analysis of different huntites, magnesite, a natural mixture of magnesite and dolomite and nesquehonite from Iran and samples of commercial hydromagnesite - huntite in both natural and processed forms from Greece are studied using a Stanton Redcroft DTA 67-4, with the following operating conditions:

Temperature range = room temperature - 1000°C

Heating rate = 8°C/min

Chart speed = 50 mm/hr

Sensitivity = 250 microvolts.

Reference material = calcined alumina

6.5.3.1 Results

Differential thermal analysis characteristic curves of studied samples are given in Figure 6.2.

6.5.3.1.a Huntite [$Mg_3Ca(CO_3)_4$]

The DTA curves of nodular type huntite (Figure 6.2a) and alluvial type huntite (Figure 6.2b) are different from that of vein type huntite (Figure 6.2c) which is due to the presence of magnesite with the latter.

Pure huntite shows two endothermic peaks (Figure 6.2a, b), the first one represents the decomposition of the magnesium carbonate portion and the second that of the calcium carbonate portion of the mineral. The mineral huntite behaving thermally as if were a mixture of magnesite and calcite.

6.5.3.1.b Magnesite ($MgCO_3$)

Magnesite exhibits one large endothermic peak at 594°C which represents its dissociation (Figure 6.2e). Figure 6.2f represent the characteristic curves of the dissociation of a natural mixture of magnesite and dolomite. The large endothermic curve at 611°C representing the dissociation of magnesite, and two smaller endothermic peaks at 680°C and 771°C are due to dissociation of dolomite.

The exothermic reaction at 637°C, following the magnesite decomposition is due to present of iron oxide in the sample. According to Webb and Heystek (1957), the large

exothermic reaction following the magnesite decomposition and displacement of magnesite peak to higher temperatures suggest the presence of breunnerite.

Berg (1943) has observed that about one percent of sodium chloride lowers the temperature of magnesite peak by about 50°C. Gruver (1950a) found that what appears to be a sample of breunnerite gave a wider and shallower peak than did a typical sample of magnesite.

6.5.3.1.c Nesquehonite ($MgCO_3 \cdot 3H_2O$)

Beck (1950) has attributed the first doublet to the loss of two molecules of water of crystallization, the second peak at 259°C to the remaining water molecule and the third endothermic peak to the carbonate decomposition. The exothermic peak is due to the crystallization of amorphous magnesium oxide. Figure 6.2d present the DTA curve of nesquehonite with the two large, distinct and well separated breaks representing nesquehonite decomposition.

6.5.3.1.d Hydromagnesite - huntite

For the purpose of comparison, a commercial natural mixture of hydromagnesite [$3MgCO_3 \cdot Mg(OH)_2 \cdot 3H_2O$] and huntite from Greece in natural and processed form have been subjected to differential thermal analysis. The resultant curves are shown in Figure 6.2g and h respectively. In curve (f) the first peak at 66°C which is not present in curve (g) is possibly due to presence of water. This is not present in the processed sample. Other peaks are more or less similar in

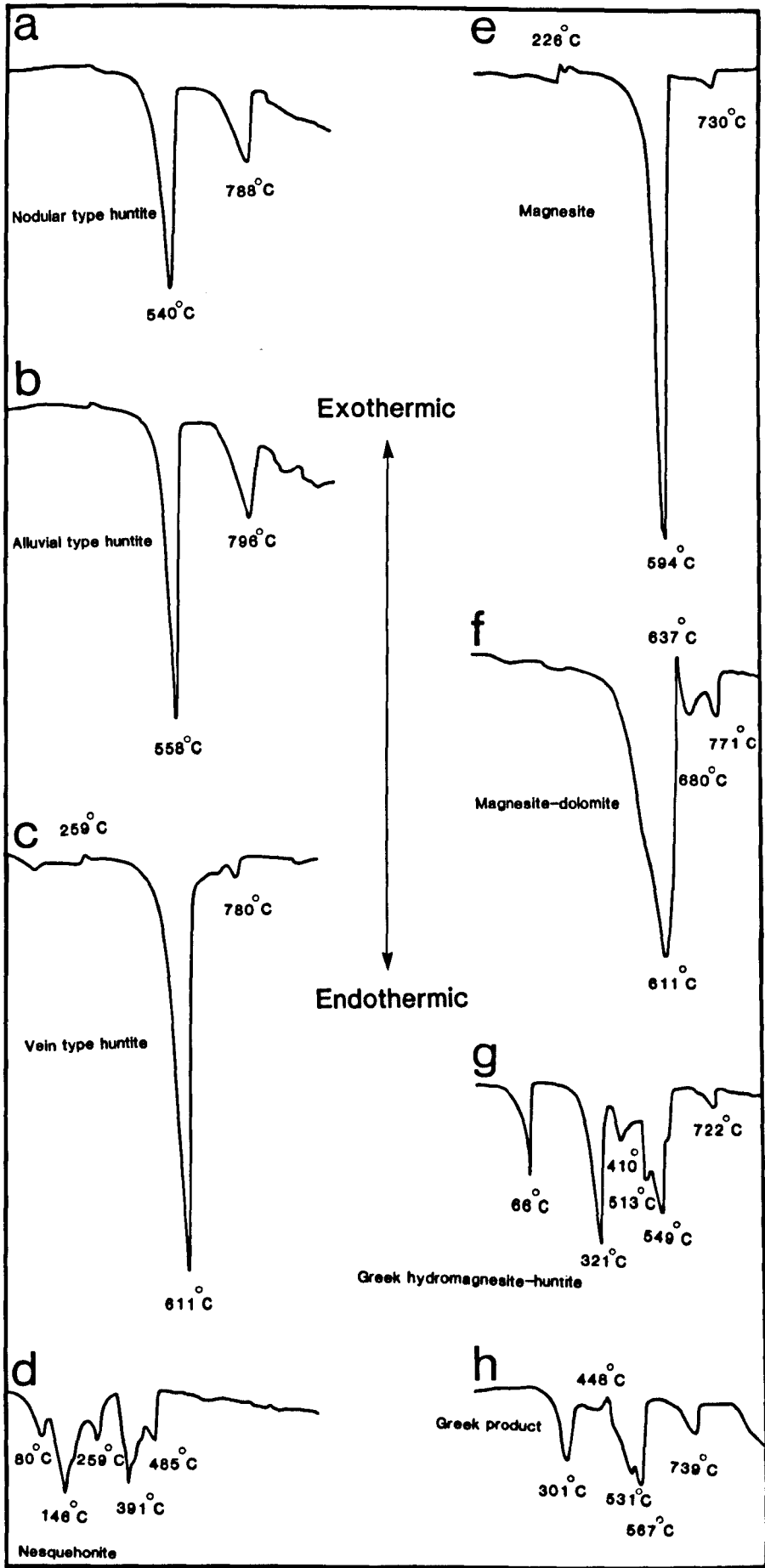


Figure 6.2 Differential thermal curves of studied specimens

both natural and processed materials.

6.5.4 Transmission electron microscopy

The minus one micron huntite crystals, and irregular and radial form nesquehonite grains have been studied using transmission electron microscope. The samples were gently disaggregated, then very small amount, of samples (approx. 1/10 gm) were diluted with distilled water and one drop placed on a carbon-coated microscope grid and allowed to dry. Samples were examined using a JEOL-JEM 100C transmission electron microscope (TEM). The operating voltage was 100KV.

6.5.4.1 Results

Huntite is present in rhombohedral crystalline form which is illustrated in Plate 39. Individual thin crystal platelets (0.2-1 μ m), generally show good rhombohedral shape with sharp or slightly rounded corners. Modulation can be seen within the huntite crystals (Plate 39e). The origin of this modulation is unknown.

Nesquehonite grains illustrate irregular and radial shapes (0.5-2 μ m). The nesquehonite grains loose water under heating by electron beam producing rounded bubbles on the surface. Transmission electron micrographs of nesquehonite are presented in Plate 40.

PLATE 39

Transmission electron micrographs of huntite.

a,b) Transmission electron micrograph of huntite crystals.

c,d) Closer view to rhombohedral huntite crystals.

e) Under focus photograph of huntite crystal to show modulation within huntite crystal structure. This modulation is within the huntite crystal and not an artifact created by the huntite over the carbon support film.

f) Similar to (e), but when the photograph is focused. The modulation structure changes slightly. The origin of this modulation is unknown.

PLATE 39

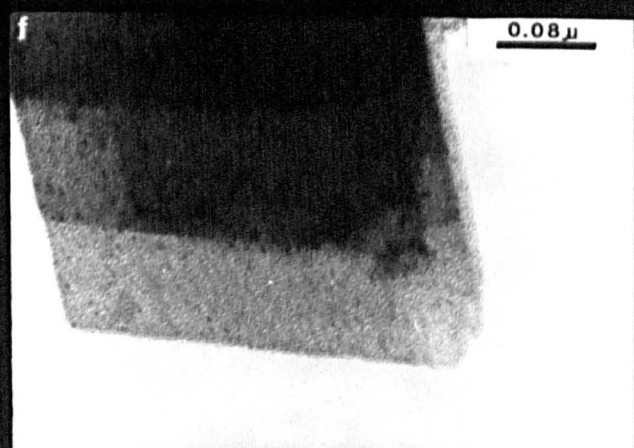
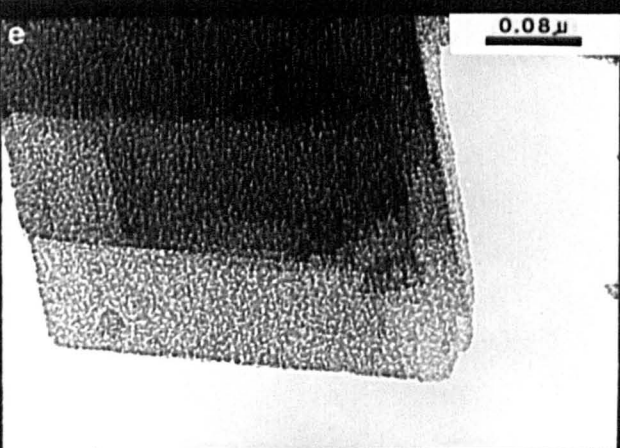
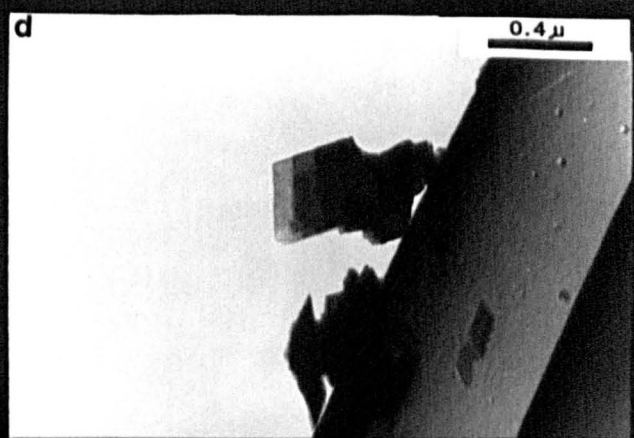
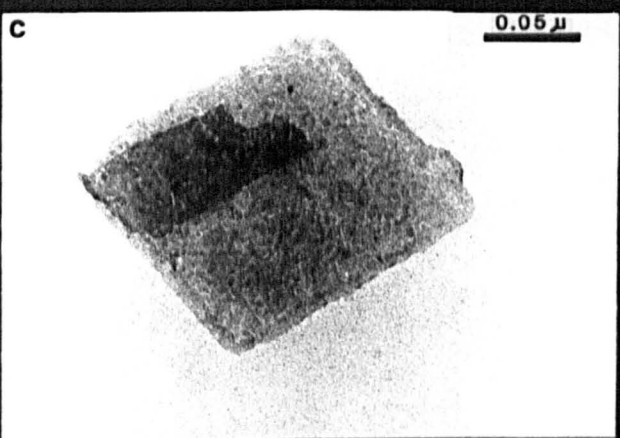
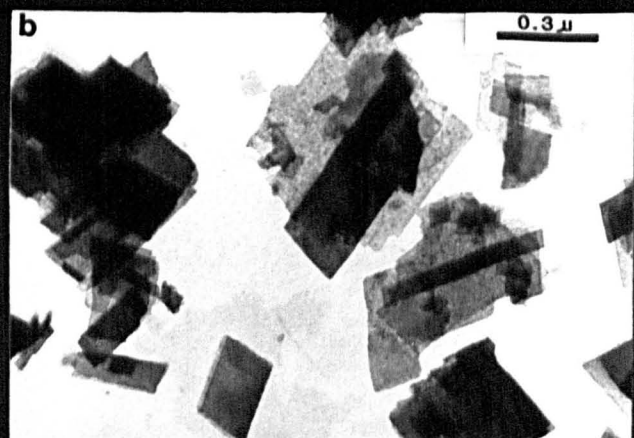
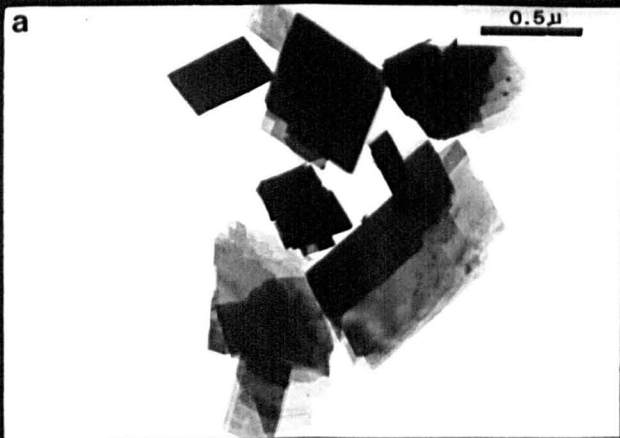


PLATE 40

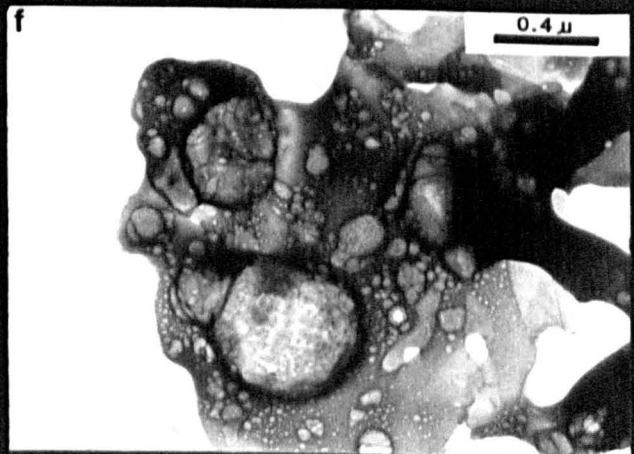
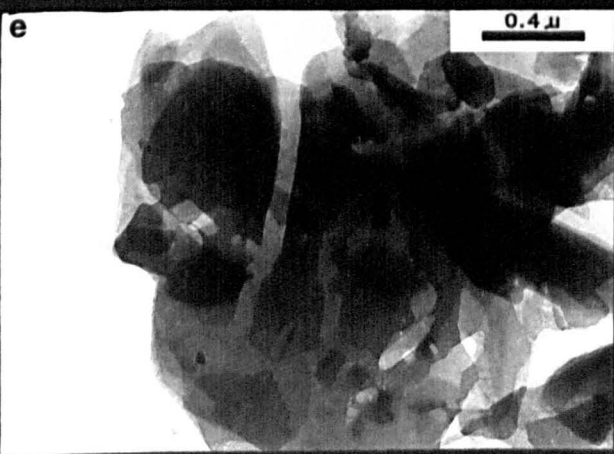
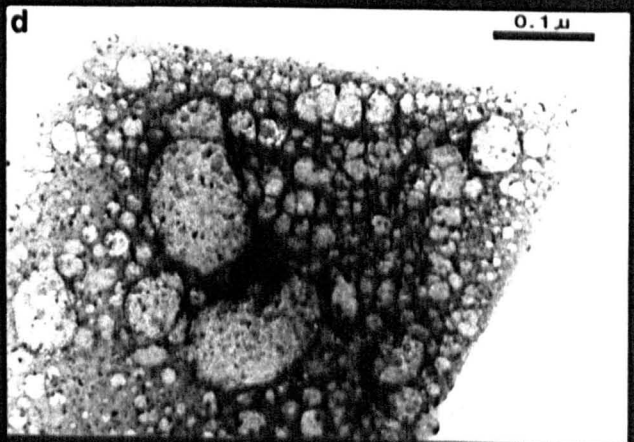
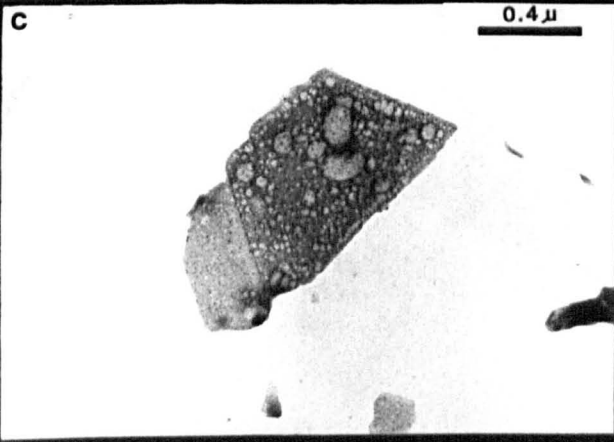
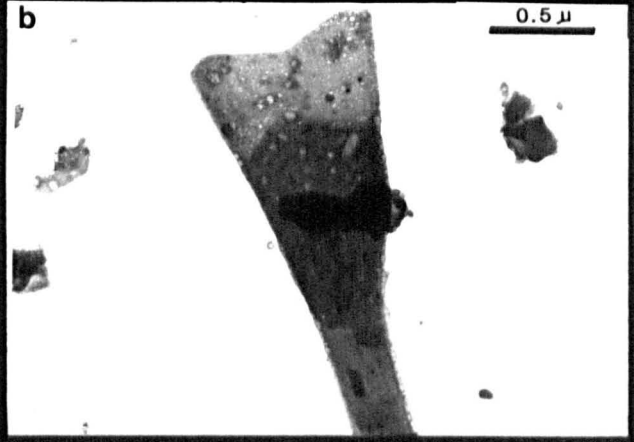
Transmission electron micrographs (TEM) of Nesquehonite.

a) Typical view of irregular nesquehonite grains.

b,c,d) Closer view of the irregular nesquehonite grains.

e,f) These two photograph demonstrate the beam damage in nesquehonite grains. Photograph (f) is taken from sample (e) after few second (approx. 20-30 seconds) showing result of heating by electron beam and subsequent loss of water.

PLATE 40



6.6 Bulk chemistry

The chemical composition of Iranian huntites, nesquehonite, magnesite - dolomite, and Grecian hydromagnesite - huntite in both natural and processed forms, were determined by British Ceramic Research Limited using a Philips 1606 X-ray fluorescence spectrometer (XRF) calibrated on magnesite. Operating condition is 40 KV, and 75 mA. Glass discs were prepared by adding 0.9 gm of sample with 9 gms of lithium tetraborate and heated up to 1200°C.

6.6.1 Results

The chemical analyses, and loss on ignition values are presented in Table 6.2.

Table 6.2 The bulk chemical composition of huntite, hydromagnesite - huntite, magnesite - dolomite and nesquehonite as determined by XRF.

oxide	Samples						
	A-H	V-H	N-H	G-Hm,H	G-P	A-M,D	NES
SiO ₂	0.88	7.40	0.00	0.51	0.37	2.00	3.70
TiO ₂	0.00	0.00	0.00	0.00	0.00	0.01	0.03
Al ₂ O ₃	0.18	0.00	0.00	0.00	0.03	0.51	0.75
Fe ₂ O ₃	0.06	0.00	0.00	0.01	0.02	0.75	0.38
CaO	13.00	9.17	13.80	4.24	6.42	3.48	0.74
MgO	33.10	36.40	32.50	40.70	39.40	42.33	33.53
K ₂ O	0.03	0.02	0.03	0.00	0.00	0.01	0.19
Na ₂ O	0.49	0.30	0.86	0.00	0.05	1.69	0.87
P ₂ O ₅	0.04	0.03	0.00	0.00	0.00	0.00	0.00
BaO	0.03	0.08	0.00	0.00	0.00	0.00	0.00
SrO	2.94	0.80	0.94	0.00	0.01	0.00	0.00
SO ₃	0.01	0.00	0.12	0.00	0.03	0.00	0.03
LOI	48.90	45.50	52.40	54.20	53.50	50.07	62.77
TOTAL	99.66	99.70	100.65	99.66	99.83	100.85	102.99
CaO/SiO ₂	15.83	1.33	0.00	8.91	18.59	1.86	0.22
Al ₂ O ₃ /Fe ₂ O ₃	4.70	0.00	0.00	0.00	1.57	1.06	3.15

Where:

A-H = Alluvial type huntite

V-H = Vein type huntite

N-H = Nodular type huntite

G-Hm,H = Grecian hydromagnesite - huntite

G-P = Grecian product

A-M,D = Ablah magnesite - dolomite

NES = Nesquehonite

All huntite samples from Iran contain SrO which is 0.80%, 0.94% and 2.94% for vein type, nodular type, and alluvial type huntites respectively.

The main impurity oxide exist in alluvial and vein type huntite samples is SiO₂, which varies between 0.88% in alluvial type and 7.40% in vein type huntite. The amount of SiO₂ in nodular type huntite is below detection limit.

In comparison to Iranian huntites, the Grecian hydromagnesite - huntite sample contains lower amount of CaO and higher percentage of MgO.

The higher percentage of SiO₂ in nesquehonite is due to difficulties in the sample collection as it is not possible to collect nesquehonite without picking other small impurity grains such as quartz (see Plate 37).

6.7 Microstructure

The microstructure of fracture surface of natural huntite, hydromagnesite - huntite, magnesite - dolomite, and nesquehonite specimens have been studied using two Cambridge scanning electron microscopes models 360 and 600.

The scanning electron micrographs are presented in Plates 41-43. Plate 41 display platy habit and very small crystalline size of huntite (<2^μm). Plate 42 compares the microstructures of magnesite - dolomite and magnesite specimens from Iran with Grecian hydromagnesite - huntite samples in both raw and processed forms and finally Plate 43 exhibits platy habit and rosette pattern of nesquehonite.

PLATE 41

Scanning electron micrographs of fracture surface of different huntite specimens.

a,b,c) Alluvial type huntite. The huntite crystals appear in the form of platey shape, with a crystal sizes of less than two micron in diameter.

d,e,f) Nodular type huntite. In this type huntite, two different shapes of grains seems to appear:

1. Platey, like photograph (d), and
2. Mixture of platey and needle shape grains which are presented in photograph e and f.

g,h) Vein type huntite. this type huntite is a mixture of magnesite and huntite. Presence of magnesite as impurity in this sample does not allow huntite grains to show their platey habits, so their grain shape is actually depends on the percentage of magnesite impurity. However in plate 41g most of grains are plates of huntite, but plate 41h is a mixture of magnesite and huntite.

PLATE 41

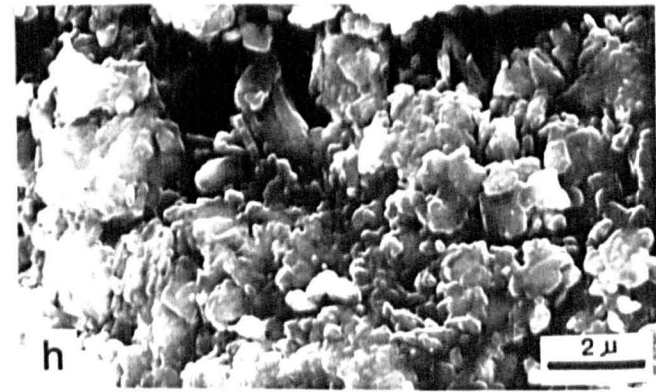
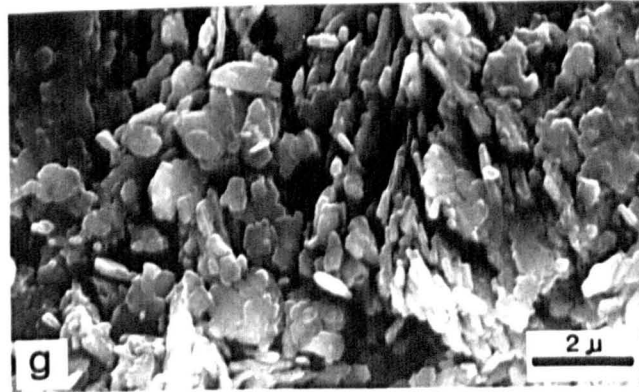
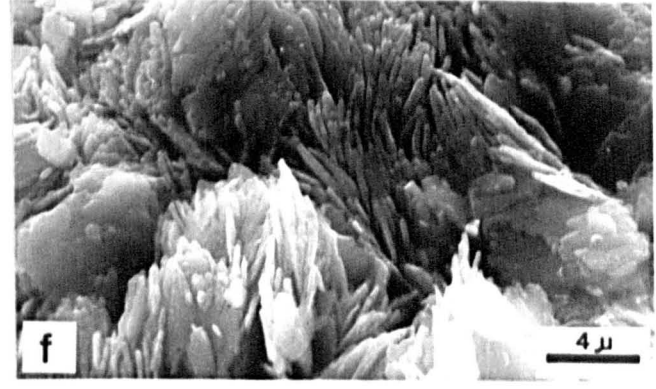
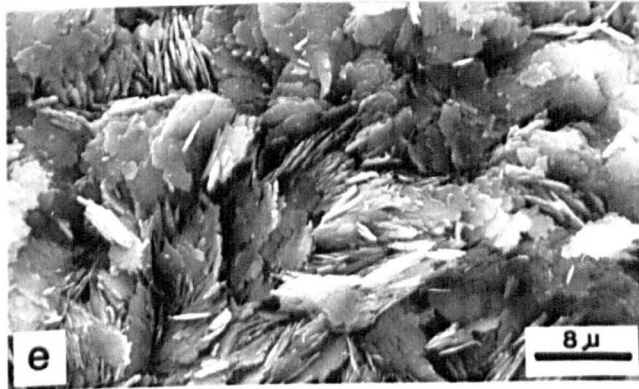
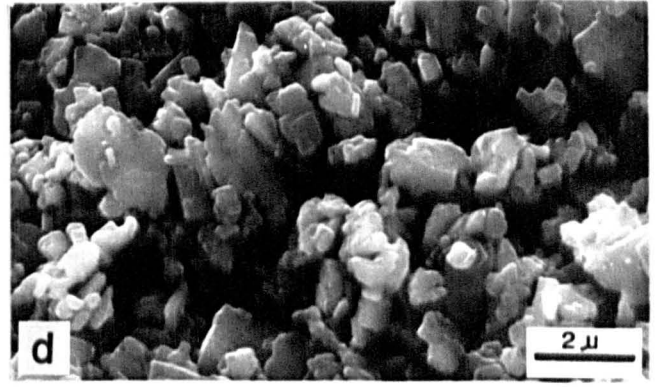
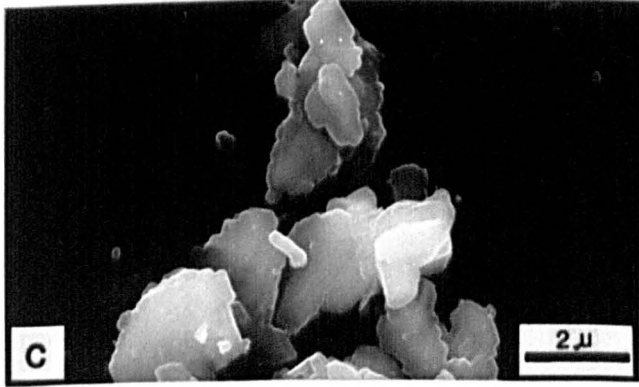
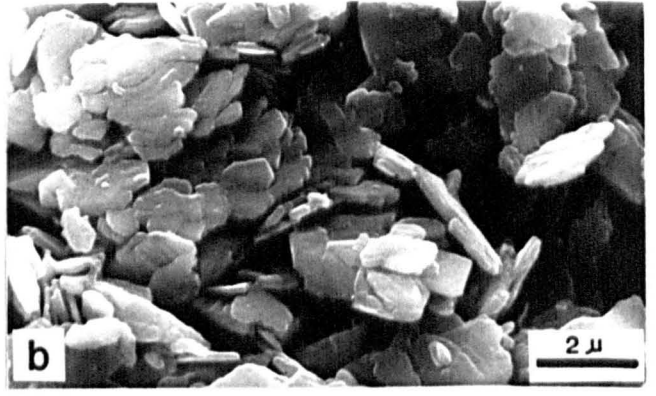
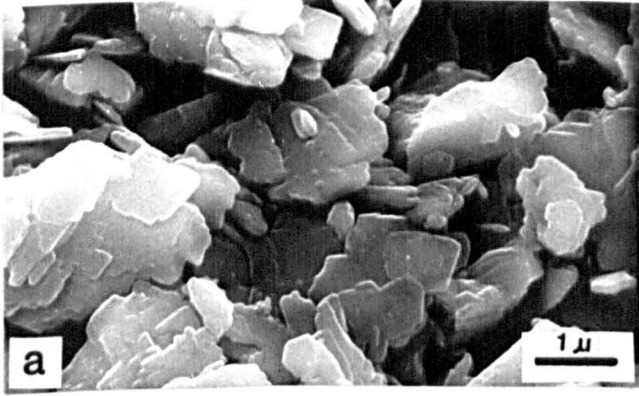


PLATE 42

Scanning electron micrographs of fracture surface of magnesite - dolomite, pure magnesite and Grecian hydromagnesite - huntite raw material and products.

a,b,c) Scanning electron micrographs of fracture surface of a mixture of magnesite and dolomite. Dolomites are mostly rounded and flower shape grains e.g (a, b). Plate 42c is close up of one of the rhombs. Identification of crystals as dolomite is based on the rhombic morphology and EDX spectrum consisting of Ca, Mg, and Fe.

d) Perfect rhombohedral crystal of magnesite in the size of about one micron.

e,f) Grecian raw materials are mostly contain hydromagnesite and huntite. Most of the grains are visible in Plate 42e and f show nearly similar structure to the natural magnesite (Plate 42d), but very small grains on the surface of hydromagnesites are huntite. Scale bar in plate 42e is belong to the small rectangular in the left hand side of photograph.

g,h) Grecian product. The Grecian hydromagnesite - huntite raw material shown in plate 42e and f are mostly hydromagnesite with few percentage of huntite, but after processing as it can be seen in plate 42g and h, they are mostly pure huntite.

PLATE 42

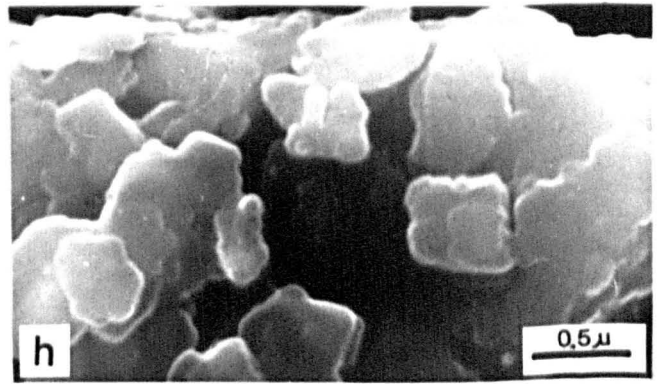
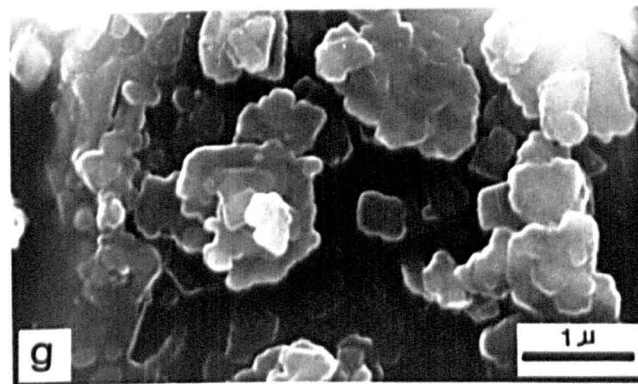
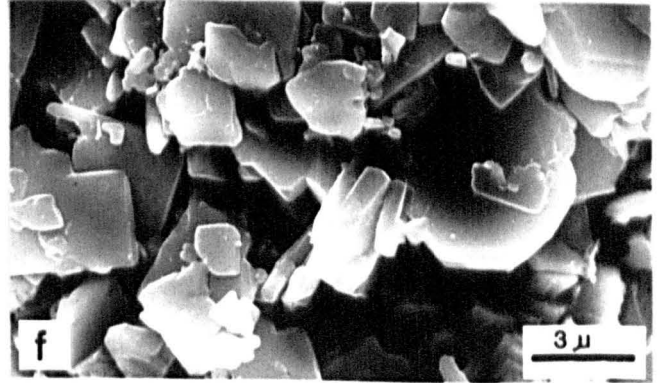
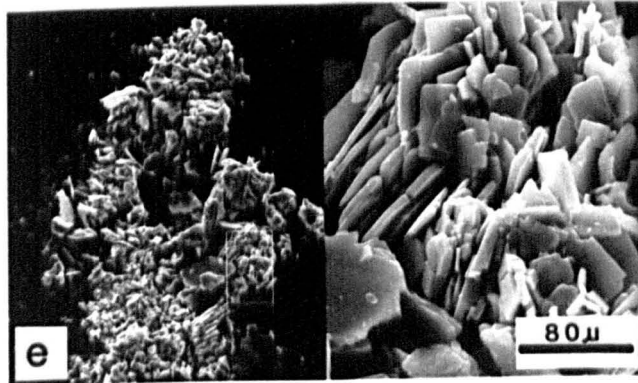
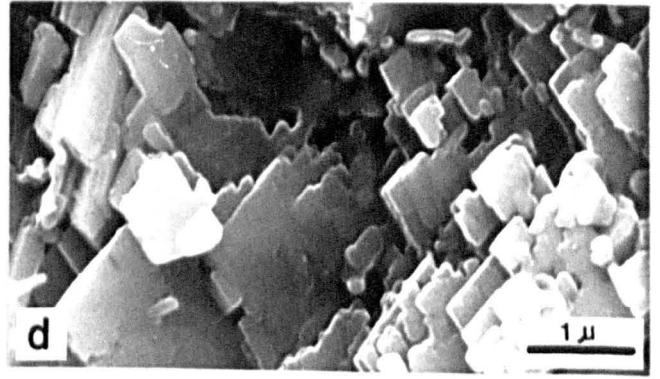
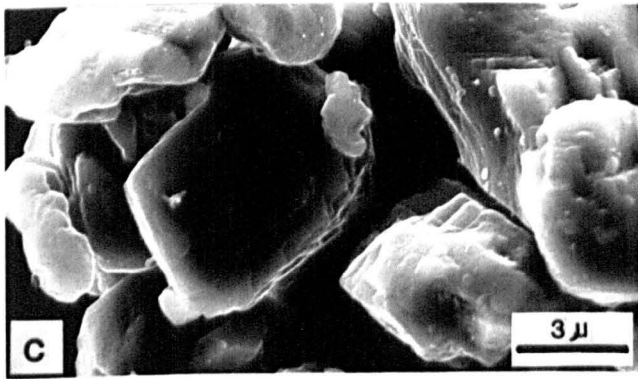
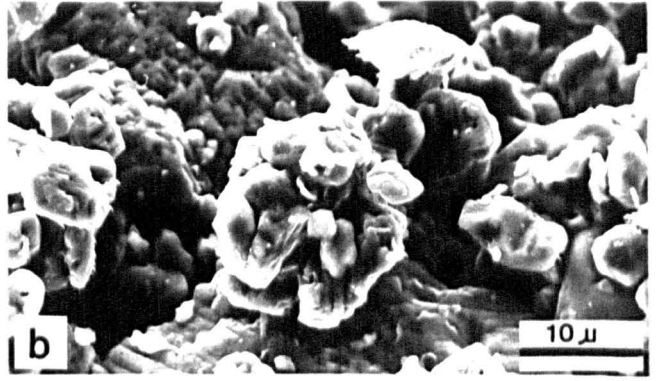
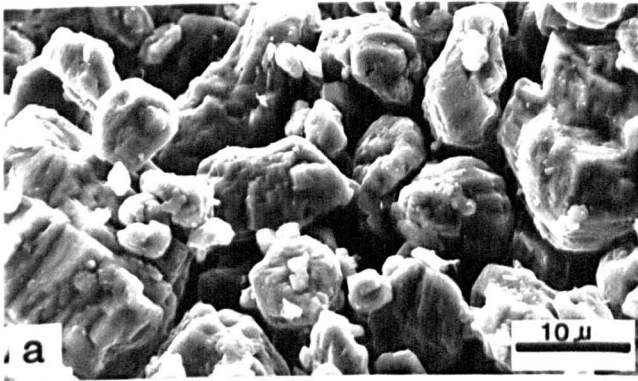
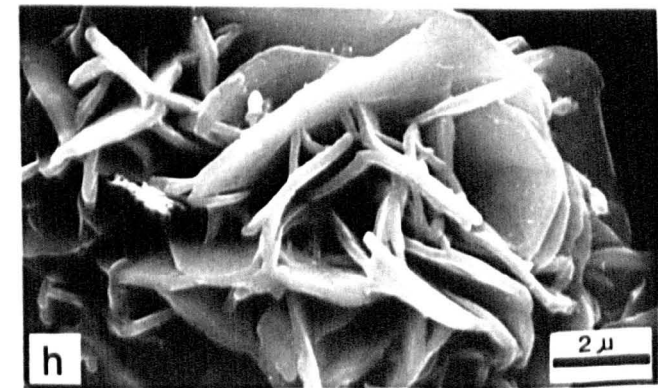
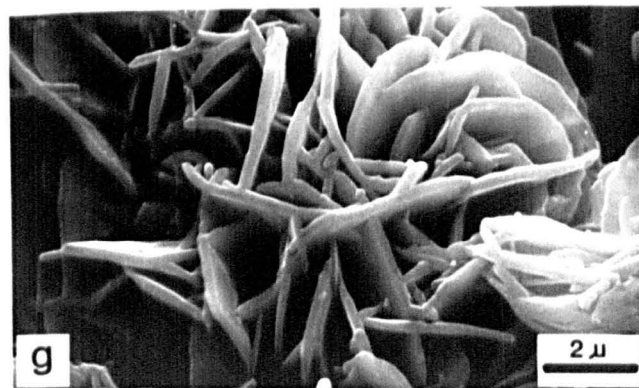
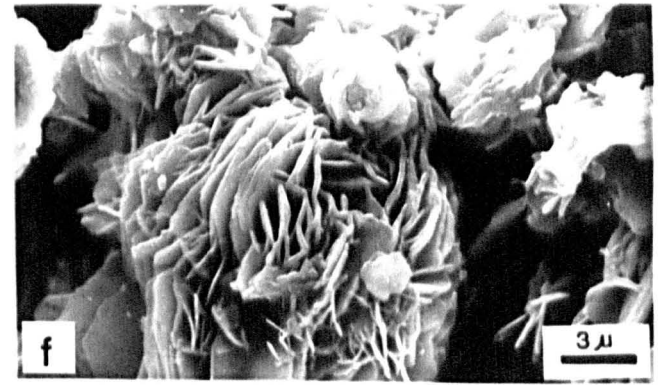
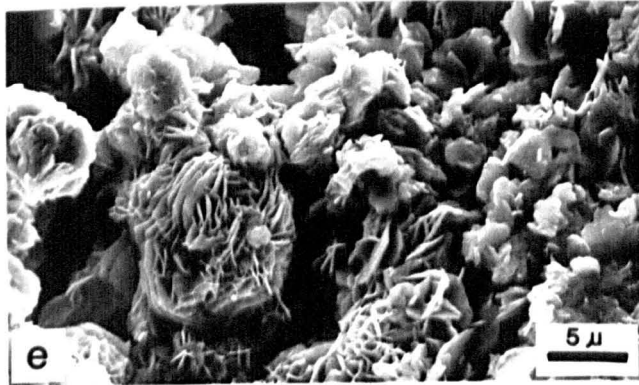
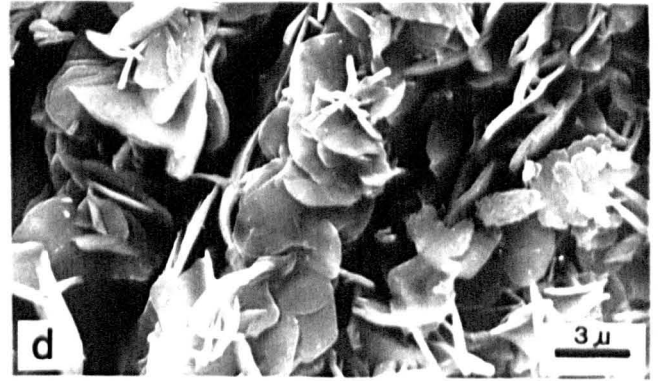
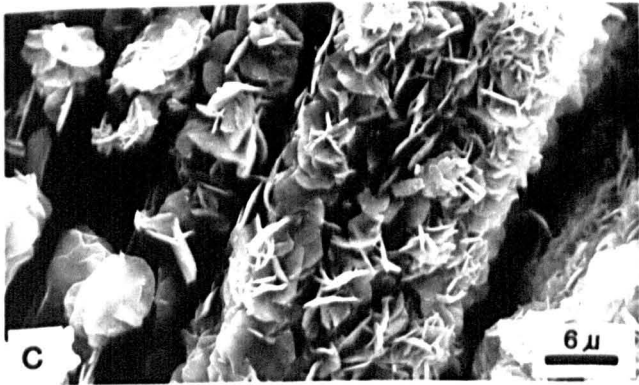
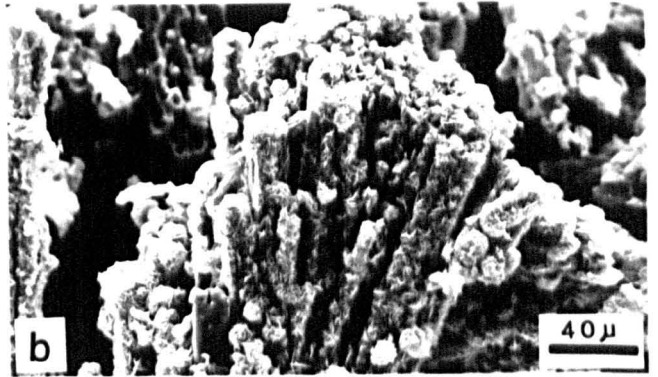
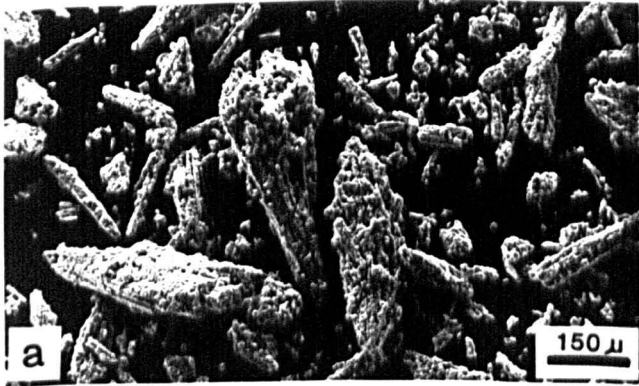


PLATE 43

Scanning electron micrographs of fracture surface of Nesquehonite.

- a) Common view of nesquehonite grains which are developed in radial forms like a fan.
- b) Closer view to the colony of Individual nesquehonite plates.
- c,d) Is close up of nesquehonite platey shape crystals. These photographs are closer view of plate 43b.
- e,f) Individual nesquehonite platelets are arranged in a rosette pattern.
- g,h) Closer view to the rosette pattern of nesquehonite.

PLATE 43



6.8 Apparent porosity, bulk density and apparent specific gravity

Porosity is the ratio of the pore or voids to the bulk volume of the specimen and usually indicated as a percentage. The total porosity is a measure of all void space of porous material and includes the sealed-off pores as well as those which are connected with the surface of test specimen. The equation for total or true porosity (PT) by percent is:

$$PT (\%) = 100 \left(1 - \frac{VG}{VB} \right)$$

Where (VB) is bulk volume and (VG) is grain volume. Alternatively and more usually, grain density is substituted for grain volume, and bulk density for bulk volume. Total porosity by percent correspondingly is:

$$PT (\%) = 100 \left(1 - \frac{DB}{DG} \right)$$

Apparent porosity (PA), otherwise called effective or net porosity, is a measure of the interconnected void space which communicates with the surface of the test specimen. It therefore does not include the sealed-off pores. Apparent porosity is obtained by determining the fluid capacity of interconnected pores, which is the pore volume (VP). The apparent porosity can be calculated by dividing the pore volume (VP) by the bulk volume (VB).

The equation for apparent porosity (PA) by percent is

$$PA (\%) = 100 \left(\frac{VP}{VB} \right)$$

Bulk density, (B) or apparent density of a specimen in grams per cubic centimetre is the ratio of its dry weight divided by the exterior volume, including pores.

$$B = \frac{D}{V_{ext}}$$

Apparent specific gravity, (T) is used to indicate the ratio of the weight of a mass of material to that of a volume of water equal to the volume of the solid material plus the sealed pores.

6.8.1 Method of measurement

The values measured in this investigation are apparent porosity, apparent specific gravity and the bulk density. These values are determined by using a modified version of the ASTM test for apparent porosity, water absorption, apparent specific gravity and bulk density of burned refractory brick by boiling water (ASTM C20-80a). Details on methods of measurement are given in Appendix 11.

6.8.2 Results and discussion

The measurement of apparent porosity (P), bulk density (B) and specific gravity (T), have been carried out by using paraffin on the natural specimens of huntite, a commercial natural mixture of hydromagnesite - huntite from Greece, nesquehonite, natural mixture of magnesite and dolomite, and magnesite. The results are presented in Table 6.3.

Table 6.3 Apparent porosity (P), bulk density (B) and apparent specific gravity (T), values of huntite, hydromagnesite - huntite, nesquehonite, magnesite - dolomite and magnesite.

Sample	P (%)	B	T
vein type huntite	5.19	3.37	3.63
Alluvial type huntite	24.66	2.81	3.73
Nodular type huntite	37.40	2.25	3.54
Hydromagnesite - huntite	31.25	2.32	3.38
Nesquehonite	26.47	3.26	4.26
Magnesite - Dolomite	10.95	3.36	3.77
Magnesite (A8 mean value)	6.84	2.81	3.01

It appears that the huntite shows a wide variation in the apparent porosity values ranging from 5.19% in vein type huntite to 37.40% in nodular type.

These variations are represent^{ative} of the variable structure in different type huntite. The lack of porosity (5.19%) in vein type huntite, may be due to presence of magnesite as impurity.

Samples with high percentage porosity like in nodular type huntite, commonly are very fine rounded and similar in size. Grains with small area of contact, which correspond to higher porosity between the grains, and the larger the volume of micropores, will cause the higher water absorption. The results also shows that the specimens with higher percentages of apparent porosity have lower bulk densities. The apparent specific gravity values show less variation in compare with porosity. However the higher the percentage of closed

porosity will cause higher apparent specific gravity.

6.9 Acid insoluble residue (AIR)

Acid insoluble residue measurement is a quick way to measure the amount of non-carbonate residues which are appears as impurities in carbonates soluble in cold 10% HCl, such as limestone, huntite and Nesquehonite. If a granular residue is obtained, it can studied with a binocular microscope or a residue can be identified by XRD.

6.9.1 Method of measurement

The acid insoluble residue (AIR) value of three different huntites and nesquehonite from Iran with samples of commercial hydromagnesite - huntite in natural and processed forms from Greece were determined using the method described in Appendix 12. Measurements were made in duplicate.

6.9.2 Result and discussion

Result of measurements are given in Table 6.4.

Table 6.4 Acid insoluble residue of specimens from Iran and Greece.

Sample	Acid Insoluble Residue (%)
Nesquehonite	5.60
Vein type huntite	7.38
Nodular type huntite	0.07
Alluvial type huntite	0.25
Greecian natural hydromagnesite - huntite	0.70
Greecian hydromagnesite - huntite product	0.30

The higher percentage of AIR in vein type huntite deposit is due to presence of magnesite in this type of deposits.

The very low percentage of AIR in both alluvial and nodular type huntite deposits indicate their high purity.

The percentage of AIR in the case of samples from Greece in both form of raw material and products are higher than alluvial and nodular type huntite from Iran, but they are purer than vein type huntite. Obviously the AIR% may decrease after mineral processing, in the case of samples from Greece this value change from 0.70% to 0.30% after processing which is still higher than alluvial and nodular type huntite deposits from Iran.

CHAPTER 7

INDUSTRIAL POTENTIAL OF HUNTITE

7.1 Introduction

The most important potential use of huntite is as a white filler in the paint industry. Oil absorption values and the colour properties suggest that huntite may make an excellent white filler in paint. However because of the chemical composition of huntite which is half way between magnesite and dolomite, a sample of huntite has been calcined at 1500°C for 96 hours to compare the dead burned huntite products with those of dead burned magnesite and dolomite.

7.2 Oil absorption

Oil absorption is the minimum quantity of oil required for the formation of a homogeneous paste that is plastic and does not crack or crumble. The value indicates the percentage of voids between the particles and the size distribution of the particles. Higher oil absorption values are obtained by small and uniform particle sizes rather than the particles with a very wide range of sizes. That is because the larger voids are created as a result of packing of small uniform sized particles.

According to Bessey and Lammiman (1955) the total quantity of oil needed to give a homogeneous paste may be regarded as made up of:

1. The quantity required to wet the surfaces of the particles.
2. The quantity required to fill any accessible voids or crevices within the particles themselves.
3. The quantity required to fill the voids between the oil wetted particles when they are closely packed.

Thus the oil absorption value is a composite of the void volume and the percentage of oil adsorped on the particle surfaces.

7.2.1 Method of measurement

The test followed procedure detailed in BS 4383, part B7 (1982).

7.2.2 Results

The weight of refined linseed oil absorbed by 100 gm of huntite, nesquehonite, magnesite, a natural mixture of magnesite - dolomite, Grecian raw and processed hydromagnesite - huntite and the British manufactured filler product (Snowcal 6ML whiting) were determined on a 5 and 10 gms of samples of minus 53 micron in size. Determinations have been carried out under the same condition and measurement are made on duplicate samples. Results are presented in Table 7.1.

Table 7.1 Oil absorption values

Sample	Oil absorption (ml/100gm)		
	1st Reading	2nd Reading	Average
Whiting (chack)	19.0	19.0	19.0
Nodular type huntite	35.0	35.0	35.0
vein type huntite	38.0	38.0	38.0
Alluvial type huntite	40.0	40.0	40.0
Nesquehonite	60.0	60.0	60.0
Greecian raw material	31.5	32.0	31.7
Greecian product	40.0	40.0	40.0
Magnesite - dolomite	17.0	16.5	16.7
Magnesite (T25)	19.0	18.0	18.5

7.2.3 Discussion

The oil absorption values of three different huntite specimens from Iran are very similar (35-40 ml/100g) because of their similarity in the particle size distribution and the purity. The Greecian raw materials (hydromagnesite - huntite) have a lower oil absorption value compared to the Iranian samples. This is due to a higher percentage of hydromagnesite impurity and greater size distribution. However the oil absorption value increases after processing of the Greecian raw material to a value similar to the Iranian material. Lower values of oil absorption have been found for magnesite, magnesite - dolomite, and whiting. The maximum value of oil absorption in this experiment is 60 ml/100gm for nesquehonite.

Fine particle size filler is required for many applications. In this case, a larger oil absorption will result from the higher surface area of the produced fine powder. This could be lowered by chemically treating the

surfaces of the particles by fatty or aliphatic acids.

7.3 Colour measurement

7.3.1 Importance of colour of industrial mineral powders

The most important property of powders for use as a filler in the great majority of applications is colour, and in most cases the filler must be white. Cheaper off-white or coloured fillers are utilized in dark coloured products where slight variation in colour does not affect the appearance of the product. When white mineral products are required (e.g. china clay in paper, whiting as a filler in plastic, TiO_2 and huntite in paints) the whiter the raw materials are the higher the price of products will become.

It is difficult to compare the published details of the colour of mineral products from one company to another because there are several ways of measuring and presenting the data. Each manufacturer generally tries to present its own product in the most favourable way. In the case of white mineral powders, 100% means "pure white" to the customer. Thus the mineral producer is likely to use the method of measurement and presentation of data which shows its product to appear as white as possible.

7.3.2 Method of measurement and preparation of specimens

Colour measurements have been made using an EEL reflectance spectrophotometer as explained in Appendix 14. Both the spectral reflectance curves and X, Y, and Z tristimulus values of the C.I.E. system have been measured

for huntite, nesquehonite, magnesite and magnesite - dolomite specimens from Iran. For comparative purpose the colour of Snowcal 6ML whiting, Supreme kaolin and the Grecian hydromagnesite - huntite product have been determined as well. A white ceramic tile which is used as a working reference has been calibrated against $MgCO_3$ standard supplied by the equipment manufacturers (see Appendix 14).

All measurements are made on pressed powder pellets prepared in the way described in Appendix 14.

7.3.3 Results

The reflectance spectrophotometric results are given in Table 7.2 and plotted in Figure 7.1. The tristimulus values (X, Y, Z) and the chromaticity coordinates (x, y, z) are presented in Table 7.3. The Y tristimulus value gives the brightness.

Table 7.2 Percentage reflectance at given wavelengths

Filter No	Sample					
	G-P	K	H	N	M-D	W
601 (4260 A°)	94.1	88.9	96.4	55.5	81.0	82.6
602 (4700 A°)	98.9	94.8	99.4	75.5	89.6	91.6
603 (4900 A°)	99.2	94.4	99.5	70.4	88.9	89.1
604 (5200 A°)	98.3	93.7	99.5	72.0	88.6	89.5
605 (5500 A°)	98.1	94.4	98.4	75.6	91.0	91.4
606 (5800 A°)	98.0	94.6	98.5	81.5	91.6	92.2
607 (6000 A°)	99.5	98.0	99.9	90.4	95.9	96.3
608 (6600 A°)	99.7	98.3	99.8	91.5	96.6	97.2
609 (6840 A°)	99.4	97.7	99.6	86.7	94.6	95.8

where:

G-P = Grecian hydromagnesite - huntite product

K = Supreme kaolin

H = Nodular type huntite

N = Nesquehonite

M-D = Ablah magnesite - dolomite powder

W = Whiting 6ML (chack)

Table 7.3 Derivation of chromaticity coordinates

filter No	Sample					
	G-P	K	H	N	M-D	W
X	99.5	97.1	99.5	84.4	94.9	95.5
Y	89.8	88.7	90.4	76.3	85.1	87.5
Z	32.1	31.1	32.8	25.4	29.7	31.1
x	0.45	0.45	0.45	0.45	0.45	0.45
Y	0.41	0.41	0.41	0.41	0.41	0.41
z	0.15	0.14	0.15	0.14	0.14	0.15

Where:

G-P = Grecian hydromagnesite - huntite product

K = Supreme kaolin

H = Nodular type huntite

N = Nesquehonite

M-D = Ablah magnesite - dolomite powder

W = Whiting 6ML (chack)

Y = Brightness

7.3.4 Discussion

The colour properties of huntite, nesquehonite, magnesite and magnesite - dolomite from Iran along with those of high quality commercial fillers, such as Supreme kaolin, whiting Snowcal 6ML (chalk) and Grecian hydromagnesite - huntite products have been determined.

The spectrophotometric curves show that the reflectance (the amount of light reflected from the surface of sample) of

huntite is higher than other samples such as the Grecian hydromagnesite - huntite product which is used at present in the paint industry as a filler.

The Brightness which is taken as the "Y" tristimulus value and corresponds with the general level of reflectivity in case of Iranian huntite is higher than the other samples.

The values of hue and purity can not be determined because of similarity of chromaticity coordinates (x, y, z) of tested samples with those of "A" source on the chromaticity chart.

7.4 Dead burned huntite

As mentioned in the introduction to this chapter the main potential use of huntite is as a white filler in paint, but because of similarity in chemistry of huntite to magnesite and dolomite, just for the purpose of laboratory investigation samples of huntite, natural mixture of hydromagnesite - huntite, magnesite - dolomite and nesquehonite have been calcined to compare the products with dead burned magnesite and dolomite. The huntite deposits are very rare and small in nature to be used in basic refractory industry such as magnesite or dolomite.

Scanning electron microscope and electron microprobe were employed to determine the microstructure, mineralogy and mineral chemistry of dead burned products to compare the results with the other basic refractories.

Plate 48 show the dead burned products (1500°C, 96 hrs) of different huntites, hydromagnesite - huntite, magnesite -

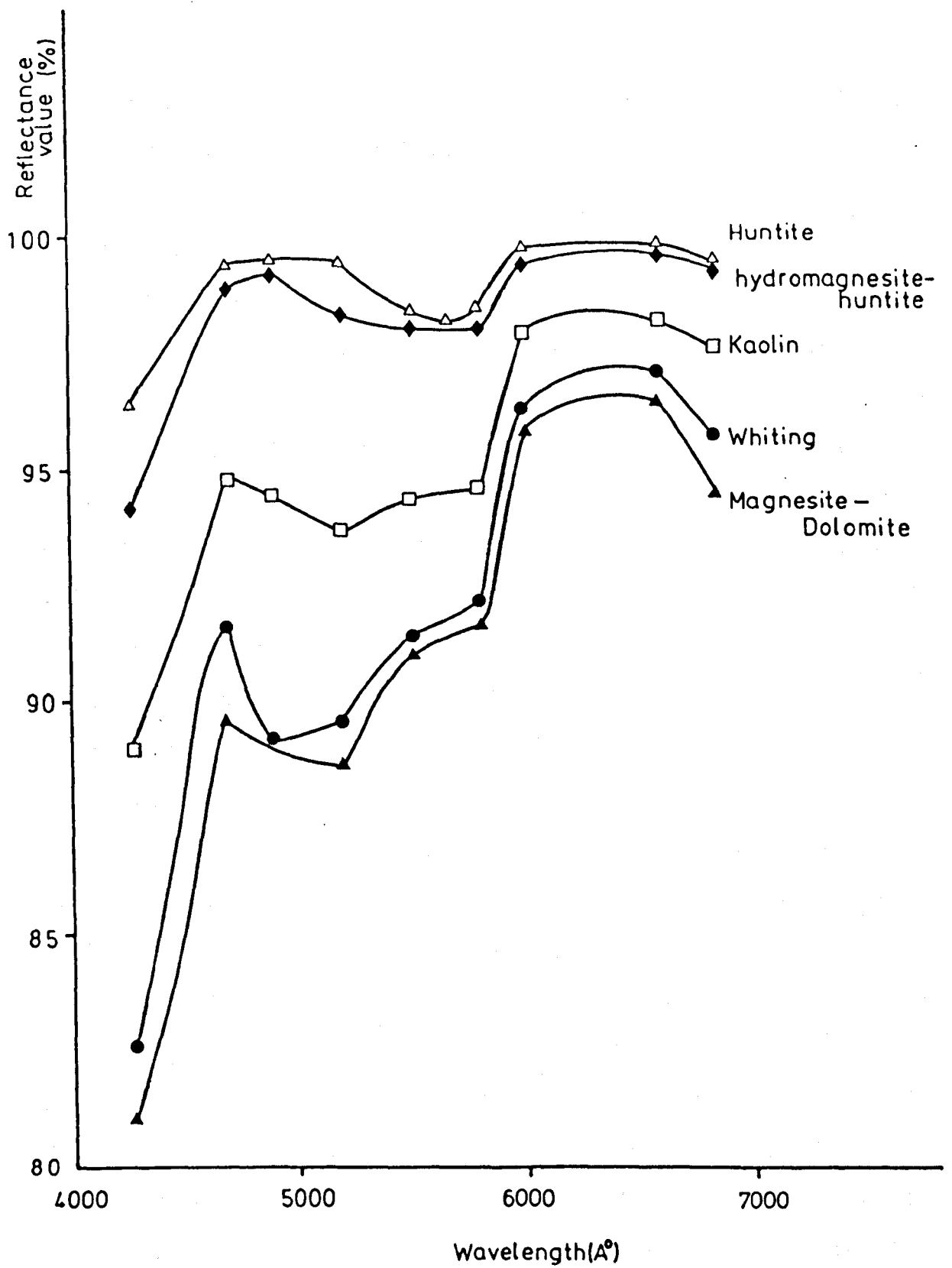


Figure 7.1 Spectro-photometric curves of studied materials

dolomite and nesquehonite. Products have different colours due to their bulk composition.

7.4.1 Microstructure

Detail information of microstructural investigations, experimental and instrumental conditions are presented in Chapter 4 and Appendix 5. The microstructure of dead burned products (1500°C, 96 hrs) of different types of huntite, a natural mixture of magnesite and dolomite and nesquehonite from Iran and a commercial natural mixture of hydromagnesite - huntite from Greece in both raw material and processed forms have been studied in both secondary and backscattered emission modes using two Cambridge scanning electron microscopes models 360 and 600. The scanning electron micrographs are presented in Plates 44-47.

The bulk chemical composition, of all samples are presented in Table 6.2. In comparison with magnesite the higher amount of CaO in huntite crystallizes as lime competing with periclase for available spaces which results in smaller periclase crystal growth (the average periclase crystalline size of dead burned huntite calcined at 1500°C for 96 hours are approximately of 5-10 microns in diameter which are only one fifth of the size of the average periclase crystals of dead burned magnesites calcined at similar condition). The microstructural observations indicate that the presence of Fe₂O₃ and to lesser extent SiO₂ promote the periclase crystalline growth (Chapter 4). The lack of these oxides in huntite also results smaller periclase grains in

dead burned huntite in compare with dead burned magnesite.

7.4.2 Description of microstructures

For the purpose of this study, different types of huntite, a natural mixture of magnesite - dolomite and nesquehonite from Iran, with two samples of natural mixture of hydromagnesite and huntite from Greece in both forms of raw material and processed have been calcined at 1500°C for 96 hours. The natural samples have a wide range of bulk chemical composition (Table 6.2) which effect directly the development of new phases, microstructural characteristic and industrial properties of products. The calcined products show different colour, due to their chemical composition (Plate 48). Polished blocks and the calcined surface of these materials were prepared for the purpose of microstructural and microprobe studies as described in Chapter 4 and App. 6.

Table 7.4 Phases determined in the calcined huntites, magnesite - dolomite, nesquehonite and hydromagnesite - huntite as determined by energy dispersive X-ray analysis (EDX)

Sample	Phases determined
Alluvial type huntite	M, C, C ₃ S, (SrO)
Vein type huntite	M, C ₃ MS ₂ , C, C ₃ S, C ₂ S
Nodular type huntite	M, C, (SrO)
Magnesite - dolomite	M, C, C ₃ S, C ₂ F, C ₂ S, C ₃ MS ₂
Hydromagnesite - huntite	M, C, C ₃ S
Nesquehonite	M, M ₂ S, CMS, C ₃ MS ₂ , C ₃ S

Where:

M = periclase, C = lime, C₃S = tricalcium silicate, SrO = strontia, C₃MS₂ = merwinite, C₂S = dicalcium silicate, C₂F = dicalcium ferrite, M₂S = forsterite and CMS = monticellite

7.4.2.1 Dead burned alluvial type huntite

The minerals identified in dead burned products of alluvial type huntite are presented in Table 7.4, and Plates 44-45 illustrate the microstructural observations in both secondary and backscattered modes. The periclase grains are very small (<10 microns) and are normally associated with lime (Plate 45c, d). SrO occurs substituted in periclase and lime and as separate phases within the products (Plate 45c, d).

In some parts of dead burned alluvial type huntite which contain higher percentage of SiO_2 and Fe_2O_3 , relatively larger periclase grains are present in association with tricalcium silicate. For example in Plate 44a larger periclase crystals are present in compare with Plate 44c.

7.4.2.2 Dead burned vein type huntite

Vein type huntite is a mixture of huntite and magnesite. The periclase grains are very small (<5 microns). The impurities are concentrated in certain areas. Larger periclase crystals (dark patches in the specimen) can be found in the parts of the dead burned sample where CaO is lacking (Plate 46a, b). The main phases identified in this sample are small and separated periclase grains (black), lime (white), and tricalcium silicate (grey) (Plate 46g).

7.4.2.3 Dead burned nodular type huntite

In this sample, the periclase grains are very small (<10 microns) which is probably due to crystallization of lime. The percentage of porosity is high and strontia (SrO) appears as a separate white patches (Plate 45g, h). Periclase and lime analysis contain few percentage of SrO as a solid solution.

7.4.2.4 Dead burned hydromagnesite - huntite from Greece

This sample contains hydromagnesite and huntite. In the dead burned product there are patches with only periclase and others with periclase and lime. The former patches presumably are a product from the hydromagnesite. The periclase crystals are also larger in these patches compared with those where lime is also present. Porosity is very high in this sample.

7.4.2.5 Dead burned magnesite - dolomite from Ablah deposit

This sample is a mixture of magnesite and dolomite. The chemical composition is presented in Table 6.2. In dead burned product, there are certain areas with larger periclase grains and small amounts of interstitial phases (Plate 47a) which are presumably a product from magnesite. Others with smaller periclase grains and higher amounts of matrix (lime, tricalcium silicate) phases are produced from dolomite (Plate 47b). The lower amount of CaO, higher percentage of MgO, Fe₂O₃ and SiO₂ are the responsible factors affecting to produce larger periclase grains from magnesite rich areas.

Most of periclase grains are separated by the matrix and there is no direct contact between periclase grains. The matrix phases are dicalcium silicate (white) and merwinite (grey). In the dolomite rich areas periclase grains are very small (around 10 microns) (Plate 47b) and the main impurity phases are lime (white) and tricalcium silicate (grey). Dicalcium ferrite rarely appears as very small white grains (Plate 47d).

7.4.2.6 Dead burned nesquehonite

The chemical composition is presented in table 6.2. In this sample the porosity is very high and the main phases are periclase (black), forsterite (grey) and monticellite (white). The mean periclase grain size is between 20-50 microns.

PLATE 44

Scanning electron micrographs of the surface of dead burned huntites, magnesite - dolomite and nesquehonite from Iran and Grecian hydromagnesite - huntite calcined at 1500°C for 96 hours.

- a) Dead burned alluvial type huntite containing an aggregate of periclase and tricalcium silicate. The periclase crystals appear more euhedral having rough surface with darker colour in compare with lighter and smooth surface tricalcium silicates. Lime also appear between the periclase grains. Periclase crystals are around 10-20 microns in diameter.
- b) Dead burned vein type huntite. This sample is a mixture of magnesite and huntite. The periclase grain sizes are around 5 microns. As it can be seen in this photograph, high concentrate of matrix (dicalcium silicate) (whiter) covered most of periclase grains (darker).
- c) Dead burned alluvial type huntite. The periclase grain sizes are around 5 microns, in some of the periclase grains, cubic cleavages are visible. Normally lime is developed between the periclase grains and most of periclase and limes contain few percentage of SrO as a solid solution.
- d) Dead burned nodular type huntite. Step like growth of periclase are visible. The periclase grain size is very small (around 10 microns). Lime as an impurity normally crystallise between the periclase grains. Periclase grains are well shaped in compare with the limes. Periclase grains contain few percentage of SrO as a solid solution.
- e) Closer view to the step like growth of periclase grains in dead burned alluvial type huntite.
- f) Dead burned Grecian hydromagnesite - huntite. This sample is a mixture of hydromagnesite and huntite with larger periclase grains (20-30 microns). The lighter interstitial grains are lime and tricalcium silicate. Cubic cleavage on the calcined surface of periclase grains are visible.
- g) Dead burned product of a natural mixture of magnesite and dolomite with a relatively large periclase grains together with a large amount of tricalcium silicate, dicalcium silicate and possibly lime separating the periclase.
- h) Dead burned nesquehonite containing coarse periclase grains and interstitial forsterite.

PLATE 44

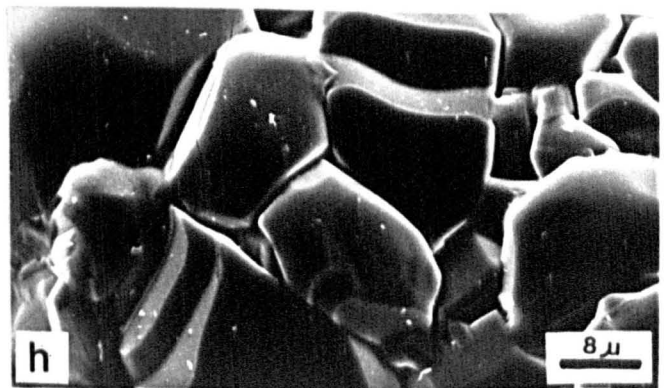
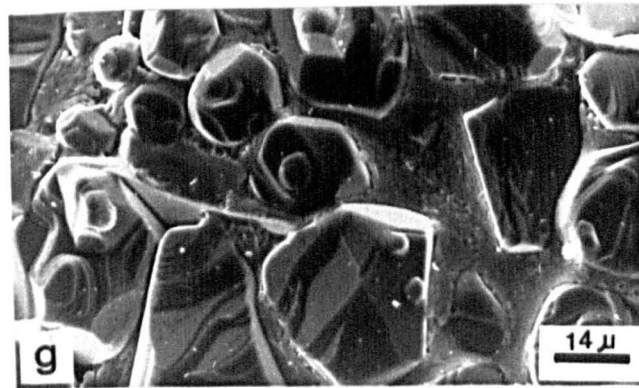
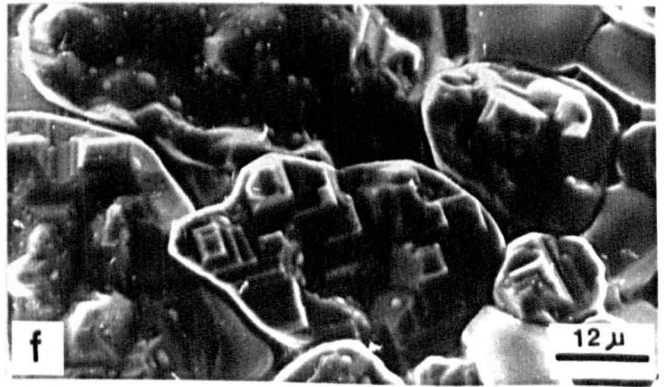
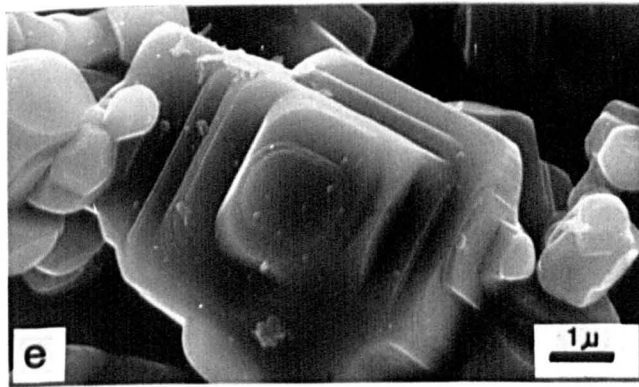
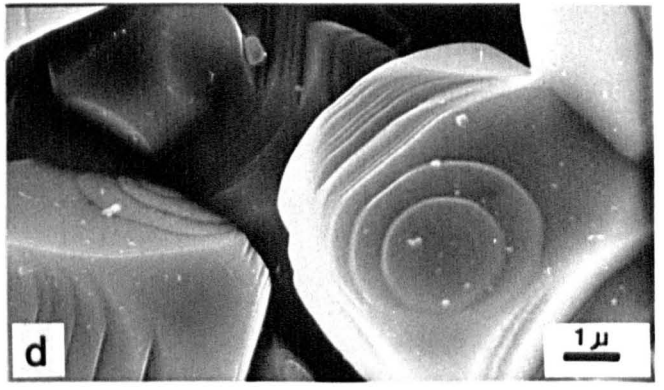
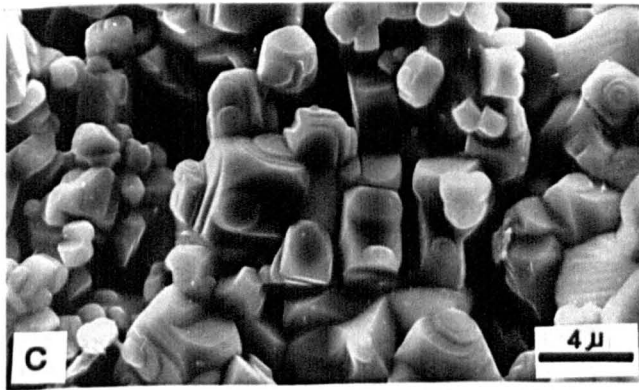
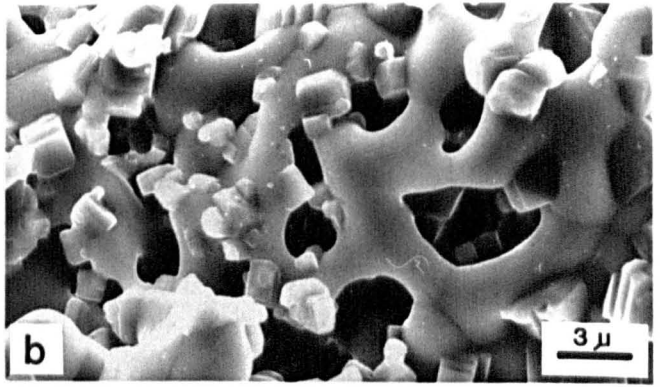
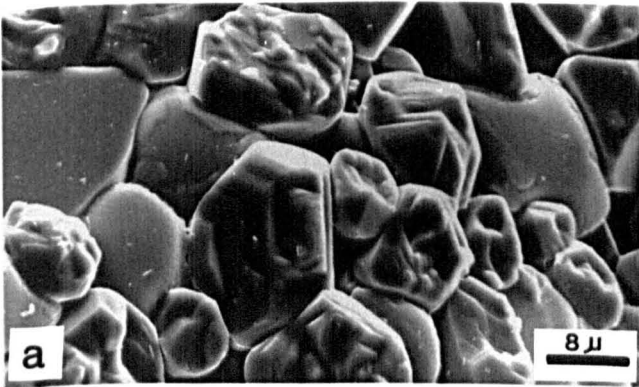


PLATE 45

Backscattered electron micrographs of dead burned huntite.

- a,b) Nodular type huntite with high percentage of porosity (black). The main phases are periclase (dark grey to black) and lime (white) which are intergrown. The grain sizes are very small. Strontia (SrO) occurs substituted in both periclase and lime crystals of dead burned nodular type huntite.
- c) Concentration of SrO (strontia) (very white) at the edge of dead burned alluvial type huntite. The main phases are periclase (black) and lime (white grey).
- d) Concentration of strontia rich area as a separate patches in dead burned alluvial type huntite. Other surrounding phases are lime (grey) and periclase (black) in a fine intergrowth. Grain sizes are small.
- e,f) Detail of strontia rich area in dead burned alluvial type huntite. The white area is SrO, grey is lime and the black grains are periclase. In dead burned alluvial type huntite SrO is detected within periclase and lime.
- g,h) Detail of strontia rich area which is intergrown with periclase (black) and lime (grey) in dead burned nodular type huntite.

PLATE 45

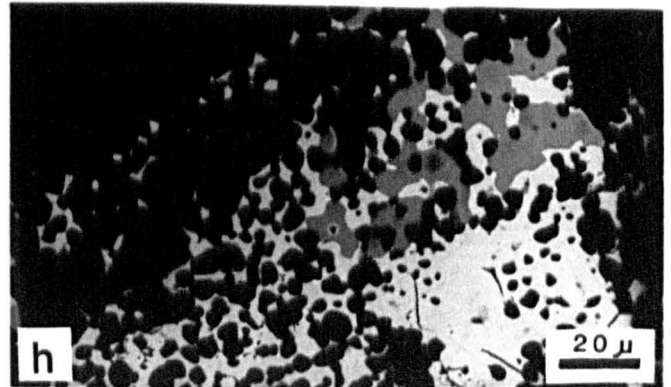
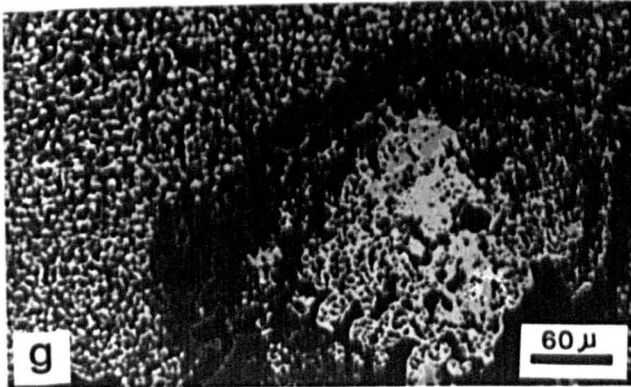
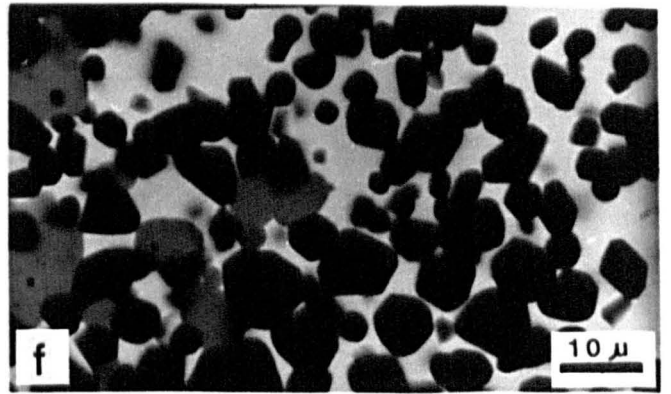
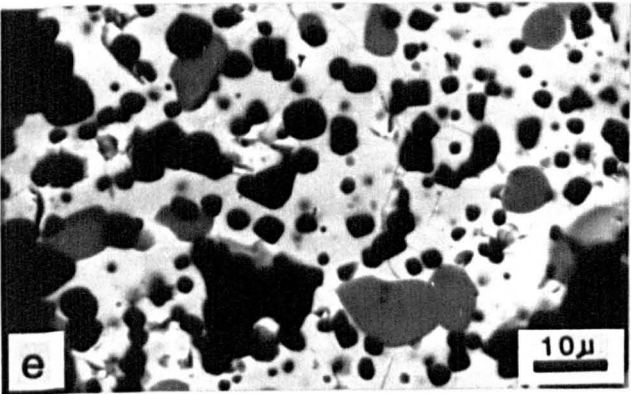
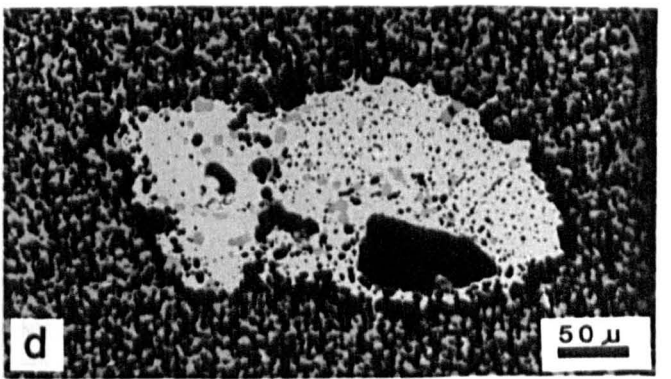
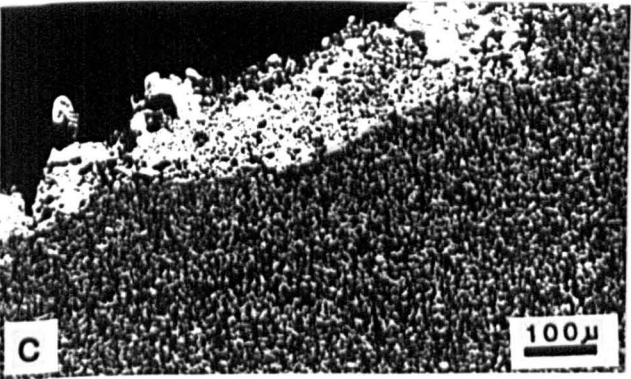
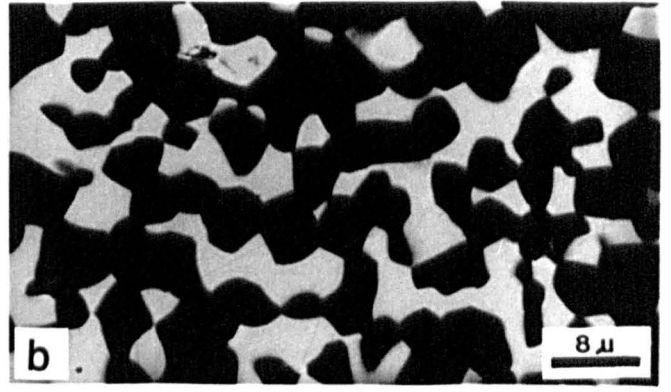
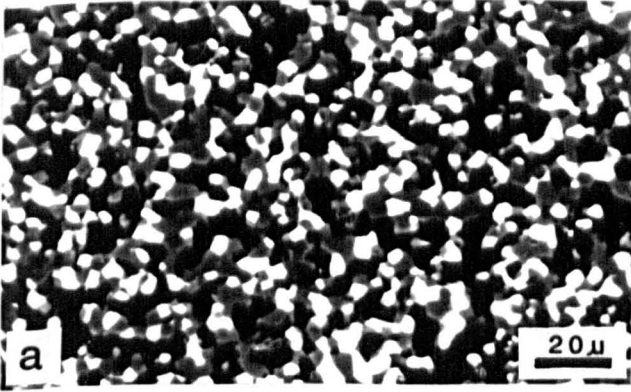


PLATE 46

Backscattered electron micrographs of dead burned huntite and a natural mixture of hydromagnesite and huntite.

a,b,c,d,e) Detail view of dead burned vein type huntite. This sample is a combination of magnesite and huntite, so the percentage of MgO is higher than other types of huntite. The grain sizes are small. Three main phases are identified, Periclase with some Ca solid solution (black), lime (white), and tricalcium silicate (grey). In Plate 46a in darker patches there are more periclase, and the whiter area has more tricalcium silicate.

f,g,h) Dead burned hydromagnesite - huntite from Greece. This sample is a natural mixture of hydromagnesite and huntite. Two main phases are identified, lime (white), and periclase (dark grey). The grain sizes are very small.

PLATE 46

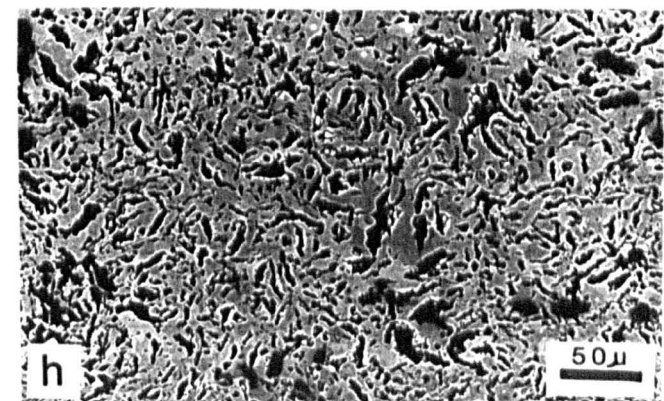
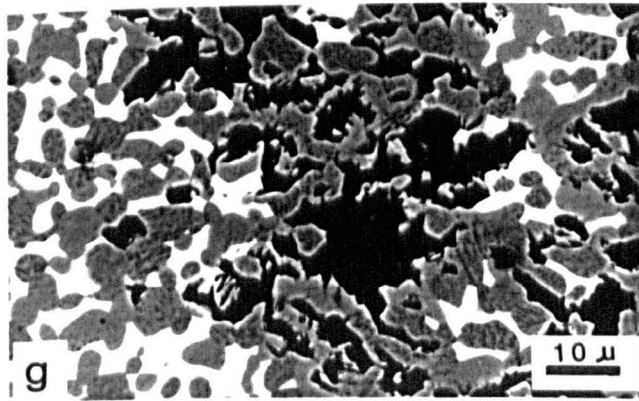
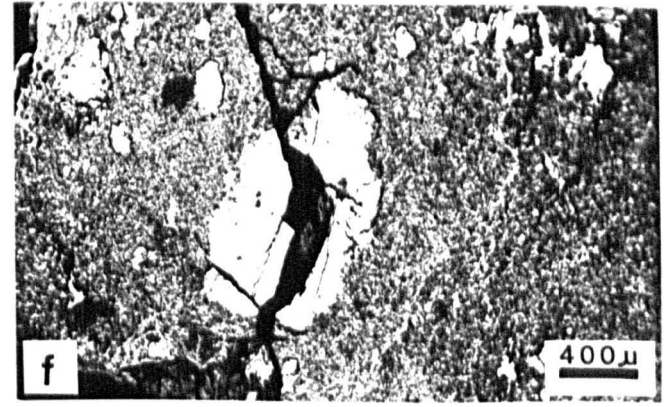
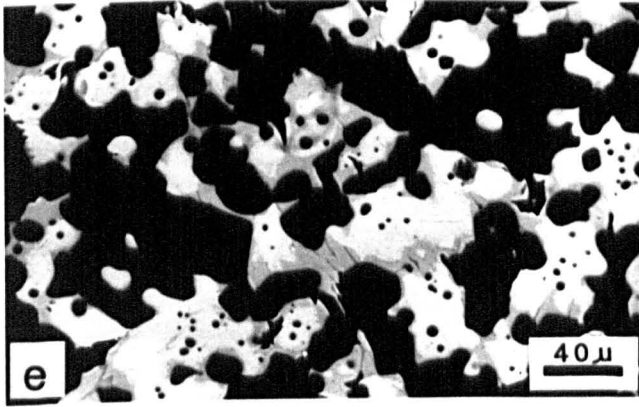
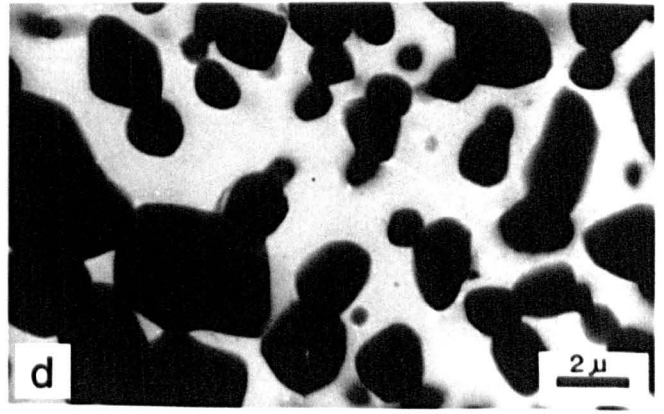
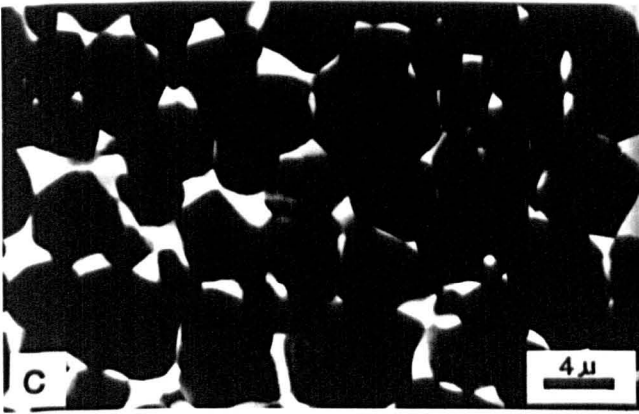
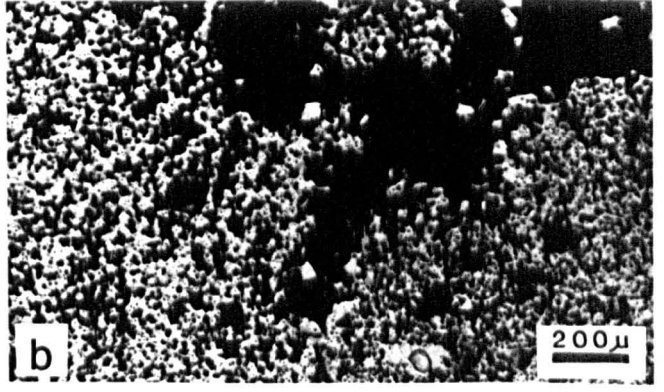
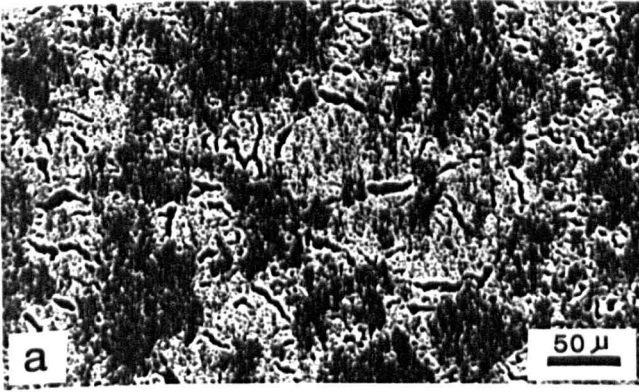


PLATE 47

Backscattered electron micrographs of dead burned magnesite - dolomite and nesquehonite.

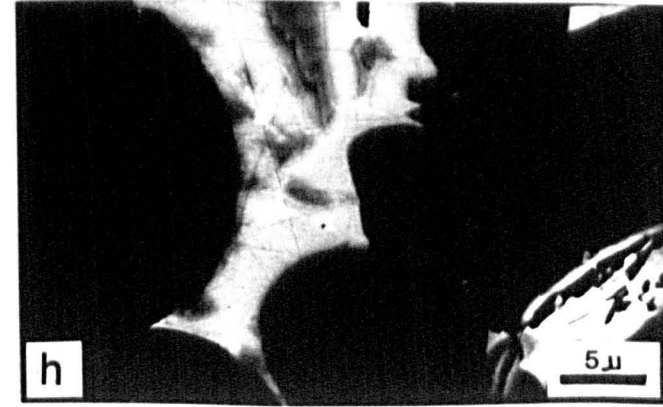
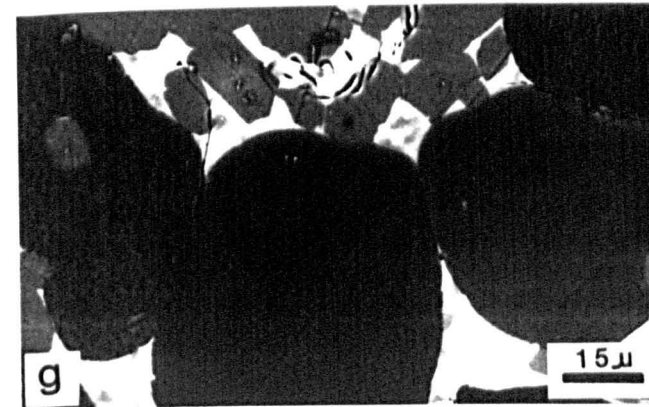
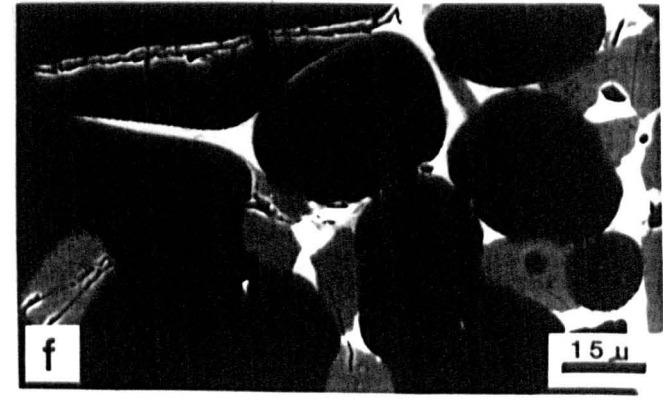
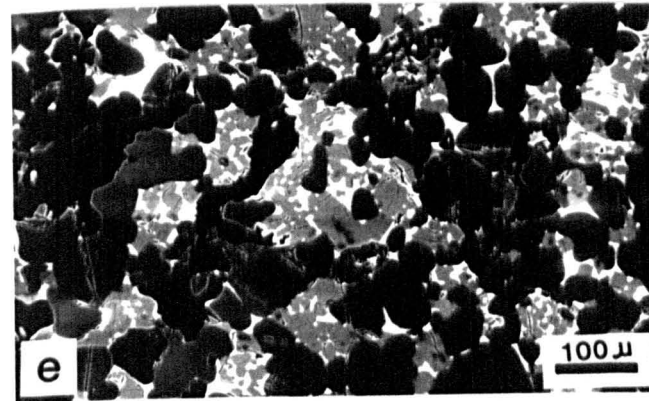
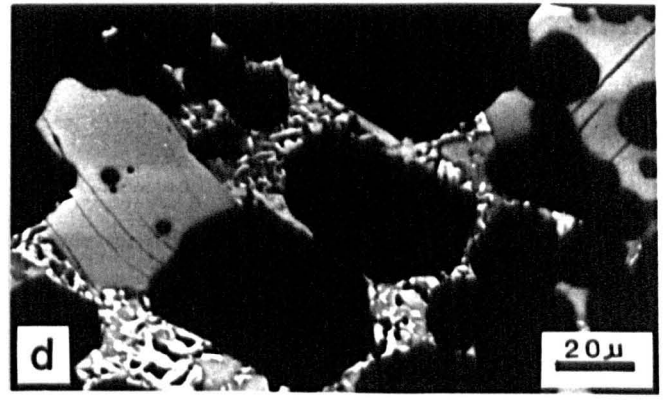
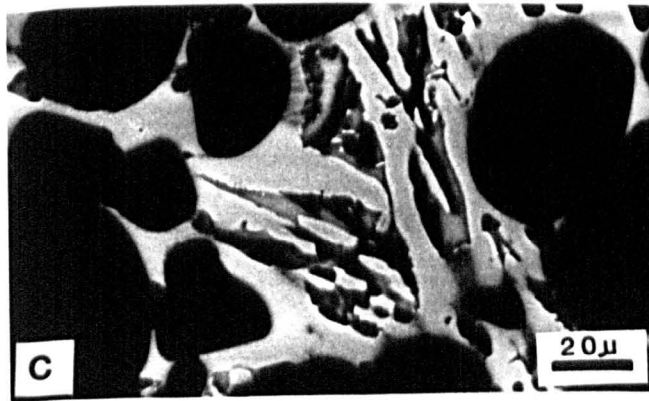
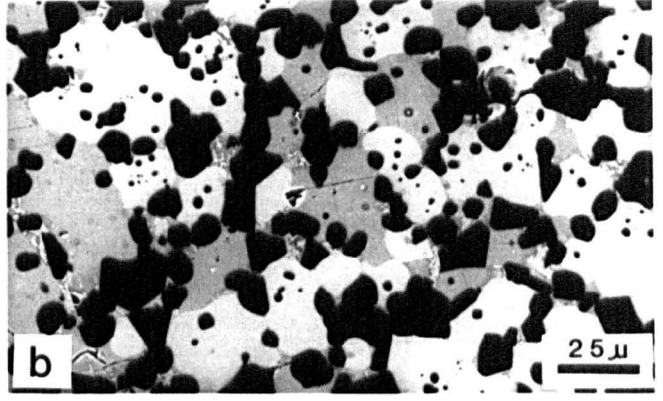
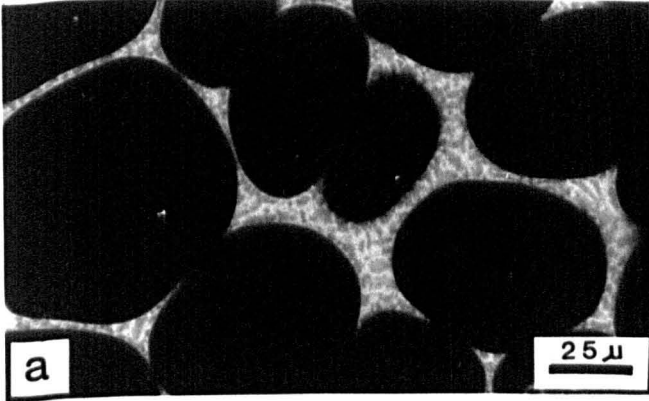
1. Dead burned magnesite - dolomite

- a) Common view to the rounded periclase grains without direct periclase grain contacts and the matrix. In matrix, two main phases identified. The white grains are tricalcium silicate and the grey part is merwinite.
- b) In this photograph three main phases identified, little rounded and black grains are Periclase with the minor amount of CaO and FeO as solid solution. White grains are lime, and the grey patches are tricalcium silicate.
- c) Three different phases are visible in this photograph, Periclase which appears like a black rounded and without direct grain contact. The whiter grey grains are tricalcium silicate, and the darker grey phase is merwinite. The grain sizes are large, but lime particles start to hydrate and as a result lots of holes are visible.
- d) Three main phases are present. Periclase with small amount of CaO solid solution (black), tricalcium silicate (grey) and dicalcium ferrite (very small white).

2. Dead burned nesquehonite

- e) Common view to the Dead burned nesquehonite, showing three main phases, periclase (very dark grey), forsterite (grey) and the white grains are monticellite. This sample is very porous.
- f,g) Closer view of the dead burned nesquehonite showing three main phases. Periclase (black), forsterite (grey) and the white matrix is monticellite.
- h) Detailed study of the matrix area, in this photograph the black grains are forsterite. The white area is tricalcium silicate containing minor amounts of Ti, Al and Fe impurities. The grey patches are monticellite and the little whiter parts inside the matrix area are ferrite.

PLATE 47



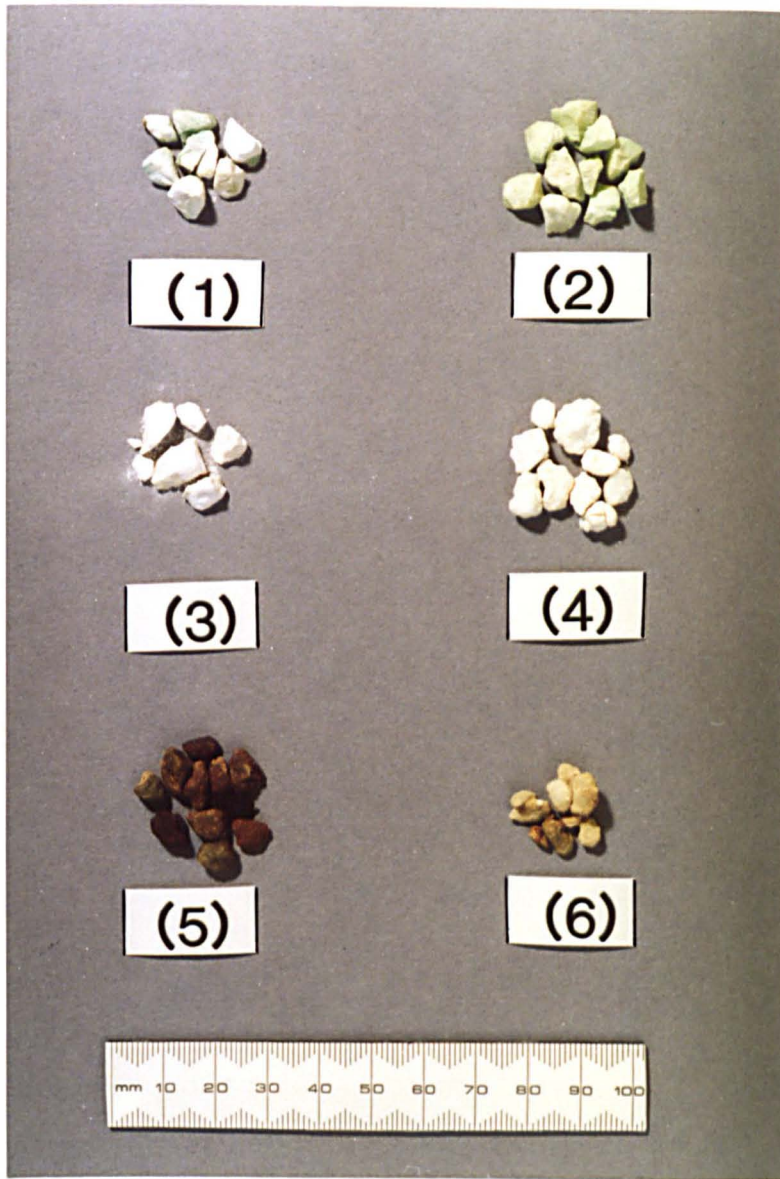


PLATE 48 A colour photograph of dead burned huntites (1-3), hydromagnesite-huntite (4), magnesite dolomite (5), and nesquehonite (6).

7.5 Mineralogy of dead burned huntite, hydromagnesite -
Huntite, magnesite - dolomite and nesquehonite as determined
by electron microprobe.

7.5.1 General

Huntite [$Mg_3Ca(CO_3)_4$], crystallizes in the trigonal system. The structure of huntite is similar to that of calcite, but the Mg and Ca ions are ordered. The unit cell has $a_x = 6.075 \text{ \AA}$, $a_y = 102^\circ 56'$; $a_z = 9.505 \text{ \AA}$, $c = 7.821 \text{ \AA}$ (for more detail see Deer et al. 1962, 1983).

7.5.2 Instrumental

Electron microprobe analysis of dead burned huntite was carried out on the three different types of huntite. Also samples of dead burned magnesite - dolomite, dead burned nesquehonite ($MgCO_3 \cdot 3H_2O$) and dead burned hydromagnesite - huntite from Greece have been analysed mostly for the purpose of comparison.

7.5.3 Results

The mineral phases identified in each dead burned huntite, magnesite - dolomite, hydromagnesite - huntite and nesquehonite, calcined at 1500°C for 96 hours are presented in Table 7.5. Complete electron microprobe analyses are given in Appendix 15.

As MgO , CaO and SiO_2 are the main components in these materials, the microprobe analyses are plotted on

CaO-MgO-SiO₂ triangular diagrams. Where other oxides are found in considerable amounts, the analyses are also plotted on appropriate diagrams, e.g. MgO-Al₂O₃-SiO₂ (Figure 7.3).

Table 7.5 The mineralogy of huntites, hydromagnesite - huntite, magnesite - dolomite and nesquehonite calcined at 1500°C for 96 hours as determined by electron microprobe.

Sample	Phases determined
Alluvial type huntite	M, C, (SrO)
Vein type huntite	M, C ₂ S, C ₃ MS ₂
Nodular type huntite	M, C, (SrO)
Magnesite - Dolomite	M, C, C ₃ S, C ₃ A
Nesquehonite	M, CMS, M ₂ S, SP
Hydromagnesite - Huntite	M, C

Where:

M = periclase, C = lime, SrO = strontia, C₂S = dicalcium silicate, C₃MS₂ = merwinite, C₃S = tricalcium silicate, C₃A = tricalcium aluminate, CMS = monticellite, M₂S = forsterite and SP = spinel

7.5.3.1 Dead burned alluvial type huntite

As can be seen from the CaO-MgO-SiO₂ diagram (Figure 7.2a), the main phases in this sample are periclase and lime. A few periclase analyses plot slightly away from the theoretical composition of periclase show some solid solution with lime as expected. Others with more than 5% CaO are of a mixed of the 2 phases. The lime analyses are concentrated in an area slightly away from theoretical composition towards periclase. This results from the presence of a small amount of Mg within the lime and indicates a minor amount of solid solution between lime and periclase. Other analyses lying on

the join between lime and periclase are mixed analyses of periclase and lime. Strontia (SrO) present in both lime and periclase which were impossible to quantify because of the lack of suitable standards. All analyses plotted on the line joining lime and silica contain strontia and seems to be a mixture of these three phases confirmed by CaO-SrO-SiO₂ diagram (Figure 7.3e).

SrO is found mainly in distinct patches. Some calcium is generally present substituting for strontium. The microprobe analyses containing strontia (SrO) are presented under the code beginning with S (Appendix 15).

7.5.3.2 Dead burned vein type huntite

The main phases as determined by electron microprobe in this sample are periclase, dicalcium silicate, and merwinite (Figure 7.2b). As it can be seen in CaO-MgO-SiO₂ diagram, dicalcium silicate analyses plot slightly away from its theoretical composition having a clear trend towards merwinite which is due to higher percentage of MgO in these analyses. This can be interpreted either as mixed phases between dicalcium silicate and merwinite, or possibly the existence of a phase called "T". Points plotting away from the theoretical composition of merwinite are mixed analyses.

7.5.3.3 Dead burned nodular type huntite

As can be seen from CaO-MgO-SiO₂ diagram (Figure 7.2c), the main phases present are periclase and lime. As SEM study also confirmed, Strontia (SrO) is also present as a separate

patches. Also SrO occurs substituted in lime and periclase. The lime analyses are concentrated in an area slightly away from its theoretical composition towards periclase. This results from the presence of a small amount of Mg within lime and indicates a minor amount of solid solution between periclase and lime. In contrast periclase analyses show closer composition together except in one spot. The analyses lying on the line joining periclase and lime are mixed. Analyses plotting on the line joining lime and silica contain strontia and seems to be a mixture of these phases, confirmed by CaO-SrO-SiO₂ diagram (Figure 7.3e).

7.5.3.4 Dead burned nesquehonite

The main phases determined in dead burned nesquehonite are periclase, forsterite and monticellite. As can be seen in CaO-MgO-SiO₂ diagram (Figure 7.2d), monticellite analyses which are slightly away from the theoretical point display fairly wide range of composition having a trend towards forsterite which is due to forsterite solid solution in monticellite. The forsterite analyses are concentrated in an area slightly away from the theoretical composition towards monticellite. This results from the presence of a small amount of Ca within the forsterite and indicates a minor amount of solid solution between monticellite and forsterite. Other analyses lying on the join between monticellite, forsterite and periclase are mixed analyses. Very small (<5^{um}) minor phases have been observed between the monticellite grains. According to MgO-Al₂O₃-SiO₂ diagram, the

analyses are probably of mixture of spinel and monticellite.

7.5.3.5 Dead burned magnesite - dolomite

As can be seen in CaO-MgO-SiO₂ diagram (Figure 7.2e), the main phases in this sample are periclase, lime and tricalcium silicate. Tricalcium silicate analyses are concentrated in an area slightly away from the theoretical composition towards periclase which is due to higher percentage of MgO in these analyses. The only point plotted on the join between periclase and tricalcium silicate is a mixed analysis. Lime analyses which are lying slightly away from the theoretical point display a clear trend towards periclase which is due to periclase solid solution in lime. Other points which are plotting around lime displaying a wide range of composition, are mixed analyses of two or three phases.

As indicated by SEM there are some small white and grey inclusions within the tricalcium silicates. These are too small to analyse individually but their major oxides are CaO, Al₂O₃, and FeO. They may possibly be ferrite and aluminates

7.5.3.6 Dead burned hydromagnesite - huntite

Many of the analyses of this sample (periclase and lime) as can be seen in CaO-MgO-SiO₂ diagram (Figure 7.2f) are of mixed phases. This is because of small grain size (<5 μ m) of the periclase and lime.

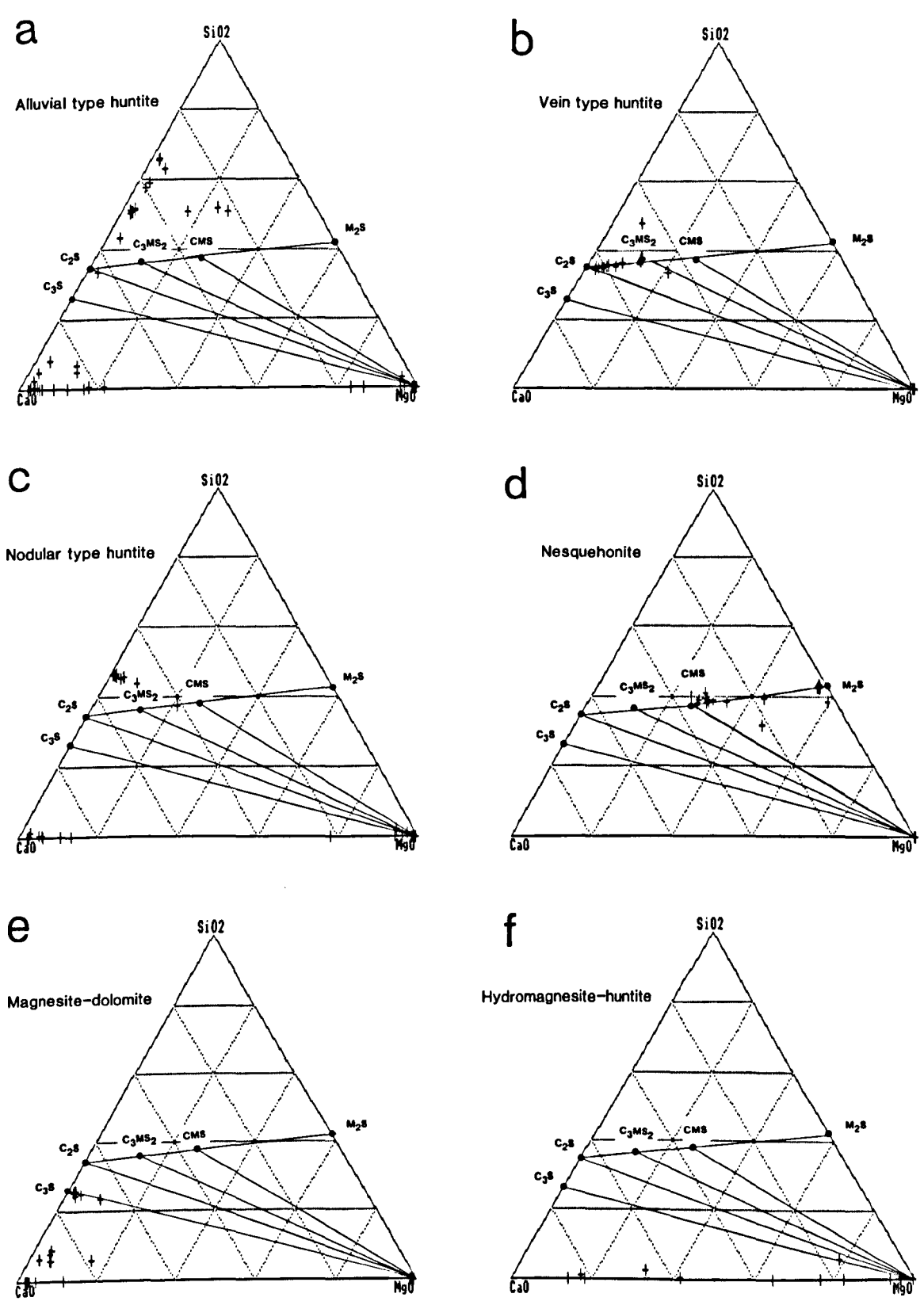


Figure 7.2 Triangular plots showing CaO-MgO-SiO₂ ratios of all microprobe analyses of dead burned huntite, nesquehonite, magnesite-dolomite and hydromagnesite-huntite (wt.%)

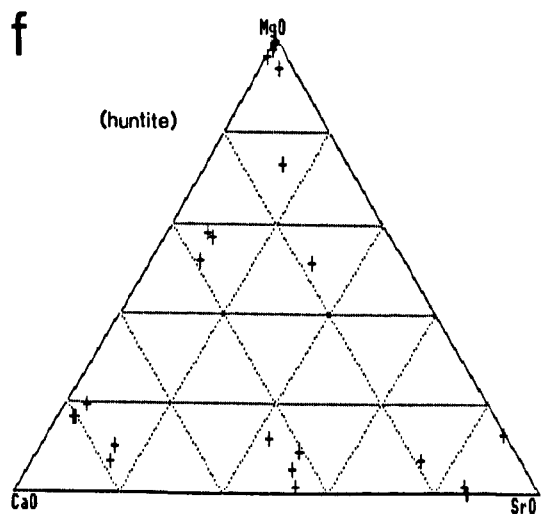
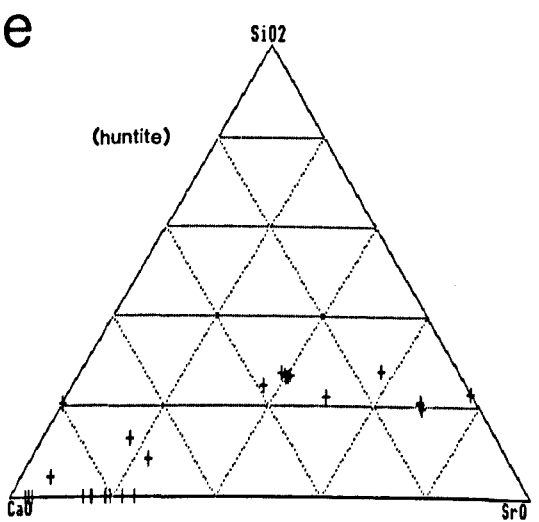
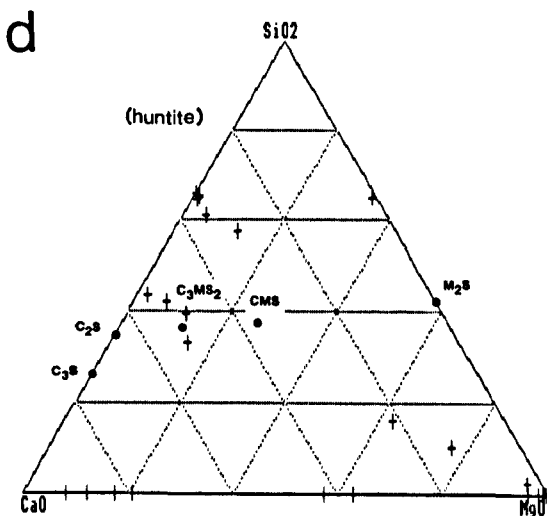
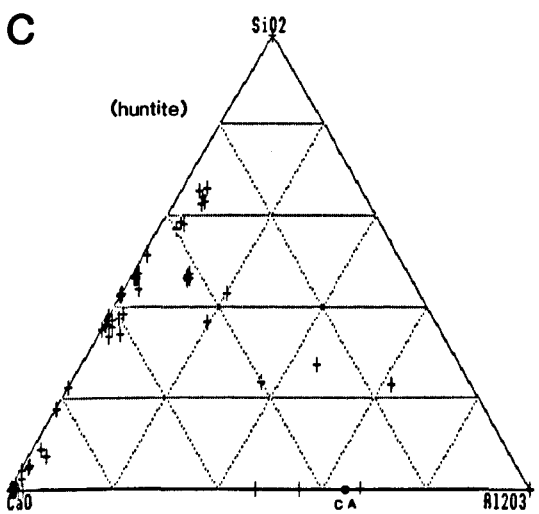
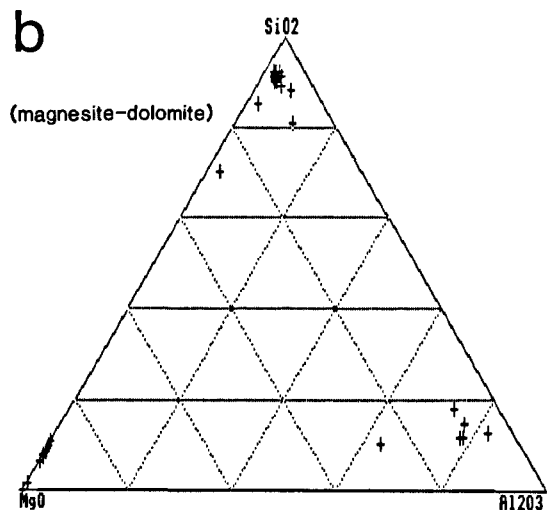
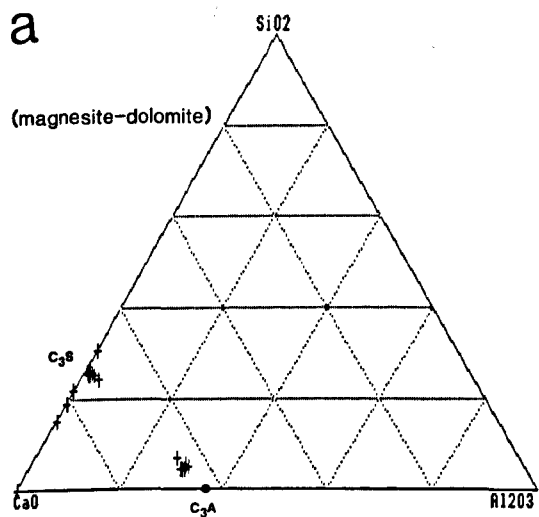


Figure 7.3 Triangular plots showing CaO-Al₂O₃-SiO₂, MgO-Al₂O₃-SiO₂, CaO-MgO-SiO₂, CaO-SrO-SiO₂ and CaO-SrO-MgO ratios of all microprobe analyses of dead burned huntite and magnesite-dolomite (wt.%)

7.6 Mineral chemistry

7.6.1 Periclase

Periclase analyses determined in dead burned products of samples, huntite, hydromagnesite - huntite, magnesite - dolomite, and nesquehonite are presented in Appendix 15 under the code beginning with P. A selection of the representative periclase analyses are given in Table 7.6.

Mineral formula of periclase is calculated on the basis of 1 oxygen.

As can be seen from Figure 7.4a, CaO is the most frequently present constituent in periclase in most of the samples. SiO₂, Al₂O₃ and FeO is also present, but to a lesser extent. SrO is only detected within periclase of dead burned alluvial and nodular type huntites. The cation relationships in periclase are presented in Figure 7.4b and 7.4c.

7.6.1.1 Results

7.6.1.1.a CaO in periclase

The electron microprobe analysis of periclase in different samples show varying amounts of CaO. Some analyses contain no CaO (i.e. are below detection limit), maximum 1.59% CaO in periclase have been detected in these analyses.

CaO in periclase increases steadily with the increase in the CaO/SiO₂ ratios of the bulk analyses. The amount of FeO in periclase in the dead burned specimens is found to rise with the rise of FeO content of bulk analyses. SiO₂ and Al₂O₃

Table 7.6 A selection of periclase analyses as determined by EPMA in dead burned huntite

Sample Code SPOT	AH-C PCAH 18	AH-C PCAH 20	AH-C PCAH 21	AH-C PCAH 24	VH-B PCVH 1	VH-B PCVH 2	VH-B PMVH 3	VH-B PCVH 4	VH-B PMVH 5	VH-B PCVH 6
SiO2	n.d.	n.d.	n.d.	0.23	0.66	n.d.	n.d.	n.d.	0.25	n.d.
TiO2	n.d.	n.d.	n.d.	n.d.	n.d.	n.d.	n.d.	n.d.	n.d.	n.d.
Al2O3	n.d.	n.d.	n.d.	n.d.	0.35	0.49	0.41	0.45	0.41	0.34
Cr2O3	n.d.	n.d.	n.d.	n.d.	n.d.	n.d.	n.d.	n.d.	n.d.	n.d.
FeO	n.d.	n.d.	n.d.	n.d.	n.d.	n.d.	n.d.	n.d.	n.d.	n.d.
MnO	n.d.	n.d.	n.d.	n.d.	n.d.	n.d.	n.d.	n.d.	n.d.	n.d.
MgO	98.10	100.43	98.23	98.10	98.01	100.87	99.86	99.92	99.10	99.22
CaO	0.82	0.82	0.80	0.79	0.79	n.d.	n.d.	0.22	0.25	n.d.
K2O	n.d.	n.d.	n.d.	n.d.	n.d.	n.d.	n.d.	n.d.	n.d.	n.d.
TOTAL	98.92	101.25	99.03	99.12	99.81	101.36	100.27	100.59	100.01	99.56

Cations on the basis of 1 oxygen

Si	0.00	0.00	0.00	0.00	0.00	0.00	0.00	0.00	0.00	0.00
Fe2	0.00	0.00	0.00	0.00	0.00	0.00	0.00	0.00	0.00	0.00
Mn	0.00	0.00	0.00	0.00	0.00	0.00	0.00	0.00	0.00	0.00
Mg	0.99	0.99	0.99	0.99	0.98	0.99	1.00	0.99	0.99	1.00
Ca	0.01	0.01	0.01	0.01	0.01	0.00	0.00	0.00	0.00	0.00
Al	0.00	0.00	0.00	0.00	0.00	0.00	0.00	0.00	0.00	0.00

Sample Code SPOT	VH-B PCVH 13	VH-B PCVH 22	VH-B PMVH 23	NH-A PCNH 12	NH-A PCNH 12	NH-A PCNH 14	NH-A PCNH 22	AMD-A PCMD 12	AMD-A PMMD 13	AMD-A PCMD 17
SiO2	0.23	n.d.	n.d.	n.d.	n.d.	n.d.	1.12	n.d.	0.37	0.24
TiO2	n.d.	n.d.	n.d.							
Al2O3	0.61	n.d.	0.50	n.d.	n.d.	n.d.	n.d.	n.d.	n.d.	n.d.
Cr2O3	n.d.	n.d.	n.d.							
FeO	n.d.	n.d.	0.29	0.27	0.27	0.27	0.36	0.45	0.39	0.70
MnO	n.d.	0.27	n.d.							
MgO	98.50	98.82	98.52	97.98	99.42	98.39	95.92	96.65	96.52	97.05
CaO	0.15	0.20	0.40	0.65	0.70	0.75	2.05	1.03	1.32	1.01
K2O	n.d.	n.d.	n.d.							
TOTAL	99.49	99.02	99.71	98.90	100.39	99.41	99.45	98.13	98.87	99.00

Cations on the basis of 1 oxygen

Si	0.00	0.00	0.00	0.00	0.00	0.00	0.01	0.00	0.00	0.00
Fe2	0.00	0.00	0.00	0.00	0.00	0.00	0.00	0.00	0.00	0.00
Mn	0.00	0.00	0.00	0.00	0.00	0.00	0.00	0.00	0.00	0.00
Mg	0.99	1.00	0.99	0.99	0.99	0.99	0.97	0.99	0.98	0.99
Ca	0.00	0.00	0.00	0.00	0.01	0.01	0.01	0.01	0.01	0.01
Al	0.00	0.00	0.00	0.00	0.00	0.00	0.00	0.00	0.00	0.00

are less frequently found in periclase. Cation relationships are given in Figure 7.4.

7.6.1.1.b FeO in periclase

FeO like CaO, is frequently present in periclase, but it is present in a comparatively narrow range. The amount of FeO in most of analyses is either below detection limit, or less than 0.7%. A maximum of 1.17% FeO have been detected. The highest FeO values in periclase were observed in dead burned nesquehonite. The microprobe analyses show that the FeO content of periclase increases as the FeO content of bulk composition increases.

7.6.1.1.c Al₂O₃ in periclase

Al₂O₃, in general, is very rarely detected in periclase in these samples. It varies from below the detection limit to a maximum of 1.29% in nesquehonite. It is possible that high values of Al₂O₃ resulted from the presence of spinel.

7.6.1.1.d SiO₂ in periclase

SiO₂ is detected from below detection limit up to a maximum of around 1%.

Comparatively high values of SiO₂ in periclase are most probably mixed from other silicates.

7.6.2 Lime

Lime analyses, as determined by the electron microprobe, are plotted on the CaO-MgO-SiO₂ diagrams as wt.% and

presented in Figure 7.4. All analyses are presented in Appendix 15 under the code beginning with L. A selection of the representative lime analyses are given in Table 7.7.

Mineral formula of lime is calculated on the basis of one oxygen. Cation relationships in lime are presented in Figure 7.4. The low total of the analyses are due to hydration of the surface. Previous experience of others (P.W. Scott personal communication) is that analyses of lime with 100% total are not possible to achieve.

MgO and SiO₂ are the most frequently oxides present in lime, Al₂O₃ and FeO are occasionally present.

7.6.2.1 Results

7.6.2.1.a MgO in Lime

The electron microprobe analyses of lime in each sample show various amount of MgO (see Appendix 15). As it can be seen from Figure 7.4d, 2-3 percent MgO exist as solid solution in lime (majority of analyses concentrate in an area around 2% MgO). The higher percentages of MgO in some cases are due to mixed analyses.

7.6.2.1.b SiO₂ in lime

SiO₂ is detected in low percentages and varies considerably. The highest values of SiO₂ in these samples are most probably the result of silicate contaminations (mixed analyses).

Table 7.7 A selection of lime analyses as determined by EPMA in dead burned huntite

Sample Code SPOT	AH-C LCAH 14	AH-C LCAH 17	AH-C LCAH 19	AH-C LCAH 23	NH-A LCNH 4	NH-A LCNH 8	NH-A LCNH 9	NH-A LCNH 10	NH-A LMNH 11	NH-A LCNH 17
SiO2	0.43	0.60	0.37	n.d.	0.24	0.68	n.d.	0.29	1.53	n.d.
TiO2	n.d.	n.d.	n.d.	n.d.	n.d.	n.d.	n.d.	n.d.	n.d.	n.d.
Al2O3	0.44	0.60	0.58	0.59	n.d.	0.20	0.20	0.34	0.33	0.26
Cr2O3	n.d.	n.d.	n.d.	n.d.	n.d.	n.d.	n.d.	n.d.	n.d.	n.d.
FeO	n.d.	n.d.	n.d.	n.d.	n.d.	n.d.	n.d.	n.d.	n.d.	n.d.
MnO	n.d.	n.d.	n.d.	n.d.	n.d.	n.d.	n.d.	n.d.	n.d.	n.d.
MgO	4.90	2.23	2.12	1.95	2.36	2.11	2.13	2.33	2.19	2.29
CaO	84.27	85.32	85.92	86.24	91.43	91.38	92.16	92.64	90.47	92.66
K2O	n.d.	n.d.	n.d.	n.d.	n.d.	n.d.	n.d.	n.d.	n.d.	n.d.
TOTAL	90.04	88.75	88.99	88.78	94.03	94.37	94.49	95.60	94.52	95.21

Cations on the basis of 1 oxygen

Si	0.00	0.01	0.00	0.00	0.00	0.01	0.00	0.00	0.01	0.00
Fe2	0.00	0.00	0.00	0.00	0.00	0.00	0.00	0.00	0.00	0.00
Mn	0.00	0.00	0.00	0.00	0.00	0.00	0.00	0.00	0.00	0.00
Mg	0.07	0.03	0.03	0.03	0.03	0.03	0.03	0.03	0.03	0.03
Ca	0.91	0.94	0.95	0.96	0.96	0.95	0.97	0.96	0.93	0.96
Al	0.01	0.01	0.01	0.01	0.00	0.00	0.00	0.00	0.00	0.00

Sample Code SPOT	NH-A LCNH 18	NH-A LCNH 19	NH-A LCNH 20	NH-A LMNH 21	NH-A LCNH 34	AMD-A LCMD 8	AMD-A LMMD 9	AMD-A LCMD 16	AMD-A LCMD 18	AMD-A LMMD 19
SiO2	n.d.	0.68	0.64	0.82	n.d.	0.19	0.20	0.20	0.19	n.d.
TiO2	n.d.	n.d.	n.d.							
Al2O3	0.21	n.d.	0.40	0.26	0.30	n.d.	n.d.	n.d.	n.d.	n.d.
Cr2O3	n.d.	n.d.	n.d.							
FeO	n.d.	n.d.	n.d.	n.d.	n.d.	n.d.	0.36	n.d.	0.37	0.32
MnO	n.d.	n.d.	0.31							
MgO	2.06	4.52	5.33	2.16	5.70	2.19	2.17	2.82	2.26	2.31
CaO	32.12	90.05	89.83	92.01	87.14	95.42	94.50	95.45	95.79	94.40
K2O	n.d.	n.d.	n.d.							
TOTAL	34.39	95.25	96.20	95.25	93.14	97.80	97.23	98.47	98.61	97.34

Cations on the basis of 1 oxygen

Si	0.00	0.01	0.01	0.01	0.00	0.00	0.00	0.00	0.00	0.00
Fe2	0.00	0.00	0.00	0.00	0.00	0.00	0.00	0.00	0.00	0.00
Mn	0.00	0.00	0.00	0.00	0.00	0.00	0.00	0.00	0.00	0.00
Mg	0.08	0.06	0.07	0.03	0.08	0.03	0.03	0.04	0.03	0.03
Ca	0.91	0.92	0.91	0.95	0.91	0.97	0.96	0.96	0.96	0.96
Al	0.01	0.00	0.00	0.00	0.00	0.00	0.00	0.00	0.00	0.00

Sample Code SPOT	AMD-A LCMD 20	AMD-A LCMD 23	AMD-A LCMD 29	AMD-A LMMD 30	AMD-A LCMD 31	AMD-A LMMD 32	AMD-B LCMD 18	AMD-B LCMD 19	AMD-B LCMD 24
SiO2	n.d.	0.26	n.d.	n.d.	0.21	0.23	n.d.	n.d.	0.29
TiO2	n.d.								
Al2O3	n.d.								
Cr2O3	n.d.								
FeO	n.d.								
MnO	n.d.								
MgO	2.36	2.40	2.24	2.46	2.14	2.27	1.93	4.36	2.36
CaO	94.11	96.17	98.46	97.16	95.62	94.60	93.37	91.69	93.69
K2O	n.d.								
TOTAL	96.47	98.83	100.70	99.62	97.97	97.10	95.30	96.05	96.34

Cations on the basis of 1 oxygen

Si	0.00	0.00	0.00	0.00	0.00	0.00	0.00	0.00	0.00
Fe2	0.00	0.00	0.00	0.00	0.00	0.00	0.00	0.00	0.00
Mn	0.00	0.00	0.00	0.00	0.00	0.00	0.00	0.00	0.00
Mg	0.03	0.03	0.03	0.03	0.03	0.03	0.03	0.06	0.03
Ca	0.97	0.96	0.97	0.97	0.97	0.96	0.97	0.94	0.96
Al	0.00	0.00	0.00	0.00	0.00	0.00	0.00	0.00	0.00

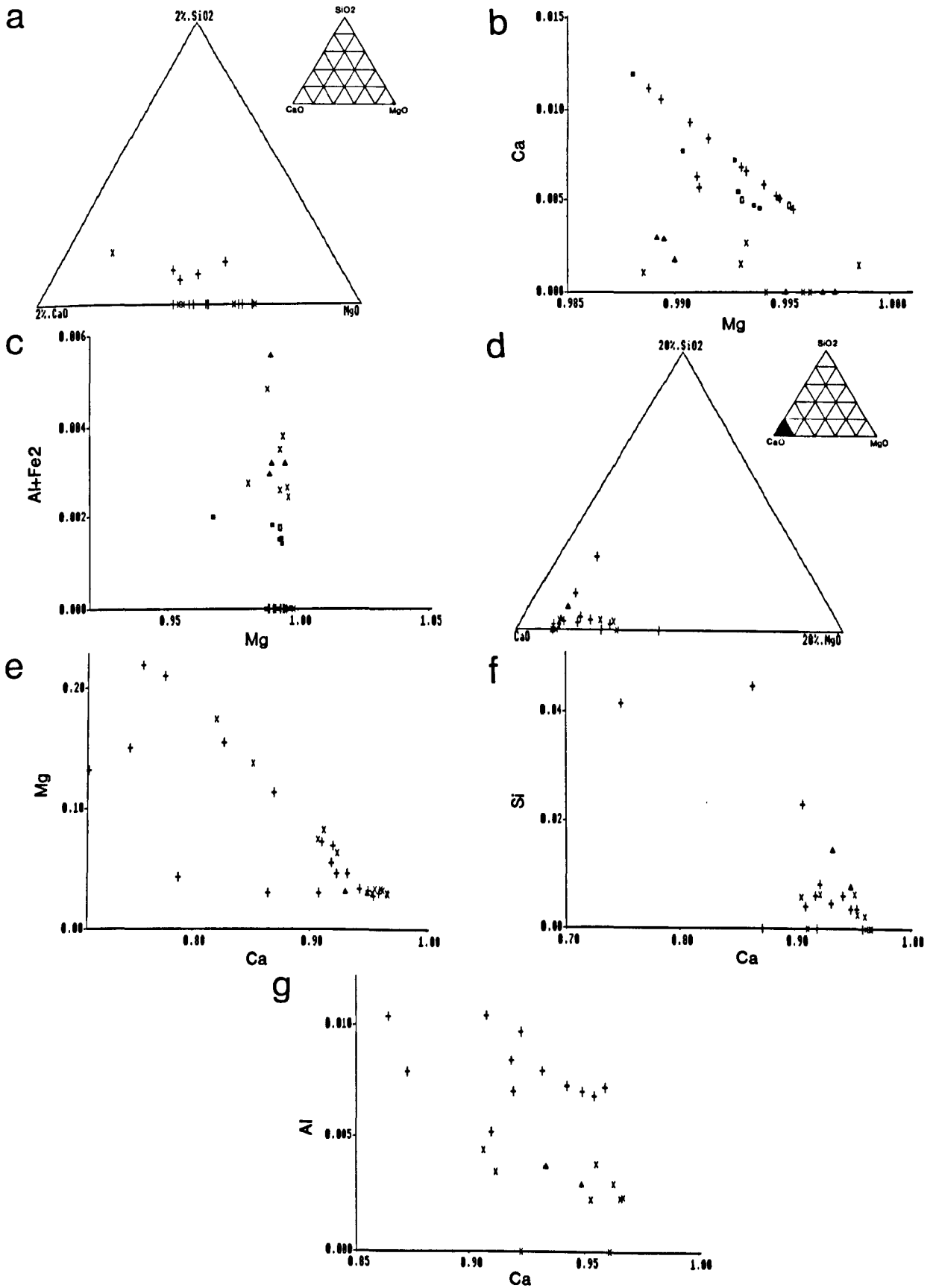


Figure 7.4 Triangular plots (wt.%) and cation relationships of periclase (a, b, c) and lime (d, e, f, g)

7.6.2.1.c Al₂O₃ and FeO in lime

Al₂O₃ and FeO, in general are frequently detected in these samples. Al₂O₃ in huntites varies from below detection limit to a maximum of 0.79% in alluvial type huntite. However FeO has been detected in much lesser amount and only in Ablah magnesite - dolomite.

The relationship between the cations are shown in Figure 7.4e, f and g. There is an inverse relationship between Ca and Mg. Si shows no significant variation when plotted against Mg and Ca.

Fe and Al are the minor cations which are occasionally present. There is no definite relationship between these three minor cations against Mg or Ca.

7.6.3 Monticellite

Monticellite is present only in Nesquehonite. The monticellite analyses are plotted on the CaO-MgO-SiO₂ diagram (Figure 7.5a). The monticellite analyses show a wide composition range with a clear trend towards forsterite. The mineral formula of monticellite analyses are calculated on the basis of four oxygens. Complete sets of analyses with their mineral formula are given in Table 7.8 under the code beginning with M.

There is an inverse relationship between Mg and Ca (Figure 7.5b). Most of the analyses are higher in Mg and lower in Ca than the theoretical monticellite. These are the analyses which lie between monticellite and forsterite.

Table 7.8 Monticellite analyses as determined by EPMA in dead burned Nesquehonite

Sample Code	NES-A MCNA	NES-A MCNA	NES-C MCNC	NES-C MCNC	NES-C MCNC
SPOT	12	14	11	12	16
SiO2	38.33	38.12	35.54	37.31	37.94
TiO2	0.46	0.39	0.60	0.24	0.27
Al2O3	0.72	0.94	2.83	0.32	0.75
Cr2O3	n.d.	n.d.	n.d.	n.d.	n.d.
FeO	n.d.	n.d.	0.64	n.d.	0.44
MnO	n.d.	n.d.	n.d.	n.d.	n.d.
MgO	27.52	28.65	25.51	28.62	29.61
CaO	31.13	30.99	32.51	30.22	29.27
K2O	n.d.	n.d.	n.d.	n.d.	n.d.
TOTAL	98.16	99.09	97.63	96.71	98.28

Cations on the basis of 4 oxygens

Si	1.01	0.99	0.95	0.99	0.99
Al	0.02	0.03	0.09	0.01	0.02
Fe2	0.00	0.00	0.01	0.00	0.01
Mn	0.00	0.00	0.00	0.00	0.00
Mg	1.08	1.11	1.02	1.14	1.15
Ca	0.88	0.86	0.93	0.86	0.82

Si shows no significant variation when plotted against Mg and Ca. (for more detail about monticellite see Chapter 4, section 4.6.2).

7.6.4 Forsterite

Forsterite is present only in calcined nesquehonite and is plotted on the system CaO-MgO-SiO_2 as wt.% (Figure 7.5c). (more detail about forsterite are given in Chapter 4, section 4.6.3). The forsterite analyses are recalculated on the basis of four oxygens and the complete analyses with their mineral formula are presented in Table 7.9 under the code beginning with F. There is an inverse relationship between Mg and Ca, but Si is almost constant (Figure 7.5d). Al_2O_3 has been found in one analysis.

7.6.5 Merwinite

Merwinite has been found in ^{Calcined} vein type huntite. The microprobe analyses of merwinite are plotted on the CaO-MgO-SiO_2 diagram as wt.% which is given in Figure 7.5e Complete microprobe analyses of merwinite are given in Table 7.10 and Appendix 15 under the code beginning with "MR". Al_2O_3 and FeO are occasionally present. The cations calculated on the basis of eight oxygens. There is an inverse relationship between Mg and Ca and Si.

7.6.6 Dicalcium silicate

Dicalcium silicate has been found in calcined vein type huntite which was originally a mixture of huntite and

Table 7.9 Forsterite analyses as determined by EPMA in dead burned nesquehonite

Sample Code SPOT	NES-A FCNA 6	NES-A FMNA 7	NES-A FCNA 8	NES-A FCNA 9	NES-A FCNA 10	NES-A FCNA 11	NES-C FCNC 1	NES-C FCNC 3	NES-C FCNC 4	NES-C FCNC 7
SiO2	37.47	41.96	41.89	42.24	42.14	42.37	41.65	41.55	43.12	41.80
TiO2	n.d.	n.d.	n.d.	n.d.	n.d.	n.d.	n.d.	n.d.	n.d.	n.d.
Al2O3	0.42	n.d.	n.d.	n.d.	n.d.	n.d.	n.d.	n.d.	n.d.	0.00
Cr2O3	n.d.	n.d.	n.d.	n.d.	n.d.	n.d.	n.d.	n.d.	n.d.	n.d.
FeO	n.d.	n.d.	n.d.	n.d.	n.d.	n.d.	n.d.	n.d.	n.d.	n.d.
MnO	n.d.	n.d.	n.d.	n.d.	n.d.	n.d.	n.d.	n.d.	n.d.	n.d.
MgO	57.76	53.49	54.66	54.54	54.66	53.92	53.34	53.36	54.62	53.82
CaO	2.17	2.22	1.98	1.82	2.29	2.16	2.53	2.09	1.77	1.87
K2O	n.d.	n.d.	n.d.	n.d.	n.d.	n.d.	n.d.	n.d.	n.d.	n.d.
TOTAL	97.82	97.67	98.53	98.60	99.09	98.45	97.52	97.00	99.51	97.49
Cations on the basis of 4 oxygens										
Si	0.91	1.01	1.00	1.01	1.00	1.01	1.01	1.01	1.02	1.01
Al	0.01	0.00	0.00	0.00	0.00	0.00	0.00	0.00	0.00	0.00
Fe2	0.00	0.00	0.00	0.00	0.00	0.00	0.00	0.00	0.00	0.00
Mn	0.00	0.00	0.00	0.00	0.00	0.00	0.00	0.00	0.00	0.00
Mg	2.10	1.92	1.95	1.94	1.94	1.92	1.92	1.93	1.92	1.94
Ca	0.06	0.06	0.05	0.05	0.06	0.06	0.07	0.05	0.04	0.05

Table 7.10 Merwinite analyses as determined by EPMA in dead burned huntite

Sample Code	VH-B MRVH	VH-B MRVH	VH-B MRVH	VH-B MRVH	VH-B MRVH	VH-B MRVH
SPOT	10	14	15	24	26	28
SiO2	36.36	35.92	36.22	55.11	35.46	36.20
TiO2	0.26	n.d.	n.d.	n.d.	n.d.	n.d.
Al2O3	n.d.	n.d.	n.d.	0.86	n.d.	n.d.
Cr2O3	n.d.	n.d.	n.d.	n.d.	n.d.	n.d.
FeO	n.d.	n.d.	n.d.	n.d.	n.d.	n.d.
MnO	n.d.	n.d.	n.d.	n.d.	n.d.	n.d.
MgO	11.80	11.68	12.21	8.58	11.50	12.01
CaO	47.68	47.98	47.80	51.76	48.11	48.59
K2O	n.d.	n.d.	n.d.	n.d.	n.d.	n.d.
TOTAL	96.10	95.58	96.23	116.31	95.07	96.80

Cations on the basis of 8 oxygens

Si	2.06	2.04	2.04	2.45	2.03	2.03
Al	0.00	0.00	0.00	0.05	0.00	0.00
Fe2	0.00	0.00	0.00	0.00	0.00	0.00
Mn	0.00	0.00	0.00	0.00	0.00	0.00
Mg	1.00	0.99	1.03	0.57	0.98	1.01
Ca	2.89	2.92	2.89	2.46	2.95	2.93

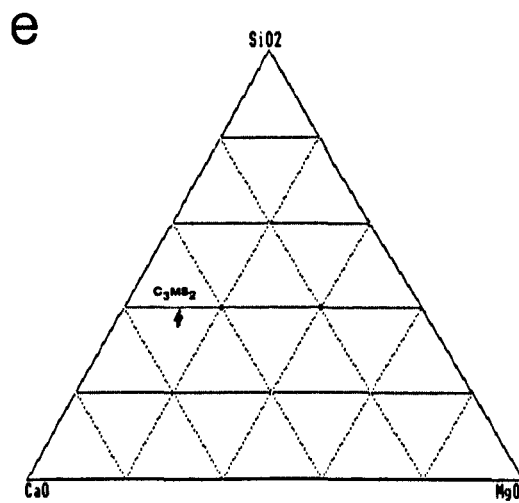
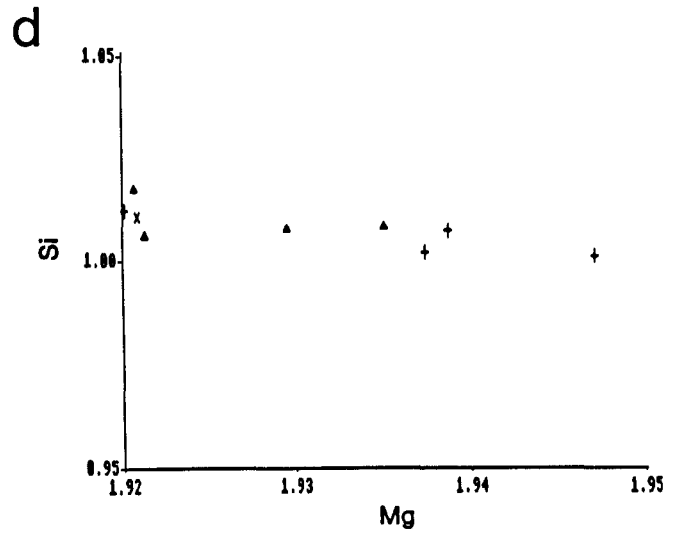
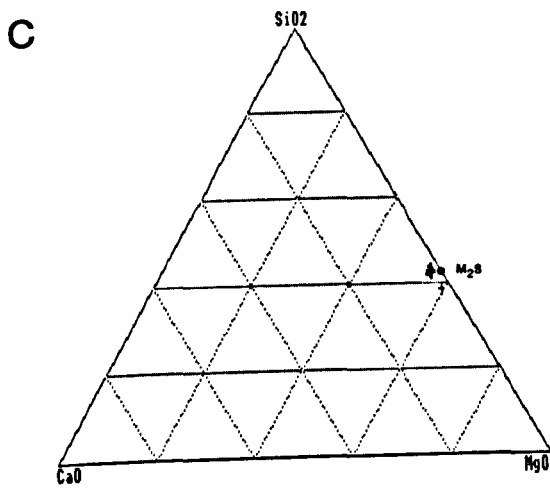
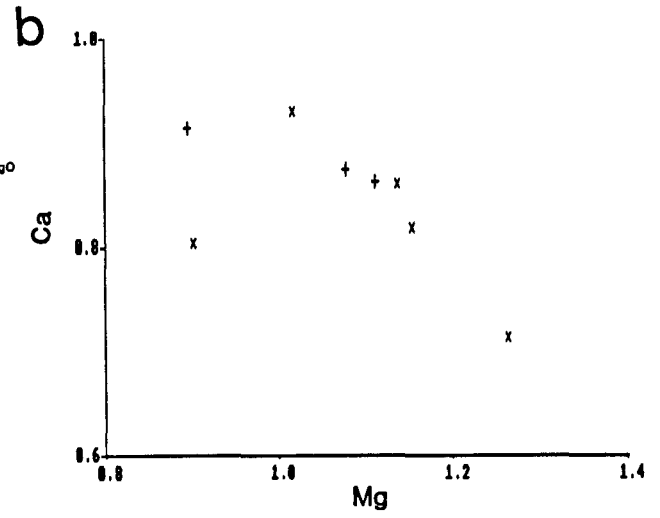
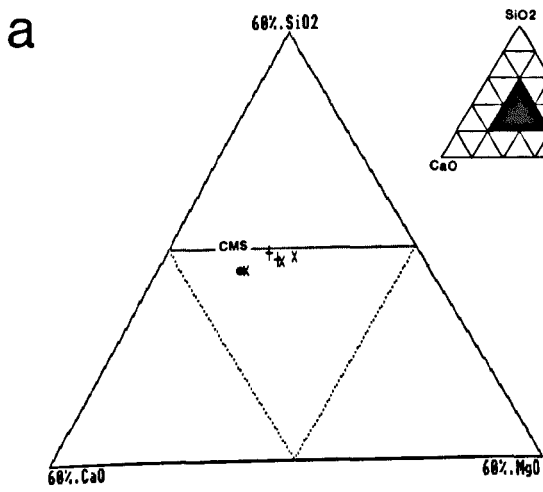


Figure 7.5 Triangular plots (wt.%) and cation relationships of monticellite (a, b), forsterite (c, d) and merwinite (e)

magnesite. The microprobe analyses of dicalcium silicates are plotted on the CaO-MgO-SiO₂ diagram as wt.%, and given in Figure 7.6a. The complete set of analyses are presented in Table 7.11 under the code beginning with D.

There is a distinct trend towards merwinite which is probably due to solid solution between merwinite and dicalcium silicate. Most of the analyses are distributed on the join dicalcium silicate and merwinite (Figure 7.6a). Comparatively high contents of Al₂O₃ and MgO were also determined. As dicalcium silicate is present in association with merwinite, it is possible to obtain mixed analyses which result a higher MgO content, also MgO can be picked up from periclase.

The MgO in these analyses ranges between 1.85-4.49% and Al₂O₃, between below detection limit up to 3.72%. As it can be seen from Figure 7.6b. There is an inverse relationship between Ca and Mg.

7.6.7 Tricalcium silicate

Tricalcium silicate has been found mainly in ~~Ca~~ natural mixtures of magnesite - dolomite sample. The microprobe analyses of tricalcium silicate are plotted on the CaO-MgO-SiO₂ as wt.% and it is given in Figure 7.6c. The MgO content varies between 1.27-2.18 wt.%. The higher percentage of MgO in tricalcium silicate is due to mix analysis. A comparatively high content of Al₂O₃ and FeO were also determined. The tricalcium silicate analyses are calculated on the basis of five oxygens and presented in Table 7.12

Table 7.11 Dicalcium silicate analyses as determined by EPMA
in dead burned huntite

Sample Code SPOT	VH-B DCVH 19	VH-B DCVH 20	VH-B DCVH 21	VH-B DCVH 25	VH-B DCVH 27	VH-B DCVH 29	VH-B DCVH 30	VH-B DCVH 31
SiO2	34.51	33.22	34.00	34.40	34.44	33.35	34.32	32.50
TiO2	n.d.	n.d.	n.d.	n.d.	0.26	n.d.	n.d.	n.d.
Al2O3	n.d.	1.75	n.d.	0.26	n.d.	0.77	1.20	3.72
Cr2O3	n.d.							
FeO	n.d.							
MnO	n.d.							
MgO	4.49	2.90	4.28	1.85	3.44	4.12	4.23	2.12
CaO	56.25	58.47	57.06	59.85	58.38	57.63	57.26	58.41
K2O	n.d.							
TOTAL	95.25	96.34	95.34	96.36	96.52	95.87	97.01	96.75
Cations on the basis of 4 oxygens								
Si	1.02	0.97	1.00	1.01	1.01	0.98	0.99	0.95
Al	0.00	0.06	0.00	0.01	0.00	0.03	0.04	0.13
Fe2	0.00	0.00	0.00	0.00	0.00	0.00	0.00	0.00
Mn	0.00	0.00	0.00	0.00	0.00	0.00	0.00	0.00
Mg	0.20	0.13	0.19	0.08	0.15	0.18	0.18	0.09
Ca	1.77	1.84	1.80	1.88	1.83	1.82	1.77	1.82

Table 7.12 Tricalcium silicate analyses as determined by EPMA in dead burned magnesite - dolomite

Sample Code SPOT	AMD-A TCMD 10	AMD-A TCMD 14	AMD-A TMMD 15	AMD-A TCMD 24	AMD-A TMMD 25	AMD-A TCMD 26	AMD-A TMMD 27	AMD-A TCMD 28	AMD-A TCMD 33	AMD-A TMMD 34
SiO2	24.53	24.49	24.73	25.08	24.47	22.59	24.57	24.65	24.90	25.07
TiO2	n.d.									
Al2O3	0.63	0.86	0.68	0.74	1.95	3.13	0.48	1.06	0.69	0.90
Cr2O3	n.d.	n.d.	n.d.	n.d.	0.28	n.d.	n.d.	n.d.	n.d.	n.d.
FeO	n.d.	0.41	0.43	0.55	0.60	1.77	0.47	0.34	n.d.	0.42
MnO	n.d.	n.d.	n.d.	n.d.	0.30	n.d.	n.d.	n.d.	n.d.	n.d.
MgO	1.73	1.87	1.58	1.64	1.27	2.18	1.60	1.39	1.60	1.68
CaO	69.75	69.58	69.97	70.22	68.55	66.80	69.64	70.10	69.52	69.70
K2O	n.d.									
NiO	n.d.									
TOTAL	96.64	97.21	97.39	98.23	97.42	96.47	96.76	97.54	96.71	97.77

Cations on the basis of 5 oxygens

Si	0.96	0.96	0.96	0.97	0.95	0.89	0.96	0.96	0.97	0.97
Al	0.03	0.04	0.03	0.03	0.09	0.15	0.02	0.05	0.03	0.04
Fe2	0.00	0.01	0.01	0.02	0.02	0.06	0.02	0.01	0.00	0.01
Mn	0.00	0.00	0.00	0.00	0.01	0.00	0.00	0.00	0.00	0.00
Mg	0.10	0.11	0.09	0.09	0.07	0.13	0.09	0.08	0.09	0.10
Ca	2.93	2.91	2.92	2.90	2.86	2.82	2.93	2.92	2.91	2.89

Sample Code SPOT	AMD-B TCMD 3	AMD-B TCMD 14	AMD-B TMMD 15	AMD-B TCMD 16	AMD-B TCMD 20	AMD-B TCMD 23	AMD-B TCMD 25
SiO2	24.73	24.26	24.21	24.85	24.83	23.93	24.53
TiO2	n.d.	n.d.	n.d.	n.d.	n.d.	n.d.	n.d.
Al2O3	0.64	0.57	0.78	0.75	0.77	0.94	1.33
Cr2O3	n.d.	n.d.	n.d.	n.d.	n.d.	n.d.	n.d.
FeO	0.38	0.55	0.40	0.59	0.48	n.d.	0.70
MnO	n.d.	n.d.	n.d.	n.d.	n.d.	n.d.	n.d.
MgO	1.50	1.58	1.74	1.34	1.71	1.70	1.63
CaO	69.78	69.14	68.91	68.80	69.19	68.71	68.06
K2O	n.d.	n.d.	n.d.	n.d.	n.d.	n.d.	n.d.
NiO	n.d.	n.d.	n.d.	n.d.	n.d.	n.d.	n.d.
TOTAL	97.03	96.10	96.04	96.33	96.98	95.28	96.25

Cations on the basis of 5 oxygens

Si	0.97	0.96	0.96	0.98	0.97	0.95	0.96
Al	0.03	0.03	0.04	0.03	0.04	0.04	0.06
Fe2	0.01	0.02	0.01	0.02	0.02	0.00	0.02
Mn	0.00	0.00	0.00	0.00	0.00	0.00	0.00
Mg	0.09	0.09	0.10	0.08	0.10	0.10	0.10
Ca	2.92	2.93	2.92	2.90	2.89	2.93	2.86

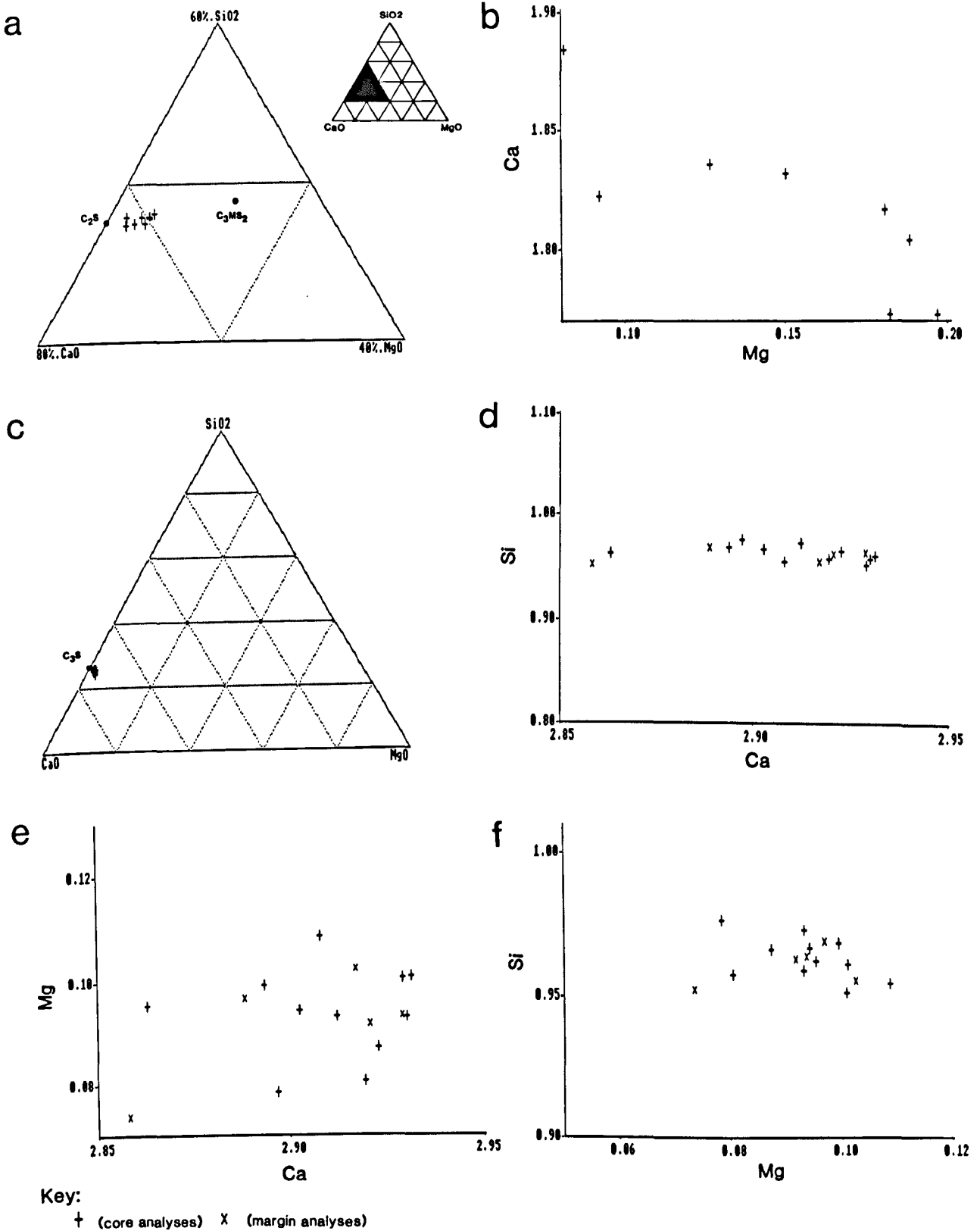


Figure 7.6 Triangular plots (wt.%) and cation relationships of dicalcium silicate (a, b) and tricalcium silicate (c, d, e, f)

under the code beginning with T. Cation relationship are shown in Figure 7.6d, e and f.

7.7 Comparison and evaluation

The phase assemblage of the dead burned huntites, a natural mixture of magnesite and dolomite, nesquehonite and a natural mixture of hydromagnesite and huntite, as predicted from the bulk composition (Figure 7.7) and determined mineral phases using SEM and EPMA are given in Table 7.13. Plots of bulk composition (wt.%) of the natural samples on the CaO-MgO-SiO₂ diagram are presented in Figure 7.7.

7.7.1 Discussion of the predicted and determined phase assemblages

The maximum number of phases which can be assumed at equilibrium conditions, are two silicate (or one silicate and lime), one spinel and one ferrite (see Chapter 4, section 4.7 for more information). As can be seen from Table 7.13 most of samples contain two and rarely three silicate phase, with a maximum of one spinel and one ferrite phase. This may suggest that equilibrium is perfectly attained. As it can be seen from Table 7.13, almost all the predicted phases are among the determined phases. As the close agreement between the predicted and determined phases indicates, it is possible to predict the general mineralogy of the final product from the bulk chemical analyses using a knowledge of phase equilibria.

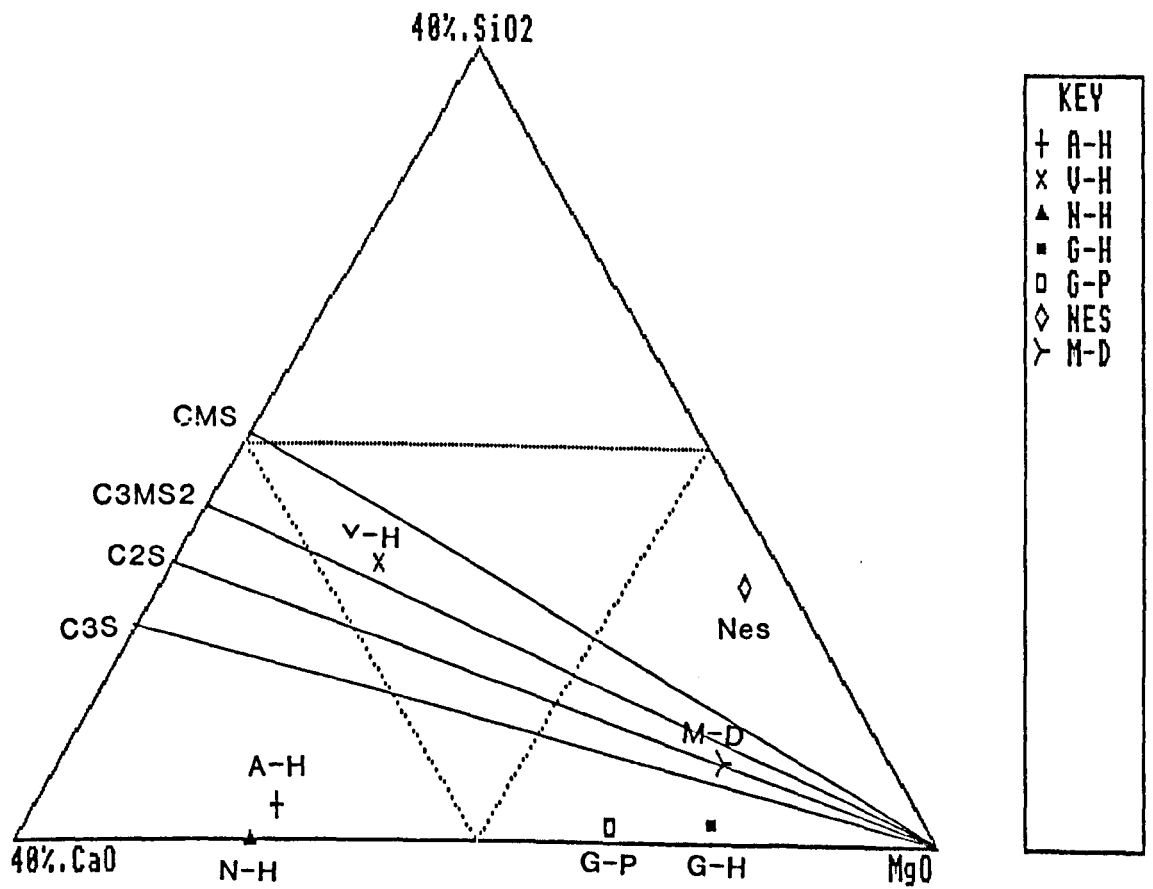


Figure 7.7 Plots of the bulk chemistry of the natural huntite, hydromagnesite - huntite, magnesite - dolomite and nesquehonite

Table : 7.13 Predicted and determined phase assemblages of the natural dead burned huntite, Hydromag-huntite, mag-dol, and Nesquohuntite calcined at 1500°C for 96 hours.

Sample	CaO/SiO ₂ mole ratio	Al ₂ O ₃ /Fe ₂ O ₃ mole ratio	Predicted phase Assemblages	Determined phase assemblages	
				SEM	EPMA
A-H	15.83	4.70	M-C-C3S	SEM	M-C-C3S-(SrO)
				EPMA	M-C-(SrO)
N-H	0.00	0.00	M-C-C3S	SEM	M-C-(SrO)
				EPMA	M-C-(SrO)
v-H	1.33	0.00	M-CMS-C3MS2-C2S	SEM	M-C3MS2-C-C3S-C2S
				EPMA	M-C2S-C3MS2
G-Hm,H	8.91	0.00	M-C-C3S	SEM	M-C-C3S
				EPMA	M-C
M-D	1.86	1.06	M-C3MS2-C2S-C3S	SEM	M-C-C3S-C2F-C2S-C3A-C3MS2
				EPMA	M-C-C3S-C3A
Ncs	0.17-0.27	3.42-2.88	M-CMS-M2S	SEM	M-M2S-C3MS2-CMS-C3S
				EPMA	M-CMS-M2S-SP

CHAPTER 8

SUMMARY AND CONCLUSION

8.1 Natural magnesite

One of the most important commercial types of magnesite deposits occurs in belts of ultramafic rocks and consists of cryptocrystalline magnesite resulting from alteration of serpentinite. Of the type of magnesite deposits so far known in the world, only the vein and hydrothermal - sedimentary types are found in eastern Iran. These magnesite deposits are formed near the surface as fracture filling most probably by ascending hydrothermal solutions. The investigated magnesite deposits have formed within the flysch and ophiolite melange belt of eastern Iran. The most important formation exposed in the area consists of Upper Cretaceous ophiolites and Upper Cretaceous - Middle Eocene flysch formations. The ophiolite unit mainly serpentinite is the host rock of the magnesite deposits. Several generations of magnesite are recognised in the area ranging from Middle Eocene and continuing until the present.

Magnesites of the investigated deposits are compact, cryptocrystalline and have a very fine uniform texture.

The investigated magnesite deposits are in general of low impurity content. The main impurities which are present in the majority of samples are dolomite and quartz, but also some other impurities such as chlorite, calcite, mica and plagioclase are present to a minor extent in some samples. By selective mining and simple beneficiation techniques, it is possible to obtain a high quality magnesite or concentrate which could be used for most industrial applications.

8.2 Dead burned magnesite

The most important properties of dead burned magnesite relevant to its major use as a basic refractory raw material are bulk chemistry, mineralogy, bulk density, crystal size of periclase, degree of direct bonding, porosity and hydration tendency. An evaluation of the dead burned magnesites from Iran as refractory raw materials have been made by taking all above properties into consideration together.

X-ray diffraction analyses of dead burned magnesites from Iran calcined at different temperatures (1400, 1500 and 1600°C) for different times (6, 24, 96 and 108 hrs) indicate that quartz exists nearly in constant amount at lower temperatures, but it disappears completely at 1600°C and 108 hours. In contrast to quartz and lime which also tends to disappears or reduce in amount at higher temperatures probably due to reaction, dicalcium silicate, tricalcium silicate and merwinite are present at higher temperatures of calcination.

In samples with a suitable CaO/SiO₂ ratio monticellite and forsterite appear at 1400°C and above at all times. Monticellite and forsterite becomes less concentrated at higher temperatures.

Spinel is only present in very small amount, at higher firing temperatures.

The calcined products show different colour, due to their minor impurities. Dead burned product of magnesite with 0.5% Fe₂O₃ is dark brown. With increasing Al₂O₃ the colour changes

to pale brown and greenish brown. When the major impurity is CaO (approx. 2.5%) the dead burned product is green, while increasing amount of SiO₂ changes the product to white colour. There is no relationship between the colour of the grain and the mineralogy.

The present detailed electron microscopic observations of dead burned magnesites indicate that the periclase grains either have a smooth surface structure appearance, or an irregular aggregate like texture. The matrix is concentrated at the periclase crystal boundaries particularly at the triple points. Periclase grains are larger at increased calcination temperatures and times. The amount of periclase - periclase grain contact reduces by increasing the amount of impurities. However high purity may not always be the most important factor required for industry. The high purity samples studied in this work (A3, T2, T26) usually cracked after calcination, a few percentage of matrix materials reducing this effect (A14, T15). In dead burned magnesites where only lower percentages of impurities are present, they concentrate at the triple points of polygonal periclase grains (e.g. samples A3 and T2), but in sample with higher amount of impurities (A14, T15), the matrix can fill in between periclase grains which results in smaller and rounded periclase grains with lower direct grain contact. Also some matrix materials have been found on the surface of periclase grains which is due to migration of impurities to the surface during the calcination process. Periclase grains appear in two main shapes, spherical mostly when the percentage of

interstitial materials is high and polygonal in purer samples. Step like growths are present on the surface of some periclase grains.

The periclase grain size is variable, the variation is dependent on the sintering temperature, duration of burning, the size of particles and the level of impurities. Insufficient sintering results in a very small grain size.

The electron microprobe analysis indicate, that the most frequently constituents present in the periclase grains in the samples are CaO and FeO. SiO₂ and Al₂O₃ are occasionally detected.

The present results confirm that CaO in periclase increases steadily with the increase in the CaO/SiO₂ ratio of the bulk chemistry. The amount of FeO in periclase in the dead burned magnesites is found to rise with the rising FeO content of the chemical composition. SiO₂ and Al₂O₃ are less frequently present in periclase.

Wide ranges in the mineral compositions of the forsterite, monticellite and dicalcium silicate in dead burned magnesite have been found probably due to solid solution, although many analyses represents mixed analyses.

Tricalcium silicate has been found mainly in a dead burned product of a natural mixture of magnesite and dolomite. The bulk of the analyses plot, slightly away from the theoretical composition of tricalcium silicate probably arising from a small amount of solid solutions of MgO.

The maximum number of impurity phases which can be found in the dead burned magnesite at equilibrium conditions are

two silicates (or one silicate and lime), one spinel (or spinel solid solution) and one ferrite (or ferrite solid solution). All of dead burned samples in this study contain most commonly two and occasionally three silicates, with a maximum of one spinel and one ferrite phase. Where a higher number of silicate phases is present, equilibrium within the grain is not completely achieved. Almost all the predicted phases are among the determined phases. As the close agreement between the predicted and determined phases indicates, it is possible to suggest the general mineralogy of the final dead burned product from the bulk chemical analyses of their raw materials using phase equilibrium diagrams.

High temperature resistance of the studied natural dead burned magnesites may be classified by considering the melting point of all phases present in the dead burned product. According to this, samples containing monticellite and forsterite as matrix (A14, T15) would have a lower temperature resistance in comparison with samples containing dicalcium and tricalcium silicate interstitial materials (T2, T26).

The porosity in the dead burned magnesites studied is in general very low. The pores are usually isolated and developed mainly at the periclase crystal boundaries, and occasionally within them.

Larger periclase grains are produced when magnesite calcined at higher temperatures and times. Presence of small amounts of FeO can promote the crystal growth of periclase.

The degree of direct bounding in the natural dead burned magnesite not only changes from one sample to another, but also within a single magnesia grain. At particle boundaries where interstitial phases are high in proportion there is almost no direct contact between periclase crystals. Consequently, where the matrix is high in amount, the contact of periclase grains is low. The present study confirms that generally samples containing monticellite, forsterite as interstitial phases ($\text{CaO/SiO}_2 < 2:1$) exhibits comparatively lower periclase - periclase grains contact. With an increase in CaO/SiO_2 ratio of the silicate phase (i.e. dicalcium and tricalcium silicates) ($\text{CaO/SiO}_2 > 2:1$) the bonding, in general is found to increase. Higher degree of direct bonding have been observed when the sample contain comparatively lower amount of matrix. When it contains free lime, dead burned magnesia can easily hydrate when exposed to the atmosphere. This can ultimately cause the refractory to disintegrate.

8.2.1 Comparison and recommendation

The chemical composition of natural magnesites from Iran are compared with some commercial natural magnesites and pelletized sea water magnesia products (Chester, 1973) in Table 8.1.

Table 8.1 Comparison of bulk composition of unprocessed natural magnesites from Iran with other products

Origin	SiO ₂	Al ₂ O ₃	Fe ₂ O ₃	CaO	Cr ₂ O ₃	MgO
INM (A)	2.38	0.21	1.36	1.84	- -	94.10
INM (T)	3.86	0.45	0.26	3.62	- -	91.55
GNM	1.60	0.07	0.54	2.90	0.01	94.87*
TNM	1.16	0.04	0.61	2.28	0.02	95.88*
ANM	0.86	0.56	3.91	2.75	0.02	91.82*
BSM1	0.80	0.40	1.30	0.80	0.02	96-97*
BSM2	0.80	0.40	1.30	1.60	0.50	95-96*
BSM (GA)	2.00	0.60	1.40	2.20	- -	93-94*
BSM (GB)	0.90	0.40	5.00	1.60	- -	91-93*
BSM (GC)	3.20	0.50	1.40	0.90	- -	93-95*
BSM (GD)	2.50	0.70	5.00	4.50	- -	87-89*
SSM1	0.50	0.20	0.20	0.60	0.02	98-99*
SSM2	0.80	0.20	0.20	1.60	0.30	96-97*

Where:

INM (A) = Iranian natural magnesite (Afzalabad deposit) (means value). INM (T) = Iranian natural magnesite (Torshak deposit) (means value), GNM = Grecian natural magnesite, TNM = Turkish natural magnesite, ANM = Austrian natural magnesite, BSM = British sea water magnesia, (GA-GD) = Grade A-D, SSM = Sardinian sea water magnesia, * = MgO (by diff.). All analysis in wt.%, - - = not determined.

The Iranian magnesites in general compare favourably with magnesite from elsewhere especially with the British sea water magnesias (BSM).

Magnesite samples from Torshak contain higher amounts of impurities such as SiO₂ and CaO compared with the Afzalabad deposit. The higher CaO/SiO₂ ratio in the Torshak deposit will produce higher melting point matrix materials. The higher percentage of Fe₂O₃ in the Afzalabad magnesites results in ferrite with low melting points in dead burned products.

For the production of high duty magnesia bricks, the following comments are relevant:

1. Angular shaped MgO crystals with high degree of direct periclase - periclase crystal contact are required. This can be achieved by simple beneficiation of the Iranian magnesites to reduce the amounts of impurities, specially CaO, SiO₂, Fe₂O₃ and by maintaining the CaO/SiO₂ ratio of around 2:1. In this case the matrix phases which are mostly dicalcium silicate forms at the triple point of the periclase grains (e.g. samples A3 and T2). Lower CaO/SiO₂ ratios (samples A14 and T15) produces low melting matrix phases such as monticellite (m.pt.1502°C), merwinite (m.pt.1575°C) and forsterite (m.pt.1900°C) which is liquify at lower temperatures than dicalcium silicate melting point (2130°C), hence lower melting temperature of product, (the melting point of periclase is 2800°C). However if the CaO/SiO₂ remain high, considerable quantities of dicalcium silicate may be formed during dead burning and this can lead to "dusting" of refractories in service. Minimum amounts of impurity phases should isolated in pockets at MgO crystal intersections.
2. A crystal diameter of >40 microns is required. This can be achieved by calcining the studied magnesites in excess of 1500°C with the CaO/SiO₂ ratio of around 2:1. Samples containing small amounts of iron oxide can produce very large periclase grains (Sample A3 with 0.49% Fe₂O₃ has an average grain size of 122 microns when it calcined at

1600°C). It should be noticed in this case the possibility exists for forming low melting point ferrite.

3. Pores that are present should preferably be isolated within the crystals and should not form a continuous network at the crystal boundaries. Crystal shape and diameter is dependent on firing temperature, time and chemical composition particularly with respect to the CaO/SiO₂ ratio. The lower the porosity, the greater the amount of material to resist chemical attack.
4. The poor hydration resistance properties should be overcome by lowering the CaO impurity to a level which eliminates the presence of free CaO in the dead burned product and by increasing the fired bulk density.
5. Refractory grade magnesia should have a high density to maximise slag resistance and high temperature strength properties. It is generally considered the raw material should have a density of at least 3.35-3.4, to achieve this property. The bulk density of dead burned samples from Iran calcined in the range of 1400-1600°C are between 3.33 to 3.55.

In considering the commercial extraction of these potential magnesite deposits a detailed sampling, drilling and testing programmes would be vital in order adequately to assess and to check for any intervening zones of inferior quality within its body. By selective mining and simple beneficiation techniques, it should be possible to obtain a high quality magnesite.

8.3 Caustic calcined magnesite

Caustic magnesia is a type magnesium oxide (MgO) which can be obtained by decomposition of magnesium carbonate or magnesium hydroxide just above the temperature of thermal decomposition ($700-1200^{\circ}C$), in this case the products are more reactive and is suitable for variety of chemical and other applications.

The effect of time and temperature on the transformation of natural magnesites from Iran into caustic calcined magnesia have been studied to establish the ideal industrial properties of these materials to produce caustic calcined magnesia to use by the chemical and allied industries.

The time - temperature - transformation of magnesite to periclase in the range of $500-1200^{\circ}C$ and time range of 1/4-8 hours is characterized by two curves, showing the starting and finishing points of magnesite - periclase transformation. The area between the two curves indicates the intermediate stage of transformation (i.e. both magnesite and periclase are present together). At the lower calcination temperatures the phase transformation is taking place slowly and longer calcination times are required, but at higher temperatures the phase transformation is taking place very quickly.

The crystalline size increases comparatively sharply at temperatures higher than $1000^{\circ}C$ for larger calcination times, but at temperatures between $600^{\circ}C$ and $1100^{\circ}C$ the increase in the crystallite size with the time is small.

The LOI decreases, as the calcination temperature and time

increase, the LOI values are very high at 500°C for all the calcination times. The LOI values are less variable with different times at 900°C and almost constant at 1000°C for all the calcination times. For lower calcination temperatures such as 600°C, the surface area goes through a maximum and after this time the surface area value start to decrease with increasing the time. There is no maximum peak recognised at 500°C, probably because of insufficient calcination time. The highest value of surface area is obtained for a sample calcined at 600°C for two hours time, but this corresponds to a high residual loss on ignition of 5-10%. The surface area changes rapidly with different times for the temperatures between 500°C to 900°C, but for temperature higher than 1000°C, the surface area values show only small differences with various calcination times.

The iodine number curves and contours are similar in shape to the surface area measurements, however the errors in this method is higher than the surface area measurement. For lower calcination temperatures such as 600-800°C, the iodine number values goes through a maximum and after this time the iodine adsorption numbers starts to decrease with increasing the time. At 500°C there is no maximum peak recognised, because of shortage of calcination time (max. 8 hrs in this study). At all calcination temperatures and after maximum 2 hours time, the iodine number decreases except at 500°C for all calcination times and at 700°C for 1/4 hour calcination time, where the iodine number increase, with increasing time.

The present electron microscopy observations of caustic

calcined magnesite indicate the transformation of magnesite to periclase at different calcination temperature (500-1200°C). From perfectly shaped magnesite crystal at lower temperatures to a mixture of magnesite - periclase and then pure periclase at higher temperatures. The highest value of surface area and iodine number are obtained when the decomposition of magnesite is just complete. Relatively high value, of surface area and iodine number are also found at intermediate decomposition, (i.e. when magnesite and periclase are present together). The industrial properties, (SA, IN, LOI, CS) of the caustic calcined magnesites from Iran compare well with the existing medium and high quality commercial synthetic products.

8.3.1 Recommendation

Caustic calcined magnesite with different industrial properties can be made by varying the calcination temperature and time. The commercial products could have a wide range of properties. High quality magnesia have a large variation in surface area and iodine number values and specification for individual products span a large part of this range. This reflects a very closely controlled reaction and the manufactures make specific MgO's for specific customers.

High quality magnesia could be produced from Iranian magnesites in a narrow range of temperatures and times. The medium quality product can be made rapidly within 30 minutes between 800-1000°C. At lower temperature (600-800°C) formation of this medium quality magnesia, which is superior

to existing synthetic products, is largely independent of time in the range of 2-8 hours. The latter appears to present an easier way to manufacture a consistent product.

Temperature is the most important factor affecting the production of medium quality magnesia. Increase of calcination temperature beyond 800°C is likely to lead a rapid deterioration of surface area and hence product quality.

8.4 Huntite

Many occurrences of huntite are present very close to magnesite deposits of Nehbandan area. This area lies within the ophiolite complex of eastern Iran. In the investigated area three different modes of occurrence of huntite have been recognised: vein type, nodular type and alluvial type huntite. These deposits are presumably formed from alteration products of magnesite deposits. The majority of alluvial type huntites are entirely pure huntite. Magnesite and quartz are rarely present as impurities in alluvial type huntite. Serpentinite and hydromagnesite are the main impurities in nodular type huntite. Vein type huntite is a mixture of huntite and magnesite and all samples contain various amounts of magnesite.

The microstructural study of huntite indicate they have platy habit and very small crystalline size (<2µm). Very low acid insoluble residue (AIR) in both alluvial and nodular type huntite deposits indicate their high purity.

The most important industrial application of huntite is

to use it as a white filler in the paint industry. Oil absorption values and the colour properties suggest that huntite may make an excellent white filler in paint.

The oil absorption value indicates the percentage of voids between the periclase and the size distribution of particles. Higher oil absorption values are obtained by small and uniform particle sizes rather than the particles with very wide range of sizes. The oil absorption values of three different huntite specimens from Iran are very similar, because of their similarity in the particle size and purity. The oil absorption property of Iranian huntite is similar to some manufacture fillers.

A fine particle size filler is required for many applications. In this case a larger oil absorption will result from the higher surface area of the produced fine powder.

The colour measurement investigation show that the reflectance of huntite from Iran is higher than other examined commercial products. The brightness value of Iranian huntite which corresponds with general level of reflectivity is higher than the other products.

The present work indicate, that huntite is not suitable for use as a refractory raw material, but because of its special chemical composition which is between magnesite and dolomite, a sample of huntite have been calcined at 1500°C for 96 hours to compare the dead burned products with those of dead burned magnesite and dolomite.

In comparison with magnesite, a higher percentage of CaO

which crystallises as lime competing with periclase for available spaces which results in smaller periclase crystal growth (the average periclase grain size of dead burned huntite at 1500°C for 96 hours is 5-10 times smaller than the average periclase grains of dead burned magnesite calcined at similar condition).

The present work show that strontia (SrO) occurs substituted in periclase and lime and as separate patches within the dead burned products of alluvial and nodular types huntite.

Huntite is not suitable to use as a raw material to produce dead burned magnesia because:

- 1) The deposits are very rare and small in the nature.
- 2) The level of undesirable impurities such as CaO is high, as a result the periclase grains are very small.
- 3) huntite would not give dense products due to high porosity.

8.4.1 Exploitation and processing

Total extent of huntite is unknown. Presently, the exploitation is not organised, but the mineral is exploited from the small ore bodies without any systematics.

Naturally occurring huntite is always associated with other impurities such as silica, serpentine, dolomite etc. It is, therefore, necessary to process it before packing. During this study, ^{The} following method was found to be satisfactory for the processing of huntite.

water is added to huntite and other impurities. Since huntite has natural tendency to crumble in water and the

impurities like silica, serpentine and other carbonate minerals have tendency to sink. Therefore, it is possible to separate impurities either by sieving or by hydrocycling. Then one could pump out the water with huntite and dry the content. Finally, the dried material is ready for the shipment as almost pure huntite.

APPENDIX 1

HAND SPECIMEN DESCRIPTION

- A1. This is cryptocrystalline variety of somewhat impure magnesite where small veins of altered serpentine are present.
- A2. This is a sample of *magneite*. It is yellowish gray and compact with conchoidal fractures.
- A3. Sample is white in colour and compact in appearance. It is cryptocrystalline with conchoidal fracture.
- A4. Same as A3.
- A5. This is whitish gray in colour. The surface is characterized by the cauli-flower structure and mostly exhibits the conchoidal fracture.
- A6. same as A5.
- A7. same as A1.
- A8. This is cryptocrystalline sample with high purity which is apparent from the bright white colour. It is compact in appearance with conchoidal fracture.
- A9. This is white in colour with compact appearance and cryptocrystalline texture.
- A10. same as A1.
- A11. This sample has cauli-flower surface. It is whitish gray in colour and shows conchoidal fracture.
- A12. same as A7.
- A13. Yellowish gray dolomite sample with compact appearance and of cryptocrystalline nature.

- A14. This is an impure sample. It seems to be a mixture of magnesite and dolomite. The colour is pale gray with conchoidal fracture.
- T1. This is white in colour and compact in nature with conchoidal fracture. Grain size is cryptocrystalline.
- T2. same as T1.
- T3. same as T1 and T2.
- T4. same as T1 and T2 and T3
- T5. White in colour and smooth in appearance with cryptocrystalline grains.
- T6. same as T1.
- T7. same as T2.
- T8. same as T7.
- T9. This sample is similar to that of T26 except it is softer than T26.
- T10. same as T8.
- T11. This sample is whitish gray in colour and massive in appearance with a few fractures.
- T12. Colour is whitish gray and the sample has somewhat chalky appearance.
- T13. Similar to T26 but slightly softer.
- T14. White, compact sample with cryptocrystalline grains and conchoidal fracture.
- T15. same as T26 but soft.
- T16. same as T15.

- T17. Yellowish white in colour and massive in appearance with a few tiny cavities. The grain size is mostly cryptocrystalline.
- T18. same as T14.
- T19. White, cryptocrystalline magnesite with cauli-flower surface and and compact appearance.
- T20. same as T19.
- T21. Gray in colour and compact in appearance. cryptocrystalline with conchoidal fracture.
- T22. same as T5 but with chalky surface.
- T23. same as T1.
- T24. same as T1.
- T25. same as T1 but with a few cracks.
- T26. White in colour and massive in appearance with cauli-flower surface. Dominated by the conchoidal fracture with slight porosity at places.
- T27. same as T25.

APPENDIX 2

BULK CHEMISTRY

A2.1 Experimental

The bulk chemical analyses have been carried out for the natural magnesite specimens collected from Torshak and Afzalabad deposits of eastern Iran.

X-ray fluorescence spectrometry (XRF) was employed for this purpose.

A2.2 Procedures

A2.2.1. Loss on ignition (LOI)

A pre - calcined silica crucible (1000°C) was allowed to cool in a dessicator and weighed accurately to ± 0.0001 g. Approx. 5g of pulverised sample was accurately weighed into the silica crucible and placed in the furnace which was heated gradually to 1000°C. The sample was left to soak at 1000°C for two hours in the furnace. It was then removed, allowed to cool in a dessicator and re-weighed to 0.0001 g. The loss in weight expressed on a percentage of the original weight is taken on the LOI.

A2.3 XRF sample preparation

The cleaned and dried specimens were first crushed by a fly press to less than two centimetres. The material was then ground in a tema mill for 90 seconds (three runs each thirty seconds).

A2.4 Pressed powder pellet preparation

About 7g. of each powdered samples were mixed with 11-13 drops of moviol 18.88 (Hoechst chemical Ltd) and then pressed in a mould to high pressure (15000 Kg). Then the pressed powder pellets were air dried before using with the X-ray fluorescence spectrometer.

A2.5 Calibration

Prior to bulk chemical analysis, it was necessary to calibrate the Philips PW 1212 X-ray fluorescence spectrometer for different oxides.

MgO, Fe₂O₃, SiO₂, and CaO were calibrated on standards from high purity natural magnesite specimens of known composition (Kimyongur 1984). These oxides were determined on pressed powder pellets.

The calibration curves of MgO, Fe₂O₃, SiO₂, CaO and the calibration factors obtained are presented in Figures A2.1. Also calibration curves were checked statistically by using the following equations to find out the slope and intercepts of the calibration curves.

$$m = \frac{\sum(xy) - \sum(x) \sum(y)/n}{\sum(x^2) - (\sum x^2)/n}$$

$$c = \frac{\sum(y)}{n} - \frac{m \sum(x)}{n}$$

Where:

c = intercept

m = slope

n = number of pairs of values

X = oxides%

y = count ratios

The calibration factors and intercepts found for the pressed powder pellets are as follows:

	MgO	Fe ₂ O ₃	SiO ₂	CaO
K =	10.01	1.853	26.21	1.789
C =	12.01	-0.016	-0.029	-0.079

where:

K = calibration factors

C = intercept

The minor oxides (Al₂O₃, TiO₂ and K₂O) were also determined on pressed powder pellets and calibrated using the following spiking procedure.

10 gms mixture of 90 and 95 percent from one of the purest natural magnesite specimens collected from Afzalabad deposit (sample A8) of known minerals, analysed by XRD were mixed very well with 10 and 5 percent larvikite of known composition, using a mechanical mixer. The mixtures were micronized for five minutes and then dried at 105°C before making pellets.

Table A2.1 chemical analysis of larvikite

SiO ₂	59.41
Al ₂ O ₃	18.21
TiO ₂	1.10
Fe ₂ O ₃	4.63
MnO	0.13
MgO	1.36
CaO	3.41
Na ₂ O	6.22
K ₂ O	4.13

The best fit lines were drawn through the data by plotting the count ratios against weight percentages. Calibration curves of Al₂O₃, K₂O and TiO₂ are presented in Figure A2.1.

The calibration factors and intercepts found for pressed powder pellets are as follows:

	K ₂ O	TiO ₂	Al ₂ O ₃
K =	2.22	1.24	21.39
C =	0.00	0.00	0.00

where:

K = calibration factor

C = intercept

Na₂O calibration as previously determined by Mr Middleton

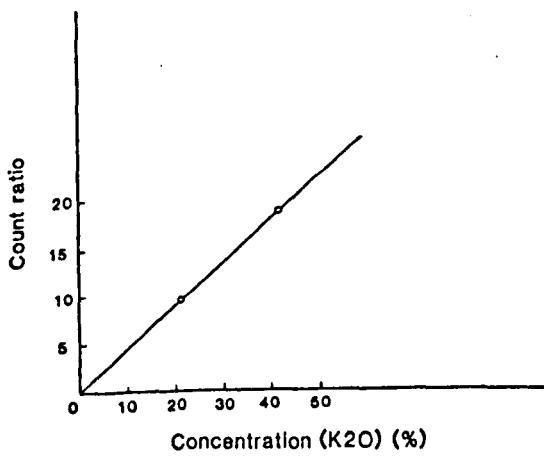
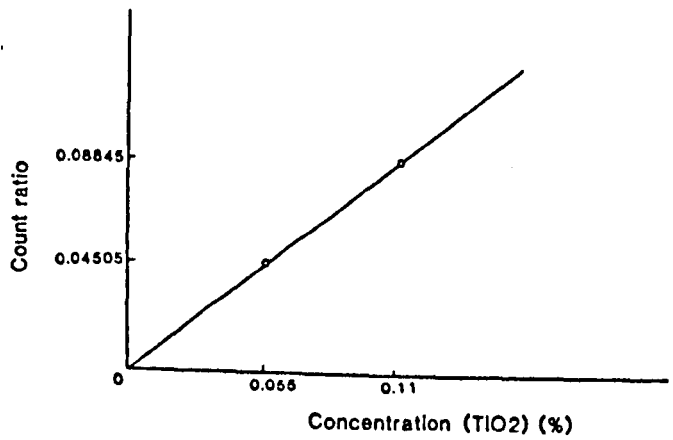
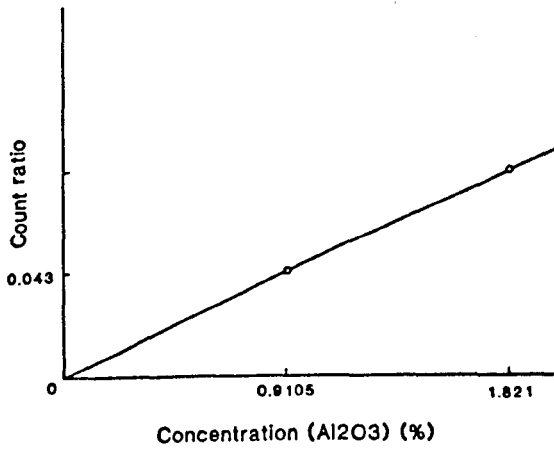
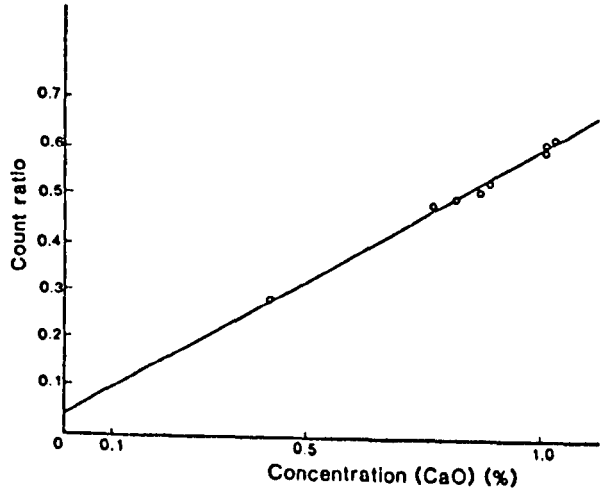
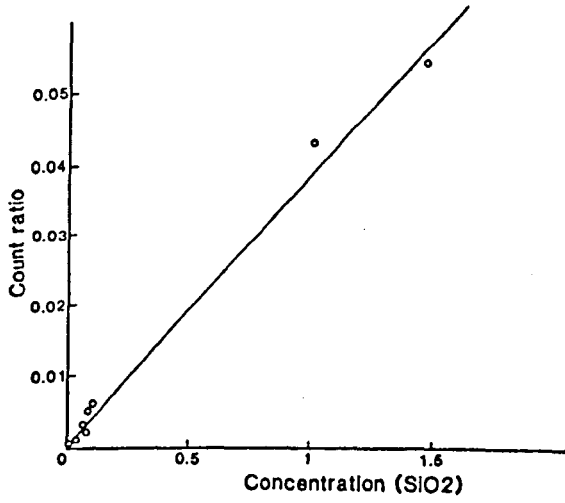
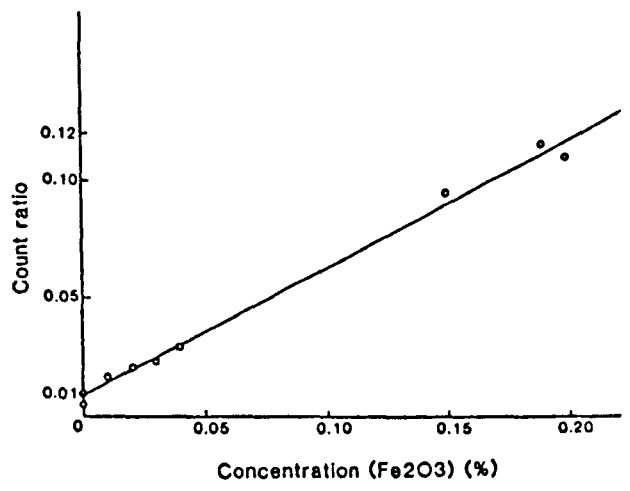
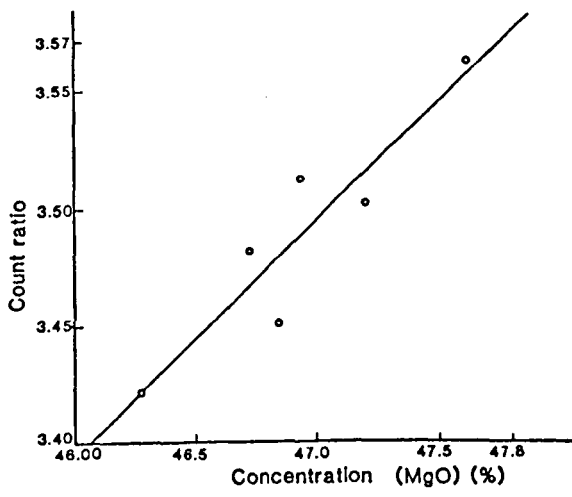


Figure A2.1 Calibration curves as determined on press powder pellets

(Geology Department, Hull university) was used in this study. The calibration factor used for Na₂O is 13.00.

A2.6 Instrumental condition

The XRF instrumental condition used for determination of the major and minor oxides (MgO, CaO, SiO₂, Fe₂O₃, Al₂O₃, TiO₂, Na₂O, and K₂O) of natural magnesites samples collected from eastern part of Iran is presented in Table A2.2.

Table A2.2 XRF instrumental condition

Element	Kv	mA	crystal	Time=	counter	collimator
Mg	60	28	TLAP	20	F	coarse
Fe	60	28	LiF	20	F	Fine
Ti	60	28	LiF	40	F	Fine
Si	60	28	PE	20	F	coarse
Ca	60	28	LiF	20	F	Fine
Al	60	28	PE	40	F	Fine
Na	60	28	TLAP	100	F	Coarse
K	60	28	TLAP	40	F	coarse

where:

TLAP = thallium acid phthalate

LiF = lithium fluoride

PE = pentaerythritol

F = Flow counter

APPENDIX 3

X-RAY DIFFRACTION ANALYSIS

x-ray diffraction has been employed to determine the different phases both in natural magnesite, huntite and their dead burned products in various times and temperatures of firing (6, 24, 96 and 108 hrs) (1400, 1500, 1600°C) Also it has been used in caustic calcined products for two objectives to determine:

1. The transformation of magnesite to periclase.
2. The crystalline size of periclase.

A3.1. Sample preparation

The particle size suitable for x-ray diffraction work is less than 40 micron (Zussman 1977). In order to achieve a similar size range, the samples were first crushed by fly press machine to less than 2 cm, and then followed by hand grinding in an agate pestle and mortar.

A3.2. INSTRUMENTAL (natural magnesite)

Ni filtered, CuK-alpha radiation was used for all analyses on a Philips X-ray diffraction unit. Operation conditions as shown below:

tube current 40 Kv, 30 mA
count rate 1x10³ cps
time Constant 4 seconds
scanning speed 1/2°2θ/min
chart speed 10 mm/min
range (2θ) 5-60 degrees

A3.3. Instrumental conditions for dead burned magnesite

Ni filtered Cu radiation at 40mA and 40Kv
scanning rang (2θ) 20-65 degrees
scanning speed 1/2°2θ/min
time constant 4 second
count range 4x10² cps
chart speed 10 mm/min

A3.4. Instrumental conditions for caustic calcined magnesite experiments

1. Transformation of magnesite to periclase.

The analyses were carried out with a Philips PW 1050 diffractometer using Ni filtered Cu radiation at 40 mA and 40 Kv, Operating conditions varied depending on the sample run as below:

count rate	4×10^2 cps
time constant	4 second
scanning range	30-80 degrees
scanning rate	$1/2^\circ 2\theta/\text{min}$
chart speed	10 mm/min

A3.5. Instrumental conditions for natural huntite

Ni filtered Cu radiation at 40 mA and 40 Kv	
Scanning range (2θ)	5-65 degrees
Scanning speed	$1/2^\circ 2\theta/\text{min}$
Time constant	4 second
count range	1×10^3 cps
chart speed	10 mm/min

In the case of some samples it was necessary to change the count rate to 2×10^3 cps. Pressed cavity mounts were used for all samples.

2. The crystalline size determination of periclase from X-ray line broadening

The instrumental conditions in the case of present of magnesite and periclase in the caustic calcined products are different and shown as below:

If sample contains magnesite only or magnesite and periclase use CuK-beta reflection at $29.42^\circ 2\theta$ can be used to measure the magnesite crystalline size only. If sample

contains periclase and magnesite together, reliable results not obtainable on periclase unless with the high proportion of periclase, in which CuK-alpha reflection at $36.95^{\circ}2\theta$ may be used.

If sample contains periclase only CuK-beta reflection at $38.60^{\circ}2\theta$ can be used to measured the mean periclase size

Unfiltered CuK-beta radiation was used for analyses on a philips X-ray diffraction unit. Operation conditions varied depending on the sample as shown below:

tube current	40mA, 40Kv
count rate	4×10^3 cps
time constant	10 second
scanning rate	$1/8^{\circ}2\theta/\text{min}$
chart speed	50 mm/min

In the case of some sample it was found necessary to change the count rate to 1×10^3 and 2×10^3 cps.

1. General

The theory and methods of calculating the crystallite size from line broadening have been presented in detail by Klug and Alexander (1974).

The basis for the determination of crystallite size from X-ray diffraction line broadening is determination of pure diffraction breadth (ρ) due to crystallite size and the calculation of the crystallite size (D) from the Scherrer equation:

$$D = \frac{K \lambda}{\beta \cos \theta}$$

where K : crystallite shape constant

λ : X-ray wavelength (\AA)

θ : Bragg angle

There are three main factors which contribute to the broadening of X-ray lines, namely: crystallite size, the geometry of the instrument and K-alpha separation. Crystal imperfections such as strain, deformation and mosaic structure also contribute to the line broadening. In the present study the crystallites are assumed to be free of crystal imperfections.

2. Procedure

Unfiltered Cu radiation is used to obtain K-beta lines of (200) reflection of periclase, in order to avoid correction for K-alpha doublets.

The observed diffraction peak breadth at half-maximum intensity (B) is measured.

Quartz standard which is strain free and does not have mosaic structure, with particle size in the range 1-10 microns is used to determine instrumental broadening (b) The determined relationship between 2θ and half-height breadth (b) using CuK-beta for the quartz standard is given in Figure A3.2. (after Kimyongur, 1984) Using the curve 'Low angle reflection' in Figure A3.1 (taken from Klug and Alexander,

1974, p.641, Figure. 9.9) which gives the relationship between b/B and β/B , the pure diffraction breadth (beta) is determined.

The crystallite size (D) is calculated from the Scherrer equation given earlier. The crystallite shape constant (K) is equal to 0.9 when "beta" is taken as half the maximum line breadth (Klug and Alexander, 1974). The "beta" is converted to radian measure before solving the Scherrer equation. The experimental procedure for X-ray line broadening is also given in Rau (1962) and Bartam (1967).

The instrumental conditions used in the scanning of the quartz standard is as follows:

radiation	Cuk-beta (no filter)
current	25mA, 40 KV
scanning rate	1/8° 2θ/min
time constant	10 sec
count range	2x10 ² -4x10 ³ cps
scanning range	18.40° - 71.40°
chart speed	50 mm/min

Crystallite size determination by X-ray Line Broadening is said to be applicable to sizes up to 1000 Å (Rau (1962), Bartam (1967)). The higher the values, the greater the error.

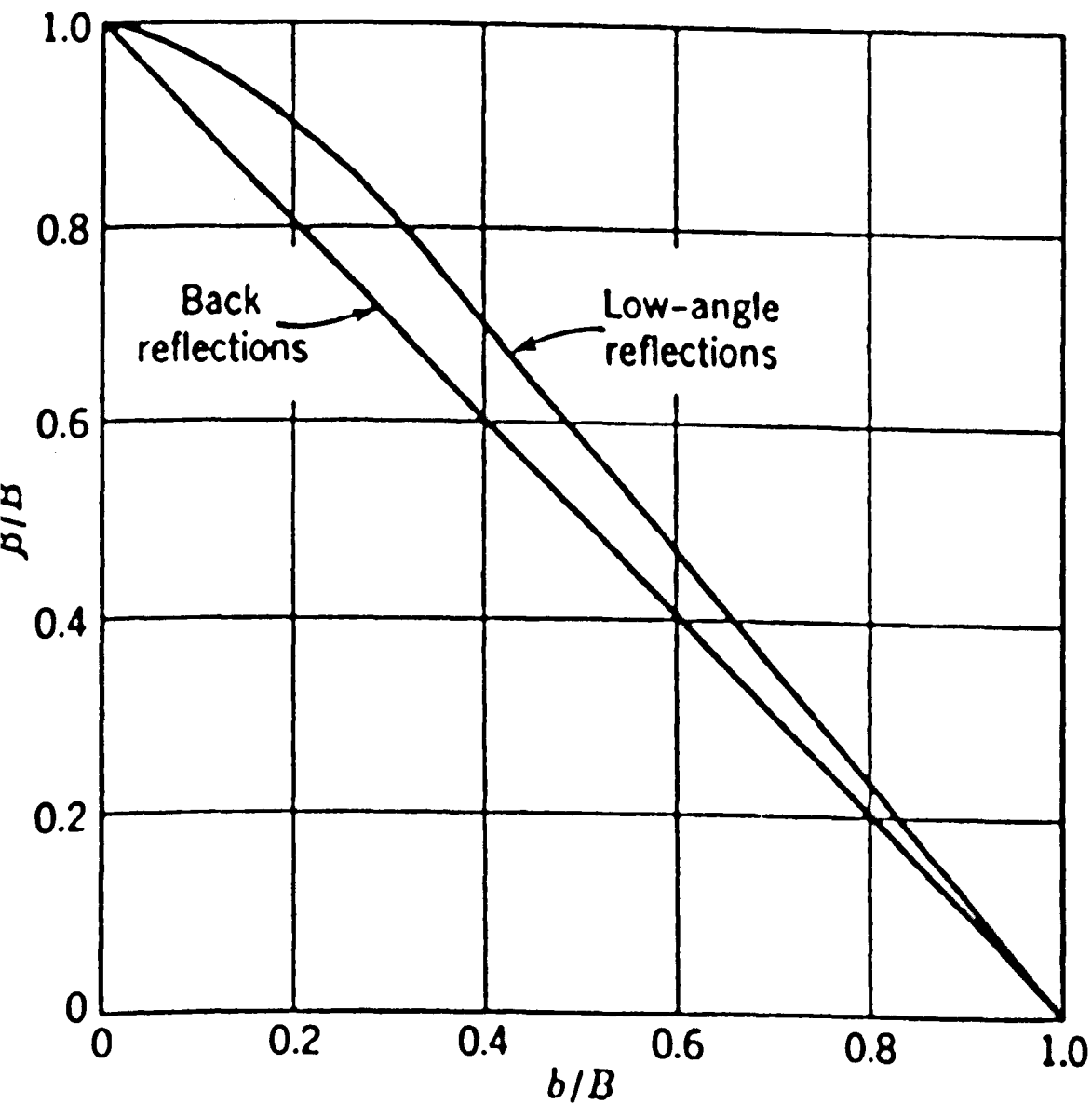


Figure A3.1 Curves for correcting X-ray diffractometer line breadth for instrumental broadening (after Klug and Alexander, 1974)

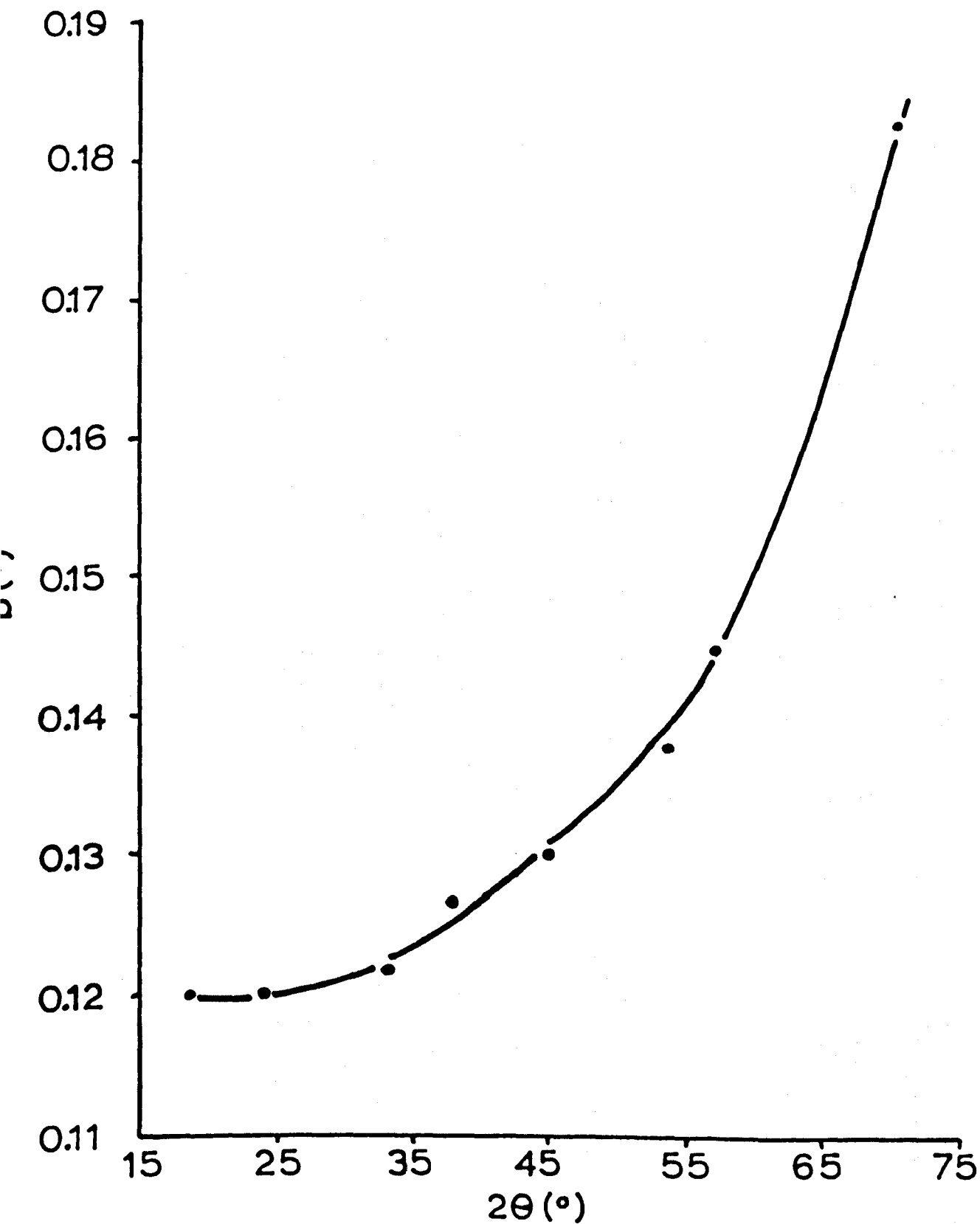


Fig. A3.2 Instrumental broadening as a function of diffraction angle 2θ (quartz standard, 1-10 μ particle diameter using $\text{CuK}\beta$)

APPENDIX 4

Electron microprobe analyses of natural magnesite

Sample Code SPOT	A1 DL-C 1	A1 DL-M 2	A1 MG-C 3	A1 MG-M 4	A1 DL-C 5	A1 DL-M 6	A1 MG-C 7	A1 MG-M 8	A1 DL-C 9	A1 MG-C 10
SiO2	n.d.	n.d.	0.18	0.18	n.d.	0.22	n.d.	n.d.	n.d.	n.d.
TiO2	n.d.									
Al2O3	n.d.									
Cr2O3	n.d.									
FeO	0.68	0.53	0.35	n.d.	0.87	1.81	0.46	1.31	n.d.	1.79
MnO	n.d.									
MgO	21.30	21.03	41.31	41.31	21.20	21.10	40.87	40.63	20.94	40.86
CaO	28.08	28.09	0.22	0.55	26.98	27.01	0.29	0.55	29.22	0.48
K2O	n.d.									
TOTAL	50.06	49.66	42.06	42.05	49.05	50.14	41.62	42.50	50.16	43.14
Sample Code SPOT	A1 MG-C 11	A1 MG-C 12	A1 DL-C 13	A1 MG-C 14	A1 MG-C 15	A1 MG-M 16	A1 MG-C 17	A1 MG-C 18	A1 MG-C 19	A1 MG-C 20
SiO2	n.d.	0.19	0.31	n.d.	n.d.	n.d.	n.d.	n.d.	0.17	n.d.
TiO2	n.d.									
Al2O3	n.d.									
Cr2O3	n.d.									
FeO	n.d.	0.87	n.d.	2.13	n.d.	n.d.	n.d.	n.d.	n.d.	n.d.
MnO	n.d.									
MgO	41.77	41.03	20.66	40.93	41.96	41.93	40.98	41.63	40.92	42.51
CaO	0.30	0.31	29.76	0.89	0.72	0.67	0.19	0.14	0.13	0.15
K2O	n.d.									
TOTAL	42.06	42.40	50.72	43.95	42.68	42.60	41.16	41.77	41.22	42.66
Sample Code SPOT	A1 MG-C 21	A1 MG-M 22	A1 DL-M 23	A1 DL-C 24	A1 DL-C 25	A1 MG-C 26	A1 MG-C 27	A1 MG-C 28	A6 MX-C 1	A6 MG-C 2
SiO2	n.d.	1.12								
TiO2	n.d.									
Al2O3	0.00	n.d.								
Cr2O3	n.d.	n.d.	n.d.	n.d.	n.d.	n.d.	0.22	n.d.	n.d.	n.d.
FeO	0.25	2.99	1.87	n.d.	0.30	2.45	n.d.	n.d.	n.d.	0.99
MnO	n.d.									
MgO	42.23	40.77	21.85	21.36	21.85	41.98	43.33	42.73	42.28	40.90
CaO	0.39	1.02	28.82	30.11	29.53	0.70	0.43	0.23	0.22	0.53
K2O	n.d.									
TOTAL	42.87	44.78	52.54	51.47	51.67	45.13	43.99	42.97	42.50	43.55

N-MAG

Sample Code SPOT	A6 MG-C 3	A6 MG-C 4	A6 MX-C 5	A6 MG-C 6	A6 MX-C 7	A6 MX-C 8	A6 MX-C 9	A6 MG-C 10	A6 MG-M 11	A6 MG-C 12
SiO2	n.d.	0.17	2.66	0.86	3.10	1.67	1.92	n.d.	0.18	n.d.
TiO2	n.d.									
Al2O3	n.d.									
Cr2O3	n.d.									
FeO	0.67	0.36	0.78	0.39	0.41	0.54	0.54	n.d.	n.d.	n.d.
MnO	n.d.									
MgO	40.88	41.49	40.35	41.03	39.43	41.08	40.55	41.36	41.32	41.66
CaO	1.48	0.96	0.36	0.57	0.59	0.49	0.50	0.68	0.76	0.54
K2O	n.d.									
TOTAL	43.03	42.98	44.16	42.85	43.52	43.78	43.51	42.04	42.26	42.20
Sample Code SPOT	A6 SI-C 13	A6 SI-C 14	A6 SI-C 15	A6 MG-C 16	A6 MG-M 17	A6 MG-C 18	A6 MG-C 19	A6 MG-M 20	A6 SI-C 21	A6 MX-C 22
SiO2	90.75	91.11	90.26	0.17	n.d.	n.d.	0.17	0.16	90.38	2.92
TiO2	n.d.									
Al2O3	n.d.									
Cr2O3	n.d.									
FeO	n.d.									
MnO	n.d.	0.67								
MgO	n.d.	n.d.	n.d.	41.64	41.78	41.68	41.90	41.09	n.d.	40.14
CaO	n.d.	n.d.	n.d.	0.54	0.45	1.06	0.95	1.07	n.d.	0.50
K2O	n.d.									
TOTAL	90.75	91.11	90.26	42.35	42.23	42.74	43.02	42.33	90.38	44.23
Sample Code SPOT	A6 MX-C 23	A6 MX-C 24	A12 MG-C 1	A12 MG-M 2	A12 MG-M 3	A12 MG-C 4	A12 MG-C 5	A12 MG-M 6	A12 MG-C 7	A12 MG-C 8
SiO2	3.06	4.97	n.d.	0.22	0.74	n.d.	n.d.	n.d.	n.d.	n.d.
TiO2	n.d.									
Al2O3	n.d.									
Cr2O3	n.d.									
FeO	0.55	0.80	1.87	0.58	2.22	2.52	2.55	2.80	n.d.	2.62
MnO	n.d.									
MgO	40.63	39.54	40.56	41.36	38.86	40.32	40.62	40.12	41.54	40.69
CaO	0.41	0.53	0.84	0.68	0.93	1.37	1.14	1.07	0.89	1.35
K2O	n.d.									
TOTAL	44.65	45.85	43.27	42.84	42.74	44.21	44.32	43.99	42.43	44.66

N-MAG

Sample Code SPOT	A12 MG-M 9	A12 MG-C 10	A12 MG-M 11	A12 MG-C 12	A12 MG-C 13	A12 MG-M 14	A12 MG-C 15	A12 MG-C 16	A12 MG-M 17	A12 MG-M 18
SiO2	n.d.	n.d.	n.d.	n.d.	n.d.	n.d.	n.d.	n.d.	n.d.	0.22
TiO2	n.d.	n.d.	n.d.	n.d.	n.d.	n.d.	n.d.	n.d.	n.d.	n.d.
Al2O3	n.d.	n.d.	n.d.	n.d.	n.d.	n.d.	n.d.	n.d.	n.d.	n.d.
Cr2O3	n.d.	n.d.	n.d.	n.d.	n.d.	n.d.	n.d.	n.d.	n.d.	n.d.
FeO	1.32	2.20	1.31	0.20	2.34	2.53	2.38	2.61	2.82	0.45
MnO	n.d.	n.d.	n.d.	n.d.	n.d.	n.d.	n.d.	n.d.	n.d.	n.d.
MgO	40.84	39.96	40.74	41.41	40.08	40.55	40.82	40.83	40.32	41.11
CaO	1.13	1.08	1.32	1.03	1.16	0.99	0.77	1.04	1.15	1.00
K2O	n.d.	n.d.	n.d.	n.d.	n.d.	n.d.	n.d.	n.d.	n.d.	n.d.
TOTAL	43.28	43.24	43.38	42.64	43.58	44.07	43.97	44.48	44.28	42.78

Sample Code SPOT	A12 MG-C 19	A12 MG-C 20	A12 MG-M 21	A12 MG-C 22	A12 MG-M 23	A12 MG-C 24	A12 MG-C 25	A12 MG-C 26	A12 MG-C 27	A12 MG-C 28
SiO2	n.d.	n.d.	n.d.	n.d.	n.d.	n.d.	0.21	n.d.	n.d.	n.d.
TiO2	n.d.									
Al2O3	n.d.									
Cr2O3	n.d.									
FeO	2.16	1.94	1.26	1.51	3.46	1.01	n.d.	1.83	n.d.	2.40
MnO	n.d.									
MgO	39.65	41.09	41.83	39.63	40.17	41.24	39.64	40.41	41.61	39.86
CaO	1.05	0.89	0.49	1.38	1.33	0.69	0.92	0.54	0.85	1.56
K2O	n.d.									
TOTAL	42.86	43.92	43.59	42.52	44.97	42.94	40.77	42.77	42.46	43.82

Sample Code SPOT	A12 MG-C 29	A12 MG-M 30	A12 MG-C 31	A12 MG-C 32	A12 MG-C 33	A12 MG-C 34	A12 MG-C 35	A12 MG-M 36	A12 MG-C 37	A12 MG-C 38
SiO2	n.d.	n.d.	n.d.	n.d.	n.d.	0.17	n.d.	n.d.	n.d.	n.d.
TiO2	n.d.									
Al2O3	n.d.									
Cr2O3	n.d.	n.d.	0.27	n.d.						
FeO	2.18	1.84	2.41	2.35	1.23	1.28	2.71	2.22	n.d.	2.65
MnO	n.d.									
MgO	40.36	40.52	41.01	40.38	41.25	41.66	39.96	39.88	40.63	39.93
CaO	1.18	0.55	0.66	0.67	0.47	0.51	0.95	1.24	0.62	1.19
K2O	n.d.									
TOTAL	43.72	42.91	44.35	43.40	42.94	43.62	43.62	43.34	41.25	43.78

N-MAG										
Sample Code SPOT	A12 MG-C 39	A12 MG-M 40	A12 MG-M 41	A12 MG-C 42	A12 MG-C 43	A12 MG-C 44	A12 MG-M 45	A12 MG-C 46	A12 MG-M 47	A12 MG-C 48
SiO2	0.17	n.d.	n.d.	n.d.	n.d.	n.d.	0.57	0.16	0.16	n.d.
TiO2	n.d.									
Al2O3	n.d.									
Cr2O3	n.d.									
FeO	n.d.	0.34	1.20	0.94	0.27	0.86	1.12	0.24	n.d.	0.29
MnO	n.d.									
MgO	41.97	41.89	40.62	41.41	40.47	40.12	40.65	41.32	41.04	41.98
CaO	0.40	1.11	0.41	0.45	0.72	0.90	0.52	0.37	0.54	0.42
K2O	n.d.									
TOTAL	42.54	43.34	42.23	42.80	41.46	41.88	42.86	42.09	41.74	42.69
Sample Code SPOT	A12 MG-M 49	A12 MG-C 50	T2 MG-C 1	T2 MG-C 2	T2 MG-C 3	T2 MG-C 4	T2 MX-C 5	T2 MG-C 6	T2 MX-C 7	T2 MG-C 8
SiO2	0.17	n.d.	0.68	0.28	0.34	0.77	1.16	0.28	3.68	0.71
TiO2	n.d.									
Al2O3	n.d.									
Cr2O3	n.d.	n.d.	0.00	0.00	0.00	0.00	0.00	0.00	0.00	0.00
FeO	2.75	2.37	n.d.							
MnO	n.d.									
MgO	39.79	39.85	40.69	41.53	40.85	40.58	39.85	41.23	38.86	40.12
CaO	1.14	1.25	2.27	2.02	2.08	2.32	2.17	2.25	2.94	2.46
K2O	n.d.									
TOTAL	43.85	43.46	43.63	43.83	43.27	43.67	43.18	43.76	45.47	43.30
Sample Code SPOT	T2 MG-C 9	T2 MG-C 10	T2 MG-C 11	T15 MX-C 1	T15 MX-C 2	T15 MX-C 3	T15 MX-C 4	T15 MX-C 5	T15 MX-C 6	T15 MX-C 7
SiO2	0.32	0.19	0.43	0.11	2.39	4.28	6.39	3.36	3.74	2.42
TiO2	n.d.									
Al2O3	n.d.									
Cr2O3	0.00	0.00	0.00	n.d.						
FeO	n.d.									
MnO	n.d.									
MgO	41.08	41.29	41.64	38.92	37.19	34.00	33.23	37.00	34.35	34.71
CaO	2.24	2.49	2.27	4.62	2.16	2.10	2.09	2.46	2.16	2.12
K2O	n.d.									
TOTAL	43.64	43.97	44.33	43.65	41.74	40.38	41.71	42.81	40.26	39.25

Sample Code SPOT	N-MAG									
	T15 MX-C 8	T26 DL-C 1	T26 MG-C 2	T26 DL-C 3	T26 MG-C 4	T26 DL-C 5	T26 MG-C 6	T26 DL-C 7	T26 MG-C 8	T26 DL-C 9
SiO2	2.28	n.d.	0.20	n.d.	n.d.	n.d.	0.26	n.d.	0.24	n.d.
TiO2	n.d.									
Al2O3	n.d.									
Cr2O3	n.d.									
FeO	n.d.									
MnO	n.d.									
MgO	34.04	18.46	40.45	21.84	40.15	19.21	40.57	21.04	38.72	19.67
CaO	2.16	33.49	0.85	30.45	0.93	32.81	1.15	29.76	1.21	33.35
K2O	n.d.									
TOTAL	38.48	51.95	41.51	52.29	41.08	52.02	41.98	50.81	40.17	53.02

Sample Code SPOT	T26 MG-C 10	T26 DL-C 11	T26 MG-C 12	T26 DL-C 13	T26 MX-C 14	T26 MX-M 15	T26 DL-M 16	T26 MX-M 17	T26 DL-C 18	T26 MX-M 19
	SiO2	n.d.	n.d.	n.d.	n.d.	0.20	n.d.	n.d.	n.d.	n.d.
TiO2	n.d.									
Al2O3	n.d.									
Cr2O3	n.d.									
FeO	n.d.									
MnO	n.d.									
MgO	40.12	21.94	38.22	21.45	39.51	27.54	23.54	29.02	18.96	28.87
CaO	2.78	28.94	0.84	30.40	3.05	22.97	26.45	19.48	32.81	19.91
K2O	n.d.									
TOTAL	42.91	50.88	39.06	51.86	42.76	50.52	49.99	48.50	51.77	48.79

Sample Code SPOT	T26 DL-C 20	T26 DL-M 21	T26 DL-C 22	T26 MX-M 23
	SiO2	n.d.	0.17	n.d.
TiO2	n.d.	n.d.	n.d.	n.d.
Al2O3	n.d.	n.d.	n.d.	n.d.
Cr2O3	n.d.	n.d.	n.d.	n.d.
FeO	n.d.	n.d.	n.d.	n.d.
MnO	n.d.	n.d.	n.d.	n.d.
MgO	21.86	25.66	19.48	38.18
CaO	31.29	26.94	33.75	8.78
K2O	n.d.	n.d.	n.d.	n.d.
TOTAL	53.15	52.77	53.23	46.96

APPENDIX 5

SCANNING ELECTRON MICROSCOPE

Instrumental

The Scanning Electron Microscope consists of an electron optical column and an electronics console (Figure A 5.1). The coated sample is placed in the sample chamber, and evacuated to high vacuum. Instead of using light, as in the petrographic microscope, the SEM image is formed by an internally generated electron beam. This beam is created by heating a very thin tungsten filament (Figure A 5.1) in the electron gun until the filament emits electrons. The electrons are accelerated through the column by a 0.2-40 KV accelerating voltage, demagnified and focused through a series of electromagnetic lenses into a finely focused beam, which bombards the sample. The final diameter of the beam is typically 100 angstroms in most commercial SEM's. Additional components include a stigmator for controlling the shape of the beam and apertures to minimize lens defects (aberrations), which in light microscopy severely limits the resolution. It is the interaction of the primary electron beam with the sample which generates various forms of radiation, such as secondary electrons, characteristic X-rays, Auger electrons, and back scatter electrons. All of these reactions occur simultaneously. It is possible to both observe and analyse the elemental composition of an isolated mineral in a matter of seconds.

The microstructural study on flat surfaces are carried out with the Cambridge Instruments models 600 and 360 Scanning Electron Microscopes. The SEM 600 equipped with a K.E.Developments Limited solid state back scattered electron detector and Link System model 860 energy dispersive X-ray analyser.

Since the efficiency of the backscatter detector is relatively poor, a higher than normal spot size was used. This reduces the spatial resolution, but improves the number contrast.

Secondary electron (SE) emission

Free electrons that leave the specimen, liberated by the inelastic scattering reaction, are known as secondary electrons. These electrons have no relationship with the material from which they were liberated, and have an energy less than 50 electron volts. The energy of the incident electron beam, at conventional scanning electron microscope accelerating voltages, does not play any part of relation to the number of secondary electrons emitted by the inelastic scattering reaction. At these high voltage levels the relationship between the material making up the specimen and the emission of secondary electrons is fairly constant. Only at very low atomic numbers does the secondary emission relate to atomic number.

The most advanced advantageous use of pure secondary images is in the observation of fine surface structures. Secondary electron imaging uses very low accelerating

voltages (<5KV). Almost all low KV operating techniques follow the high resolution procedures, as lower accelerating voltages degrade image resolution to a considerable degree.

Backscattered electron (BSE) emission

Backscattered electrons are incident beam electrons that have been re-emitted from the specimen through multiple scattering. They have an energy up to the incident beam energy, and are usually very near to that energy. The emission of backscattered electrons from a specimen is related to the atomic number of the material involved, the higher the atomic number the higher the backscatter coefficient. The emission of backscattered electrons also relates to the energy of the incident electron beam, the higher the incident electrons energy, the greater its ability to move through the specimen material, and the higher the probability of its emerging as backscattered electrons.

**Scanning Electron Microscope
and
Energy Dispersive X-Ray Spectrometer**

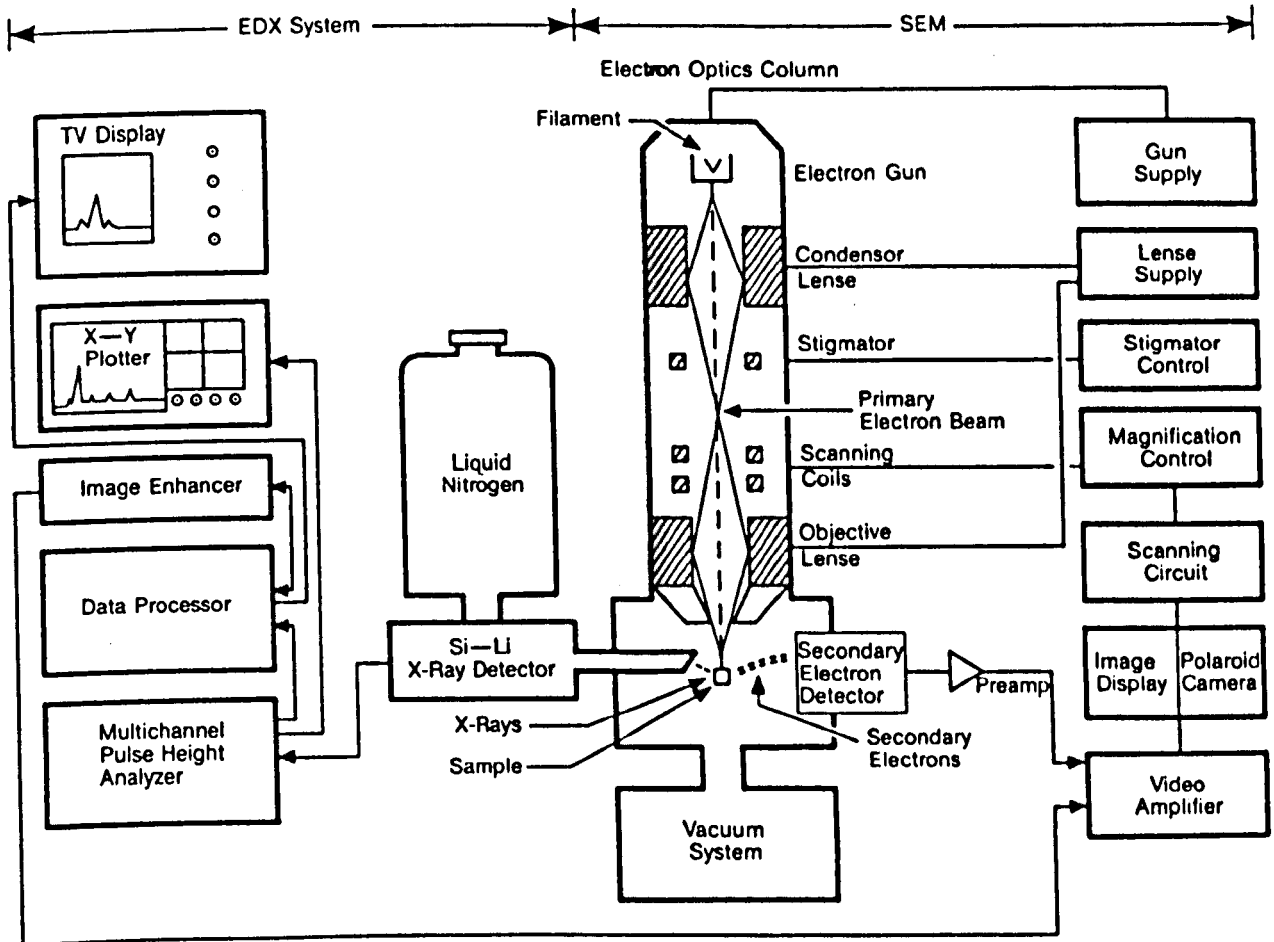


Figure A5.1

Schematic showing SEM/EDX System
(from Welton 1984)

APPENDIX 6

PROCEDURE FOR PREPARATION OF POLISHED BLOCKS OF MATERIALS SUSCEPTIBLE TO HYDRATION

(This procedure is taken from Kimyongur 1984)

There are three stages in preparing polished blocks of materials which consist of loose grains (0.5-3.0 cm in diameter), such as magnesia grains: a) moulding; b) grinding and c) polishing. If the material is in powder or fine granular form, it needs first to be impregnated. When the material is large in size, it has to be cut using a diamond saw into a suitable size for embedding in the mould.

a) Moulding

The procedure for moulding the magnesia grains is as follows:

1. Grease the block mould with a non-reacting agent (silicone grease is used here).
2. Place the selected grains in the block mould.
3. Prepare moulding resin following the instructions (Araldite MY735 (resin) and Araldite HY951 (hardener) in the ratio of 5:1 is used in this study) and pour it into the block mould. Avoid air bubbles being trapped under the specimen. Evacuate in a desiccator if necessary.
4. Leave the blocks to 'cure' for approximately 24 hours.
5. Remove the blocks from the mould.

b) Grinding

Steps in grinding the blocks are summarized below:

1. using dry grinding:
 - i) grind the back of the block,
 - ii) grind the front of the block to remove the moulding resin. Bevel the sharp edges of the block in order to avoid damaging the polishing laps.
2. Using carborundum grit size 400 (38 microns) and paraffin prepare a slurry on a glass plate.
3. Grind the surface to be examined until a smooth surface of the specimen is obtained.
4. Clean thoroughly the surface of the polished blocks and the glass plate.
5. repeat steps 2, 3 and 4 for grit size 600 (30 microns), 800 (22 microns) and 1200 (15 microns).

After grinding with grit 1200 the block should have a reasonably smooth and shiny surface. The block is now ready for polishing.

c) Polishing (Engis polishing machine is used here).

The procedure and the conditions are as follows:

1. Drill a shallow hole into the back of the block.
2. Place 6 micron (3000 grit size) diamond paste on the polishing lap.
3. Fit thoroughly cleaned blocks to the polishing heads.
4. Spray a lubricant on the lap.
5. Polish using 2.27 kg (5lb) weight at speed 70 rpm for

approximately 2 hours.

6. Repeat steps 1 to 5 using the following diamond pastes, weights and polishing times:

<u>diamond paste</u>	<u>Weight</u>	<u>speed (rpm)</u>	<u>time (hr)</u>
3um (8000 grit size)	1.8 Kg (41b)	75	1
1um (14000 grit size)	1.8 kg (41b)	90	1

Examine the quality of polish at each grade and repeat the polish if necessary.

APPENDIX 7

Electron microprobe analyses of dead burned magnesite

Sample Code SPOT	A3-1A PC16 1	A3-1A PC16 2	A3-1A PC16 3	A3-1A MX16 4	A3-1A MX16 5	A3-1A DC16 6	A3-1A DC16 7	A3-1A DC16 8	A3-1A PC16 9	A3-1A PM16 10
SiO2	n.d.	n.d.	n.d.	23.31	31.62	33.81	33.38	33.90	0.19	n.d.
TiO2	n.d.									
Al2O3	n.d.	1.62	n.d.	n.d.	n.d.	0.24	0.57	0.29	n.d.	n.d.
Cr2O3	n.d.	n.d.	n.d.	0.25	n.d.	n.d.	n.d.	n.d.	n.d.	n.d.
FeO	0.55	0.80	0.56	n.d.	n.d.	n.d.	n.d.	n.d.	0.70	0.73
MnO	n.d.									
MgO	99.81	98.47	98.75	37.43	7.53	0.36	0.51	n.d.	100.37	98.75
CaO	0.23	0.32	n.d.	41.75	60.16	64.52	63.69	64.44	0.20	n.d.
K2O	n.d.									
TOTAL	100.58	101.21	99.31	102.74	99.31	98.93	98.16	98.63	101.47	99.48

Sample Code SPOT	A3-1A PC16 11	A3-1A DC16 12	A3-1A DM16 13	A3-1A MX16 14	A3-1A MX16 15	A3-1A PC16 16	A3-1A PC16 17	A3-1A PM16 18	A3-1A PC16 19	A3-1A DC16 20
SiO2	n.d.	34.00	33.54	13.13	0.00	n.d.	n.d.	n.d.	0.29	33.57
TiO2	n.d.									
Al2O3	n.d.	0.30	0.40	14.51	10.34	2.12	n.d.	n.d.	n.d.	0.26
Cr2O3	n.d.									
FeO	0.38	n.d.	n.d.	1.59	1.10	0.58	0.69	0.40	0.54	n.d.
MnO	n.d.									
MgO	100.10	1.56	0.40	49.52	91.06	99.35	100.11	100.07	100.63	0.53
CaO	n.d.	63.54	65.22	22.34	0.31	n.d.	0.21	n.d.	n.d.	64.47
K2O	n.d.									
TOTAL	100.48	99.40	99.57	101.09	102.82	102.06	101.01	100.47	101.46	98.82

Sample Code SPOT	A3-1A DC16 21	A3-1A DC16 22	A3-1A PC16 23	A3-1A MX16 24	A3-1A DC16 25	A3-1A DC16 26	A3-1B DC16 1	A3-1B PC16 2	A3-1B PM16 3	A3-1B PC16 4
SiO2	33.80	33.37	n.d.	22.21	33.16	34.24	34.23	n.d.	n.d.	n.d.
TiO2	n.d.	n.d.	n.d.	n.d.	0.33	n.d.	n.d.	n.d.	n.d.	n.d.
Al2O3	0.24	1.30	n.d.	12.75	1.10	0.46	0.28	n.d.	n.d.	0.60
Cr2O3	n.d.	n.d.	n.d.	n.d.	n.d.	n.d.	n.d.	n.d.	n.d.	n.d.
FeO	n.d.	n.d.	0.55	0.71	n.d.	n.d.	n.d.	0.73	0.45	0.57
MnO	n.d.	n.d.	n.d.	n.d.	n.d.	n.d.	n.d.	n.d.	n.d.	n.d.
MgO	1.87	0.68	99.93	25.30	4.59	1.07	0.82	99.79	99.43	97.91
CaO	63.31	63.96	n.d.	43.41	59.47	64.04	64.33	0.25	0.19	0.29
K2O	n.d.	n.d.	n.d.	n.d.	n.d.	n.d.	n.d.	n.d.	n.d.	n.d.
TOTAL	99.22	99.31	100.48	104.38	98.65	99.82	99.66	100.77	100.07	99.37

DB.MG1

Sample Code SPOT	A3-1B PM16 5	A3-1B DC16 6	A3-1B DC16 7	A3-1B DC16 8	A3-1B DC16 9	A3-1B DC16 10	A3-1B DC16 11	A3-1B SP16 12	A3-1B MX16 13	A3-1B SP16 14
SiO2	n.d.	33.79	33.83	33.90	33.86	33.53	34.03	10.48	5.34	11.43
TiO2	n.d.	0.48	0.24	0.42						
Al2O3	n.d.	0.79	0.51	0.31	0.49	0.86	n.d.	45.71	35.49	44.90
Cr2O3	n.d.									
FeO	0.75	n.d.	n.d.	n.d.	n.d.	n.d.	n.d.	3.96	3.08	4.05
MnO	n.d.									
MgO	100.93	1.89	0.44	0.34	1.80	0.75	0.31	20.67	49.99	20.08
CaO	n.d.	62.93	63.89	65.81	63.67	62.44	63.96	10.31	10.76	19.50
K2O	n.d.									
TOTAL	101.68	99.40	98.66	100.36	99.82	97.57	98.29	91.60	104.90	100.37
Sample Code SPOT	A3-1B PC16 15	A3-1B PM16 16	A3-1B PC16 17	A3-1B PC16 18	A3-1B DC16 19	A3-1B PC16 20	A3-1B PC16 21	A3-2A DC16 1	A3-2A DM16 2	A3-2A PM16 3
SiO2	0.18	0.17	n.d.	n.d.	33.26	0.29	0.18	33.84	33.41	0.19
TiO2	n.d.									
Al2O3	n.d.	2.10	n.d.	0.81	0.45	n.d.	n.d.	n.d.	0.26	0.28
Cr2O3	n.d.									
FeO	0.70	1.08	0.76	0.77	0.30	0.82	0.65	n.d.	0.37	1.01
MnO	n.d.									
MgO	99.26	97.69	101.10	98.22	1.17	98.32	98.89	0.25	0.32	100.00
CaO	n.d.	0.16	0.15	0.24	63.37	0.52	0.20	64.65	64.67	n.d.
K2O	n.d.									
TOTAL	100.14	101.20	102.01	100.04	98.55	99.95	99.92	98.74	99.03	101.47
Sample Code SPOT	A3-2A PC16 4	A3-2A DC16 5	A3-2A DC16 6	A3-2A DC16 7	A3-2A PC16 8	A3-2A PM16 9	A3-2A DC16 10	A3-2A MX16 11	A3-2A DC16 12	A3-2A DM16 13
SiO2	n.d.	33.68	33.79	34.28	n.d.	0.18	33.68	18.69	33.75	34.28
TiO2	n.d.	n.d.	n.d.	0.23	n.d.	n.d.	n.d.	n.d.	n.d.	n.d.
Al2O3	0.41	0.23	n.d.	n.d.	n.d.	n.d.	0.45	27.10	0.39	0.51
Cr2O3	n.d.									
FeO	1.03	n.d.	n.d.	n.d.	0.81	1.13	n.d.	4.03	n.d.	n.d.
MnO	n.d.									
MgO	98.48	n.d.	0.70	0.48	99.39	99.23	0.20	21.38	1.73	1.44
CaO	0.27	64.48	64.17	64.73	n.d.	0.65	64.97	32.19	63.02	63.50
K2O	n.d.									
TOTAL	100.18	98.40	98.66	99.72	100.19	101.19	99.30	103.38	98.88	99.73

DB.MG1

Sample Code SPOT	A3-2A PC16 14	A3-2A DM16 15	A3-2A DC16 16	A3-2B DC16 1	A3-2B PC16 2	A3-2B PC16 3	A3-2B PC16 4	A3-2B DC16 5	A3-2B PC16 6	A3-2B PC16 7
SiO2	n.d.	30.21	33.47	33.16	n.d.	n.d.	n.d.	33.68	n.d.	n.d.
TiO2	n.d.	n.d.	n.d.	n.d.	n.d.	n.d.	n.d.	n.d.	n.d.	n.d.
Al2O3	0.45	7.11	1.30	0.26	n.d.	0.64	n.d.	0.63	n.d.	n.d.
Cr2O3	n.d.	n.d.	n.d.	n.d.	n.d.	n.d.	n.d.	n.d.	n.d.	n.d.
FeO	1.00	0.89	n.d.	n.d.	0.75	0.89	0.92	n.d.	0.74	1.10
MnO	n.d.	n.d.	n.d.	n.d.	n.d.	n.d.	n.d.	n.d.	n.d.	n.d.
MgO	99.90	0.44	2.62	0.38	99.74	99.58	99.22	0.58	101.94	99.85
CaO	0.30	59.50	61.20	63.90	n.d.	0.29	0.13	64.17	n.d.	n.d.
K2O	n.d.	n.d.	n.d.	n.d.	n.d.	n.d.	n.d.	n.d.	n.d.	n.d.
TOTAL	101.65	98.16	98.59	97.69	100.50	101.41	100.28	99.07	102.69	100.95

Sample Code SPOT	A3-2B DM16 8	A3-2B DC16 9	A3-2B DC16 10	A3-2B DC16 11	A3-2B PC16 12	A3-2B PM16 13	A3-2B DC16 14	A3-2B PC16 15	A3-2B PC16 16	A3-2B PM16 17
SiO2	33.38	33.21	33.99	33.95	n.d.	n.d.	33.93	0.18	0.19	0.23
TiO2	n.d.	n.d.	n.d.	n.d.	n.d.	n.d.	n.d.	n.d.	n.d.	n.d.
Al2O3	0.54	0.23	0.29	n.d.	0.31	n.d.	0.35	0.45	0.48	0.51
Cr2O3	n.d.	n.d.	n.d.	n.d.	n.d.	n.d.	n.d.	n.d.	n.d.	n.d.
FeO	0.35	n.d.	n.d.	n.d.	0.98	1.00	n.d.	0.93	1.00	1.07
MnO	n.d.	n.d.	n.d.	n.d.	n.d.	n.d.	n.d.	n.d.	n.d.	n.d.
MgO	0.44	0.26	n.d.	0.34	98.83	100.54	0.46	97.83	99.42	98.81
CaO	64.05	64.72	64.73	64.59	0.16	n.d.	64.34	0.35	0.16	0.37
K2O	n.d.	n.d.	n.d.	n.d.	n.d.	n.d.	n.d.	n.d.	n.d.	n.d.
TOTAL	98.75	98.42	99.00	98.87	100.29	101.55	99.08	99.75	101.25	100.99

Sample Code SPOT	A3 SP16 1	A3 SP16 2	A3 DC16 3	A3 DC16 4	A3 SP16 5	A3 MX16 6	A3 SP16 7	A3 SP16 8	A3 SP16 9	A3 SP16 10
SiO2	2.17	0.37	33.47	33.85	0.27	9.34	1.47	8.17	5.85	8.75
TiO2	n.d.	0.25	n.d.	n.d.	n.d.	0.48	n.d.	0.53	0.36	0.29
Al2O3	56.58	64.24	n.d.	n.d.	58.55	36.54	61.59	49.09	54.57	48.35
Cr2O3	n.d.	n.d.	n.d.	n.d.	0.20	n.d.	n.d.	n.d.	n.d.	n.d.
FeO	7.15	5.90	n.d.	n.d.	7.07	3.61	6.62	4.28	4.95	3.93
MnO	n.d.									
MgO	29.86	29.65	1.03	0.38	31.19	13.73	27.16	21.39	23.94	22.07
CaO	3.93	0.51	63.35	64.92	0.42	37.11	2.02	15.42	9.23	15.66
K2O	n.d.									
TOTAL	99.69	100.91	97.85	99.15	97.69	100.81	98.86	98.87	98.90	99.05

DB.MG1

Sample Code SPOT	A3 SP16 11	A3 MR15 1	A3 MX15 2	A3 MR15 3	A3 MX15 4	A3 PM15 5	A3 PC15 6	A3 PC15 7	A3 PC15 8	A3 PM15 9
SiO2	1.33	36.56	26.52	36.16	32.54	0.29	n.d.	n.d.	n.d.	n.d.
TiO2	0.27	n.d.								
Al2O3	56.21	n.d.								
Cr2O3	n.d.	n.d.	n.d.	n.d.	n.d.	n.d.	n.d.	n.d.	n.d.	n.d.
FeO	6.93	n.d.	0.83	n.d.	0.47	2.23	2.22	2.15	2.10	1.99
MnO	n.d.	n.d.	n.d.	n.d.	n.d.	n.d.	n.d.	n.d.	n.d.	n.d.
MgO	26.56	12.18	39.35	11.98	3.89	96.47	97.70	96.76	96.12	95.96
CaO	2.02	50.29	36.23	50.43	56.87	n.d.	0.14	n.d.	0.16	0.23
K2O	n.d.	n.d.	n.d.	n.d.	n.d.	n.d.	n.d.	n.d.	n.d.	n.d.
TOTAL	93.33	99.03	102.93	98.57	93.77	98.99	100.06	98.91	98.38	98.18

Sample Code SPOT	A3 PC15 10	A3 PM15 11	A3 PC15 12	A3 PM15 13	A3 PC15 14	A3 PM15 15	A3 PC15 16	A3 PM15 17	A3 MX15 18	A3 MR15 19
SiO2	n.d.	n.d.	0.20	n.d.	n.d.	n.d.	n.d.	n.d.	32.61	36.35
TiO2	n.d.									
Al2O3	n.d.									
Cr2O3	n.d.									
FeO	1.94	2.00	2.16	1.99	2.33	1.95	2.26	2.12	0.32	0.42
MnO	n.d.									
MgO	96.55	96.65	96.68	96.50	97.01	96.99	96.56	96.51	22.16	12.14
CaO	n.d.	n.d.	0.31	0.16	0.16	0.14	n.d.	n.d.	45.75	50.10
K2O	n.d.									
TOTAL	98.49	98.65	99.35	98.65	99.50	99.08	98.82	98.63	100.84	99.01

Sample Code SPOT	A3 MR15 20	A3 MR15 21	A3 MR15 22	A3 MX15 23	A3 PC14 1	A3 PC14 2	A3 PC14 3	A3 PM14 4	A3 PC14 5	A3 PM14 6
SiO2	35.35	37.27	34.90	24.37	0.24	0.30	n.d.	n.d.	n.d.	0.21
TiO2	n.d.	n.d.	n.d.	n.d.	n.d.	n.d.	n.d.	n.d.	n.d.	n.d.
Al2O3	n.d.	n.d.	n.d.	n.d.	n.d.	n.d.	n.d.	n.d.	n.d.	n.d.
Cr2O3	n.d.	n.d.	n.d.	n.d.	n.d.	n.d.	n.d.	n.d.	n.d.	n.d.
FeO	n.d.	0.31	n.d.	0.93	1.58	1.55	1.60	1.40	1.72	1.42
MnO	n.d.	n.d.	n.d.	n.d.	n.d.	n.d.	n.d.	n.d.	n.d.	0.24
MgO	13.44	12.37	13.51	44.78	95.40	98.02	97.26	96.52	95.71	95.33
CaO	49.65	51.82	48.90	32.25	0.65	0.46	0.34	0.28	0.38	0.29
K2O	n.d.	n.d.	n.d.	n.d.	n.d.	n.d.	n.d.	n.d.	n.d.	n.d.
TOTAL	98.44	101.77	97.31	102.33	97.87	100.33	99.20	98.20	97.81	97.49

DB.MG1

Sample Code SPOT	A3 PC14 7	A3 PM14 8	A3 PC14 9	A3 PC14 10	A3 PM14 11	A3 PC14 12	A3 PM14 13	A3 PC14 14	A3 PC14 15	A3 PC14 16
SiO2	n.d.	n.d.	0.21	n.d.	0.19	n.d.	0.19	n.d.	0.25	n.d.
TiO2	n.d.	n.d.	n.d.	n.d.	n.d.	n.d.	n.d.	n.d.	n.d.	n.d.
Al2O3	n.d.	n.d.	n.d.	n.d.	n.d.	n.d.	n.d.	n.d.	n.d.	n.d.
Cr2O3	n.d.	n.d.	n.d.	n.d.	n.d.	n.d.	n.d.	n.d.	n.d.	n.d.
FeO	1.36	1.48	1.50	1.51	1.50	1.26	1.17	1.36	1.48	1.50
MnO	n.d.	n.d.	n.d.	n.d.	n.d.	n.d.	n.d.	n.d.	n.d.	n.d.
MgO	95.67	96.60	96.15	97.89	98.34	96.81	97.72	95.47	96.06	95.87
CaO	0.33	0.33	0.35	0.37	0.32	0.30	0.33	0.33	0.33	0.35
K2O	n.d.	n.d.	n.d.	n.d.	n.d.	n.d.	n.d.	n.d.	n.d.	n.d.
TOTAL	97.36	98.41	98.21	99.77	100.35	98.37	99.41	97.16	98.12	97.72

Sample Code SPOT	A3 FR14 17	A3 FR14 18	A3 FR14 19	A3 FR14 20	A3 FR14 21	A14-1A MC16 1	A14-1A MM16 2	A14-1A PC16 3	A14-1A PC16 4	A14-1A MC16 5
SiO2	6.27	5.38	6.39	6.60	8.15	39.01	38.92	0.19	n.d.	38.16
TiO2	0.46	n.d.	n.d.	0.37	0.35	n.d.	n.d.	n.d.	n.d.	0.23
Al2O3	n.d.	n.d.	n.d.	n.d.	n.d.	n.d.	n.d.	n.d.	1.18	n.d.
Cr2O3	n.d.	n.d.	n.d.	n.d.	n.d.	n.d.	n.d.	n.d.	n.d.	n.d.
FeO	32.73	21.44	32.37	32.27	21.48	n.d.	n.d.	0.53	0.63	n.d.
MnO	n.d.	n.d.	n.d.	n.d.	n.d.	n.d.	n.d.	n.d.	n.d.	n.d.
MgO	14.46	42.34	11.91	12.27	23.79	29.61	29.56	97.21	99.11	26.88
CaO	39.92	29.74	40.01	41.47	41.27	30.58	30.97	n.d.	n.d.	33.10
K2O	n.d.	n.d.	n.d.	n.d.	n.d.	n.d.	n.d.	n.d.	n.d.	n.d.
TOTAL	93.84	98.90	90.68	92.98	95.04	99.19	99.45	97.93	100.92	98.38

Sample Code SPOT	A14-1A PC16 6	A14-1A PC16 7	A14-1A PM16 8	A14-1A MC16 9	A14-1A MC16 10	A14-1A FC16 11	A14-1A MC16 12	A14-1A MC16 13	A14-1A FC16 14	A14-1A FC16 15
SiO2	n.d.	n.d.	n.d.	36.61	37.81	41.64	38.83	38.73	41.32	42.05
TiO2	n.d.	n.d.	n.d.	n.d.	n.d.	n.d.	n.d.	n.d.	n.d.	n.d.
Al2O3	0.43	0.37	n.d.	0.56	0.29	n.d.	n.d.	n.d.	0.89	0.68
Cr2O3	n.d.	n.d.	n.d.	n.d.	n.d.	n.d.	n.d.	n.d.	n.d.	n.d.
FeO	0.68	0.44	0.54	n.d.	n.d.	0.43	n.d.	n.d.	n.d.	0.44
MnO	n.d.	n.d.	n.d.	n.d.	n.d.	n.d.	n.d.	n.d.	n.d.	n.d.
MgO	99.56	98.85	98.49	32.73	31.38	52.22	28.50	29.76	52.91	53.15
CaO	n.d.	n.d.	n.d.	29.78	30.12	4.12	31.71	30.72	3.76	3.73
K2O	n.d.	n.d.	n.d.	n.d.	n.d.	n.d.	n.d.	n.d.	n.d.	n.d.
TOTAL	100.66	99.66	99.03	99.67	99.60	98.40	99.04	99.21	98.88	100.06

DB.MG1

Sample Code SPOT	A14-1A FC16 16	A14-1A MX16 17	A14-1A FC16 18	A14-1A PC16 19	A14-1A MC16 20	A14-1A MC16 21	A14-1A MC16 22	A14-1B FC16 1	A14-1B FM16 2	A14-1B FC16 3
SiO2	41.97	32.67	41.96	n.d.	35.37	38.91	39.04	42.08	41.22	42.38
TiO2	n.d.	n.d.	n.d.	n.d.						
Al2O3	1.02	0.52	0.69	0.28	2.00	n.d.	n.d.	0.45	0.40	0.79
Cr2O3	n.d.	n.d.	n.d.	n.d.						
FeO	0.31	0.28	n.d.	0.77	0.47	n.d.	n.d.	n.d.	0.37	n.d.
MnO	n.d.	n.d.	n.d.	n.d.						
MgO	54.08	43.26	53.94	99.69	35.22	29.23	30.25	53.79	52.80	54.14
CaO	3.12	26.50	3.30	n.d.	27.84	31.42	29.84	3.09	4.13	4.11
K2O	n.d.	n.d.	n.d.	n.d.						
TOTAL	100.52	103.23	99.90	100.74	100.89	99.56	99.13	99.41	98.94	101.42

Sample Code SPOT	A14-1B MC16 4	A14-1B FC16 5	A14-1B FC16 6	A14-1B MC16 7	A14-1B MC16 8	A14-1B MX16 9	A14-1B PM16 10	A14-1B MX16 11	A14-1B MC16 12	A14-1B FC16 13
SiO2	39.18	41.81	41.97	38.43	37.66	n.d.	0.17	28.73	39.21	42.24
TiO2	n.d.	0.45	n.d.	n.d.						
Al2O3	0.38	0.69	0.69	n.d.	n.d.	6.88	n.d.	16.66	0.32	0.37
Cr2O3	n.d.	n.d.	n.d.	n.d.						
FeO	n.d.	n.d.	0.29	n.d.	n.d.	0.93	0.80	0.49	n.d.	n.d.
MnO	n.d.	n.d.	n.d.	n.d.						
MgO	30.33	53.96	52.81	29.63	31.14	93.53	98.99	27.16	31.03	53.01
CaO	30.65	2.98	4.41	30.51	29.85	n.d.	n.d.	24.47	29.78	4.83
K2O	n.d.	n.d.	n.d.	n.d.						
TOTAL	100.54	99.44	100.17	98.57	98.65	101.34	99.95	97.96	100.35	100.46

Sample Code SPOT	A14-1B FC16 14	A14-1B MC16 15	A14-1B MC16 16	A14-1B PC16 17	A14-1B PM16 18	A14-1B PC16 19	A14-1B PM16 20	A14-1B MC16 21	A14-1B MC16 22	A14-1B PC16 23
SiO2	41.70	37.10	38.87	0.21	n.d.	n.d.	n.d.	38.52	38.55	n.d.
TiO2	n.d.	0.28	n.d.	n.d.	n.d.	n.d.	n.d.	n.d.	0.23	n.d.
Al2O3	0.58	0.63	0.44	0.79	0.48	0.76	0.37	n.d.	0.37	0.74
Cr2O3	n.d.									
FeO	0.43	n.d.	n.d.	0.56	0.60	0.77	0.43	n.d.	n.d.	0.69
MnO	n.d.									
MgO	54.56	31.34	29.66	98.07	98.46	98.80	99.44	29.00	30.35	98.49
CaO	3.52	29.13	31.29	n.d.	n.d.	n.d.	n.d.	31.07	30.17	n.d.
K2O	n.d.									
TOTAL	100.78	98.47	100.27	99.63	99.54	100.33	100.24	98.58	99.67	99.92

DB.MG1

Sample Code SPOT	A14 SP16 1	A14 SP16 2	A14 SP16 3	A14 SP16 4	A14 SP16 5	A14 SP16 6	A14 SP16 7	A14 SP16 8	A14 SP16 9	A14 PC16 10
SiO2	0.34	0.63	n.d.	0.85	3.94	1.28	1.11	1.28	2.58	n.d.
TiO2	1.42	1.46	2.10	1.98	2.25	1.78	1.19	1.46	2.05	n.d.
Al2O3	68.69	65.78	65.80	64.00	58.93	62.26	53.00	53.17	56.62	0.44
Cr2O3	n.d.									
FeO	1.96	2.18	2.60	2.71	2.06	2.24	1.67	2.11	2.08	0.44
MnO	n.d.									
MgO	29.85	29.37	29.85	29.22	29.76	32.08	43.86	44.45	36.82	99.10
CaO	0.14	0.32	n.d.	n.d.	2.25	0.29	0.28	0.18	1.19	n.d.
K2O	n.d.									
TOTAL	102.39	99.75	100.36	98.77	99.18	99.94	101.09	102.65	101.34	99.99

Sample Code SPOT	A14 PC16 11	A14 PC16 12	A14-A PC15 1	A14-A PM15 2	A14-A PC15 3	A14-A PM15 4	A14-A PM15 5	A14-A PC15 6	A14-A MX15 7	A14-A MX15 8
SiO2	n.d.	0.23	n.d.	0.20	n.d.	n.d.	n.d.	n.d.	37.25	37.34
TiO2	n.d.	n.d.	n.d.	n.d.	n.d.	n.d.	n.d.	n.d.	0.61	0.39
Al2O3	0.55	0.58	0.40	n.d.	n.d.	n.d.	n.d.	0.33	5.86	7.87
Cr2O3	n.d.	n.d.	n.d.	n.d.	n.d.	n.d.	n.d.	n.d.	n.d.	0.25
FeO	1.00	0.64	0.67	0.48	0.56	0.90	0.78	0.79	0.64	0.92
MnO	n.d.	n.d.	n.d.	n.d.	n.d.	n.d.	n.d.	n.d.	n.d.	n.d.
MgO	98.27	99.42	98.51	98.98	98.74	99.20	98.70	99.22	22.78	19.44
CaO	n.d.	n.d.	n.d.	0.00	n.d.	0.14	n.d.	n.d.	31.41	31.69
K2O	n.d.	n.d.	n.d.	n.d.	n.d.	n.d.	n.d.	n.d.	n.d.	n.d.
TOTAL	99.82	100.87	99.58	99.66	99.30	100.24	99.48	100.34	98.55	97.90

Sample Code SPOT	A14-A MC15 9	A14-A MX15 10	A14-A MX15 11	A14-A MC15 12	A14-A MX15 13	A14-A MC15 14	A14-A MC15 15	A14-A MC15 16	A14-B PC15 1	A14-B PM15 2
SiO2	33.78	9.09	36.42	38.77	37.06	34.55	38.19	38.11	n.d.	0.25
TiO2	n.d.	n.d.	0.87	0.26	0.44	0.34	n.d.	0.25	n.d.	n.d.
Al2O3	2.53	1.97	12.94	1.12	5.26	2.26	4.10	3.10	n.d.	0.35
Cr2O3	n.d.	n.d.	n.d.	n.d.	n.d.	n.d.	n.d.	n.d.	n.d.	n.d.
FeO	0.56	0.80	1.28	0.43	0.54	0.39	0.60	0.50	0.57	0.66
MnO	n.d.	n.d.	n.d.	n.d.	n.d.	n.d.	n.d.	n.d.	n.d.	n.d.
MgO	36.10	79.46	16.21	29.06	23.85	35.20	23.98	25.38	98.92	98.83
CaO	26.68	8.30	30.15	31.50	31.50	27.71	33.07	31.93	n.d.	n.d.
K2O	n.d.	n.d.	n.d.	n.d.	n.d.	n.d.	n.d.	n.d.	n.d.	n.d.
TOTAL	99.65	99.62	97.87	101.14	98.65	100.45	99.94	99.27	99.49	100.09

DB.MG1

Sample Code SPOT	A14-B PC15 3	A14-B PM15 4	A14-B FC15 5	A14-B MX15 6	A14-B MC15 7	A14-B MC15 8	A14-B MC15 9	A14-B FC15 10	A14-B MC15 11	A14-B FC15 12
SiO2	n.d.	n.d.	42.66	41.08	38.72	38.21	38.48	42.17	38.76	42.17
TiO2	n.d.	n.d.	n.d.							
Al2O3	n.d.	0.37	0.00							
Cr2O3	n.d.	n.d.	n.d.							
FeO	0.80	0.69	n.d.	n.d.	n.d.	n.d.	n.d.	0.27	n.d.	n.d.
MnO	n.d.	n.d.	n.d.							
MgO	98.41	98.57	54.22	49.14	28.98	29.78	30.35	53.41	29.63	53.08
CaO	n.d.	n.d.	3.02	8.66	30.99	30.23	30.07	3.15	31.24	3.27
K2O	n.d.	n.d.	n.d.							
TOTAL	99.21	99.26	99.90	98.88	98.69	98.22	98.90	99.00	100.00	98.52

Sample Code SPOT	A14-B MC15 13	A14-B FC15 14	A14-B PC15 15	A14-B MC15 16	A14-B FC15 17	A14-B MX15 18	A14-A PC14 1	A14-A PC14 2	A14-A FC14 3	A14-A FC14 4
SiO2	37.12	42.46	n.d.	39.63	41.73	23.81	n.d.	n.d.	39.65	41.90
TiO2	n.d.	n.d.	n.d.	n.d.	n.d.	0.47	n.d.	n.d.	n.d.	n.d.
Al2O3	n.d.	n.d.	n.d.	0.39	n.d.	6.53	0.54	0.42	1.92	n.d.
Cr2O3	n.d.	n.d.	n.d.	n.d.	n.d.	n.d.	n.d.	n.d.	n.d.	n.d.
FeO	n.d.	n.d.	0.58	n.d.	n.d.	0.65	0.56	0.58	n.d.	n.d.
MnO	n.d.	n.d.	n.d.	n.d.	n.d.	n.d.	n.d.	n.d.	n.d.	n.d.
MgO	32.67	53.76	98.47	32.17	53.67	49.41	97.66	98.38	39.36	52.38
CaO	28.16	3.19	n.d.	28.20	3.00	21.27	n.d.	n.d.	17.60	4.08
K2O	n.d.	n.d.	n.d.	n.d.	n.d.	n.d.	n.d.	n.d.	0.32	n.d.
TOTAL	97.95	99.41	99.05	100.39	98.40	102.14	98.76	99.38	98.85	98.36

Sample Code SPOT	A14-A FC14 5	A14-A MX14 6	A14-A MC14 7	A14-A PC14 8	A14-A FC14 9	A14-A FC14 10	A14-A MC14 11	A14-A MX14 12	A14-A MC14 13	A14-A MC14 14
SiO2	41.84	29.66	38.29	0.24	41.58	41.42	37.55	26.53	39.02	37.42
TiO2	n.d.	1.00	n.d.	n.d.	n.d.	n.d.	n.d.	n.d.	n.d.	0.35
Al2O3	n.d.	22.05	n.d.	0.54	n.d.	0.84	1.45	n.d.	0.40	2.23
Cr2O3	n.d.	n.d.	n.d.	n.d.	n.d.	n.d.	n.d.	n.d.	n.d.	n.d.
FeO	n.d.	1.05	n.d.	0.53	n.d.	n.d.	n.d.	0.36	n.d.	n.d.
MnO	n.d.	n.d.	n.d.	n.d.	n.d.	n.d.	n.d.	n.d.	n.d.	n.d.
MgO	53.27	11.89	29.31	96.70	52.23	50.25	29.07	51.60	30.03	27.85
CaO	3.52	21.43	30.15	0.16	4.57	5.34	30.80	21.72	30.26	31.05
K2O	n.d.	3.88	n.d.	n.d.	n.d.	n.d.	0.19	n.d.	n.d.	0.18
TOTAL	98.63	90.96	97.75	98.17	98.38	97.85	99.06	100.21	99.71	99.08

DB.MG1

Sample Code SPOT	A14-A MC14 15	A14-A MC14 16	A14-A PC14 17	A14-A PC14 18	A14-A PM14 19	A14-A PC15 20	A14-A MX14 21	A14-A MX14 22	A14-A MX14 23	A14-A MX14 24
SiO2	36.37	36.50	0.23	0.36	n.d.	0.19	39.43	40.14	25.64	18.24
TiO2	0.51	n.d.	n.d.	n.d.	n.d.	n.d.	0.25	n.d.	1.10	0.92
Al2O3	4.07	n.d.	0.49	0.61	0.39	0.32	2.06	3.15	23.18	21.92
Cr2O3	n.d.									
FeO	0.53	n.d.	0.62	0.66	0.70	0.64	n.d.	n.d.	1.11	1.29
MnO	n.d.									
MgO	26.11	34.81	99.07	99.32	98.81	98.24	39.90	46.69	26.71	39.46
CaO	30.93	27.72	n.d.	0.28	n.d.	n.d.	16.80	7.17	11.40	10.34
K2O	0.52	n.d.	n.d.	n.d.	n.d.	n.d.	0.28	0.76	4.93	3.74
TOTAL	99.04	99.03	100.41	101.23	99.90	99.39	98.72	97.91	94.07	95.91

Sample Code SPOT	A14-A MX14 25	A14-A MX14 26	A14-A PC14 27	A14-A PM14 28	A14-B MC14 1	A14-B FC14 2	A14-B PC14 3	A14-B FC14 4	A14-B FC14 5	A14-B FC14 6
SiO2	21.51	22.37	n.d.	n.d.	38.76	41.53	0.19	41.89	41.85	41.37
TiO2	0.75	1.12	n.d.	n.d.	0.29	n.d.	n.d.	n.d.	n.d.	n.d.
Al2O3	7.98	25.77	0.33	0.53	0.36	0.67	0.63	n.d.	n.d.	n.d.
Cr2O3	n.d.	n.d.	n.d.	n.d.	n.d.	n.d.	n.d.	n.d.	n.d.	n.d.
FeO	0.88	0.87	0.65	0.42	n.d.	0.28	0.88	n.d.	n.d.	0.28
MnO	n.d.	n.d.	n.d.	n.d.	n.d.	n.d.	n.d.	n.d.	n.d.	n.d.
MgO	52.08	24.45	98.22	97.99	28.25	53.12	97.92	53.09	54.64	53.50
CaO	16.70	13.59	0.18	n.d.	30.61	2.99	n.d.	3.08	2.92	2.98
K2O	0.43	4.83	n.d.	n.d.	n.d.	n.d.	n.d.	n.d.	n.d.	n.d.
TOTAL	100.33	93.00	99.38	98.94	98.27	98.59	99.62	98.06	99.41	98.13

Sample Code SPOT	A14-B FC14 7	A14-B PC14 8	A14-B MC14 9	A14-B MC14 10	A14-B PC14 11	A14-B MX14 12	A14-B PC14 13	A14-B FC14 14	A14-B MC14 15	A14-B MC14 16
SiO2	41.81	0.28	36.92	37.96	0.19	39.94	n.d.	38.31	38.22	39.18
TiO2	n.d.	n.d.	0.25	n.d.	n.d.	n.d.	n.d.	n.d.	n.d.	0.22
Al2O3	0.52	0.61	0.66	n.d.	0.81	n.d.	0.63	5.68	n.d.	0.40
Cr2O3	n.d.	n.d.	n.d.	n.d.	n.d.	n.d.	n.d.	n.d.	n.d.	n.d.
FeO	n.d.	0.77	n.d.	n.d.	0.83	0.27	0.86	0.54	n.d.	n.d.
MnO	n.d.	n.d.	n.d.	n.d.	n.d.	n.d.	n.d.	n.d.	n.d.	n.d.
MgO	54.36	96.04	29.28	30.26	97.42	49.26	96.77	51.40	28.81	32.34
CaO	3.25	n.d.	31.06	29.43	n.d.	8.40	n.d.	2.97	30.84	27.47
K2O	n.d.	n.d.	n.d.	n.d.	n.d.	n.d.	n.d.	n.d.	n.d.	n.d.
TOTAL	99.94	97.70	98.17	97.65	99.25	97.87	98.26	98.90	97.87	99.61

DB.MG1

Sample Code SPOT	A14-B MC14 17	A14-B FC14 18	A14-B FC14 19	A14-B FC14 20	A14-B MX14 21	A14-B FC14 22	A14-B FC14 23	A14-B FC14 24	A14-B MC14 25	A14-B MX14 26
SiO2	38.78	36.34	32.42	26.58	25.19	38.87	38.89	36.91	37.67	25.86
TiO2	n.d.	n.d.	0.49	0.51	1.67	n.d.	0.23	n.d.	0.25	0.95
Al2O3	0.44	6.41	5.86	3.28	17.29	0.76	5.82	0.60	0.66	22.32
Cr2O3	n.d.	n.d.	n.d.	0.00	n.d.	n.d.	n.d.	n.d.	n.d.	n.d.
FeO	n.d.	0.58	0.63	0.77	1.41	0.45	n.d.	0.33	n.d.	1.91
MnO	n.d.									
MgO	30.41	52.65	54.63	64.29	39.79	58.25	50.73	51.95	28.02	33.10
CaO	29.33	2.64	3.93	4.59	6.46	6.69	3.21	8.17	31.16	14.65
K2O	n.d.	n.d.	1.13	0.62	3.51	n.d.	0.13	0.12	n.d.	n.d.
TOTAL	98.96	98.62	99.09	100.64	95.32	105.02	99.01	98.08	97.76	98.79

Sample Code SPOT	A14-B SP14 27	A14-B SP14 28	A14-B SP14 29	A14-B SP14 30	A14-B SP14 31
SiO2	3.57	0.29	n.d.	7.00	10.17
TiO2	0.76	0.35	0.50	0.78	0.52
Al2O3	60.09	54.54	51.63	45.28	49.22
Cr2O3	n.d.	n.d.	n.d.	n.d.	n.d.
FeO	3.01	3.90	2.68	2.81	2.58
MnO	n.d.	n.d.	n.d.	n.d.	n.d.
MgO	29.05	41.44	42.42	31.54	30.98
CaO	1.77	0.20	0.17	3.97	4.36
K2O	n.d.	n.d.	n.d.	n.d.	n.d.
TOTAL	98.25	100.72	97.40	91.38	97.83

SPINEL

Sample Code SPOT	A3-1B SP16 12	A3-1B SP16 14	A3 SP16 1	A3 SP16 2	A3 SP16 5	A3 SP16 7	A3 SP16 8	A3 SP16 9	A3 SP16 10	A3 SP16 11
SiO2	10.48	11.43	2.17	0.37	0.27	1.47	8.17	5.85	8.75	1.33
TiO2	0.48	0.42	n.d.	0.25	n.d.	n.d.	0.53	0.36	0.29	0.27
Al2O3	45.71	44.90	56.58	64.24	58.55	61.59	49.09	54.57	48.35	56.21
Cr2O3	n.d.	n.d.	n.d.	n.d.	0.20	n.d.	n.d.	n.d.	n.d.	n.d.
FeO	3.96	4.05	7.15	5.90	7.07	6.62	4.28	4.95	3.93	6.93
MnO	n.d.	n.d.	n.d.	n.d.	n.d.	n.d.	n.d.	n.d.	n.d.	n.d.
MgO	20.67	20.08	29.86	29.65	31.19	27.16	21.39	23.94	22.07	26.56
CaO	10.31	19.50	3.93	0.51	0.42	2.02	15.42	9.23	15.66	2.02
K2O	n.d.	n.d.	n.d.	n.d.	n.d.	n.d.	n.d.	n.d.	n.d.	n.d.
TOTAL	91.60	100.37	99.69	100.91	97.69	98.86	98.87	98.90	99.05	93.33

Cations on the basis of 24 oxygens

Si	2.54	2.80	0.44	0.07	0.05	0.29	1.92	1.27	2.06	0.28
Al	13.08	12.96	13.41	14.49	13.59	14.51	13.63	14.00	13.39	14.05
Ti	0.09	0.08	0.00	0.04	0.00	0.00	0.09	0.06	0.05	0.04
Fe3	0.00	0.00	1.20	0.94	1.16	0.90	0.00	0.00	0.00	1.23
Fe2	0.80	0.83	0.00	0.00	0.00	0.20	0.84	0.90	0.77	0.00
Mn	0.00	0.00	0.00	0.00	0.00	0.00	0.00	0.00	0.00	0.00
Mg	7.48	7.33	8.95	8.46	9.16	8.09	7.51	7.77	7.73	8.40
Cr	0.00	0.00	0.00	0.00	0.03	0.00	0.00	0.00	0.00	0.00
Zn	0.00	0.00	0.00	0.00	0.00	0.00	0.00	0.00	0.00	0.00

Sample Code SPOT	A14 SP16 1	A14 SP16 2	A14 SP16 3	A14 SP16 4	A14 SP16 5	A14 SP16 6	A14 SP16 7	A14 SP16 8	A14 SP16 9	A14-B SP14 27
SiO2	0.34	0.63	n.d.	0.85	3.94	1.28	1.11	1.28	2.58	3.57
TiO2	1.42	1.46	2.10	1.98	2.25	1.78	1.19	1.46	2.05	0.76
Al2O3	68.69	65.78	65.80	64.00	58.93	62.26	53.00	53.17	56.62	60.09
Cr2O3	n.d.									
FeO	1.96	2.18	2.60	2.71	2.06	2.24	1.67	2.11	2.08	3.01
MnO	n.d.									
MgO	29.85	29.37	29.85	29.22	29.76	32.08	43.86	44.45	36.82	29.05
CaO	0.14	0.32	n.d.	n.d.	2.25	0.29	0.28	0.18	1.19	1.77
K2O	n.d.									
TOTAL	102.39	99.75	100.36	98.77	99.18	99.94	101.09	102.65	101.34	98.25

Cations on the basis of 24 oxygens

Si	0.06	0.12	0.00	0.17	0.78	0.24	0.20	0.23	0.49	0.71
Al	15.12	14.90	14.79	14.65	13.76	14.01	11.42	11.30	12.56	14.07
Ti	0.20	0.21	0.30	0.29	0.33	0.26	0.16	0.20	0.29	0.11
Fe3	0.31	0.35	0.42	0.44	0.01	0.36	0.26	0.32	0.33	0.28
Fe2	0.00	0.00	0.00	0.00	0.33	0.00	0.00	0.00	0.00	0.22
Mn	0.00	0.00	0.00	0.00	0.00	0.00	0.00	0.00	0.00	0.00
Mg	8.31	8.41	8.49	8.46	8.79	9.13	11.96	11.95	10.33	8.60
Cr	0.00	0.00	0.00	0.00	0.00	0.00	0.00	0.00	0.00	0.00
Zn	0.00	0.00	0.00	0.00	0.00	0.00	0.00	0.00	0.00	0.00

SPINEL

Sample Code	A14-B SP14	A14-B SP14	A14-B SP14	A14-B SP14	T15-A SP15	T15-A SP15
SPOT	28	29	30	31	23	24
SiO2	0.29	n.d.	7.00	10.17	8.52	5.51
TiO2	0.35	0.50	0.78	0.52	0.33	0.93
Al2O3	54.54	51.63	45.28	49.22	48.60	54.34
Cr2O3	n.d.	n.d.	n.d.	n.d.	n.d.	n.d.
FeO	3.90	2.68	2.81	2.58	0.00	n.d.
MnO	n.d.	n.d.	n.d.	n.d.	n.d.	n.d.
MgO	41.44	42.42	31.54	30.98	34.86	26.04
CaO	0.20	0.17	3.97	4.36	6.58	6.18
K2O	n.d.	n.d.	n.d.	n.d.	n.d.	n.d.
TOTAL	100.72	97.40	91.38	97.83	98.89	93.00

Cations on the basis of 24 oxygens

Si	0.05	0.00	1.52	2.09	1.73	1.21
Al	11.88	11.53	11.61	11.91	11.65	14.09
Ti	0.05	0.07	0.13	0.08	0.05	0.15
Fe3	0.60	0.42	0.51	0.00	0.00	0.00
Fe2	0.00	0.00	0.00	0.44	0.00	0.00
Mn	0.00	0.00	0.00	0.00	0.00	0.00
Mg	11.42	11.98	10.23	9.48	10.57	8.54
Cr	0.00	0.00	0.00	0.00	0.00	0.00
Zn	0.00	0.00	0.00	0.00	0.00	0.00

DB.MG2

Sample Code	T2-2A DC16	T2-2A PC16	2-2A PC16	T2-2A DC16	T2-2A MX16	T2-2A MX16	T2-2A MX16	T2-2A MX16	T2-2A PC16	T2-2A PM16
SPOT	1	2	3	4	5	6	7	8	9	10
SiO2	35.35	0.19	n.d.	34.31	36.41	2.92	34.07	35.65	n.d.	0.32
TiO2	n.d.									
Al2O3	n.d.									
Cr2O3	n.d.									
FeO	n.d.									
MnO	n.d.									
MgO	5.37	100.87	100.29	0.67	10.05	93.91	11.25	5.93	99.91	100.07
CaO	59.02	0.38	0.27	64.56	53.93	4.65	56.28	58.23	0.23	0.29
K2O	n.d.									
TOTAL	99.74	101.44	100.56	99.54	100.39	101.48	101.60	99.81	100.14	100.68
Sample Code	T2-2A MX16	T2-2A MX16	T2-2A PC16	T2-2A PC16	T2-2A PC16	T2-2A MX16	T2-2A PC16	T2-2A PC16	T2-2A PM16	T2-2A PC16
SPOT	11	12	13	14	15	16	17	18	19	20
SiO2	34.23	4.32	n.d.	0.34	n.d.	34.97	n.d.	n.d.	n.d.	n.d.
TiO2	n.d.									
Al2O3	n.d.									
Cr2O3	n.d.									
FeO	n.d.	n.d.	n.d.	n.d.	n.d.	0.29	n.d.	n.d.	n.d.	n.d.
MnO	n.d.									
MgO	7.40	90.52	100.62	99.73	100.84	4.36	100.01	100.45	100.69	100.42
CaO	57.95	6.26	0.31	0.32	0.32	60.01	0.45	0.27	0.24	0.27
K2O	n.d.									
TOTAL	99.58	101.10	100.93	100.39	101.16	99.63	100.46	100.72	100.93	100.69
Sample Code	T2-2A MX16	T2-2A DM16	T2-2B PC16	T2-2B MX16	T2-2B PC16	T2-2B PC16	T2-2B MX16	T2-2B MX16	T2-2B PC16	T2-2B MX16
SPOT	21	22	1	2	3	4	5	6	7	8
SiO2	35.55	34.85	n.d.	19.80	n.d.	0.19	21.36	23.10	0.25	19.81
TiO2	n.d.									
Al2O3	n.d.									
Cr2O3	0.30	n.d.								
FeO	n.d.									
MnO	n.d.									
MgO	50.30	1.04	100.05	30.08	99.07	99.30	20.20	13.89	98.46	31.68
CaO	58.53	63.45	0.83	52.35	1.08	0.99	57.57	64.66	0.94	52.59
K2O	n.d.									
TOTAL	144.68	99.34	100.88	102.23	100.15	100.48	99.13	101.65	99.65	104.08

DB.MG2

Sample Code SPOT	T2-2B PC16 9	T2-2B PC16 10	T2-1A DC16 1	T2-1A DC16 2	T2-1A DC16 3	T2-1A DC16 4	T2-1A PC16 5	T2-1A DC16 6	T2-1A MX16 7	T2-1A PC16 8
SiO2	0.23	n.d.	35.50	33.70	33.43	34.42	0.22	33.98	32.54	0.18
TiO2	n.d.	n.d.	n.d.	n.d.	n.d.	n.d.	n.d.	n.d.	n.d.	n.d.
Al2O3	n.d.	n.d.	n.d.	n.d.	n.d.	n.d.	n.d.	n.d.	n.d.	n.d.
Cr2O3	n.d.	n.d.	n.d.	n.d.	n.d.	n.d.	n.d.	n.d.	n.d.	n.d.
FeO	n.d.	n.d.	n.d.	n.d.	n.d.	n.d.	n.d.	n.d.	n.d.	n.d.
MnO	n.d.	n.d.	n.d.	n.d.	n.d.	n.d.	n.d.	n.d.	n.d.	n.d.
MgO	99.01	98.96	3.32	0.33	n.d.	0.43	99.95	1.66	9.70	100.82
CaO	0.85	0.83	62.22	63.37	61.81	64.54	0.73	64.38	57.36	0.65
K2O	n.d.	n.d.	n.d.	n.d.	n.d.	n.d.	n.d.	n.d.	n.d.	n.d.
TOTAL	100.09	99.79	101.04	97.40	95.24	99.39	100.90	100.02	99.60	101.65

Sample Code SPOT	T2-1A MX16 9	T2-1A PC16 10	T2-1A DC16 11	T2-1A PC16 12	T2-1A DC16 13	T2-1A PC16 14	T2-1A PC16 15	T2-1A PC16 16	T2-1A DC16 17	T2-1B PC16 1
SiO2	30.25	0.52	34.48	0.19	34.21	n.d.	0.17	0.55	34.40	n.d.
TiO2	n.d.	n.d.	n.d.	n.d.	n.d.	n.d.	n.d.	n.d.	n.d.	n.d.
Al2O3	n.d.	n.d.	n.d.	n.d.	n.d.	n.d.	n.d.	n.d.	n.d.	n.d.
Cr2O3	n.d.	n.d.	n.d.	n.d.	n.d.	n.d.	n.d.	n.d.	n.d.	n.d.
FeO	n.d.	n.d.	n.d.	n.d.	n.d.	n.d.	n.d.	n.d.	n.d.	n.d.
MnO	n.d.	n.d.	n.d.	n.d.	n.d.	n.d.	n.d.	n.d.	n.d.	n.d.
MgO	14.68	98.80	n.d.	100.50	1.10	100.75	98.66	99.50	0.99	99.94
CaO	56.71	1.08	63.89	0.58	63.81	0.57	0.70	1.15	64.17	0.91
K2O	n.d.	n.d.	n.d.	n.d.	n.d.	n.d.	n.d.	n.d.	n.d.	n.d.
TOTAL	101.64	100.40	98.37	101.27	99.12	101.32	99.53	101.20	99.56	100.85

Sample Code SPOT	T2-1B PC16 2	T2-1B PC16 3	T2-1B MX16 4	T2-1B MX16 5	T2-1B MX16 6	T2-1B PC16 7	T2-1B PC16 8	T2-1B MX16 9	T2 DC15 1	T2 DC15 2
SiO2	0.22	n.d.	5.66	22.42	24.61	0.21	n.d.	0.28	33.79	33.93
TiO2	n.d.	n.d.	n.d.							
Al2O3	n.d.	0.93	0.52							
Cr2O3	n.d.	n.d.	n.d.							
FeO	n.d.	n.d.	n.d.							
MnO	n.d.	n.d.	n.d.							
MgO	97.44	99.42	81.15	17.62	7.26	97.75	98.93	40.04	2.71	3.10
CaO	0.91	0.91	14.82	61.81	67.61	0.80	1.03	62.75	61.15	60.52
K2O	n.d.	n.d.	n.d.							
TOTAL	98.57	100.33	101.63	101.85	99.48	98.76	99.96	103.07	98.58	98.07

DB.MG2

Sample Code SPOT	T2 DC15 3	T2 DC15 4	T2 DC15 5	T2 DC15 6	T2 DC15 7	T2 PC15 8	T2 PM15 9	T2 PC15 10	T2 PM15 11	T2 DC15 12
SiO2	33.69	33.85	33.59	34.36	34.42	0.23	0.82	n.d.	n.d.	35.51
TiO2	n.d.	n.d.	n.d.							
Al2O3	1.65	1.34	1.79	0.41	0.29	0.48	0.48	n.d.	0.64	1.24
Cr2O3	n.d.	n.d.	n.d.							
FeO	n.d.	n.d.	n.d.							
MnO	n.d.	n.d.	n.d.							
MgO	4.26	2.58	3.62	2.85	2.89	98.94	96.32	99.13	99.14	3.15
CaO	59.10	61.01	60.09	61.59	61.77	0.26	0.93	0.33	0.26	64.75
K2O	n.d.	n.d.	n.d.							
TOTAL	98.70	98.78	99.09	99.21	99.37	99.91	98.55	99.46	100.04	104.65

Sample Code SPOT	T2 PC15 13	T2 PC15 14	T2 PC15 15	T2 PC15 16	T2 MX15 17	T2 PC14 1	T2 PC14 2	T2 MX14 3	T2 MX14 4	T2 MX14 5
SiO2	0.28	n.d.	n.d.	n.d.	9.25	0.24	1.02	1.56	1.27	1.42
TiO2	n.d.	n.d.	n.d.	n.d.	n.d.	n.d.	n.d.	n.d.	n.d.	n.d.
Al2O3	0.83	0.54	0.69	0.46	30.98	n.d.	n.d.	n.d.	n.d.	n.d.
Cr2O3	n.d.	n.d.	n.d.	n.d.	n.d.	n.d.	n.d.	n.d.	n.d.	n.d.
FeO	n.d.	n.d.	n.d.	n.d.	n.d.	n.d.	n.d.	n.d.	n.d.	n.d.
MnO	n.d.	n.d.	n.d.	n.d.	n.d.	n.d.	n.d.	n.d.	n.d.	n.d.
MgO	100.39	100.08	100.25	98.74	36.90	97.83	95.57	94.96	94.93	94.46
CaO	0.48	0.21	0.20	0.27	28.27	0.72	2.23	3.00	2.46	3.16
K2O	n.d.	n.d.	n.d.	n.d.	n.d.	n.d.	n.d.	n.d.	n.d.	n.d.
TOTAL	101.98	100.83	101.14	99.47	105.40	98.79	98.82	99.52	98.66	99.04

Sample Code SPOT	T2 MX14 6	T2 MX14 7	T2 PC14 8	T2 MX14 9	T2 MX14 10	T2 MX14 11	T2 MX14 12	T2 PC14 13	T2 MX14 14	T2 MX14 15
SiO2	1.65	3.70	0.90	2.13	0.81	3.23	1.97	0.62	1.17	1.60
TiO2	n.d.	n.d.	n.d.	n.d.	n.d.	n.d.	n.d.	n.d.	n.d.	n.d.
Al2O3	n.d.	n.d.	n.d.	n.d.	n.d.	n.d.	n.d.	n.d.	n.d.	n.d.
Cr2O3	n.d.	n.d.	n.d.	n.d.	n.d.	n.d.	n.d.	n.d.	n.d.	n.d.
FeO	n.d.	n.d.	n.d.	n.d.	n.d.	n.d.	n.d.	n.d.	n.d.	n.d.
MnO	n.d.	n.d.	n.d.	n.d.	n.d.	n.d.	n.d.	n.d.	n.d.	n.d.
MgO	93.98	87.33	96.64	93.75	94.43	88.62	94.69	97.80	94.18	93.32
CaO	4.57	9.59	2.60	4.40	5.57	8.82	3.99	1.86	3.72	3.60
K2O	n.d.	n.d.	n.d.	n.d.	n.d.	n.d.	n.d.	n.d.	n.d.	n.d.
TOTAL	100.20	100.62	100.14	100.28	100.81	100.67	100.65	100.28	99.07	98.52

DB.MG2

Sample Code SPOT	T2 PC14 16	T2 MX14 17	T2 MX14 18	T2 MX14 19	T2 MX14 20	T2 MX14 21	T2 PC14 22	T2 MX14 23	T2 MX14 24	T2 MX14 25
SiO2	1.14	0.96	1.34	1.74	3.29	0.72	0.95	1.66	3.13	2.10
TiO2	n.d.	n.d.	n.d.	n.d.						
Al2O3	n.d.	n.d.	n.d.	n.d.						
Cr2O3	n.d.	n.d.	n.d.	n.d.						
FeO	n.d.	n.d.	n.d.	n.d.						
MnO	n.d.	n.d.	n.d.	n.d.						
MgO	95.95	95.19	93.81	92.62	88.42	91.20	94.57	93.28	89.54	93.02
CaO	2.68	3.07	3.30	4.06	7.43	6.34	3.26	3.29	8.33	4.94
K2O	n.d.	n.d.	n.d.	n.d.						
TOTAL	99.77	99.22	98.45	98.42	99.14	98.26	98.78	98.23	101.00	100.06
Sample Code SPOT	T2 PC14 26	T2 MX14 27	T2 MX14 28	T2 MX14 29	T2 MX14 30	T2 MX14 31	T2 PC14 32	T2 MX14 33	T2 PC14 34	T2 MX14 35
SiO2	3.86	2.53	2.62	2.86	1.54	3.91	0.64	2.07	1.05	6.67
TiO2	n.d.	n.d.	n.d.	n.d.						
Al2O3	n.d.	n.d.	n.d.	n.d.						
Cr2O3	n.d.	n.d.	n.d.	n.d.						
FeO	n.d.	n.d.	n.d.	n.d.						
MnO	n.d.	n.d.	n.d.	n.d.						
MgO	88.31	93.40	91.65	89.00	93.76	87.33	98.40	92.16	95.07	81.64
CaO	7.19	5.17	6.81	8.03	3.54	2.27	1.73	4.83	3.86	13.30
K2O	n.d.	n.d.	n.d.	n.d.						
TOTAL	99.36	101.10	101.08	99.89	98.84	93.51	100.77	99.06	99.98	101.61
Sample Code SPOT	T2 PC14 36	T2 MX14 37	T2 PC14 38	T2 MX14 39	T2 MX14 40	T2 MX14 41	T15-1A PC16 1	T15-1A PC16 2	T15-1A PM16 3	T15-1A PC16 4
SiO2	1.18	18.77	1.05	2.48	1.61	1.08	0.18	n.d.	n.d.	n.d.
TiO2	n.d.	n.d.	n.d.	n.d.						
Al2O3	n.d.	n.d.	n.d.	n.d.						
Cr2O3	n.d.	n.d.	n.d.	n.d.						
FeO	n.d.	n.d.	0.23	n.d.	n.d.	n.d.	n.d.	n.d.	n.d.	n.d.
MnO	n.d.	n.d.	n.d.	n.d.						
MgO	94.51	23.35	95.58	92.16	94.66	95.97	101.41	100.92	100.19	99.79
CaO	2.72	39.60	3.11	4.53	3.04	2.59	n.d.	n.d.	n.d.	n.d.
K2O	n.d.	n.d.	n.d.	n.d.						
TOTAL	98.41	81.72	99.97	99.17	99.31	99.64	101.59	100.92	100.19	99.79

DB.MG2

Sample Code	T15-1A PM16	T15-1A MC16	T15-1A MC16	T15-1A PC16	T15-1A FC16	T15-1A FC16	T15-1A MC16	T15-1A PC16	T15-1A PM16	T15-1A FC16
SPOT	5	6	7	8	9	10	11	12	13	14
SiO2	0.20	39.40	39.17	n.d.	42.37	42.77	39.92	n.d.	0.18	43.05
TiO2	n.d.									
Al2O3	n.d.									
Cr2O3	n.d.									
FeO	n.d.									
MnO	n.d.									
MgO	101.09	31.97	32.37	100.54	54.50	54.74	32.10	100.20	100.58	54.41
CaO	n.d.	28.13	28.18	n.d.	3.12	3.03	28.73	n.d.	n.d.	3.02
K2O	n.d.									
TOTAL	101.29	99.50	99.73	100.54	99.99	100.54	100.75	100.20	100.76	100.47
Sample Code	15-1A FM16	T15-1A MX16	T15-1A MX16	T15-1A FM16	T15-1A PC16	T15-1A PM16	T15-1A MC16	T15-1B FC16	T15-1B MX16	15-1B FC16
SPOT	15	16	17	18	19	20	21	1	2	3
SiO2	42.64	37.10	12.21	42.03	n.d.	0.22	39.22	42.21	41.83	42.91
TiO2	n.d.									
Al2O3	n.d.									
Cr2O3	n.d.									
FeO	n.d.									
MnO	n.d.									
MgO	54.71	37.28	86.33	56.10	100.38	100.87	32.19	54.06	43.67	54.56
CaO	2.90	27.49	1.03	2.99	n.d.	n.d.	29.24	2.89	16.07	2.93
K2O	n.d.									
TOTAL	100.26	101.86	99.57	101.12	100.38	101.08	100.65	99.15	101.57	100.39
Sample Code	T15-1B PC16	T15-1B MC16	T15-1B MC16	T15-1B PC16	T15-1B PM16	T15-1B PC16	T15-1B FC16	T15-1B FC16	T15-1B MC16	T15-1B MM16
SPOT	4	5	6	7	8	9	10	11	12	13
SiO2	0.21	39.09	39.79	n.d.	0.20	n.d.	42.71	41.81	39.96	39.15
TiO2	n.d.									
Al2O3	n.d.									
Cr2O3	n.d.									
FeO	n.d.									
MnO	n.d.									
MgO	100.73	31.02	31.84	100.74	100.43	100.96	53.85	51.08	31.93	32.35
CaO	n.d.	30.11	29.08	n.d.	n.d.	n.d.	3.28	6.65	28.87	28.30
K2O	n.d.									
TOTAL	100.94	100.23	100.71	100.74	100.63	100.96	99.84	99.55	100.75	99.81

DB.MG2

Sample Code	T15-1B FM16	T15-1B FC16	T15-1B MX16	T15-1C PC16	T15-1C PC16	T15-1C PC16	T15-1C PM16	T15-1C PC16	T15-1C PM16	T15-1C MC16
SPOT	14	15	16	1	2	3	4	5	6	7
SiO2	42.89	42.81	42.06	0.19	n.d.	n.d.	n.d.	0.22	n.d.	39.64
TiO2	n.d.									
Al2O3	n.d.									
Cr2O3	n.d.									
FeO	n.d.									
MnO	n.d.									
MgO	53.49	55.07	49.91	98.64	99.36	99.68	101.56	99.53	100.82	32.21
CaO	4.19	3.24	8.35	n.d.	n.d.	n.d.	n.d.	n.d.	n.d.	28.19
K2O	n.d.									
TOTAL	100.57	101.13	100.32	98.83	99.36	99.68	101.56	99.75	100.82	100.04
Sample Code	T15-1C MC16	T15-1C MM16	T15-1C FM16	T15-1C FC16	T15-1C FM16	T15-1C MC16	T15-1C MM16	T15-1C FC16	T15-1C FM16	T15-1C FC16
SPOT	8	9	10	11	12	13	14	15	16	17
SiO2	38.81	39.19	43.10	42.85	42.72	39.54	38.63	43.29	42.80	42.40
TiO2	n.d.									
Al2O3	n.d.									
Cr2O3	n.d.									
FeO	n.d.									
MnO	n.d.									
MgO	32.65	30.66	55.29	54.19	55.10	31.90	31.80	55.01	54.84	54.01
CaO	28.34	29.31	3.09	3.19	3.09	29.79	30.20	3.11	3.00	2.93
K2O	n.d.									
TOTAL	99.81	99.16	101.48	100.22	100.92	101.22	100.63	101.41	100.64	99.35
Sample Code	T15-2 PC16	T15-2 PM16	T15-2 PC16	T15-2 PM16	T15-2 FC16	T15-2 MC16	T15-2 MC16	T15-2 MC16	T15-2 FC16	T15-2 MX16
SPOT	1	2	3	4	5	6	7	8	9	10
SiO2	n.d.	n.d.	0.34	n.d.	42.16	39.24	39.54	39.97	42.12	19.57
TiO2	n.d.	4.24								
Al2O3	n.d.	0.47								
Cr2O3	n.d.									
FeO	n.d.									
MnO	n.d.									
MgO	99.43	100.00	98.62	99.54	55.13	32.09	31.06	31.62	51.27	17.23
CaO	n.d.	n.d.	n.d.	n.d.	3.04	28.55	28.84	29.26	6.43	28.84
K2O	n.d.	0.39								
TOTAL	99.43	100.00	98.97	99.54	100.33	99.87	99.44	100.84	99.82	70.73

DB.MG2

Sample Code SPOT	T15-2 MX16 11	T15-2 MC16 12	T15-2 MC16 13	T15-2 FC16 14	T15-2 FC16 15	T15-2 MC16 16	T15-2 MC16 17	T15-2 FM16 18	T15-2 FC16 19	T15-2 MC16 20
SiO2	20.99	39.44	39.07	43.05	41.64	39.09	39.51	42.76	42.87	39.06
TiO2	4.20	n.d.	n.d.	n.d.	n.d.	0.28	n.d.	n.d.	n.d.	n.d.
Al2O3	0.48	n.d.								
Cr2O3	n.d.									
FeO	n.d.									
MnO	n.d.									
MgO	17.36	31.37	32.07	53.92	52.43	31.20	30.67	54.19	54.53	30.58
CaO	28.87	29.21	28.45	2.95	3.21	29.27	29.55	3.24	3.12	29.95
K2O	0.20	n.d.								
TOTAL	72.11	100.02	99.59	99.92	97.27	99.84	99.72	100.19	100.52	99.60
Sample Code SPOT	T15-2 MM16 21	T15-2 FC16 22	T15-2 FM16 23	T15-A FC15 1	T15-A FC15 2	T15-A FC15 3	T15-A FC15 4	T15-A FC15 5	T15-A FC15 6	T15-A MC15 7
SiO2	38.46	42.78	43.21	41.57	41.94	41.70	41.99	42.37	41.88	39.72
TiO2	n.d.									
Al2O3	n.d.									
Cr2O3	n.d.									
FeO	n.d.									
MnO	n.d.									
MgO	33.50	53.99	54.31	48.66	50.96	50.23	50.34	50.41	51.39	31.76
CaO	28.07	3.06	2.90	7.13	6.71	6.87	6.92	6.69	6.64	27.52
K2O	n.d.									
TOTAL	100.03	99.83	100.41	97.36	99.61	98.80	99.25	99.47	99.91	99.00
Sample Code SPOT	T15-A MC15 8	T15-A MC15 9	T15-A FC15 10	T15-A FC15 11	T15-A PC15 12	T15-A PM15 13	T15-A PC15 14	T15-A PM15 15	T15-A FC15 16	T15-A FC15 17
SiO2	39.56	39.34	42.02	41.81	n.d.	n.d.	n.d.	n.d.	42.07	41.47
TiO2	n.d.									
Al2O3	n.d.									
Cr2O3	n.d.									
FeO	n.d.									
MnO	n.d.									
MgO	30.52	31.64	50.37	50.01	100.34	99.70	99.35	99.06	51.11	51.15
CaO	29.46	28.77	6.14	6.97	n.d.	n.d.	n.d.	n.d.	6.53	5.85
K2O	n.d.									
TOTAL	99.54	99.75	98.53	98.79	100.34	99.70	99.35	99.06	99.71	98.47

DB.MG2

Sample Code SPOT	T15-A FM15 18	T15-A FC15 19	T15-A FC15 20	T15-A MC15 21	T15-A MM15 22	T15-A SP15 23	T15-A SP15 24	T15-B MX15 1	T15-B MX15 2	T15-B FC15 3
SiO2	42.07	41.85	42.02	39.23	39.34	8.52	5.51	39.08	37.89	42.07
TiO2	n.d.	n.d.	n.d.	n.d.	n.d.	0.33	0.93	n.d.	n.d.	n.d.
Al2O3	n.d.	n.d.	n.d.	n.d.	n.d.	48.60	54.34	n.d.	n.d.	n.d.
Cr2O3	n.d.									
FeO	n.d.	n.d.	n.d.	n.d.	n.d.	0.00	n.d.	n.d.	n.d.	n.d.
MnO	n.d.									
MgO	50.53	49.93	49.89	30.52	31.24	34.86	26.04	33.20	36.43	50.77
CaO	6.62	6.89	6.85	28.45	29.33	6.58	6.18	26.34	24.62	6.79
K2O	n.d.									
TOTAL	99.22	98.67	98.76	98.20	99.91	98.89	93.00	98.62	98.94	99.63
Sample Code SPOT	T15-B FC15 4	T15-B FC15 5	T15-B FC15 6	T15-B MC15 7	T15-B MC15 8	T15-B FC15 9	T15-B FC15 10	T15-B FM15 11	T15-B MC15 12	T15-B MM15 13
SiO2	41.88	42.23	41.83	39.66	39.58	41.62	40.49	42.10	39.16	40.07
TiO2	n.d.									
Al2O3	n.d.									
Cr2O3	n.d.									
FeO	n.d.									
MnO	n.d.									
MgO	49.79	50.19	50.28	33.24	33.62	50.46	51.79	50.06	33.80	33.49
CaO	7.70	7.71	6.80	26.40	26.05	7.12	6.77	7.01	26.03	26.03
K2O	n.d.									
TOTAL	99.37	100.13	98.91	99.30	99.25	99.20	99.05	99.17	98.99	99.59
Sample Code SPOT	T15-B MC15 14	T15-B FC15 15	T15-B PC15 16	T15-B PM15 17	T15-B PC15 18	T15-B PM15 19	T15-B PC15 20	T15-B PM15 21	T15 FC14 1	T15 FM14 2
SiO2	39.53	42.00	n.d.	0.27	n.d.	0.21	0.22	1.15	41.82	42.03
TiO2	n.d.									
Al2O3	n.d.									
Cr2O3	n.d.									
FeO	n.d.									
MnO	n.d.									
MgO	33.91	50.80	98.97	98.89	100.06	99.45	99.08	97.68	52.53	54.61
CaO	25.46	7.28	n.d.	0.19	n.d.	n.d.	n.d.	0.52	4.13	2.60
K2O	n.d.									
TOTAL	98.90	100.08	98.97	99.35	100.06	99.66	99.30	99.35	98.48	99.24

DB.MG2

Sample Code SPOT	T15 FC14 3	T15 MX14 4	T15 FC14 5	T15 MX14 6	T15 FM14 7	T15 MC14 8	T15 MM14 9	T15 MX14 10	T15 MX14 11	T15 MX14 12
SiO2	41.92	29.49	40.92	28.33	42.30	39.05	37.97	28.63	40.99	31.25
TiO2	n.d.	n.d.	n.d.	n.d.	n.d.	n.d.	n.d.	n.d.	n.d.	n.d.
Al2O3	n.d.	n.d.	n.d.	n.d.	n.d.	n.d.	n.d.	n.d.	n.d.	n.d.
Cr2O3	n.d.	n.d.	n.d.	n.d.	n.d.	n.d.	n.d.	n.d.	n.d.	n.d.
FeO	n.d.	n.d.	n.d.	n.d.	n.d.	n.d.	n.d.	n.d.	n.d.	n.d.
MnO	n.d.	n.d.	n.d.	n.d.	n.d.	n.d.	n.d.	n.d.	n.d.	n.d.
MgO	53.58	47.82	54.80	51.01	53.93	29.72	29.78	22.24	44.65	24.68
CaO	2.86	2.47	3.35	3.04	3.65	30.55	29.15	21.59	13.44	23.73
K2O	n.d.	n.d.	n.d.	n.d.	n.d.	n.d.	n.d.	n.d.	n.d.	n.d.
TOTAL	98.36	79.78	99.07	82.38	99.88	99.32	96.90	72.46	99.08	79.66
Sample Code SPOT	T15 MC14 13	T15 MX14 14	T15 MX14 15	T15 MX14 16	T15 PC14 17	T15 FC14 18	T15 FC14 19	T15 MX14 20	T15 MX14 21	T15 MX14 22
SiO2	39.06	2.33	8.70	2.63	0.77	42.27	42.30	4.06	2.44	3.57
TiO2	n.d.	n.d.	n.d.	n.d.	n.d.	n.d.	n.d.	n.d.	n.d.	n.d.
Al2O3	n.d.	n.d.	n.d.	n.d.	n.d.	n.d.	n.d.	n.d.	n.d.	n.d.
Cr2O3	n.d.	n.d.	n.d.	n.d.	n.d.	n.d.	n.d.	n.d.	n.d.	n.d.
FeO	n.d.	n.d.	n.d.	n.d.	n.d.	n.d.	n.d.	n.d.	n.d.	n.d.
MnO	n.d.	n.d.	n.d.	n.d.	n.d.	n.d.	n.d.	n.d.	n.d.	n.d.
MgO	34.18	93.85	85.22	92.96	97.20	52.93	54.13	87.10	93.46	91.31
CaO	25.42	1.75	5.94	1.61	0.50	3.64	3.45	2.59	1.63	2.97
K2O	n.d.	n.d.	n.d.	n.d.	n.d.	n.d.	n.d.	n.d.	n.d.	n.d.
TOTAL	98.66	97.93	99.86	97.20	98.47	98.84	99.88	93.75	97.53	97.85
Sample Code SPOT	T15 MX14 23	T26-1A PC16 1	T26-1A PM16 2	T26-1A PC16 3	T26-1A PM16 4	T26-1A PC16 5	T26-1A DC16 6	T26-1A DC16 7	T26-1A DC16 8	T26-1A PC16 9
SiO2	10.14	0.18	n.d.	0.18	n.d.	n.d.	32.83	32.88	32.77	n.d.
TiO2	n.d.	n.d.	n.d.	n.d.	n.d.	n.d.	n.d.	n.d.	n.d.	n.d.
Al2O3	n.d.	0.32	n.d.	1.18	n.d.	0.48	1.29	0.33	0.26	n.d.
Cr2O3	n.d.	n.d.	n.d.	n.d.	n.d.	n.d.	n.d.	n.d.	n.d.	n.d.
FeO	n.d.	n.d.	n.d.	n.d.	n.d.	n.d.	0.34	n.d.	n.d.	n.d.
MnO	n.d.	n.d.	n.d.	n.d.	n.d.	n.d.	n.d.	n.d.	n.d.	n.d.
MgO	82.71	98.46	99.90	97.62	99.08	98.30	1.55	0.44	1.26	98.72
CaO	7.09	n.d.	0.23	0.56	n.d.	0.19	61.75	62.97	62.98	0.18
K2O	n.d.	n.d.	n.d.	n.d.	n.d.	n.d.	n.d.	n.d.	n.d.	n.d.
TOTAL	99.94	98.96	100.13	99.54	99.08	98.97	97.76	96.62	97.27	98.90

DB.MG2

Sample Code SPOT	T26-1A PM16	T26-1A DC16	T26-1A PC16	T26-1A PC16	T26-1A MX16	T26-1A DC16	T26-1A PC16	T26-1A DC16	T26-1B PC16	T26-1B PC16
	10	11	12	13	14	15	16	17	1	2
SiO2	n.d.	32.82	n.d.	n.d.	29.44	33.26	0.22	33.77	n.d.	n.d.
TiO2	n.d.									
Al2O3	n.d.	n.d.	0.89	n.d.	0.66	0.31	n.d.	0.65	n.d.	n.d.
Cr2O3	n.d.									
FeO	n.d.									
MnO	n.d.									
MgO	98.21	1.50	96.52	98.17	10.53	0.43	98.97	0.97	99.01	99.38
CaO	0.16	62.50	0.41	0.15	56.48	63.36	0.18	64.15	n.d.	n.d.
K2O	n.d.									
TOTAL	98.37	96.82	97.82	98.32	97.11	97.36	99.37	99.54	99.01	99.38
Sample Code SPOT	T26-1B MX16	T26-1B DC16	T26-1B PC16	T26-1B PC16	T26-1B DM16					
	3	4	5	6	7	8	9	10	11	12
SiO2	0.66	21.24	32.72	3.83	33.55	11.94	33.27	n.d.	n.d.	33.71
TiO2	n.d.	0.29	n.d.	n.d.	n.d.	0.26	n.d.	n.d.	n.d.	n.d.
Al2O3	26.08	21.59	3.70	10.49	0.56	42.42	0.70	n.d.	0.98	0.36
Cr2O3	n.d.									
FeO	0.54	n.d.								
MnO	n.d.									
MgO	69.73	4.29	5.11	70.68	2.14	2.44	2.02	98.78	99.16	1.37
CaO	1.01	48.01	57.46	13.14	61.82	40.18	61.96	0.22	n.d.	63.14
K2O	n.d.									
TOTAL	98.02	95.42	98.99	98.14	98.07	97.24	97.95	99.00	100.14	98.58
Sample Code SPOT	T26-1B MX16	T26-1B PC16	T26-2A PC16	T26-2A PM16	T26-2A PC16	T26-2A PM16	T26-2A MX16	T26-2B PC16	T26-2B PM16	T26-2B PC16
	13	14	1	2	3	4	5	1	2	3
SiO2	11.45	0.23	n.d.	0.21	n.d.	0.19	16.22	0.36	n.d.	0.24
TiO2	n.d.									
Al2O3	37.10	0.49	n.d.	n.d.	n.d.	n.d.	2.12	n.d.	n.d.	n.d.
Cr2O3	n.d.									
FeO	0.62	n.d.								
MnO	n.d.									
MgO	12.84	98.81	99.58	98.35	98.70	99.48	51.69	98.27	99.52	98.49
CaO	36.18	0.34	0.34	0.39	0.50	0.41	33.10	0.79	0.75	0.87
K2O	n.d.									
TOTAL	98.19	99.87	99.92	98.95	99.20	100.08	103.13	99.42	100.27	99.60

DB.MG2

Sample Code SPOT	T26-2B PM16 4	T26-2B PC16 5	T26-2B PM16 6	T26-2B PC16 7	T26 MX16 8	T26-2B MX16 9	T26-2B MX16 10	T26 MX15 1	T26 MX15 2	T26 MX15 3
SiO2	n.d.	n.d.	n.d.	n.d.	0.76	14.58	21.11	0.21	0.53	0.43
TiO2	n.d.	n.d.	n.d.	n.d.	n.d.	n.d.	n.d.	n.d.	n.d.	n.d.
Al2O3	n.d.	n.d.	n.d.	n.d.	n.d.	n.d.	n.d.	n.d.	n.d.	n.d.
Cr2O3	n.d.	n.d.	n.d.	n.d.	n.d.	n.d.	n.d.	n.d.	n.d.	n.d.
FeO	n.d.	n.d.	n.d.	n.d.	n.d.	n.d.	n.d.	n.d.	n.d.	n.d.
MnO	n.d.	n.d.	n.d.	n.d.	n.d.	n.d.	n.d.	n.d.	n.d.	n.d.
MgO	98.55	99.30	98.26	99.61	95.17	58.60	33.64	52.57	73.04	33.81
CaO	0.94	0.80	0.98	0.61	2.58	27.24	44.64	46.44	31.11	46.22
K2O	n.d.	n.d.	n.d.	n.d.	n.d.	n.d.	n.d.	n.d.	n.d.	n.d.
TOTAL	99.49	100.10	99.24	100.22	98.51	100.42	99.39	99.22	104.68	80.46
Sample Code SPOT	T26 MX15 4	T26 MX15 5	T26 PC15 6	T26 PC15 7	T26 PC15 8	T26 MX15 9	T26 PC15 10	T26 PC15 11	T26 PC15 12	T26 PC15 13
SiO2	0.41	n.d.	n.d.	n.d.	n.d.	2.51	n.d.	0.19	0.52	n.d.
TiO2	n.d.	n.d.	n.d.	n.d.	n.d.	n.d.	n.d.	n.d.	n.d.	n.d.
Al2O3	n.d.	n.d.	n.d.	n.d.	n.d.	n.d.	n.d.	n.d.	n.d.	n.d.
Cr2O3	n.d.	n.d.	n.d.	n.d.	n.d.	n.d.	n.d.	n.d.	n.d.	n.d.
FeO	n.d.	n.d.	n.d.	n.d.	n.d.	n.d.	n.d.	n.d.	n.d.	n.d.
MnO	n.d.	n.d.	n.d.	n.d.	n.d.	n.d.	n.d.	n.d.	n.d.	n.d.
MgO	26.35	75.01	100.73	99.84	100.20	93.95	100.34	100.12	97.53	97.68
CaO	57.58	19.18	0.67	0.56	0.69	6.31	0.61	0.62	1.47	0.71
K2O	n.d.	n.d.	n.d.	n.d.	n.d.	n.d.	n.d.	n.d.	n.d.	n.d.
TOTAL	84.34	94.19	101.40	100.40	100.89	102.77	100.95	100.93	99.52	98.39
Sample Code SPOT	T26 MX15 14	T26 PC15 15	T26 PC15 16	T26 PC15 17	T26 PC15 18	T26 PC15 19	T26 PC15 20	T26 MX15 21	T26 PC15 22	T26 PC15 23
SiO2	0.25	0.29	1.03	1.08	n.d.	n.d.	0.24	n.d.	n.d.	n.d.
TiO2	n.d.	n.d.	n.d.	n.d.	n.d.	n.d.	n.d.	n.d.	n.d.	n.d.
Al2O3	n.d.	n.d.	n.d.	n.d.	n.d.	n.d.	n.d.	n.d.	n.d.	n.d.
Cr2O3	n.d.	n.d.	n.d.	n.d.	n.d.	n.d.	n.d.	n.d.	n.d.	n.d.
FeO	n.d.	n.d.	n.d.	n.d.	n.d.	n.d.	n.d.	n.d.	n.d.	n.d.
MnO	n.d.	n.d.	n.d.	n.d.	n.d.	n.d.	n.d.	n.d.	n.d.	n.d.
MgO	36.63	99.77	96.41	95.64	98.87	98.53	99.61	96.27	98.84	98.74
CaO	44.96	0.57	2.41	2.54	0.52	0.88	0.55	4.08	0.76	0.69
K2O	n.d.	n.d.	n.d.	n.d.	n.d.	n.d.	n.d.	n.d.	n.d.	n.d.
TOTAL	81.84	100.63	99.85	99.26	99.39	99.41	100.40	100.35	99.60	99.43

DB.MG2

Sample Code SPOT	T26 MX15 24	T26 MX15 25	T26 MX15 26	T26 MX15 27	T26 MX15 28	T26 MX15 29	T26 MX15 30	T26 PC14 1	T26 PC14 2	T26 PC14 3
SiO2	n.d.	0.33	n.d.	n.d.	n.d.	0.27	0.22	0.20	0.22	0.44
TiO2	n.d.									
Al2O3	n.d.									
Cr2O3	n.d.									
FeO	n.d.									
MnO	n.d.									
MgO	28.19	23.54	50.26	25.53	96.60	29.17	77.47	97.82	98.63	92.33
CaO	57.66	62.41	35.33	55.97	1.11	52.82	23.16	0.48	1.57	0.98
K2O	n.d.									
TOTAL	85.85	86.28	85.59	81.50	97.71	82.26	100.85	98.50	100.42	93.75
Sample Code SPOT	T26 MX14 4	T26 MX14 5	T26 PC14 6	T26 MX14 7	T26 PC14 8	T26 MX14 9	T26 PC14 10	T26 PC14 11	T26 PC14 12	T26 MX14 13
SiO2	2.73	0.47	0.37	6.55	0.24	0.91	0.53	0.52	0.55	0.19
TiO2	n.d.									
Al2O3	n.d.									
Cr2O3	n.d.									
FeO	n.d.									
MnO	n.d.									
MgO	86.01	94.78	96.66	46.76	97.06	93.30	95.61	96.73	98.37	92.17
CaO	2.90	1.15	1.32	45.72	1.22	3.54	1.15	1.28	1.15	0.69
K2O	n.d.									
TOTAL	91.64	96.40	98.35	99.03	98.52	97.75	97.29	98.53	100.07	93.05
Sample Code SPOT	T26 MX14 14	T26 PC14 15	T26 PC14 16	T26 PC14 17	T26 PC14 18	T26 PC14 19	T26 MX14 20	T26 PC14 21	T26 PC14 22	T26 MX14 23
SiO2	0.25	0.18	0.30	n.d.	0.72	n.d.	0.46	0.22	n.d.	n.d.
TiO2	n.d.									
Al2O3	n.d.									
Cr2O3	n.d.									
FeO	n.d.									
MnO	n.d.									
MgO	95.13	98.08	98.85	96.58	96.31	96.78	94.33	97.02	98.47	75.14
CaO	0.84	0.42	0.51	2.16	1.38	1.97	3.32	0.63	0.59	0.85
K2O	n.d.									
TOTAL	96.22	98.68	99.66	98.74	98.41	98.75	98.11	97.87	99.06	75.99

DB.MG2

Sample Code SPOT	T26						
	PC14 24	PC14 25	PC14 26	PC14 27	MX14 28	PC14 29	MX14 30
SiO2	0.18	0.23	n.d.	0.28	0.57	0.34	n.d.
TiO2	n.d.						
Al2O3	n.d.						
Cr2O3	n.d.						
FeO	n.d.						
MnO	n.d.						
MgO	98.49	98.24	97.74	95.56	92.77	97.99	94.95
CaO	1.15	0.74	2.37	0.59	1.31	0.86	2.90
K2O	n.d.						
TOTAL	99.82	99.21	100.11	96.43	94.65	99.19	97.85

APPENDIX 8

LOSS ON IGNITION

The following procedure is used for the determination of the amounts of volatile constituents in caustic calcined magnesites.

A8.1 Apparatus

Small furnace heated to 1000°C, Silica Crucibles, Desiccator, Furnace Tongs, Balance capable of weighing to 0.0001 gm.

A8.2 Method of measurement

1. The furnace should be cleaned from any contaminants or other material inside.
2. The furnace must be switched on and fixed on 1000° C.
3. Previously cleaned and dried crucibles is placed in the furnace and calcine at 1000°C for one hour, then they removed from the furnace using the tongs and placed on a ceramic brick to cool and then placed in a desiccator.
4. The samples is ground to a loose powder and placed in an oven at 105°C to remove the moisture. After at least two hours the samples are removed and placed in a desiccator to be cool.
5. five grams of sample accurately weighed and placed into the previously calcined and weighed crucible.
6. The crucible is placed Very gradually in the hot furnace

(1000°C) for at least two hours.

7. The crucibles plus contents are removed from the furnace and allowed to be cold on a ceramic brick and finally placed in the desiccator. The crucibles plus contents are weighed when they completely cold.

The Loss of ignition is calculated as follows:

$$\text{LOI (\%)} = \frac{W1 - W2}{W1} \times 100$$

Where:

W1 = Weight of original dry sample

W2 = Weight after ignition at 1000°C

APPENDIX 9
SURFACE AREA MEASUREMENT

A9.1 General

Determination of surface area of caustic calcined magnesite have been made using the Area-meter II manufactured by Strohlein Labortechnik Ltd. The method is based on BET method and applied for the determination of the specific surface area of solid substances.

Solid substances have the characteristic property of adsorbing gas molecules on their surface. The dependence of the gas quantity adsorbed on the pressure of an uniform gas above the surface area at constant temperature is called adsorption isotherm. The principal of this method is to determine the amount of nitrogen required to form a complete monomolecular layer on the surface area of the solid substances by adsorption in low temperature (i.e. at -195.8°C which is the boiling point of liquid nitrogen at atmospheric pressure). Since the area occupied by the nitrogen molecule is known, this can be multiplied by the number of gas molecules to give the total surface of solid substance under test. This adsorption method permits the determination of the external surface area and as far as it is accessible by the measuring gas, also the determination of the internal surface area. The method also allows the determination of the specific surface area in the range of about $0.1 \text{ m}^2/\text{g}$ up to $1000 \text{ m}^2/\text{g}$. The weight of the sample to be evaluated needs to

be adjusted according to the expected surface area.

For example, The optimum weight for sample with surface area of about 1000 m²/g should be 0.3 g. while 10 m²/g require an optimum of 2 gm. with the small surface area below 1m²/g, the weight increases up to 30 gm.

Other advantages of this method is its high speed (half hour for one complete measurement including evaluation). It is also possible to evaluate more bulky materials up to 18 mm.

A9.2 Measurements

The principle of the measurement is the based on the use of two glass adsorption vessels of the same volumes; one of them is filled with the sample (measuring vessel) while the other remains empty (reference vessel). Both vessels are purged at ambient temperature with the nitrogen at atmospheric pressure, and then cooled in the cold bath to the temperature of liquid nitrogen. The adsorption of the nitrogen on the sample results in a pressure difference between measuring and reference vessel which is indicated on differential manometer. After the suitable amounts of sample are weighed directly into the measuring vessel, the vessel is placed on a hot plate set at 115°C for several hours. During heating the vessel is purged with nitrogen. The purpose of heating and purging is to remove any foreign molecules or moisture which might be adsorbed to the sample. Afterwards the vessels are cooled down to ambient temperature. Both vessels are then purged with nitrogen at atmospheric pressure

in water bath at ambient temperature in order to reach equilibrium. After around 10 minutes the nitrogen flow is shut off and the vessels are cooled to the temperature of liquid nitrogen for about 15 minutes. The volume of nitrogen adsorbed by the sample results in a pressure difference between the sample and the empty vessel which is indicated on the differential manometer that is filled by low vapour pressure liquid (coloured dibutylphthalate). It should be mentioned that the differential pressure on the manometer is preferred to be between 50 and 350 mm.

A9.3 Calculation

After the pressure difference is obtained from the manometer, the surface area can be evaluated without any loss of accuracy with the aid of the nomogram shown in Figure A9.2 and the following formula:

$$S_g = \frac{A \Delta h}{m} + \frac{B}{p}$$

where:

- S_g = specific surface area (m^2/g)
- Δh = pressure difference on manometer (mm)
- A = coefficient
- m = sample weight (g)
- B = coefficient
- p = specific weight of sample

The value of the coefficient (A) depends on barometric

pressure and on the pressure difference on the differential manometer. To determine the coefficient (A) on the nomogram the measured values on the left scale (pressure difference on manometer) and the vertical right scale (atmospheric pressure) are joined by a straight line and the value of the coefficient A is read on the intersection with the centre scale. Coefficient (B) is introduced so as to take into account the change in the adsorption vessel volume due to the use of large weights in case of samples having very small surface areas. This coefficient is obtained by joining the barometric pressure difference on the left scale of the nomogram to the point corresponding to the barometric pressure on the sloping scale on the right side; Where it intersects the B scale, the appropriate value is read off. In this work the coefficient is neglected because it has no significant effect on the results.

A schematic view of the apparatus, the area meter II, and Areameter-Nomogram are shown in Figures A9.1 and A9.2.

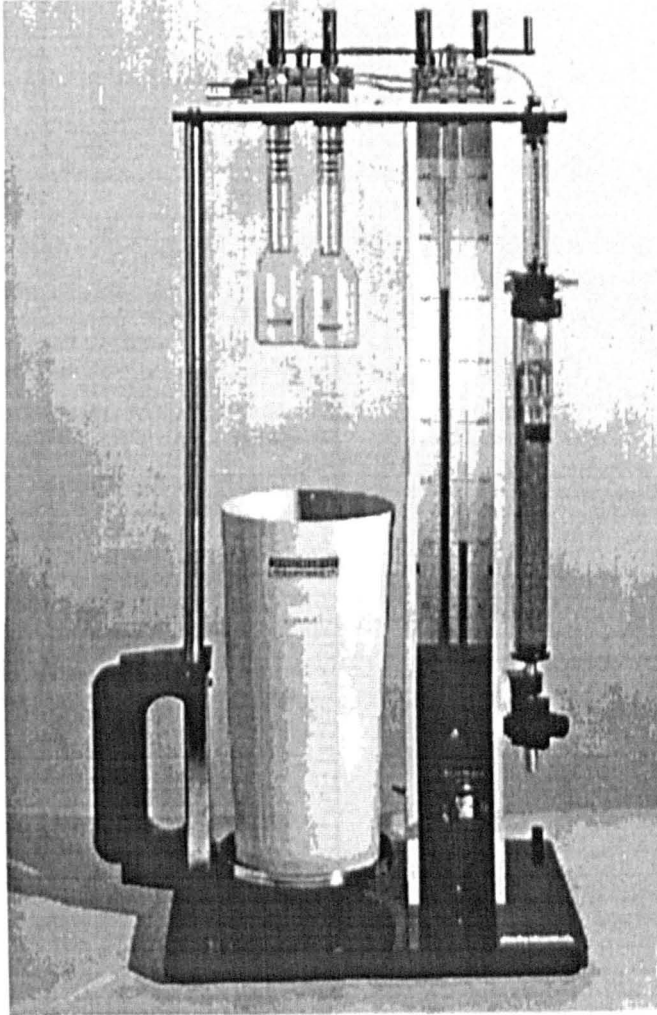
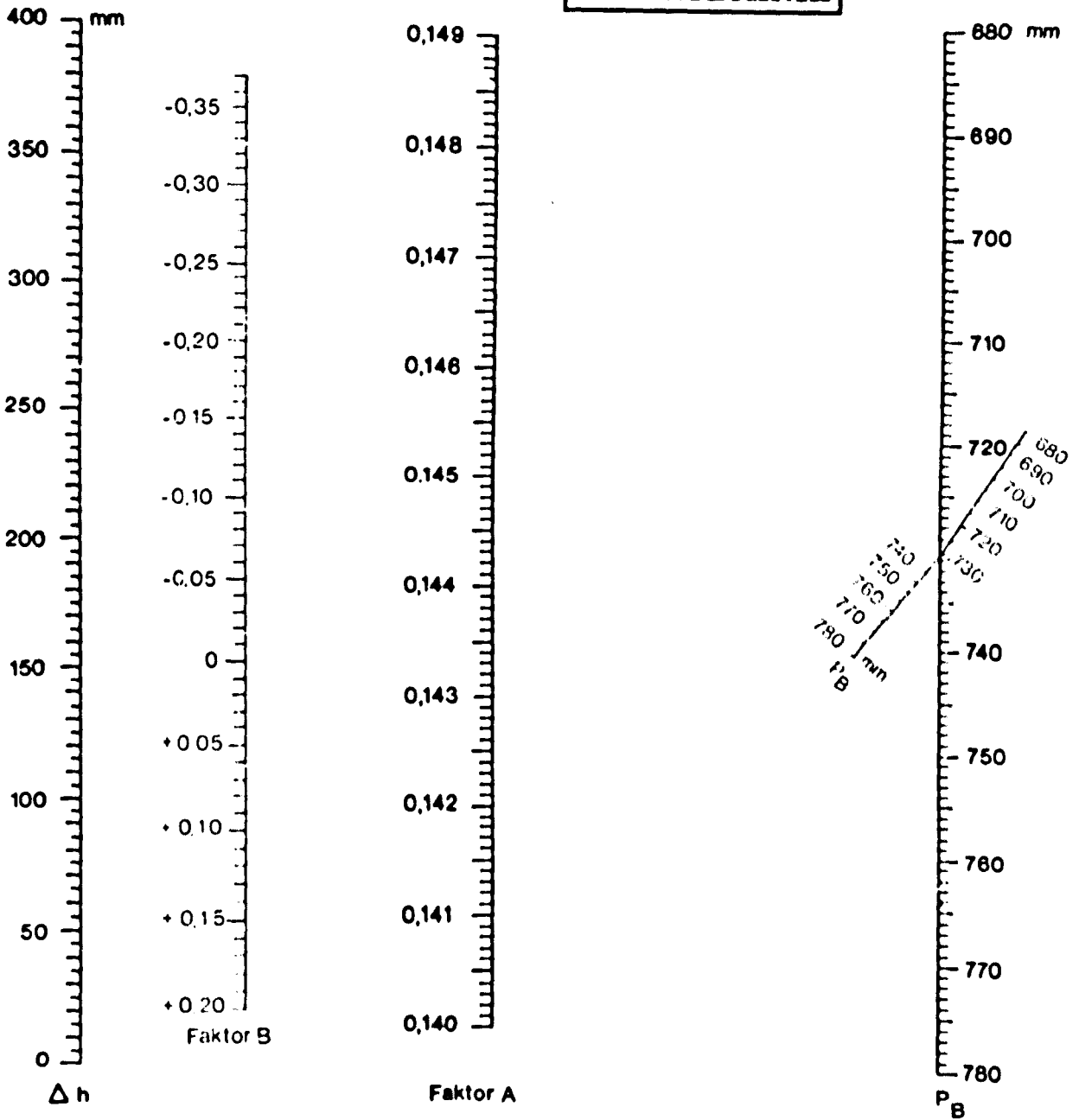


Figure A9.1 Area meter II used for measuring surface area.

Figure A9.2 AREA meter-Nomogramm



$$S_g = \frac{A \cdot \Delta h}{m} \cdot \frac{B}{\rho_p} \left(\frac{m^2}{g} \right)$$

APPENDIX 10

DETERMINATION OF IODINE ADSORPTION NUMBER

The method is adopted from British Standard 4398 (1969)

A10.1 Reagents

a) Iodine solution (0.1N)

Dissolve 12.69g of iodine in one litre of carbon tetrachloride (CCl₄).

b) Sodium thiosulphate solution (0.05)

Dissolve 12.409g of sodium thiosulphate pentahydrate (Na₂S₂O₅.5H₂O) in approximately 500 ml of distilled water in a one litre volumetric flask. Add 5ml of pentan-1-ol and shake the solution in the flask to mix thoroughly. Dilute to 1000 ml with the distilled water. Shake the solution in the flask to obtain uniform dilution.

c) Starch indicator

Dissolve 2g of soluble starch in 1000 ml of nearly boiling distilled water.

A10.2 Procedure

a) Weigh about 2g of the sample and place it in a glass bottle of approximately 200 ml.

b) Pipette 100ml of the iodine solution into the bottle and stopper immediately.

c) Shake the bottle in a mechanical shaker for approximately 30 minutes.

- d) Immediately after shaking, centrifuge and then decant the iodine solution completely in one smooth movement into a 250ml beaker, leaving the magnesium oxide in the bottom of the bottle.
- e) pipette 20 ml of this solution into 250 ml conical flask.
- f) Titrate the iodine solution with the sodium thiosulphate solution until a pale yellow colour remains.
- g) Add approximately 5 ml of the starch indicator and continue titrating until one drop of the sodium thiosulphate solution causes the blue colour to disappear leaving a colourless solution.
- h) Read the burette to the nearest 0.1 ml.
- i) Make a blank determination following the same steps, but omitting the sample.

A10.3 Calculation

Calculate the iodine adsorption number in milligrams of iodine per gram of magnesium oxide as follows:

$$I = (B-S) \frac{N}{M} \times 126.9$$

where:

I = iodine adsorption number (mg/g)

B = volume of the sodium thiosulphate solution (in millilitres) required for titration of the blank

S = volume of the sodium thiosulphate solution (in
millilitres required for titration of the sample

M = weight of the test portion (in grams).

N = normality of the sodium thiosulphate solution.

Appendix 11

MEASUREMENT OF APPARENT POROSITY, APPARENT SPECIFIC GRAVITY, AND BULK DENSITY

The values are determined using a modified version of A.S.T.M. test method (C20-80a). The main differences are that the suspended weight is measured directly using a top pan balance and in the case of dead burned magnesite paraffin is used instead of water for liquid saturation to prevent any possibility of hydration.

A11.1 Sampling and test specimens

For each measurement, approximately 50 grams of granular and representative specimen in the size range of 10-20 mm are selected. All loosely adhering particles are removed from each sample.

A11.2 Dry weight, (D)

The test specimens are dried by heating to 105° C in an oven. Then the dry weight (D) is determined in gms to nearest 0.1 gm. The drying procedure may be omitted only when the test specimens are known to be dry, as may be the case with samples taken directly from kilns.

A11.3 Saturation

The test specimen is placed in an electrically heated flask container fitted with a reflux condenser, and the

sample in the flask is covered with water (in the case of refractories with liquid paraffin) and then brought to boil for two hours. During the boiling period, they are kept entirely covered with liquid, without any contact with the heated bottom of the container.

After the boiling period, the test specimens are cooled to room temperature while still completely covered in the liquid for at least 12 hours before weighing.

A11.4 Suspended weight, (S)

The cool samples are removed from the liquid and the suspended weight (S) is determined for each test specimen after boiling and while it is suspended in the same liquid through the instrumentation shown in Figure A11.1.

This instrument has a perforated glass beaker to use as a sample holder. The latter is held by a metallic ring which is connected to a base through an arm and stand. The arm has a counter balance at its end to equalize for the weight of the beaker and its contents. Initially the empty perforated beaker is lowered to a predetermined depth into a two litre beaker containing water or paraffin. This is done by lowering the arm shown in the diagram. The balance is then tared, and the sample holder is lifted out afterwards. The empty sample holder is filled with the material and lowered again to the same depth and the reading on the balance scale is recorded. This reading gives the suspended weight (S grams) of the sample.

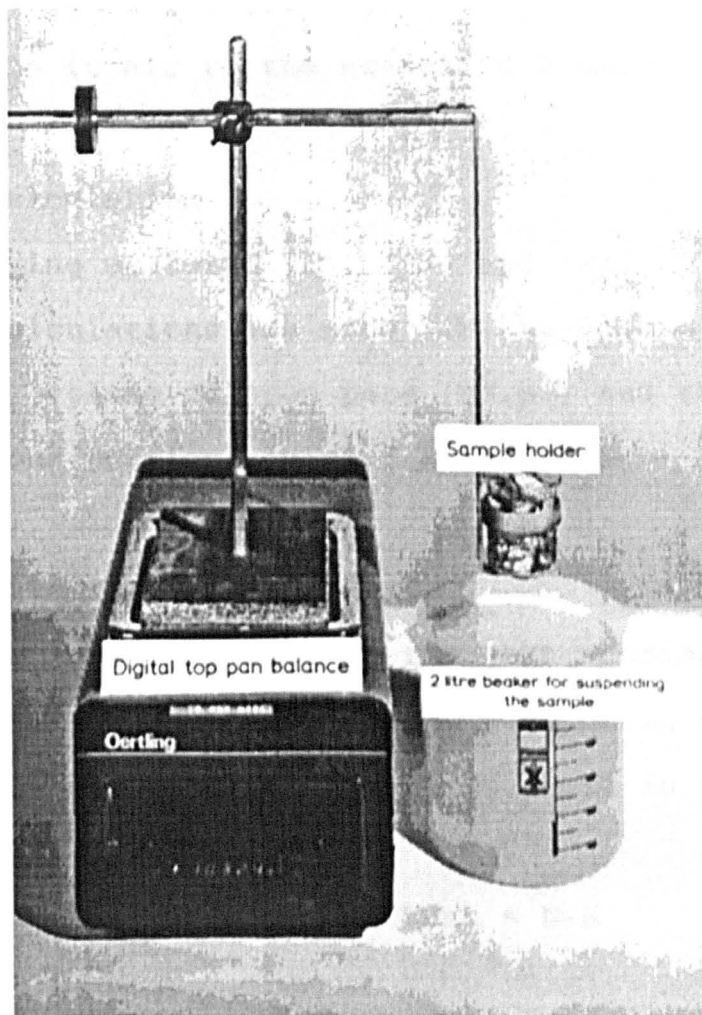


Figure A11.1 Apparatus for measuring suspended weight.

All.5 Saturated Weight, (W)

After determining the suspended weight, each specimen is dried lightly with a moistened smooth linen or cotton cloth to remove all drops of water from the surface. Then the saturated weight (W), in grams is determined by weighing the materials in air to the nearest 0.1 gm.

All.6 Calculation

Having measured (D), (S), and (W), to the nearest 0.1 gram, calculations are made for the volume of exterior (vext.), volume of open pore (vo.p.) and the volume of impervious portions (vimp.) as follows:

All.7 Exterior Volume, (Vext)

The (vext.) volume of the test specimen in cubic centimetres can be obtained by subtracting the suspended weight from the saturated weight, both in grams, as follows:

$$V_{ext} = W - S$$

All.8 Volumes of Open Pores (Vo.p) and Impervious Portions (Vimp)

These values can be determined by using the following formulas:

$$V_{o.p} = W - D$$

$$V_{imp} = D - S$$

Note: This assumes that 1 cm³ of water weighs 1 gram at room temperature. As with periclase paraffin is used, hence the

right sides of the above formulas must be divided by the density of paraffin (0.82 gm/cm³, at 18°C).

Using the calculated volumes, the apparent porosity (P) which express as a percentage of the relationship of the volume of the open pores in the specimen to its exterior volume is found as follows:

$$P (\%) = \frac{V_{o.p}}{V_{ext}} \times 100$$

Bulk density (B) (gm/cm³) is given by the relation:

$$B = \frac{D}{V_{ext}}$$

The apparent specific gravity is calculated by the following formula:

$$T = \frac{D}{V_{imp}}$$

Water Absorption, A is given by the relation

$$A (\%) = \frac{V_{o.p}}{D} \times 100$$

Note: Apparent porosity can also be determined as follows:

$$P (\%) = A \times B$$

The repeatability of the method was tested by determination of ten separate portions of one magnesite sample. The results are presented in Table A||.} together with Mean and Standard deviation for each property.

Table AIII. Data obtained after repetitive tests on magnesite

Sample	D	S	W	Vext.	V.op.	Vimp	P (%)	B	T
1	24.89	16.7	25.49	8.79	0.60	8.19	6.83	2.83	3.04
2	22.45	15.1	23.02	7.92	0.57	7.35	7.20	2.83	3.05
3	24.40	16.4	25.02	8.62	0.62	8.00	7.19	2.83	3.05
4	24.35	16.2	24.97	8.77	0.62	8.15	7.06	2.78	2.99
5	22.49	14.9	23.00	8.10	0.51	7.59	6.30	2.78	2.96
6	23.53	15.9	24.16	8.26	0.63	7.63	7.63	2.85	3.08
7	24.18	16.2	24.71	8.51	0.53	7.98	6.23	2.84	3.03
8	24.79	16.6	25.30	8.70	0.51	8.19	5.86	2.85	3.03
9	28.64	18.9	29.29	10.39	0.65	9.74	6.26	2.76	2.94
10	20.84	13.8	21.44	7.64	0.60	7.04	7.85	2.73	2.96
Mean							6.84	2.81	3.01
S.D							0.66	0.04	0.05

Where:

D = Weight of dry sample (gm)

S = Weight of suspended sample (gm)

W = Weight of saturated sample (gm)

P = Apparent porosity in percentage

B = Bulk density (gm/Cm³)

T = Apparent specific gravity

S.D = Standard deviation

Vext. = Exterior volume (Cm³)

V.op. = Open pore volume (Cm³)

Vimp. = Impervious portion value (Cm³)

The apparent specific gravity values show little variation, which is due to presence of similar portion of

small closed porosities within the specimen. Closed porosity can be calculate as follows:

$$\text{Closed porosity (\%)} = 100 \left(1 - \frac{\text{Apparent specific gravity}}{\text{True specific gravity}} \right)$$

The apparent specific gravity (T), bulk density (B), and apparent porosity (P), values relation are shown as follow:

$$P (\%) = \frac{T-B}{T} \times 100$$

The total porosity can be calculate by adding the apparent and closed porosities.

APPENDIX 12

DETERMINATION OF ACID INSOLUBLE RESIDUE (AIR)

A12.1 Equipment and reagents

1. 10 percent cold hydrochloric acid.
2. Distilled water.
3. Filter paper number 5.
4. Large plastic plastic beakers for containing the sample and acid during dissolution.
5. Glass rod.
6. Wash bottle of distilled water.
7. A set of watch glasses to contain the filters and residue.
8. Buchner flask and funnel.
9. A vacuum pump.

A12.2 Procedure

- a) Weight out 5g of the sample accurately up to four decimal places and place it in a 2000 ml plastic beaker.
- b) Carefully add HCl 10% to the samples and stir the the content with a glass rod and allow it to stand for around 10 minutes.
- c) Add some more acid and stir the solution and continue adding the 10% HCl and string the solution until no further gas bubbles are evolved (a colourless solution will appear in the beaker).
- d) Weigh the filter papers very accurately up to four decimal places.

- e) Mark all filter papers, beakers and the watch glasses to prevent any mistake.
- f) place the filter paper on the surface of the funnel of Buchner flask and turn on the vacuum pump.
- g) Decant the acid solution and residues in smooth movement on the surface of filter paper and wait until all solution are passed through the filter.
- h) wash the filter carefully several time with distilled water (make sure no acid is remained in the filter).
- i) Place the filter papers in 105°C oven for two hours to dry the moisture.
- j) Remove the filter papers from oven and allow them to be cool, when they completely cold weigh the filter papers plus contents up to four decimal place.
- k) describe the residue under binocular microscope.

A12.3 Calculation

The acid insoluble residue is calculated as follows:

$$\text{AIR (\%)} = \frac{\text{Weight of (R+M) + A}}{\text{Weight of sample}}$$

where:

R = residue

M = moisture

A = correction factor

Note 1. Weight of (R+M) can be calculate by subtract the weight of filter paper before experimental from weight of

filter paper and residue after drying in oven.

Note 2. Correction factor is the amount of moisture in the original filter paper and it can be measured by subtracting the weight of original filter paper before and after drying.

APPENDIX 13

DETERMINATION OF OIL ABSORPTION VALUE

The method used follows BS 3483: part B7 British standard method for testing pigments for paints.

In accordance with this method, refined linseed oil, complying with the BS 242 and having an acid value of 5.0 mg to 7.0 mg of KOH per gram is combined with the appropriate quantity of pigment.

A13.1 Apparatus

1. Ground glass or marble plate, at least 300 mm x 400 mm.
2. Palette knife, of steel with a taped blade of the approximate dimensions 140 mm to 150 mm long, 20 mm to 25 mm wide at its widest point and not less than 12.5 mm wide at narrowest point.
3. Burette, 10 ml capacity, graduated in 0.1 ml division, complying with BS 846.

A13.2 Test Portion

Weigh of the quantity of the pigment under test in accordance with the expected oil absorption, as it shown in Table A13.1.

Table A13.1 Mass of pigment for test

Expected oil absorption value of pigment	Mass of the test portion
(ml/100g)	(g)
less than 10	20
10 to 30	10
30 to 50	5
50 to 80	2
Over 80	1

A13.3 Determination

The appropriate quantity of sample is placed on a glass plate and four or five drops of linseed oil are added slowly at a time the burette. After each addition the oil is rubbed into the pigment with the palette knife. The addition of oil is continue in this rate until conglomerate of oil and pigment are formed. From this point, the addition of oil is one drop at a time and each addition is followed by thoroughly rubbing with the palette knife. when a paste of smooth consistency has been formed the addition of oil is ceased. This paste should just spread without cracking or crumbling and should only adhere to the plate. The quantity of oil used is readed from the burette. The time needed for

completion of the test is between 20 and 25 minutes.

A13.4 Results

The oil absorption value can be calculate either as the volume or the mass of oil required per 100 gm of pigment by means of the formula:

On the volume/mass basis, oil absorption value = $100 \frac{V}{m}$.
On the mass/Mass basis, oil absorption value = $93 \frac{V}{m}$
Where V is the volume of oil required in millilitres and m is the mass in grams of test portion. The results is reported to the nearest ml or gm.

APPENDIX 14

COLOUR MEASUREMENT OF MINERAL POWDERS

A14.1 The nature of colour

The radiation of wavelengths in the visible spectrums from approximately 4000 A° (violet) to 7000 A° (red) are responds to the human eye. The "average eye" being most sensitive to light is approximately 5600 A°.

The sensation known as colour is considered to result from the brain from energy transmitted by the optic nerves from the retina of the eye. The human eye is sensitive to only a very small amount of the electromagnetic spectrum. This fraction is called the visible light, or "white" light.

A14.2 Attribution of colour

HUE is the dominant wavelength reflectance for any sample. e.g. wavelength ranges between 4500-4900 A° is blue and 6300-7800 A° is red. Each member of the continuous series of spectrum colours is a hue.

SATURATION or PURITY is the proportion of density of colour measured against white light (of zero colour). Different people receive different impressions of colour in that some individuals are able to distinguish only differences in light intensities and not differences in wavelength.

BRIGHTNESS is the light intensity of the colour. Two specimens may have the same hue and saturation values but if

their brightness levels are not the same, they will appear in two different colours.

A14.3 The Reflectance Spectrophotometer

The instrument commonly used for measuring colour is the reflectance spectrophotometer. This is an instrument which measure the amount of light reflected from the surface of the specimen. The light is filtered so that only a chosen narrow band of the spectrum is measured. The amount of light reflected usually varies with the different filters.

A14.4 Sample preparation

For the purpose of reflectance measurement of powders, it is great important to have an even-grained, clean and flat surface. This is carried out using the Hull university D.I.Y. powder press equipments which are contain of the following parts as it shown in Figure A14.1.

- A) Hollow cylinder fitted with ground glass plate and three centering screws.
- B) Piston with screw which fits into (A).
- C) Sample holder comprising hollow metal disc fitted with a base. The base screws into the disc to form the sample holder.
- D) A small cylinder which screw into the hollow metal disc of the sample holder. This hollow cylinder contains the powder whilst pressing the sample and is made so that the piston (B) closely fits inside it.
- E) A tool for screwing the sample base into the hollow metal disc.

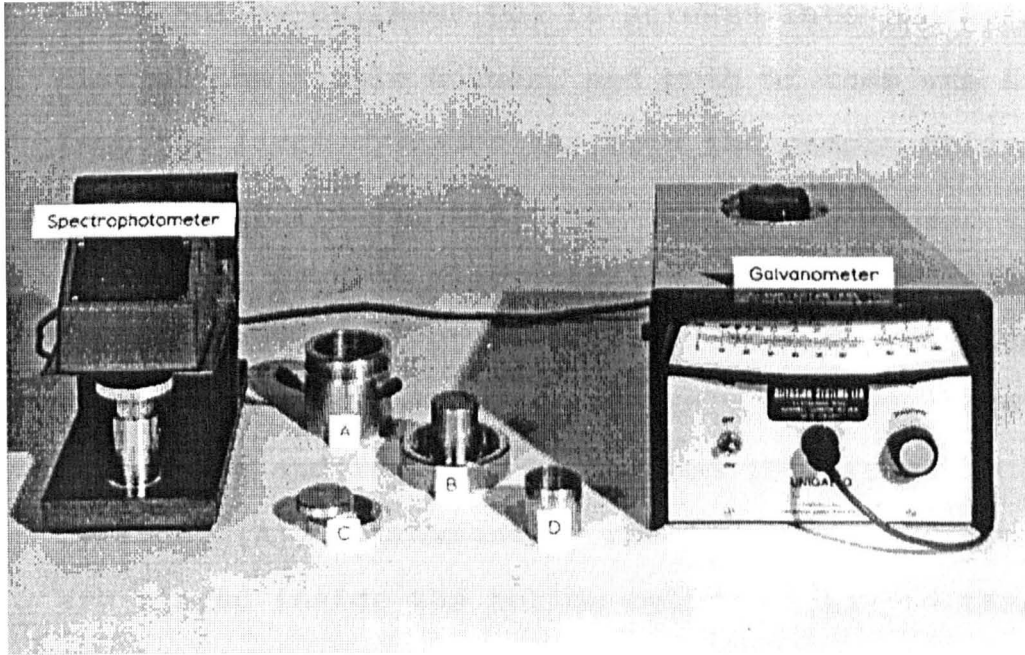


Figure A14.1 EEL reflectance spectrophotometer and components of the powder press.

F) A tea-spoon.

A14.5 Procedure

1. All parts of the press should be cleaned thoroughly with tissue paper to remove any dust or remains of previous sample.
2. Small hollow cylinder (D) is screwed into the hollow metal disc of the sample holder, and both of them are fitted into the large cylinder (A) with the sample holder flat against the glass plate.
3. Piston (B) is next placed inside the cylinder and loosely screwed down. Each of the three screws are tightened so that the sample holder is certainly clamped. After unscrewing and removing the piston (B), from the large cylinder (A), approximately two level teaspoons of powder are placed inside the hollow cylinder (D) and tamped lightly to evenly distribute and close pack the powder.
4. The piston (B) is then fitted and screwed down firmly and evenly so that the powder is firmly pressed into the specimen holder.
5. After removing the piston (B) again, the hollow cylinder (D) is carefully un-screwed from the hollow metal disc of the sample holder (C). Blow onto the surface of the sample to remove surplus loose powder.
6. The base of the sample holder is then screwed into the hollow metal disc. The sample is ready for reflectivity determinations after unscrewing the centering screws, inverting the cylinder and removing the sample holder

carefully.

A14.6 Calibration and Standardization

The principal of measurement is based on comparing the reflectance of the specimen to be measured with a white standard. A close approach to perfect whiteness is attained by various standards like titanium oxide, magnesium carbonate, barium sulphate or magnesium oxide.

For the EEL spectrophotometer, the standard used is magnesium carbonate, but for the practical purpose this has been replaced by a ceramic tile, which has been calibrated against the magnesium carbonate block using two sets of filters (the nine filters (601-609) and the tristimulus (X,Y,Z) filters) and has values as follows:

<u>Filter No</u>	<u>% Reflectance</u>
601	79.3
602	89.7
603	87.4
604	87.3
605	88.6
606	89.8
607	95.2
608	95.9
609	93.3
X	93.4
Y	84.5
Z	29.7

A14.7 Methods of colour specification

Colour specification may be done by several method. Two of the method, which can be carried out with the EEL reflectance spectrophotometer, by a simple change of filters, are as follows:

a) The spectrophotometric curve

The colour of the sample is represented by a graph of wavelength of light plotted against intensity of reflected light. This is made by the use of the nine-filters wheel (filters (601-609) which have the following wavelengths and colours

Table A14.1

Filter No	Colour	Wavelength (A°)
601	violet	4260
602	blue	4700
603	blue-green	4900
604	green	5200
605	yellow-green	5500
606	yellow	5800
607	orange	6000
608	red	6600
609	deep red	6840

procedure for measuring the spectrophotometric curve.

1. With the 601 filter in position, place the tile under the spectrophotometric head and adjust the galvanometer sensitivity control anti-clockwise until the reading corresponds with the calibrated value at this filter (79.3%).

2. Replace the tile by the sample and read the galvanometer.
3. Turn the wheel to the next filter, and with the standard once again under the spectrophotometric head. adjust the sensitivity to the values and repeat the procedure as before with each filter.
4. The plot of reflectance measurement against wavelength of light is the spectrophotometric curve. A pure white sample has no change in reflectance when using the normal light. A grey sample is similar but the overall values are less, due to absorption. A blue sample has greatest reflection at the blue end of the spectrum due to the reflection of the blue wavelength component of the light.

b) The C.I.E. colour system

Colours are more easy to compare if numerical values are used. The commission international de 'Eclairage developed the C.I.E. colour system. According to this system, three values, X, Y, and Z which are called the tristimulus values and correspond to red, green and blue colour respectively, are determined by the use of the tristimulus filters (X,Y,Z) wheel. This is carried out in the same manner as for the determination of the spectral curve.

Functions x, y, and z, which are called chromaticity coordination can be derived from X, Y, and Z, as follows:

$$\begin{array}{ccc}
 \begin{array}{c} X \\ x = \frac{\quad}{X + Y + Z} \end{array} &
 \begin{array}{c} Y \\ y = \frac{\quad}{X + Y + Z} \end{array} &
 \begin{array}{c} Z \\ z = \frac{\quad}{X + Y + Z} \end{array}
 \end{array}$$

Because the sum of x , y , and z is unity, thus only x and y are needed. These functions can be plotted on the chromaticity chart (Figure A14.2). All the spectrum colours fall on the spectrum locus which is an inverted U-shaped curve whose extreme ends are jointed by a straight line, the purple line. The centre of the spectrum locus is white. Ideal white lights plots at $x = 0.33$, $y = 0.33$ in the chromaticity diagram. The source light used to illuminate the sample in the EEL reflectance spectrophotometer approximates to source A ($x = 0.4476$, $y = 0.4075$) which corresponds to a tungsten filament lamp. Once the chromaticity coordinates (x and y) of a colour are known, the colour can be plotted on the chromaticity diagram. A line can be drawn from the achromatic point (standard illuminate point A) through the sample plot to the wavelength on the spectrum locus.

The hue of sample can be indicated by the particular value found in the spectrum locus which is known as the dominant wavelength.

The purity is specified as the ratio of the distance of the specimen point from the achromatic point to the distance from the spectrum locus to the achromatic point expressed in percentage. The purity varies from zero at the achromatic point to unity at the spectrum locus. However, its value and that of the dominant wavelength depend on the achromatic point to which the chromaticity coordinates are related. This is because there are two other sources other than the tungsten filament lamp (source A). These are source (B) ($x =$

0.3485, $y = 0.3518$) and source (C) ($x = 0.3101$, $y = 0.3163$) which are intended to present direct sunlight and daylight respectively.

The third colour dimension, the brightness, is taken as the Y tristimulus value. The C.I.E. system was arranged so that the percentage reflectance of a sample when measured using the Y filter is a measure of the percentage visual brightness.

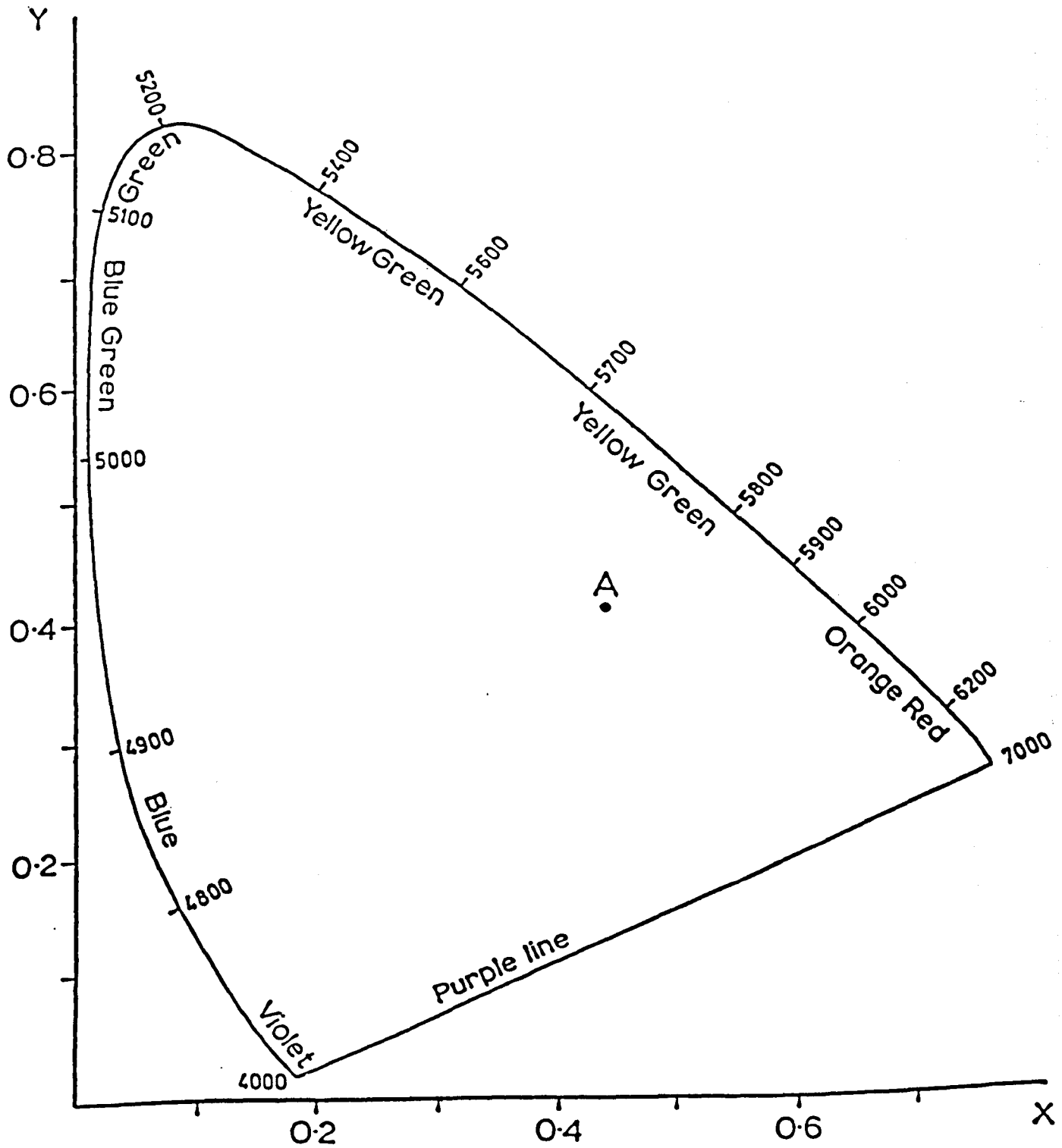


Figure A14.2 Chromaticity Chart

APPENDIX 15

Electron microprobe analyses of dead burned huntite,
hydromagnesite - huntite, magnesite - dolomite and
nesquehonite

Sample Code SPOT	AH-C SCAH 1	AH-C SCAH 2	AH-C SCAH 3	AH-C SCAH 4	AH-C SCAH 5	AH-C PCAH 6	AH-C SCAH 7	AH-C MXAH 8	AH-C PCAH 9	AH-C MXAH 10
SiO2	18.73	19.35	18.89	18.76	18.97	n.d.	19.32	2.87	n.d.	n.d.
TiO2	n.d.									
Al2O3	4.51	4.37	4.44	4.50	4.33	n.d.	4.34	1.32	n.d.	n.d.
Cr2O3	n.d.	0.39	n.d.							
FeO	n.d.									
MnO	n.d.									
MgO	0.89	1.10	0.83	0.89	0.96	97.13	1.07	87.24	97.46	94.11
CaO	17.18	17.12	17.51	17.61	17.24	0.61	17.00	2.45	1.15	3.45
K2O	n.d.									
TOTAL	41.31	42.33	41.67	41.76	41.50	97.74	41.73	93.88	98.61	97.56
Sample Code SPOT	AH-C SCAH 11	AH-C PCAH 12	AH-C PCAH 13	AH-C LCAH 14	AH-C MXAH 15	AH-C MXAH 16	AH-C LCAH 17	AH-C PCAH 18	AH-C LCAH 19	AH-C PCAH 20
SiO2	19.13	n.d.	n.d.	0.43	0.33	n.d.	0.60	n.d.	0.37	n.d.
TiO2	n.d.									
Al2O3	4.27	n.d.	n.d.	0.44	0.68	n.d.	0.60	n.d.	0.58	n.d.
Cr2O3	n.d.									
FeO	n.d.									
MnO	n.d.									
MgO	0.68	96.91	97.91	4.90	10.70	94.23	2.23	98.10	2.12	100.43
CaO	17.60	1.45	0.94	84.27	79.11	4.51	85.32	0.91	85.92	0.82
K2O	n.d.									
TOTAL	41.68	98.36	98.85	90.04	90.82	98.74	88.75	99.01	88.99	101.25
Sample Code SPOT	AH-C PCAH 21	AH-C LCAH 22	AH-C LCAH 23	AH-C PCAH 24	AH-C LCAH 25	AH-B SCAH 1	AH-B SCAH 2	AH-B SCAH 3	AH-B PCAH 4	AH-B PCAH 5
SiO2	n.d.	n.d.	n.d.	0.23	n.d.	23.07	22.75	22.12	0.19	n.d.
TiO2	n.d.									
Al2O3	n.d.	0.58	0.59	n.d.	0.66	1.28	1.26	1.52	n.d.	n.d.
Cr2O3	n.d.	n.d.	n.d.	n.d.	n.d.	0.44	n.d.	n.d.	n.d.	n.d.
FeO	n.d.									
MnO	n.d.									
MgO	98.23	4.57	1.95	98.10	7.64	1.10	0.93	7.29	97.76	97.38
CaO	0.80	83.31	86.24	0.79	80.38	15.04	15.77	14.28	0.87	1.27
K2O	n.d.									
TOTAL	99.03	88.46	88.78	99.12	88.68	40.93	40.71	45.21	98.82	98.65

HUNT

Sample Code SPOT	AH-B SCAH 6	AH-B SCAH 7	AH-B MXAH 8	AH-B MXAH 9	AH-B LCAH 10	AH-B MXAH 11	AH-B LCAH 12	AH-B MXAH 13	AH-B SCAH 14	AH-B SCAH 15
SiO2	19.80	16.75	n.d.	0.49	0.79	0.51	0.35	6.63	26.07	26.12
TiO2	n.d.	n.d.	n.d.	n.d.	n.d.	n.d.	n.d.	n.d.	0.36	n.d.
Al2O3	1.27	1.05	0.30	0.72	0.79	0.68	0.54	1.16	2.37	1.91
Cr2O3	0.35	0.37	n.d.	0.37						
FeO	n.d.	n.d.	n.d.	n.d.	n.d.	n.d.	n.d.	n.d.	n.d.	n.d.
MnO	n.d.	n.d.	n.d.	n.d.	n.d.	n.d.	n.d.	n.d.	n.d.	n.d.
MgO	1.41	1.35	82.37	19.48	2.97	14.79	1.73	2.60	0.76	0.75
CaO	24.08	31.60	16.61	72.61	82.47	70.74	82.44	66.77	12.94	12.75
K2O	n.d.	n.d.	n.d.	n.d.	n.d.	n.d.	n.d.	n.d.	n.d.	n.d.
TOTAL	46.91	51.12	99.28	93.30	87.02	86.72	85.06	77.16	42.50	41.90
Sample Code SPOT	AH-B LCAH 16	AH-B SCAH 17	AH-B PCAH 18	AH-B MXAH 19	AH-B MXAH 20	AH-B PCAH 21	AH-B LCAH 22	AH-B SCAH 23	AH-B PCAH 24	AH-B LCAH 25
SiO2	4.09	24.68	n.d.	n.d.	2.27	n.d.	3.97	24.81	n.d.	0.45
TiO2	n.d.	n.d.	n.d.	n.d.	n.d.	n.d.	n.d.	n.d.	n.d.	n.d.
Al2O3	0.80	2.10	n.d.	0.36	0.92	n.d.	0.86	1.37	n.d.	0.64
Cr2O3	n.d.	n.d.	n.d.	n.d.	n.d.	n.d.	n.d.	n.d.	n.d.	n.d.
FeO	n.d.	n.d.	n.d.	n.d.	n.d.	n.d.	n.d.	n.d.	n.d.	n.d.
MnO	n.d.	n.d.	n.d.	n.d.	n.d.	n.d.	n.d.	n.d.	n.d.	n.d.
MgO	1.83	1.83	98.31	84.10	3.53	98.43	9.66	11.44	98.01	2.97
CaO	73.26	12.78	1.55	13.27	26.29	0.70	66.41	11.87	0.72	82.44
K2O	n.d.	n.d.	n.d.	n.d.	n.d.	n.d.	n.d.	n.d.	n.d.	n.d.
TOTAL	79.98	41.39	99.86	97.73	33.01	99.13	80.90	49.49	98.73	86.50
Sample Code SPOT	AH-B LCAH 9.9999	AH-B SCAH 27	AH-B MXAH 28	AH-B LCAH 29	VH-B PCVH 1	VH-B PCVH 2	VH-B PMVH 3	VH-B PCVH 4	VH-B PMVH 5	VH-B PCVH 6
SiO2	2.17	24.10	n.d.	0.60	0.66	n.d.	n.d.	n.d.	0.23	n.d.
TiO2	n.d.	n.d.	n.d.	n.d.	n.d.	n.d.	n.d.	n.d.	n.d.	n.d.
Al2O3	0.83	1.67	0.73	0.68	0.35	0.49	0.41	0.45	0.41	0.34
Cr2O3	n.d.	n.d.	n.d.	n.d.	n.d.	n.d.	n.d.	n.d.	n.d.	n.d.
FeO	n.d.	n.d.	n.d.	n.d.	n.d.	n.d.	n.d.	n.d.	n.d.	n.d.
MnO	n.d.	n.d.	n.d.	n.d.	n.d.	n.d.	n.d.	n.d.	n.d.	n.d.
MgO	1.92	12.72	14.37	3.58	98.01	100.87	99.86	99.92	99.10	99.22
CaO	79.55	10.80	73.43	81.21	0.79	n.d.	n.d.	0.22	0.25	n.d.
K2O	n.d.	n.d.	n.d.	n.d.	n.d.	n.d.	n.d.	n.d.	n.d.	n.d.
TOTAL	84.47	49.29	88.53	86.07	99.81	101.36	100.27	100.59	100.01	99.56

HUNT

Sample Code SPOT	VH-B PMVH 7	VH-B PCVH 8	VH-B PMVH 9	VH-B MRVH 10	VH-B MXVH 11	VH-B MXVH 12	VH-B PCVH 13	VH-B MRVH 14	VH-B MRVH 15	VH-B MXVH 16
SiO2	0.19	n.d.	0.23	36.36	34.23	32.84	0.23	35.92	36.22	33.77
TiO2	n.d.	n.d.	n.d.	0.26	0.25	n.d.	n.d.	n.d.	n.d.	n.d.
Al2O3	n.d.	0.31	n.d.	n.d.	2.21	n.d.	0.61	n.d.	n.d.	1.82
Cr2O3	n.d.									
FeO	n.d.	n.d.	n.d.	n.d.	n.d.	0.31	n.d.	n.d.	n.d.	n.d.
MnO	n.d.									
MgO	98.47	98.17	97.55	11.80	7.63	20.29	98.50	11.68	12.21	6.33
CaO	n.d.	n.d.	n.d.	47.68	51.97	43.75	0.15	47.98	47.80	53.99
K2O	n.d.									
TOTAL	98.66	98.48	97.78	96.10	96.29	97.19	99.49	95.58	96.23	95.91
Sample Code SPOT	VH-B PCVH 17	VH-B PMVH 18	VH-B DCVH 19	VH-B DCVH 20	VH-B DCVH 21	VH-B PCVH 22	VH-B PMVH 23	VH-B MRVH 24	VH-B DCVH 25	VH-B MRVH 26
SiO2	n.d.	0.24	34.51	33.22	34.00	n.d.	n.d.	55.11	34.40	35.46
TiO2	n.d.									
Al2O3	0.33	0.37	n.d.	1.75	n.d.	n.d.	0.50	0.86	0.26	n.d.
Cr2O3	n.d.									
FeO	n.d.	n.d.	n.d.	n.d.	n.d.	n.d.	0.29	n.d.	n.d.	n.d.
MnO	n.d.									
MgO	98.23	96.71	4.49	2.90	4.28	98.82	98.52	8.58	1.85	11.50
CaO	0.37	0.41	56.25	58.47	57.06	0.20	0.40	51.76	59.85	48.11
K2O	n.d.									
TOTAL	98.93	97.73	95.25	96.34	95.34	99.02	99.71	116.31	96.36	95.07
Sample Code SPOT	VH-B DCVH 27	VH-B MRVH 28	VH-B DCVH 29	VH-B DCVH 30	VH-B DCVH 31	NH-A SCNH 1	NH-A SCNH 2	NH-A SCNH 3	NH-A LCNH 4	NH-A PCNH 5
SiO2	34.44	36.20	33.35	34.32	32.50	26.06	29.24	28.08	0.24	n.d.
TiO2	0.26	n.d.								
Al2O3	n.d.	n.d.	0.77	1.20	3.72	0.50	0.59	0.64	n.d.	n.d.
Cr2O3	n.d.	n.d.	n.d.	n.d.	n.d.	n.d.	0.44	n.d.	n.d.	n.d.
FeO	n.d.	n.d.	n.d.	n.d.	n.d.	0.76	0.73	0.83	n.d.	n.d.
MnO	n.d.									
MgO	3.44	12.01	4.12	4.23	2.12	14.34	1.82	4.90	2.36	96.40
CaO	58.38	48.59	57.63	57.26	58.41	28.35	32.93	30.54	91.43	0.69
K2O	n.d.									
TOTAL	96.52	96.80	95.87	97.01	96.75	70.01	65.75	64.99	94.03	97.09

HUNT

Sample Code SPOT	NH-A PCNH 6	NH-A PCNH 7	NH-A LCNH 8	NH-A LCNH 9	NH-A LCNH 10	NH-A LMNH 11	NH-A PCNH 12	NH-A PMNH 13	NH-A PCNH 14	NH-A MXNH 15
SiO2	n.d.	n.d.	0.68	n.d.	0.29	1.53	n.d.	n.d.	n.d.	2.33
TiO2	n.d.									
Al2O3	n.d.	n.d.	0.20	0.20	0.34	0.33	n.d.	n.d.	n.d.	n.d.
Cr2O3	n.d.									
FeO	0.25	n.d.	n.d.	n.d.	n.d.	n.d.	0.27	0.32	0.27	0.36
MnO	n.d.									
MgO	97.79	97.73	2.11	2.13	2.33	2.19	97.98	99.42	98.39	92.83
CaO	0.63	0.62	91.38	92.16	92.64	90.47	0.65	0.70	0.75	4.08
K2O	n.d.									
TOTAL	98.67	98.35	94.37	94.49	95.60	94.52	98.90	100.44	99.41	99.60
Sample Code SPOT	NH-A PMNH 16	NH-A LCNH 17	NH-A LCNH 18	NH-A LCNH 19	NH-A LCNH 20	NH-A LMNH 21	NH-A PCNH 22	NH-A SCNH 23	NH-A SCNH 24	NH-A SCNH 25
SiO2	n.d.	n.d.	n.d.	0.68	0.64	0.82	1.12	28.43	28.95	29.31
TiO2	n.d.									
Al2O3	n.d.	0.26	0.21	n.d.	0.40	0.26	n.d.	0.43	0.52	0.57
Cr2O3	n.d.	0.41								
FeO	n.d.	n.d.	n.d.	n.d.	n.d.	n.d.	0.36	0.74	0.79	0.57
MnO	n.d.									
MgO	97.65	2.29	2.06	4.52	5.33	2.16	95.92	2.08	0.80	0.88
CaO	0.64	92.66	93.12	90.05	89.83	92.01	2.05	31.40	31.83	32.97
K2O	n.d.									
TOTAL	98.29	95.21	95.39	95.25	96.20	95.25	99.45	63.08	62.89	64.71
Sample Code SPOT	NH-A SCNH 26	NH-A SCNH 27	NH-A SCNH 28	NH-A SCNH 29	NH-A SCNH 30	NH-A PCNH 31	NH-A MXNH 32	NH-A PCNH 33	NH-A LCNH 34	NH-A PCNH 35
SiO2	28.77	29.08	28.80	28.92	28.43	n.d.	n.d.	n.d.	n.d.	n.d.
TiO2	n.d.									
Al2O3	0.49	0.56	0.46	0.54	0.51	n.d.	n.d.	n.d.	0.30	n.d.
Cr2O3	0.37	n.d.	n.d.	0.30	n.d.	n.d.	n.d.	n.d.	n.d.	n.d.
FeO	0.57	0.94	0.81	0.92	1.16	0.26	n.d.	0.32	n.d.	n.d.
MnO	n.d.									
MgO	2.40	1.06	0.71	0.50	0.39	94.80	91.86	96.23	5.70	95.46
CaO	31.63	33.05	32.59	33.14	32.55	0.73	5.58	1.05	87.14	0.96
K2O	n.d.									
TOTAL	64.23	64.69	63.37	64.32	63.04	95.79	97.44	97.60	93.14	96.42

HUNT

Sample Code	NH-A MXNH	NH-A PCNH	NH-A MXNH	NH-A MXNH	NH-A MXNH	NES-A PCNA	NES-A PMNA	NES-A PMNA	NES-A PCNA	NES-A PCNA
SPOT	36	37	38	39	40	1	2	3	4	5
SiO2	0.28	n.d.	0.18	n.d.	n.d.	n.d.	0.24	n.d.	0.17	0.18
TiO2	n.d.									
Al2O3	0.33	n.d.	n.d.	0.33	n.d.	1.27	1.28	1.05	1.07	1.07
Cr2O3	n.d.									
FeO	n.d.	n.d.	n.d.	n.d.	n.d.	1.17	1.01	0.86	1.10	0.99
MnO	n.d.									
MgO	9.89	94.60	92.21	12.50	74.57	95.82	95.78	95.06	94.40	94.75
CaO	84.81	1.59	3.61	81.44	20.91	n.d.	n.d.	n.d.	n.d.	n.d.
K2O	n.d.									
TOTAL	95.31	96.19	96.00	94.27	95.48	98.26	98.31	96.97	96.74	96.99
Sample Code	NES-A FCNA	NES-A FMNA	NES-A FCNA	NES-A FCNA	NES-A FCNA	NES-A FCNA	NES-A MCNA	NES-A MXMA	NES-A MCNA	NES-A MXMA
SPOT	6	7	8	9	10	11	12	13	14	15
SiO2	37.47	41.96	41.89	42.24	42.14	42.37	38.33	32.05	38.12	26.74
TiO2	n.d.	n.d.	n.d.	n.d.	n.d.	n.d.	0.46	1.27	0.39	3.22
Al2O3	0.42	n.d.	n.d.	n.d.	n.d.	n.d.	0.72	4.39	0.94	24.10
Cr2O3	n.d.									
FeO	n.d.	0.51	n.d.	2.98						
MnO	n.d.									
MgO	57.76	53.49	54.66	54.54	54.66	53.92	27.52	19.86	28.65	17.87
CaO	2.17	2.22	1.98	1.82	2.29	2.16	31.13	28.24	30.99	20.16
K2O	n.d.									
TOTAL	97.82	97.67	98.53	98.60	99.09	98.45	98.16	86.32	99.09	95.07
Sample Code	NES-C FCNC	NES-C PCNC	NES-C FCNC	NES-C FCNC	NES-C PCNC	NES-C PMNC	NES-C FCNC	NES-C PCNC	NES-C PMNC	NES-C PCNC
SPOT	1	2	3	4	5	6	7	8	9	10
SiO2	41.65	0.19	41.55	43.12	0.19	0.21	41.80	0.21	0.19	0.18
TiO2	n.d.									
Al2O3	n.d.	1.26	n.d.	n.d.	1.21	1.29	0.00	1.09	1.27	1.24
Cr2O3	n.d.									
FeO	n.d.	1.10	n.d.	n.d.	1.13	0.95	n.d.	1.09	1.08	0.84
MnO	n.d.									
MgO	53.34	95.77	53.36	54.62	96.28	95.86	53.82	96.14	96.94	95.42
CaO	2.53	n.d.	2.09	1.77	n.d.	n.d.	1.87	n.d.	n.d.	n.d.
K2O	n.d.									
TOTAL	97.52	98.32	97.00	99.51	98.81	98.31	97.49	98.53	99.48	97.68

HUNT										
Sample Code SPOT	NES-C MCNC 11	NES-C MCNC 12	NES-C MXNC 13	NES-C MXNC 14	NES-C MXNC 15	NES-C MCNC 16	NES-C MXNC 17	NES-C MXNC 18	AMD-A PCMD 1	AMD-A PCMD 2
SiO2	35.54	37.31	36.65	36.34	22.68	37.94	33.24	14.71	n.d.	n.d.
TiO2	0.60	0.24	0.41	0.54	2.79	0.27	1.39	2.70	n.d.	n.d.
Al2O3	2.83	0.32	2.42	6.13	32.15	0.75	11.00	45.16	n.d.	n.d.
Cr2O3	n.d.									
FeO	0.64	n.d.	0.44	0.70	2.05	0.44	1.06	3.47	0.38	0.59
MnO	n.d.	0.26	n.d.							
MgO	25.51	28.62	32.67	39.65	17.50	29.61	22.89	21.31	96.21	96.57
CaO	32.51	30.22	25.76	16.12	19.31	29.27	28.43	9.84	0.71	0.73
K2O	n.d.									
TOTAL	97.63	96.71	98.35	99.48	96.48	98.28	98.01	97.19	97.56	97.89
Sample Code SPOT	AMD-A PCMD 3	AMD-A PCMD 4	AMD-A PCMD 5	AMD-A PCMD 6	AMD-A PMMD 7	AMD-A LCMD 8	AMD-A LMMD 9	AMD-A TCMD 10	AMD-A MXMD 11	AMD-A PCMD 12
SiO2	n.d.	n.d.	0.21	0.18	n.d.	0.19	0.20	24.53	23.02	n.d.
TiO2	n.d.									
Al2O3	n.d.	0.63	0.85	n.d.						
Cr2O3	n.d.									
FeO	0.43	0.35	0.42	0.40	0.46	n.d.	0.36	n.d.	0.67	0.45
MnO	n.d.									
MgO	95.62	96.34	96.37	96.35	95.88	2.19	2.17	1.73	8.90	96.65
CaO	0.92	0.91	0.87	0.99	1.06	95.42	94.50	69.75	65.34	1.03
K2O	n.d.									
TOTAL	96.97	97.60	97.87	97.92	97.40	97.80	97.23	96.64	98.78	98.13
Sample Code SPOT	AMD-A PMMD 13	AMD-A TCMD 14	AMD-A TMMD 15	AMD-A LCMD 16	AMD-A PCMD 17	AMD-A LCMD 18	AMD-A LMMD 19	AMD-A LCMD 20	AMD-A PCMD 21	AMD-A PMMD 22
SiO2	0.37	24.49	24.73	0.20	0.24	0.19	n.d.	n.d.	n.d.	n.d.
TiO2	n.d.									
Al2O3	n.d.	0.86	0.68	n.d.						
Cr2O3	n.d.									
FeO	0.39	0.41	0.43	n.d.	0.70	0.37	0.32	n.d.	0.69	0.45
MnO	0.27	n.d.	n.d.	n.d.	n.d.	n.d.	0.31	n.d.	n.d.	n.d.
MgO	96.52	1.87	1.58	2.82	97.05	2.26	2.31	2.36	95.89	95.50
CaO	1.32	69.58	69.97	95.45	1.01	95.79	94.40	94.11	0.91	1.08
K2O	n.d.									
TOTAL	98.87	97.21	97.39	98.47	99.00	98.61	97.34	96.47	97.49	97.03

HUNT

Sample Code	AMD-A LCMD	AMD-A TCMD	AMD-A TMMD	AMD-A TCMD	AMD-A TMMD	AMD-A TCMD	AMD-A LCMD	AMD-A LMMD	AMD-A LCMD	AMD-A LMMD
SPOT	23	24	25	26	27	28	29	30	31	32
SiO2	0.26	25.08	24.47	22.59	24.57	24.65	n.d.	n.d.	0.21	0.23
TiO2	n.d.									
Al2O3	n.d.	0.74	1.95	3.13	0.48	1.06	n.d.	n.d.	n.d.	n.d.
Cr2O3	n.d.	n.d.	0.28	n.d.						
FeO	n.d.	0.55	0.60	1.77	0.47	0.34	n.d.	n.d.	n.d.	n.d.
MnO	n.d.	n.d.	0.30	n.d.						
MgO	2.40	1.64	1.27	2.18	1.60	1.39	2.24	2.46	2.14	2.27
CaO	96.17	70.22	68.55	66.80	69.64	70.10	98.46	97.16	95.62	94.60
K2O	n.d.									
TOTAL	98.83	98.23	97.42	96.47	96.76	97.54	100.70	99.62	97.97	97.10

Sample Code	AMD-A TCMD	AMD-A TMMD	AMD-B PCMD	AMD-B PMMD	AMD-B TCMD	AMD-B MXMD	AMD-B MXMD	AMD-B MXMD	AMD-B MXMD	AMD-B MXMD
SPOT	33	34	1	2	3	4	5	6	7	8
SiO2	24.90	25.07	0.29	n.d.	24.73	23.89	3.25	3.57	3.38	5.21
TiO2	n.d.	n.d.	n.d.	n.d.	n.d.	n.d.	0.25	n.d.	0.37	n.d.
Al2O3	0.69	0.90	n.d.	n.d.	0.64	0.63	21.22	21.72	22.08	20.84
Cr2O3	n.d.									
FeO	n.d.	0.42	0.68	0.58	0.38	0.51	17.02	14.08	16.96	15.13
MnO	n.d.	n.d.	n.d.	n.d.	n.d.	n.d.	1.33	0.70	1.04	0.87
MgO	1.60	1.68	94.77	96.50	1.50	3.48	2.88	9.00	2.78	2.39
CaO	69.52	69.70	0.65	0.76	69.78	67.89	47.63	45.01	47.47	49.39
K2O	n.d.									
TOTAL	96.71	97.77	96.39	97.84	97.03	96.40	93.58	94.08	94.08	93.83

Sample Code	AMD-B PCMD	AMD-B PMMD	AMD-B MXMD	AMD-B MXMD	AMD-B MXMD	AMD-B TCMD	AMD-B TMMD	AMD-B TCMD	AMD-B PCMD	AMD-B LCMD
SPOT	9	10	11	12	13	14	15	16	17	18
SiO2	n.d.	n.d.	4.35	3.34	3.72	24.26	24.21	24.85	n.d.	n.d.
TiO2	n.d.	n.d.	n.d.	0.37	n.d.	n.d.	n.d.	n.d.	n.d.	n.d.
Al2O3	n.d.	n.d.	22.62	21.72	23.51	0.57	0.78	0.75	n.d.	n.d.
Cr2O3	0.19	n.d.								
FeO	n.d.	0.58	15.58	17.24	8.45	0.55	0.40	0.59	0.76	n.d.
MnO	0.13	n.d.	0.42	1.34	n.d.	n.d.	n.d.	n.d.	n.d.	n.d.
MgO	96.00	95.41	2.42	2.97	1.38	1.58	1.74	1.34	96.00	1.93
CaO	0.65	0.63	48.77	47.57	52.48	69.14	68.91	68.80	1.12	93.37
K2O	n.d.									
TOTAL	96.97	96.62	94.16	94.55	89.54	96.10	96.04	96.33	97.88	95.30

Sample Code SPOT	HUNT									
	AMD-B	MIC-A	MIC-A	MIC-A						
	LCMD	TCMD	PCMD	MXMD	TCMD	LCMD	TCMD	MXMA	MXMA	MXMA
	19	20	21	22	23	24	25	1	2	3
SiO2	n.d.	24.83	n.d.	0.22	23.93	0.29	24.53	0.38	0.69	n.d.
TiO2	n.d.									
Al2O3	n.d.	0.77	n.d.	n.d.	0.94	n.d.	1.33	n.d.	n.d.	n.d.
Cr2O3	n.d.									
FeO	n.d.	0.48	0.42	n.d.	n.d.	n.d.	0.70	n.d.	n.d.	n.d.
MnO	n.d.	n.d.	0.26	n.d.						
MgO	4.36	1.71	96.29	11.16	1.70	2.36	1.63	76.60	93.35	95.84
CaO	91.69	69.19	1.00	86.32	68.71	93.69	68.06	23.35	3.01	3.56
K2O	n.d.									
TOTAL	96.05	96.98	97.97	97.70	95.28	96.34	96.25	100.33	97.05	99.40
Sample Code SPOT	MIC-A MXMA	MIC-A MXMA	MIC-A PCMA	MIC-A MXMA						
	4	5	6	7	8	9	10	11	12	13
SiO2	n.d.	n.d.	n.d.	2.73	n.d.	1.20	0.35	5.95	n.d.	0.20
TiO2	n.d.									
Al2O3	n.d.									
Cr2O3	n.d.									
FeO	n.d.	n.d.	n.d.	n.d.	0.00	n.d.	n.d.	n.d.	n.d.	n.d.
MnO	n.d.									
MgO	68.66	95.61	97.78	33.88	18.62	17.29	84.42	78.37	95.45	13.96
CaO	37.76	3.47	0.57	70.01	83.16	85.68	17.83	15.59	3.66	85.85
K2O	n.d.									
TOTAL	106.42	99.08	98.35	106.62	101.78	104.17	102.60	99.91	99.11	100.01
Sample Code SPOT	MIC-A MXMA	MIC-A MXMA								
	14	15								
SiO2	n.d.	0.49								
TiO2	n.d.	n.d.								
Al2O3	n.d.	n.d.								
Cr2O3	n.d.	n.d.								
FeO	n.d.	n.d.								
MnO	n.d.	n.d.								
MgO	92.97	39.45								
CaO	6.24	55.75								
K2O	n.d.	n.d.								
TOTAL	99.21	95.69								

ABLAHA

Sample Code SPOT	AMD-A PCMD 1	AMD-A PCMD 2	AMD-A PCMD 3	AMD-A PCMD 4	AMD-A PCMD 5	AMD-A PCMD 6	AMD-A PCMD 7	AMD-A LCMD 8	AMD-A LMMD 9	AMD-A TCMD 10
SiO2	n.d.	n.d.	n.d.	n.d.	0.21	0.18	n.d.	0.19	0.20	24.53
TiO2	n.d.									
Al2O3	n.d.	0.63								
Cr2O3	n.d.									
FeO	0.38	0.59	0.43	0.35	0.42	0.40	0.46	n.d.	0.36	n.d.
MnO	0.26	n.d.								
MgO	96.21	96.57	95.62	96.34	96.37	96.35	95.88	2.19	2.17	1.73
CaO	0.71	0.73	0.92	0.91	0.87	0.99	1.06	95.42	94.50	69.75
K2O	n.d.									
NiO	n.d.	n.d.	0.41	0.35	n.d.	n.d.	n.d.	n.d.	n.d.	n.d.
TOTAL	97.56	97.89	97.38	97.95	97.87	97.92	97.40	97.80	97.23	96.64

Sample Code SPOT	AMD-A MXMD 11	AMD-A PCMD 12	AMD-A PMMD 13	AMD-A TCMD 14	AMD-A TMMD 15	AMD-A LCMD 16	AMD-A PCMD 17	AMD-A LCMD 18	AMD-A LMMD 19	AMD-A LCMD 20
SiO2	23.02	n.d.	0.37	24.49	24.73	0.20	0.24	0.19	n.d.	n.d.
TiO2	n.d.									
Al2O3	0.85	n.d.	n.d.	0.86	0.68	n.d.	n.d.	n.d.	n.d.	n.d.
Cr2O3	n.d.									
FeO	0.67	0.45	0.39	0.41	0.43	n.d.	0.70	0.37	0.32	n.d.
MnO	n.d.	n.d.	0.27	n.d.	n.d.	n.d.	n.d.	n.d.	0.31	n.d.
MgO	8.90	96.65	96.52	1.87	1.58	2.82	97.05	2.26	2.31	2.36
CaO	65.34	1.03	1.32	69.58	69.97	95.45	1.01	95.79	94.40	94.11
K2O	n.d.									
NiO	n.d.	0.42	0.49	n.d.	n.d.	n.d.	0.38	n.d.	n.d.	n.d.
TOTAL	98.78	98.55	99.36	97.21	97.39	98.47	99.38	98.61	97.34	96.47

Sample Code SPOT	AMD-A PCMD 21	AMD-A PMMD 22	AMD-A LCMD 23	AMD-A TCMD 24	AMD-A TMMD 25	AMD-A TCMD 26	AMD-A TMMD 27	AMD-A TCMD 28	AMD-A LCMD 29	AMD-A LMMD 30
SiO2	n.d.	n.d.	0.26	25.08	24.47	22.59	24.57	24.65	n.d.	n.d.
TiO2	n.d.									
Al2O3	n.d.	n.d.	n.d.	0.74	1.95	3.13	0.48	1.06	n.d.	n.d.
Cr2O3	n.d.	n.d.	n.d.	n.d.	0.28	n.d.	n.d.	n.d.	n.d.	n.d.
FeO	0.69	0.45	n.d.	0.55	0.60	1.77	0.47	0.34	n.d.	n.d.
MnO	n.d.	n.d.	n.d.	n.d.	0.30	n.d.	n.d.	n.d.	n.d.	n.d.
MgO	95.89	95.50	2.40	1.64	1.27	2.18	1.60	1.39	2.24	2.46
CaO	0.91	1.08	96.17	70.22	68.55	66.80	69.64	70.10	98.46	97.16
K2O	n.d.									
NiO	n.d.									
TOTAL	97.49	97.03	98.83	98.23	97.42	96.47	96.76	97.54	100.70	99.62

ABLAHA

Sample Code SPOT	AMD-A LCMD 31	AMD-A LMMD 32	AMD-A TCMD 33	AMD-A TMMD 34	AMD-B PCMD 1	AMD-B PMMD 2	AMD-B TCMD 3	AMD-B MXMD 4	AMD-B MXMD 5	AMD-B MXMD 6
SiO2	0.21	0.23	24.90	25.07	0.29	n.d.	24.73	23.89	3.25	3.57
TiO2	n.d.	n.d.	n.d.	n.d.	n.d.	n.d.	n.d.	n.d.	0.25	n.d.
Al2O3	n.d.	n.d.	0.69	0.90	n.d.	n.d.	0.64	0.63	21.22	21.72
Cr2O3	n.d.	n.d.	n.d.	n.d.	n.d.	n.d.	n.d.	n.d.	n.d.	n.d.
FeO	n.d.	n.d.	n.d.	0.42	0.68	0.58	0.38	0.51	17.02	14.08
MnO	n.d.	n.d.	n.d.	n.d.	n.d.	n.d.	n.d.	n.d.	1.33	0.70
MgO	2.14	2.27	1.60	1.68	94.77	96.50	1.50	3.48	2.88	9.00
CaO	95.62	94.60	69.52	69.70	0.65	0.76	69.78	67.89	47.63	45.01
K2O	n.d.	n.d.	n.d.	n.d.	n.d.	n.d.	n.d.	n.d.	n.d.	n.d.
NiO	n.d.	n.d.	n.d.	n.d.	n.d.	0.47	n.d.	n.d.	n.d.	n.d.
TOTAL	97.97	97.10	96.71	97.77	96.39	98.31	97.03	96.40	93.58	94.08

Sample Code SPOT	AMD-B MXMD 7	AMD-B MXMD 8	AMD-B PCMD 9	AMD-B PMMD 10	AMD-B MXMD 11	AMD-B MXMD 12	AMD-B MXMD 13	AMD-B TCMD 14	AMD-B TMMD 15	AMD-B TCMD 16
SiO2	3.38	5.21	n.d.	n.d.	4.35	3.34	3.72	24.26	24.21	24.85
TiO2	0.37	n.d.	n.d.	n.d.	n.d.	0.37	n.d.	n.d.	n.d.	n.d.
Al2O3	22.08	20.84	n.d.	n.d.	22.62	21.72	23.51	0.57	0.78	0.75
Cr2O3	n.d.	n.d.	0.19	n.d.						
FeO	16.96	15.13	n.d.	0.58	15.58	17.24	8.45	0.55	0.40	0.59
MnO	1.04	0.87	0.13	n.d.	0.42	1.34	n.d.	n.d.	n.d.	n.d.
MgO	2.78	2.39	96.00	95.41	2.42	2.97	1.38	1.58	1.74	1.34
CaO	47.47	49.39	0.65	0.63	48.77	47.57	52.48	69.14	68.91	68.80
K2O	n.d.	n.d.	n.d.	n.d.	n.d.	n.d.	n.d.	n.d.	n.d.	n.d.
NiO	n.d.	n.d.	0.37	n.d.						
TOTAL	94.08	93.83	97.34	96.62	94.16	94.55	89.54	96.10	96.04	96.33

Sample Code SPOT	AMD-B PCMD 17	AMD-B LCMD 18	AMD-B LCMD 19	AMD-B TCMD 20	AMD-B PCMD 21	AMD-B MXMD 22	AMD-B TCMD 23	AMD-B LCMD 24	AMD-B TCMD 25
SiO2	n.d.	n.d.	n.d.	24.83	n.d.	0.22	23.93	0.29	24.53
TiO2	n.d.								
Al2O3	n.d.	n.d.	n.d.	0.77	n.d.	n.d.	0.94	n.d.	1.33
Cr2O3	n.d.								
FeO	0.76	n.d.	n.d.	0.48	0.42	n.d.	n.d.	n.d.	0.70
MnO	n.d.	n.d.	n.d.	n.d.	0.26	n.d.	n.d.	n.d.	n.d.
MgO	96.00	1.93	4.36	1.71	96.29	11.16	1.70	2.36	1.63
CaO	1.12	93.37	91.69	69.19	1.00	86.32	68.71	93.69	68.06
K2O	n.d.								
NiO	n.d.	n.d.	n.d.	n.d.	0.45	n.d.	n.d.	n.d.	n.d.
TOTAL	97.88	95.30	96.05	96.98	98.42	97.70	95.28	96.34	96.25

REFERENCES

- ANDERSON, C.A. (ed.), 1973. Microprobe analysis. Wiley and sons, New York. 1-81.
- ASTM C20-80a, 1982. Standard method of apparent porosity, water absorption, apparent specific gravity and bulk density of burned refractory brick and shapes by boiling water. *Amer. Soc for testing materials*.
- BAIN, G. W. 1924. Types of magnesite deposits and their origin. *Econ. Geol.* 19-5, 412-413.
- BAOGUI, Z. & YUEMING, Z. 1975. Huntite from a certain deposit in China. *Geochimica.* 4, 285-290.
- BARTRAM, S. F. 1967. Crystallite size determination from line broadening and spotty patterns. In: Kaelble, E. F. *Hand book of X-rays*. Macgraw-Hill, New York 17.1-17.18.
- BATES, R. L. 1969. Magnesite, in 'Geology of the industrial rocks and minerals'. Dover publications Inc, New york. 296-305.
- BAUMGART, W. 1984. Refractories. In: BAUMGART ET AL. (ed.). *Process Mineralogy of Ceramic Materials*. Ferdinand Enke Publishers. Stuttgart. 80-103.
- BECK, C. W. 1950. D.t.a. of carbonates. *Amer. Min.* 35, 985-1013.
- BELOV, N. V., BELOVA, E. N., ANDIANOVA, N. N. & SMIRNOVA, R. F. 1951. (Determination of the parameters in the olivine (forsterite) structure with the harmonic three-dimensional synthesis.) *DOKI. AKAD. Nauk SSSR*: 81, 399-402. (in Russian)
- BERG, L. G. 1943. Influence of salt on dissociation of dolomite. (*C.R. Acad. Sci., USSR.*). 38, 24-27
- BESSEY, G. E. & LAMMIMAN, K. N. 1955. Void volume and oil absorption. *J. oil and colour chemists*. November, 694-708.
- BHATIA, M., RAMANUJAM, M. & HOHMANN, E. H. 1968. Beneficiation of Salem Magnesite. *Indian Journal of Technology.* 16, 73-75.
- BIGGAR, G. M. and O'HARA, M. J. 1969. Monticellite and forsterite crystalline solutions. *Jour. Amer. Ceram. Soc.* 52, 249-252.
- BIGGAR, G. M. 1971. Phase Relationships of Bredigite ($\text{Ca}_5\text{MgSi}_3\text{O}_{12}$) and of The Quaternary compound ($\text{Ca}_6\text{MgAl}_8\text{SiO}_{21}$) in the System $\text{CaO-MgO-Al}_2\text{O}_3\text{-SiO}_2$ *Cement and Concrete Research.* 1, 493-513.
- BIRLE, J. D., GIBBS, G. V., MOORE, P. B. and SMITH, J. V. 1968. Crystal structures of natural olivines. *Amer. Miner.* 53, 807-824.

- BRAGG, W. L. & BROWN, G. B. 1926. Die struktur des olivins. *Z. Krist.* 63, 538-556.
- BREDIG, M. A. 1950. Polymorphism of calcium orthosilicate. *Jour. Amer. Ceram. Soc.* 33, 183-192.
- BRITISH STANDARD 4398. 1969. Specification for compounding ingredients for rubber test mixes. HMSO, London.
- BRITISH STANDARD 4383, part B7, 1982, Method of testing pigment for paint. HMSO, London.
- BUDNIKOV, P. P. 1964. Magnesite refractories, In: *'The technology of ceramics and refractories'*. MIT Press. Cambridge. Mass. 248-270.
- CHESTERS, J. H. 1973. Magnesite, In: *'refractories, production and properties'*. The Iron and Steel Institute, London. 118-176.
- CHESTERS, J. H. 1957. Steel plant refractories. Testing, Research and Development. The United Steel Companies, Sheffield, LTD. 233 PP.
- CLARK, F. W. 1924. The data of geochemistry. U.s.g.s. Bull. 70 et seq. 770, 23-24.
- COLE, W. F. & LANCUCKI, C. J. 1975. Huntite from Deer Park, Victoria, Australia. *Amer. Miner.* 60, 1130-1131.
- COOPE, B. M. 1981. Magnesite - A tale of two markets. 'IM' Refractories Survey. 49-56.
- COOPE, B. M. 1981. An introduction to refractories. 'IM' Refractories Survey 7-47.
- COOPE, B. M. 1981. Caustic magnesia markets - agricultural oversupply and industrial underdemand. *Industrial Minerals*. February. 43-51.
- COOPE, B. M. 1983. Magnesia markets-refractory contraction and caustic stagnation. *Industrial Minerals*. August. 57-87.
- COOPE, B. 1987. The world magnesia industry. Smaller but fitter... and purer! *Industrial Minerals*. February. 21-48.
- DEER, W. A., HOWIE, R. A. & ZUSSMAN, J. 1962. Rock forming minerals. Volume 5. William Clowes and Sons, LTD. London and Beccles. 226-322, non-silicates. 1-4, 56-88.
- DEER, W. A., HOWIE, R. A. & ZUSSMAN, J. 1982. Rock-forming minerals. Volume 1A. Orthosilicates, Second edition. Wiley & Sons, Inc. New York. 3-336, 352-375.

- DEER, W. A., HOWIE, R. A. & ZUSSMAN, J. 1983. An introduction to the rock forming minerals. Longman Group LTD, England. 72-76, 473-503, 58, 1-10, 403, 242-249, 424-433 pp.
- DEER, W. A., HOWIE, R. A. & ZUSSMAN, J. 1986. Rock-forming minerals. Volume 1B: Second edition, Disilicates and ring silicates. Copublished with John Wiley and Sons, Inc. New York. 285-334, 248-255, 256-262.
- DELIARENA, G. J. 1959. Nuevas observaciones sobre la magnesita sedimentaria. *Estud. Geol.* 15.
- DESTOMBES, J. P. 1956. Magnesites (giobertites) des pyre'ne's occidentales. *Bull. Soc. Geol. Fr.* 6,6.
- DEWENDRA, J. D., WILSON, C. M. & BRETT, N. H. 1982. A Quantitative Investigation of Phase Compositions in Magnesia-R₂O₃-Silicate Systems. Part 1-Solid Solubility of Binary Mixtures of Al₂O₃, Cr₂O₃ and Fe₂O₃ in the Periclase Phase. *Trans. J. Br. Ceram. Soc.* 81, 185-189.
- DEWENDRA, J. D., WILSON, C. M. & BRETT, N. H. 1983. A Quantitative Investigation of Phase Compositions in Magnesia-R₂O₃ Silicate Systems. Part 2: Solubility of Ternary Mixtures of Al₂O₃, Cr₂O₃ and Fe₂O₃ in the Periclase, Spinel and Liquid Phases. *Trans. J. Br. Ceram. Soc.* 82, 64-68.
- DEWENDRA, J. D., WILSON, C. M. & BRETT, N. H. 1983. A Quantitative Investigation of Phase Compositions in Magnesia-R₂O₃-Silicate Systems. Part 3: Microstructural Features in MgO-R₂O₃-CaO.SiO₂ Systems at 1700°C. *Trans. J. Brit. Ceram. Soc.* 82, 87-90.
- DEWENDRA, J. D., WILSON, C. M. & BRETT, N. H. 1983. A Quantitative Investigation of Phase Compositions in Magnesia - R₂O₃-Silicate Systems. Part 4: A Study of Commercial Magnesia-Chrome Mixtures. *Trans. J. Br. Ceram. Soc.* 82, 132-136.
- DICKSON, E. M. 1981. Refractories - practice and trends, in 'Raw materials for the refractories industry - an Industrial Minerals Consumer Survey', edited by Coope, B. M. and DICKSON, E. M. *Metal Bulletin PLC*, London. 37-43.
- DUNCAN, L. R. & McCracken, W. H. 1981. The impact of energy on refractory raw materials. *Industrial Minerals*. Januray. 19-27.
- DUNHAM, A. C. and WILKINSON, F. C. F. 1978. Accuracy, precision and detection limits of energy dispersive electron microprobe analyses of silicates. X-ray

Spectromy. 7, 50-56.

- FAUST, G. T. 1953. Huntite, $Mg_3Ca(CO_3)_4$, a new mineral. *Amer. Miner.* 38, 4-23.
- FERGUSON, J. B. & MERWIN, H. E. 1919. Ternary system CaO-MgO-SiO₂. *Amer. Jour. Sci.*, 4th ser. 48, 81-123.
- FLETCHER, K. E. 1965. The effect of Fe³⁺ and Al³⁺ on the Polymorphism of Tricalcium Silicate. *Tran. Brit. Ceram. Soc.* 64, 377-385.
- FOROGLOU, Z., MALISSA, H. & GRASSERBAUER, M. 1980. Microstructural Characterization Study of Magnesia Derived from Natural Microcrystalline Magnesite. *Trans. J. Brit. Ceram. Soc.* 79, 91-97.
- FROST, M. T. 1982. The Magnesite Deposit at Main Creek, Savage River, Tasmania. *Econ. Geol.* 77, 1901-1911.
- FULLMAN, R. L. 1953. Measurement of particle sizes of opaque bodies. *Trans. Amer.* 197, 447-452.
- GHOSH, N., BHASKARA RAO, P. PAUL, A. K. & RAINA, K. S. 1979. Review, The Chemistry of dicalcium silicate mineral. *Jour. Mat. Sci.* 14, 1554-1567.
- GOLDSMITH, J. R. 1983. Phase relations of rhombohedral carbonates, in 'Carbonates: mineralogy and chemistry', edited by Reader, R. *J. Mineralogical Society of America*, Washington. 49-76.
- GOLDSTEIN, J. I., NEWBURY, D. E., ECHLIN, P., JOY, D. C., FIORI, C. and LIFSHIN, E. 1981. Scanning electron microscopy and X-ray microanalysis. Plenum Press, New York and London. 75-87, 157-164 and 305-392.
- GRUVER, R. M. 1950a. D. T. A. of ceramic materials, I. *J. Amer. Ceram. Soc.* 33, 96-101.
- GUINIER, A. & REGOURD, M. 1968. Session I Structure of Portland Cement Minerals. Principal Paper Structure of Portland Cement Minerals. *Cement Association of Japan, Proceeding of the 5th International symposium on the Chemistry of Cement.* Tokyo. 1-43.
- GUINIER, A. and REGROUD, M. 1968. Structure of portland cement minerals. Proceedings of the 5th International Symposium on the Chemistry of Cement, Tokyo. *Cement Association of Japan.* 1, 1-32.
- GUTT, W. 1965. The system dicalcium silicate-merwinite. *Nature.* 207, 184-185.

- GUTT, W. 1966. High temperature equilibria in polycrystalline silicate systems, Ph.D. Thesis, London.
- GUTT, W. and NURSE, R. W. 1974. The phase composition of portland cement clinker. Building Research Establishment, Current Paper 96/74. 1-13.
- HALL, R. J. & SPENCER, D. R. F. 1973. A review of the Production and Properties of Sea-Water Magnesia. *InterCeram*. 3, 212-218.
- HANKE, K. 1965. Beiträge zu Kristallstrukturen vom Olivin-Typ. *Beitr. Min. Petr.* 11, 535-558.
- HANKE, K. & ZEMANN, J. 1963. Verfeinerung der Kristallstruktur von Olivin. *Naturw.* 50, 91-92.
- HATFIELD, T. & RICHMOND, C. 1970. The Solubility of Monticellite in Forsterite. *Brit. Ceram. Soc. Trans.* 69, 99-101.
- HARBEN, P. W., & BATES, R. L. 1984. Magnesite and magnesia. In: *Geology of the nonmetallics*. Metal Bulletin Inc. 347-355.
- HENNEY, J. W. & JONES, J. W. S. 1969. The Solid Solubility of CaO and SiO₂ in MgO and its Effect on the MgO-CaO-SiO₂ System at 1750°C. *Trans. Brit. Ceram. Soc.* 68, 201-203.
- HIMMELBAUER, A. 1933. Magnesite. In: O. Stutzer: Die wichtigsten Lagerstätten der Nichterze 5.
- HURLBUT, JR. C. S. and KLEIN, C. 1977. Manual of mineralogy. 19th edition. Wiley and Sons, New York and London. 196-301.
- ILIC, M. 1966. Genetske odlike magnezitskih ležišta detritičnog tipa. Referati vi savetovanja geologa, SFRJ.
- ILIC, M. 1968. Problems of the Genesis and Genetic Classification of Magnesite Deposits. *Geologický zborník, Geologica Carpathica*. 19, 149-160.
- INSLEY, H. and FRECHETTE, V. D. 1955. Microscopy of ceramics and cements. Academic Press, New York. 83-84 and 131-136.
- JEFFERY, J. W. 1952. The tricalcium silicate phase. London. 30-48.
- JONES, D. G. & MELFORD, D. A. 1969. Comparison of the High temperature Constitution of Sea-water Magnesites with that of Natural Greek Material. *Trans. Brit. Ceram. Soc.* 68, 241-247.

- JOST, K. H., ZIEMER, B. & SEYDEL, R. 1977. Redetermination of the structure of beta - dicalcium silicate. *Acta. Cryst.* B33, 1696-1700.
- JUHASZ, A. Z. 1982. Mechanochemical reaction of carbonate minerals. *Acta Geologica Academiae Scientiarum Hungaricae.* 25, 247-270.
- KAZAKOV, A. V. 1957. Tikhomirova M. M. Plotnikova V. I. Sistema karbonatnykh ravnovesii (dolomit, magnezit). *Trudy geol. Instituta AN SSSr.* 152.
- KEYVANFAR, M. 1987. Comparative exploration report of magnesite deposits. *Geological Survey of Iran.* 1, in Persian.
- KIMYONGUR, N. 1984. The industrial mineralogy of magnesite with particular reference to material from Turkey. Unpublished Ph.d. Thesis, University of Hull, England. 352 pp.
- KIMYONGUR, N. & SCOTT, P. W. 1986. Calcined natural magnesite-influence of time and temperature on the transformation and resulting industrial properties. *Materials Science Forum.* 7, 83-90.
- KLUG, H. P. & ALEXANDER, L. E. 1974. X-ray diffraction procedures. 2nd edition. Wiley and Sons, New York. 142-166 and 618-708.
- KURODA, Y. 1969. Crystal structure of olivine and its chemical bonds. *J. Japanese Assoc. Min. Petr. and Econ. Geol.* 62, 66-79.
- LAMING, J. 1971. Raw Materials and Refractories Performance. *The Refractories Journal.* June, 6-21.
- LAPHAM, D. M. & BARNES, J. H. 1971. Unusual Minerals Found in Pennsylvania. *Pennsylvania Geology.* 2, 2-3.
- LARSON, E. S. & FOSHAG, W. F. 1921. Merwinite, a new mineral from the contact zone at Crestmore, California. *Amer. Min.* 6, 143-148.
- LEVIN, E. M., ROBBINS, C. R. & McMURDIE, H.F. 1964. Phase diagrams for ceramists. The American Ceramic Society, Columbus, Ohio.
- LONG, J. V. P. 1977. Electron Probe Microanalysis, In: 'physical methods in determinative mineralogy', edited by Zussman, J. 2nd edition. Academic Press, London and New York. 273-341.
- MARTIN, C. 1956. Origin of crystalline magnesite deposits. *Bull. Geol. Soc. Amer.* 71, 12.

- McCALL, G. J. H. 1985. East Iran Project-area No.1, (North Makran and South Baluchestan). *Geological Survey of Iran*. Report No.57.
- MIDGLEY, C. M. 1952. The crystal structure of B - dicalcium silicate. *Acta Cryst.* 5, 307-312.
- MIDGLEY, H. G. & FLETCHER, K. E. 1963. The Role of Alumina and Magnesia in the Polymorphism of Tricalcium Silicate. *Trans. Brit. Ceram. Soc.* 62, 917-937.
- MIDGLEY, H. G. 1974. Proceedings of the 6th International Congress on the Chemistry of Cement, Moscow (Stroiizdat, Moscow) Suppl paper, Section 1. Mineralogie und Geochemie Carbonatischer Ablagerungen in europaischen Hohlen - ein Beitrag Zur Bildung und Diagenese von speleothemen. *N. Jb. Miner. Abh.* 126, 268-291.
- MOORE, P. B. & ARAKI, T. 1972, Atomic Arrangement of Merwinite, $\text{Ca}_3\text{Mg}(\text{SiO}_4)_2$, An Unusual Dense-Packed Structure of Geophysical Interest. *Amer. Miner.* 57, 1355-1374.
- MORTL, G. 1986. A user view of challenges for the magnesite industry. *Industrial Minerals*. July, 29-49.
- MUAN, A. & OSBORN, E. F. 1965. Phase equilibria among oxides in steelmaking. Pergamon Press. Oxford, London and New York. 236 pp.
- NABAVI, M. H. 1976. An introduction to the geology of Iran. *Geological Survey of Iran, (In Persian)*. 109 PP
- NASRABADI, K. E. 1986. A mineralogical investigation and industrial assessment of pegmatitic feldspars from the Mashhad area, Iran. Unpublished M.Sc. Thesis, University of Hull, England.110 PP.
- NISHIHARA, H. 1956. Origin of The Bedded Magnesite Deposits of Manchuria. *Econ. Geol.* 51, 698-711.
- NORTON, F. H. 1968. Refractories. Fourth edition. McGraw-Hill book Company. 79-89.
- NURSE, R. W. 1952. The dicalcium silicate phase. *Proceedings of the 3rd International Symposium on the Chemistry of Cement, London*. 56-77.

- NURSE, R. W., WELCH, J. H. & GUTT, W. 1959. High temperature phase equilibria in the system dicalcium silicate - tricalcium phosphate. *Jour. Chem. Soc.* 220, 1077-1983.
- NURSE, R. W. 1968. Session I-2 Phase Equilibria and Formation of Portland Cement Minerals. *Proceedings of the 5th International Symposium on the Chemistry of Cement, Tokyo.* 1, 77-89.
- OHANIAN, T. 1983. The Birjand ophiolite, an intracontinental transform structure, Eastern Iran. Geodynamic project (Geotraverse) in Iran. Final report. Report No.51. 239-245.
- OSBORN, E. F. and MUAN, A. 1960. phase equilibrium diagram of the system CaO-MgO-siO₂, in 'Phase diagrams for ceramists', edited by Levin, E. M. et al. *American Ceramic Society, Columbus, Ohio, 1964.* 210.
- PALFREYMAN, M. 1974. Refractory-grade magnesia in Canada. *CIM Bulletin*, 148-154.
- PETRASCHECK, W. 1931. Die Magnesite und siderite der Alpen. *Sitzgsber. Akad. Wiss. Wien. Math-nath.* K1 141.
- PETRASCHECK, W. E. 1961. Lagerstättenlehre. ZW. Anf. Wien Springer verlag.
- PHEMISTER, J. 1943. Merwinite as an artificial mineral. *Min. Mag.* 26, 225-230.
- RAIT, J. R. 1950. Basic refractories, their chemistry and their performance. Iliffe and Sons Ltd. London. 19-31.
- RAU, R. C. 1962. Routine crystallite-size determination by X-ray diffraction line broadening. *Advances in X-ray Analysis.* 5, 105-116.
- REDLICH, K. A. 1934. Die Typen der Magnesitlagerstätten. Ihre Bildung. Geologische stellung untersuchung. *Z. Prakt. Geol.* 42.
- REED, S. J. B. 1975. Electron microprobe analysis. Cambridge University Press, Cambridge. 400 PP.
- REEDER, R. J. 1983. Crystal chemistry of the rhombohedral carbonates, In: 'Carbonates: mineralogy and chemistry', edited by Reeder, R. J. Mineralogical Society of America, Washington. 1-47.
- RICKER, R. W. and OSBORN, E. F. 1954. Additional phase equilibrium data for the system CaO-MgO-SiO₂. *Jour. Amer. Ceram. Soc.* 37, 133-139.

- RIGBY, G. R., RICHARDSON, H. M. & BALL, F. 1947. The Mineralogical Composition of Magnesite Bricks. *Trans. Brit. Ceram. Soc.* 46, 313-329.
- ROY, D. M. 1956. Subsolidus data for the joint Ca_2SiO_4 - CaMgSiO_4 and stability of merwinite. *Miner. Mag.* 31, 187-194.
- SCHLAUDT, C. M. & ROY, D. M. 1965. *J. Amer. Ceram. Soc.* 48-248.
- SCHLAUDT, C. M. and ROY, D. M. 1966. The join Ca_2SiO_4 - CaMgSiO_4 . *Jour. Amer. Ceram. Soc.* 49, 430-432.
- SHAYAN, A. & SANDY, M. J. 1983. Carbonate minerals from a Basalt Quarry at Fyansford, Victoria, Australia. *The Australian Mineralogist.* July, 236-240.
- SKINNER, B. J. 1958. Huntite from Tea Tree Gully, South Australia. *Amer. Miner.* 43, 159-163.
- SMITH, D. K., MAJUMDAR, A. J. & ORDWAY, F. 1965. The crystal structure of Y - dicalcium silicate. *Acta cryst.* 18, 787-795.
- SPEER, J. A. and RIBBE, P. H. 1982. Miscellaneous orthosilicates, in 'Orthosilicates', edited by Ribbe, P. H. 2nd edition. Mineralogical Society of America, Washington. 383-450.
- SPENCER, D. R. F. 1969. *Trans. Brit. Ceram. Soc.* 68, 173.
- SPENCER, D. R. F. & COLMAN, D. S. 1970. Science of ceramics. The Swedish Institute for silicate Research, (Ed. C. Brosset and E. Knopp). 5, 15.
- SPENCER, D. R. F., BEAMOND, T. W. & COLEMAN, D. S. 1971. The Solubility of CaO in MgO and its Effect on the CaO-MgO-SiO_2 System at 1800°C. *Trans. Brit. Ceram. Soc.* 70, 31-33.
- SPENCER, D. R. F. 1972. Basic Refractory Raw Materials. *Trans. Brit. Ceram. Soc.* 71, 123-134.
- SPENCER, D. R. F. 1979. Refractories in the Eighties. *Refract. Jour.* May/June, 12-28.
- STOCKLIN, J., EFTEKHAR-NEZHAD, J. & HUSHMAND-ZADEH, A. 1972. Central Lut reconnaissance, East Iran. *Geological Survey of Iran*, report No. 22. 1-62.
- STOCKLIN, J., SETUDEHNIA, A. 1977. Stratigraphic lexicon of Iran. *Geological Survey of Iran*, report No. 18.

- STRUNZ, H. 1976. Mineralien aus Nordost - Bayern. *Der Aufschluss*. 27, 77-80.
- SVERDRUP, H. V. M., JOHNSON, M. W., & FLEMING, R. H. 1942. *The Oceans* (Published prentice-Hall, INC).
- TAKIN, M. 1972. Iranian geology and continental drift in the Middle East: *Nature*. No.5334. 235, 147-150.
- TATARINOVE, P. M. 1946. Magnezit. Kurs mestorozhdenii poleznykh iskopaemykh. Gostoptekhizdat. Moskva-Leningrad. (In Russian).
- TURKDOGAN, E. T. 1980. Calcination, reduction, roasting and sintering, In: 'Physical chemistry of high temperature technology'. Academic Press, New York and London. 290-341.
- UCHIKAWA, H. & TSUKIYAMA, K. 1971. Polymorphic Transformations of Tricalcium Silicate. *Yonyo Kyokai Shi*. 79, 183-188.
- VEEN, A. W. L. & ARNDT, W. 1973. Huntite and aragonite nodules in a vertisol near Katherine, Northern Territory, Australia. *Nature; Phys. Sci.* No. 106. 241, 37-40.
- WARNER, R. D. & LUTH, W. C. 1973. Two-Phase Data for the Joint Monticellite (CaMgSiO_4)-Forsterite (Mg_2SiO_4): Experimental Results and Numerical Analysis. *Amer. Miner.* 58, 998-1008.
- WEBB, T. L. & HEYSTER, H. 1957. The carbonate minerals. In: MACKENZIE, R. C. (ed.). *The differential thermal investigation of clays*. Mineralogical society, London. 329-342.
- WEBSTER, R. and JACKSON, B. 1975. The property requirements for fired magnesite refractories used in oxygen steelmaking vessels. *Trans. Brit. Ceram. Soc.* 74, 233-241.
- WELLS, O. C. 1974. *Scanning electron microscopy*: New York, McGraw - Hill, 421 PP.
- WELTON, J. E. 1984. SEM petrology atlas. Chevron oil field research company. Amer. Assoc, Petroleum. Geologist. U.S.A. 237 PP.
- WENK, H. R. & RAYMOND, K. N. 1973. Four new refinements of olivine. *Z. Krist.* 137, 86-105.

- WHITE, J. 1962. Basic refractories: A survey of present knowledge. *Journal of the Iron and Steel Institute*. August, 611-621.
- WHITE, J. 1963. The Changing Pattern in Refractories Technology. *The Refractories Journal*. April, 126-140 and 160.
- WHITE, J. 1966. Current refractories research and its applications. *The Refract. Jour.* February, 414-433.
- WHITE, J. 1968. Phase distribution in ceramics, in 'Ceramic microstructures', edited by Fulrath, R. M. and Pask, J. A. Wiley and Sons, New York and London. 728-762.
- WHITE, J. and RICHMOND, C. 1970. Recent developments in research on basic refractories 2, Microstructural Relationships in Basic Refractories. *The Refract. Jour.* November 6-19.
- WHITE, J. 1970. Magnesia-based refractories. In: Alper, A. M. (ed.) High temperature oxides, part I: Magnesia, lime and chrome refractories. *Refractory materials, Volume 5-1*. Academic Press, New York. 76-141
- WICKEN, O. M. and DUNCA, L. R. 1984. Magnesite and related minerals, In: 'Industrial minerals and rocks', edited by Lefond, S. J. AIME. New York. 2, 881-896.
- YI YANG, H. 1973. New Data on Forsterite and Monticellite Solid Solutions. *Amer. Miner.* 58, 343-345.
- YAMAGUCHI, G., ONO, Y. & KAWAMURA, S. 1962. The solid solution ranges of Al_2O_3 and Fe_2O_3 in the high temperature modifications of $2CaO \cdot SiO_2$, *Review of the 16th General Meeting, Japan cement Engineering Assoc.* May, Tokyo. 35-36.
- YAMAGUCHI, G. & SUZUKI, K. 1967. Structural analysis of merwinite. *Yogyo Kyokaishi (J. Ceram. Assoc. Japan)*, 75, 220-229.
- ZUSSMAN, J. 1977. X-ray diffraction, In: 'Physical methods in determinative mineralogy', edited by Zussman, J. Academic Press, London and New York. 391-473.